



ISSN: 1728-144X
e-ISSN: 1735-9244



International Journal of Engineering

Journal Homepage: www.ije.ir



TRANSACTIONS B: APPLICATIONS

Volume 36, Number 11, November 2023

Materials and Energy Research Center

INTERNATIONAL JOURNAL OF ENGINEERING
Transactions B: Applications

DIRECTOR-IN-CHARGE
H. Omidvar

EDITOR IN CHIEF
G. D. Najafpour

ASSOCIATE EDITOR
A. Haerian

EDITORIAL BOARD

- | | | | |
|------|--|-------|--|
| S.B. | Adeloju, Charles Sturt University, Wagga, Australia | A. | Mahmoudi, Bu-Ali Sina University, Hamedan, Iran |
| K. | Badie, Iran Telecomm. Research Center, Tehran, Iran | O.P. | Malik, University of Calgary, Alberta, Canada |
| M. | Balaban, Massachusetts Ins. of Technology (MIT), USA | G.D. | Najafpour, Babol Noshirvani Univ. of Tech., Babol, Iran |
| M. | Bodaghi, Nottingham Trent University, Nottingham, UK | F. | Nateghi-A, Int. Ins. Earthquake Eng. Seis., Tehran, Iran |
| E. | Clausen, Univ. of Arkansas, North Carolina, USA | S. E. | Oh, Kangwon National University, Korea |
| W.R. | Daud, University Kebangsaan Malaysia, Selangor, Malaysia | M. | Osanloo, Amirkabir Univ. of Tech., Tehran, Iran |
| M. | Ehsan, Sharif University of Technology, Tehran, Iran | M. | Pazouki, MERC, Karaj, Iran |
| J. | Faiz, Univ. of Tehran, Tehran, Iran | J. | Rashed-Mohassel, Univ. of Tehran, Tehran, Iran |
| H. | Farrahi, Sharif University of Technology, Tehran, Iran | S. K. | Sadrnezhad, Sharif Univ. of Tech, Tehran, Iran |
| K. | Firoozbakhsh, Sharif Univ. of Technology, Tehran, Iran | R. | Sahraeian, Shahed University, Tehran, Iran |
| A. | Haerian, Sajad Univ., Mashhad, Iran | A. | Shokuhfar, K. N. Toosi Univ. of Tech., Tehran, Iran |
| H. | Hassanpour, Shahrood Univ. of Tech., Shahrood, Iran | R. | Tavakkoli-Moghaddam, Univ. of Tehran, Tehran, Iran |
| W. | Hogland, Linnaeus Univ, Kalmar Sweden | T. | Teng, Univ. Sains Malaysia, Gelugor, Malaysia |
| A.F. | Ismail, Univ. Tech. Malaysia, Skudai, Malaysia | P. | Tiong, Nanyang Technological University, Singapore |
| M. | Jain, University of Nebraska Medical Center, Omaha, USA | X. | Wang, Deakin University, Geelong VIC 3217, Australia |
| M. | Keyanpour rad, Materials and Energy Research Center, Karaj, Iran | H. | Omidvar, Amirkabir Univ. of Tech., Tehran, Iran |

EDITORIAL ADVISORY BOARD

- | | | | |
|-------|--|-------|---|
| S. T. | Akhavan-Niaki, Sharif Univ. of Tech., Tehran, Iran | A. | Kheyroddin, Semnan Univ., Semnan, Iran |
| M. | Amidpour, K. N. Toosi Univ. of Tech., Tehran, Iran | N. | Latifi, Mississippi State Univ., Mississippi State, USA |
| M. | Azadi, Semnan university, Semnan, Iran | H. | Oraee, Sharif Univ. of Tech., Tehran, Iran |
| M. | Azadi, Semnan University, Semnan, Iran | S. M. | Seyed-Hosseini, Iran Univ. of Sc. & Tech., Tehran, Iran |
| F. | Behnamfar, Isfahan University of Technology, Isfahan | M. T. | Shervani-Tabar, Tabriz Univ., Tabriz, Iran |
| R. | Dutta, Sharda University, India | E. | Shirani, Isfahan Univ. of Tech., Isfahan, Iran |
| M. | Eslami, Amirkabir Univ. of Technology, Tehran, Iran | A. | Siadat, Arts et Métiers, France |
| H. | Hamidi, K.N.Toosi Univ. of Technology, Tehran, Iran | C. | Triki, Hamad Bin Khalifa Univ., Doha, Qatar |
| S. | Jafarmadar, Urmia Univ., Urmia, Iran | | |

TECHNICAL STAFF

M. Khavarpour; M. Mohammadi; V. H. Bazzaz, R. Esfandiar; T. Ebadi

DISCLAIMER

The publication of papers in International Journal of Engineering does not imply that the editorial board, reviewers or publisher accept, approve or endorse the data and conclusions of authors.

International Journal of Engineering *Transactions A: Basics* (ISSN 1728-1431) (EISSN 1735-9244)

International Journal of Engineering *Transactions B: Applications* (ISSN 1728-144X) (EISSN 1735-9244)

International Journal of Engineering *Transactions C: Aspects* (ISSN 2423-7167) (EISSN 1735-9244)

Web Sites: www.ije.ir & www.ijeir.info E-mails: ije.editor8@gmail.com, Tel: (+9821) 88771578, Fax: (+9821) 88773352
Materials and Energy Research Center (MERC)

CONTENTS

Transactions B: Applications

F. Altalib, H. R. Tavakoli, S. K. Hashemi	The Post-fire Behavior of Lightweight Structural Concrete is Improved by Nano-SiO ₂ and Steel Fibers	1942-1960
N. Nurbaiti, A. E. Tontowi, M. G. Widystuti, H. V. Hoten, F. Ibrahim, N. Muna, R. Febrian, D. P. Perkasa, M. K. Herliansyah	Process Parameter Optimization of 3D-Printer Machine Using Response Surface Method for Printing Hydroxyapatite/Collagen Composite Slurry	1961-1971
H. O. Sayevand, S. Khorshidi, B. Keshavarzian	Investigation of Shell Side Overall Performance of a Novel Shell-and-Double-Concentric –tube Heat Exchanger with Simple and Perforated Helical Baffles	1972-1981
A. Nasirifar, M. Khodaparast	Development of Light Dynamic Penetrometer for Application in Dense Soil	1982-1992
Y. Yusmaniar, E. Julio, A. Rahman, S. D. Yudanto, F. B. Susetyo	Synthesis of Polyvinyl Alcohol-Chitosan Composite Film using Nanocellulose from Coconut Fibers (<i>Cocos nucifera</i>)	1993-2003
K. Y. Leong, H. Jaafar, L. Tajul, Z. A. Zailani, R. Hamidon, M. Z. M. Zain	Effect of Inclined Angle in Trimming of Ultra-high Strength Steel Sheets Having Inclined and Curved Shapes	2004-2014
M. Mohammadzadeh, H. Bagheri, S. Ghader	Experimental Investigation and Thermodynamic Modeling of Zn ⁺² and Ni ⁺² Extraction from Zn Plant Residue using D2EHPA	2015-2027
A. Mohammadjani, F. Zamani	A Multiple Kernel Learning based Model with Clustered Features for Cancer Stage Detection using Gene Datasets	2028-2037
B. Y. Yegane	An Integrated Production-distribution Problem of Perishable Items with Dynamic Pricing Consideration in a Three-echelon Supply Chain	2038-2051
A. Torkaman, K. Badie, A. Salajegheh, M. H. Bokaei, S. F. Fatemi Ardestani	A Hybrid Approach to Detect Researchers' Communities Based on Deep Learning and Game Theory	2052-2062
Z. Nassrullah	Evaluating Traffic Performance on Basra City Urban Roads Network	2063-2072
S. Mohammadi, M. Yadegari	Exploring Factors Influencing Cryptocurrency Adoption: A Comprehensive Modeling Based on Fuzzy Cognitive Maps Approach	2073-2086

P. Jalili, M. D. Afifi, B. Jalili, A. Mirzaei, D. D. Ganji	Numerical Study and Comparison of Two-dimensional Ferrofluid Flow in Semi-porous Channel under Magnetic Field	2087-2101
M. Rohani, H. Farsi, S. Mohamadzadeh	Deep Multi-task Convolutional Neural Networks for Efficient Classification of Face Attributes	2102-2111
A. M. Jabbar, D. H. Mohammed, Q. A. Hasan	A Numerical Study to Investigate Shear Behavior of High-strength Concrete Beams Externally Retrofitted with Carbon Fiber Reinforced Polymer Sheets	2112-2123
G. Chhajed, B. Garg	Novel Scheme for Data Hiding in Binary Images using Cover Pattern Histogram	2124-2136



The Post-fire Behavior of Lightweight Structural Concrete is Improved by Nano-SiO₂ and Steel Fibers

F. Altalib, H. R. Tavakoli*, S. K. Hashemi

School of Civil Engineering, Babol Noshirvani University of Technology, Babol, Iran

PAPER INFO

ABSTRACT

Paper history:

Received 20 June 2023

Received in revised form 21 July 2023

Accepted 22 July 2023

Keywords:

Lightweight Concrete

Nano-SiO₂

Steel Fiber

High Temperature

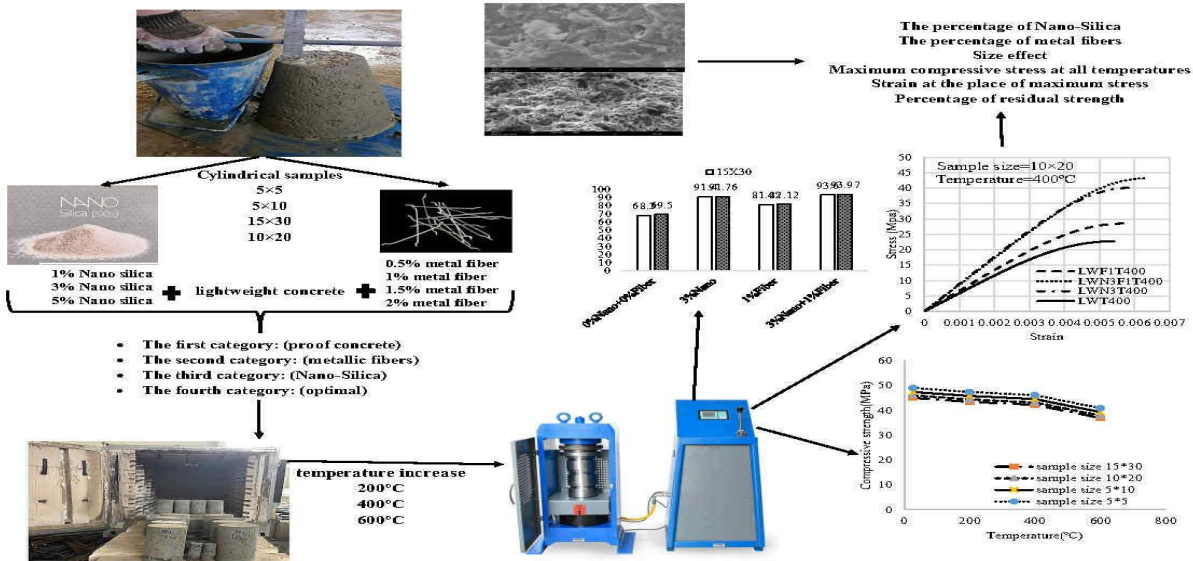
Weight Loss

Size Effect

The primary goal of the engineering design of building is to reduce the weight of the structure and its resistance to fires and earthquakes because fires are inevitable. Hence, the direction of this study was to use lightweight concrete because of its unique advantages in weight loss and fire resistance due to its thermal insulation property. It was also intended to enhance the strength and behavior of this concrete at high temperatures. For this purpose, four mixing designs samples without fibers and nano-SiO₂, samples with different proportions of nano-SiO₂, samples with different proportions of fibers, and samples with both fibers and nano-SiO₂ together were prepared. The results showed damage to samples free of nano-SiO₂ and fibers, changing their color, reducing their resistance and reducing their weight. But adding nano-SiO₂ fibers or using them together leads to improving the properties of concrete at all temperatures. Due to nano-SiO₂, its pozzolanic interactions improve the microstructure, and the fibers prevent cracks in concrete. This study also dealt with the effect of changing the size of the samples on the compressive strength, and the results showed an increase in the resistance of the samples with small sizes, and resulted factors for converting the resistance of non-standard samples into a standard.

doi: 10.5829/ije.2023.36.11b.01

Graphical Abstract



*Corresponding Author Institutional Email: tavakoli@nit.ac.ir (H. R. Tavakoli)

1. INTRODUCTION

Concrete is the most widely used material in construction worldwide due to its ease of use and low cost. Its compressive strength is one of the most significant reasons for accepting this material. The concrete used in this study is lightweight concrete (LWC), as its use by engineers has increased in recent years because the heavy structure and traditional materials will have many consequences for the structure. If the weight is less, it will increase the structure's safety and resistance to fire and earthquakes without affecting its strength. It entered the application of LWC after the production and manufacture of light concrete in the early twentieth century in 1917, after which many lightweight concrete buildings and bridges were built in the world, including the largest concrete building with 52 floors and a height of 215 meters in Houston, Texas, the Park Plaza Hotel building. It is among the buildings constructed between 1920 and 1930. The 42-story building in Chicago, the TWA terminal at New York Airport in 1960, Dulles Airport in Washington in 1962, a church in Norway in 1965, a bridge in Wiesbaden, Germany, in 1966, and a water bridge in Rotterdam, Netherlands, in 1968. This type of bridge was built in the Netherlands, England, Italy, and Scotland in the 1970s and 1980s, along with other buildings where it was used for LWC. FIP has published some significant lightweight concrete projects, demonstrating their astronomical use. Also, LWC significantly reduces construction costs, which can be examined in two aspects:

1. Reducing the dead load on the building: This factor decreases the cost of the skeleton and the foundation. Note: Reducing the building's dead load will reduce damage during an earthquake or fire.

2. Saving energy consumption: Due to the ease of cutting and drilling this type of concrete, we will witness a decrease in the cost of operating the facility, and during the operation of the building, due to the insulation of the building structure, there will be a significant decrease in the cost.

Also, LWC has other benefits. The volume of waste in this type of concrete is less than ordinary concrete, as the issue of the environment and its pollution has been taken into account recently, and natural materials that do not destroy the environment are of particular interest attention. Destroying LWC requires less energy than standard concrete because smaller machines can be used. In addition, because this type of concrete contains air, the volume of waste during demolition is smaller than normal concrete. Thus, using LWC spread due to its essential advantages, such as lightness, thermal insulation, reduced production and transportation costs, and sufficient earthquake resistance. Lightweight

concrete can withstand high temperatures and fire due to its low thermal conductivity and specific heat. Considering all the previous advantages of LWC, specifications for this type of concrete and how to improve these properties under certain conditions have been studied. In fact, LWC is known for its potential ability to withstand high temperatures and fire due to its low thermal conductivity and specific heat. However, this does not mean high temperatures do not affect LWC. Elevated temperatures may lead to severe discoloration, a change in concrete compressive strength, a reduction in weight and modulus of elasticity, and a change in concrete appearance [1]. One of the significant problems with LWC applications in industry and structures at high temperatures is that the favorable properties of concrete are reduced at high temperatures.

Nistratov et al. [2] used the regeneration of fibers made from waste composites and found that the minimum temperature to destroy the carbon plastic matrix is 410 °C and that adding 1% of the fibers led to their growth of 37% due to their high density and low porosity. In his study, Moosaei et al. [3] improved the ductility of light aggregate concrete by integrating hybrid steel and polypropylene fibers. He found a significant increase in compressive ductility and the ability to absorb energy.

Toric et al. [4] have investigated the mechanical properties of LWC after exposure to high temperatures. Concrete samples in four concrete mixtures were heated to 600 °C and subjected to various tests after 90 days. The results indicate that the compressive strength has decreased by 20%. Poon et al. [5] indicated that high temperatures weakened concrete's compressive strength and hardness.

Considering that LWC has lower strength due to the lower specific weight of this type of concrete, researchers have always tried to improve its mechanical properties by adding admixtures. They also have improved properties at elevated temperatures. These additives are steel fiber and nano-SiO₂. Wang et al. [6] studied lightweight concrete (SFLWC). They used two types of concrete with steel fibers and steel fibers with knurled ends and wrinkled shapes. The results showed that the higher the temperature, the higher the axial peak.

The strain significantly increased while the axial compressive strength and modulus of elasticity decreased. Concrete hardness rises at lower temperatures and decreases at higher temperatures. However, steel fibers can enhance the material's ability to absorb energy as well as its specific and residual durability. Mohammadi and Bagheripour [7] studied the engineering properties of self-compressing lightweight concrete (SCLWC) after adding fibers to it and found

that the compressive strength was improved by adding 1% fine steel fibers. Goaiz et al. [8], Mohammed and Kadhim [9] showed that adding fiber increased compressive strength. A study by Varghese et al. [10] showed that carbon fiber-reinforced concrete samples had better residual shear strength than others. Combining carbon and basalt fibers into concrete reduced microcracking in samples exposed to elevated temperatures. Some researchers stated that the fibers do not have a noticeable effect on the compressive strength of concrete [11-13]. According to literature, it can be said that the use of fiber cannot provide a complete improvement in LWC. Düğenci et al. [14] have stated in their research that the compressive strength and modulus of elasticity of concrete-containing fibers decrease significantly with increasing temperature. Lau and Anson [15] showed that steel fibers increase resilience to heat and cracking. Among the additions that attracted researchers' interest in improving the behavior of concrete and making the microstructure dense and homogeneous at high temperatures is nano-SiO₂ due to its interaction with calcium oxide produced through the decomposition of cement hydrates at high temperatures.

According to literature [16, 17], adding nanomaterials such as alcofine and replacing it with cement can improve compressive strength and reduce environmental pollution.

Bastami et al. [18] investigated changes in concrete's compressive and tensile strengths due to heat modification with nano-SiO₂. This study tested six samples with different percentages of nano-SiO₂ and two without nano-SiO₂. After making the samples, they were heated to 400, 600, and 800 degrees Celsius. The results showed that adding nano-SiO₂ increased compressive and tensile strengths and permeability, flaking, and mass loss. Horszczaruk et al. [19] studied the effect of high temperatures on the performance of concrete containing nano-SiO₂. In this research, concrete with 5% different nano-SiO₂ and three edge temperatures of 200 °C was made and tested. The analysis of mass loss, bending, and compressive strength and observation with SEM was done for samples. Based on the results, an ideal nano-SiO₂ content improved the thermal resistance. Brzozowsk et al. [20] found that nanoparticles enhanced the behavior of concrete at high temperatures in cement mortar containing quartz and magnetite aggregates. Researchers [21-24] found that adding 4% of nano-SiO₂ by replacing it with cement improved compressive strength, and whenever it exceeded 4%, its positive effect decreased. Ahmadi et al. [25] found in their study that adding nano-SiO₂ as an alternative to cement 1, 3, and 5% improves the microstructure of cement and increases its compressive strength.

The purpose of this study was to design a mixture of nano-SiO₂ and fibers to improve the behavior of LWC after fire exposure. For this purpose, four mixing designs with nine groups of samples were made. Designing the first mixing for control samples and designing the second mixing with different weight ratios 1%, 3% and 5% nano-SiO₂ by replacing it with the weight of cement and subtracting the third mixing for different volume ratios of 0.5, 1, 1.5 and 2% fibers. The results showed that the best percentage for nano-SiO₂ is 3%, and the optimal percentage for fiber is 1%. Thus, a composite fourth mixing design consisting of 3% nano-SiO₂ and 1% steel fibers was made. After that, the samples were exposed to different temperatures of 200, 400, and 600 °C, and a comparison was made between them and the control samples. These groups contain samples of different sizes (10×20, 15×30, 5×10 and 5×5 cm). The purpose of the difference in the size of the samples was to show the effect of size on compressive strength. The results showed that the smaller the size of the sample, the greater the compressive strength.

2. MATERIALS AND METHODS

This section describes the quality and quantity of materials used to prepare concrete samples.

2. 1. Materials

2. 1. 1. Aggregates The lightweight aggregate in this study is Light Weight Expanded Clay Compound (LECA). Figure 1 shows the LECA model used in this research. Specific gravity and water absorption tests were also performed on the samples. The maximum LECA size is limited to 12 mm. The maximum amount of these samples was determined using the sieve analysis test according to "ASTM C330" [26]. Also, the mechanical and physical parameters of the LECA assemblies are presented in Table 1. Sand with a maximum grain size of 4.75 mm was used as a fine aggregate according to ASTM C33 [27]. Figure 2 shows the results of the sieve analysis test performed on fine sand and silica.



Figure 1. LECA was used in this study

Portland cement type 2 was used in this investigation. Based on the manufacturer's information, its chemical, physical, and mechanical properties are summarized in Table 2. This Portland cement type produces moderate heat due to its reaction with water. In addition to that, it has balanced resistance to salts, sulfates, and chlorides. Also, this cement is suitable for

pouring concrete in hot weather. This cement may not be used in facilities subject to sulfate attacks. Less heat is produced due to the slow reaction of cement with water, so this type of cement can be used in relatively large constructions, such as massive and large-sized foundations.

TABLE 1. A LECA aggregate's mechanical and physical characteristics

Elements	Na ₂ O	Al ₂ O ₃	SiO ₂	P ₂ O ₅	SO ₃
wL%	0.376	2.163	4.141	19.298	0.116
Elements	Cl	K ₂ O	CaO	TiO ₂	MnO
wL%	0.011	0.808	58.95	0.221	0.1
Elements	Fe ₂ O ₃	Ni	Cu	Zn	Rb
wL%	2.982	0.009	0.006	0.01	0.003
Elements	Sr	Bn	LOI		
wL%	0.025	0.086	6.47		

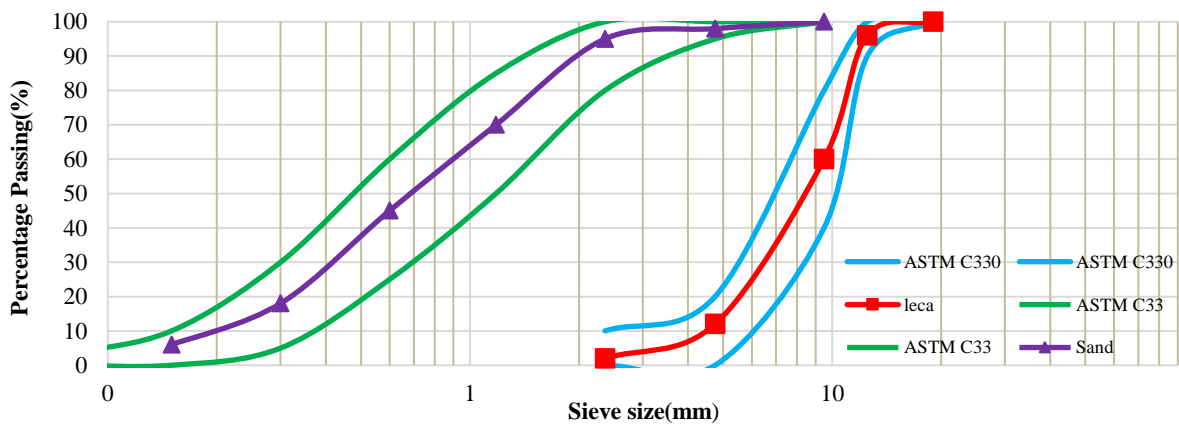


Figure 2. The sieve analysis test of coarse and fine aggregates was used in this research

TABLE 2. Characteristics of the cement used in this research

Elements	Na ₂ O	Al ₂ O ₃	SiO ₂	P ₂ O ₅	SO ₃
wL%	1.735	16.353	63.259	0.201	0.331
Elements	Cl	K ₂ O	CaO	TiO ₂	MnO
wL%	0.098	3.114	4.159	0.532	0.112
Elements	Fe ₂ O ₃	Ni	Cu	Zn	Rb
wL%	5.566	0.006	0.006	0.015	0.009
Elements	Sr	Zr	Ba	Pb	LOI
wL%	0.043	0.017	0.047	0.014	0.5
Elements	MgO	Cr			
wL%	3.869	0.014			

The third-generation superplasticizer based on carboxylate is an Abadgaran Construction Chemical Industries product.

This study relied on Nano Sadra's nano-SiO₂ [28]. White in color, with 99% pure nano-SiO₂ powder has a particle size of 11-13 nm. The microstructure has been verified using a transmission electron microscope (TEM) and X-ray diffraction (XRD) images. A transmission electron microscope (TEM) is a high-resolution, ultra-magnification instrument for the structural characterization of materials. XRD analysis, or X-ray powder diffraction analysis, another name for X-ray spectroscopy, is a technology used to learn about the chemical makeup and crystal structure of the natural and artificial objects without destroying them. X-ray patterns are like fingerprints in that they can identify specific crystal structures. The TEM photo with different resolutions (a) 0.1 nm, (b) 150 nm, (c) 40 nm, (d) 300 nm and X-ray XRD diagram are presented in Figures 3 and 4. TEM device model: EM10C-100KV device, Zeiss, Germany, was used in our work.

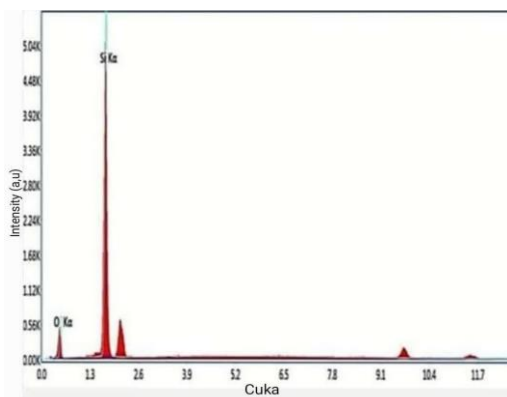
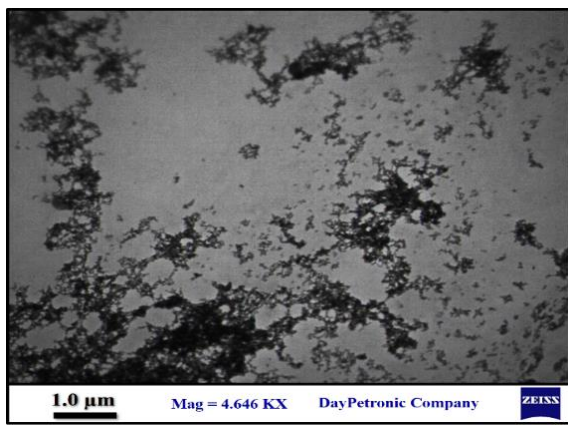
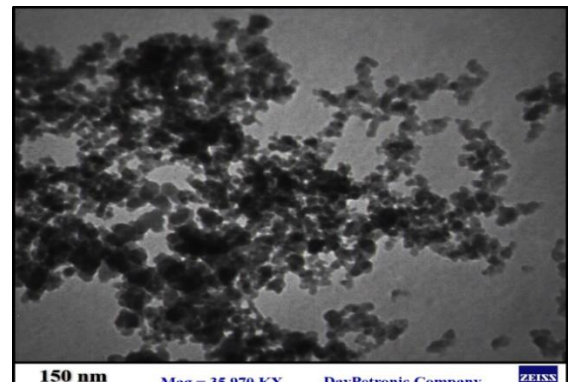


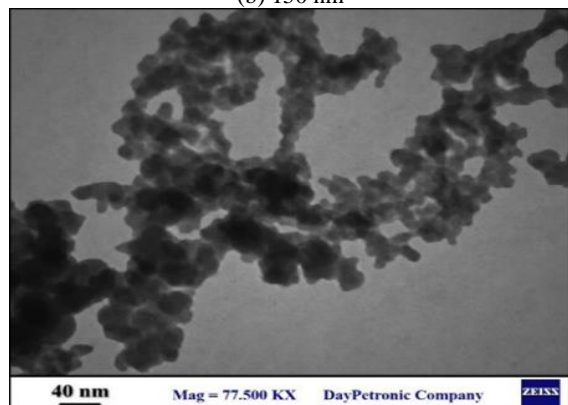
Figure 3. The XRD chart of nano-SiO₂



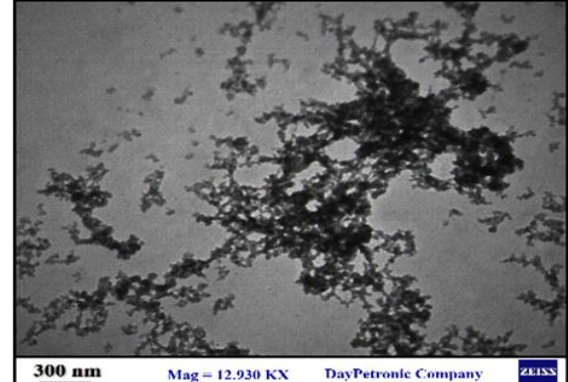
(a) 0.1 nm



(b) 150 nm



(c) 40 nm



(d) 300 nm

Figure 4. TEM image of nano-SiO₂ at different accuracies

Among different types of fibers, steel fibers are often applied for construction purposes and improve concrete properties more effectively than other fibers [30]. Steel fibers with short and discrete lengths are available in lengths of up to 80 mm and cross-sectional areas ranging from 0.1 to 1.5 mm² [29]. Ki Mix Company supplied the steel fibers used in this study. It has a straight shape with a hooked end. Table 3 displays information about steel fiber properties. Figure 5 shows the shape of the steel fibers used in this study.

TABLE 3. The mechanical and physical properties of steel fibers are presented.

Tensile strength (MPa)	L/D	Diameter (mm)	Length (mm)	cross-section shape	Appearance
1200	62.5	0.8	5	circle	straight

**Figure 5.** The shape of the fibers with knotted ends used

2.2. Concrete Mixture

In this study, the mixing design in the standard "ACI 211.2" [30] was used in making preliminary samples, and then the design was modified several times until a mixing design with a suitable slab between 50 and 80 mm was obtained. The LWC mixing technique per cubic meter used in this study is shown in Table 4.

The nano- SiO_2 weight ratio is added by replacing it with the cement weight. Three percentages were used in this study: 1, 3 and 5% nano- SiO_2 .

To distribute nano- SiO_2 powder uniformly, it is mixed well with cement for 2 minutes until a homogeneous mixture is obtained for use as a concrete admixture. All dry materials are combined in a mixer for two minutes, and then water containing plasticizers is gradually added to the mixture. Then, in a mixture containing fibers, steel fibers are added to the mixture. After the materials are completely mixed in the mixer, the fresh concrete is poured in three layers into the required molds arranged in advance. Concrete mixtures are compacted on a vibrating table. Molds were opened after 24 hours. Mold samples were taken and cured by covering them with nylon and a damp cloth for 28 days,

TABLE 4. The LWC mixing plan used in this research

Cement (kg/m ³)	Coarse aggregate (Leca) (kg/m ³)	Fine aggregate (sand) (kg/m ³)	Water to cement ratio	Superplasticizer percentage	28 days' compressive strength f_c (MPa)	Specific Weight γ (kg/m ³)
450	350	850	0.38	1%	30	1910

as shown in Figure 6. Then they were exposed to free air. Ninety days after being prepared, some samples were put in the oven for thermal testing. Some samples were heated to 200 °C, 400 °C, and 600 °C, while others were stored at 25 °C at room temperature. Twelve samples were made for each mixing plant and temperature. Three samples were made with cylindrical molds of different dimensions (15×30, 10×20, 5×10, and 5×5 cm) to observe the effect of size. Table 5 also shows the number of samples and tests performed on them. Table 6 represents the subtraction admixture characteristics of the samples.

TABLE 5. Number of samples

Experiment	Sample dimension (cm)	Sample shape	Number of samples
Compressive strength and modulus of elasticity	10×20	Cylindrical	108
Compressive strength and modulus of elasticity	15×30	Cylindrical	48
Compressive strength	5×10	Cylindrical	48
Compressive strength	5×5	Cylindrical	96

TABLE 6. LWC mixture plan

Nano- SiO_2 (%) (weight percentage of cement)	steel fibers (%)	Volume percent	Plan
1	-	-	The first category (control samples)
2	-	0.5	
3	-	1	The second category (metallic fibers)
4	-	1.5	
5	-	2	
6	1	-	
7	3	-	The third category (Nano- SiO_2)
8	5	-	
9	3	1	The fourth category (optimal)



Figure 6. Samples under occurring

2.3. Expose the Samples to Temperature The samples were heated for 48 hours, or 2880 minutes, at 100 °C before the temperature required for surface drying was reached. This method may help prevent cracking in the samples at high temperatures [31]. After that, the samples were heated to 200, 400, and 600°C. The electronic oven is set through the control panel at 5 degrees per minute. When the samples are heated inside the furnace, the oven temperature is set to the required degree. The oven temperature it reaches is known through the furnace side keyboard. In order to measure the temperature, samples must arrive, which is done with a digital thermometer attached to a wire outside the furnace. This wire was carefully placed inside the concrete paste inside a cube mold with 100 x 100 x 100 mm dimensions. We enter the mold with the rest of the samples when the samples are heated. The other end of the wire protrudes through a small hole in the oven side, on the outside, to connect to the thermometer in Figure 7 (a) the samples after exposure to temperatures, (b) the arrangement of the samples to enter the oven, (c) the thermometer to measure the temperature of the sample. This can be seen in the graphs obtained from the digital thermometer in Figure 8, showing the temperature change inside the sample and in the furnace. (A) samples after exposure to temperature 200°C, (b) samples after exposure to temperature 400°C, (c) samples after exposure to temperature 600°C.

2.3. Test Procedure Three studies were conducted for this research. Firstly, to study the effect of steel fibers and nano-SiO₂ on the compressive strength and modulus of elasticity of light structural concrete and to find the optimal ratio of steel fibers and nano-SiO₂. Secondly, to examine the effect of temperature on concrete compressive strength, and finally, to examine the effect of concrete sample size on compressive strength.

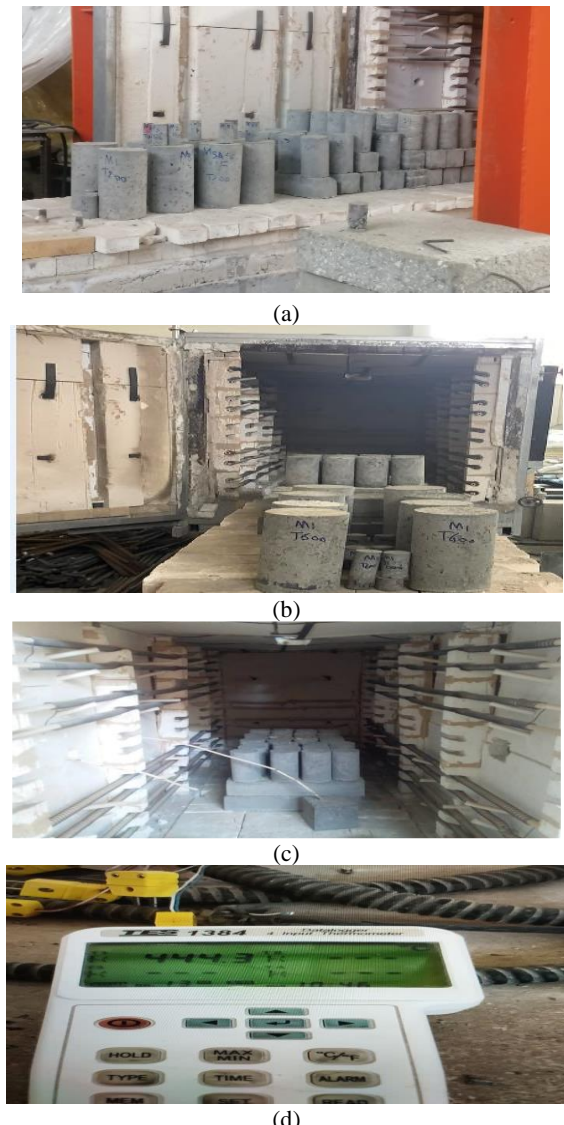


Figure 7. Samples in the electrical furnace

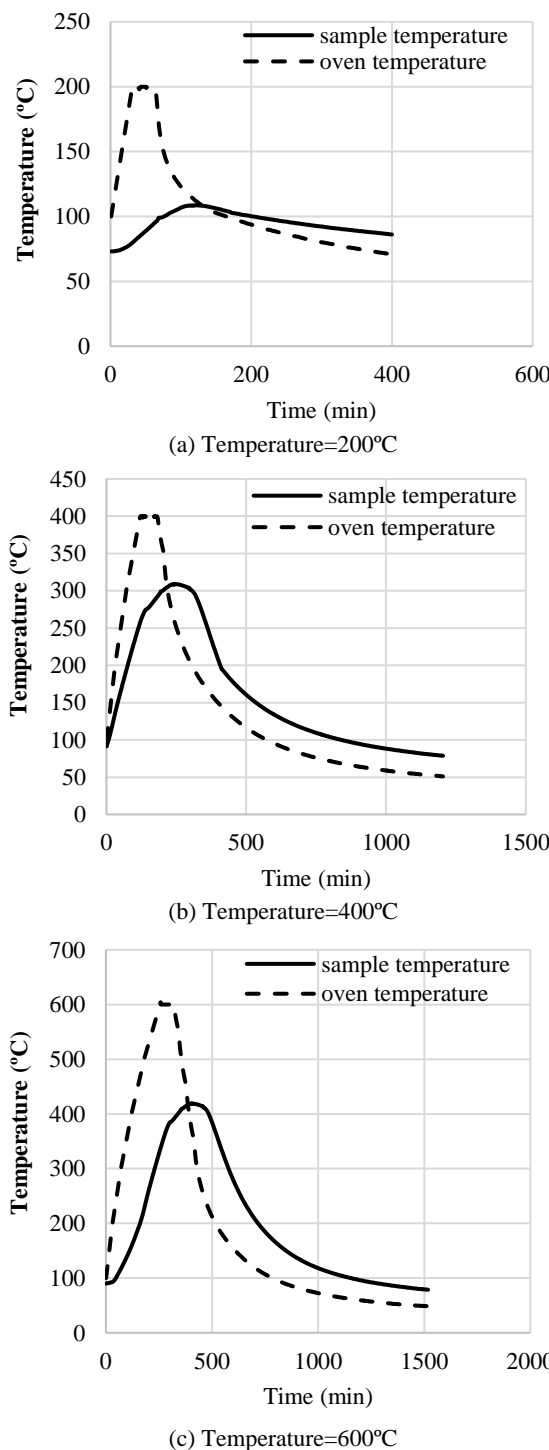


Figure 8. The graphs of the temperature increment on the samples

2. 4. Mechanical Experiment Samples were prepared for various tests based on a predetermined mixing plan and method, including thermal and mechanical loading. The uniaxial compression test, (μ , modulus of elasticity) test, and compressive stress-strain

curve were used in this study to check the mechanical properties of the samples. The compressive strength test was performed according to the ASTM C39 standard [32]. The samples' elastic modulus was determined based on the ASTM C469 standard [33]. This study used an instrument with a capacity of 2000 kN and an accuracy of 1 kN to measure stress-strain curves (Figure 9). This test was performed according to the ASTM C617 standard [34].

3. RESULTS AND DISCUSSION

In the results section, investigate the behavior of LWC containing nano- SiO_2 , fibers, or both at different temperatures by knowing the compressive strength, elastic modulus, stress-strain curve, and the effect of the different sizes of the samples on the compressive strength.

3. 1. Effect of Nano- SiO_2 and Steel Fibers on LWC Compressive Strength at Room Temperature

The compressive strength results for different steel fibers and nano- SiO_2 proportions in LWC for all sample sizes can be seen in Tables 7 and 8 and Figures 10 to 13.

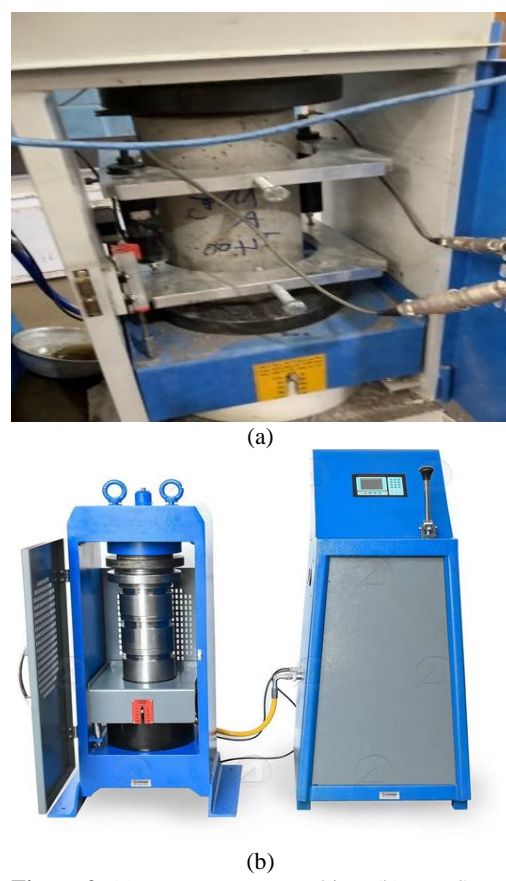


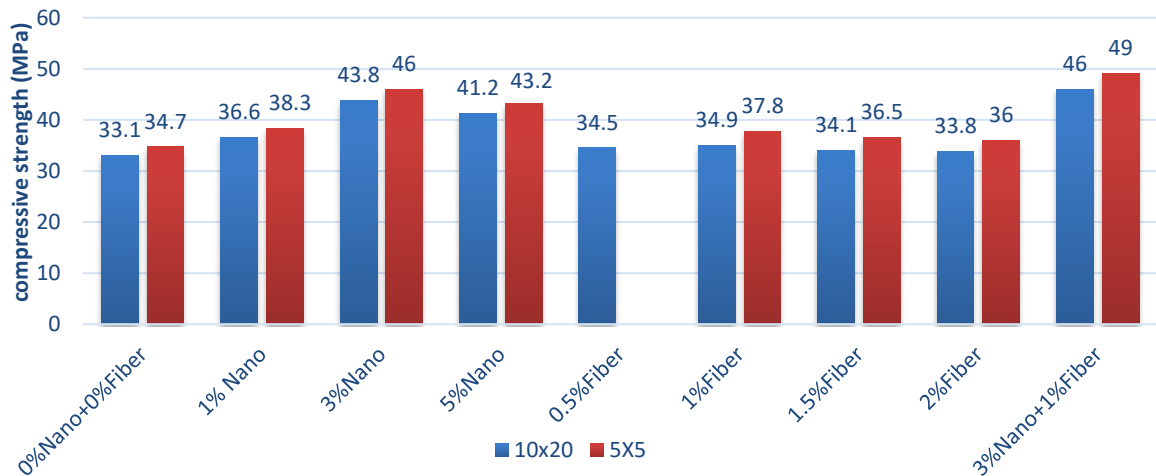
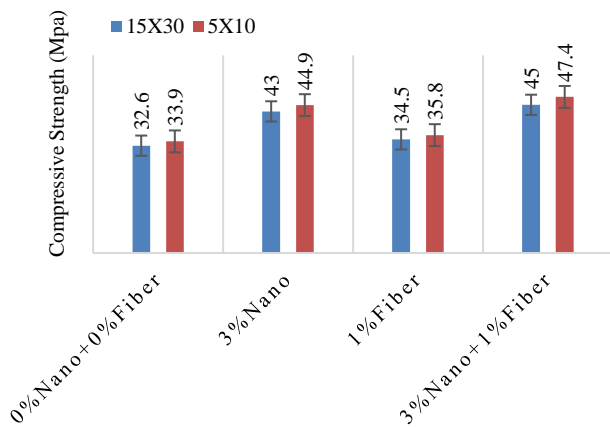
Figure 9. (a) Pressure Test Machine; (b) Test Setup

TABLE 7. The compressive strength (MPa) at 25°C for 15×30 and 5×10

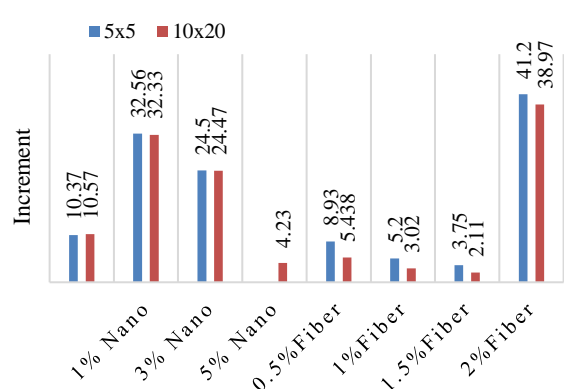
Size sample(cm)	Control	3%Nano	1%Fiber	3%Nano+1%Fiber
15×30	32.6	43	34.5	45
5×10	33.9	44.9	35.8	47.4

TABLE 8. The compressive strength at 25°C for 10×20 and 5×5

Size sample (cm)	Control	1% Nano	3% Nano	5% Nano	0.5% Fiber	1% Fiber	1.5% Fiber	2% Fiber	3% Nano+1% Fiber
10×20	33.1	36.6	43.8	41.2	34.5	34.9	34.1	33.8	46
5×5	34.7	38.3	46	43.2	34.5	37.8	36.5	36	49

**Figure 10.** The compressive strength at 25°C for 10×20cm and 5×5cm size samples**Figure 11.** The compressive strength at 25°C for 15×30cm and 5×10cm size samples

To select the most suitable nano- SiO₂ and the highest fiber ratio, 10 × 20 cm molds were used. The largest percentage of nano- SiO₂, as shown in the results, is 3%,

**Figure 12.** Differences from control samples at 25°C (%)

and the highest percentage of fiber is 1%. The positive effect of nano- SiO₂ decreases when the ratio exceeds 3%. This can be explained by the fact that a certain amount of calcium hydroxide crystals were produced

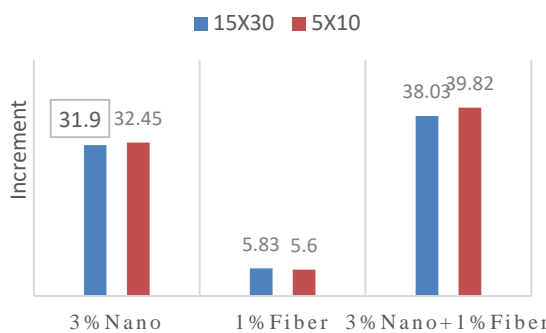


Figure 13. Differences from control samples at 25°C (%)

during the interaction of water with cement, which reacts with nano- SiO_2 which from this fusion produces a gel (hydra silicate calcium). When more nano- SiO_2 than required is added, it reacts with calcium hydroxide, and the excess nano- SiO_2 is precipitated and replaced by the spent cement, which reduces the strength of the cement paste and reduces the adhesion between the aggregate and the cement paste. The reason why nanoparticles cause an increase in compressive strength can be explained as follows: The reaction between cement and water, known as the pozzolanic reaction, leads to the formation of vast amounts of calcium hydroxide crystals. $\text{Ca}(\text{OH})_2$, a hexagonal crystal present in the transition zone between the cement paste matrix and the aggregate, breaks concrete's strength. Because of nano- SiO_2 has a high specific surface area, it is highly reactive and reacts rapidly with $\text{Ca}(\text{OH})_2$ to form a calcium silicate gel. As a result of the pozzolanic reaction, the size, and concentration of calcium hydroxide crystals are reduced, and a dense, high-strength H-S-C gel (calcium silicate hydrate) is produced, which fills the voids in the transition zone to enhance the strength and durability of concrete, known as micro-filling. The average diameter of H-S-C gel particles is about 10 nm. Therefore, filling the existing pores creates a denser and homogeneous viscous paste matrix, as previously shown by other researchers [35]. However, we note from the results that adding 2% of the fibers reduces the compressive strength because the fibers prevent cracks growth. Its principal function is to repair cracks, leading to a decrease in compressive strength. Also, we noted from the results that the highest compressive strength was in the compain mixture design, as it increased by 39%. The reason for this increase is that by adding nano- SiO_2 to the mixture containing fibers, the strength of the concrete increases due to an increase in density of the mixture and the increase in the contact surface between the fibers and the cement paste.

3. 2. Mechanical Properties of LWC at High Temperatures

Figure 14 shows the compressive

strength of all sample sizes of LWC at 200°C, 400°C, and 600°C, as well as control samples.

As shown in the above figure, the compression strength decreases with increasing temperature in all sample sizes, and this is because heat damages the load-bearing mechanical structure of concrete, and the mechanical properties of concrete change permanently. Figure 15 compares changes in compressive strength after heat exposure for samples of three different sizes.

Figure 15 reveals that as concrete's temperature rises, particularly between 400°C and 600°C, the material's compressive strength decreases dramatically. The values of the percentage weight loss of the samples due to heat are presented in comparing form in Figure 16.

As shown in Figure 16, with the increase in temperature experienced by the sample and an increase in the duration of exposure to the appointed temperature, the weight loss of the samples increases. This weight loss is related to the amount of water in the concrete structure, the decomposition of calcium hydroxide into quicklime and water, the evaporation of

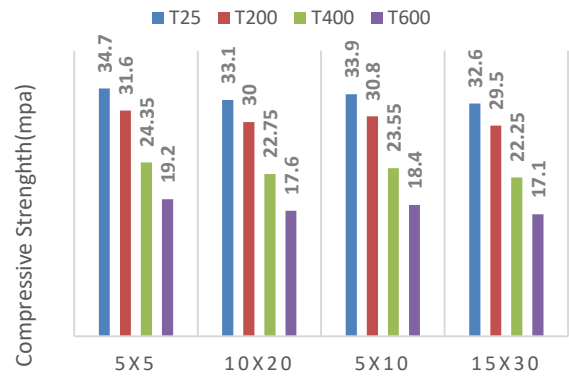


Figure 14. LWC compressive strength at high temperatures

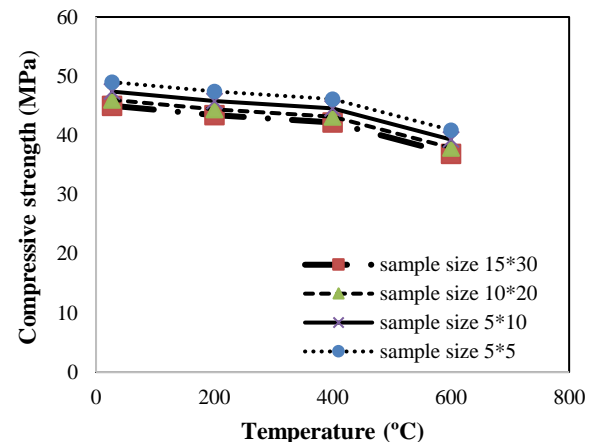


Figure 15. LWC compressive strength exposed to high temperatures

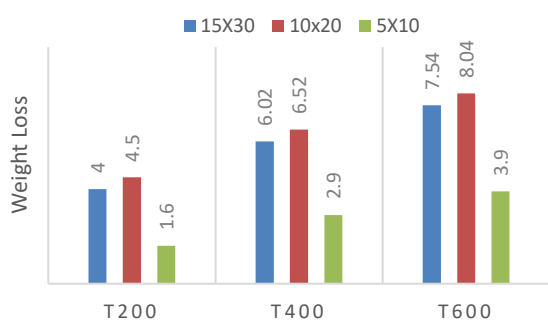


Figure 16. Weight loss percentage (%) of LWC due to high temperature

produced water, the separation of surface absorption water from CSH layers, and the decomposition of aggregates. All of these phenomena become more intense as temperatures and heating times increased. This result has been confirmed in the literature [21, 26]. Figure 17 shows residual compressive strength following exposure to high temperatures for different sample sizes compared to control samples.

The 600°C temperature had a significant effect on the residual compressive strength of the concrete. Figure 17 shows that lightweight concrete compressive strength decreased with temperature increase. It can also be seen that the smaller the sample size, the greater its residual resistance.

3. 3. Effect of Temperature on LWC Containing Nano-SiO₂ and Fibers

Tables 9 and 10 and Figure 18 show the compressive strength, weight loss, and residual compressive strength of all sample sizes at 200°C, 400°C, and 600°C.

TABLE 9. Residual compressive strength and weight loss of LWC containing nano-SiO₂ and fibers at high temperatures for 15×30 and 5×10 samples

Parameter	temp	Size sample (cm)	0%Nano+0%Fiber	3%Nano	1%Fiber	3%Nano+1%Fiber
Residual %	T200	15×30	90.5	96.3	94.5	96.4
		5×10	90.9	96.4	94.7	96.6
	T400	15×30	68.3	91.4	81.45	93.6
		5×10	69.5	91.76	82.12	93.97
	T600	15×30	52.45	73.56	65.5	82
		5×10	54.28	74.7	66.76	82.91
Weight loss%	T200	15×30	4	2.9	3.5	2.5
		5×10	1.6	1.28	1.46	1.06
	T400	15×30	6.02	5.33	4.6	4.2
		5×10	2.9	2.5	2.7	2.1
	T600	15×30	7.54	7.16	6.6	6.2
		5×10	3.9	3.5	3.6	3.2

The results showed the state of deterioration of the samples and the weight reduction when the temperature rose to 600. However, the nano- SiO₂ and the fibers helped somewhat in improving the resistance at the temperature of 600. We note that the effectiveness of the nano- SiO₂ decreased at high temperatures and became similar to the behavior of the fibers because, before the temperature rise, the nanoparticles improved the microstructure. After the high temperature here, the fibers played like a bridge in preventing cracks. Also, we notice that at high temperatures, the concrete color changed and became pinkish, as shown in Figure 19. As shown in the figures, the lack of fibers and nano-SiO₂ in the sample indicates the amount of crack. The wear due to compressive load and failure at the place where the load is applied is very high. By adding 1% steel fiber, this amount of failure is greatly reduced.

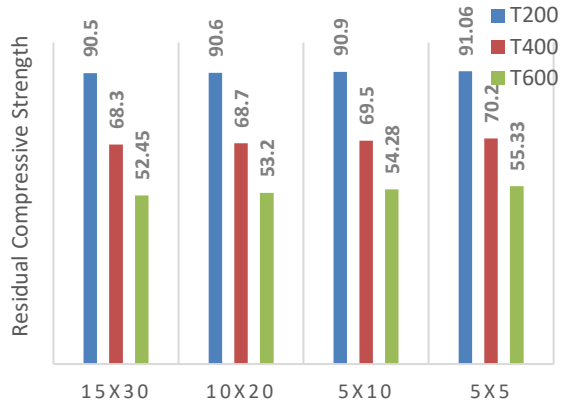
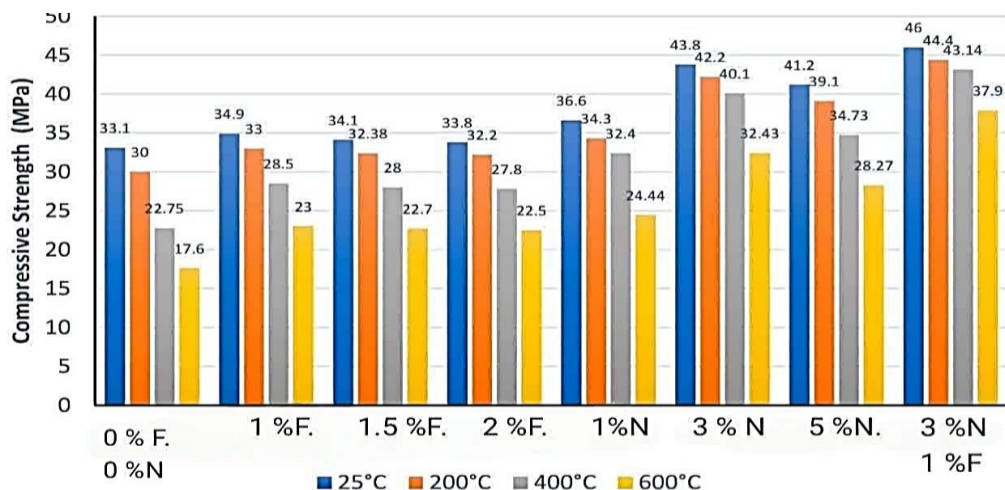
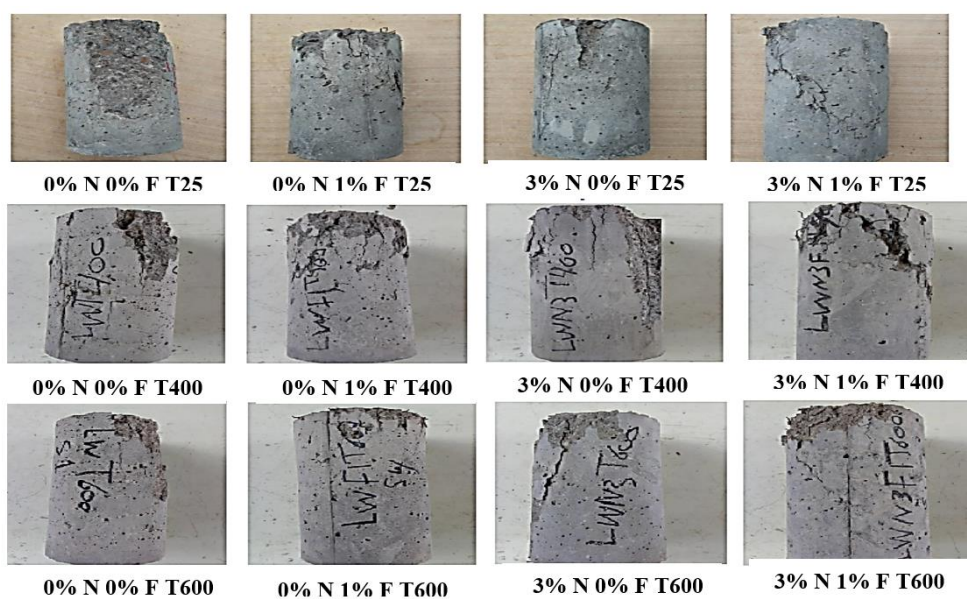


Figure 17. Residual compressive strength after high-temperature exposure

TABLE 10. Residual compressive strength and weight loss of LWC containing nano-SiO₂ and fibers at high temperatures for 10×20 and 5×5 samples

Parameter	temp	Size sample (cm)	0% Nano+ 0% Fiber	1% Nano	3% Nano	5% Nano	1% Fiber	1.5% Fiber	2% Fiber	3% Nano+ 1% Fiber
Residual %	T200	10×20	90.6	93.7	96.3	94.9	94.6	94.95	95.3	96.5
		5×5	91.06	93.9	96.5	95.1	94.9	95.3	95.6	96.7
	T400	10×20	68.7	88.5	91.6	84.3	81.7	82.1	82.25	93.8
		5×5	70.2	89.03	91.96	85.02	83.07	83.29	83.33	94.16
Weight loss%	T600	10×20	53.2	66.78	74.04	68.62	65.9	66.57	66.57	82.4
		5×5	55.33	68.25	75.28	69.9	68.57	70.96	68.61	83.47
	T200	10×20	4.5	3.8	3.3	2.9	4	4.1	4.3	3
		5×5	6.52	5.9	5.73	5.4	5.1	5.25	5.6	4.7
	T600	10×20	8.04	7.7	7.56	7.2	7.1	7.5	7.8	6.7

**Figure 18.** Compressive strength of samples at different temperatures**Figure 19.** Pictures of samples' compression test

In the sample with nano- SiO_2 , the failure rate is lower compared to the control sample, and the most satisfactory results are related to the sample with 1% of fibers. and 3% silica nanoparticle is that the amount of local corrosion and damage in the sample is greatly reduced, and a small prevalence was found in the sample. According to the figures, the process obtained at 400 °C is similar to that at 25 °C.

Furthermore, compared with the 25 °C samples, only the damage rate of the samples increased, and the resistance also decreased. According to the figures, the orientation obtained at 600 °C is similar to the directions at 25 and 400 °C. Moreover, only the damage rate of the samples increased compared to 25 and 400 °C, and the resistance also decreased. The method of cracking and damage to the samples with fibers and samples has separate nano- SiO_2 , and the presence of this material affects the crack pattern in the parts.

3. 4. Modulus of Elasticity

The elasticity modulus elasticity was calculated according to Equation (1):

$$E = [(S_2 - S_1) / (\varepsilon_2 - 0.000050)] \quad (1)$$

{Where (E) is the modulus of elasticity in MPa, (S_2) is the stress corresponding to 40% of the ultimate load, (S_1) is the stress corresponding to the longitudinal strain of 50 millionths in MPa, and (ε_2) is the longitudinal strain produced by stress S_2 .}

According to Figure 20 and Table 11, the effect of nano- SiO_2 and steel fibers on the modulus of elasticity of LWC has been investigated in all mix designs.

Results show that the modulus of elasticity of LWC increases when the amount of nano- SiO_2 and steel fibers increases. In general, by adding 1% steel fibers and 3% nano- SiO_2 , the most significant impact on improving concrete's modulus of elasticity has been observed.

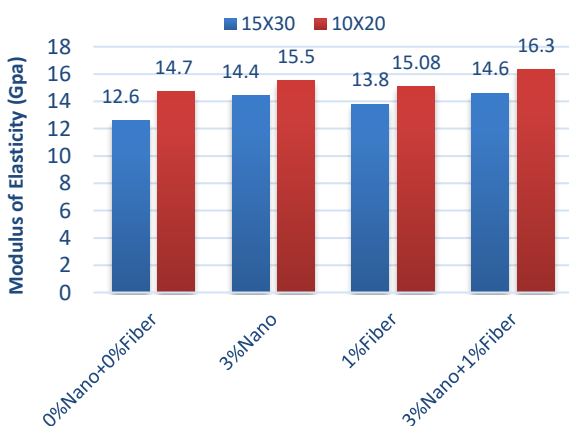


Figure 20. Comparison of the modulus of elasticity (GPa) of all concrete specimens

TABLE 11. The modulus of elasticity (GPa) of all concrete specimens

Sample Size	Temperature (°C)	0% Nano+0% Fiber	3% Nano	1% Fiber	3% Nano+1% Fiber
15x30	25	12.6	14.4	13.8	14.6
10x20	25	14.7	15.5	15.08	16.3
15x30	200	9.8	11.09	9.41	11.3
10x20	200	10	12.03	11.07	12.7
15x30	400	5.66	8.3	6.3	8.5
10x20	400	6.1	8.9	7.13	9.1
15x30	600	3.26	5.3	4.11	5.6
10x20	600	3.5	5.4	4	5.7

Other studies [36] corroborate this finding. The elasticity of concrete's constituent materials, most notably cement paste, affects the concrete's modulus of elasticity. Therefore, the elasticity modulus improves by adding nano- SiO_2 . This is also linked to reduced porosity in cement paste and enhanced compressive strength. Denser concrete results from increasing its elasticity modulus. The findings of other researchers [37] corroborate this. In general, when the compressive strength increases, the modulus of elasticity also increases, and when the porosity in the cement paste is reduced by adding nano- SiO_2 and metal fibers, the modulus of elasticity increases.

3. 5. Compressive Stress-strain Relationship between LWC and Strain at Peak Strength

Figures 21 and 22 show that adding steel fibers and nano- SiO_2 to LWC changes its behavior after maximum compressive stress, making the compressive stress-strain curve tangent less steep.

The maximum stress-strain curve was observed by adding 1% fiber and 3% nano- SiO_2 for all sample sizes. The increase in the modulus of elasticity with the

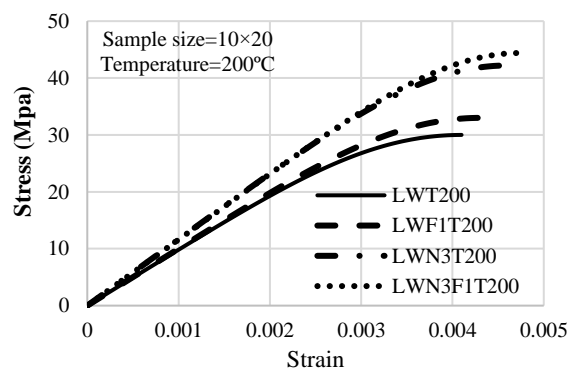


Figure 21. The stress-strain diagram of 10x20 cm samples for all LWC mix designs

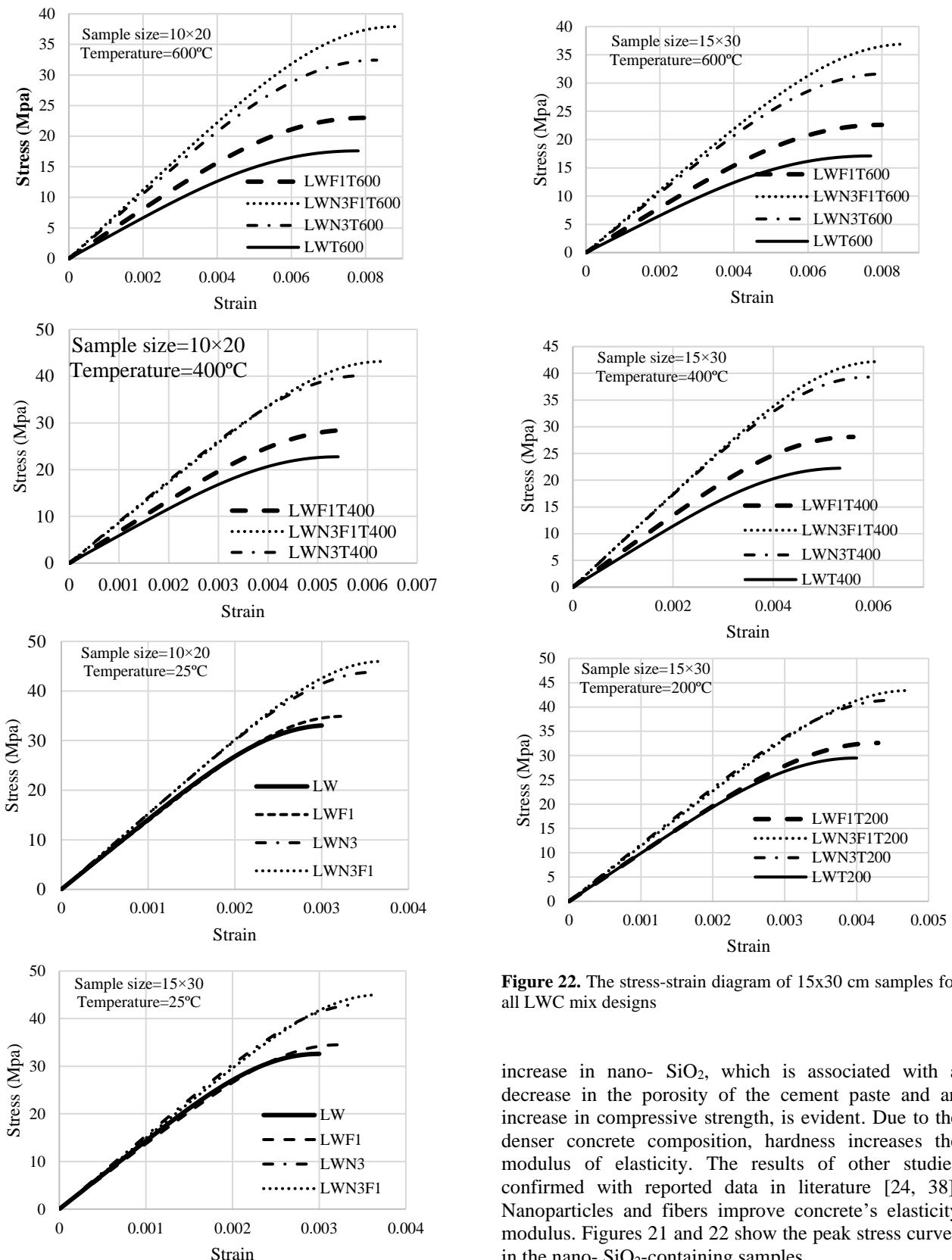


Figure 22. The stress-strain diagram of 15x30 cm samples for all LWC mix designs

increase in nano- SiO₂, which is associated with a decrease in the porosity of the cement paste and an increase in compressive strength, is evident. Due to the denser concrete composition, hardness increases the modulus of elasticity. The results of other studies confirmed with reported data in literature [24, 38]. Nanoparticles and fibers improve concrete's elasticity modulus. Figures 21 and 22 show the peak stress curves in the nano- SiO₂-containing samples.

3. 6. SEM Images of LWC Samples In Figures 23 and 24, images prepared by SEM are shown. Figure 23 shows a concrete structure without nano-SiO₂ and steel fiber, and Figure 24 shows concrete in the presence of 3% nano-SiO₂.

As shown in the figures above, the microstructure of concrete containing nano-SiO₂ has been significantly improved and is more uniform than regular concrete. Large, clustered calcium hydroxide crystals can be seen in the control sample when no nano-SiO₂ is present. However, in the sample with nano-SiO₂, the calcium hydroxide crystals reacted with the silica to produce a very resistant H-S-C gel with a very dense, compact structure. In this way, using nano-SiO₂ in concrete significantly improves its microstructure, increases the cement matrix density, and strengthens the transition zone between the aggregate and the cement paste. Figure 24 shows the structure of concrete without nano-SiO₂ and steel fiber at a temperature of 600°C and Figure 25 shows concrete in the presence of 3% nano-SiO₂ at the same temperature of 600°C.

It is evident from the images obtained from the SEM test that applying high heat to concrete has caused fundamental changes in the microstructure of concrete and the cement paste matrix. The effects of temperature on concrete can be attributed to the non-hydration of cement paste, increase in porosity, decrease in available moisture, thermal expansion, change in pore pressure, decrease in strength, and thermal cracking caused by incompatibility, creep, and thermal separation. The microstructure of induced concrete is greatly affected and structurally weakened when ordinary concrete images are taken at high temperatures. According to the pictures, the creation of a tree structure, the presence of numerous capillary pores caused by the evaporation of the water in the capillary spaces in the hydrated calcium silicate gel (H-S-C), and the decrease in the amount of hydrated H-S-C gel in the dark areas are evident, which indicates the weakness in the concrete microstructure after applying high temperature to the concrete.

Additionally, in 2018, Wang et al. [24] investigated the effect of nano-SiO₂ on the compressive strength and

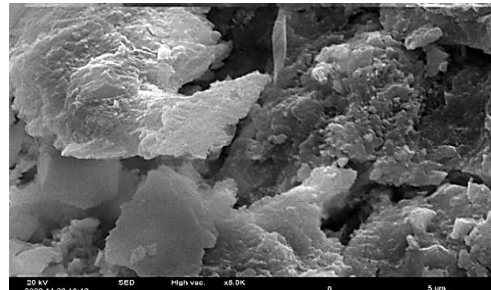


Figure 23. SEM picture of an LWC sample at 25°C

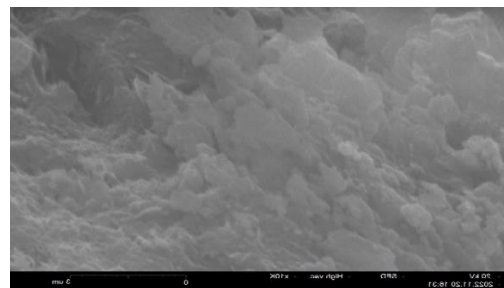


Figure 24. SEM image of a LWC sample containing 3% nano-SiO₂ at 25°C

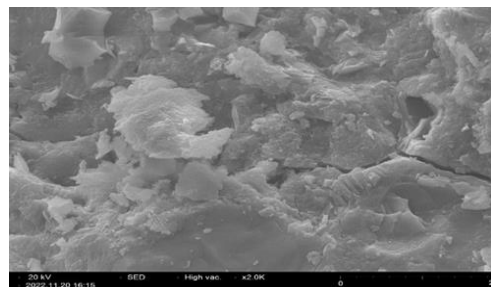


Figure 25. SEM picture of an LWC sample at 600°C

shrinkage of LWC made from artificial aggregates and found similar outcomes.

3. 7. Effect of Sample Size on Mechanical Properties An analysis of the effect of sample size on compressive strength is shown in Figures 26-30.

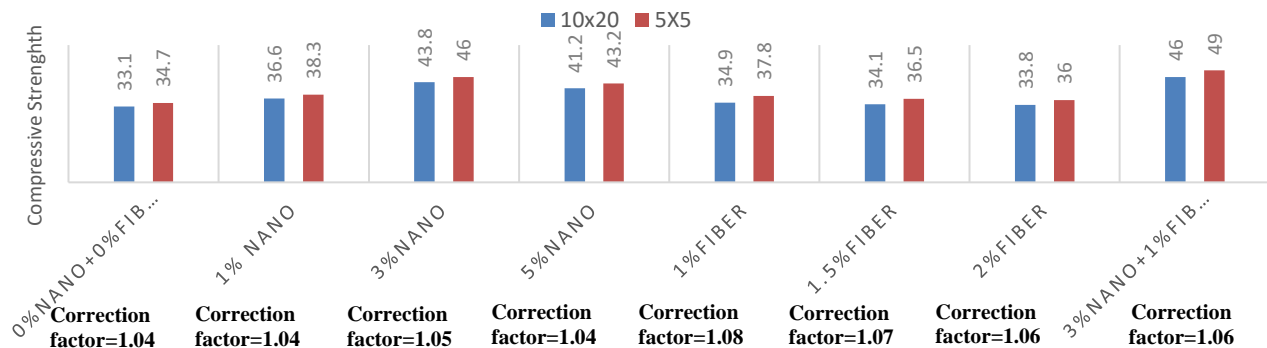


Figure 26. The effect of sample size on compressive strength at 25°C

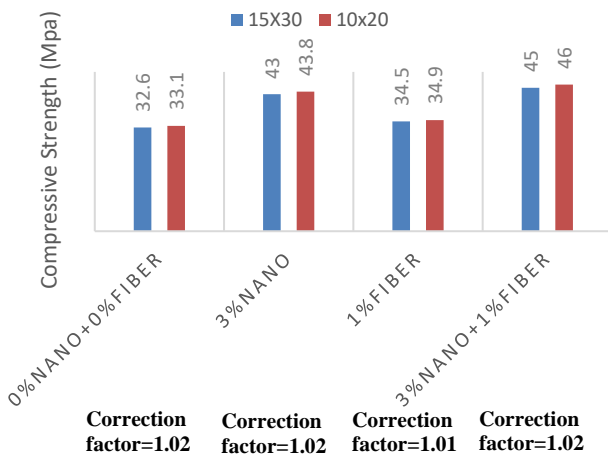


Figure 27. The effect of sample size with dimensions 15x30 cm and 10x20 cm

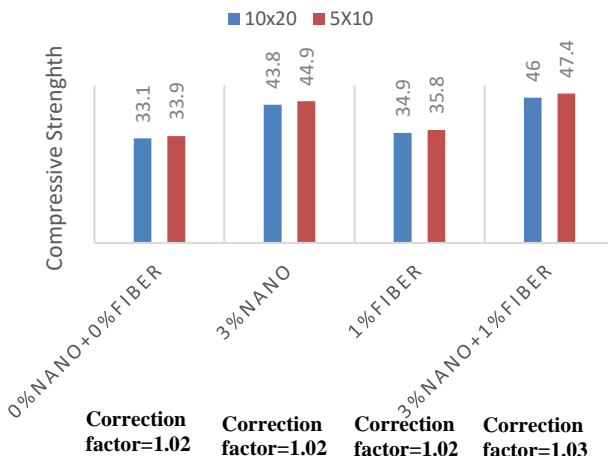


Figure 28. The effect of sample size with dimensions 5x10 cm and 10x20 cm

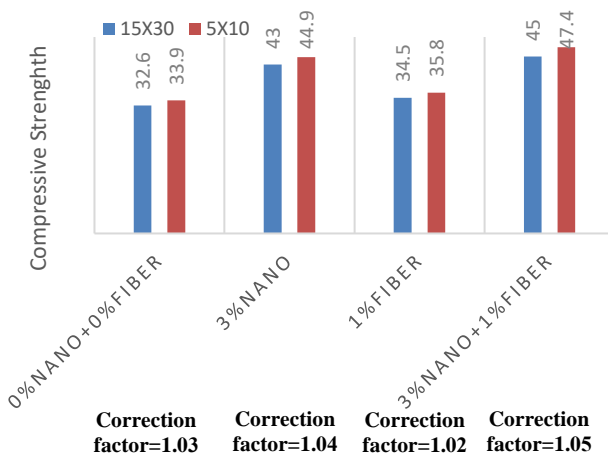


Figure 29. The effect of sample size with dimensions 15x30 and 5x10

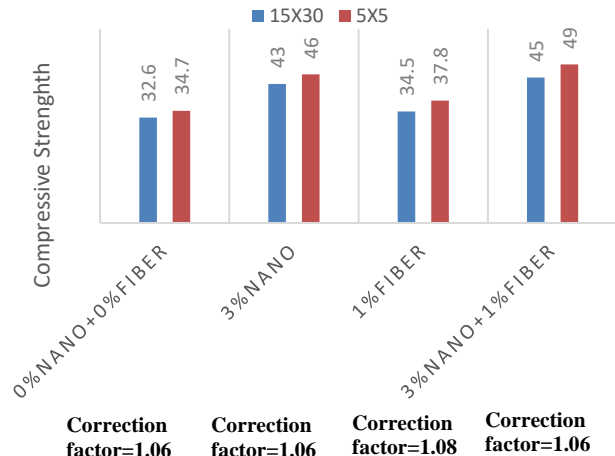


Figure 30. The effect of sample size with dimensions 15x30 cm and 5x5 cm

The effect of sample size is clearly seen in the results, as shown in the above figures. By reducing the dimensions and volume of the sample, the compressive strength increases. From the results it can be seen that the factors extracted by multiplying them by the resistance of the non-standard samples, the resistance of the standard sample is obtained according to the standard specifications [39].

4. CONCLUSIONS

This paper studied LWC behavior after exposure to high temperatures. It also examined its behavior when nano-SiO₂ fibers, fibers, or both are added at high temperatures. This study also examined the effect of changing the sample dimensions on the compressive strength of the samples. For this, four mixing designs were made with nine groups, each containing sufficient samples of different sizes. The samples were exposed to temperatures of 200, 400, and 600 °C. Then their behavior was verified by analyzing the curves of compressive strength, pressure, strain, modulus of elasticity, and residual strength. The results were as follows:

- The ultimate compressive strength was observed when 3% nano-SiO₂ or 1% steel fibers were added to the mixture separately, with an average increase in compressive strength of 32.33% and 4.23%, respectively. Thus a composite mixture of 3% nano-SiO₂ and 1% fibers was made.

- When samples were exposed to high temperatures, their compressive strength and weight decreased. This is not preferred in concrete used in construction. The fibers' ability to stop the cracks' formation and the nano-SiO₂'s ability to reaction

pozzolanic and form a gel that helps fill the pores in weak areas in the concrete contributed to limiting this behavior.

- The composite mixture of nano-sio2 and fibers had the best behavior to retain the residual strength of the samples (ratio of high heat resistance to ambient temperature resistance) after exposure to high temperatures, the residual compressive strength values for the composite mixture were (96.5%, 93.8%, and 82.4%) at exposure to a temperature of 200, 400, and 600, respectively.

- In the results obtained from the stress-strain curves, we notice increased stress and peak tension in designs containing nano-SiO₂ material. During this period, fine cracks have not appeared yet. For this reason, we note that the effectiveness of the fibers is low, and the effectiveness of nano-SiO₂ is higher because the fibers in the temperature act as a bridge to prevent cracks and nano-SiO₂ improve the microstructure in a period before exposure to temperatures.

- The effect of different sample sizes on the results was investigated. When the sample size decreased, the resistivity value increased. A comparison was made between standard and non-standard samples, and appropriate factors were extracted to convert them into standard samples.

This was a preliminary study of LWC behavior with nano-SiO₂ and fibers under static loads. It is suggested to study its behavior with nano-SiO₂ fibers under dynamic loads and with different strain rates to know the endurance of this type of concrete under earthquakes or explosions. It is also proposed to study its behavior by adding other types of fibers.

5. ACKNOWLEDGMENTS

This research was funded by Babol Noshirvani University of Technology under Grant No. BUT/388011/1401.

6. REFERENCES

1. Arioiz, O., "Effects of elevated temperatures on properties of concrete", *Fire Safety Journal*, Vol. 42, No. 8, (2007), 516-522. <https://doi.org/10.1016/j.firesaf.2007.01.003>
2. Nistratov, A.V., Klimenko, N.N., Pustynnikov, I.V. and Vu, L.K., "Thermal regeneration and reuse of carbon and glass fibers from waste composites", *Emerging Science Journal*, Vol. 6, (2022), 967-984. <https://doi.org/10.28991/ESJ-2022-06-05-04>
3. Moosaei, H., Zareei, A. and Salemi, N., "Elevated temperature performance of concrete reinforced with steel, glass, and polypropylene fibers and fire-proofed with coating", *International Journal of Engineering, Transactions B: Applications*, Vol. 35, No. 5, (2022), 917-930. <https://doi.org/10.5829/ije.2022.35.05b.08>
4. Torić, N., Boko, I., Juradin, S. and Baloević, G., "Mechanical properties of lightweight concrete after fire exposure", *Structural Concrete*, Vol. 17, No. 6, (2016), 1071-1081. <https://doi.org/10.1002/suco.201500145>
5. Poon, C.S., Shui, Z. and Lam, L., "Compressive behavior of fiber reinforced high-performance concrete subjected to elevated temperatures", *Cement and Concrete Research*, Vol. 34, No. 12, (2004), 2215-2222. <https://doi.org/10.1016/j.cemconres.2004.02.011>
6. Wang, H., Wei, M., Wu, Y., Huang, J., Chen, H. and Cheng, B., "Mechanical behavior of steel fiber-reinforced lightweight concrete exposed to high temperatures", *Applied Sciences*, Vol. 11, No. 1, (2020), 116. <https://doi.org/10.3390/app11010116>
7. Mohammadi, Y. and Asilb, M.B., "Utilization of steel micro-fiber and carbon nanotubes in self-compacting lightweight concrete", *International Journal of Engineering, Transactions B: Applications*, Vol. 36, No. 5, (2023), 955-964. <https://doi.org/10.5829/ije.2023.36.05b.12>
8. Goaiz, H.A., Jabir, H.A., Abdulrehman, M.A. and Al-Gasham, T., "Evaluation of lightweight concrete core test including steel bars", *International Journal of Engineering, Transactions C: Aspects*, Vol. 36, No. 6, (2023), 1121-1128. <https://doi.org/10.5829/ije.2023.36.06c.10>
9. Mohammed, T. and Kadhim, H., "Static and dynamic behavior of high-strength lightweight reinforced concrete one-way ribbed slabs", *International Journal of Engineering, Transactions A: Basics*, Vol. 35, No. 4, (2022), 732-739. <https://doi.org/10.5829/ije.2022.35.04A.13>
10. Varghese, A., Anand, N. and Arulraj, P., "Influence of fiber on shear behavior of concrete exposed to elevated temperature", *International Journal of Engineering, Transactions A: Basics*, Vol. 33, No. 10, (2020), 1897-1903. <https://doi.org/10.5829/ije.2020.33.10a.08>
11. Grabois, T.M., Cordeiro, G.C. and Toledo Filho, R.D., "Fresh and hardened-state properties of self-compacting lightweight concrete reinforced with steel fibers", *Construction and Building Materials*, Vol. 104, (2016), 284-292. <https://doi.org/10.1016/j.conbuildmat.2015.12.060>
12. Balandran, R., Zhou, F., Nadeem, A. and Leung, A., "Influence of steel fibres on strength and ductility of normal and lightweight high strength concrete", *Building and Environment*, Vol. 37, No. 12, (2002), 1361-1367. [https://doi.org/10.1016/S0360-1323\(01\)00109-3](https://doi.org/10.1016/S0360-1323(01)00109-3)
13. Almasabha, G., Murad, Y., Alghossoon, A., Saleh, E. and Tarawneh, A., "Sustainability of using steel fibers in reinforced concrete deep beams without stirrups", *Sustainability*, Vol. 15, No. 6, (2023), 4721. <https://doi.org/10.3390/su15064721>
14. Düğenci, O., Haktanır, T. and Altun, F., "Experimental research for the effect of high temperature on the mechanical properties of steel fiber-reinforced concrete", *Construction and Building Materials*, Vol. 75, (2015), 82-88. <https://doi.org/10.1016/j.conbuildmat.2014.11.005>
15. Lau, A. and Anson, M., "Effect of high temperatures on high performance steel fibre reinforced concrete", *Cement and Concrete Research*, Vol. 36, No. 9, (2006), 1698-1707. <https://doi.org/10.1016/j.cemconres.2006.03.024>
16. Ali, A.A., Al-Attar, T.S. and Abbas, W.A., "A statistical model to predict the strength development of geopolymer concrete based on SiO₂/Al₂O₃ ratio variation", *Civil Engineering Journal*, Vol. 8, No. 3, (2022), 454-471. <https://doi.org/10.28991/CEJ-2022-08-03-0>
17. Balamuralikrishnan, R. and Saravanan, J., "Effect of addition of alcocofine on the compressive strength of cement mortar cubes", *Emerging Science Journal*, Vol. 5, No. 2, (2021), 155-170. <https://doi.org/10.1016/j.cscm.2023.e01968>

18. Bastami, M., Baghbadrani, M. and Aslani, F., "Performance of nano-silica modified high strength concrete at elevated temperatures", *Construction and Building Materials*, Vol. 68, (2014), 402-408. <http://dx.doi.org/10.1016/j.conbuildmat.2014.06.026>
19. Horszczaruk, E., Sikora, P., Cendrowski, K. and Mijowska, E., "The effect of elevated temperature on the properties of cement mortars containing nanosilica and heavyweight aggregates", *Construction and Building Materials*, Vol. 137, (2017), 420-431. <https://doi.org/10.1016/j.conbuildmat.2017.02.003>
20. Brzozowski, P., Strzałkowski, J., Rychtowski, P., Wróbel, R., Tryba, B. and Horszczaruk, E., "Effect of nano-SiO₂ on the microstructure and mechanical properties of concrete under high temperature conditions", *Materials*, Vol. 15, No. 1, (2021), 166. <https://doi.org/10.3390/ma15010166>
21. Beigi, M.H., Berenjian, J., Omran, O.L., Nik, A.S. and Nikbin, I.M., "An experimental survey on combined effects of fibers and nanosilica on the mechanical, rheological, and durability properties of self-compacting concrete", *Materials & Design*, Vol. 50, (2013), 1019-1029. <https://doi.org/10.1016/j.matdes.2013.03.046>
22. Yu, R., Spiesz, P. and Brouwers, H., "Effect of nano-silica on the hydration and microstructure development of ultra-high performance concrete (UHPC) with a low binder amount", *Construction and Building Materials*, Vol. 65, (2014), 140-150. <https://doi.org/10.1016/j.conbuildmat.2014.04.063>
23. Mohamed, A.M., "Influence of nano materials on flexural behavior and compressive strength of concrete", *HBRC Journal*, Vol. 12, No. 2, (2016), 212-225. <https://doi.org/10.1016/j.hbrcj.2014.11.006>
24. Wang, X., Huang, Y., Wu, G., Fang, C., Li, D., Han, N. and Xing, F., "Effect of nano-SiO₂ on strength, shrinkage and cracking sensitivity of lightweight aggregate concrete", *Construction and Building Materials*, Vol. 175, (2018), 115-125. <https://doi.org/10.1016/j.conbuildmat.2018.04.113>
25. Ahmadi, S., Honarbakhsh, A., Zhiani, R. and Tavakoli, D., "Effects of kcc-1/ag nanoparticles on the mechanical properties of concrete", *International Journal of Engineering, Transactions A: Basics*, Vol. 35, No. 7, (2022), 1388-1397. <https://doi.org/10.5829/ije.2022.35.07a.17>
26. Concreate, A., "Standard specification for lightweight aggregates for structural concrete", ASTM International, (2017).
27. C33, A., "Astm C33 standard specifications for concrete aggregates", ASTM Standard Book, (2003).
28. Elvin, G., *Nanotechnology for green building, green technology forum*, (2007).
29. Carnovale, D.J., "Behaviour and analysis of steel and macro-synthetic fibre reinforced concrete subjected to reversed cyclic loading: A pilot investigation", University of Toronto Toronto, ON, Canada, (2013),
30. INSTITUTE, A.C., *Aci 213r-14: Guide for structural lightweight-aggregate concrete*. 2014, Farmington Hills.
31. Bamonte, P., Gambarova, P.G. and Meda, A., "Today's concretes exposed to fire—test results and sectional analysis", *Structural Concrete*, Vol. 9, No. 1, (2008), 19-29. <http://dx.doi.org/10.1680/stco.2008.9.1.19>
32. ASTM, C., "Astm c39: Standard test method for compressive strength of cylindrical concrete specimens", ASTM international West Conshohocken, PA, USA, (2001). <https://www.admet.com/testing-applications/testing-standards/astm-c39-concrete-cylinder-compression-testing/>
33. Concrete, A.I.C.C.o. and Aggregates, C., "Standard test method for static modulus of elasticity and poisson's ratio of concrete in compression1, Astm international, (2014).
34. Astm, A., "C617/c617m 15—standard practice for capping cylindrical concrete specimens", ASTM American Society for Testing and Materials—Committee C09 on Concrete and Concrete Aggregates—Subcommittee C, Vol. 9, (2015).
35. Haruehansapong, S., Pulngern, T. and Chucheepsakul, S., "Effect of the particle size of nanosilica on the compressive strength and the optimum replacement content of cement mortar containing nano- SiO₂", *Construction and Building Materials*, Vol. 50, (2014), 471-477. <https://doi.org/10.1016/j.conbuildmat.2013.10.002>
36. Voutetaki, M.E., Naoum, M.C., Papadopoulos, N.A. and Chalioris, C.E., "Cracking diagnosis in fiber-reinforced concrete with synthetic fibers using piezoelectric transducers", *Fibers*, Vol. 10, No. 1, (2022), 5. <https://doi.org/10.3390/fib10010005>
37. Sobolev, K. and Ferrara, M., "How nanotechnology can change the concrete word-part 1", *Am Ceram Bull*, Vol. 84, No. 10, (2005), 15-17. <http://dx.doi.org/10.1002/9780470588260.ch16>
38. Huang, R., Li, S., Meng, L., Jiang, D. and Li, P., "Coupled effect of temperature and strain rate on mechanical properties of steel fiber-reinforced concrete", *International Journal of Concrete Structures and Materials*, Vol. 14, No., (2020), 1-15. <http://dx.doi.org/10.1186/s40069-020-00423-y>
39. Standard, B., "Testing hardened concrete", Compressive Strength of Test Specimens, BS EN, (2009), 12390-12393.

COPYRIGHTS

©2023 The author(s). This is an open access article distributed under the terms of the Creative Commons Attribution (CC BY 4.0), which permits unrestricted use, distribution, and reproduction in any medium, as long as the original authors and source are cited. No permission is required from the authors or the publishers.

**Persian Abstract**

پژوهش

هدف اولیه در طراحی مهندسی ساختمان، کاهش وزن سازه و افزایش مقاومت آن در برابر آتش سوزی و زلزله است زیرا در سازه‌ها، آتش سوزی اجتناب ناپذیر است. در این مقاله از بتن سبک به دلیل مزایای ویژه آن بخصوص کاهش وزن و افزایش مقاومت در دماهای بالا به دلیل خاصیت عایق حرارتی آن استفاده شده است. همچنین با افزودن نانو سیلیس یا الیاف فلزی یا هر دو به بتن سبک، به بررسی رفتار بتن سبک پرداخته شده است. برای این منظور در چهار دسته کلی طرح اختلاط بتن ارائه شده است: نمونه‌های بدون الیاف و نانو سیلیس، نمونه‌هایی با درصدهای مختلف نانو سیلیس و نمونه‌هایی با درصدهای مختلف الیاف فلزی و نمونه‌هایی با الیاف و نانو سیلیس با هم. نتایج نشان داد که در دماهای بالا به نمونه‌های بدون نانو سیلیس و الیاف فلزی آسیب وارد شده است. تغییر رنگ، کاهش مقاومت فشاری و کاهش وزن نمونه‌ها بدلیل آسیب بتن در دماهای بالا بوده است. با افزودن نانو سیلیس و الیاف فلزی، خواص بتن را در تمام دماها بهبود یافته است، زیرا واکنش پوزولانی نانو سیلیس، ساختار بتن را بهبود می‌بخشد و الیاف فلزی از ایجاد ترک در بتن جلوگیری می‌کند. این مطالعه همچنین به بررسی تاثیر تغییر ابعاد نمونه‌ها بر روی مقاومت فشاری پرداخته است و نتایج نشان دهنده افزایش مقاومت نمونه‌های با اندازه کوچکتر است.



Process Parameter Optimization of 3D-Printer Machine Using Response Surface Method for Printing Hydroxyapatite/Collagen Composite Slurry

N. Nurbaiti^{a,b}, A. E. Tontowi^{*a}, M. G. Widyastuti^c, H. V. Hoten^{a,b}, F. Ibrahim^a, N. Muna^a, R. Febrian^a, D. P. Perkasa^d, M. K. Herliansyah^a

^a Mechanical and Industrial Engineering Department, Universitas Gadjah Mada, Yogyakarta, Indonesia

^b Mechanical Engineering Department, Bengkulu University, Indonesia

^c Oral and Maxillofacial Surgery Department Gadjah Mada, Yogyakarta, Indonesia

^d National Nuclear Energy Agency, Indonesia

PAPER INFO

Paper history:

Received 05 May 2023

Received in revised form 11 July 2023

Accepted 12 July 2023

Keywords:

Hydroxyapatite

Collagen

Slurry

3D Printer

Optimum Parameter

Printability

ABSTRACT

Nowadays, various 3D-Printer technologies are commercially available. However, those printers could only be used for a certain material provided by the printer manufacturers. For new material, the commercial printer could not be employed directly and needs to be modified and its printing parameter has to be optimized to fit the property of the new material. This paper aimed to find the optimum parameters (print speed and layer height) based on printability material. The new material that would be developed was a composite of bioceramic powder (hydroxyapatite) and polymer (collagen) in the form of slurry with ratios of 99.84% (w/v) and 0.16% (w/v). While the printer was a commercial 3D-Printer machine with modification on its cartridge container and bracket. The printing parameters were layer height (0.65, 1.0, 1.35 mm) and print speed (14.4, 25, 35.6 mm/min). Optimization of the printing parameter used Response Surface Method (RSM) with 13 sets of specimens. Test specimens for defining printable material were printed in the form of line shape and a rectangular shape for case study. Printability as a responding of the optimum parameter setting was defined on the basis of 5%-maximum dimension error of the printed specimen compared to the 3D-CAD data. Data obtained was analyzed using ANOVA. The results show that the optimum setup printing parameter were 10.009 mm/min for print speed and 0.505 mm for layer height, respectively with the error dimension obtained from the experiment was 0.013 mm² (0.59%) lower than that of the permitted error of 5% (0.125 mm²).

doi: 10.5829/ije.2023.36.11b.02

NOMENCLATURE

ξ_i	Natural Variable	T_L	Target length (mm)
Y	First-order response surface model	W	Width (mm)
β	Intercept	T_w	Target width (mm)
x	Independent variables	H	Height (mm)
ε	Error	T_h	Target height (mm)
L	Length (mm)		

1. INTRODUCTION

Biomaterials have a major impact to improve the quality life of many patients through of functional restorations engineering of body tissues [1]. The requirement of biomaterials are non-carcinogenic nature, non-pyrogenic, non-toxic, absolutely blood compatible, and non-

inflammatory [2]. One of the biomaterials purposes is used for biomedical applications and their condition can interact with live body tissues. Metals, ceramics, composites and polymers are classified as biomaterials [3]. Metals like stainless steel, titanium and magnesium alloys are used for biomaterials. However, they have

*Corresponding Author Email: [\(A. E. Tontowi\)](mailto:alvaedytontowi@ugm.ac.id)

some drawbacks such as toxic ions, inflammatory, allergic reactions, and high modulus [4].

Hydroxyapatite (HA) is one such bioceramic that has bioactive properties [5]. It has, thromboresistance, chemical inertia, and physical characteristics similar to bone. HA has a similar composition to bone minerals and excellent biocompatibility; therefore, widely used as a bone substitute [6–8]. However, synthetic HA is brittle, rigid, has low solubility, and poor processability [9, 10]. Moreover, the biodegradation time of HA is 130 months after implantation [11]. Collagen is a natural polymer providing favorable biological conditions. It stimulates the generation and differentiation of cells as an extracellular matrix [12] but they have poor mechanical properties [13]. Combining bioceramic (HA) and polymer (collagen) will overcome the drawback of them. This composite improves mechanical and biological properties, such as resistance to failure [14–17]. Structure of collagen resembles a rope, triple helix, high strength, and tensile strength [18]. Research and commercial studies of composites HA/collagen began around the 1980's [19].

Additive manufacturing techniques allow the construction of objects point by point, line by line, or layer by layer [20, 21]. There are two basic steps of 3D printing. Firstly the object design via computer software and secondly, the object deposition/ formation via a 3D printer [22]. The International Organization for Standardization (ISO) and American Society for Testing and Materials (ASTM) classify 3D printing technologies into seven different categories, namely binder jetting (BJ), direct energy deposition, material extrusion, Material Jetting, Powder Bed Fusion, Sheet Lamination, and Photopolymerization [4]. Three dimensional printing technology using slurry was explained by Lin et al. [23] and Putlyaev et al. [24]. Lin et al. [23] described using stereolithography and direct ink writing for slurry ceramic. Ceramic slurry for stereolithography should have long-term stability and suitable rheological behavior to enable a smooth flow for printing and homogeneity of the printed part. In terms of viscosity, the slurry has to be ideally comparable to the resin (<3000 mPa·s). In contrast, Direct Ink Writing (DIW) is more economical and faster, including fabrication, drying, and sintering. However, the challenge is after the extrusion process such as crack happens.

Putlyaev et al.[24] produced bioceramic scaffolds using stereolithographic 3D printing of light-cured slurries containing a mixed calcium sodium phosphate $\text{Ca}_{2.5}\text{Na}(\text{PO}_4)_2$ composition. Extrusion-based bioprinting is 3D printing that is widely used to print organs. This is related to rheological properties [25].

The science that studies the deformation and flow of materials is called rheology [26]. Material rheology is related to cell behavior. It correlates between particle mobility and cell speed across length scales [27].

Characterization of rheology is important to the design of concentrated dispersions of ceramic particles (also called slurries). Furthermore, the rheological properties of these viscoelastic fluids determine in which ways these formulations can be utilized or further processed. However, in the biomaterials research field, the rheology of ceramic formulations is often treated neglectfully thought of the complexities involved [28].

Design of experiment (DoE) as a collection of data is adopted by RSM [29]. RSM was introduced by Box and Wilson in 1951 [30, 31]. It is useful not only in the engineering sector but also in a variety of other fields [32]. It is the best combination of mathematical and statistical techniques for non-linear relationships among multi-objective inputs, their response, and to predict multivariant optimization. It is necessary because the sample point must be chosen to create a credible model with the fewest feasible tests [33, 34].

The main advantage of RSM is the decreased required number of experimental runs in predicting the optimum state compared to other optimizing techniques and avail a systematic, satisfactory result compared to the one-factor model [32, 35–37]. It is principally based on the fit of practical equations on experimental data determined from the given design [38]. It employs linear and polynomial equations (quadratic, cubic, or higher-order functions). RSM offers a unique capability for developing an empirical link between factor variables and experimental design procedure responses [39].

The purpose of this research was to get the printability and optimum parameter process of 3D-printer machine using response surface method for printing (HA/collagen) composite slurry.

2. METHODS

2. 1. Materials HA 04238 type (density 1.0 g/cm³, molecular weight 502.31 g/mol, density 1.0 g/cm³ at 20 °C) was purchased from Sigma Aldrich and collagen which is synthesis from mackerel (Scomberomous SP) skin that was used as raw materials. Characterization of collagen with amino acid analysis using High Performance Liquid Chromatography (HPLC) with Thermo Dionex UltiMate 3000 in the Organic Chemistry Laboratory, Faculty of Mathematics and Natural Sciences, Universitas Gadjah Mada. The concentrations of the amino acids of the collagen (in ppm) are aspartic acid 41.68, glutamicacid 71.28, serine 22.47, glycine 103.93, threonine 19.61, arginine 65.05, alanine 62.44, tyrosine 12.20, methionine 10.80, valine 18.44, phenylalan in 21.16, ileucine 13.60, leucine 21.83, and lysine 34.95. The solvents used acetic acid (glacial 100%) to dissolve (HA/collagen) composite and Sodium Hydroxide to balance pH, which was purchased from Sigma Aldrich.

2. 2. Material Preparation

Preparation of (HA/collagen) composite slurry collagen was carried out by dissolving collagen in acetic acid solution ($\text{pH}=2$) at low concentration of 0.2% (w/v) and stirring for 30 minutes. HA powder was mixed gradually into the collagen solution with ratio of 99.84% (w/v) and 0.16% (w/v). During mixing, stirring using magnetic stirrer was carried out for the first step from 250 rpm to 800 rpm and stirring was continued by hand stirring to form slurry composite. To adjust pH, Sodium Hydroxide 0.4 M ($\text{pH}=14$) was used. The slurry composite was kept at room temperature.

2. 3. 3D-Bioprinter System

A modified 3D-Bioprinter was used for printing specimens. This 3D printer machine was a commercial machine (Eazao Zero type, Qingdao Eazao Intelligent Technology Co., Ltd., China) (Figure 1). Modification has been carried out on the cartridge container and bracket in order to fit to the limited use of slurry composite materials. The nozzle was a hollow needle with diameter of 1.5 mm.

2. 4. Specimen Preparation

Two types of printed specimens were used in this research. First was specimens in the form of a line shape for defining printable material and second was a rectangular shape for a case study. The dimensions of line were 20 mm long x 1.5 mm wide x 1.5 mm height. While, the dimensions of rectangular shape were 20 mm long x 20 mm wide x 5 mm height. The height of the rectangular specimen was composed by several layer of line. The dimensions of printing line and rectangular specimen are shown in Figure 2. All specimens were printed following the Design of Experiment.

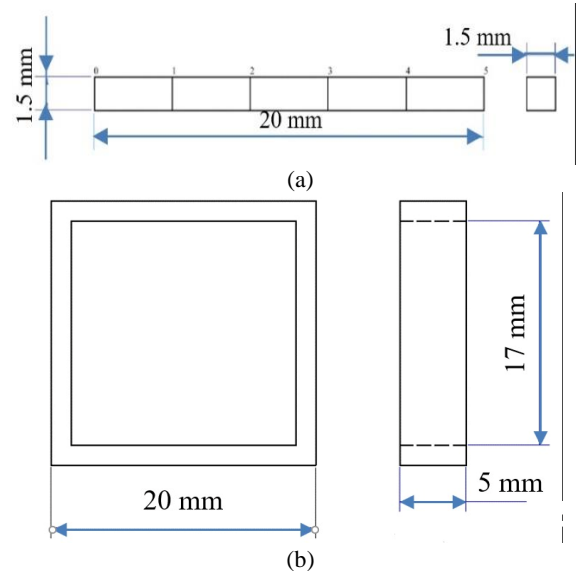


Figure 2. The dimensions of specimens (a) line (b) rectangular

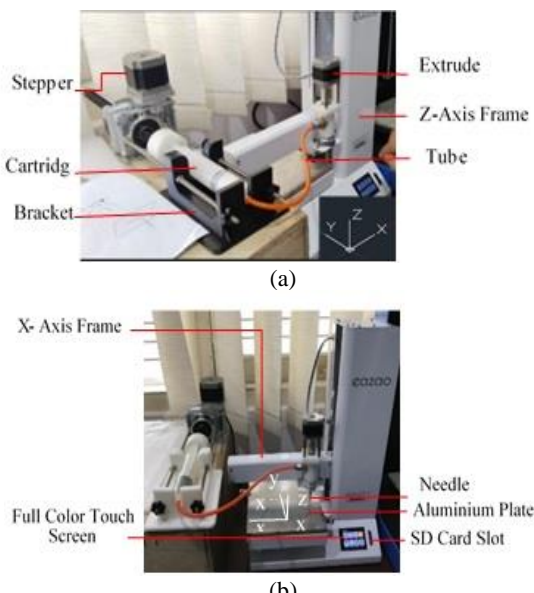


Figure 1. (a) and (b) 3D bioprinter based on slurry extrusion

The printing process begins with leveling of the aluminium table plate of the machine. The gap between upper surface of the table and edge of nozzle/needle was set up of 0.1mm. Next, the slurry was transferred from the mixing container into the cartridge using a micro spatula and ready for printing. On the touch screen, select the back putter (out) menu. In this, piston within the cartridge will push the slurry material into the plastic air tubing, enter to the extruder and the material comes out through the needle. Select the file of specimen that has been prepared and press the print menu. The percentage of composite slurry material was 1% (in the range of 1%-10%). Data of printed specimens was gathered by measuring dimension of specimen using a MiViewCap microscope.

2. 5. Printability and Optimization Method

Optimization of printing parameter process is important for obtaining printability. For the 3D bioprinter there are five printing parameter process including ambient temperature, nozzle diameter, flow rate, print speed, and layer height. The ambient temperature was set up at room temperature and diameter nozzle is 1.5 mm. The flow rate of the slurry from the nozzle was $10 \text{ mm}^3/\text{s}$. In this study only print speed and layer height were optimized as printing process parameters. While, the ambient temperature, nozzle diameter and flow rate were set up as fixed value. To determine the optimum parameters, each parameter had to be set into three levels and two factors as described in Table 1. The two factors include A: Print Speed (mm/min) and B: layer height (mm) with coded levels high (+1), low (-1), and center points (0). The actual values of the print speed representing levels were 14.4, 25, and 35.6 mm/min. While, the layer height

TABLE 1. Factor and level used based on the standard in the Eazao Zero machine

Factor	Level		
	-1	0	+1
A: Print Speed (mm/min)	14.4	25	35.6
B: Layer Height (mm)	0.65	1	1.35

representing levels were 0.65, 1, 1.35 mm. These values were taken from the data sheet specification of Eazao Zero machine. The print speed was between 10 - 40 mm/min. While the layer height was between 0.5 - 1.5 mm.

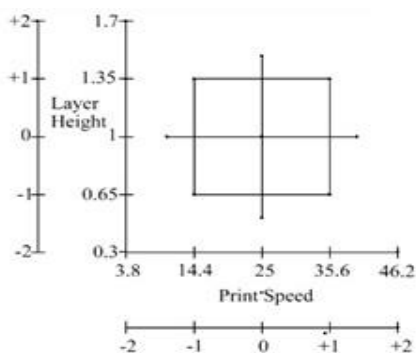
The range of each level was obtained through the Coded Value Equation [40]. The equation of coded value is as Equation (1):

$$x_i = \frac{\xi_i - \frac{(high+low)}{2}}{\frac{(high-low)}{2}} \quad (1)$$

In this study, there are two factors so it uses the central composite design that is shown in Figure 3.

Figure 3 shows 2^2 designs with four axial runs. The maximum and minimum values of the print speed are 35.6 mm/s and 14.4 mm/s while the layer height are 1.35 mm and 0.65 mm.

Based on the Central Composite Design (2 levels), 13 observations were obtained as shown in Table 2.

**Figure 3.** Central Composite Design**TABLE 2.** Design of experiment (DoE)

No	Coded Variable		Actual Variable	
	Print Speed	Layer Height	A	B
1	0	0	25	1
2	-1.414	0	10.009	1
3	1.414	0	39.99	1
4	0	0	25	1
5	-1	1	14.4	1.35
6	0	0	25	1

7	0	0	25	1
8	-1	-1	14.4	0.65
9	0	-1.414	25	0.505
10	0	0	25	1
11	1	1	35.6	1.35
12	1	-1	35.6	0.65
13	0	1.414	25	1.494

Printability is defined as the ability to form and preserve reproducible using 3D printing from bioink material [41]. The printability test is carried out by printing line with 3D bioprinter based on slurry extrusion. The DoE was used for the dimensional error test. Each printed product from each parameter will be separated into 5 areas in the X, Y and Z directions. Then these values were compared with the dimension on the CAD drawings. Dimensions measured were in the wet conditions of the specimen. The result was calculated by the sum of multiplication between different dimensions and the target in the form of width and height. Furthermore, the average and percentage of error dimensions were determined. It is printable when it has a dimensional error of no more than 5%.

Optimization was obtained using RSM with Minitab 18 software for getting optimum parameters of the print speed and layer height that are started by doing first-order tests. The RSM regression model is generally quadratic full equation or reduced form [42]. This test is calculated by the following mathematical Equation (2) (RSM equation):

$$Y = \beta_0 + \beta_1 x_1 + \beta_2 x_2 + \beta_{11} x_1^2 + \beta_{22} x_2^2 + \beta_{12} x_1 x_2 + \varepsilon \quad (2)$$

Moreover, a lack of fit test is carried out to identify the type of error that occurred. Data is valid and normally distributed when the p-value is greater than α otherwise data is not valid and not normally distributed when the p-value is less than α . The difference between the proposed model and the experimental data can be calculated using dimensional error and a mathematical model will be obtained. Furthermore, the results will be analyzed using the Analysis of Variance (ANOVA). Finally, the interaction between these parameters will be obtained which shows the optimum results for each interaction. Validation can be carried out by comparing the dimensional error result in RSM based on Equation (2) and the dimensional error from the experiment.

3. RESULTS AND DISCUSSION

Based on the design of the experiment HA/collagen composites were printed using 13 sets of specimens.

Specimens are illustrated in Figure 4. As Figure 4 shows the printability material composite HA/Collagen. Printability and dimensional error from the experiment are shown in Table 3 and Figure 5.

Table 3 shows the error dimensions for 13 sets of specimens from 13 parameters. Parameters 8 and 9 have allowable error limits. Their respective values are 0.104 mm^2 (4.61%) and 0.085 mm^2 (3.76%). In this study, the maximum allowable limit value is 0.1125 mm^2 (5%).

Figure 5 shows the printability of material composite. Parameters 8 and 9 are printable. Parameter 9 is the most printable. Positive value indicates the average surface dimensional error of the five specimen points exceeds the surface dimension size of the CAD drawing. This means that there is deformation that occurs between one layer and the next layer in the wet condition. Conversely, a negative value indicates an error its surface dimension shrinks compared to the CAD drawing surface.

The Analysis of Variance (ANOVA) is tested to determine whether the error occurs systematically or not. After the ANOVA test, the primary effect parameter analysis is carried out, which has the most significant influence. It shows in Table 4.

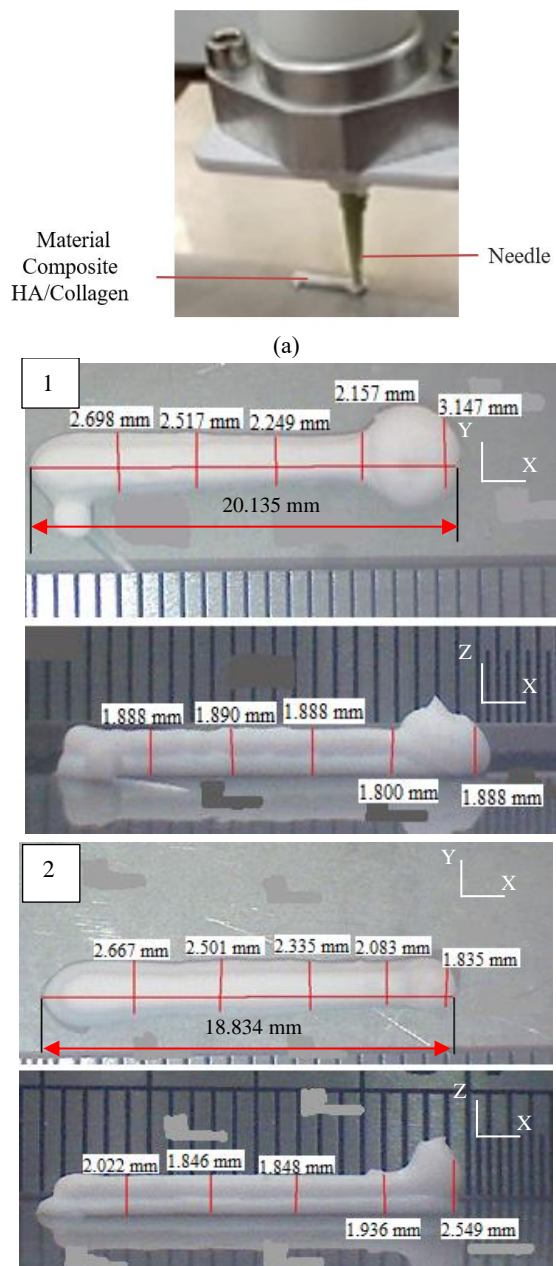
TABLE 3. Dimensional error for 13 sets of specimens

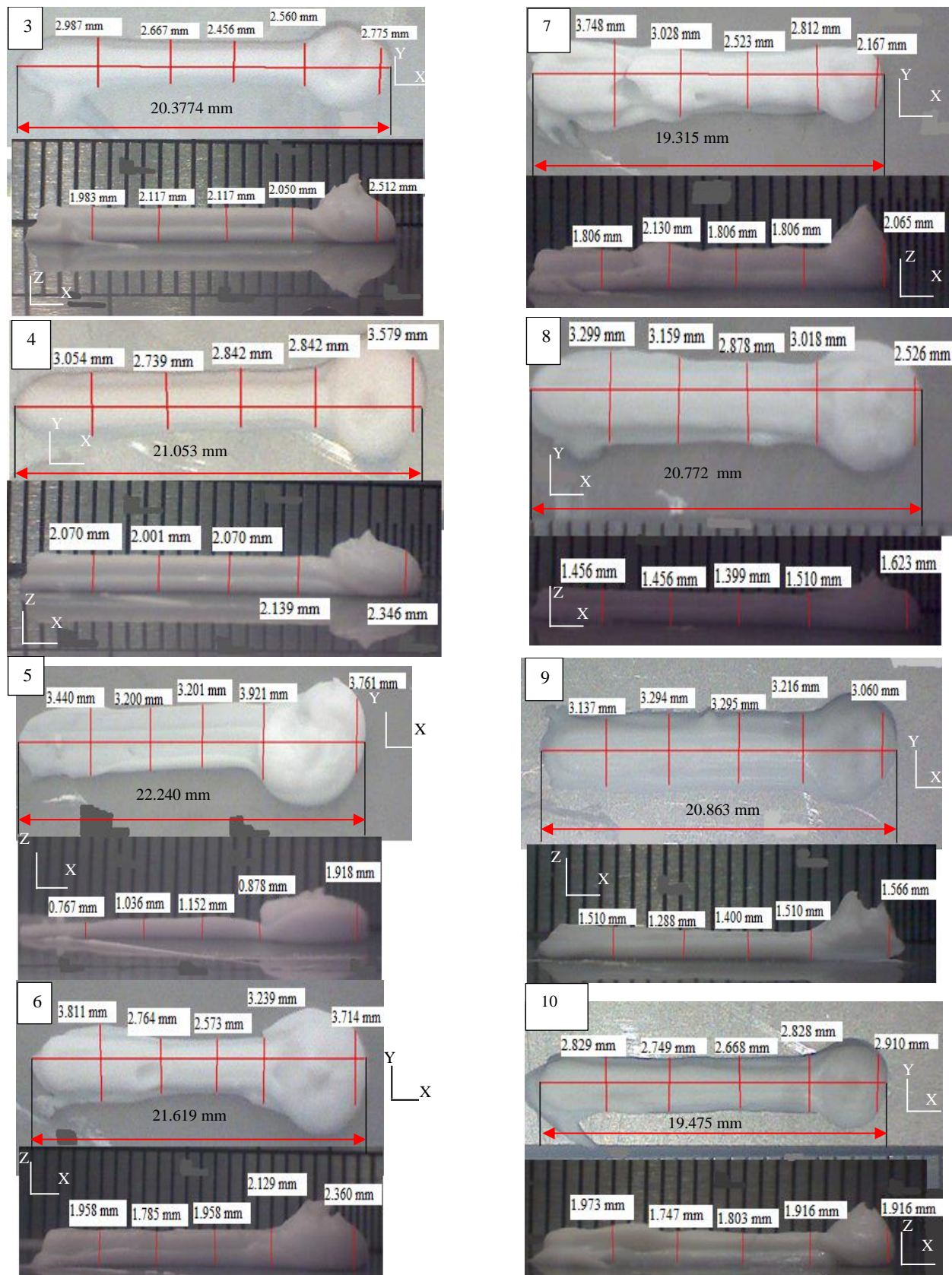
Actual Variable A	Dimensional Error (mm^2) B	The mean of Dimensional error (mm^2)	Percentage of dimensional error (%)	Actual Variable
25	1	1.988	0.398	17.67
10.009	1	1.852	0.370	16.46
39.99	1	3.901	0.780	34.68
25	1	3.845	0.769	34.18
14.4	1.35	-3.262	-0.652	28.99
25	1	4.275	0.855	38.00
25	1	2.742	0.548	24.37
14.4	0.65	-0.519	-0.104	4.61
25	0.505	-0.423	-0.085	3.76
25	1	2.430	0.486	21.60
35.6	1.35	-3.187	-0.637	28.33
35.6	0.65	2.788	0.558	24.79
25	1.494	-1.769	-0.354	15.72

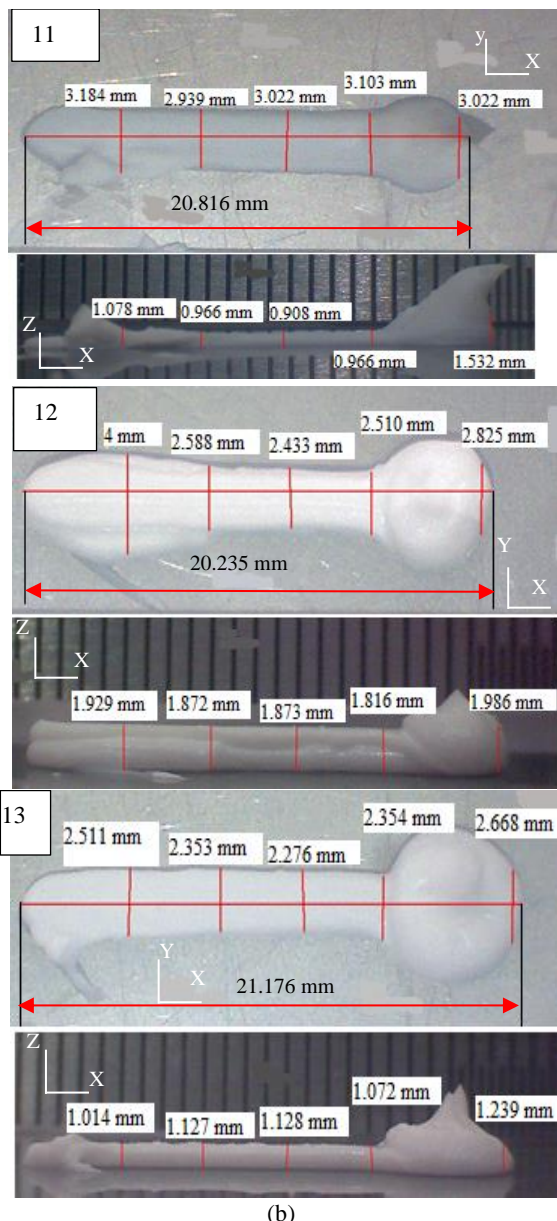
TABLE 4. ANOVA for print speed and layer height

Source	DF	Adj SS	Adj MS	F-Value	P-Value
Model	5	13.151	2.6301	4.18	0.044
Linear	2	6.446	3.223	5.12	0.043
A	1	3.249	3.249	5.16	0.057
B	1	3.196	3.196	5.08	0.059

Square	2	5.348	2.674	4.25	0.062
A ²	1	0.0039	0.0039	0.01	0.939
B ²	1	5.2168	5.2168	8.28	0.024
2-way Interaction	1	1.374	1.374	2.18	0.183
A*B	1	1.374	1.374	2.18	0.183
Error	7	4.408	0.629		
Lack-of-Fit	3	0.668	0.223	0.24	0.866
Pure Error	4	3.739	0.935		
Total	12	17.558			







(b)

Figure 4. (a) 3D printing process. (b) printing for 13 sets of specimens

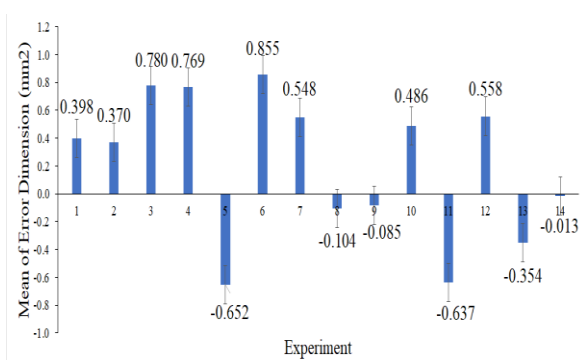


Figure 5. Printability test for 13 sets of specimens

Table 4 shows a lack of fit value of 0.866, which means that it is greater than the α value for the confidence interval 95% ($\alpha=5\%$) so that the model used (which is estimated based on data) is suitable for a relationship between variables. Moreover, the parameter that has a significant effect is the quadratic layer height because it has p-value smaller than the α value. Regarding these interactions, the regression model Equation (3) is obtained.

$$Yg = -7.33 + 0.06A + 16.01B - 7.108B^2 \quad (3)$$

The effect parameters process on response can be presented in a Pareto chart as shown in Figure 6.

Figure 6 shows the effect of layer height quadratically is the most influential dimensional error. The interaction of two same parameters also has an effect. This indicates that the relationship between the parameters and the dimensional error response follows a curved line or is not linear.

Figure 7 shows the effect parameters machine versus error dimension. A linear curve was shown between print speed and dimensional error. It means that print speed increases when the dimensional error increases. Contrarily, the error dimension will decrease if the print speed is lowered. Furthermore, layer height and error dimension form a parabolic curve. Layer height increases then the dimensional error that occurs will increase until it reaches the maximum point (about 1.12 mm). It means that the dimensional error maximum for 13 parameters is 1.12 mm. After that, the dimension error will decrease even though the layer height increased to 1.5 mm.

It is necessary to obtain the optimum value of each of these parameters based on the interaction between them. The surface plot of the interactions between these parameters are illustrated in Figure 8. Moreover, optimum parameter results are shown in Figure 9.

Figure 9 shows the results of the analysis optimum values for the process parameters (print speed and layer height) are 10.009 mm/min and 0.5050 mm, respectively.

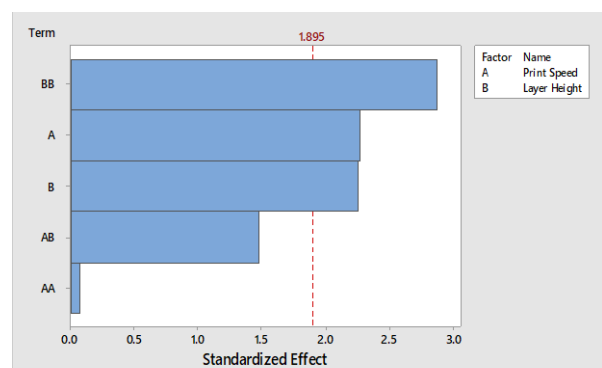


Figure 6. Pareto Chart between Print Speed and Layer Height versus Dimensional Error

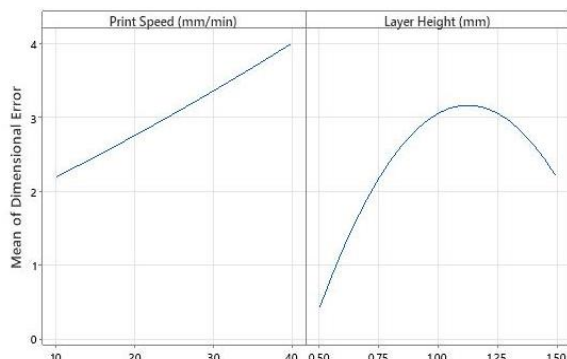


Figure 7. The effect of 3D Printer parameters machine versus error dimension

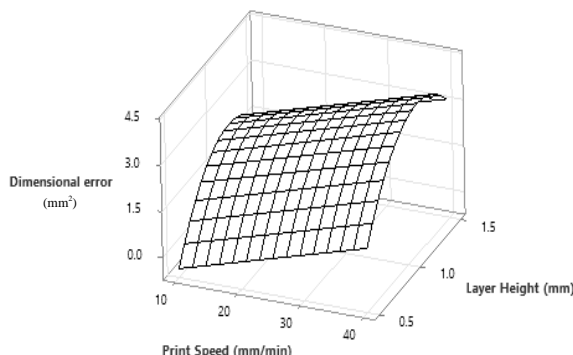


Figure 8. Surface Plot Print Speed and Layer Height versus Dimensional Error

Dimensional error results using these optimum parameters from analysis with a value of -1.5994 mm^2 .

Print composite materials using the optimum parameters is shown in Figure 10 in line.

Figure 10a shows the print results in line product. Figure 10b shows five points with the same scale on the Y and Z axes. The mean dimensional error is 0.013 mm^2 (0.59%). Part product for the case study is shown in Figure 11.

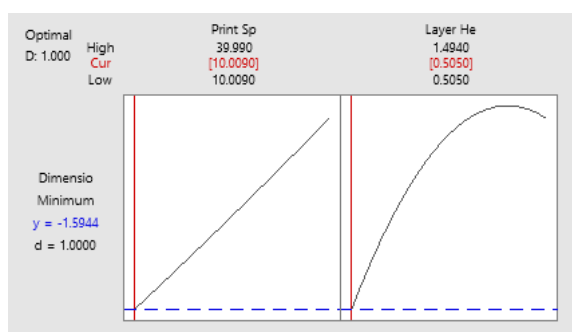


Figure 9. Optimum parameter results

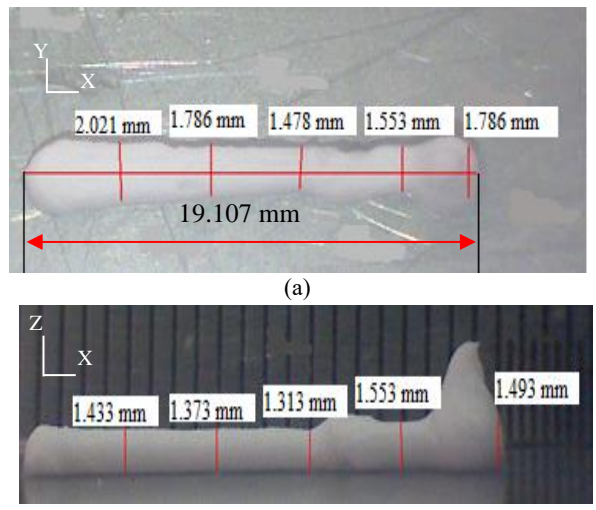


Figure 10. (a) Printing of line product dimension in the Y axis (b) dimension in the Z axis

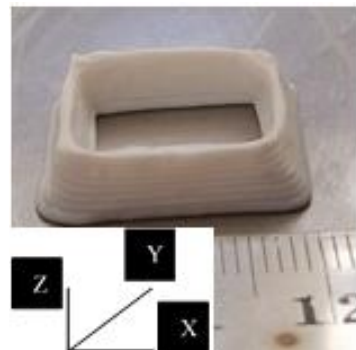


Figure 11. Product using optimum parameters

4. CONCLUSION

Optimum parameter process of 3D printer machine for printing (hydroxyapatite/collagen) composite slurry was successfully obtained. Composite slurry (hydroxyapatite/collagen) was prepared with ratios of 99.84% (w/v) and 0.16% (w/v). The printing process was carried out using commercial machine (3D printer Eazao Zero) with modified cartridge and bracket because composite slurry is used in limited quantities. There are two parameters used in this study namely print speed and layer height with 13 set specimens. The optimum process parameter values for print speed and layer height were 10.009 mm/min and 0.505 mm, respectively. Furthermore, the printability test shows a dimensional error of the optimum parameter of about 0.013 mm^2 (percentage of error dimension 0.59%). Regarding the result, it is printable because of the permissible error limit of 5% (0.013 mm^2).

5. ACKNOWLEDGEMENTS

This research was supported by the Department of Mechanical & Industrial Engineering, Faculty of Engineering, Universitas Gadjah Mada. Research Grant 2022.

6. REFERENCES

- Ronoh, K., Mwema, F., Dabees, S., and Sobola, D. "Advances in sustainable grinding of different types of the titanium biomaterials for medical applications: A review." *Biomedical Engineering Advances*, Vol. 4, (2022), 100047. <https://doi.org/10.1016/J.BEA.2022.100047>
- Agarwal, K. M., Singh, P., Mohan, U., Mandal, S., and Bhatia, D. "Comprehensive study related to advancement in biomaterials for medical applications." *Sensors International*, Vol. 1, (2020), 100055. <https://doi.org/10.1016/J.SINTL.2020.100055>
- Ajmal, S., Athar Hashmi, F., and Imran, I. "Recent progress in development and applications of biomaterials." *Materials Today: Proceedings*, Vol. 62, (2022), 385-391. <https://doi.org/10.1016/J.MATPR.2022.04.233>
- Kanwar, S., and Vijayavenkataraman, S. "Design of 3D printed scaffolds for bone tissue engineering: A review." *Bioprinting*, Vol. 24, (2021), e00167. <https://doi.org/10.1016/J.BPRINT.2021.E00167>
- Annur, D., Bayu, F., Supriadi, S., and Suharno, B. "Electrophoretic Deposition of Hydroxyapatite/Chitosan Coating on Porous Titanium for Orthopedic Application." *Evergreen*, Vol. 9, No. 1, (2022), 109-114. <https://doi.org/10.5109/4774222>
- Kumar, M., Ghosh, S., Kumar, V., Sharma, V., and Roy, P. "Tribo-mechanical and biological characterization of PEGDA/bioceramics composites fabricated using stereolithography." *Journal of Manufacturing Processes*, Vol. 77, (2022), 301-312. <https://doi.org/10.1016/J.JMAPRO.2022.03.024>
- Tontowi, A. E., Raharjo, K. P., Sihaloho, R. I., and Baroroh, D. K. "Comparison of design method for making composite of (PMMA/HA/Sericin)." *Materials Science Forum*, Vol. 901 MSF, (2017), 85-90. <https://doi.org/10.4028/www.scientific.net/MSF.901.85>
- Van Hoten, H., Gunawarman, Mulyadi, I. H., Mainil, A. K., Bismantolo, P., and Nurbaiti. "Parameters optimization in manufacturing nanopowder bioceramics of eggshell with pulvrisette 6 machine using taguchi and ANOVA method." *International Journal of Engineering, Transactions A: Basics*, Vol. 31, No. 1, (2018), 45-49. <https://doi.org/10.5829/ije.2018.31.01a.07>
- You, B. C., Meng, C. E., Mohd Nasir, N. F., Mohd Tarmizi, E. Z., Fhan, K. S., Kheng, E. S., Abdul Majid, M. S., and Mohd Jamir, M. R. "Dielectric and biodegradation properties of biodegradable nano-hydroxyapatite/starch bone scaffold." *Journal of Materials Research and Technology*, Vol. 18, (2022), 3215-3226. <https://doi.org/10.1016/J.JMRT.2022.04.014>
- Bhat, S., Uthappa, U. T., Altalhi, T., Jung, H. Y., and Kurkuri, M. D. "Functionalized Porous Hydroxyapatite Scaffolds for Tissue Engineering Applications: A Focused Review." *ACS Biomaterials Science and Engineering*, (2021). <https://doi.org/10.1021/acsbiomaterials.1c00438>
- Ou, M., and Huang, X. "Influence of bone formation by composite scaffolds with different proportions of hydroxyapatite and collagen." *Dental Materials*, Vol. 37, No. 4, (2021), e231-e244. <https://doi.org/10.1016/J.DENTAL.2020.12.006>
- Arahira, T., and Todo, M. "Development of novel collagen scaffolds with different bioceramic particles for bone tissue engineering." *Composites Communications*, Vol. 16, (2019), 30-32. <https://doi.org/10.1016/J.COCO.2019.08.012>
- Ambekar, R. S., and Kandasubramanian, B. "Progress in the Advancement of Porous Biopolymer Scaffold: Tissue Engineering Application." *Industrial and Engineering Chemistry Research*, Vol. 58, No. 16, (2019), 6163-6194. <https://doi.org/10.1021/acs.iecr.8b05334>
- Ramesh, N., Moratti, S. C., and Dias, G. J. "Hydroxyapatite-polymer biocomposites for bone regeneration: A review of current trends." *Journal of Biomedical Materials Research - Part B Applied Biomaterials*, Vol. 106, No. 5, (2018), 2046-2057. <https://doi.org/10.1002/jbm.b.33950>
- Chai, Y., Okuda, M., Otsuka, Y., Ohnuma, K., and Tagaya, M. "Comparison of two fabrication processes for biomimetic collagen/hydroxyapatite hybrids." *Advanced Powder Technology*, Vol. 30, No. 7, (2019), 1419-1423. <https://doi.org/10.1016/J.APT.2019.04.012>
- Mallick, M., Are, R. P., and Babu, A. R. "An overview of collagen/bioceramic and synthetic collagen for bone tissue engineering." *Materialia*, Vol. 22, (2022), 101391. <https://doi.org/10.1016/J.MTLA.2022.101391>
- Nemati, N. H., and Mirhadi, S. M. "Study on Polycaprolactone Coated Hierarchical Meso/Macroporous Titania Scaffolds for Bone Tissue Engineering." *International Journal of Engineering, Transactions A: Basics*, Vol. 35, No. 10, (2022), 1887-1894. <https://doi.org/10.5829/ije.2022.35.10a.08>
- Sharma, S., Rai, V. K., Narang, R. K., and Markandeywar, T. S. "Collagen-based formulations for wound healing: A literature review." *Life Sciences*, Vol. 290, (2022), 120096. <https://doi.org/10.1016/J.LFS.2021.120096>
- Maher, M., Castilho, M., Yue, Z., Glattauer, V., Hughes, T. C., Ramshaw, J. A. M., and Wallace, G. G. "Shaping collagen for engineering hard tissues: Towards a printomics approach." *Acta Biomaterialia*, Vol. 131, (2021), 41-61. <https://doi.org/10.1016/J.ACTBIO.2021.06.035>
- Lamnini, S., Elsayed, H., Lakhdar, Y., Baino, F., Smeacetto, F., and Bernardo, E. "Robocasting of advanced ceramics: ink optimization and protocol to predict the printing parameters - A review." *Helijon*, Vol. 8, No. 9, (2022), e10651. <https://doi.org/10.1016/J.HELIYON.2022.E10651>
- Tagliaferri, S., Panagiotopoulos, A., and Mattevi, C. "Direct ink writing of energy materials." *Materials Advances*, Vol. 2, No. 2, (2021), 540-563. <https://doi.org/10.1039/d0ma00753f>
- Mohammed, A. A., Algahtani, M. S., Ahmad, M. Z., Ahmad, J., and Kotta, S. "3D Printing in medicine: Technology overview and drug delivery applications." *Annals of 3D Printed Medicine*, Vol. 4, (2021), 100037. <https://doi.org/10.1016/j.stlm.2021.100037>
- Lin, K., Sheikh, R., Romanazzo, S., and Iman, R. "3D Printing of Bioceramic Scaffolds — Barriers to the Clinical Translation: From Promise to Reality, and Future Perspectives." *Materials*, Vol. 12, No. 17, (2019), 2660.
- Putlyayev, V. I., Yevdokimov, P. V., Mamonov, S. A., Zorin, V. N., Klimashina, E. S., Rodin, I. A., Safranova, T. V., and Garshev, A. V. "Stereolithographic 3D Printing of Bioceramic Scaffolds of a Given Shape and Architecture for Bone Tissue Regeneration." *Inorganic Materials: Applied Research*, Vol. 10, No. 5, (2019), 1101-1108. <https://doi.org/10.1134/S2075113319050277>
- Zhang, T., Zhao, W., Xiahou, Z., Wang, X., Zhang, K., and Yin, J. "Bioink design for extrusion-based bioprinting." *Applied Materials Today*, Vol. 25, (2021), 101227. <https://doi.org/10.1016/J.APMT.2021.101227>

26. Lu, C., Zhang, Z., Shi, C., Li, N., Jiao, D., and Yuan, Q. "Rheology of alkali-activated materials: A review." *Cement and Concrete Composites*, Vol. 121, (2021), 104061. <https://doi.org/10.1016/J.CEMCONCOMP.2021.104061>
27. McGlynn, J. A., Druggan, K. J., Croland, K. J., and Schultz, K. M. "Human mesenchymal stem cell-engineered length scale dependent rheology of the pericellular region measured with bi-disperse multiple particle tracking microrheology." *Acta Biomaterialia*, Vol. 121, (2021), 405-417. <https://doi.org/10.1016/J.ACTBIO.2020.11.048>
28. Maas, M., Hess, U., and Rezwan, K. "The contribution of rheology for designing hydroxyapatite biomaterials." *Current Opinion in Colloid & Interface Science*, Vol. 19, No. 6, (2014), 585-593. <https://doi.org/10.1016/J.COCLIS.2014.09.002>
29. Ghelich, R., Jahannama, M. R., Abdizadeh, H., Torknik, F. S., and Vaezi, M. R. "Central composite design (CCD)-Response surface methodology (RSM) of effective electrospinning parameters on PVP-B-Hf hybrid nanofibrous composites for synthesis of HfB₂-based composite nanofibers." *Composites Part B: Engineering*, Vol. 166, (2019), 527-541. <https://doi.org/10.1016/J.COMPOSITESB.2019.01.094>
30. Hadiyat, M. A., Sophia, B. M., and Wibowo, B. S. "Response Surface Methodology Using Observational Data: A Systematic Literature Review." *Applied Sciences (Switzerland)*, Vol. 12, No. 20, (2022). <https://doi.org/10.3390/app122010663>
31. Vahdani, M., Ghazavi, M., and Roustaei, M. "Prediction of mechanical properties of frozen soils using response surface method: An optimization approach." *International Journal of Engineering, Transactions A: Basics*, Vol. 33, No. 10, (2020), 1826-1841. <https://doi.org/10.5829/IJE.2020.33.10A.02>
32. Singh, D. K., and Tirkey, J. V. "Modeling and multi-objective optimization of variable air gasification performance parameters using Syzygium cumini biomass by integrating ASPEN Plus with Response surface methodology (RSM)." *International Journal of Hydrogen Energy*, Vol. 46, No. 36, (2021), 18816-18831. <https://doi.org/10.1016/J.IJHYDENE.2021.03.054>
33. Waila, V. C., Sharma, A., and Yusuf, M. "Optimizing the Performance of Solar PV Water Pump by Using Response Surface Methodology." *Evergreen*, Vol. 9, No. 4, (2022), 1151-1159. <https://doi.org/10.5109/6625726>
34. Reddy, S. S., and Reddy, M. A. K. "Optimization of calcined bentonite caly utilization in cement mortar using response surface methodology." *International Journal of Engineering, Transactions A: Basics*, Vol. 34, No. 7, (2021), 1623-1631. <https://doi.org/10.5829/IJE.2021.34.07A.07>
35. Sun, W., Feng, L., Abed, A. M., Sharma, A., and Arsalanloo, A. "Thermoeconomic assessment of a renewable hybrid RO/PEM electrolyzer integrated with Kalina cycle and solar dryer unit using response surface methodology (RSM)." *Energy*, Vol. 260, (2022), 124947. <https://doi.org/10.1016/J.ENERGY.2022.124947>
36. Cao, C., Zhao, Y., Dai, D., Zhang, X., Song, Z., Liu, Q., Liu, G., Gao, Y., Zhang, H., and Zheng, Z. "Simulation analysis and optimization of laser preheating SiC ceramics based on RSM." *International Journal of Thermal Sciences*, Vol. 185, (2023), 108070. <https://doi.org/10.1016/J.IJTHERMALSCI.2022.108070>
37. Karkare, Y. Y., Sathe, V. S., and Chavan, A. R. "RSM-CCD optimized facile and efficient microwave-assisted green synthesis of Aripiprazole intermediate." *Chemical Engineering and Processing - Process Intensification*, Vol. 173, (2022), 108819. <https://doi.org/10.1016/J.CEP.2022.108819>
38. Hosseinpour, M., Soltani, M., Noofeli, A., and Nathwani, J. "An optimization study on heavy oil upgrading in supercritical water through the response surface methodology (RSM)." *Fuel*, Vol. 271, (2020), 117618. <https://doi.org/10.1016/J.FUEL.2020.117618>
39. Isaac, R., and Siddiqui, S. "Sequestration of Ni(II) and Cu(II) using FeSO₄ modified Zea mays husk magnetic biochar: Isotherm, kinetics, thermodynamic studies and RSM." *Journal of Hazardous Materials Advances*, Vol. 8, (2022), 100162. <https://doi.org/10.1016/J.HAZADV.2022.100162>
40. Myer, H. R., Montgomery, C. D., and Anderson-cook, M. C. Response Surface Methodology (Vol. 21). Wiley. Retrieved from <http://journal.um-surabaya.ac.id/index.php/JKM/article/view/2203>
41. Naghieh, S., and Chen, X. "Printability-A key issue in extrusion-based bioprinting." *Journal of Pharmaceutical Analysis*, Vol. 11, No. 5, (2021), 564-579. <https://doi.org/10.1016/j.jpha.2021.02.001>
42. Karimi, Y., Rashahmadi, S., and Hasanzadeh, R. "The effects of newmark method parameters on errors in dynamic extended finite element method using response surface method." *International Journal of Engineering, Transactions A: Basics*, Vol. 31, No. 1, (2018), 50-57. <https://doi.org/10.5829/ije.2018.31.01a.08>

COPYRIGHTS

©2023 The author(s). This is an open access article distributed under the terms of the Creative Commons Attribution (CC BY 4.0), which permits unrestricted use, distribution, and reproduction in any medium, as long as the original authors and source are cited. No permission is required from the authors or the publishers.

**Persian Abstract****چکیده**

امروزه فناوری های مختلف چاپگر سه بعدی به صورت تجاری در دسترس هستند. با این حال، این چاپگرها را فقط می توان برای مواد خاصی که توسط تولیدکنندگان چاپگر ارائه می شد استفاده کرد. برای مواد جدید، چاپگر تجاری را نمی توان مستقیماً به کار گرفت و باید اصلاح شود و پارامتر چاپ آن باید بهینه شود تا با ویژگی ماده جدید مطابقت داشته باشد. هدف این مقاله یافتن پارامترهای بهینه (سرعت چاپ و ارتفاع لایه) بر اساس مواد قابل چاپ است. ماده جدیدی که قرار بود ساخته شود کامپوزیت پودر بیوسرامیک (هیدروکسی آپاتیت) و پلیمر (کلارن) به شکل دوغاب با نسبت های ۹۹.۸۴ (w/v) و ۰.۱۶ (w/v) % بود. در حالی که این چاپگر یک دستگاه چاپگر سه بعدی تجاری بود که در ظرف کارتیج و برآکت آن تغییراتی ایجاد شده بود. پارامترهای چاپ ارتفاع لایه (۰.۶۵، ۱.۰، ۱.۳۵ میلی متر) و سرعت چاپ (۱۴.۴، ۲۵.۶، ۳۵.۶ میلی متر در دقیقه) بود. بهینه سازی پارامتر چاپ با استفاده از روش سطح پاسخ (RSM) با ۱۳ مجموعه نمونه. نمونه های آزمایشی برای تعریف مواد قابل چاپ به شکل خط و به شکل مستطیل برای مطالعه موردنی چاپ شدند. قابلیت چاپ به عنوان پاسخ به تنظیمات پارامتر بهینه بر اساس ۵٪ حداقل خطای ابعاد نمونه چاپ شده در مقایسه با داده های ۳CAD تعریف شد. داده های به دست آمده با استفاده از آنالیز واریانس تجزیه و تحلیل شد. نتایج نشان می دهد که پارامتر چاپ را اندازی بهینه به ترتیب ۱۰۰۰۹ میلی متر در دقیقه برای سرعت چاپ و ۰/۵۰۵۰ میلی متر برای ارتفاع لایه بود که بعد خطای به دست آمده از آزمایش ۰/۱۳ میلی متر مربع (۵۹٪ درصد) کمتر از خطای مجاز درصد بود. (۱۲۵ میلی متر مربع).



Investigation of Shell Side Overall Performance of a Novel Shell-and-Double-Concentric –tube Heat Exchanger with Simple and Perforated Helical Baffles

H. O. Sayevand*, S. Khorshidi, B. Keshavarzian

Mechanical Engineering Department, Bu-Ali Sina University, Hamedan, Iran

PAPER INFO

Paper history:

Received 27 May 2023

Received in revised form 06 August 2023

Accepted 20 August 2023

Keywords:

Heat Exchanger

Shell-and-double-concentric-tube

Perforated

Helical Baffles

A B S T R A C T

In this study, the overall performance of a heat exchanger shell-and-double-concentric-tube with simple and perforated helical baffles is investigated in the shell side of the heat exchanger using ANSYS FLUENT 19.2. A comparison between the shell-side with simple helical baffles of the heat exchanger (SHB-SDCTHEX) and the one with perforated helical baffles (PHB-SDCTHEX) using numerous mass flow rates is carried out. For the perforated helical baffles heat transfer rate Q , thermo-hydraulic performance $Q/\Delta P$ and effectiveness ε are around 26.7%, 55.5% and 26.6% higher than the same parameters for the simple helical baffles of the heat exchanger, respectively. It is also observed that the flow and temperature distribution for the perforated helical baffles are more uniform with higher flow turbulence than the simple helical baffles of the heat exchanger. So, the perforated helical baffles could be a better choice for the designers and manufacturers with respect to the simple helical baffles of the heat exchanger.

doi: 10.5829/ije.2023.36.11b.03

NOMENCLATURE

A	Heat transfer area (m^2)	σ_ε	Prandtl number of ε
c_p	Specific heat ($J/kg.K$)	Γ	Generalized diffusion coefficient
d_2	Inside diameter of inner tube (mm)	ε	Dissipation rate of turbulence (m^2/s^3)
d_1	The outside diameter of inner tube (mm)	ε	effectiveness
D_2	Inside diameter of the outer tube (mm)	Abbreviations	
D_1	Outside diameter of the outer tube (mm)	CFD	Computational fluid dynamics
h	Heat transfer coefficient ($W/m^2.K$)	HE	Heat exchanger
L	Length (m)	STHEX	Shell-and-tube HE
k	Turbulent kinetic energy (m^2/s^2)	SDCTHEX	Shell-and-double-concentric-tube HE
m	Mass flow rate (kg/s)	SHB- SDCTHEX	Shell-and-double-concentric-tube HE with simple helical baffle
M	mesh used	S&T	Shell and tube
N	Number	PHB-SDCTHEX	Shell-and-double-concentric-tube HE with perforated helical baffle
Q	Heat transfer rate (W)	Subscripts	
Δp	Pressure drop (pa)	av	Average
T	Temperature (K)	a	Annulus
ΔT_m	Logarithmic temperature difference (K)	h	Hydraulic
U	Overall heat transfer coefficient ($W/m^2.K$)	inner	Hydraulic
V	Velocity (m/s)	i	Inner
Greek symbol		in	Inlet
μ	Dynamic viscosity ($kg/m.s$)	min	Minimum
v	Kinematic viscosity (m^2/s)	max	Maximum
v_t	Turbulent Kinematic viscosity (m^2/s)	out	Outlet
λ	Thermal conductivity ($W/m.K$)	s	Shell-side
ρ	Density (kg/m^3)	t	Tube-side
σ_k	Prandtl number of k	w	Wall-side

*Corresponding Author Email: h.sayeh@basu.ac.ir (H. O. Sayevand)

1. INTRODUCTION

HEs are one of the principal supplies utilized extensively in chemical industry, steam production, and oil refineries. Among all groups of heat exchangers (HE), the shell and tube (S&T) one has had many applications in heat transfer technology [1-4] and is the most appropriate for higher pressure operations. Many investigations have been engaged to improve S&T HE efficiency and numerous approaches have been adopted for this purpose. One of the most important concerns of the industry has always been increasing heat transfer for various uses, and efforts have been made in this field. For example, the use of porous materials, Induced vibrations, nano-fluids, and nanoparticles in fluid have always been investigated to increase heat transfer in heat exchangers and energy storage systems [5-14]. One of these practical approaches is using various baffles on shell-side to change the flow direction and mix the fluid. So far, researchers have investigated several baffles with diverse formations such as segmental and double segmental baffles [15, 16], ring supports [17], helical baffles [18-27] and rod baffles [28-30] using empirical, numerical and analytical approaches. Hosseinzade et al. [31] investigated the effect of two different fins (longitudinal-tree like) on energy storage using the phase changer method. Using the analytical method can reveal the possible defects in S&T design, but it cannot identify where these faults are [15]. CFD (numerical approach) can conceive the distribution of temperature and fluid flow particularly on the shell-side, which can facilitate estimating the weak points, and so denoting the possible rectifications to be applied for efficiency improvement [15]. In addition, economic efficiency, flow field observation, and time expenditure are some privileges of the numerical approach concerning to the empirical approach [32]. As a result, several numerical investigations have been accomplished on S&T HE. Bougriou and Baadache [33] researched on SDCTHEX. Difference between the SDCTHEX and classical S&T HE is that the S&T HE tube has been replaced by the double concentric tube. As a result of adding the inner tube, the SDCTHEX has a larger heat transfer area than the S&T HE. Subsequently, increasing the area of heat transfer would make the HE more compact for a specific amount of heat transfer. This causes reducing the cost of manufacturing and the dimensions of the device.

Shahril et al. [15] studied the SDCTHEX and S&T HE with segmental baffle and made a comprehensive comparison of both types of the HE. They revealed that a SDCTHEX is equivalent to a S&T HE if the S&T HE is used with two tube passes and one shell, where hot oil flows in the inner tube and shell. In contrast, water flows in the annulus they found that the average of $Q/\Delta P$ parameter for SDCTHEX is around 343% higher than

that of the S&T HE. They realized that apart from their advantages, using the segmental baffles has also some disadvantages as follows: (1) higher pressure drop in shell-side because of abrupt constriction and distension of flow and severity of flow contact with shell wall and baffles, (2) creation of dead spots in the junction of the segmental baffle and the shell resulting in low heat transfer coefficient, (3) They found that the average of $Q/\Delta P$ parameter for SDCTHEX is around 343% higher than that of the S&T HE. In recent years, to crack these weaknesses, rod baffles, deflecting baffles, and disk-and-doughnut baffles have been evolved [1]. But, none of these baffles could eliminate the defects listed above. Instead, baffles with helical shapes could be a suitable option to substitute segmental baffles by avoiding the cons cited above [34].

Finding a suitable design in heat exchangers to increase thermal efficiency along with reducing pressure drop has always been the focus of the industry. Therefore, a lot of research has been done on the types of fins and even their arrangement and this research has always continued. Helical fins are one of the types of fins used in shell-tube heat exchangers in order to increase heat transfer. Nevertheless, helical baffles cannot thoroughly flow the fluid uniformly across the shell-side as this issue can cause a low heat transfer coefficient in some spots of the shell-side. In this study, the perforated helical baffle is provided to resolve this issue. It is made by creating orifices on the simple helical baffle to allow the flow to cross through these orifices. This new type of fin, by affecting the amount of fluid flow turbulence, makes the thermal efficiency and performance of perforated fins much higher than its simple state, and the pressure drop of the fluid flow is also lower. This issue can be very important for the construction of shell and tube heat exchangers. Due to the fact that higher efficiency and smaller dimensions with lower pressure drop will be the result of using this type of fin.

2. DESCRIPTION OF THE SYSTEM

The perspective views of the SHB-SDCTHEX and the PHB-SDCTHEX are depicted in Figure 1. The length of the HE for the shell and tubes is 1270 mm and 1286 mm, respectively. The internal shell diameter is 337 mm with 55 concentric tubes placed inside the shell in a staggered arrangement. For the inner tubes of SHB-SDCTHEX and PHB-SDCTHEX the internal and external diameters are 8 mm and 12 mm, and 20 mm and 24 mm for the outer tubes, respectively. Also, the diameter of the orifices in the perforated helical baffle is 8 mm. The AISI 1042-annealed steel is adopted as the material for the baffles and tubes, by density = 7840 kg/m³, specific heat c_p = 460 J/kg.K and thermal conductivity λ = 50 w/m.K

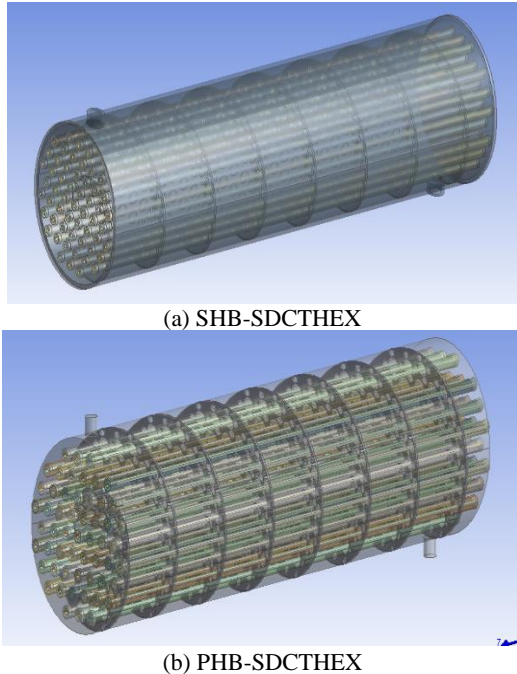


Figure 1. Perspective views of the SHB-SDCTHEX and PHB-SDCTHEX

[20]. The thickness and the section angle for both baffles are 5 mm and 20°, respectively. Also, the working fluids are engine oil and water. Engine oil flows inside the shell and the inner tube as the hot fluid, while water flows inside the annulus as the cold fluid. The properties of the working fluids are described in ANSYS FLUENT 19.2 using the piecewise-linear function of temperature and also can be obtained from literature [35].

3. NUMERICAL ANALYSIS:

3.1. Model Development The equations of the momentum, continuity, energy, k and ε are shown as below. The steady state, incompressible and turbulent flow assumptions are engaged [15]:

Continuity equation:

$$\frac{\partial u_i}{\partial x_i} = 0 \quad (1)$$

Momentum equation:

$$\frac{\partial u_i u_j}{\partial x_i} = -\frac{1}{\rho} \frac{\partial \rho}{\partial x_i} + \frac{\partial}{\partial x_j} ((v + v_t)(\frac{\partial u_j}{\partial x_i} + \frac{\partial u_i}{\partial x_j})) \quad (2)$$

Energy equation:

$$\frac{\partial u_i T}{\partial x_i} = \frac{\partial}{\partial x_i} ((\frac{v}{p_r} + \frac{v_t}{p_{r_t}}) \frac{\partial T}{\partial x_i}) \quad (3)$$

Turbulent kinetic energy k equation:

$$\frac{\partial u_i k}{\partial x_i} = \frac{\partial}{\partial x_i} \left(\left(v + \frac{v_t}{\sigma_k} \right) \frac{\partial k}{\partial x_i} \right) + \Gamma - \varepsilon \quad (4)$$

Turbulent energy dissipation ε equation:

$$\frac{\partial u_i \varepsilon}{\partial x_i} = \frac{\partial}{\partial x_i} \left(\left(v + \frac{v_t}{\sigma_\varepsilon} \right) \frac{\partial \varepsilon}{\partial x_i} \right) - C_2 \frac{\varepsilon^2}{k + \sqrt{v \varepsilon}} \quad (5)$$

where:

$$\Gamma = -\bar{u}_i \bar{u}_j \frac{\partial u_i}{\partial x_j} = v_t (\frac{\partial u_i}{\partial x_j} + \frac{\partial u_j}{\partial x_i}) \frac{\partial u_i}{\partial u_i}, v_t = C_\mu \frac{k^2}{\varepsilon} \quad (6)$$

The $k - \varepsilon$ turbulence model practical constants are: $C_2 = 1.2$, $\sigma_k = 1.0$, $\sigma_\varepsilon = 1.2$. Also, C_μ has a constant value for a high Reynolds number. However, C_μ was considered a function of the strain and rotation rate [36].

3. 2. Boundary Conditions and Numerical Approach

Numerical analysis is accomplished by applying CFD software ANSYS FLUENT 19.2. The working fluids for both samples of the HE SHB-SDCTHEX and PHB-SDCTHEX are engine oil and water. The engine oil flows in the shell and the inner tubes with the same m_s , and water is allocated as working fluid in the annulus.

The boundary conditions are explained for the SHB-SDCTHEX and the PHB-SDCTHEX as follows:

(1) The shell-side inlet:

$$m_s = 20 \text{ (kg/s)}, T_{s,in} = 393 \text{ (°k)}, V_{s,in} = 68.26 \text{ (m/s)}.$$

(2) The inner tube side inlet:

$$m_t = 20 \text{ (kg/s)}, T_{t,in} = 393 \text{ (°k)}.$$

(3) The annulus side inlet:

$$m_a = 10.14 \text{ (kg/s)}, T_{t,in} = 293 \text{ (°k)}.$$

(4) The outlet boundary condition: pressure outlet.

(5) Wall boundary conditions: non-slip boundary, the coupled thermal boundary is applied for the wall of the tubes and baffles. Also, adiabatic condition is used for thermal boundary of the shell wall.

Pressure-based and double-precision solver is used here. For the near wall zone, the realizable $k - \varepsilon$ and scalable wall function is employed for all simulations. The SIMPLE and the second-order-upwind difference scheme are set in the simulations.

Simulations are carried out under the following assumptions:

(1) The fluid properties of the working are constant.

(2) The gravity effect is ignored.

(3) Thermal radiation is negligible.

Data reduction:

Heat transfer balance for the shell and the inner tube is gained:

$$Q_a = Q_s + Q_i \quad (7)$$

where:

$$Q_a = m_a c_{pa} (T_{(a,out)} - T_{(a,in)})$$

$$Q_s = m_s c_{ps} (T_{(s,in)} - T_{(s,out)}) \quad (8)$$

$$Q_i = m_i c_{pi} (T_{(i,in)} - T_{(i,out)})$$

The mean heat transfer rate (Q_{av}) is defined by:

$$Q_{av} = (Q_a + Q_{s,i})/2$$

$$\text{Where } Q_{s,i} = Q_s + Q_i$$

Due to the counter flow of the water in the annulus side, the logarithmic average temperature difference between the shell and the annulus is obtained by:

$$\Delta T_{m_{1,2}} = \frac{(T_{s,in} - T_{a,out}) - (T_{s,out} - T_{a,in})}{\ln \frac{(T_{s,in} - T_{a,out})}{(T_{s,out} - T_{a,in})}} \quad (9)$$

The total heat transfer coefficient from the shell side to the annulus side is obtained by:

$$U_{1,2} = \frac{Q_s}{N_a \pi D_1 L_a F \Delta T_{m_{1,2}}} \quad (10)$$

The convection heat transfer coefficient of the shell side is obtained from:

$$h_s = \frac{1}{\frac{1}{U_{1,2}} - \frac{1}{h D_2} - \frac{D_1}{2 \lambda_a} \ln \frac{D_1}{D_2}} \quad (11)$$

3.3. Validation 3D geometry configurations of the HE were constructed using the Solid Works software. As shown in Figure 2, the computational mesh, by the workbench in ANSYS FLUENT, is generated with an unstructured grid. For grid study of the SHB-SDCTHEX model, five various meshes (M1: 6954315, M2: 11753218, M3: 12853619, M4: 13998340, and M5: 15697562 elements) were considered. In order to choose the best mesh that is favorable for the problem in terms of economy and accuracy of the results, by comparing the pressure drop and the heat transfer coefficient obtained for the meshes. The M4 was considered for further calculations (it should be noted that the residual squared errors for the flow field and pressure is considered 10^{-5} for convergence). Comparing the results obtained in this research with the results of the Bell-Delaware approach described by Shahril et al. [15] is used for the heat transfer coefficient of shell side and the shell side pressure drop for the SHB-SDCTHEX and PHB-SDCTHEX in Figures 3 and 4. The maximum difference

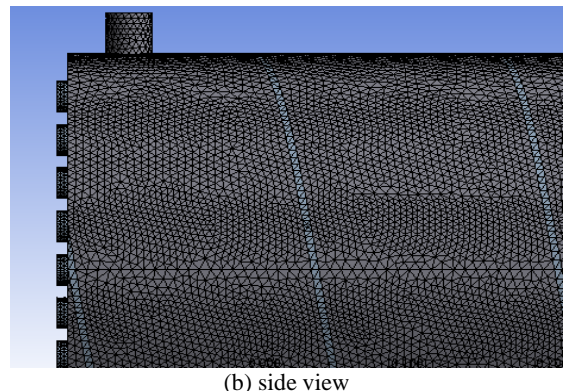
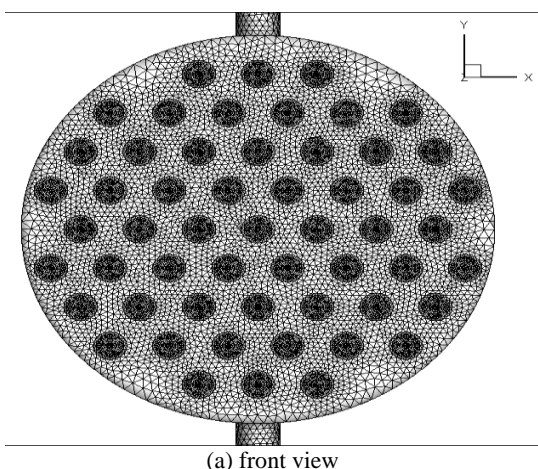


Figure 2. Local Views of the grid system for SHB-SDCTHEX and PHB-SDCTHEX.

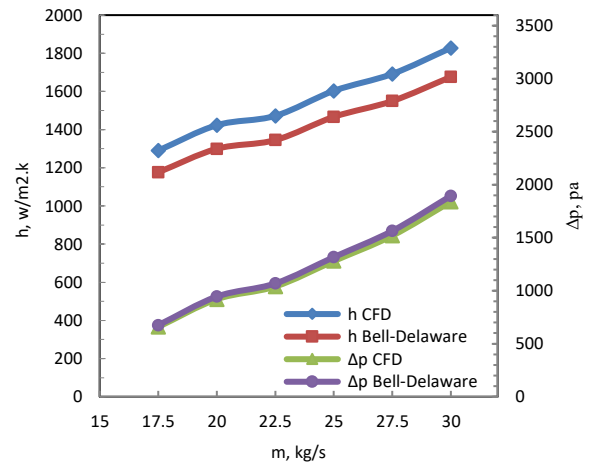


Figure 3. Comparison between the numerical calculations and the Bell-Delaware approach for the shell side of the SHB-SDCTHEX

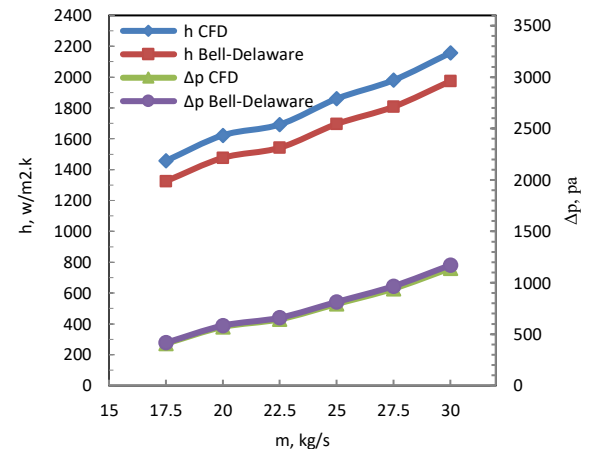


Figure 4. Comparison between the numerical calculations and the Bell-Delaware approach for the shell side of the PHB-SDCTHEX

between the shell side heat transfer coefficient in this study and the Bell-Delaware approach is around 8.6%, and, this difference is about 2.8% for the shell side pressure drop. Similarly, in Figure 4, the maximum deviation for the (PHB-SDCTHEX) is approximately 8.9% and 2.5% for shell side heat transfer coefficient and the shell side pressure drop. With this comparison, it can be said that the results have acceptable accuracy.

4. RESULTS AND DISCUSSION

4. 1. Velocity and Pressure Distributions

Velocity profiles of the shell side of the SHB-SDCTHEX and the PHB-SDCTHEX are illustrated in Figures 5 and 6. Also, the so called active zones (A) and dead zones (D) are determined for both HE. Active zones have higher turbulent flow and velocity magnitude than the dead zones. Figure 5 shows that the helical flow has a higher velocity magnitude in the central zones of the shell side. This is due to the helical baffle and its section angle and dead zones, which are created far from central zones with low velocity magnitude and creates less turbulence and non-uniform flow across the shell in the SHB-SDCTHEX. Figure 6 depicts that dead zones are eliminated in the PHB-SDCTHEX, and the flow is more uniform concerning to the SHB-SDCTHEX. When the flow crosses through the orifices, it becomes more turbulent. Velocity profiles at the inlet zones for the SHB-SDCTHEX and the PHB-SDCTHEX are depicted in Figures 5(b) and 6(b). It can be found that the flow distribution is more stable and uniform at the inlet of the PHB-SDCTHEX compared with the SHB-SDCTHEX. Similarly, velocity distributions at the outlet zones for both models are shown in Figures 5(c) and 6(c). The flow distributions are also stable at the outlet zones. Pressure distributions across the shell side for the SHB-SDCTHEX and the PHB-SDCTHEX are illustrated in Figure 7. Because of the uniform distribution of flow across the shell side, the gradient of pressure for the PHB-SDCTHEX is lower than the pressure gradient for the SHB-SDCTHEX.

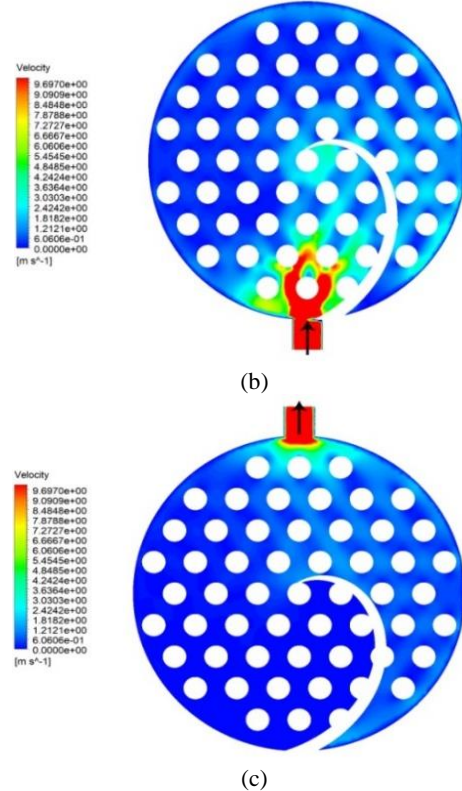
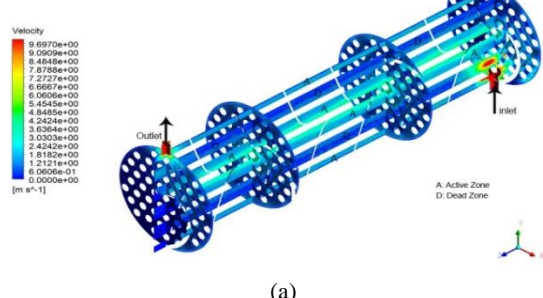
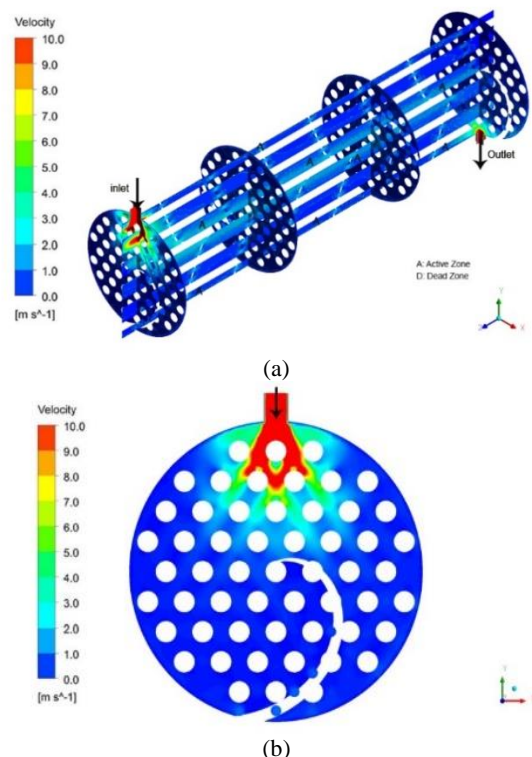


Figure 5. Velocity profiles for the SHB-SDCTHEX: (a) 3D profile (b) inlet zone (c) outlet zone with $m_s = 20$ (kg/s)



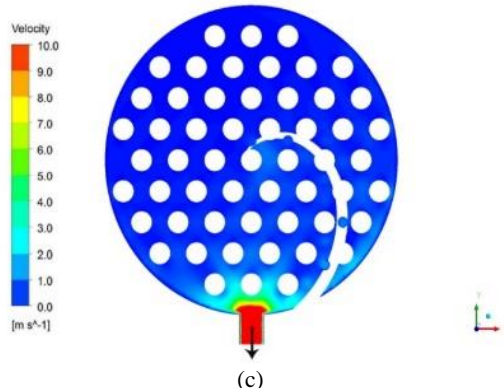


Figure 6. Velocity profiles for the PHB-SDCTHEX: (a) 3D profile (b) inlet zone (c) outlet zone with $m_s = 20$ (kg/s)

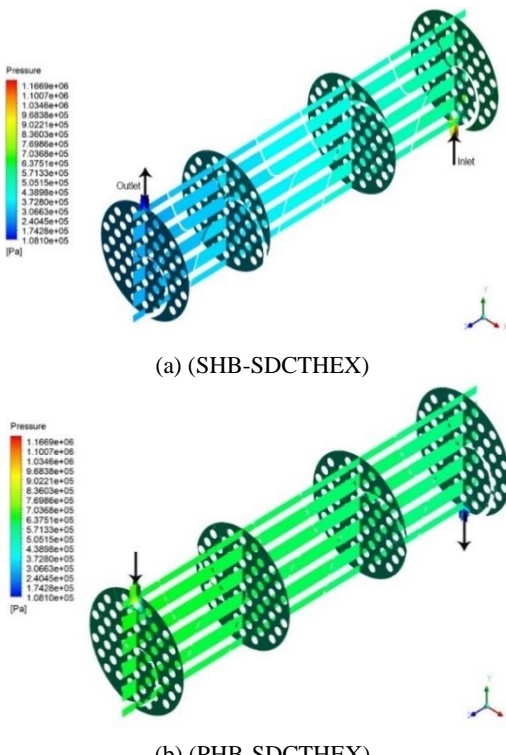


Figure 7. Pressure distributions across the shell side: (a) for the SHB-SDCTHEX and (b) for the PHB-SDCTHEX with $m_s = 20$ (kg/s)

4.2. Temperature Distributions For the SHB-SDCTHEX and the PHB-SDCTHEX in the shell temperature distributions are depicted in Figures 8 and 9 in four various zones. Due to a simple helical baffle, with the same m_s , the outlet and inlet temperature difference on the shell side is 9.9 K and 13 K for the SHB-SDCTHEX and the PHB-SDCTHEX, respectively. As the contours illustrate, active zones (A) have a higher heat transfer coefficient than dead zones (D). The results

also reveal that the local temperature in the dead zones (D) is higher than that for the active zones (A). As can be seen, the temperature distributions of the PHB-SDCTHEX are more uniform with compare to the SHB-SDCTHEX, and temperature drop happens ahead for the PHB-SDCTHEX with respect to the SHB-SDCTHEX.

4.3. Overall Performance Comparison To make a comparison between the performance of the SHB-SDCTHEX and the PHB-SDCTHEX, for various m_s parameters of the heat transfer rate (Q), pressure drop (ΔP), and thermo-hydraulic efficiency ($Q/\Delta P$) are used. Figure 8 shows that the heat transfer rate is enhanced for both models with an increasing mass flow rate (m_s). Increasing the value of m_s increases the amount of the convective heat transfer coefficient (h). Also, the heat transfer rate for PHB-SDCTHEX has increased by about 14.9% compared to SHB-SDCTHEX. In PHB-SDCTHEX the trend of increase of the heat transfer rate is more than that for the SHB-SDCTHEX. This is due to eliminating the dead zones by perforating the simple

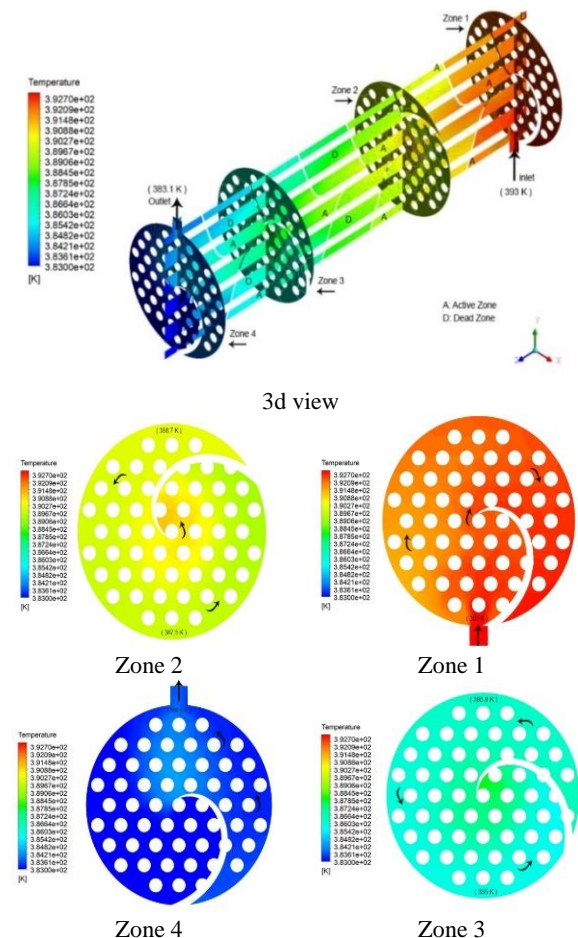


Figure 8. Temperature distribution across the shell side for the (SHB-SDCTHEX) with $m_s = 20$ (kg/s) in various zones

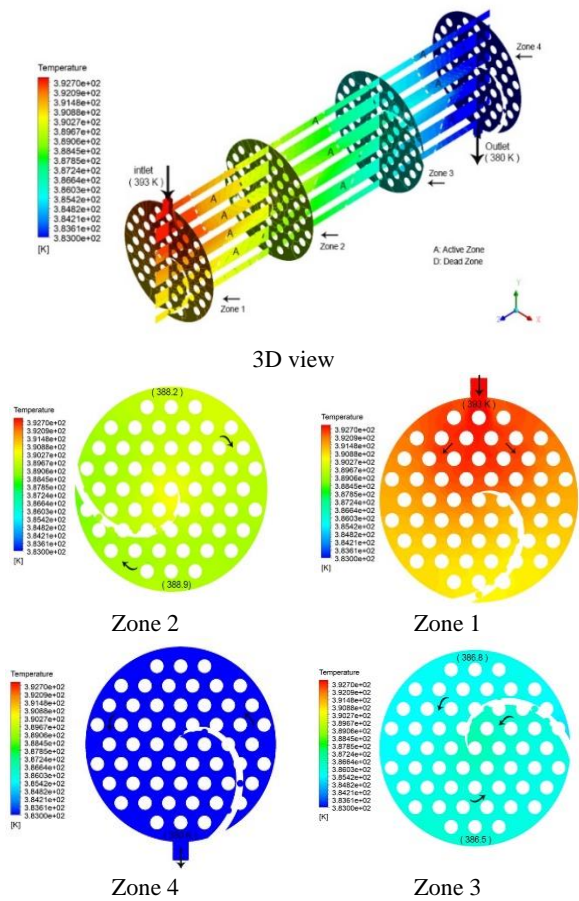


Figure 3. Temperature distribution across the shell side for the (PHB-SDCTHEX) with $m_s = 20$ (kg/s) in various zones

helical baffle. Variations of the pressure drop are depicted in Figure 9. Notably, the pressure drop is an essential parameter from the cost point of view when modeling a S&T HE. The reason is that less pressure drop results in less pumping power and operating costs. Figure 9 indicates that pressure drop for the PHB-SDCTHEX is reduced by around 38.4% compared with the SHB-SDCTHEX. Also, increasing the m_s increases the pressure drop.

According to Figure 9, the growth of pressure drop for the PHB-SDCTHEX is less than that for the SHB-SDCTHEX. For evaluating the efficiency of a HE, the heat transfer rate and the pressure drop cannot be employed independently. Variations of The thermo-hydraulic performance ($Q/\Delta P$) for both models are demonstrated in Figure 10.

It can be noticed from this figure that the ($Q/\Delta P$) for the PHB-SDCTHEX is around 74% more than that of the SHB-SDCTHEX for the same m_s ($m_s = 20$ kg/s). Likewise, the ($Q/\Delta P$) decreases with the increasing m_s . The effectiveness (ε) of a HE is expressed as follows [15]:

$$\varepsilon = \frac{Q_{av}}{Q_{max}} = \frac{Q_{av}}{(mc_p)_{min}(T_{s,in} - T_{a,in})} \quad (12)$$

In Figure 11, the pressure drop in both HEs are compared for different mass flow rates. It can be clearly seen that the pressure drop in both types of HEs increases with an increase in mass flow rate. In all flow rates, the pressure drop in SHB-SDCTHEX is always higher than PHB-SDCTHEX, and with an increase in flow rate, this difference also increases. The thermo-hydraulic performance for different values of mass flow for both HEs is shown in Figure 12. It can be seen that the maximum performance is at lower flow rates, and this parameter will decrease with an increase in flow rate of mass. Also, considering mass flow rates, the thermo-hydraulic performance of PHB-SDCTHEX is always higher than SHB-SDCTHEX, for the same flow rate. Figure 13 shows variation of the effectiveness as a function of m_s .

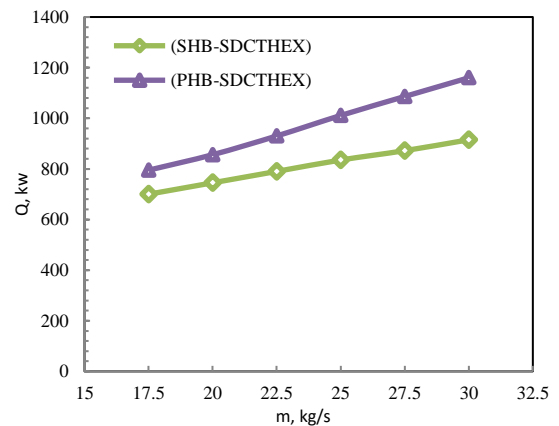


Figure 4. Variations of the heat transfer rate contrast with m_s for SHB-SDCTHEX and PHB-SDCTHEX

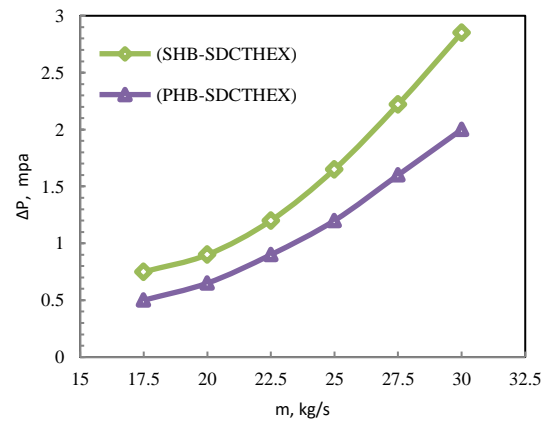


Figure 5. Variations of pressure drop contrast with m_s for SHB-SDCTHEX and PHB-SDCTHEX

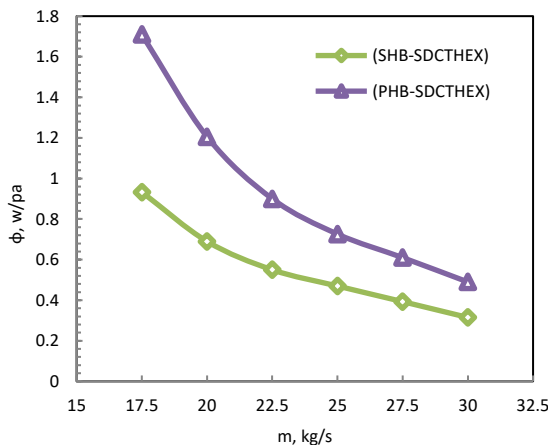


Figure 12. Variations of thermo-hydraulic performance contrast with m_s for SHB-SDCTHEX and PHB-SDCTHEX

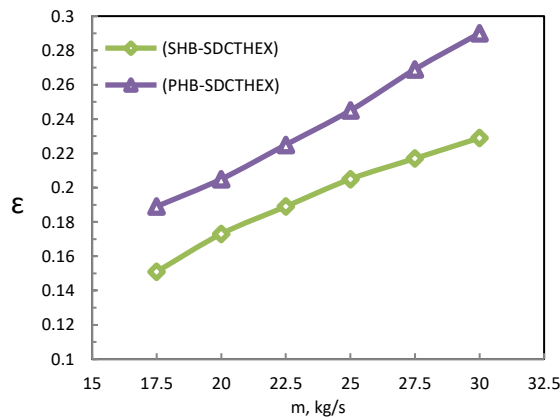


Figure 13. Variations of effectiveness contrast m_s for SHB-SDCTHEX and PHB-SDCTHEX.

Increasing m_s increases the effectiveness. For the PHB-SDCTHEX the effectiveness is around 25% more than that of the SHB-SDCTHEX. Therefore, based on the evaluation of the above parameters, the PHB-SDCTHEX is considered a convenient alternative to the SHB-SDCTHEX.

5. CONCLUSION

In this research, a shell-and-double-concentric-tube HE with a perforated helical baffle PHB-SDCTHEX is compared with a shell-and-double-concentric-tube HE with a simple helical baffle SHB-SDCTHEX using CFD. The pressure drop of the fluid flow in the shell part of this type of heat exchanger will be reduced by using the new fin used, and the heat transfer in this exchanger will significantly increase. This can be considered for the design of new converters with smaller dimensions and higher efficiency. In the following, we can point out the

advantages of the serious fin compared to the simple helical fin in this type of converter as follows:

(1) Using perforated helical baffles makes the flow distribution further uniform and turbulent. Consequently, dead zones are eliminated across the shell side due to the orifices created on the simple helical baffle. It is noted that the existence of the dead zones leads to a higher temperature than other zones on the shell side and less Q happens within the dead zones due to higher temperature.

(2) Q raises for the PHB-SDCTHEX around 14.9% compared with the SHB-SDCTHEX in the same conditions. It is noted that the Q increases with the increasing m_s . Also, the trend of growth of Q for the PHB-SDCTHEX is higher than that for the SHB-SDCTHEX.

(3) ΔP for the PHB-SDCTHEX decreases by about 38.4% compared with the SHB-SDCTHEX for the same m_s ($m_s = 20 \text{ kg/s}$). Also, ΔP increases by increasing the m_s . Notably, the trend of growth of ΔP for the PHB-SDCTHEX is lower than that of the SHB-SDCTHEX.

(4) For comprehensive efficiency, the thermo-hydraulic performance ($Q/\Delta P$) and the effectiveness (ϵ) of the PHB-SDCTHEX are raised by about 74% and 25%, respectively; compared with the SHB-SDCTHEX for the same m_s . Likewise, $(Q/\Delta P)$ is reduced by increasing the m_s . On the other hand, the effectiveness increases by increasing m_s . It should, however, be noted that most deviation of the $(Q/\Delta P)$ and the (ϵ) in both models occurs at the minimum and maximum m_s , respectively.

6. REFERENCES

1. Sivarajan, C., Rajasekaran, B. and Krishnamohan, N., "Comparision of numerical heat transfer in conventional and helically baffled heat exchanger", *IJERA*, Vol. 2, No. 2, (2012), 1278-1282.
2. Asgari Tahery, A., Jafarmadar, S. and Khalil Arya, S., "Hydraulic network modeling to analyze stream flow effectiveness on heat transfer performance of shell and tube heat exchangers", *International Journal of Engineering, Transactions C Aspects*, Vol. 30, No. 6, (2017), 904-911. doi: 10.5829/ije.2017.30.06c.11.
3. Thakur, G., Singh, G., Thakur, M. and Kajla, S., "An experimental study of nanofluids operated shell and tube heat exchanger with air bubble injection", *International Journal of Engineering, Transactions A: Basics*, Vol. 31, No. 1, (2018), 136-143. doi: 10.5829/ije.2018.31.01a.19.
4. Singh, G. and Nandan, A., "Experimental study of heat transfer rate in a shell and tube heat exchanger with air bubble injection", *International Journal of Engineering, Transactions B: Applications*, Vol. 29, No. 8, (2016), 1160-1166. doi: 10.5829/idosi.ije.2016.29.08b.16.
5. Hosseinzadeh, K., Moghaddam, M.E., Hatami, M., Ganji, D. and Ommi, F., "Experimental and numerical study for the effect of aqueous solution on heat transfer characteristics of two phase close thermosyphon", *International Communications in Heat and Mass Transfer*, Vol. 135, (2022), 106129. <https://doi.org/10.1016/j.icheatmasstransfer.2022.106129>

6. Moghaddam, M.E., Abandani, M.H.S., Hosseinzadeh, K., Shafii, M.B. and Ganji, D., "Metal foam and fin implementation into a triple concentric tube heat exchanger over melting evolution", *Theoretical and Applied Mechanics Letters*, Vol. 12, No. 2, (2022), 100332. <https://doi.org/10.1016/j.taml.2022.100332>
7. Hosseinzadeh, K., Moghaddam, M.E., Asadi, A., Mogharrebi, A. and Ganji, D., "Effect of internal fins along with hybrid nano-particles on solid process in star shape triplex latent heat thermal energy storage system by numerical simulation", *Renewable Energy*, Vol. 154, (2020), 497-507. <https://doi.org/10.1016/j.renene.2020.03.054>
8. Hosseinzadeh, K., Mogharrebi, A., Asadi, A., Paikar, M. and Ganji, D., "Effect of fin and hybrid nano-particles on solid process in hexagonal triplex latent heat thermal energy storage system", *Journal of Molecular Liquids*, Vol. 300, (2020), 112347. <https://doi.org/10.1016/j.molliq.2019.112347>
9. Keshavarzian, B. and Sayehvand, H.-O., "Validation of the local thermal equilibrium assumption for free convection boundary layer flow over a horizontal cylinder embedded in an infinite saturated porous medium", *Results in Physics*, Vol. 44, (2023), 106112. doi: 10.1016/j.rinp.2022.106112.
10. Keshavarzian, B. and Khosravi, M., "Numerical investigation of the structural frequencies effects on flow induced vibration and heat transfer", *Journal of Materials and Environmental Science*, Vol. 6, No. 7, (2015), 1949-1956.
11. Keshavarzian, B., Abad, J.M.N., Mir, M., Keshavarzian, M. and Alizadeh, R., "The optimization of natural frequency on the cross flow-induced vibration and heat transfer in a circular cylinder with lstm deep learning model", *Journal of the Taiwan Institute of Chemical Engineers*, (2023), 104969. <https://doi.org/10.1016/j.jtice.2023.104969>
12. Keshavarzian, B. and Sayehvand, H.-O., "Validity of the boundary layer assumptions for natural convection around a cylinder in a porous medium", *Results in Engineering*, Vol. 18, (2023), 101069. doi: 10.1016/j.rineng.2023.101069.
13. Keshavarzian, B. and Sayehvand, H.-o., "The effect of the flow and solid matrix parameters on the nusselt number for free convection over horizontal cylinder by considering the boundary layer and local thermal non-equilibrium model", *Journal of Thermal Analysis and Calorimetry*, (2022), 1-10. doi: 10.1007/s10973-022-11801-x.
14. Mohammadi, M., Hosseinzadeh, K. and Ganji, D.D., "Numerical analysis on the impact of axial grooves on vortex cooling behavior in gas turbine blade's leading edge", *Proceedings of the Institution of Mechanical Engineers, Part E: Journal of Process Mechanical Engineering*, (2023), 09544089231163113. doi: 10.1177/09544089231163113.
15. Shahril, S., Quadir, G., Amin, N. and Badruddin, I.A., "Thermo hydraulic performance analysis of a shell-and-double concentric tube heat exchanger using cfd", *International Journal of Heat and Mass Transfer*, Vol. 105, (2017), 781-798. doi: 10.1016/j.ijheatmasstransfer.2016.10.021.
16. Mukherjee, R., "Effectively design shell-and-tube heat exchangers", *Chemical Engineering Progress*, Vol. 94, No. 2, (1998), 21-37.
17. Xianhe, D. and Songjiu, D., "Investigation of heat transfer enhancement of roughened tube bundles supported by ring or rod supports", *Heat Transfer Engineering*, Vol. 19, No. 2, (1998), 21-27. doi: 10.1080/01457639808939917.
18. Xiao, X., Zhang, L., Li, X., Jiang, B., Yang, X. and Xia, Y., "Numerical investigation of helical baffles heat exchanger with different prandtl number fluids", *International Journal of Heat and Mass Transfer*, Vol. 63, (2013), 434-444. doi: 10.1016/J.IJHEATMASSTRANSFER.2013.04.001.
19. Zhang, J.-F., Guo, S.-L., Li, Z.-Z., Wang, J.-P., He, Y.-L. and Tao, W.-Q., "Experimental performance comparison of shell-and-tube oil coolers with overlapped helical baffles and segmental baffles", *Applied Thermal Engineering*, Vol. 58, No. 1-2, (2013), 336-343. doi: 10.1016/j.applthermaleng.2013.04.009.
20. Taher, F.N., Movassag, S.Z., Razmi, K. and Azar, R.T., "Baffle space impact on the performance of helical baffle shell and tube heat exchangers", *Applied Thermal Engineering*, Vol. 44, (2012), 143-149. doi: 10.1016/j.applthermaleng.2012.03.042.
21. Picón-Núñez, M., García-Castillo, J. and Alvarado-Briones, B., "Thermo-hydraulic design of single and multi-pass helical baffle heat exchangers", *Applied Thermal Engineering*, Vol. 105, (2016), 783-791. doi: 10.1016/J.APPLTHERMALENG.2016.04.034.
22. Shinde, S. and Chavan, U., "Numerical and experimental analysis on shell side thermo-hydraulic performance of shell and tube heat exchanger with continuous helical frp baffles", *Thermal Science and Engineering Progress*, Vol. 5, (2018), 158-171. doi: 10.1016/J.TSEP.2017.11.006.
23. Du, T., Chen, Q., Du, W. and Cheng, L., "Performance of continuous helical baffled heat exchanger with varying elliptical tube layouts", *International Journal of Heat and Mass Transfer*, Vol. 133, (2019), 1165-1175. doi: 10.1016/J.IJHEATMASSTRANSFER.2018.12.142.
24. Chen, J., Lu, X., Wang, Q. and Zeng, M., "Experimental investigation on thermal-hydraulic performance of a novel shell-and-tube heat exchanger with unilateral ladder type helical baffles", *Applied Thermal Engineering*, Vol. 161, (2019), 114099. doi: 10.1016/j.applthermaleng.2019.114099.
25. Tang, H., Chen, Y., Wu, J. and Yang, S., "Numerical investigation of the performances of axial separation helical baffle heat exchangers", *Energy Conversion and Management*, Vol. 126, (2016), 400-410. doi: 10.1016/J.ENCONMAN.2016.08.003.
26. Naqvi, S., Elfeky, K., Cao, Y. and Wang, Q., "Numerical analysis on performances of shell side in segmental baffles, helical baffles and novel clamping anti-vibration baffles with square twisted tubes shell and tube heat exchangers", *Energy Procedia*, Vol. 158, (2019), 5770-5775. doi: 10.1016/J.EGYPRO.2019.01.553.
27. Pawar, S. and Sunnapwar, V.K., "Experimental and cfd investigation of convective heat transfer in helically coiled tube heat exchanger", *Chemical Engineering Research and Design*, Vol. 92, No. 11, (2014), 2294-2312. doi: 10.1016/j.cherd.2014.01.016.
28. Sepehr, M., Hashemi, S.S., Rahjoo, M., Farhangmehr, V. and Alimoradi, A., "Prediction of heat transfer, pressure drop and entropy generation in shell and helically coiled finned tube heat exchangers", *Chemical Engineering Research and Design*, Vol. 134, (2018), 277-291. doi: 10.1016/j.cherd.2018.04.010.
29. You, Y., Zhang, F., Fan, A., Dai, F., Luo, X. and Liu, W., "A numerical study on the turbulent heat transfer enhancement of rodbaffle heat exchanger with staggered tubes supported by round rods with arc cuts", *Applied Thermal Engineering*, Vol. 76, (2015), 220-232. doi: 10.1016/J.APPLTHERMALENG.2014.11.048.
30. Liu, J., Liu, Z. and Liu, W., "3d numerical study on shell side heat transfer and flow characteristics of rod-baffle heat exchangers with spirally corrugated tubes", *International Journal of Thermal Sciences*, Vol. 89, (2015), 34-42. doi: 10.1016/J.IJTHERMALSCI.2014.10.011.
31. Hosseinzadeh, K., Moghaddam, M.E., Asadi, A., Mogharrebi, A., Jafari, B., Hasani, M. and Ganji, D., "Effect of two different fins (longitudinal-tree like) and hybrid nano-particles (MOS_2-TiO_2) on solidification process in triplex latent heat thermal energy storage system", *Alexandria Engineering Journal*, Vol. 60, No. 1, (2021), 1967-1979. <https://doi.org/10.1016/j.aej.2020.12.001>.
32. Yang, J. and Liu, W., "Numerical investigation on a novel shell-and-tube heat exchanger with plate baffles and experimental

- validation", *Energy Conversion and Management*, Vol. 101, (2015), 689-696. doi: 10.1016/J.ENCONMAN.2015.05.066.
33. Bougriou, C. and Baadache, K., "Shell-and-double concentric-tube heat exchangers", *Heat and Mass Transfer*, Vol. 46, (2010), 315-322. doi: 10.1007/s00231-010-0572-z.
34. Lutcha, J. and Nemcansky, J., "Performance improvement of tubular heat exchangers by helical baffles", *Chemical Engineering Research and Design*; (UK), Vol. 68, No. A3, (1990).
35. Shah, R.K. and Sekulic, D.P., "Fundamentals of heat exchanger design, John Wiley & Sons, (2003).
36. Yang, J.-F., Zeng, M. and Wang, Q.-W., "Numerical investigation on shell-side performances of combined parallel and serial two shell-pass shell-and-tube heat exchangers with continuous helical baffles", *Applied Energy*, Vol. 139, (2015), 163-174. doi: 10.1016/J.APENERGY.2014.11.029.

COPYRIGHTS

©2023 The author(s). This is an open access article distributed under the terms of the Creative Commons Attribution (CC BY 4.0), which permits unrestricted use, distribution, and reproduction in any medium, as long as the original authors and source are cited. No permission is required from the authors or the publishers.



Persian Abstract

چکیده

عملکرد کلی یک مدل حرارتی پوسته-لوله دوگانه با در نظر گرفتن فین های ساده و مارپیچ نصب شده در قسمت پوسته، توسط نرم افزار تجاری ANSYS FLUENT 19.2 مورد بررسی قرار گرفته است. برای مقادیر مختلف دبی ورودی سیال، مقایسه جامعی برای مدل حرارتی با فین ساده و مارپیچ صورت گرفته است. در مدل حرارتی با فین مارپیچ نرخ انتقال حرارت، عملکرد حرارتی-هیدرولیکی مدل و بازده مدل به ترتیب 26.7% , 55.5% و 26.6% بالاتر از این مقادیر برای مدل حرارتی با فین ساده محاسبه گردید. همچنین توزیع جریان و دما در مدل با فین های مارپیچ یکنواخت تر با تلاطم بالاتر می باشد. بنابراین، مدل با فین های مارپیچ میتواند انتخاب بهتری برای طراحان مدل حرارتی باشد.



Development of Light Dynamic Penetrometer for Application in Dense Soil

A. Nasirifar^a, M. Khodaparast^{*b}

^a University of Qom, Faculty of Engineering, Qom, Iran

^b University of Qom, Faculty of Engineering, Civil Engineering Department, Qom, Iran

PAPER INFO

Paper history:

Received 31 May 2023

Received in revised form 30 July 2023

Accepted 05 August 2023

Keywords:

Dynamic Probing Test

Cone Dynamic Resistance

Cone Tip Angle

Repeatability

Dense Soil

A B S T R A C T

The dynamic probing test is effective for compaction control in road embankments and pavement layers. However, challenges exist to its use in dense soil types to obtain valid results. The main purpose of this research is to use light weight penetrometer in dense soils and obtain valid results. This study developed and tested three light dynamic penetrometers with different cone geometries in dense soils and compared their results with those of conventional dynamic penetrometers. Over 72 dynamic penetration tests were performed in the field in dense natural soil. The results showed a 50% reduction in the number of blows compared to the dynamic probing light penetrometer (DPL). The coefficients of variation of the results of 8.6% to 15.9% indicate desirable repeatability. To further evaluate the efficiency of these penetrometers, the correlations between their results and the soil characteristics of the dry unit weight in place, compaction percentage and peak shear strength were assessed by statistical residual analysis. This approach showed that these relationships were satisfactory.

doi: 10.5829/ije.2023.36.11b.04

1. INTRODUCTION

The dynamic penetration test is a method of identifying soil strength characteristics. In this method, the dynamic energy resulting from the fall of a hammer having a certain weight from a certain height will cause a rod with a conical tip to penetrate the ground. The number of blows required for the rod to penetrate into the soil is a criterion for measuring the hardness and density of materials. The penetration depth at each step is usually 10 to 20 cm and the test result is denoted as N_{10} and N_{20} . The dynamic penetration index (DPI), which is measured as the number of millimetres per impact (mm/blow), also can be used. In general, an increase in the strength or hardness of the soil will cause the DPI to decrease [1, 2]. Various techniques can be used for soil improvement in road embankment and geotechnical engineering [3].

A conventional dynamic probe used in soil mechanics in Iran and other countries is the dynamic probing light (DPL). However, the large amount of energy required for penetration into hard and dense soil prevents the use penetrometers such as the DPL in this type of soil. In

current standards, including BS EN ISO 22476-2, ASTM D 6951 [4] and the national standard of Iran 12305-2 [1], the maximum number of blows allowed to penetrate 10 cm of soil is limited to 50 blows. However, the results of penetration testing with light probes such as the DPL in hard and dense soil indicate that this limit can be quickly exceeded, which reduces its validity. The standards recommend that heavier dynamic penetrometers should be used in such situations, but field experiments show that the weight of equipment such as the heavier types of penetrometers strongly decreased the tendency to use this test.

This study investigated the use of a light penetrometer in dense soil. To achieve this purpose, the energy produced by the penetrometer must be increased adequately. There are two general solutions to increase energy. Increasing the hammer weight and height of the fall or changing in the geometry of the cone.

The present study changed the geometry of the cone, including the diameter and angle of the cone tip, to allow penetration tests to be carried out in dense and hard soil. It will also be possible to investigate the effect of the

*Corresponding Author Email: [\(M. khodaparast\)](mailto:khodaparast@qom.ac.ir)

change in the cone tip angle on the penetration power. Twelve urban areas were selected to test the efficiency of the new penetrometer. It was evaluated and compared with other standard penetrometers and was found to be a suitable dynamic penetrometer as an alternative to the DPL penetrometer. By conducting penetrations tests in the specific soil with different penetrometers, the amount of changes in the results can be checked. In other words, the independence of results from the type of penetrometers can be evaluated.

1. 1. Applications of Dynamic Penetration Test

The method and equipment used in this test are basic, making them a fast and economical method of evaluating important in situ soil resistance parameters. Figure 1 shows the schematic of cone penetration into the soil per hammer blow.

Studies are being done on the applied components of this test, such as evaluation of the unit weight [5, 6] and relative density [7-9]. The relationships between DPI and other soil parameters from various laboratory and field studies are summarized in Table 1. Other important parameters such as compaction percentage [10, 11] and shear strength [12-14] also stated in this table.

1. 2. Dynamic Cone Resistance Parameter (q_d)

Another way to use the results of this test is to calculate the dynamic cone resistance parameter (q_d). It is assumed that the penetration of a dynamic penetrometer cone into the soil corresponds to a pile. Pile foundations

are used in civil structures to transfer the structural load to the depth of the soil or rock layers [15]. Pile-driving theory measures the soil resistance against the number of dynamic blows. The cone dynamic resistance parameter is presented as:

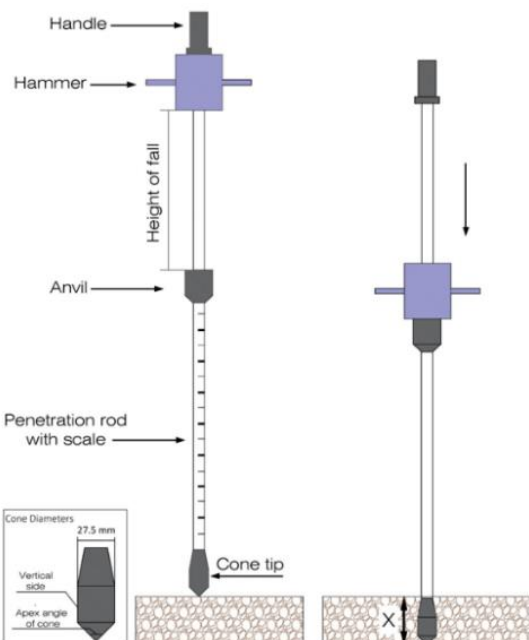


Figure 1. Schematic of dynamic penetration steps

TABLE 1. Correlations between dynamic penetrometer results and soil engineering properties

Reference	Correlation	Description	Soil type
Harison [16]	$\text{Log}(\text{CBR}) = 2.81 - 1.32 \times \text{log}(\text{DPI})$	Laboratory tests	Granular and cohesive soils
Livneh et al. [17]	$\text{Log}(\text{CBR}) = 2.46 - 1.12 \times \text{log}(\text{DPI})$	Field and laboratory tests	Granular and cohesive soils
Chennarapu et al. [5]	$\gamma_d = 2.67 (\text{DPI})^{-0.131}$	Field tests	Silty sand
Hamid et al. [6]	$\gamma_d = 2.02 (\text{DPI})^{-0.04}$	Laboratory tests	Poorly graded sand
Mohammadi et al. [9]	$\text{Dr} = 189.93 (\text{DPI})^{-0.53}$	Laboratory tests	Poorly graded sand
MacRobert et al. [8]	$\text{Dr} = 148 - 50 \times \text{log}(\text{DPI})$	Laboratory tests	Sandy soils
L. Lin et al. [18]	$\text{Dr} = -80.63 + 37.63 \times \text{log}(D_{50}^{-0.34} C_u^{-0.17} q_d)$	Field and laboratory tests	Granular soils
Ampadu and Arthur [11]	$\text{Log}(\text{Rc}) = 2.148 - 0.337 \times \text{log}(\text{DPI})$	Laboratory tests	Granular soils
Khodaparast et al. [10]	$\text{Rc} = 16.654 \times q_d^{0.193}$	Field and laboratory tests	Fine grained soils
Fakher et al. [19]	$C_u = 2.5 \text{ M}$	Field tests	Soft clay
Lee et al. [20]	$\phi^\circ = 45.6 - 0.2 \times \frac{\text{DPI}}{D_{50}}$	Laboratory tests	Silty sand soil
Lee et al. [12]	$\phi^\circ = 0.0116 \times q_{d,n} + 47.8$	Laboratory tests	Poorly graded sand with low fines content
Kim and Lee [13]	$\tau_f = 223.8 (\text{DPI})^{-0.9}$	Laboratory tests	Silty sand soil

Note:

CBR: California bearing ratio (%); DPI: dynamic penetration index (mm/blow); γ_d : dry unit weight of soil (kN/m^3); Dr: relative density (%); D_{50} : Average particle diameter (mm); C_u : Uniformity coefficient; q_d : dynamic cone resistance (kPa); Rc: Compaction percentage (%) ; Cu: undrained shear strength (kPa); M: number of blows for 100 mm penetration; ϕ : friction angle of soil (degrees); $q_{d,n}$: normalized dynamic cone resistance (kPa); τ_f : Peak shear strength (kPa)

$$q_d = \left(\frac{M}{M+m} \right) \cdot \frac{M \cdot g \cdot h}{A \cdot x} \quad (1)$$

where A is the cross-sectional area of the cone; x is the penetration length of the cone per blow, h is the height of the hammer fall, M is the hammer mass, m is the mass of the penetrometer without a hammer and g is the gravity acceleration. The advantage of q_d is that, due to the contribution of the penetrometer energy, the geometry of the cone and the mass of its attachments, the value of this parameter has little dependence on the type of penetrometer selected [21].

One factor affecting the results of the dynamic penetration test is the overburden stress in the soil mass. This stress increases as the depth increases. An increase in the overburden stress and the subsequent increase in lateral pressure on the penetration cone will affect the penetration results differently depending on the soil type. Some researchers believe that the results of penetration tests should be modified depending on the depth. In the standard penetration test (SPT), this correction is referred to as the overburden correction [22].

In dynamic penetration tests, vertical stress can also affect the results. Lee et al. [12] eliminated the effect of the confining pressure on the dynamic cone resistance by introducing the normalized dynamic cone resistance ($q_{d,n}$) as:

$$q_{d,n} = \frac{\left(\frac{q_d}{P_a} \right)}{\left(\frac{\sigma_m}{P_a} \right)^{0.5}} \quad (2)$$

where q_d is the dynamic cone resistance, P_a is a reference value such as the atmospheric pressure (100 kPa) and σ_m is the mean principal stress [12].

2. MATERIALS AND METHODS

2. 1. Introducing the Three New Dynamic Penetrometer

The standards provide specific work criteria for each impact (E_n) generated by a hammer

falling on an anvil as the parameter that determines the amount of energy produced by the penetrometer. To increase the penetration power, it is possible to increase the potential energy of the hammer (m. g. h) or reduce the cross-sectional area of the penetration cone (A) as:

$$E_n = \frac{M \cdot g \cdot h}{A} \quad (3)$$

Increasing the potential energy requires an increase in the mass of the hammer and height of the fall. This will increase the energy consumed by the operator and will reduce the acceptance of the penetrometer. Thus, an increase in the mass and height of the hammer should be avoided whenever possible. The use of motorized penetrometers is recommended to solve this problem, but transportation and other limitations of these penetrometers should be taken into consideration.

After conducting initial field tests and reviewing the characteristics of dynamic penetrometers for different standards, three new dynamic penetration instruments (ADP25, ADP60 and ADP90) with the specifications presented in Table 2 and Figure 2 were developed.

2. 2. Field and Laboratory Tests

A series of tests then were performed to evaluate the repeatability of

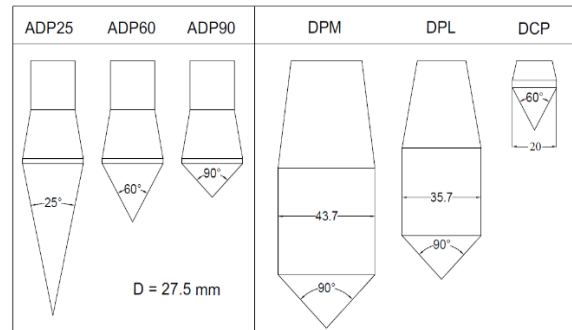


Figure 2. Specifications and appearance of penetrometer cones showing dimensions

TABLE 2. Characteristics of novel and standard penetrometers

Penetrometer	DPL	DPM	DCP	ADP25	ADP60	ADP90
Hammer mass (kg)	10	30	8	10	10	10
Height of fall (mm)	500	500	575	500	500	500
Cone diameter (mm)	35.7	43.7	20	27.5	27.5	27.5
Cone tip angle (deg)	90	90	60	25	60	90
Specific work per blow (kJ /m ²)	49	98	143	82.6	82.6	82.6
Standards	BS EN ISO 22476-2		ASTM D 6951		Introduced in this study	
Reference	[2]		[4]		-	

the results at four sites in accordance with the national standards of Iran 12305-2 and BS EN ISO 22476-2. The efficiency of the penetrometers was determined in hard and dense soils at 12 sites and, as a method of comparison, the results of the DPL and DPM types for BS EN ISO 22476-2 and type DCP for ASTM D 6951 [4] were determined. Figure 3 shows the research methodology in this article.

Dynamic penetration tests were carried out using the six penetrometers (DPL- DPM- DCP- ADP25- ADP60-ADP90) in natural soil in 12 areas around the city of Qom that have high density hard soil. The penetration depths in these tests were from the ground surface to a depth of 60 cm. The results were recorded in terms of the penetration number (N_{10}), which indicates the number of blows required for the penetration of the cone to a depth of 10 cm into the soil. Figure 4(b) shows the distance between the points of the penetration tests. Because of the possibility of soil surface tamping and proper establishment of the penetrometer in the soil, the initial 10 cm results were omitted.

The soil in these locations primarily comprised silt and sandy clay, which have high resistance and compaction due to low humidity. Table 3 shows the characteristics and classes of these soils according to ASTM D2487 (Unified Soil Classification System) [23]. The particle-size distribution curve of these materials is shown in Figure 5. Because of the low penetration depth, dryness of materials and the larger diameter of the cone on the penetration rod, the friction between the soil and the penetration rod were largely ineffective [15, 24, 25].

During in situ tests was observed that pulling out the penetration rod after performing test was easy. There is no friction between penetration rod and soil almost and so that the penetration rod can be entered into the initial cavity without any force.

According to what is mentioned in penetration test standards, the tip of the penetration cone should be checked and replaced in case of injury. The high density and hardness of the materials, likewise a low-angle cone, increase the injury of the cone tip. Hence, in this research, the cones were review before commencement of penetrations tests and were replaced if needed.

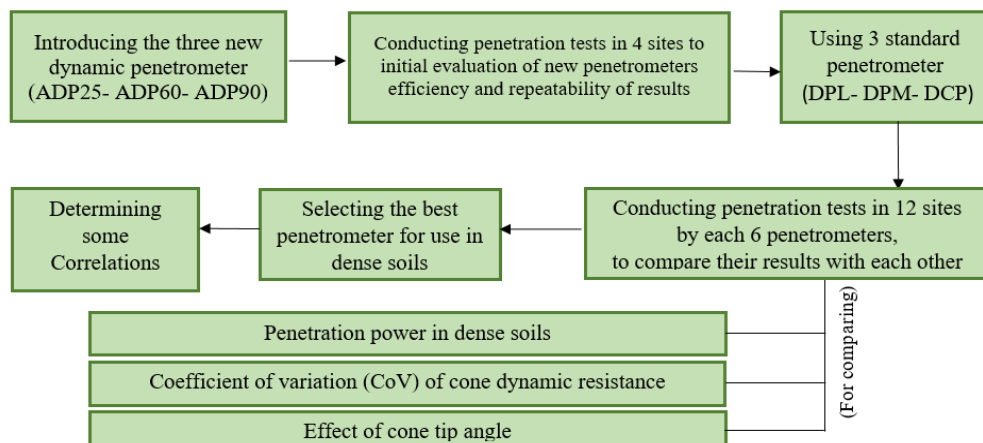


Figure 3. The process of conducting penetration tests in this research

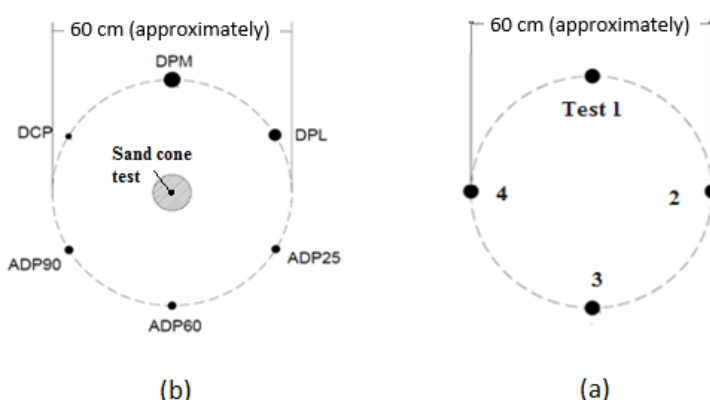
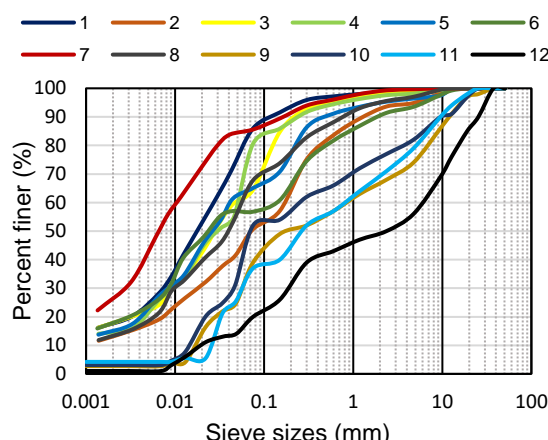
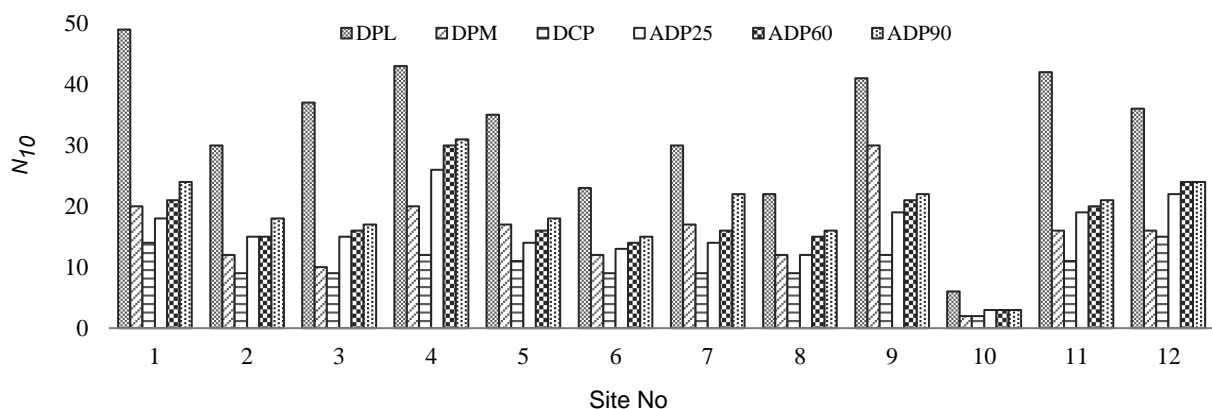


Figure 4. Spacing of penetration test points: (a) repeatability tests; (b) tests using different penetrometers

TABLE 3. Soil properties of penetration sites

Site No	Soil Type	Materials Percentage (%)			γ	ω
		Fines	Sand	Gravel		
1	CL	86	13	1	1.76	2.5
2	ML	51	44	5	1.76	3
3	ML	64	35	1	1.81	3.6
4	CL-ML	80	18	2	1.76	6.5
5	CL-ML	65	31	4	1.71	5.6
6	ML	57	37	6	1.92	7.8
7	CL-ML	86	14	0	1.75	9
8	ML	68	29	3	1.59	4.2
9	SC-SM	39	35	26	2.02	6.9
10	ML	52	30	18	1.64	12.3
11	SC-SM	37	42	21	1.9	8.2
12	GC-GM	20	36	44	1.9	3.3

Note:

 γ : unit weight of soil (gr/cm^3); ω : Moisture Content (%)**Figure 5.** Particle-size distribution curves of soils**Figure 6.** Average of N_{10} at depths of 10 to 60 cm for all dynamic penetration tests

Researchers have effective factors such as the length of penetration rods (depth of penetration), the fall of the hammer without conflict with the guidance rod and the fixing of the connections, in the amount of energy dissipation [15, 26, 27]. In this study, due to the short length of the penetration rod and continuous examination of the connections. Energy dissipation are negligible and the amount of energy transferred to the cone is assumed to be equal to the value of the theory.

Rebounding of cones and penetrating rods is an issue that can occur in very hard (often gravelly) soils. In these soils, due to the extremely high density and hardness of the soil, the penetrometer is not able to penetrate in the soil. In this situation, the energy from the hammer falling is returned to the penetrometer and caused interferes in measurement of penetration depth. In this study, such soils were not encountered and this problem was not observed.

In order to further expand the application of the developed penetrometers, the correlation between the results of the most appropriate new penetrometer and the soil resistance parameters have been presented. For this purpose, in-situ unit weight tests (ASTM D 1556 [28]), compaction tests (ASTM D 1557 09 [29]) and direct shear tests (ASTM D 3080 [30]) were performed.

3. RESULTS AND DISCUSSION

3. 1. Efficiency of Developed Penetrometers

Figure 6 shows the average penetration numbers (N_{10}) for depths of 10 to 60 cm for all dynamic penetration tests performed at the 12 locations. The penetration number for cones ADP25, ADP60 and ADP90 decreased by 50%, 46% and 40%, respectively, compared to the DPL penetrometer. Also, the N_{10} of the instrumented ADP25 was equal to that of the DPM penetrometer, a semi-heavypenetrometer (hammer weight of 30 kg), which indicates proper performance of the designed cones. In

the specifications of the new penetrometers, the decrease in the number of blows was caused by a decrease in the cross-sectional area of the penetration cone and a change in the angle of the tip. The lowest value of the N_{10} parameter is related to the DCP penetrometer, which has the highest amount of specific work for each impact (E_n).

It should be noted that the small diameter of the cone in this penetrometer (18 mm) compared to other penetrometers causes it to quickly become defective in the penetration tests in dense and hard soils.

3. 2. Repeatability of Developed Penetrometer Test Results

The coefficient of variation (CoV) was used to evaluate the repeatability of the results of the in-situ penetration tests. The CoV of each random variable was obtained by dividing the standard deviation (S) by the mean of the data (\bar{X}) (Equation (4)) and is expressed as a percentage [1, 10]. In this study, the repeatability of the results of the penetration tests was determined by calculating the CoV of N_{10} obtained from 48 penetration tests.

$$\text{CoV} (\%) = \frac{S}{\bar{X}} \times 100 \quad (4)$$

Studies have shown that increasing of the soil compaction and stiffness will increase the CoV of the dynamic penetration test results [9]. Figure 7 also shows that an increase in the CoV was caused by an increase in the number of penetrations. The average CoV was calculated and is shown in Table 4. The instrumented ADP25 with a CoV of 8.56% had the most repeatable results of the developed penetrometers.

3. 2. 1. Effect of Cone Tip Angle on CoV Table 4 shows that the lowest CoV was for the ADP25 penetrometer, which could be attributed to the power the penetrometer. Although the specific work per impact (E_n) was the same for all three penetrometers, the difference in the cone tip angle increased the penetration power of the ADP25 penetrometer. As a result, the CoV

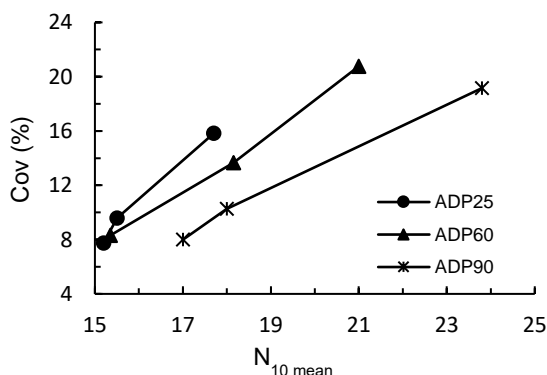


Figure 7. Variation in CoV(%) values due to the increase of N_{10} mean

TABLE 4. Mean of CoV (%) for N_{10}

CoV (%)		
ADP25	ADP60	ADP90
8.56	15.86	11.39

of the results was less than of other the two penetrometers. During the penetration tests, when the density and hardness of the soil increases significantly and the penetrometer is not able to penetrate into the soils (N_{10} more than 30), the repeatability of the results decreased and the number of blows irregularly increased. Therefore, in most studies and standards, the acceptable number of blows for penetration of 10 cm into the soil was limited to 3 to 50 blows.

3. 2. 2. CoV of Cone Dynamic Resistance Parameter (q_d)

The cone dynamic resistance parameter is an intrinsic feature of the soil and should not change if the penetrometer is changed. But, in practice, because factors such as energy wasted and the cone tip angle are not included in Equation (1), there are differences between the values of this parameter as measured by different penetrometers. In this study, the effect of the cone tip angle on the cone dynamic resistance also was clearly observed. One challenge of dynamic probing test is the independence of the results from the type of penetration used. In this study, in order to evaluate these changes, the CoV that relates to repeatability was used. Table 5 shows the mean CoV (q_d) of all six penetrometers and the states in which the developed penetrometers (ADP25, ADP60 and ADP90) and the standard ones (DPL, DPM and DCP) differed.

Table 5 indicates that the value of the dynamic cone resistance obtained from the six different penetrometers had a CoV of less than 20%, which indicates that q_d was independent of the type of penetrometer. The calculation of the CoV of q_d has not been done in previous research and a recommended value for it was not available. The recommended value of the CoV of the results of common penetration tests such as SPT was 30% and for the static cone penetration test (CPT) was 15 to 35% [31]. Therefore, the CoV obtained for the dynamic penetration test was considered acceptable.

3. 3. Correlation of ADP25 Penetrometer Results and Soil Engineering Properties

Dynamic penetrometer tests were done using the three new penetrometers and their results were estimated in terms of penetration power in hard and dense soil and the repeatability of results. Based on these results, ADP25 was selected as the penetrometer on which to further explore the abilities of this device. The correlation between the results for ADP25 and the dry unit weight,

compaction percentage and peak shear strength of the soil are presented below.

3.3.1. Dry Unit Weight (γ_d) To determine the correlation between the in-situ dry unit weight and ADP25 penetrometer results, the sand cone test was performed at the site of dynamic penetration tests. After measuring the moisture content of the samples, the dry unit weight was obtained. Figure 8 and Table 6 show the diagram and correlations for the dry unit weight.

Figure 9 shows the comparison of dry unit weight versus DPI in the present study with data reported by Chennarapu et al. [5]. As can be seen the trend observed between DPI and dry unit weight in two research is similar. Though the dry density values in this study are lower than those from Chennarapu et al. [5]. The lower DPI values for a given Dry unit weight from the present study when compared to Chennarapu et al. [5] could be

TABLE 5. Mean of CoV (%) for q_d

DPL-DPM-DCP	ADP25-ADP60-ADP90	All penetrometers
17.9	11.93	18.3

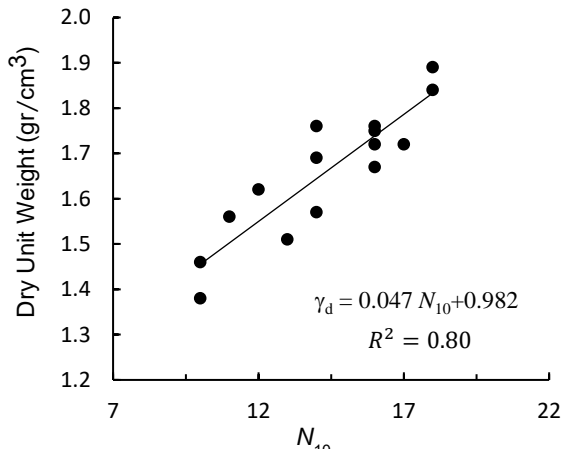


Figure 8. Correlation of γ_d and N_{10}

TABLE 6. Correlations of γ_d and dynamic penetration test results

Correlations	R ²
$\gamma_d = -0.084 \text{ DPI} + 2.27$	0.79
$\gamma_d = 3.59 \text{ DPI}^{-0.396}$	0.80
$\gamma_d = 0.047 N_{10} + 0.98$	0.80
$\gamma_d = 0.087 q_d + 0.98$ γ_d in (gr/cm ³) and q_d in kPa.	0.80

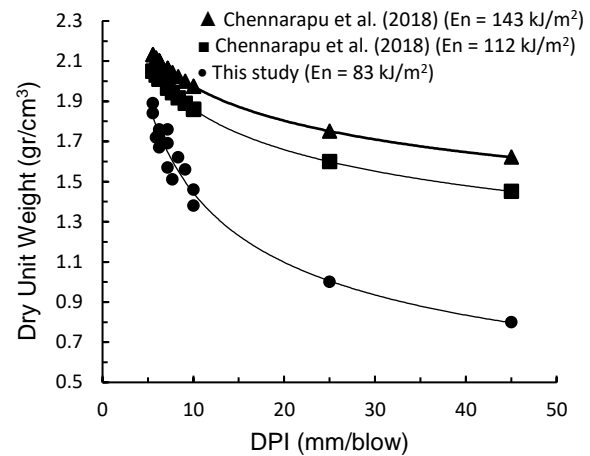


Figure 9. Comparison of Dry unit weight versus DPI in the present study with Chennarapu et al. [5]

due to the different penetrometers and soil type used in the two studies. The specific work per blow (En) parameter of this research penetrometer is equal to 83 (kJ/m²), while the specific work per blow used penetrometer in Chennarapu et al. [5] is equal to 143 and 112 (kJ/m²), respectively.

The correlation based on the DPI and N_{10} parameters are specific to the used penetrometer in the research, in other words, the values of these parameters will change by changing the penetrometer properties such as hammer weight, fall height and cone diameter. As mentioned earlier, due to the considering of physical and geometric characteristics of penetrometers in dynamic cone resistance equation (Equation (1)), this parameter is not dependent on the type of penetrometers and can use the correlations provided by it, in other penetrometers [21, 31].

Most statistical methods, such as regression, which are used to calculate the correlation between penetrometer results and other soil parameters, will exhibit adequate reliability when the data distribution is normal (or near normal). The standard residual analysis method can be used to evaluate the validity of a linear regression model and derive correlations [32]. In this method, the normality of the data distribution is investigated. Standard residuals are the differences between the actual observation values and those obtained from the correlation. Figure 10 shows the standard residuals versus the calculated γ_d and Figure 11 presents the normal probability plots.

In a standard residual plot, values having a normal distribution show no obvious pattern or unusual structure. If about 95% of these values range from -2 to +2 on the vertical axes, the distribution of the residuals is considered to be normal and the correlation has adequate confidence. In a normal probability plot, when the data

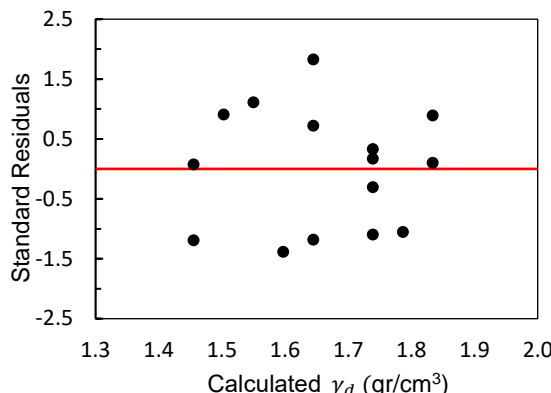


Figure 10. Standard residuals vs. calculated dry unit weight

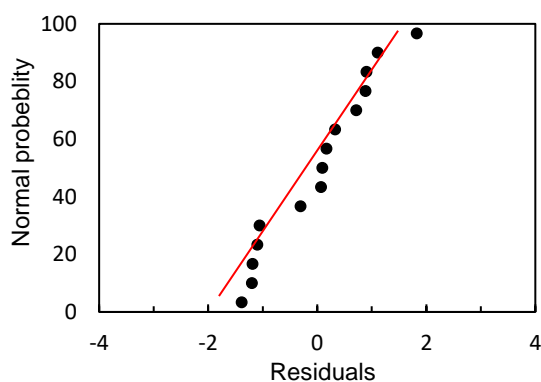


Figure 11. Normal probability of γ_d and N_{10} correlation

distribution is normal, the points will be on a straight line. The proximity of points to the straight line is representative a normal data distribution. The observation points that are some distance from the line indicate the existence of outliers [32, 33]. The results of residual analysis with the appropriate coefficient of determination (R^2) indicate acceptable correlation between the dry unit weight and N_{10} .

3. 3. 2. Compaction Percentage (R_c) The compaction percentage is an important index for assessing the quality of the road subgrade; thus, an easy and fast estimation of this index is desirable. Accordingly, the modified proctor compaction test was performed on the materials from the eight selected locations. Because of the effect of moisture content (ω) on the dry unit weight, this parameter also formed a component of the calculations. Figure 12 and Table 7 show the diagram and correlations of the compaction percentage used to estimate the results of the penetration test. In the horizontal axis of Figure 12, the parameter N_{10}/ω is used (N_{10} divided by ω) because ω is effective in calculating of R_c . The results of the standard residual analysis confirm the accuracy and validity of the correlation.

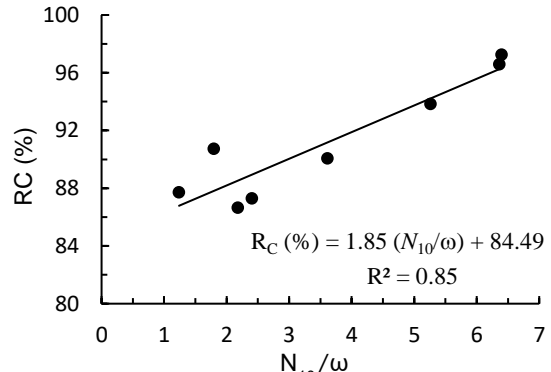


Figure 12. Compaction percentage vs. N_{10}/ω

TABLE 7. Compaction percentage vs. ADP25 device penetration results

Correlations	R^2
$R_C (\%)=1.85(N_{10}/\omega) + 84.50$	0.85
$R_C (\%)=113.43(DPI \times \omega)^{-0.063}$	0.73
$R_C (\%)=3.39(q_d/\omega) + 84.50$	0.85
q_d in kPa.	

3. 3. 3. Peak Shear Strength (τ_f) The direct shear test was performed on samples taken from the materials gathered from the eight locations and the soil shear strength was evaluated based on the results of dynamic penetration tests. In the direct shear tests, vertical stresses of 10, 30 and 50 kPa were used and their mean shear strength was applied as the peak shear strength.

Previous studies have estimated the angle of internal friction using the results of the penetration test [4, 7-14, 16-18]. The shear strength of fine-grained soil results from the internal friction angle and cohesion of the soil. The coarse grain fraction and the moisture content of such soil has a direct effect on its shear behaviour; therefore, the internal friction angle, which is only representative of the frictional resistance of the soil, cannot properly correlate with the results of the dynamic penetration test. It is apparent that the correlation between the results of the dynamic penetration test and soil shear strength in which the cohesion resistance also participates is more accurate than the internal friction angle. Figure 13 shows the correlation between the internal friction angle and the penetration index. It can be seen that the coefficient of determination of the proposed correlation was not appropriate. Figures 14 to 16 and Table 8 show the correlations between the peak shear strength and the penetration results.

According to the results of the figures above, it is clear that in fine-grained soils, the correlation between the results of dynamic penetration tests and the peak shear strength of the soil had greater accuracy than the internal friction angle.

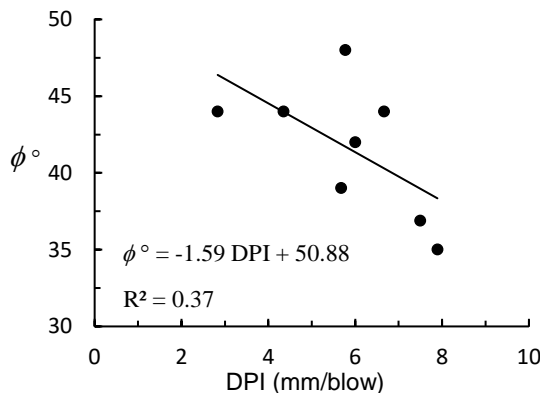


Figure 13. Correlation of internal friction angle and DPI

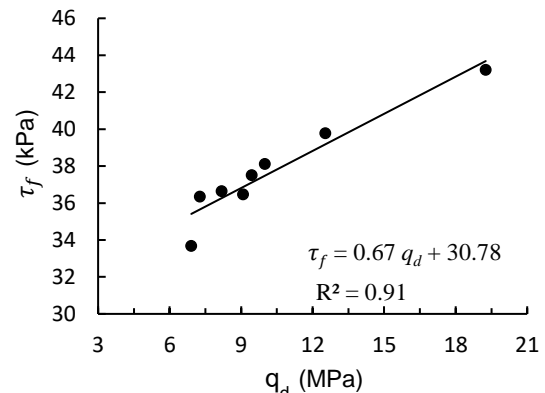
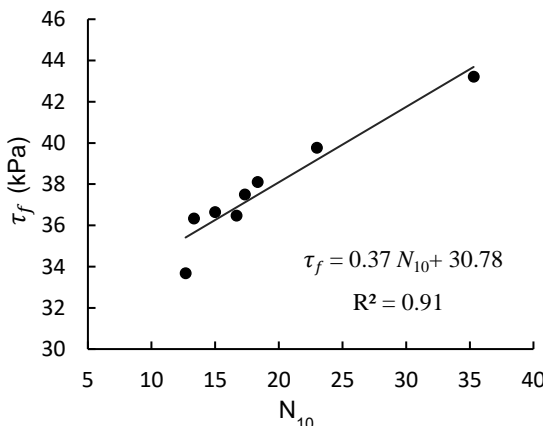
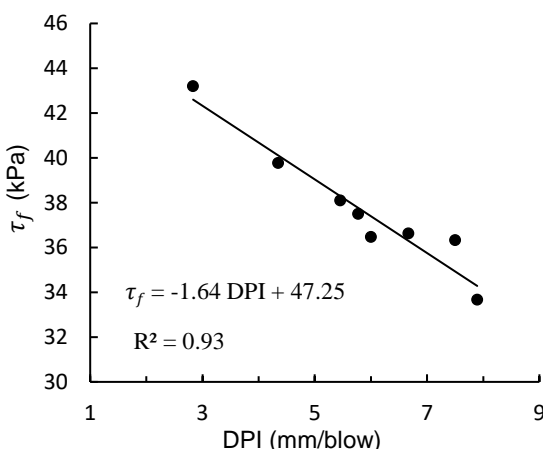
Figure 16. Correlation of peak shear strength and q_d (MPa)Figure 14. Correlation of peak shear strength and N_{10} 

Figure 15. Correlation of peak shear strength and DPI

3.3.4. Correlation of Peak Shear Strength (τ_f) and Normalized Cone Dynamic Resistance ($q_{d,n}$)

In this study, the normalized cone dynamic resistance was calculated using Equation (2). Figure 17 shows the correlation between ($q_{d,n}$) and the peak shear strength.

TABLE 8. Correlations of peak shear strength and penetration results of ADP25

Correlations	R ²
τ_f (kPa) = $0.37 N_{10} + 30.78$	0.91
τ_f (kPa) = -1.64 DPI + 47.25	0.93
τ_f (kPa) = $0.67 q_d$ (Mpa) + 30.78	0.91

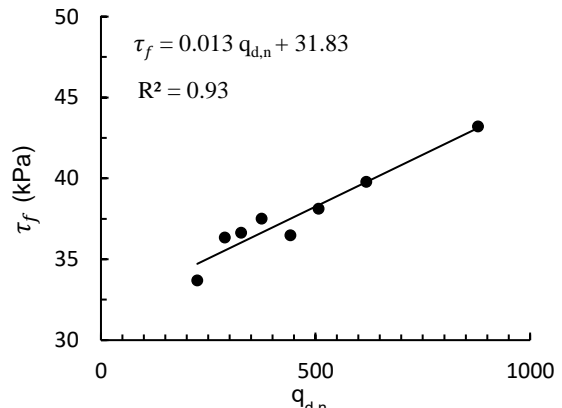


Figure 17. Correlation of peak shear strength and normalized cone dynamic resistance

This figure shows that an acceptable correlation was obtained between these parameters. Since overburden stress and lateral pressure can have a significant effect on the results of dynamic penetration test, using this correlation can get more accurate results. Therefore, this correlation is of higher importance and value than other provided relationships.

4. CONCLUSION

This study investigated the efficacy of light penetrometers for use in hard and dense soil.

consequently, three light dynamic penetrometers with different cone geometries were developed and then were practically evaluated in 12 urban locations with dense and hard sandy fine-grained soil.

To further evaluate the efficiency of these penetrometers, the correlations between their results and the soil characteristics of the dry unit weight in place, compaction percentage and peak shear strength were assessed. Based on the field testing carried out in the present study, the following conclusions are drawn:

1. The penetration numbers (N_{10}) of the three penetrometers (ADP25, ADP60 and ADP90), which differ only in the cone tip angle, were shown to have decreased 50%, 46% and 40%, respectively, compared to those for the DPL penetrometer. According to the method of performing this test, which is usually carry out manually by the operator, reducing the number of blow with the proposed device (ADP25) was very profitable and would increase the accuracy of the test by the operator. Thus, it seems that the ADP25 penetrometer can be used as a suitable alternative for the DPL penetrometer, especially in relatively hard and dense soils.
2. The coefficient of variation (CoV) of the three penetrometers results were calculated 8.56%, 15.86% and 11.39%, respectively, which seems to be appropriate compared to other penetration tests. Based on the results of penetration tests performed in this study, the ADP25 penetrometer showed the best penetrability in hard and dense soil and had the most repeatable results. Thus, this device can be a suitable alternative to the DPL penetrometer. In this way, the ADP25 penetration has a adequate performance in terms of repeatability of the results, and it can be used more reliably in practical soil mechanics studies instead of conventional dynamic penetrometers.
3. The CoV of the cone dynamic resistance (q_d) obtained by performing penetration tests with six different penetrometers at the 12 unit locations was calculated and was shown to be equal to 18.3%. It can be concluded that this parameter was independent of the type of penetrometer used.
4. The correlations between the ADP25 penetrometer results and the dry unit weight, compaction percentage and peak shear strength have been presented. Standard residual analysis was used in addition to the coefficient of determination (R^2) to investigate the accuracy and validity of the proposed correlations. The results of both methods confirmed the acceptability of the presented relationships and were in satisfactory agreement. Also the normalized cone dynamic resistance, which corrects the effect of overburden pressure on penetration test results, was also investigated. The correlation between peak shear strength and this novel and valuable parameter showed high accuracy.

5. REFERENCES

1. Ghorashi, S., Khodaparast, M. and Rajabi, A., "Evaluation of dynamic probing testing effect in hand excavated pit on test results using numerical modeling", *International Journal of Engineering, Transactions B: Applications*, Vol. 33, No. 8, (2020), 1553-1559. <https://doi.org/10.5829/ije.2020.33.08b.13>
2. Ghorashia, S., Khodaparast, M. and Qomib, M.K., "Compaction quality control of coarse-grained soils using dynamic penetration test results through correlation with relative compaction percentages", *International Journal of Engineering, Transactions C: Aspects*, Vol. 36, No. 3, (2023), 473-480. <https://doi.org/10.5829/ije.2023.36.03c.06>
3. Mohammadi, M., Khodaparast, M. and Rajabi, A.M., "Effect of nano calcium carbonate (nano caco3) on the strength and consolidation properties of clayey sand soil", *Road Materials and Pavement Design*, Vol. 23, No. 10, (2022), 2394-2415. <https://doi.org/10.1080/14680629.2021.1976255>
4. ASTM, D., "6927", Standard test method for Marshall stability and flow of asphalt mixtures. Annual Book of ASTM Standards, ASTM International, West Conshohocken, PA, (2015).
5. Chennarupu, H., Garala, T.K., Chennareddy, R., Balunaini, U. and Venkata Narasimha Reddy, G., "Compaction quality control of earth fills using dynamic cone penetrometer", *Journal of Construction Engineering and Management*, Vol. 144, No. 9, (2018), 04018086. [https://doi.org/10.1061/\(ASCE\)CO.1943-7862.0001530](https://doi.org/10.1061/(ASCE)CO.1943-7862.0001530)
6. Hamid, A.M., Al-Amoudi, O.S.B. and Aiban, S.A., "Assessing the effect of density and water level on the degree of compaction of sand using dynamic cone penetration test", *Arabian Journal for Science and Engineering*, Vol. 44, (2019), 4921-4930. <https://doi.org/10.1007/s13369-018-3641-0>
7. Mohajerani, A., Nguyen, B.T., Wang, Z., Antequera, M., Sohanpal, J., Conte, J.S., Yap, W.J., Malliaras, I. and Gao, X., "A practical technique for the compaction control of sand in road construction: Using a dynamic lightweight cone penetrometer", *Road Materials and Pavement Design*, Vol. 22, No. 1, (2021), 200-214. <https://doi.org/10.1080/14680629.2019.1634123>
8. MacRobert, C., Bernstein, G. and Nchabeleng, M., "Dynamic cone penetrometer (DCP) relative density correlations for sands", (2019). <https://doi.org/10.28927/SR.422201>
9. Mohammadi, S., Nikoudel, M., Rahimi, H. and Khamehchiyan, M., "Application of the dynamic cone penetrometer (DCP) for determination of the engineering parameters of sandy soils", *Engineering Geology*, Vol. 101, No. 3-4, (2008), 195-203. <https://doi.org/10.1016/j.enggeo.2008.05.006>
10. Khodaparast, M., Rajabi, A. and Mohammadi, M., "The new empirical formula based on dynamic probing test results in fine cohesive soils", *International Journal of Civil Engineering*, Vol. 13, No. 2, (2015), 105-113. <https://doi.org/10.22068/IJCE.13.2.105>
11. Ampadu, S.I. and Arthur, T.D., "The dynamic cone penetrometer in compaction verification on a model road pavement", *Geotechnical Testing Journal*, Vol. 29, No. 1, (2005), 70-79. <https://doi.org/10.1520/GTJ12306>
12. Lee, J.-S., Kim, S.Y., Hong, W.-T. and Byun, Y.-H., "Assessing subgrade strength using an instrumented dynamic cone penetrometer", *Soils and Foundations*, Vol. 59, No. 4, (2019), 930-941. <https://doi.org/10.1016/j.sandf.2019.03.005>
13. Kim, S.Y. and Lee, J.-S., "Energy correction of dynamic cone penetration index for reliable evaluation of shear strength in frozen sand-silt mixtures", *Acta Geotechnica*, Vol. 15, (2020), 947-961. <https://doi.org/10.1007/s11440-019-00812-y>
14. Eslami, A., Akbarimehr, D., Aflaki, E. and Hajitaheriha, M.M., "Geotechnical site characterization of the lake urmia super-soft sediments using laboratory and cptu records", *Marine*

- Georesources & Geotechnology**, Vol. 38, No. 10, (2020), 1223-1234. <https://doi.org/10.1080/1064119X.2019.1672121>
15. Khodaparast, M., Hosseini, S.H. and Moghtadai, H., "Determination of blast impact range and safe distance for a reinforced concrete pile under blast loading", **International Journal of Engineering, Transactions B: Applications**, Vol. 36, No. 2, (2023), 384-397. <https://doi.org/10.5829/ije.2023.36.02b.17>
 16. Harison, J., Grant, M., Nataatmadja, A. and Woodman, G., "Correlation between California bearing ratio and dynamic cone penetrometer strength measurement of soils", **Proceedings of the Institution of Civil Engineers**, Vol. 87, No. 1, (1989), 119-125. <https://doi.org/10.1680/iicep.1987.204>
 17. Livneh, M., Ishai, I. and Livneh, N.A., "Effect of vertical confinement on dynamic cone penetrometer strength values in pavement and subgrade evaluations", **Transportation Research Record**, (1995), 1-1.
 18. Lin, L., Li, S., Sun, L., Li, T. and Yin, J., "Assessing relative density of carbonate granular soil via dynamic cone penetration field and model tests", **Marine Georesources & Geotechnology**, Vol. 39, No. 12, (2021), 1472-1480. <https://doi.org/10.1080/1064119X.2020.1850950>
 19. Fakher, A., Khodaparast, M. and Jones, C., "The use of the mackintosh probe for site investigation in soft soils", **Quarterly Journal of Engineering Geology and Hydrogeology**, Vol. 39, No. 2, (2006), 189-196. <https://doi.org/10.1144/1470-9236-05-039>
 20. Lee, C., Kim, K.-S., Woo, W. and Lee, W., "Soil stiffness gauge (ssg) and dynamic cone penetrometer (DCP) tests for estimating engineering properties of weathered sandy soils in Korea", **Engineering Geology**, Vol. 169, (2014), 91-99. <https://doi.org/10.1016/j.enggeo.2013.11.010>
 21. Butcher, A., McElmeel, K. and Powell, J., "Dynamic probing and its use in clay soils", in Proceedings of the international conference on Advances in site investigation practice, (Craig C.(eds)). Thomas Telford, London. (1996), 383-395.
 22. Khodaparast, M., Rajabi, A.M. and Derakhshan, M., "Development of practical correlations between cone penetration resistance and spt values for various types of soils", **Iranian Journal of Science and Technology, Transactions of Civil Engineering**, Vol. 43, No. 1, (2019), 1-10. <https://doi.org/10.1007/s40996-019-00319-2>
 23. Soil, A.C.D.-o. and Rock, "Standard practice for classification of soils for engineering purposes (unified soil classification system) 1", ASTM International, (2017).
 24. Stefanoff, G., Sanglerat, G., Bergdahl, U. and Melzer, K., "Dynamic probing (DP): International reference test procedure", in International Symposium on penetration testing; ISOPT-1. 1. (1988), 53-70.
 25. Meardi, G., "Discussion: The correlation of cone size in the dynamic cone penetration test with the standard penetration test", **Géotechnique**, Vol. 21, No. 2, (1971), 184-190.
 26. Matsumoto, T., Phan, L.T., Oshima, A. and Shimono, S., "Measurements of driving energy in spt and various dynamic cone penetration tests", **Soils and Foundations**, Vol. 55, No. 1, (2015), 201-212. <https://doi.org/10.1016/j.sandf.2014.12.016>
 27. Sun, Y., Cheng, Q., Lin, J., Lammers, P.S., Berg, A., Meng, F., Zeng, Q. and Li, L., "Energy-based comparison between a dynamic cone penetrometer and a motor-operated static cone penetrometer", **Soil and Tillage Research**, Vol. 115, (2011), 105-109. <https://doi.org/10.1016/j.still.2011.06.005>
 28. Standard, A., "D1556-07: Standard test method for density and unit weight of soil in place by the sand-cone method", ASTM International, West Conshohocken, PA, (2007).
 29. D, A.S., Standard test methods for laboratory compaction characteristics of soil using modified effort. 2009, American Society for Testing and Materials (ASTM) International West.
 30. ASTM, D-., "Standard test method for direct shear test of soils under consolidated drained conditions", D3080/D3080M, Vol. 3, No. 9, (2011).
 31. Ameratunga, J., Sivakugan, N. and Das, B.M., *Correlations of soil and rock properties in geotechnical engineering*. 2016, Springer.
 32. Montgomery, D.C. and Runger, G.C., "Applied statistics and probability for engineers", John Wiley & Sons, (2010).
 33. Lin, L., Li, S., Liu, X. and Chen, W., "Prediction of relative density of carbonate soil by way of a dynamic cone penetration test", **Géotechnique Letters**, Vol. 9, No. 2, (2019), 154-160. <https://doi.org/10.1680/gjgele.18.00165>

COPYRIGHTS

©2023 The author(s). This is an open access article distributed under the terms of the Creative Commons Attribution (CC BY 4.0), which permits unrestricted use, distribution, and reproduction in any medium, as long as the original authors and source are cited. No permission is required from the authors or the publishers.



Persian Abstract

چکیده

آزمایش نفوذسنجی دینامیکی، می تواند به طور موثر در جهت کنترل تراکم خاکریزها و لایه های راهسازی مورد استفاده قرار گیرد، اما یکی از چالش های موثر در این امکان استفاده از نفوذسنجهای دینامیکی رده سبک در خاک های متراکم و کسب نتایج صحیح از آن می باشد. خلاصه وجود چنین نفوذسنجهایی در موارد زیادی مشاهده می شود. در این پژوهش، با بکارگیری سه نفوذسنج دینامیکی جدید رده سبک با هندسه مخروط متفاوت و مقایسه نتایج آنها با سه نوع نفوذسنج دینامیکی متداول، از طریق انجام بیش از ۷۲ آزمون نفوذسنجی دینامیکی در زمین های طبیعی متراکم، به بررسی امکان بهره گیری از نفوذسنج دینامیکی در خاک های متراکم پرداخته شده است. نتایج نفوذسنجی با آزارهای طراحی شده، کاهش ۵۰ درصدی تعداد ضربات نسبت به نفوذسنج سبک نوع DPL را نشان می دهد. همچنین محدوده ضریب تغییرات نتایج ۱۵/۸۶ تا ۸/۵۶ مطابقت تکرار پذیری آنهاست. در نتیجه استفاده از کاوشگرهای مذکور به عنوان جایگزینی برای نفوذسنج های سبک متداول می تواند مورد توجه قرار گیرد. همچنین به جهت ارزیابی بیشتر کارایی این کاوشگرهای روابط همبستگی میان نتایج آنها و برخی مشخصات مهم خاک مانند وزن مخصوص خشک در محل، درصد تراکم و مقاومت برشی نهایی، ارائه گردیده و به روش آماری آنالیز باقیمانده ها، مورد سنجش و رضایت قرار گرفت.



Synthesis of Polyvinyl Alcohol-Chitosan Composite Film using Nanocellulose from Coconut Fibers (*Cocos nucifera*)

Y. Yusmaniar^{*a}, E. Julio^a, A. Rahman^a, S. D. Yudanto^b, F. B. Susetyo^c

^aDepartment of Chemistry, Universitas Negeri Jakarta, Jakarta, Indonesia

^bResearch Center for Metallurgy - National Research and Innovation Agency, Serpong, Indonesia

^cDepartment of Mechanical Engineering, Universitas Negeri Jakarta, Jakarta, Indonesia

PAPER INFO

Paper history:

Received 14 May 2023

Received in revised form 13 July 2023

Accepted 14 Jul 2023

Keywords:

Coconut Husk

Nano-Composite

Tensile Strength

Biodegradability

ABSTRACT

In this research, polyvinyl alcohol (PVA)-chitosan composite films were produced using nanocellulose from coconut fibers (*Cocos nucifera*) in an Indonesian plantation in order to enhance mechanical properties and biodegradability. The process began by separating lignin and hemicellulose by delignification, bleaching, and then cellulose hydrolysis to produce nanocellulose. The PVA was mixed with chitosan with specific compositions and added the nanocellulose in 0%, 1%, 3%, and 5% concentrations, respectively. A tensile test was conducted to obtain tensile strength and elongation break. Biodegradability test was also carried out to determine the level of mass losses. Based on SEM observations, addition of nanocellulose appears to increase the reactivity of the formation of PVA-chitosan composite films, which are characterized by a reduction in film thickness. Addition of 5% nanocellulose resulted in a high quality of nano-composite. The tensile strength, fracture elongation and biodegradability of the composite film were 31.50 MPa, 39.9% and 9.04%, respectively.

doi: 10.5829/ije.2023.36.11b.05

NOMENCLATURE

W_0	Initial mass of sample	W_t	Mass of sample after 30 days
-------	------------------------	-------	------------------------------

1. INTRODUCTION

In recent time, the community became very interested in fresh food of good quality and long shelf life. Plastic-based packaging also became a public concern because of its quality and cleanliness [1]. In the meantime, plastic is a synthetic polymer of long-chain hydrocarbons derived from petroleum. It consists of a polymerization of a similar monomer in long chains [2]. The majority of monomers used in manufactured food packaging, such as ethylene and propylene, are fossil fuel-based compounds. They are widely used for their advantages, including strength, lightness and stability. However, it is difficult to decompose by microorganisms in the environment, caused serious environmental challenges [3, 4].

The development of biodegradable plastic is known as a composite, composed of several materials having

different superior properties [5, 6]. Research on composites for biodegradable plastics, such as polyvinyl alcohol (PVA)-chitosan, has received considerable attention due to its nature as an ecological polymer [7, 8]. Chitosan is one of the most suitable materials for coating and food packaging due to its good film-formation and high antimicrobial properties against pathogenic microorganisms and bacteria (both gram-positive/negative) [9]. The films have disadvantage of poor resistance to humid air, which limits their use for food packaging [10]. The strength and thermal stability of chitosan films were improved by a number of biodegradable synthetic polymers, including polyvinyl alcohol (PVA), polycaprolactone, and polylactic acid [11, 12]. However, there are limitations to PVA-chitosan films, such as their poor mechanical properties [13]. As a result, addition of other materials to PVA-chitosan films,

*Corresponding Author Email: yusmaniar@unj.ac.id (Y. Yusmaniar)

such as nanometric fillers, is essential for improving the physical properties of the composite polymer [14].

Cellulose is among the lignocellulosic polymers, widely examined for its biodegradability, low density, and good mechanical properties [15-17]. Several types of research have also been carried out on cellulose to convert it into a material with many superior values, including conversion to nanocellulose [18-20]. Meanwhile, researchers have focused more on nanocellulose in the technology sector due to its high mechanical strength (high strength and modulus), large surface area, good aspect ratio, environmental friendly nature, and low-cost requirements [21-23].

Agroindustrial waste, such as coconut fibers (*Cocos nucifera*), contains a large amount of cellulose with a percentage of 43.44%. This cellulose enhances the value of the fiber because waste is generally not reused [24]. Coconut fiber has a tensile strength of 7.9 MPa to 11.6 MPa, which may improve the mechanical properties of composite films [25].

Previous research that isolated nanocellulose from coconut fibers discovered that it could be used as a reinforcing agent in composites [26]. Wu et al. [27] have blended PVA with nanocellulose from coconut coir fiber (China), increasing the composition of nanocellulose in composite films from 1% to 3 % increases tensile strength from 55 to 60 MPa. Arun et al. [24] added 2% of nanocellulose from a coconut shell (India) into PVA, a resulting tensile strength of 6.35 ± 0.37 N/mm². Wang et al. [28] prepared nanocellulose from waste coconut shell (Sri Langka) and mixed it with cement. Increasing nanocellulose content increases flexural strength and compressive strength. Li et al. [29] isolated nanocellulose from a coconut shell (China) and mixed it with PVA-chitosan. Nanocellulose content increased from 0 to 3%, resulted in an increase in tensile strength from 25 MPa to 34 MPa. Unfortunately, increasing nanocellulose content to 5% decreased tensile strength. Poornachandhra et al. [30] investigated the alkali-acid hydrolysis method and resulted in nanocellulose from coconut coir fiber (India) with a diameter < 40 nm under conditions of 45% acid, 50 °C for 60 minutes. Nurdiana et al. [31] isolated nanocellulose from coconut husk (Malaysia). Based on the regression equation, the optimum preparation condition of the nanocellulose (sulphuric acid is 64.61 wt.%, the reaction temperature is 44.55 °C, and the reaction time is 58.54 minutes), resulted in 44.84% of yield.

Based on the mentioned above, no research has been conducted on composite film (nanocellulose from coconut husk) with the main objective of investigation on mechanical properties and biodegradability. Li et al. [29] isolated nanocellulose from coconut shell (China) and mixed with PVA-chitosan only to investigate the mechanical properties. For this reason, this research synthesized a biodegradable PVA-chitosan film with

nanocellulose derived from coconut fiber (*Cocos nucifera*) in Indonesian plantation to improve mechanical properties and biodegradability. Nanocelluloses were characterized by FTIR, SEM and XRD. Moreover, PVA-chitosan with nanocellulose was characterized with FTIR. A tensile and a biodegradable tests were also carried out.

2. EXPERIMENTAL METHOD

2. 1. Material The coconut fiber was obtained from a local plantation. NaOH, NaClO, chitosan (66000 g/mol of molecular weight and 92% of deacetylation degree), acetic acid, acetate buffer and sulphuric acid were purchased through Sigma-Aldrich and Merck. The PVA was purchased from Gohsenol (Molecular weight: 22000 g/mol). Deionized water was applied to all experiments.

2. 2. Extraction and Purification of Nanocellulose

The coconut husk was pre-washed and dried to separate fiber and bran. The fiber was cut and sieved into a 40 mesh size [27], mixed with water for 2 hours at 50 °C and dried with oven for 24 hours at 50 °C. After drying, the fibers were heated to 80 °C with a 2% NaOH solution for 2 hours for the delignification process with a repetition and then dried [32].

Furthermore, the dried fibers were bleached using 1.70% NaClO and acetate buffer at 60 - 70 °C with 2 repetitions, which were also washed and dried [33]. The dried fibers were hydrolyzed using 55% sulphuric acid at 45 °C for 45 minutes [34, 35]. The resulting nanocellulose was centrifuged with deionized water at 5000 rpm until the pH was neutral [35]. Then, the precipitate was dialyzed to obtain a constant pH due to the removal of excess sulphate and dissolved sugar due to hydrolysis to sulphuric acid. A centrifuge tube was used to conduct the dialyzed process for 10 minutes at 5000 rpm [36].

2. 3. Preparation of PVA-Chitosan Solution The PVA 3% solution was prepared by dissolving it in deionized water (90 °C) and continuously stirring for approximately 2 hours [37]. A 1.5% chitosan solution was prepared by dissolving with 2 v/v% acetic acid at 100 °C and continuously stirring for approximately 1.5 hours [38]. Both solutions were cooled at room temperature, mixed in a 7:3 ratio, then sonicated for 15 minutes [11].

2. 4. Preparation of Composite Films The composite film was made by adding nanocellulose (0%, 1%, 3%, and 5%) based on the percentage of the total mass [39]. Then the mixture was poured into a plastic mould. After 72 hours, the mixture was de-bubbled and transferred to an oven (60 °C) for around 24 hours for

drying. Afterwards, the mixed films were vacuumed at 80 °C for 24 hours to remove excess water [40].

Composite film samples were made by adding 0%, 1%, 3% and 5% nanocellulose identified as 0-NC, 1-NC, 3-NC and 5-NC, respectively.

2. 5. Characterization The nanocellulose was characterized by FTIR (SHIMADZU Prestige-21 FTIR), SEM (JSM-6510LA), and Panalytical EMPYREAN X-ray diffractometer (XRD) using Cu K α radiation with $\lambda = 1.5406 \text{ \AA}$ at a 2 θ range from 10° - 90°. The mechanical properties of composite films were determined using a Strograph universal test machine. Each sample was tested under ASTM D1882. Triplicate measurement was conducted.

The biodegradation test was performed using the soil burial method. The ground was collected at the Universitas Negeri Jakarta in Indonesia. The soil was dried at room temperature (three days) and complemented with urea for 6 g/kg to resulting an active microbial flora. The composite films were dehydrated under vacuum at 50 °C to obtained constant mass (W_0). The composite films were then coated with synthetic net and buried in the mixed soil-urea. The biodegradability test was conducted under aerobic conditions (25 °C) at 50% relative humidity for 30 days. After 30 days, the samples were washed and dehydrated under vacuum until they obtained a constant mass (W_1). Triplicate biodegradation test measurement was conducted. Percentage mass loss was calculated by following equation [41, 42].

$$\% \text{ Mass loss} = \left[\frac{W_0 - W_1}{W_0} \right] \times 100 \quad (1)$$

3. RESULT AND DISCUSSION

3. 1. FTIR Results of Nanocellulose The FTIR characterization results on the delignified, bleached, and untreated coconut fibers are shown in Figure 1. A wavenumber 3296 cm⁻¹ showed the stretching vibration of the O-H group [43], the wavenumber 2970 cm⁻¹ did not show, but the peak at this wavenumber showed C-H stretching from the alkyl groups [11]. The wavenumber 2898 cm⁻¹ showed the vibration of the C-H group [44]. Meanwhile, a wavenumber 1736 cm⁻¹ showed stretching vibrations in the C=O group owned by hemicellulose and lignin, where the peak was lost in the delignification and bleaching spectra due to this process [45]. Similar behaviour was also found in Julie Chandra's report due to chemical treatment [46].

At 1655 cm⁻¹, there was a peak, which showed the bending of the O-H group in the H₂O molecule [47]. While the wavenumbers 1606 cm⁻¹ and 1512 cm⁻¹ were absent, the peak at this wavenumber revealed vibrations

of the C=O group on the aromatic framework of lignin [48, 49]. A wavenumber of 1425 cm⁻¹ was a bending vibration of the C-H group discovered in lignin and cellulose [50]. The peak at 1371 cm⁻¹ was the bending vibration of the C-H group in cellulose, lignin, and hemicellulose [51], while 1159 cm⁻¹ was C-O-C asymmetric stretching vibration in cellulose, lignin, and hemicellulose [49]. The peak at 895 cm⁻¹ was a stretch vibration in the glucose ring of the cellulose [52].

Results from characterization of hydrolyzed coconut fibers are presented in Figure 2. A wavenumber 3338 cm⁻¹ was the stretch vibration of the O-H group [53], while the C-H group was 2909 cm⁻¹ [54]. The peak at 1636 cm⁻¹ showed the bending vibration of the O-H functional group on the H₂O molecule [55]. Furthermore, a wavenumber at 1362 cm⁻¹ was the bending vibration of the C-H functional group in cellulose [35], while the S=O group contained in the SO₄²⁻ ion was 1200 cm⁻¹. This ion was generated through the use of sulphuric acid in cellulose hydrolysis. Consequently, the sulphate ion forms hydrogen bonds to the hydroxyl groups in cellulose [56].

Chandra et al. [46] reported that the absence of a peak may occur as a result of chemical treatment. Based on Figures 1 and 2, chemical treatment could disappear a wave number of 1736 cm⁻¹. This condition means hemicellulose and lignin have been removed. In addition, after bleaching, a wavenumber 1655 cm⁻¹ which showed the bending of the O-H group in the H₂O molecule, also disappeared.

3. 2. SEM Image of Nanocellulose Figure 3 shows the morphology of the nanocellulose. It shows the cylindrical rods, which tend to form agglomerations. The nanocellulose's diameter ranged from 66.97 nm – 144.70 nm, with a length of 1046 nm – 1267 nm. Those sizes were resulting when treated with 55% sulphuric acid at 45°C for 45 minutes.

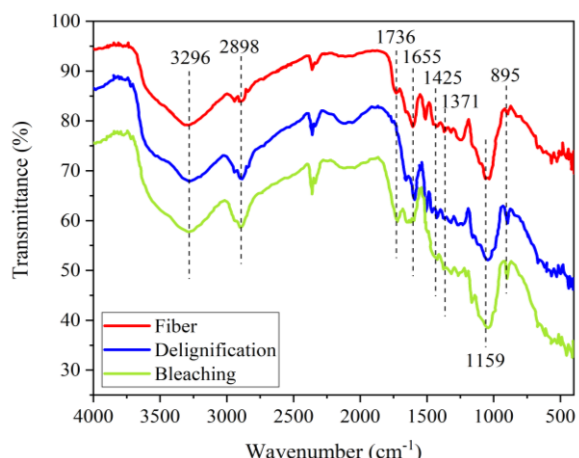


Figure 1. FTIR spectrum of coconut fibers

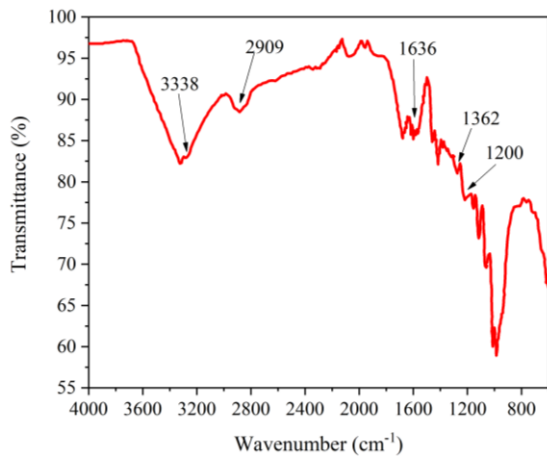


Figure 2. FTIR spectrum of nanocellulose

Lu et al. [57] treated sweet potato residue in 65 wt.% sulfuric acid (120 minutes and 55 °C), resulting in nanocellulose with a diameter of 20-40 nm. Pereira et al. [58] treated bleached banana pseudostem fiber in 62 wt.% sulfuric acid (70 minutes and 45 °C), resulting in nanocellulose with a diameter of 7.2 ± 1.9 nm and length 135 ± 12 nm. Ogundare et al. [59] treated discarded cigarette filters in 55 wt.% sulfuric acid (45 minutes and 45 °C), resulting in nanocellulose with a diameter of 8 nm and length 143 nm. Gan et al. [60] treated empty fruit bunch in 62 wt.% sulfuric acid (60 minutes and 45 °C), resulting in nanocellulose with a diameter less than 50 nm. Yang et al. [61] treated corn husk in 55 wt.% sulfuric acid (1.5 hour and 45 °C), resulting in nanocellulose with a diameter 26.9 ± 3.35 nm. Chen et al. [62] treated alpha cellulose in 0.8 M sulfuric acid (1 hour and 82.2 °C), resulting in nanocellulose with a diameter of 18.36 ± 7.34 nm. Wulandari et al. [35] treated sugarcane bagasse in 50 wt.% sulfuric acid (10 minutes and 40 °C), resulting in nanocellulose with a diameter 95.9 nm. Kouadri and Satha [63] treated *Citrullus colocynthis* in 40 wt.% sulfuric acid (4 hours and room temperature), resulting in nanocellulose with a diameter less than 100 nm. Sampath et al. [64] treated microcrystalline cellulose in 64 wt% sulfuric acid (60 minutes and 45 °C), resulting in nanocellulose with a diameter of 40 nm to 50 nm and length 200 nm to 300 nm.

Based on mentioned above, the source of the cellulose, sulfate concentration, time, and temperature are factors which affect the size of the nanocellulose [65].

3.3. XRD Result of Nanocellulose Figure 4 shows the nanocellulose diffraction pattern. Most of the cellulose phase is found to be semi-crystalline or amorphous, according to the diffraction pattern. Although the peak of the cellulose phase at the indexed plane (200) appears at an angle of $2\theta = 22.64^\circ$, the peak intensity is quite low and broad [66–68]. Through intra-

molecular and inter-molecular hydrogen bonding, cellulose molecules combine to form the semi-crystalline peak in this plane [68]. This is depicted in the insert in Figure 4, which shows the magnified diffraction pattern over the angle range of $2\theta = 15$ – 40° . Kamal et al. [69] also stated that X-ray diffraction investigations revealed the existence of the amorphous cellulose phase.

3.4. Results of Nanocomposite Films

FTIR analysis was used to detect changes in functional groups or the formation of new bonds due to the addition of nanocellulose as a filler in the PVA-chitosan matrix. The results of FTIR characterization of composite films with various concentrations of nanocellulose are shown in Figure 5.

Peaks are widening at wavenumbers from 3100 cm^{-1} to 3550 cm^{-1} in the four PVA-chitosan film spectra due to the vibrations of 2 different functional groups, namely the stretching vibration of the O–H group together with PVA and the N–H group in chitosan [70]. Furthermore, wavenumber 1648 cm^{-1} was a stretching vibration of C=O from acetate [71]. The wavenumber 1564 cm^{-1} was the vibration of the N–H group in chitosan, which shifted from literature [72], indicating the presence of intermolecular bonds of chitosan with the SO_4^{2-} group on

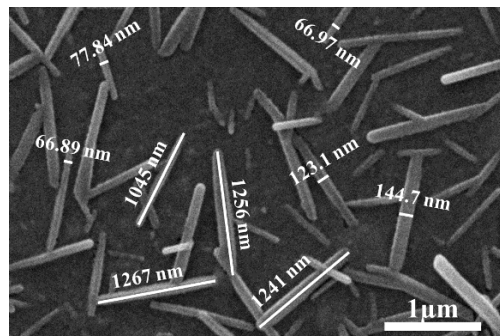


Figure 3. SEM image from nanocellulose

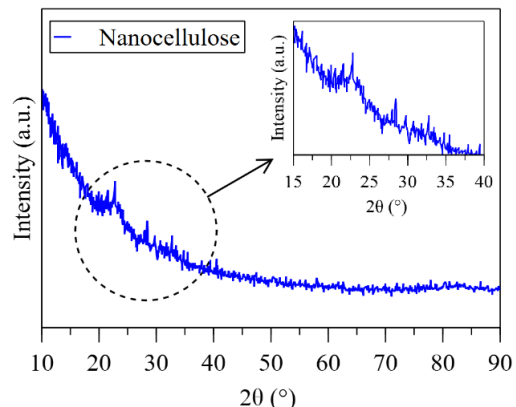


Figure 4. XRD spectrum of nanocellulose. Inset image shows the magnification at $2\theta = 15$ – 40°

nanocellulose surface. Meanwhile, peak at wavenumber 1433 cm^{-1} was the bending vibration of the C–H group on CH_2 in the nanocellulose [73]. The wavenumber of 1126 cm^{-1} was a stretching vibration of the asymmetric C–O group in PVA during the peak at 924 cm^{-1} for the C–C structure of the saccharides in chitosan and cellulose [74, 75]. Furthermore, the wavenumber of 851 cm^{-1} was a bending vibration of the C–O group on the monosaccharide ring in chitosan [76].

The characteristic spectral peaks of PVA-chitosan are due to the presence of good miscibility and chemical interaction between amino-hydroxyl group in PVA and the hydroxyl group in chitosan [11]. Furthermore, the presence of nanocellulose in composite films results in the disappearance or reduction of a certain intensity of FTIR peaks [77]. Wavenumber at $3500\text{--}2750\text{ cm}^{-1}$ reduced with a presence nanocellulose indicating the formation of intermolecular hydrogen bond between PVA-chitosan-nanocellulose in composite films [75]. Presenting nanocellulose in the composite films exhibit wave numbers 1648 cm^{-1} , 1564 cm^{-1} , 1433 cm^{-1} , 1126 cm^{-1} , 924 cm^{-1} , and 851 cm^{-1} . With increasing nanocellulose content, the vibration of the N–H group in chitosan wave number at approximately 1564 cm^{-1} and the stretching vibration of the asymmetric C–O group in PVA wave number at approximately 1126 cm^{-1} are decreased.

3. 5. Results of SEM Cross-section of Nanocomposite Films

The results of the SEM cross-section of nanocellulose added PVA-chitosan films showed that the mixture of PVA and chitosan produced homogeneous films. This showed a good interaction between PVA, chitosan, and the addition of nanocellulose as a filler. The results for SEM films are presented in Figure 6. Adding 1% nanocellulose, the thickness was reduced from $38.9\text{ }\mu\text{m}$ to $17\text{ }\mu\text{m}$. In contrast, adding 3% nanocellulose, the thickness

increases from $17\text{ }\mu\text{m}$ to $24.6\text{ }\mu\text{m}$. This behaviour needs further investigation. Moreover, by adding 5% nanocellulose, the thickness was reduced from $24.6\text{ }\mu\text{m}$ to $12.1\text{ }\mu\text{m}$. Generally, the addition of nanocellulose can reduce the thickness compared to the absence of the nanocellulose. Smaller thickness is found on addition of nanocellulose to 5%.

Hajji et al. [11] found pure chitosan and PVA thicknesses of $80\text{ }\mu\text{m}$ and $30\text{ }\mu\text{m}$. Due to the increased solubility, exhibiting PVA in the blended films would decrease the thickness. PVA-chitosan with a ratio of 70:30 resulting thickness $30\text{ }\mu\text{m}$. This result is slightly different from the present study, probably because of different preparation. In the present study, the PVA solution was stirred at $90\text{ }^\circ\text{C}$ for 2 hours. The chitosan solution was also stirred in the meantime for 1.5 hours at $100\text{ }^\circ\text{C}$. Both solutions were naturally cooled to room temperature. PVA-chitosan was mixed in a 7:3 ratio, and then subjected to a 15-minute sonication process. Whereas Hajji et al. [11] conducted a stirring of the solution for 6 hours at $80\text{ }^\circ\text{C}$ (PVA) and stirred the solution for 24 hours at $25\text{ }^\circ\text{C}$ (chitosan). Based on chitosan weight, glycerol was added to the chitosan solution at 10% (w/w). Both solutions were mixed in a 7:3 ratio [11].

3. 6. Results of Tensile Analysis of Nanocomposite Film

The tensile strength results obtained from the films tested are presented in Figure 7. PVA-chitosan films demonstrate a tensile strength of 22.43 MPa , which increased to 24.78 MPa when nanocellulose was added at 1%. Tensile strength was 28.05 MPa by adding 3% nanocellulose and 31.50 MPa by 5%. As a result, the increase in nanocellulose concentration increases tensile strength due to had a high surface area. This led to the formation of intermolecular interactions through hydrogen or ionic bonds in the PVA-chitosan polymer matrix at nanocellulose fillers [77]. Hydrogen bonds are

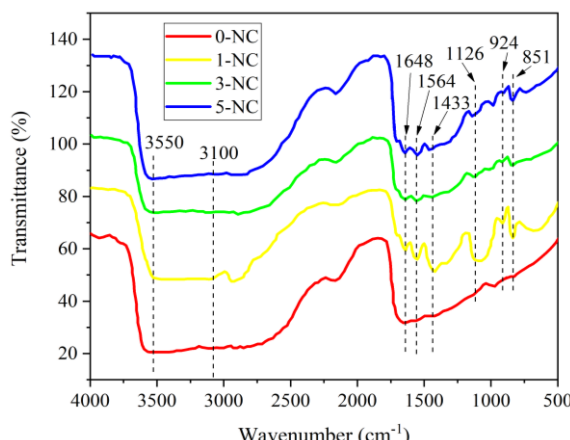


Figure 5. FTIR spectrum of composite films containing different percentages 0%, 1%, 3% and 5% of nanocellulose

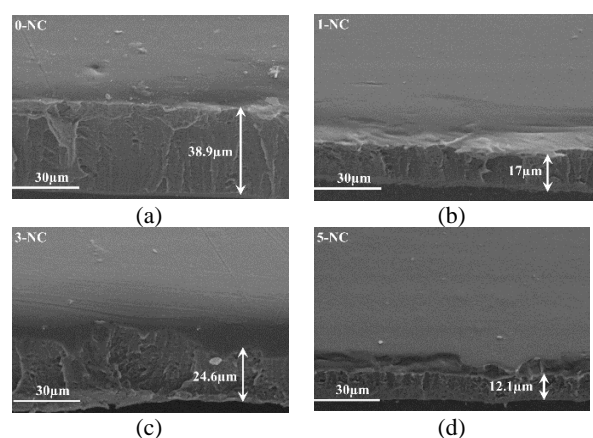


Figure 6. SEM images of nanocomposite film containing different percentages (a) 0%, (b) 1%, (c) 3% and (d) 5% of nanocellulose

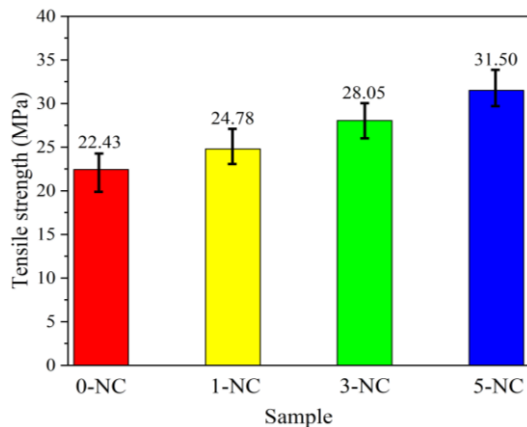


Figure 7. Effect of nanocellulose addition on the tensile strength

formed in order to increase the strength of the polymer [78]. Yudhanto et al. [79] has found that increasing nanocellulose composition from 2 to 5% lead to an increase in tensile strength. Moreover, Perumal et al. [80] blended PVA-chitosan-nanocellulose and resulting tensile strength increase with an increase in nanocellulose composition (1, 3 and 5%).

The present research has less tensile strength than another report due to acetic acid at PVA-chitosan synthesis. Abdolrahimi et al. [81] reported that an increase in acetic acid concentration in the composite promoted decreased tensile strength. Compared with Wu et al. [27], this research resulting less tensile strength due to the presence of chitosan (30%) in the composite films. Hajii et al. [11] found the tensile strength of pure PVA and chitosan to be 53.4 and 3.75 MPa, respectively. An increase in chitosan composition results in a reduction in tensile strength. Yu et al. [13] mixed PVA with chitosan in a 3:2 ratio. The PVA-chitosan mixture reportedly has a tensile strength of 27 MPa.

Another factor influence tensile strength is size of the nanocellulose. Modified cellulose to nanometer size induce the mechanical properties as regard to common cellulose fiber due to surface area and active interface [82]. In the present research, nanocellulose's diameter ranged from 66.97 nm – 144.70 nm, with a length of 1046 nm – 1267 nm which is higher than other research (Figure 3) [65]. Wu et al. [27] have blended PVA with nanocellulose with size 5.6 ± 1.5 nm, increasing the composition of nanocellulose in composite films from 1% to 3 % increased the tensile strength from 55 to 60 MPa.

Compared with synthetic packaging, the present research has more or similar tensile strength. Su and Zhang [83] reported tensile strength of high-density polyethylene is 29.3 MPa. Rhim et al. [84] found polypropylene is 31 -38 MPa. Boldt et al. [85] and AlMaadeed et al. [86] found low-density polyethylene is 20 MPa.

Figure 8 shows that adding nanocellulose as a filler increased the elongation at the break of the PVA-chitosan films, which is similar to other report [79]. Hajii et al. [11] found elongation at break pure PVA and chitosan are 38.4 and 454 %. Yudhanto et al. [79] have found that increasing nanocellulose composition from 2 to 5% lead to an increase in elongation at break from 51 % to 110 %. Zhou et al. [87] found that exhibit 10% nanocellulose would increase elongation at break from 6 to 11 %. Moreover, Mandal and Chakrabarty [82] also found similar behaviour, by increasing nanocellulose content from 2.5 to 5 wt.% would increase elongation at break from 160 to 190 %. It seems that tensile strength and elongation at break have a linear relationship, which perfectly agrees with another result [29].

3. 7. Result of Biodegradable Test of Nanocomposite Films

The biodegradation test was carried out using the soil burial method. When buried, this is a direct contact test between the films and the soil. This condition could degrade the films by action of microorganism, fungi, bacteria, or other in soil [88]. The mass loss (%) amount results of the biodegradation test were calculated by Equation (1) is presented in Figure 9. Based on Figure 9, the nanocellulose filler addition affected the composite films mass degraded during soil burial. In nanocellulose-free PVA-chitosan films, the degradation mass during the biodegradation process was 2.11%. Furthermore, at the 1% nanocellulose addition, the degraded mass was 4.80%, and it was 8.62% at 3% of nanocellulose. In addition to 5%, the highest percentage of mass degradation was 9.04%. This behavior could due to denser structure of the PVA-chitosan restricted the destructive enzymatic activity, therefore, by increasing nanocellulose content, would increase mass loss.

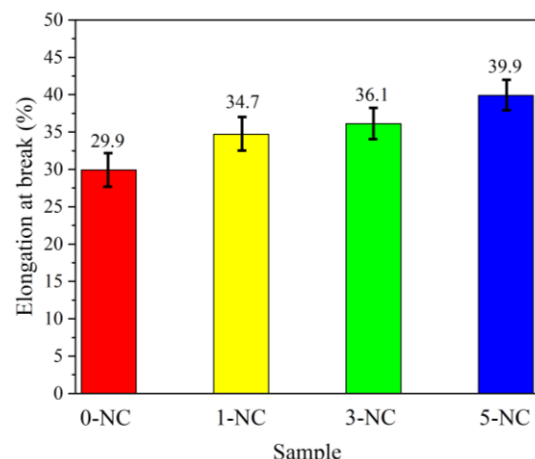


Figure 8. Effect of nanocellulose addition on the elongation at break

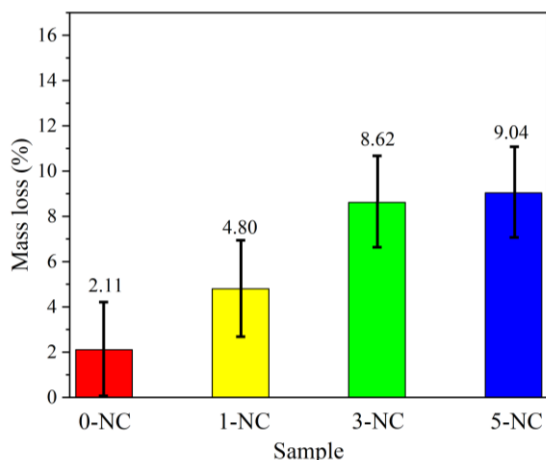


Figure 9. Effect of nanocellulose addition on biodegradation tests

Perumnal et al. [80] have found by adding 5% in PVA-chitosan lead to increase mass loss from 4 to 5% (investigated in 30 days). Van Nquyen and Lee [89] have found, by adding 0.75 g nanocellulose in 3.325 g PVA would enhance degradation rate from 10 % to 19 %. Moreover, Luzi et al. [90] has found the presence nanocellulose increases microbial attack to the surface leading to roughness and formation of crevice.

4. CONCLUSIONS

The PVA-chitosan films with nanocellulose filler from coconut fibers have been successfully fabricated. The morphology of nanocellulose is obtained as cylindrical rods, which tend to form agglomerations. The nanocellulose's diameter ranged from 66.97 nm – 144.70 nm, with a length of 1.046 μm – 1.267 μm . With an increase in nanocellulose content, the vibration of the N–H group in chitosan wave number at approximately 1564 cm^{-1} and the stretching vibration of the asymmetric C–O group in PVA wave number at approximately 1126 cm^{-1} were decreased. Increasing the nanocellulose concentration, increases the tensile strength, elongation at break and biodegradability. Higher the tensile strength, elongation at break and biodegradability is found in the 5-NC sample. Due to its tensile strength and biodegradability, PVA-chitosan-nanocellulose, a product of synthesis, offers a potential replacement for synthetic packaging.

5. ACKNOWLEDGMENTS

This project had financial support from Hibah PENELITIAN DASAR FAKULTAS with contract number 54 /SPK PENELITIAN/5.FMIPA/2021.

6. REFERENCES

- Wyrwa, J., and Barska, A. "Innovations in the food packaging market: active packaging." *European Food Research and Technology*, Vol. 243, No. 10, (2017), 1681-1692. <https://doi.org/10.1007/s00217-017-2878-2>
- Senthil Kumar, P., Bharathikumar, M., Prabhakaran, C., Vijayan, S., and Ramakrishnan, K. "Conversion of waste plastics into low-emissive hydrocarbon fuels through catalytic depolymerization in a new laboratory scale batch reactor." *International Journal of Energy and Environmental Engineering*, Vol. 8, No. 2, (2017), 167-173. <https://doi.org/10.1007/s40095-015-0167-z>
- Yang, X. G., Wen, P. P., Yang, Y. F., Jia, P. P., Li, W. G., and Pei, D. S. "Plastic biodegradation by in vitro environmental microorganisms and in vivo gut microorganisms of insects." *Frontiers in Microbiology*, Vol. 13, (2023). <https://doi.org/10.3389/fmicb.2022.1001750>
- Sheikh, K., and Shahrajabian, H. "Experimental study on mechanical, thermal and antibacterial properties of hybrid nanocomposites of PLA/CNF/Ag." *International Journal of Engineering, Transactions B: Applications*, Vol. 34, No. 2, (2021), 500-507. <https://doi.org/10.5829/IJE.2021.34.02B.23>
- Ashok, A., Abhijith, R., and Rejeesh, C. R. "Material characterization of starch derived bio degradable plastics and its mechanical property estimation." In *Materials Today: Proceedings* (Vol. 5, pp. 2163-2170). Elsevier Ltd. <https://doi.org/10.1016/j.matpr.2017.09.214>
- Furutate, S., Kamoi, J., Nomura, C. T., Taguchi, S., Abe, H., and Tsuge, T. "Superior thermal stability and fast crystallization behavior of a novel, biodegradable α -methylated bacterial polyester." *NPG Asia Materials*, Vol. 13, No. 1, (2021). <https://doi.org/10.1038/s41427-021-00296-x>
- Gasti, T., Dixit, S., Sataraddi, S. P., Hiremani, V. D., Masti, S. P., Chougale, R. B., and Malabadi, R. B. "Physicochemical and Biological Evaluation of Different Extracts of Edible Solanum nigrum L. Leaves Incorporated Chitosan/Poly (Vinyl Alcohol) Composite Films." *Journal of Polymers and the Environment*, Vol. 28, No. 11, (2020), 2918-2930. <https://doi.org/10.1007/s10924-020-01832-6>
- Haque, A. N. M. A., and Naebe, M. "Flexible water-resistant semi-transparent cotton gin trash/poly (vinyl alcohol) bio-plastic for packaging application: Effect of plasticisers on physicochemical properties." *Journal of Cleaner Production*, Vol. 303, (2021), 126983. <https://doi.org/10.1016/j.jclepro.2021.126983>
- Liu, Y., Wang, S., and Lan, W. "Fabrication of antibacterial chitosan-PVA blended film using electrospray technique for food packaging applications." *International Journal of Biological Macromolecules*, Vol. 107, (2018), 848-854. <https://doi.org/10.1016/j.ijbiomac.2017.09.044>
- Priyadarshi, R., and Rhim, J. W. "Chitosan-based biodegradable functional films for food packaging applications." *Innovative Food Science and Emerging Technologies*, Vol. 62, (2020), 102346. <https://doi.org/10.1016/j.ifset.2020.102346>
- Hajji, S., Chaker, A., Jridi, M., Maalej, H., Jellouli, K., Boufi, S., and Nasri, M. "Structural analysis, and antioxidant and antibacterial properties of chitosan-poly (vinyl alcohol) biodegradable films." *Environmental Science and Pollution Research*, Vol. 23, No. 15, (2016), 15310-15320. <https://doi.org/10.1007/s11356-016-6699-9>
- Jacob, J., and Gopi, S. Isolation and physicochemical characterization of biopolymers. *Biopolymers and their Industrial Applications*. <https://doi.org/10.1016/b978-0-12-819240-5.00003-1>
- Yu, Z., Li, B., Chu, J., and Zhang, P. "Silica in situ enhanced PVA/chitosan biodegradable films for food packages." <https://doi.org/10.1016/j.biomaterials.2022.122000>

- Carbohydrate Polymers**, Vol. 184, (2018), 214-220. <https://doi.org/10.1016/j.carbpol.2017.12.043>
14. Abbas, W. A., Sharafeldin, I. M., Omar, M. M., and Allam, N. K. "Novel mineralized electrospun chitosan/PVA/TiO₂ nanofibrous composites for potential biomedical applications: Computational and experimental insights." **Nanoscale Advances**, Vol. 2, No. 4, (2020), 1512-1522. <https://doi.org/10.1039/d0na00042f>
 15. Collazo-Bigliardi, S., Ortega-Toro, R., and Chiralt Boix, A. "Isolation and characterisation of microcrystalline cellulose and cellulose nanocrystals from coffee husk and comparative study with rice husk." **Carbohydrate Polymers**, Vol. 191, (2018), 205-215. <https://doi.org/10.1016/j.carbpol.2018.03.022>
 16. Oracion, J. P. L., Rosa, L. B. D. La, Budlayan, M. L. M., Rodriguez, M. J. D., Manigo, J. P., Patricio, J. N., Arco, S. D., Austria, E. S., Alguno, A. C., Deocaris, C. C., and Capangpangan, R. Y. "Simple one-pot *in situ* synthesis of gold and silver nanoparticles on bacterial cellulose membrane using polyethylenimine." **Journal of Applied Science and Engineering (Taiwan)**, Vol. 24, No. 3, (2021), 351-357. [https://doi.org/10.6180/jase.202106_24\(3\).0010](https://doi.org/10.6180/jase.202106_24(3).0010)
 17. Lakshmu Naidu, A., and Kona, S. "Experimental Study of the Mechanical Properties of Banana Fiber and Groundnut Shell Ash Reinforced Epoxy Hybrid Composite." **International Journal of Engineering, Transactions A: Basics**, Vol. 31, No. 4, (2018), 659-665. <https://doi.org/10.5829/ije.2018.31.04a.18>
 18. Ramakrishnan, A., Ravishankar, K., and Dhamodharan, R. "Preparation of nanofibrillated cellulose and nanocrystalline cellulose from surgical cotton and cellulose pulp in hot-glycerol medium." **Cellulose**, Vol. 26, No. 5, (2019), 3127-3141. <https://doi.org/10.1007/s10570-019-02312-4>
 19. Ahmad Khorairi, A. N. S., Sofian-Seng, N. S., Othaman, R., Abdul Rahman, H., Mohd Razali, N. S., Lim, S. J., and Wan Mustapha, W. A. "A Review on Agro-industrial Waste as Cellulose and Nanocellulose Source and Their Potentials in Food Applications." **Food Reviews International**, Vol. 39, No. 2, (2021), 663-688. <https://doi.org/10.1080/87559129.2021.1926478>
 20. Phanthong, P., Reubroycharoen, P., Hao, X., Xu, G., Abudula, A., and Guan, G. "Nanocellulose: Extraction and application." **Carbon Resources Conversion**, Vol. 1, No. 1, (2018), 32-43. <https://doi.org/10.1016/j.crcon.2018.05.004>
 21. Zaaba, N. F., Jaafar, M., and Ismail, H. "Tensile and morphological properties of nanocrystalline cellulose and nanofibrillated cellulose reinforced PLA bionanocomposites: A review." **Polymer Engineering and Science**, Vol. 61, No. 1, (2021), 22-38. <https://doi.org/10.1002/pen.25560>
 22. Norfarhana, A. S., Ilyas, R. A., and Ngadi, N. "A review of nanocellulose adsorptive membrane as multifunctional wastewater treatment." **Carbohydrate Polymers**, Vol. 291, (2022), 119563. <https://doi.org/10.1016/j.carbpol.2022.119563>
 23. Xu, T., Du, H., Liu, H., Liu, W., Zhang, X., Si, C., Liu, P., and Zhang, K. "Advanced Nanocellulose-Based Composites for Flexible Functional Energy Storage Devices." **Advanced Materials**, Vol. 33, No. 48, (2021), 2101368. [https://doi.org/https://doi.org/10.1002/adma.202101368](https://doi.org/10.1002/adma.202101368)
 24. Arun, R., Shruthy, R., Preetha, R., and Sreejit, V. "Biodegradable nano composite reinforced with cellulose nano fiber from coconut industry waste for replacing synthetic plastic food packaging." **Chemosphere**, Vol. 291, (2022), 132786. <https://doi.org/10.1016/j.chemosphere.2021.132786>
 25. Ismail, N. F., Sulong, A. B., Muhamad, N., Tholibon, D., MdRadzi, M. K. F., and WanIbrahim, W. A. S. "Review of the Compression Moulding of Natural Fiber-Reinforced Thermoset Composites: Material Processing and Characterisations." **Pertanika Journal of Tropical Agricultural Science**, Vol. 38, No. 4, (2015), 533-547.
 26. Rosa, M. F., Medeiros, E. S., Malmonge, J. A., Gregorski, K. S., Wood, D. F., Mattoso, L. H. C., Glenn, G., Orts, W. J., and Imam, S. H. "Cellulose nanowhiskers from coconut husk fibers: Effect of preparation conditions on their thermal and morphological behavior." **Carbohydrate Polymers**, Vol. 81, No. 1, (2010), 83-92. <https://doi.org/10.1016/j.carbpol.2010.01.059>
 27. Wu, J., Du, X., Yin, Z., Xu, S., Xu, S., and Zhang, Y. "Preparation and characterization of cellulose nanofibrils from coconut coir fibers and their reinforcements in biodegradable composite films." **Carbohydrate Polymers**, Vol. 211, (2019), 49-56. <https://doi.org/10.1016/j.carbpol.2019.01.093>
 28. Wang, S., Zou, Q., Zhang, L., Zheng, W., Huang, X., and Zhang, J. "A new nanocellulose prepared from waste coconut shell fibers based on a novel ultrasonic - Active agent combination method: Preparation principle and performances in cement matrix." **Industrial Crops and Products**, Vol. 197, (2023), 116607. <https://doi.org/10.1016/j.indcrop.2023.116607>
 29. Li, G., Luo, H., Xia, W., Xu, X., and Zhang, Y. "Preparation and properties of nano coir cellulose whiskers enhanced cs/pva composite film." **Materials Science Forum**, Vol. 999, (2020), 145-154. <https://doi.org/10.4028/www.scientific.net/MSF.999.145>
 30. Poornachandhra, C., Jayabalakrishnan, R. M., Balasubramanian, G., Lakshmanan, A., Selvakumar, S., Maheswari, M., and John, J. E. "Coconut Husk Fiber: A Low-Cost Bioresource for the Synthesis of High-Value Nanocellulose." **Biointerface Research in Applied Chemistry**, Vol. 13, No. 6, (2023), 1-25. <https://doi.org/10.33263/BRIAC136.504>
 31. Nurdiana, O., Sam, S. T., and Faiq, A. M. "Optimization of the product of nanocrystalline cellulose from coconut husks." In International Conference on Advanced Manufacturing and Industry Applications (Vol. 429, 012041). IOP Conf. Series: Materials Science and Engineering. <https://doi.org/10.1088/1757-899X/429/1/012041>
 32. Silviana, S., and Dzulkarom, M. C. "Synthesis of Cassava Bagasse Starch-Based Biocomposite Reinforced Woven Bamboo Fibre with Lime Juice as Crosslinker and Epoxidized Waste Cooking Oil (EWCO) as Bioplasticizer." In The 3rd International Conference of Chemical and Materials Engineering (Vol. 1295, 012076). IOP Conf. Series: Journal of Physics: Conf. Series. <https://doi.org/10.1088/1742-6596/1295/1/012076>
 33. Van Hai, L., Pham, D. H., and Kim, J. "Effect of Bleaching and Hot-Pressing Conditions on Mechanical Properties of Compressed Wood." **Polymers**, Vol. 14, No. 14, (2022). <https://doi.org/10.3390/polym14142901>
 34. Sun, B., Zhang, M., Hou, Q., Liu, R., Wu, T., and Si, C. "Further characterization of cellulose nanocrystal (CNC) preparation from sulfuric acid hydrolysis of cotton fibers." **Cellulose**, Vol. 23, No. 1, (2016), 439-450. <https://doi.org/10.1007/s10570-015-0803-z>
 35. Wulandari, W. T., Rochliadi, A., and Arcana, I. M. "Nanocellulose prepared by acid hydrolysis of isolated cellulose from sugarcane bagasse." In 10th Joint Conference on Chemistry (Vol. 107, 012045). IOP Conference Series: Materials Science and Engineering. <https://doi.org/10.1088/1757-899X/107/1/012045>
 36. Azhar, O., Jahan, Z., Sher, F., Niazi, M. B. K., Kakar, S. J., and Shahid, M. "Cellulose acetate-polyvinyl alcohol blend hemodialysis membranes integrated with dialysis performance and high biocompatibility." **Materials Science and Engineering C**, Vol. 126, (2021), 112127. <https://doi.org/10.1016/j.msec.2021.112127>
 37. Ntshangase, N. C., Sadare, O. O., and Daramola, M. O. "Effect of silica sodalite functionalization and pva coating on performance of sodalite infused psf membrane during treatment of acid mine drainage." **Membranes**, Vol. 11, No. 5, (2021), 1-16. <https://doi.org/10.3390/membranes11050315>

38. Ramaswamy, S., Dwarampudi, L. P., Kadiyala, M., Kuppuswamy, G., Veera Venkata Satyanarayana Reddy, K., Kumar, C. K. A., and Paranjothy, M. "Formulation and characterization of chitosan encapsulated phytoconstituents of curcumin and rutin nanoparticles." *International Journal of Biological Macromolecules*, Vol. 104, , (2017), 1807-1812. <https://doi.org/10.1016/j.ijbiomac.2017.06.112>
39. de Lima, G. F., de Souza, A. G., and Rosa, D. dos S. "Nanocellulose as Reinforcement in Carboxymethylcellulose Superabsorbent Nanocomposite Hydrogels." *Macromolecular Symposia*, Vol. 394, No. 1, (2020), 1-9. <https://doi.org/10.1002/masy.202000126>
40. Li, H. Z., Chen, S. C., and Wang, Y. Z. "Preparation and characterization of nanocomposites of polyvinyl alcohol/cellulose nanowhiskers/chitosan." *Composites Science and Technology*, Vol. 115, (2015), 60-65. <https://doi.org/10.1016/j.compscitech.2015.05.004>
41. Gulati, K., Lal, S., Diwan, P. K., and Arora, S. "Investigation of Thermal, Mechanical, Morphological and Optical Properties of Polyvinyl alcohol Films Reinforced with Buddha Coconut (*Sterculia alata*) Leaf Fiber." *International Journal of Applied Engineering Research*, Vol. 14, No. 1, (2019), 170-179.
42. Nissa, R. C., Fikriyyah, A. K., Abdullah, A. H. D., and Pudjiraharti, S. "Preliminary study of biodegradability of starch-based bioplastics using ASTM G21-70, dip-hanging, and Soil Burial Test methods." In 3rd International Symposium on Green Technology for Value Chains 2018 (Vol. 277, p. 012007). IOP Conference Series: Earth and Environmental Science. <https://doi.org/10.1088/1755-1315/277/1/012007>
43. Md Salim, R., Asik, J., and Sarjadi, M. S. "Chemical functional groups of extractives, cellulose and lignin extracted from native *Leucaena leucocephala* bark." *Wood Science and Technology*, Vol. 55, No. 2, (2021), 295-313. <https://doi.org/10.1007/s00226-020-01258-2>
44. Su, G., Zhou, T., Liu, X., and Zhang, Y. "Two-step volume phase transition mechanism of poly(N-vinylcaprolactam) hydrogel online-tracked by two-dimensional correlation spectroscopy." *Physical Chemistry Chemical Physics*, Vol. 19, No. 40, (2017), 27221-27232. <https://doi.org/10.1039/c7cp04571a>
45. Yao, S. F., Chen, X. T., and Ye, H. M. "Investigation of Structure and Crystallization Behavior of Poly(butylene succinate) by Fourier Transform Infrared Spectroscopy." *Journal of Physical Chemistry B*, Vol. 121, No. 40, (2017), 9476-9485. <https://doi.org/10.1021/acs.jpcb.7b07954>
46. Julie Chandra, C. S., George, N., and NarayananKutty, S. K. "Isolation and characterization of cellulose nanofibrils from arecanut husk fibre." *Carbohydrate Polymers*, Vol. 142, , (2016), 158-166. <https://doi.org/10.1016/j.carbpol.2016.01.015>
47. Scholtzová, E., Kucková, L., Kožíšek, J., and Tunega, D. "Structural and spectroscopic characterization of ettringite mineral-combined DFT and experimental study." *Journal of Molecular Structure*, Vol. 1100, (2015), 215-224. <https://doi.org/10.1016/j.molstruc.2015.06.075>
48. Bakri, B., Putra, A. E. E., Mochtar, A. A., Renreng, I., and Arsyad, H. "Sodium Bicarbonate Treatment on Mechanical and Morphological Properties of Coir Fibres." *International Journal of Automotive and Mechanical Engineering*, Vol. 15, No. 3, (2018), 5562-5572. <https://doi.org/https://doi.org/10.15282/ijame.15.3.2018.12.0427>
49. Moosavinejad, S. M., Madhoushi, M., Vakili, M., and Rasouli, D. "Evaluation of degradation in chemical compounds of wood in historical buildings using Ft-Ir And Ft-Raman vibrational spectroscopy." *Maderas: Ciencia y Tecnología*, Vol. 21, No. 3, (2019), 381-392. <https://doi.org/10.4067/S0718-221X2019005000310>
50. Chen, C., Luo, J., Qin, W., and Tong, Z. "Elemental analysis, chemical composition, cellulose crystallinity, and FT-IR spectra of *Toona sinensis* wood." *Monatshefte Fur Chemie*, Vol. 145, No. 1, (2014), 175-185. <https://doi.org/10.1007/s00706-013-1077-5>
51. Bose, S., and Das, C. "Sawdust: From wood waste to pore-former in the fabrication of ceramic membrane." *Ceramics International*, Vol. 41, No. 3, (2015), 4070-4079. <https://doi.org/10.1016/j.ceramint.2014.11.101>
52. Ling, Z., Chen, S., Zhang, X., and Xu, F. "Exploring crystalline-structural variations of cellulose during alkaline pretreatment for enhanced enzymatic hydrolysis." *Bioresource Technology*, Vol. 224, (2017), 611-617. <https://doi.org/10.1016/j.biotech.2016.10.064>
53. Turki, A., El Oudiani, A., Msahli, S., and Sakli, F. "Investigation of OH bond energy for chemically treated alfa fibers." *Carbohydrate Polymers*, Vol. 186, (2018), 226-235. <https://doi.org/10.1016/j.carbpol.2018.01.030>
54. Han, D., Lu, D., and Meng, F. "Dielectric and photoluminescence properties of fine-grained BaTiO₃ ceramics co-doped with amphoteric Sm and valence-variable Cr." *RSC Advances*, Vol. 9, No. 8, (2019), 4469-4479. <https://doi.org/10.1039/c8ra09326a>
55. Heperkan, D., and Gökmen, E. "Application of fourier transform infrared (FTIR) spectroscopy for rapid detection of fumonisin B2 in raisins." *Journal of AOAC International*, Vol. 99, No. 4, (2016), 899-905. <https://doi.org/10.5740/jaoacint.16-0156>
56. Chang, J. K. W., Duret, X., Berberi, V., Zahedi-Niaki, H., and Lavoie, J. M. "Two-step thermochemical cellulose hydrolysis with partial neutralization for glucose production." *Frontiers in Chemistry*, Vol. 6, (2018), 117. <https://doi.org/10.3389/fchem.2018.00111>
57. Lu, H., Gui, Y., Zheng, L., and Liu, X. "Morphological, crystalline, thermal and physicochemical properties of cellulose nanocrystals obtained from sweet potato residue." *Food Research International*, Vol. 50, No. 1, (2013), 121-128. <https://doi.org/10.1016/j.foodres.2012.10.013>
58. Pereira, A. L. S., Nascimento, D. M. D., Souza Filho, M. D. S. M., Morais, J. P. S., Vasconcelos, N. F., Feitosa, J. P. A., Brígida, A. I. S., and Rosa, M. D. F. "Improvement of polyvinyl alcohol properties by adding nanocrystalline cellulose isolated from banana pseudostems." *Carbohydrate Polymers*, Vol. 112, (2014), 165-172. <https://doi.org/10.1016/j.carbpol.2014.05.090>
59. Ogundare, S. A., Moodley, V., and van Zyl, W. E. "Nanocrystalline cellulose isolated from discarded cigarette filters." *Carbohydrate Polymers*, Vol. 175, (2017), 273-281. <https://doi.org/10.1016/j.carbpol.2017.08.008>
60. Gan, P. G., Sam, S. T., Bin Abdullah, M. F., Bin Zulkepli, N. N., and Yeong, Y. F. "Characterization of nanocrystalline cellulose isolated from empty fruit bunch using acid hydrolysis." *Solid State Phenomena*, Vol. 264, (2017), 9-12. <https://doi.org/10.4028/www.scientific.net/SSP.264.9>
61. Yang, X., Han, F., Xu, C., Jiang, S., Huang, L., Liu, L., and Xia, Z. "Effects of preparation methods on the morphology and properties of nanocellulose (NC) extracted from corn husk." *Industrial Crops and Products*, Vol. 109, (2017), 241-247. <https://doi.org/10.1016/j.indcrop.2017.08.032>
62. Chen, Y. W., Lee, H. V., and Hamid, S. B. A. "Preparation of nanostructured cellulose via Cr(III)- and Mn(II)-transition metal salt catalyzed acid hydrolysis approach." *BioResources*, Vol. 11, No. 3, (2016), 7224-7241. <https://doi.org/10.15376/biores.11.3.7224-7241>
63. Kouadri, I., and Satha, H. "Extraction and characterization of cellulose and cellulose nanofibers from *Citrullus colocynthis* seeds." *Industrial Crops and Products*, Vol. 124, (2018), 787-796. <https://doi.org/10.1016/j.indcrop.2018.08.051>

64. Sampath, U. G. T. M., Ching, Y. C., Chuah, C. H., Singh, R., and Lin, P. C. "Preparation and characterization of nanocellulose reinforced semi-interpenetrating polymer network of chitosan hydrogel." *Cellulose*, Vol. 24, No. 5, (2017), 2215-2228. <https://doi.org/10.1007/s10570-017-1251-8>
65. Gan, P. G., Sam, S. T., Abdullah, M. F. bin, and Omar, M. F. "Thermal properties of nanocellulose-reinforced composites: A review." *Journal of Applied Polymer Science*, Vol. 137, No. 11, (2020). <https://doi.org/10.1002/app.48544>
66. Malgas, S., Kwanya Minghe, V. M., and Pletschke, B. I. "The effect of hemicellulose on the binding and activity of cellobiohydrolase I, Cel7A, from *Trichoderma reesei* to cellulose." *Cellulose*, Vol. 27, No. 2, (2020), 781-797. <https://doi.org/10.1007/s10570-019-02848-5>
67. Ioelevich, M. "Preparation, characterization and application of amorphized cellulose—a review." *Polymers*, Vol. 13, No. 24, (2021). <https://doi.org/10.3390/polym13244313>
68. Shi, S. C., and Liu, G. T. "Cellulose nanocrystal extraction from rice straw using a chlorine-free bleaching process." *Cellulose*, Vol. 28, No. 10, (2021), 6147-6158. <https://doi.org/10.1007/s10570-021-03889-5>
69. M. Kamal, Abdelrazek, E. M., Sellow, N. M., and Abdelghany, A. M. "Synthesis and optimization of Novel Chitosan/Cellulose Acetate Natural Polymer Membrane for water treatment." *Energies*, Vol. 6, No. 1, (2018), 1-8. <https://doi.org/https://doi.org/10.24297/jap.v14i1.7183>
70. Mallakpour, S., and Rashidimoghadam, S. "Preparation, characterization, and in vitro bioactivity study of glutaraldehyde crosslinked chitosan/poly(vinyl alcohol)/ascorbic acid-MWCNTs bionanocomposites." *International Journal of Biological Macromolecules*, Vol. 144, (2020), 389-402. <https://doi.org/10.1016/j.ijbiomac.2019.12.073>
71. Zhang, Y., Luo, B., and Sun, Y. "Properties of Ultraviolet-Shielding Composite Film Prepared from Cellulose Acetate with Eu(III) Complex." *Chemistry Select*, Vol. 5, No. 5, (2020), 1688-1693. <https://doi.org/10.1002/slct.201903237>
72. Queiroz, M. F., Melo, K. R. T., Sabry, D. A., Sasaki, G. L., and Rocha, H. A. O. "Does the use of chitosan contribute to oxalate kidney stone formation?" *Marine Drugs*, Vol. 13, No. 1, (2015), 141-158. <https://doi.org/10.3390/md13010141>
73. Adel, A. M., El-Shafei, A. M., Ibrahim, A. A., and Al-Shemy, M. T. "Chitosan/nanocrystalline cellulose biocomposites based on date palm (*Phoenix dactylifera* L.) sheath fibers." *Journal of Renewable Materials*, Vol. 7, No. 6, (2019), 567-582. <https://doi.org/10.32604/jrm.2019.00034>
74. Kong, L., Stapleton, J. J., and Ziegler, G. R. "Characterization of macromolecular orientation in κ -carrageenan fibers using polarized Fourier-transform infrared spectroscopy." *Vibrational Spectroscopy*, Vol. 94, (2018), 61-65. <https://doi.org/10.1016/j.vibspec.2017.12.004>
75. Hu, D., Qiang, T., and Wang, L. "Quaternized chitosan/polyvinyl alcohol/sodium carboxymethylcellulose blend film for potential wound dressing application." *Wound Medicine*, Vol. 16, , (2017), 15-21. <https://doi.org/10.1016/j.wndm.2016.12.003>
76. Tabarsa, M., You, S. G., Dabaghian, E. H., and Surayot, U. "Water-soluble polysaccharides from *Ulva intestinalis*: Molecular properties, structural elucidation and immunomodulatory activities." *Journal of Food and Drug Analysis*, Vol. 26, No. 2, (2018), 599-608. <https://doi.org/10.1016/j.jfda.2017.07.016>
77. Shankar, S., and Rhim, J. W. "Preparation of nanocellulose from micro-crystalline cellulose: The effect on the performance and properties of agar-based composite films." *Carbohydrate Polymers*, Vol. 135, (2016), 18-26. <https://doi.org/10.1016/j.carbpol.2015.08.082>
78. Choo, K., Ching, Y. C., Chuah, C. H., Julai, S., and Liou, N. S. "Preparation and characterization of polyvinyl alcohol-chitosan composite films reinforced with cellulose nanofiber." *Materials*, Vol. 9, No. 8, (2016), 1-16. <https://doi.org/10.3390/ma9080644>
79. Yudhanto, F., Jamasri, Rochardjo, H. S. B., and Kusumaatmaja, A. "Experimental study of polyvinyl alcohol nanocomposite film reinforced by cellulose nanofibers from agave cantala." *International Journal of Engineering, Transactions A: Basics*, Vol. 34, No. 4, (2021), 987-998. <https://doi.org/10.5829/ije.2021.34.04a.25>
80. Perumal, A. B., Sellamuthu, P. S., Nambiar, R. B., and Sadiku, E. R. "Development of polyvinyl alcohol/chitosan bio-nanocomposite films reinforced with cellulose nanocrystals isolated from rice straw." *Applied Surface Science*, Vol. 449, (2018), 591-602. <https://doi.org/10.1016/j.apsusc.2018.01.022>
81. Abdolrahimi, M., Seifi, M., and Ramezanzadeh, M. H. "Study the effect of acetic acid on structural, optical and mechanical properties of PVA/chitosan/MWCNT films." *Chinese Journal of Physics*, Vol. 56, No. 1, (2018), 221-230. <https://doi.org/10.1016/j.cjph.2017.12.018>
82. Mandal, A., and Chakrabarty, D. "Studies on the mechanical, thermal, morphological and barrier properties of nanocomposites based on poly(vinyl alcohol) and nanocellulose from sugarcane bagasse." *Journal of Industrial and Engineering Chemistry*, Vol. 20, No. 2, (2014), 462-473. <https://doi.org/10.1016/j.jiec.2013.05.003>
83. Su, J., and Zhang, J. "Comparison of rheological, mechanical, electrical properties of HDPE filled with BaTiO 3 with different polar surface tension." *Applied Surface Science*, Vol. 388, , (2016), 531-538. <https://doi.org/10.1016/j.apsusc.2015.10.156>
84. Rhim, J. W., Wang, L. F., and Hong, S. I. "Preparation and characterization of agar/silver nanoparticles composite films with antimicrobial activity." *Food Hydrocolloids*, Vol. 33, No. 2, (2013), 327-335. <https://doi.org/10.1016/j.foodhyd.2013.04.002>
85. Boldt, R., Gohs, U., Wagenknecht, U., and Stamm, M. "Effect of electron-induced reactive processing on morphology and structural properties of high-density polyethylene." *Polymer*, Vol. 95, (2016), 1-8. <https://doi.org/10.1016/j.polymer.2016.04.044>
86. Almaadeed, M. A., Nogelová, Z., Mičušík, M., Novák, I., and Krupa, I. "Mechanical, sorption and adhesive properties of composites based on low density polyethylene filled with date palm wood powder." *Materials and Design*, Vol. 53, (2014), 29-37. <https://doi.org/10.1016/j.matdes.2013.05.093>
87. Zhou, P., Luo, Y., Lv, Z., Sun, X., Tian, Y., and Zhang, X. "Melt-processed poly (vinyl alcohol)/corn starch/nanocellulose composites with improved mechanical properties." *International Journal of Biological Macromolecules*, Vol. 183, (2021), 1903-1910. <https://doi.org/10.1016/j.ijbiomac.2021.06.011>
88. Syafri, E., Sudirman, Mashadi, Yulianti, E., Deswita, Asrofi, M., Abral, H., Sapuan, S. M., Ilyas, R. A., and Fudholi, A. "Effect of sonication time on the thermal stability, moisture absorption, and biodegradation of water hyacinth (*Eichhornia crassipes*) nanocellulose-filled bengkuang (*Pachyrhizus erosus*) starch biocomposites." *Journal of Materials Research and Technology*, Vol. 8, No. 6, (2019), 6223-6231. <https://doi.org/10.1016/j.jmrt.2019.10.016>
89. Van Nguyen, S., and Lee, B. K. "Polyvinyl alcohol/cellulose nanocrystals/alkyl ketene dimer nanocomposite as a novel biodegradable food packing material." *International Journal of Biological Macromolecules*, Vol. 207, (2022), 31-39. <https://doi.org/10.1016/j.ijbiomac.2022.02.184>
90. Luzi, F., Fortunati, E., Jiménez, A., Puglia, D., Pezzolla, D., Gigliotti, G., Kenny, J. M., Chiralt, A., and Torre, L. "Production and characterization of PLA/PBS biodegradable blends reinforced with cellulose nanocrystals extracted from hemp fibres." *Industrial Crops and Products*, Vol. 93, (2016), 276-289. <https://doi.org/10.1016/j.indcrop.2016.01.045>

COPYRIGHTS

©2023 The author(s). This is an open access article distributed under the terms of the Creative Commons Attribution (CC BY 4.0), which permits unrestricted use, distribution, and reproduction in any medium, as long as the original authors and source are cited. No permission is required from the authors or the publishers.

**Persian Abstract****چکیده**

در این تحقیق، فیلم‌های کامپوزیتی پلی‌وینیل الکل - (PVA) کیتوزان با استفاده از نانوسلولز از یاف نارگیل (*Cocos nucifera*) در مزرعه‌ای اندونزی به منظور افزایش خواص مکانیکی و تجزیه‌پذیری زیستی تولید شد. این فرآیند با جداسازی لیگنین و همی سلولز با لایه برداری، سفید کردن و سپس هیدرولیز سلولز برای تولید نانوسلولز آغاز شد. PVA با کیتوزان با ترکیبات خاص مخلوط شد و نانوسلولز به ترتیب در غلاظت‌های ۰، ۱، ۳ و ۵ درصد اضافه شد. یک آزمایش کششی برای به دست آوردن استحکام کششی و شکست از دیاد طول انجام شد. تست زیست تخریب پذیری نیز برای تعیین سطح تلفات جرمی انجام شد. بر اساس مشاهدات SEM، افزودن نانوسلولز به نظر می‌رسد که واکنش‌پذیری تشکیل لایه‌های کامپوزیت PVA- کیتوسان را افزایش می‌دهد که با کاهش ضخامت لایه مشخص می‌شود. افزودن ۵ درصد نانوسلولز منجر به کیفیت بالای نانوکامپوزیت شد. استحکام کششی، از دیاد طول شکست و زیست تخریب پذیری فیلم کامپوزیت به ترتیب ۳۱/۵۰ مگاپاسکال، ۳۹/۹ درصد و ۹/۰۴ درصد بود.



Effect of Inclined Angle in Trimming of Ultra-high Strength Steel Sheets Having Inclined and Curved Shapes

K. Y. Leong^a, H. Jaafar^{*a,b}, L. Tajul^a, Z. A. Zailani^a, R. Hamidon^a, M. Z. M. Zain^{a,b}

^aFaculty of Mechanical Engineering and Technology, Universiti Malaysia Perlis, 02600, Arau, Perlis, Malaysia

^bAdvanced Material Processing and Design Research Group, Faculty of Mechanical Engineering Technology, Universiti Malaysia Perlis

PAPER INFO

ABSTRACT

Paper history:

Received 23 May 2023

Received in revised form 28 June 2023

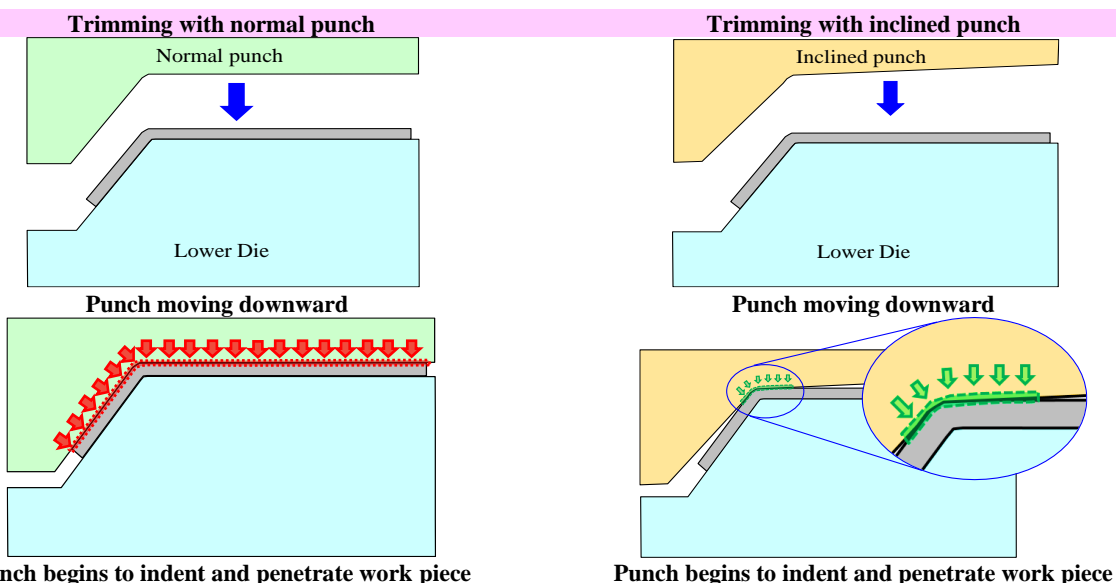
Accepted 05 July 2023

Keywords:

Trimming
Inclination Angle
Ultra-high Strength Steel
Trimming Load
Sheared Edge Quality
Shape Defects

Trimming the scrap portion of ultra-high strength steel (UHSS) components poses a significant challenge due to the inherent high strength and hardness characteristics of the material. For UHSS components with a higher geometric complexity such consisting of inclined and curved sections, sharp tilt, and small bend radius, the large trimming load results in poor sheared quality and shape defects, which commonly happen in these areas. This research investigated the effects of applying a small inclination angle to the punch in the trimming of the UHSS parts having an inclined and curved shape. The inclined punch was modified to four sets of different degrees of inclination i.e., 1°, 3°, 5°, and 10°. A comparative analysis of the trimming load, trimming energy, sheared edge quality and shape defects was conducted between these modified punches and the normal punch for their effectiveness in the trimming operation. Results showed that the application of inclination angle significantly decreased the trimming load, reduced the trimming energy, and improved the sheared edge surface quality, as well as prevented the shape defects at the inclined and curved zones as compared to the outcomes produced when trimming using the normal punch. The study suggested that the change to the punch geometry is an effective option to improve the performance of the process as well as the quality of the part, particularly in trimming the high-strength components having complex shapes.

doi: 10.5829/ije.2023.36.11b.06



*Corresponding Author Institutional Email: hasnulhadi@unimap.edu.my (H. Jaafar)

- All surfaces of the punch are in contact and conform the work piece.
- A significant force is generated to trim the scrap at once.

1. INTRODUCTION

The concern for climate change caused by green gas emissions is spreading over the world, and all nations are beginning to determine the minimum amount of green gas allowed to be emitted for all industries. Considering that CO₂ gas emissions are the primary cause of global warming, the need for remedial action by the transportation sector, especially the automotive manufacturers, to reduce the total weight of vehicles is irrefutable [1]. In conjunction with the green policies set by the environmental agency (EA), lightweight material became a pivotal point of improvement for car manufacturers, as the less-weight vehicles will indirectly release less hazardous gases from engine combustion [2, 3]. The use of lightweight steel reduces the overall weight of a car, which indirectly improves fuel efficiency, whereas high-strength enhances the safety aspects for the passengers [4]. Various studies were conducted in the transportation sector to assess the relationship between mass reduction, crash safety, and cost-effectiveness, as well as greenhouse gas emission, in order to optimize the design and the related manufacturing process [5]. Caffrey et al. [6] investigated the critical factors affecting life cycle assessments of material choice for vehicle weight reduction.

Although steel, which is both lightweight and high strength, is essential for achieving these objectives, this type of material often has reduced formability, which limits the range of uses in many car parts manufacturing processes such as stamping, rolling, punching, and flanging. As a result, to produce steel grades by focusing on both lightweight and high strength, significant effort has been expended in research over the last decades to enhance ductility and formability with appropriate toughness and fatigue resistance concurrently [7, 8]. Among the applicable and cost-effective steels that belong to this category is ultra-high strength steel (UHSS) sheet, which has a strength of up to and above 1000 MPa [9, 10]. The application of UHSS sheets has become essential in modern car manufacturing, mainly for the chassis and the body-in-white (BIW) parts of a car, as the structure made of this material can uphold high impact force in case of any collision occurs [11, 12]. The BIW of vehicle parts, such as the front pillar, center pillar, and cross member, are stamped in a mold, followed by secondary processing, such as bending and flanging, before being moved to the finishing process [13-15]. Since the formability of the UHSS is low and the

- Only small and certain surface area of the punch is in contact with the work piece.
- Small force is generated to trim the scrap only at the contacted area.
- The rest area of the scrap is gradually trimmed as the punch move further downward.

strength is high, performing the sheet metal working process, such as punching and trimming on the UHSS, is challenging [16-18].

The performance, quality, and characteristics at the sheared edge of the cutting process including blanking, punching, and trimming are determined by the process parameters, such as cutting speed, clearance, and corner radius of the punch and die [19-21]. The shape of punch and die is another critical factor in determining the part quality and shearing force. Optimizing the shapes result in a significant reduction of force, especially when trimming or cutting a high strength or thick stock [22-24]. Kolleck et al. [25] investigated the effects of increasing the die chamfer angles on the punching and stripping forces, and spring back in tight geometrical tolerances blanking of conically formed holes. Kutuniva et al. [26] proved that the cutting force of the ultra-high-strength DQ960 was reduced by the shearing angle (convex angle) of the punch. The punch force reduces by 57 % compared to a flat punch force when a shear angle of 14° is used. To get a high-quality sheared surface with a low punch force, a shear angle of 7° was used. Kurniawan et al. [27] similarly investigated the effect of punch geometry (flat shape, single shear angle (SSA), and double shear angle (DSA)) by an experiment. The results showed that using SSA and DSA punch geometry successfully reduces punch force by 18% and 13%, respectively, compared to that of flat punch geometry. FEM simulation has been performed by Bao et al. [28] to investigate the effects of the inclined edge of the punch on the blanking force and surface quality. According to the result obtained, the blanking force will decrease as the inclined edge of punch is increased in comparison to flat edge punching, and the double convex inclined edge could produce the greatest quality of the blanked surface.

Some researchers conducted experiments to the energy consumption, fatigue crack behaviour edge quality and its effect on formability during the cutting and machining processes. Shih et al. [29] used an adjustable computer-controlled shearing device to cut DP600 and the DP980 high-strength steel sheets, where it was discovered that this technique can provide a comparable outcome as compared to cutting process by high-energy laser cutting and water jet cutting procedures but with less energy consumption. Balogun et al. [30] and Zainal et al. [31] reduced the energy consumption in milling of AISI1045 steel alloy and aluminum alloy 7075, respectively, by optimizing the swept angle. Since a fatigue crack typically appears on a shear-cut edge in

automotive components, Paetzold et al. [32] looked into the relationship between the shear-cutting process (die clearance and cutting edge radius) and the fatigue behaviour in cutting of DP800 high strength steel, where the result showed that the shearing technique used has a significant impact on fatigue resistance. Feistel et al. [33] reported that different cutting parameters and strategies, including single and multi-stage shear cutting, open and closed cutting lines, die clearance, and cutting-edge geometry, have a significant effect on the edge crack sensitivity. Gläsner et al. [34] created a novel two-stage shear-cutting technique (pre-cutting, trimming) that exhibits minimal dimensional tolerance and clean edges in order to minimize the sensitivity of edge cracks. Yasutomi et al. [35] discovered that the tensile residual stress on the sheared surface, which is the source for the edge crack, is significantly decreased by shearing scrap material on the sheared edge.

While previous studies have examined the effects of shear and slant angle in the cutting and trimming processes of high-strength steel sheets, the focus has primarily been on flat-shaped parts. However, there remains a knowledge gap concerning the impact of inclined angles in the trimming process of parts with intricate geometric complexities, such as those featuring inclined and curved sections. In this study, the effects of changing the inclined angles on the trimming load, trimming energy, and quality of the sheared edge in the trimming process of ultra-high strength steel (UHSS) parts having an inclined and curved shape were compared to those of trimming with the normal flat punch and investigated.

2. EXPERIMENTAL DETAILS

2.1. Experimental Setup The experiment setup for trimming the UHSS sheet having a curved shape is shown in Figure 1. The experiments were carried out using a trimming die set which assembled at the 250 kN SHIMADZU Universal Testing Machine (UTM) as shown in Figure 2. The punch, lower die and sheet holder are made of SKH11 tool steel having a hardness of HRC50 after the heat treatment process. The JSC1180YN UHSS sheet, with dimensions of 1.22 mm x 50 mm x 40 mm in thickness, length and width, respectively, was selected as the workpiece to be trimmed. The mechanical properties of the UHSS sheet (workpiece) are given in Table 1 and were obtained from the uniaxial tensile tests, which are conducted according to the ASTM E8/E8M standard.

The top and front view of the trimming die is shown in Figure 2 (a) and (b), respectively.

The workpiece is first formed into a curved and inclined shape by a separate bending process so that a bend angle and bend radius of 60° and 5 mm are formed.

Two types of punches, i.e., the normal and inclined punches were used for the experiment. The normal punch conforms to the shape of the workpiece, whereas the inclined punch has a slight inclination of the punch edges, particularly at the inclined and straight zones. Four punches with four different inclination angles, θ , i.e., 1°, 3°, 5°, and 10°, respectively, were fabricated for the experiment and h , is the highest inclination point of the inclined punch (Figure 2(c)). The 10 mm out of 40 mm in width of the workpiece, was trimmed as scrap. The workpiece before and after trimming is shown in Figure 2 (d). The inclined, curved, and straight zones at the workpiece are divided as in Figure 2 (e) for sheared edge observation. The trimming conditions were set as in

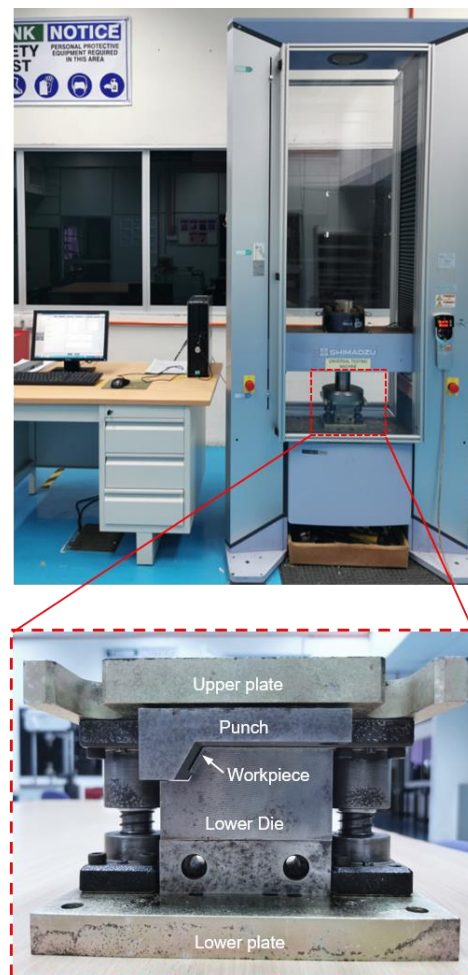


Figure 1. Setup of trimming die set and main components at the 250 kN SHIMADZU Universal Testing Machine

TABLE 1. Mechanical properties of the curved blank

Blank type	Thickness (mm)	Tensile strength (MPa)	Elongation (%)
JSC1180YN	1.22	1242	8.1

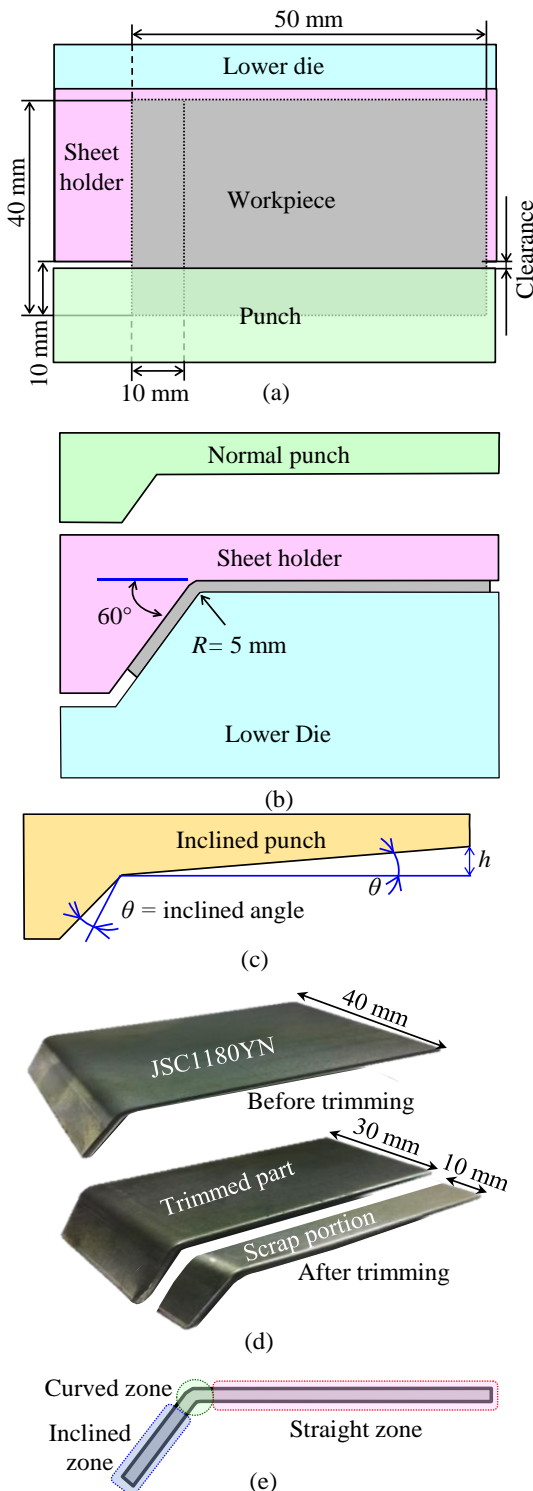


Figure 2. Experimental setup: (a) Top view (b) Front view (c) Inclined punch (d) Workpiece before and after trimming, and (e) Inclined, curved and straight zones of the work piece

Table 2 and the clearance between the punch and the lower die was set to 0.12 mm (10% of thickness). The

TABLE 2. Trimming conditions

Parameter	Set value
Inclination angle, θ	1, 3, 5, 10°
Clearance ratio to workpiece thickness, c	10 % (0.12 mm)
Trimming speed, v	4 mm/s
Bend angle	60°
Bend radius, R	5 mm

blank holder firmly held the workpiece during the trimming process until the scrap was separated from the part. For every set of inclinations, 10 pieces of blank were trimmed, and the average results were analyzed. The low-powered XOPTRON, model XST60 digital microscope with 45 times magnification is used for sheared edge observation.

3. RESULT AND DISCUSSION

3. 1. Trimming Load and Trimming Energy The relation between the trimming load and punch stroke for trimming the JSC1180YN (UHHS) sheet metal with the normal punch and inclined punch with different inclination angles is given in Figure 3. The maximum trimming load for trimming with the normal punch is about 55 kN, whereas a significant reduction at the maximum trimming load was observed when the inclined punch is used. The trimming load was large when using the normal punch because the whole area of the punch is simultaneously in contact with the blank as the trimming punch moves downward, indenting the workpiece. Due to the large contact area between the trimming punch and the part, a huge trimming load is required to simultaneously break the total bonding force in a single cutting action. A high spike of trimming load was observed within less than 1 mm of the punch stroke. In contrast, by applying an inclination angle at the punch, even for just a slight increment of $\theta = 1^\circ$ at the punch, the maximum trimming load was reduced by almost half. A further trend of reduction in maximum trimming load was observed as the angle of inclination was increased. The inclined surface of the punch causes the contact between the punch and the workpiece to be concentrated in a specific area (localized). As a result of this localized contact, the force exerted by the punch on the contact area of the workpiece is minimized. Kutuniva et al. [26] and Kurniawan et al. [27] validated the same pattern of cutting force behaviour during the indentation stage for punching the high-strength steel and titanium, respectively, when changing the punch shape. As the inclined angle is increased, a noticeable distinction is observed in the behaviour of the maximum trimming load is observed, particularly for the inclined punch $\theta = 10^\circ$.

Unlike other inclined punches ($\theta=1^\circ$, 3° , and 5°) that exhibit a sharp peak at the maximum trimming load, the inclined punch $\theta=10^\circ$ displays a flattened profile. When the inclined angle is too large, less area of the workpiece are indented by the punch at the beginning of the trimming process. Although the maximum trimming load is significantly reduced, the punch requires a longer stroke to complete the separation of the scrap. This can be seen from the interval of change of the trimming load from increasing to maximum and going back down (indicating initiation of fracture in the workpiece), where the change of interval is longer for the inclined punch $\theta=10^\circ$, compared to the others that exhibit a short change and sharp peak.

Although trimming with the normal punch results in the highest maximum trimming load, however, the punch stroke is the shortest. By changing to an inclined punch, the punch stroke to separate the part and scrap were found to become longer with an increase in inclination angle. For instance, the total trimming stroke for trimming using an inclined punch with $\theta=10^\circ$ is about 9 mm, which is more than three times that of trimming with an inclined punch with $\theta=1^\circ$. The higher angle of inclination makes it longer for the highest inclination point, h , at the punch to reach and cut the blank. Bao et al. [28] thru finite element simulation found that a slant punch takes a longer time to cut the workpiece. The comparison of the percentage change in the maximum trimming load and punch stroke for trimming with the inclined punch is given in Figure 4. The application of an inclination angle $\theta=3^\circ$, 5° , and 10° gave the most significant reduction in maximum trimming load, ranging from approximately 70% to 79%. Conversely, for the punch stroke, a huge increase in the percentage of up to more than 400% was observed when trimming with the same inclined punch $\theta=3^\circ$, 5° , and 10° . Therefore, it is essential to optimize the inclination angle to achieve a balance between

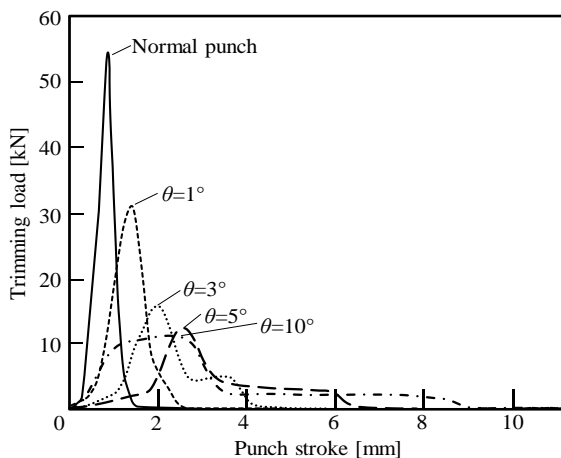


Figure 3. Comparison of load-stroke curves for trimming with normal and inclined punches

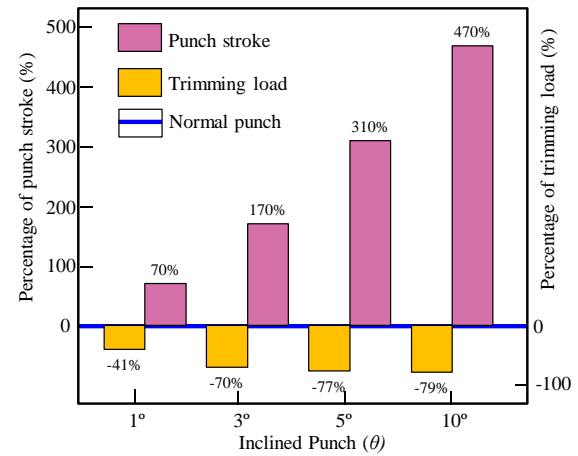


Figure 4. Percentage change in maximum trimming load and punch stroke for trimming with an inclined punch with respect to the normal punch

reducing the maximum trimming load and minimizing the increase in the punch stroke.

The energy used for trimming the JSC1180YN (UHSS) sheet using the normal and inclined punches is shown in Figure 5. The trimming energy is calculated based on the integration of the total trimming load used over the travel distance of the punch downwards until the separation of the scrap occurs, which is given by following equation:

$$W = \int_0^s F_t \cdot ds \quad (1)$$

where W is the trimming energy used measured in Joule, F_t is the trimming load, and s is the punch stroke. From the graph, the trimming energy for trimming with the normal punch is relatively higher than that of trimming with the inclined punch, except for the inclined punch $\theta=10^\circ$. When trimming with the normal punch, despite the short total punch stroke to separate the scrap from the workpiece, i.e., less than 2.5 mm, the high load generated at the beginning of the trimming process result in a high trimming energy used. When trimming with the inclined punch, by applying the inclination angle, an expressive reduction trend in trimming energy used is obtained. The inclined punch with inclination angle $\theta=3^\circ$ and 5° consumed the lowest energy of about 18 Joule. As the energy consumption depends on the travel distance of the punch stroke, the energy used for trimming with the inclined punch $\theta=10^\circ$ is the highest as it requires the longest punch stroke to cut out the scrap. The calculation shows that the punch stroke has a high impact on energy consumption, even if the trimming load is low. The selection of proper inclination angle and other parameters is important to optimize between lowering the maximum trimming load and minimizing the trimming energy [35].

The change of energy used by the inclined punches in percentage with respect to trimming with the normal

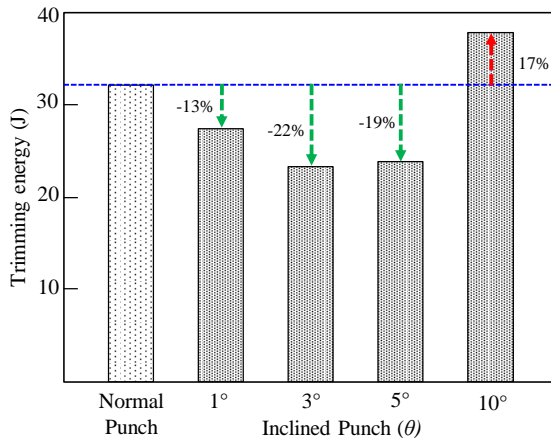


Figure 5. Trimming energy used for trimming normal punch and inclined punch

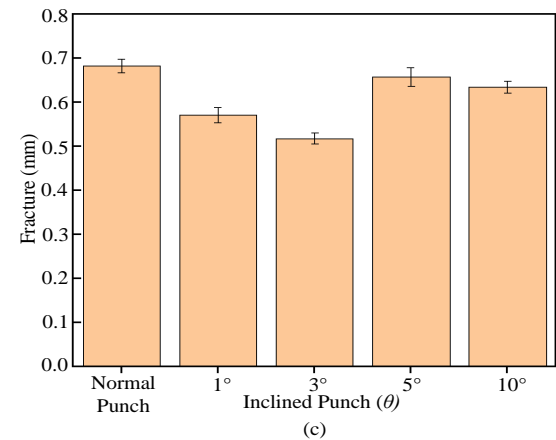
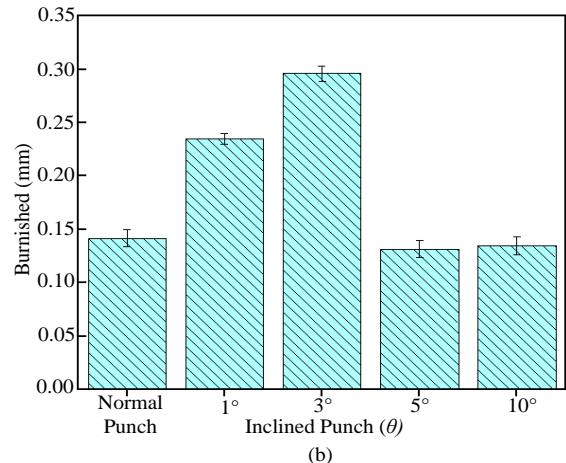
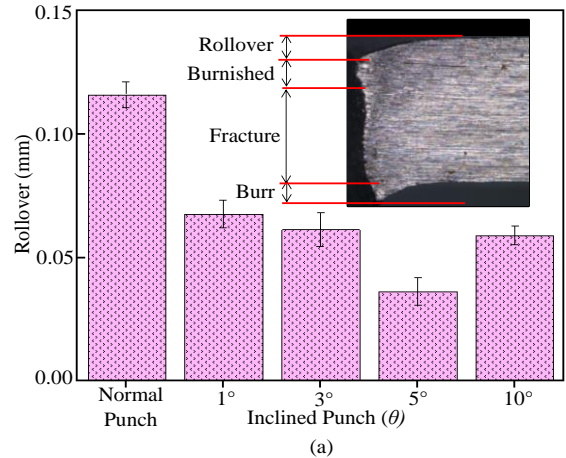
punch was compared in the same figure. The energy used by inclined punch $\theta = 1^\circ, 3^\circ$, and 5° was managed to be reduced by 13%, 22% and 19%, respectively, compared with the normal punch. However, the percentage of trimming energy was found to increase by 17% for the inclined punch $\theta = 10^\circ$, indicating too much inclination will not optimize the process even though the trimming load is reduced.

3.2. Sheared-edge Quality The quality of the four cutting zones at the sheared edge, which are the rollover, burnished, fracture and burr, based on the height produced after trimming as is shown in Figure 6. In general, the height for rollover, fracture, and burr was decreased when trimming using the inclined punch, compared to that of trimming with the normal punch. On the contrary, the height of the burnished surface was found to increase. The decrease in heights of rollover, fracture, and burr, as well as an increase in burnished surface, indicated a successful improvement in the quality of the sheared edge. However, the detailed analysis of the heights of a rollover, burnish, fracture, and burr for different angles of inclination of the inclined punch does not exhibit a direct proportionality. The rollover height (Figure 6 (a)) was found gradually decreased with an increase in the inclination angle, except for the inclined punch $\theta = 10^\circ$. For the burnished surface (Figure 6 (b)), the height was proportionally increased with an increase in inclination angle, only for the inclined punch $\theta = 1^\circ$ and 3° . Both inclined punch $\theta = 5^\circ$ and 10° were measured to have the same burnished height.

For the fracture and burr height (Figure 6 (c) and (d)), an decrease in height was only found in the directly proportional relationship for the inclined punch $\theta = 1^\circ$ and 3° . For the inclined punch $\theta = 5^\circ$ and 10° , both the fracture and burr were higher. These irregular patterns of the

relationship are attributed to the growth of the bending moment at the cutting area of both the inclined and straight zones (Figure 2 (c)), as a result of an increases in inclination angle.

The localized contact occurs when the inclined punch indents the workpiece at the start of the trimming stage, causing the material at the sheared plane to reach its limit of strain and force tolerance [32]. Thus, the higher



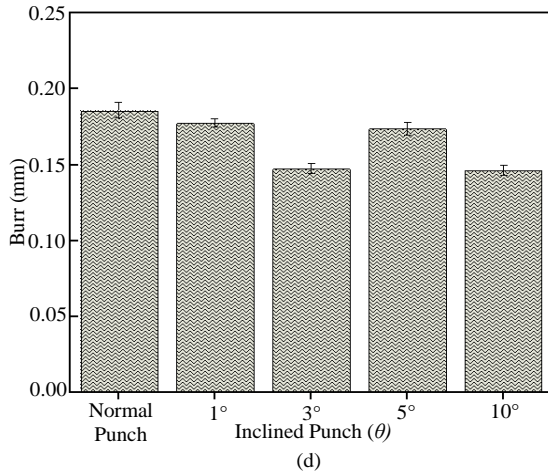


Figure 6. Height of sheared surface with different inclined punch shapes; (a) rollover, (b) burnished, (c) fracture and (d) burr

inclination angle results in greater strain and localized force, ultimately causing the workpiece to bend. Particularly, the shape of the punch used for trimming will impact the quality of the fracture surface [36].

The depth percentage of the rollover, burnished, fracture and burr at the sheared edge for trimming with normal and inclined punches are shown in Figure 7. The depth of the fracture and burnished surfaces are the most important in determining the quality of the sheared edge, where the larger the depth of the burnished and the lower the fracture surface, the better the quality of the sheared edge. For trimming with the normal punch, a large fracture but small burnished surfaces were observed at the sheared edge. In contrast, larger burnished and smaller fracture surfaces were obtained by trimming with the inclined punch. The large trimming load produced by the normal punch, compounded by the simultaneous cutting action by the flat shape of the punch on the workpiece, creates an early point of crack at the cutting area. Therefore, large fractures are created at all zones. Contrarily, the inclined shape of the punch makes the cutting action gradually occur, thus, reducing the force. As the cutting force is gradually exerted, the point of crack at the cutting area is delayed. This created a larger burnished surface at the sheared edge.

The overall percentage of the sheared edge observed in 50 mm length is shown in Figure 8. The sheared edge from the workpiece cut by the inclined punch $\theta=3^\circ$ was chosen as it produced the largest burnished and smallest fracture surfaces at the sheared edge, compared to the other inclined punches. The sheared edge of the workpiece cut by the normal punch is shown for comparison. When the workpiece is trimmed by the normal punch, the percentage of the rollover, fracture, burnished and burr were found at the same level, throughout the length, observed from 0 to 50 mm. It is a

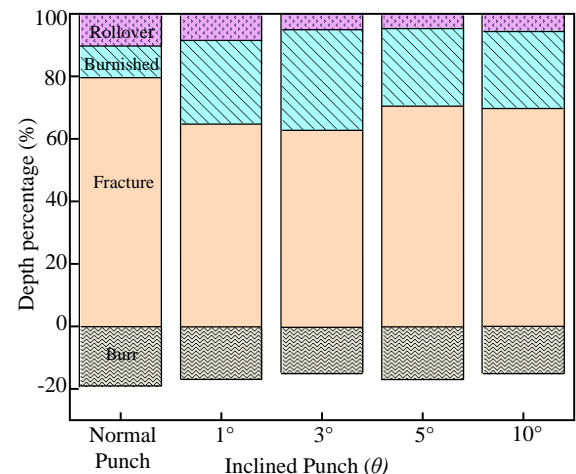


Figure 7. Depth percentage of the rollover, burnished, fracture and burr at the sheared edge for trimming with normal and inclined punches

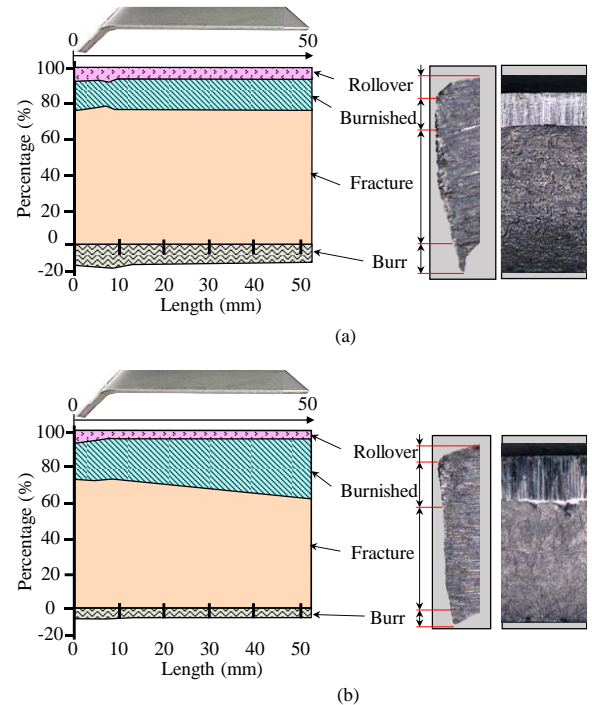


Figure 8. Percentage of the sheared edge of (a) normal punch and (b) inclined punch $\theta=3^\circ$

clear indication that all zones of the workpiece (inclined, curved, and straight) were simultaneously cut in a single action and at the same time. On the other hand, when the inclined punch is used, the percentage level of the rollover, fracture, burnished, and burr were gradually changed, obviously seen at the burnished and fracture surface, whereas for the burnished surface, the percentage level was found gradually increase from 0 to 50 mm. The fracture surface, on the other hand was

gradually decreased. This phenomenon is due to the gradual cutting action created by the inclined shape of the punch, which locally cuts the workpiece as the punch travel downward. As the bond between the part and scrap became weakest at the end of the length, the trimming process became easier and smoother, and thus created large burnished with small fracture surfaces.

3.3. Shape defect The shape of the trimmed part and scrap were observed under the microscope for the shape defects analysis and compared as in Figure 9. The inclined and curved zones were chosen for the observation as these zones exhibited clear shape defects. The workpieces observed were from those were cut by the normal punch and inclined punch $\theta=3^\circ$. The bent at the inclined and curved zones was found to be significant at both the part and the scrap portions when trimming with the normal punch. The high trimming force exerted by the punch on all contact areas at once, induced high stress. As the crack initiation begins, this high capacity of stress is abruptly released in a short stroke and time interval, resulting in the inclined and curved zones failing to absorb the sudden change in stress over the small area. Thus, the inclined and curved zones bent during the final stage of the separation. Choi et.al. [37] reported that the crack started near the flank edge of the punch and die and then propagated into the scrap side. For the inclined punch $\theta=3^\circ$, the punch gradually indented and cut the inclined and curved zones. This prevents the stress concentration on a single area. A smooth distribution of shear stress is provided during the cutting after the

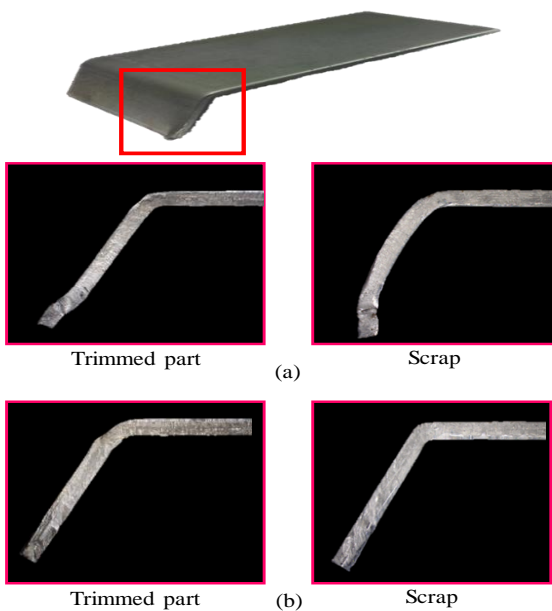


Figure 9. Shape of trimmed part and scrap after trimming process for trimming with (a) normal punch and (b) inclined punch $\theta=3^\circ$

initiation of the crack. As a result, the shape of the inclined and curved zones for both the part and scrap portions remained straight without any shape defects.

At higher magnification of observation (Figure 10), an uneven cut and bending shape was observed at the end tip of the workpiece at both the trimmed part and scrap, trimmed by the normal punch. However, with the inclined punch, the defect was prevented, and a straight cut was produced. The defect at the trimming line was observed and compared in Figure 11 for trimming with the normal and inclined punches. The high trimming force exerted by the normal punch induced high stress and resulted in an abrupt and sudden release of stress at the trimming line during the separation of the scrap.

At certain points of the trimming line, due to this sudden release of stress, a large and deep fracture has occurred (Figure 11(a)). Whereas no fracture was observed at the trimming line for trimming with the inclined punch $\theta=3^\circ$ (Figure 11(b)). The inclined surface of the punch prevented high-stress concentration at a single area of contact and therefore allowed a smooth transition of stress as the scrap was separated.

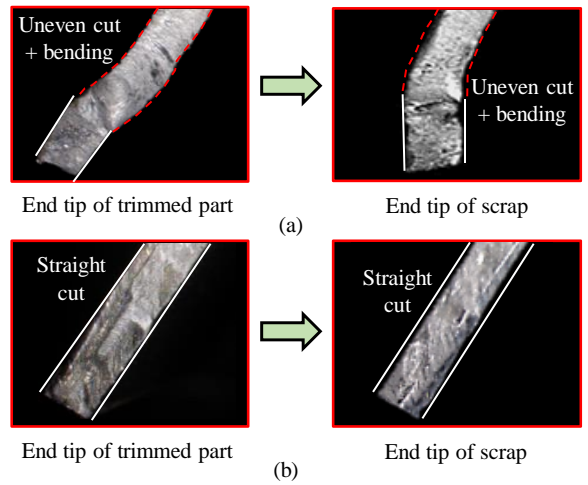


Figure 10. The shape of the end tip at trimmed part and scrap; (a) normal punch and (b) inclined punch $\theta=3^\circ$

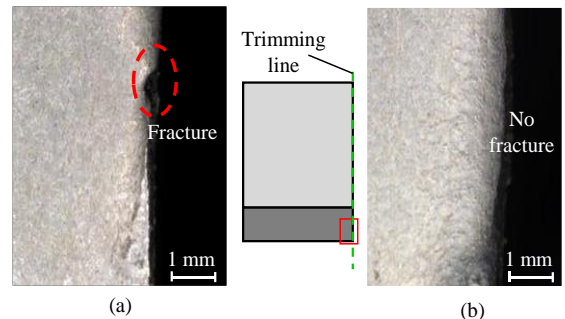


Figure 11. Trimming line at the zone with (a) normal punch and (b) inclined punch $\theta=3^\circ$

4. CONCLUSION

From this study, the trimming process of ultra-high strength steel, JSC1180YN, using both the normal and inclined punches was investigated. The high load produced during the indentation of the punch onto the workpiece is the significant factor for the sheared edge quality and shape defect. The results of the experiment showed that a significant reduction of the trimming load could be achieved by applying a small angle of inclination at the punch edge; however, the longer punch stroke is the drawback. The inclined punches ($\theta = 1^\circ, 3^\circ, 5^\circ, 10^\circ$) successfully decreased the trimming load by more than half as compared to that of trimming with the normal punch. The sheared edge quality was improved, where a larger burnished surface and a smaller fracture were obtained by the inclined punch. The inclined punch $\theta = 3^\circ$, shows the most optimal results in terms of trimming load reduction, punch stroke distance, and improvement of sheared edge quality as compared to other inclination angles. The shape of the part also remained intact without any defects and fractures when trimming with the inclined punch.

5. ACKNOWLEDGEMENT

The first author gratefully acknowledges the financial funding by the Ministry of Higher Education Malaysia under the Fundamental Research Grant Scheme [FRGS/1/2018/TK03/UNIMAP/02/9]. This research was supported by the Advanced Material Processing and Design Research Group of the Faculty of Mechanical Engineering Technology, Universiti Malaysia Perlis, for the lab facilities.

6. REFERENCES

1. Delfani, F., Kazemi, A., Seyedhosseini, S. and Niaki, S., "A green hazardous waste location-routing problem considering the risks associated with transportation and population", *International Journal of Engineering, Transactions B: Applications*, Vol. 33, No. 11, (2020), 2272-2284. doi: 10.5829/ije.2020.33.11b.18.
2. Horvath, C., Advanced steels for lightweight automotive structures, in Materials, design and manufacturing for lightweight vehicles. 2021, Elsevier.39-95.
3. Song, H., Yoo, J., Kim, S.-H., Sohn, S.S., Koo, M., Kim, N.J. and Lee, S., "Novel ultra-high-strength cu-containing medium-mn duplex lightweight steels", *Acta Materialia*, Vol. 135, (2017), 215-225. doi: 10.1016/j.actamat.2017.06.035.
4. Pyrz, M. and Krzywoblocki, M., "Crashworthiness optimization of front rail structure using macro element method and evolutionary algorithm", *Structural and Multidisciplinary Optimization*, Vol. 60, No. 2, (2019), 711-726. doi: 10.1007/s00158-019-02233-7.
5. Fallah, M., Tavakkoli-Moghaddam, R., Salamatbakhsh-Varjovi, A. and Alinaghian, M., "A green competitive vehicle routing problem under uncertainty solved by an improved differential evolution algorithm", *International Journal of Engineering, Transactions A: Basics*, Vol. 32, No. 7, (2019), 976-981. doi: 10.5829/ije.2019.32.07a.10.
6. Caffrey, C., Bolon, K., Kolwich, G., Johnston, R. and Shaw, T., *Cost-effectiveness of a lightweight design for 2020-2025: An assessment of a light-duty pickup truck*. 2015, SAE Technical Paper.
7. Luk, J.M., Kim, H.C., De Kleine, R.D., Wallington, T.J. and MacLean, H.L., "Greenhouse gas emission benefits of vehicle lightweighting: Monte carlo probabalistic analysis of the multi material lightweight vehicle glider", *Transportation Research Part D: Transport and Environment*, Vol. 62, (2018), 1-10. doi: 10.1016/j.trd.2018.02.006.
8. Hottle, T., Caffrey, C., McDonald, J. and Dodder, R., "Critical factors affecting life cycle assessments of material choice for vehicle mass reduction", *Transportation Research Part D: Transport and Environment*, Vol. 56, (2017), 241-257. doi: 10.1016/j.trd.2017.08.010.
9. Lesch, C., Kwiaton, N. and Klose, F.B., "Advanced high strength steels (ahss) for automotive applications—tailored properties by smart microstructural adjustments", *Steel research international*, Vol. 88, No. 10, (2017), 1700210. doi: 10.1002/srin.201700210.
10. Abbasian, A., Ravangard, A., Hajian Nia, I. and Mirzamohammadi, S., "Investigation of microstructure and mechanical properties of newly developed advanced high strength trip steel", *International Journal of Engineering, Transactions C: Aspects*, Vol. 35, No. 3, (2022), 567-571. doi: 10.5829/IJE.2022.35.03C.09.
11. Yi, H., Sun, L. and Xiong, X., "Challenges in the formability of the next generation of automotive steel sheets", *Materials science and technology*, Vol. 34, No. 9, (2018), 1112-1117. doi: 10.1080/02670836.2018.1424383.
12. Gronostajski, Z., Pater, Z., Madej, L., Gontarz, A., Lisiecki, L., Łukaszek-Sołek, A., Łuksza, J., Mróz, S., Muskalski, Z. and Muzykiewicz, W., "Recent development trends in metal forming", *Archives of Civil and Mechanical Engineering*, Vol. 19, No. 3, (2019), 898-941. doi: 10.1016/j.acme.2019.04.005.
13. Hamedon, Z., Abe, Y. and Mori, K., "Improvement of formability of high strength steel sheets in shrink flanging", in IOP Conference Series: Materials Science and Engineering, IOP Publishing. Vol. 114, (2016), 012001.
14. Abe, Y., Okamoto, Y., Mori, K. and Jaafar, H., "Deformation behaviour and reduction in flying speed of scrap in trimming of ultra-high strength steel sheets", *Journal of Materials Processing Technology*, Vol. 250, (2017), 372-378. doi: 10.1016/j.jmatprotec.2017.07.034.
15. Xia, P., Sabirov, I., Molina-Aldareguia, J., Verleysen, P. and Petrov, R., "Mechanical behavior and microstructure evolution of a quenched and partitioned steel during drop weight impact and punch testing", *Materials Science and Engineering: A*, Vol. 737, (2018), 18-26. doi: 10.1016/j.msea.2018.09.015.
16. Han, D., Hörrhold, R., Müller, M., Wiesenmayer, S., Merklein, M. and Meschut, G., "Shear-clinching of multi-element specimens of aluminium alloy and ultra-high-strength steel", *Key Engineering Materials*, Vol. 767, (2018), 389-396. doi: 10.4028/www.scientific.net/KEM.767.389.
17. Mori, K.-i., "Review of shearing processes of high strength steel sheets", *Journal of Manufacturing and Materials Processing*, Vol. 4, No. 2, (2020), 54. doi: 10.3390/JMMP4020054.
18. Wu, X., Bahmanpour, H. and Schmid, K., "Characterization of mechanically sheared edges of dual phase steels", *Journal of Materials Processing Technology*, Vol. 212, No. 6, (2012), 1209-1224. doi: 10.1016/j.jmatprotec.2012.01.006.
19. Patel, S.S. and Prajapati, J., "Multi-criteria decision making approach: Selection of blanking die material", *International Journal of Engineering, Transactions B: Applications*, Vol. 30, No. 5, (2017), 800-806. doi: 10.5829/idosi.ije.2017.30.05b.21.

20. Gürün, H., Göktaş, M. and Güldaş, A., "Experimental examination of effects of punch angle and clearance on shearing force and estimation of shearing force using fuzzy logic", *Transactions of FAMENA*, Vol. 40, No. 3, (2016), 19-28. doi: 10.21278/TOF.40302.
21. Suzuki, Y., Yang, M. and Murakawa, M., "Optimum clearance in the microblanking of thin foil of austenitic stainless steel jis sus304 studied from shear cut surface and punch load", *Materials*, Vol. 13, No. 3, (2020), 678. doi: 10.3390/ma13030678.
22. Rajeev, D., Dinakaran, D., Kanthavelkumaran, N. and Austin, N., "Predictions of tool wear in hard turning of aisi4140 steel through artificial neural network, fuzzy logic and regression models", *International Journal of Engineering, Transactions A: Basics*, Vol. 31, No. 1, (2018), 32-37. doi: 10.5829/ije.2018.3101a.05.
23. Senn, S. and Liewald, M., "Experimental investigation of piercing of high-strength steels within a critical range of slant angle", in *Journal of Physics: Conference Series*, IOP Publishing. Vol. 896, (2017), 012099.
24. Li, B., "Modelling and numerical simulation of cutting stress in end milling of titanium alloy using carbide coated tool", *International Journal of Engineering, Transactions A: Basics*, Vol. 28, No. 7, (2015), 1090-1098. doi: 10.5829/idosi.ije.2015.28.07a.16.
25. Kolleck, R., Vollmer, R. and Veit, R., "Investigation of a combined micro-forming and punching process for the realization of tight geometrical tolerances of conically formed hole patterns", *CIRP annals*, Vol. 60, No. 1, (2011), 331-334. doi: 10.1016/j.cirp.2011.03.141.
26. Kutuniva, K., Karjalainen, J.A. and Mäntyjärvi, K., "Effect of convex sheared punch geometry on cutting force of ultra-high-strength steel", *Key Engineering Materials*, Vol. 504, (2012), 1359-1364. doi: 10.4028/www.scientific.net/KEM.504-506.1359.
27. Kurniawan, Y. and Mahardika, M., "Suyitno, "the effect of punch geometry on punching process in titanium sheet,"", *Jurnal Teknologi*, Vol. 82, No. 2, (2020), 101-111. doi: 10.11113/jt.v82.13947.
28. Bao, H., Sun, H., Xing, R., Cheng, L. and Zhang, Z., "Finite element simulation of the punch with inclined edge in the sheet metal blanking process", *International Journal of Computing Science and Mathematics*, Vol. 9, No. 4, (2018), 377-389. doi: 10.1504/IJCSM.2018.094671.
29. Shih, H.-C., Hsiung, C.-K. and Wendt, B., *Optimal production trimming process for ahss sheared edge stretchability improvement*. 2014, SAE Technical Paper.
30. Balogun, V.A. and Edem, I.F., "Optimum swept angle estimation based on the specific cutting energy in milling aisi 1045 steel alloy", *International Journal of Engineering, Transactions A: Basics*, Vol. 30, No. 4, (2017), 1-4. doi: 10.5829/idosi.ije.2017.30.04a.18.
31. Zainal, Z., Rusli, N. and Shuaib, N., "Effect of cutting environment and swept angle selection in milling operation", *International Journal of Engineering, Transactions C: Aspects*, Vol. 34, No. 12, (2021), 2578-2584. doi: 10.5829/ije.2021.34.12c.02.
32. Paetzold, I., Dittmann, F., Feistle, M., Golle, R., Haefele, P., Hoffmann, H. and Volk, W., "Influence of shear cutting parameters on the fatigue behavior of a dual-phase steel", in *Journal of physics: conference series*, IOP Publishing. Vol. 896, (2017), 012107.
33. Feistle, M., Krinninger, M., Paetzold, I., Stahl, J., Golle, R. and Volk, W., "Design and conceptualization of a cutting tool to investigate the influence of the shear cutting process on edge crack sensitivity", in *Journal of Physics: Conference Series*, IOP Publishing. Vol. 896, (2017), 012106.
34. Gläsner, T., Sunderkötter, C., Hoffmann, H., Volk, W. and Golle, R., "Development of a 2-stage shear-cutting-process to reduce cut-edge-sensitivity of steels", in *Journal of Physics: Conference Series*, IOP Publishing. Vol. 896, (2017), 012104.
35. Yasutomi, T., Yonemura, S., Yoshida, T., Mizumura, M. and Hiwatashi, S., "Blanking method with aid of scrap to reduce tensile residual stress on sheared edge", in *Journal of Physics: Conference Series*, IOP Publishing. Vol. 896, (2017), 012098.
36. Chumrum, P., Koga, N. and Premanond, V., "Experimental investigation of energy and punch wear in piercing of advanced high-strength steel sheet", *The International Journal of Advanced Manufacturing Technology*, Vol. 79, (2015), 1035-1042. doi: 10.1007/s00170-015-6902-z.
37. Choi, H.-S., Kim, B.-M. and Ko, D.-C., "Effect of clearance and inclined angle on sheared edge and tool failure in trimming of dp980 sheet", *Journal of Mechanical Science and Technology*, Vol. 28, (2014), 2319-2328. doi: 10.1007/s12206-014-0522-7.

COPYRIGHTS

©2023 The author(s). This is an open access article distributed under the terms of the Creative Commons Attribution (CC BY 4.0), which permits unrestricted use, distribution, and reproduction in any medium, as long as the original authors and source are cited. No permission is required from the authors or the publishers.

**Persian Abstract****چکیده**

برش بخش ضایعات قطعات فولادی با استحکام فوق العاده بالا (UHSS) به دلیل ویژگی های ذاتی استحکام و سختی بالا، چالش مهمی را ایجاد می کند. برای اجزای UHSS با پیچیدگی هندسی بالاتر از جمله شامل مقاطع شبیدار و منحنی، شبیب تیز و شعاع خمش کوچک، بار پیرایشی بزرگ منجر به کیفیت برش و نقص شکل ضعیف می شود که معمولاً در این مناطق اتفاق می افتد. این تحقیق اثرات اعمال یک زاویه شبیب کوچک به پانج را در برش قطعات UHSS دارای شکل مایل و منحنی بررسی کرد. پانج مایل به چهار مجموعه با درجات شبیب متفاوت یعنی ۱ درجه، ۳ درجه، ۵ درجه و ۱۰ درجه تغییر یافت. تجزیه و تحلیل مقایسه ای از بار پیرایش، انرژی پیرایش، کیفیت لبه بشی و نقص شکل بین این پانچ های اصلاح شده و پانچ معمولی برای انرژی خشی آنها در عملیات پیرایش انجام شد. نتایج نشان داد که اعمال زاویه شبیب به طور قابل توجهی بر پیرایش را کاهش داد، انرژی پیرایش را کاهش داد و کیفیت سطح لبه برش خورده را بهبود بخشدید و همچنین از ایجاد نقص شکل در مناطق شبیدار و منحنی در مقایسه با نتایج حاصل از پیرایش با استفاده از دستگاه جلوگیری کرد. مشت معمولی این مطالعه نشان داد که تغییر در هندسه پانج یک گزینه موثر برای بهبود عملکرد فرآیند و همچنین کیفیت قطعه است، بهویژه در اصلاح اجزای با استحکام بالا که دارای اشکال پیچیده هستند.



Experimental Investigation and Thermodynamic Modeling of Zn⁺² and Ni⁺² Extraction from Zn Plant Residue using D2EHPA

M. Mohammadzadeh*, H. Bagheri, S. Ghader*

Department of Chemical Engineering, Faculty of Engineering, Shahid Bahonar University of Kerman, Kerman, Iran

PAPER INFO

ABSTRACT

Paper history:

Received 01 June 2023

Received in revised form 12 August 2023

Accepted 13 August 2023

Keywords:

Thermodynamic Modeling

Solvent Extraction

D2EHPA

Zinc Residue

Activity Coefficient

Gamma Model

Zinc plant filter cake contains valuable metals that can be reused as a source for obtaining these metals. This study describes an experimental two stage study on the extraction of zinc and nickel from waste zinc filter cake which includes acid leaching of zinc filter cake followed by organic phase aided extraction of metals from the leaching solution. To determine the optimum leaching condition a comprehensive study of the recovery of chemical elements from spent plant residues was experimentally studied at different levels of acid concentrations at different temperatures while measuring chemical elements concentration with respect to time. Experimental results showed that 99% recovery of Ni²⁺, Zn²⁺ and 89% recovery of Pb²⁺ can be achieved at following optimum conditions: 2M nitric acid, T= 358.15 K after 1.5 h of acid leaching at S/L=1/10. Then, the extraction of Zn²⁺, Ni²⁺, and Pb²⁺ was carried out by di-(2-ethylhexyl) phosphoric acid (D2EHPA) that was diluted with kerosene in equal phase ratio and the effect of extractant concentration and pH was studied at T = 298.15 K. Results showed that an increase in pH and extractant concentration can greatly increase zinc and nickel extraction to a maximum achievable amount of 95% and 90 % for Zn²⁺ and Ni²⁺, respectively by 25 (v/v%) D2EHPA at pH = 5.5 and organic to aqueous phase ratio (O/A) = 1/1. For modeling of equilibrium concentrations in organic and aqueous phases and activity coefficients calculation, Electrolyte-UNIQUAC-NRF, UNIQUAC-NRF, NRTL and NRTL-based local composition models were used. After that, adjusted parameters were successfully used for calculation of the equilibrium constant of the unknown parameters and the extraction reaction. The obtained results of thermodynamic modeling were in well agreement with the experimental data.

doi: 10.5829/ije.2023.36.11b.07

1. INTRODUCTION

In recent years, because of increasing the consumption of metals along with the simultaneous depletion of primary resources, more attention has been drawn to the recovery of metals from secondary resources, including waste residues from zinc plants. Recovering the valuable content of these resources can have both economic and ecological advantages. Some industrial wastes are classified as the main resources of different metals [1, 2]. Metals or minerals production from ores through pyro/hydro-metallurgical processes usually

causes enormous amount of residues [3, 4]. For example, zinc industrial residue, which is produced in zinc ores processing contains some valuable metals, e.g., Ni, Pb as well as Zn that can be beneficially recovered for further processing. Thus, recovering these metals from the secondary resources as well as natural minerals for the high value products, is necessary and important for effective use of these resources [5]. Nowadays, several techniques such as electrolysis, cementation, liquid-liquid extraction, precipitation, and ion exchange have been applied to separate and recover metals from zinc plant residue [6, 7]. The hydrometallurgical route is one of the most widely used approaches for recovering valuable metals from zinc plant residue which mainly involves leaching with an acid solution followed by the extraction of metal ions

*Corresponding Authors Emails:

masumeh70mohammadzadeh@gmail.com (M. Mohammadzadeh),
sattarghader@gmail.com (S. Ghader)

from leaching solution [8]. Solvent extraction, as an efficient separation and purification technology, can achieve the selective extraction of target elements and has been widely used in metal hydrometallurgy, heavy metal wastewater treatment, and other fields [8, 9].

Solvent extraction process of Ni, Zn, and Pb from aqueous solution by several commercial extractants have been studied by researchers. They were trying to understand the role and effect of influencing parameters like pH of solution and type and concentration of extractant [10, 11]. For example, acidic extractants (Cyanex 302 [12], D2EHPA [13], and Cyanex 272 [14]) and chelating extractants (LIX 984N [15], LIX 63 [16], and LIX 84 [17]) have been used for this purpose. Di-2-ethyl hexyl phosphoric acid (D2EHPA) as a classical extractant, has been widely used in extraction and separation of the divalent transition metals such as zinc, manganese, nickel, cobalt and copper [18-20]. According to the previous researches, for enhanced separation of Zn from acid solution by D2EHPA, another extractant along with D2EHPA must be used [21, 22]. For instance, Hosseini et al. [23] found the desired extraction of manganese and zinc was obtained using a mixture of Cya-nex 302 and D2EHPA. Alike results were presented by Babakhani et al. [24] for separation of Ni^{2+} and Cd^{2+} . Another report by Innocenzi and Veglio [25], revealed combination D2EHPA and Cya-nex 272 was more effective for separation of Mn^{2+} and Zn^{2+} than Cya-nex 272.

Mathematical modeling is a key step in a solvent extraction process and it is necessary for designing, controlling and optimization of the process [26-29]. Thus, an appropriate model is necessary for prediction a solute distribution coefficient and thermodynamic equilibrium constant of the extraction reaction [30]. Electrolyte solutions are very important in several chemical industries and biological processes. Since they are known non-ideal solutions even at low concentrations, or in some processes like gas sweetening, which electrolyte solutions have high concentration, accurate thermodynamic models are needed. Therefore, modeling and predicting the thermodynamic properties of electrolyte solutions is of great importance to predict an accurate model for a wide range of concentrations [31-40]. Some models such as Bromley model, Scatchard-Hildebrand model, Pitzer virial expansion equations and Guggenheim quasi-lattice model have been used for activity coefficient (γ_i) calculation of electrolyte and non-electrolyte solutions [37-50]. Although in the mentioned studies, γ_i was not calculated, or the non-ideality of a phase was ignored due to the complexity of the liquid-liquid extraction process, several of these models might not be accurate enough to correlate the activity coefficients of high concentration of aqueous electrolyte solutions. Some significant researches have been carried

out by Thomsen et al. [45], Pitzer [41, 42], Cruz and Renon [43], Zhao et al. [44], Chen et al. [46], Haghtalab and Vera [47] and Sadeghi [48] that the excess Gibbs energy functions based on the concept of local composition has been developed and are among the most successful electrolyte models. Haghtalab and Peyvandi [51] developed Electrolyte-UNIQUAC-NRF model for description the behavior of binary electrolyte and multi-component solution in a concentration range and at high temperature. This model is based on local-composition approach. Furthermore, Chen et al. [49] extended the e-NRTL model for single electrolyte solution and single solvent systems. Chen et al. [49] used Pitzer-Debye-Hückel equation [50] and local composition model based on NRTL for characterization of long and short range interactions, respectively.

In this work, we planned to examine the extraction of Zn^{2+} , Ni^{2+} , and Pb^{2+} from zinc plant filter cake (ZPFC) combined with various metal ions. First, the influences of different processes factors on the extraction of metal ions were experimentally calculated. Next, the equilibrium extraction of Ni^{2+} and Zn^{2+} ions from HNO_3 solution were model based on a thermodynamic model. Hence the Electrolyte-UNIQUAC-NRF and UNIQUAC-NRF equations were used for γ_i calculation for aqueous solution and organic phase, respectively. Finally, the result of both equations were compared with NRTL and a new NRTL-based local composition models.

2. EXPERIMENT METHOD

2. 1. Chemicals and Equipment

The ZPFC employed in the experiments was supplied from the zinc manufacturing plant in Zanjan (Iran) and was determined by the X-ray fluorescence (XRF) technique (ARL ADVANTX+, Switzerland). Nitric acid (purity of 65%) and the organic extractant, D2EHPA (purity of 97%) were prepared from Merck and kerosene was purchased from Esfahan Oil Refinery Co. (purity of 97%). Sodium hydroxide pellets (purity of 99%, Merck) were used to adjust pH values. The aqueous and organic phases were mixed using a mechanical stirrer. The operating temperature and pH values were monitored using a thermometer and pH meter, respectively. Moreover, metal ions concentrations in the aqueous and organic solutions were analyzed by AAS (Absorption Spectrophotometer) and mass balance, respectively.

2. 2. Experimental Procedure

The experimental procedure that was used in this communication is illustrated in Figure 1. The method included two main operating units: 1. leaching process of zinc filter cake and 2. solvent extraction process; the leach solution of step 1 is utilized for the separation, according to step 1,

an aqueous phase was supplied by dissolving of appropriate values of zinc filter cake and HNO_3 in distilled water. During the leaching process, the influence of acid concentration, time and operating temperature were investigated. In all experiments, 30 g of zinc plant filter cake (ZPFC) was mixed with 300 mL of HNO_3 (0.25-2 M), S/L=1/10, and after that stirred in the bottom three-necked flask at a speed equal to 600 rpm with a mechanical stirrer. The leaching process of all elements was investigated at time range of 30-120 min and temperature in the range of 298.15-358.15 K. The concentration of each ion in the leaching solution was obtained by absorption spectrophotometer and in the second step, in all solvent extraction tests, O/A=1/1. After that, 25 mL of each phase was blended on the mechanical stirrer and the pH value was continuously controlled during the experiment. Nitric acid (2 M) and sodium hydroxide (4 M) were applied to modify the pH. The organic and aqueous phases were separated at desired pH value by a separation funnel and after 10 min the equilibrium achieved. Then, the aqueous phase was sampled for analysis of the extracted ions. The percentage of extraction of metal ions were calculated using Equation (1) and the distribution ratio Zn^{2+} and Ni^{2+} from other metal ions. The ZPFC was oven-dried for 24 h at 303.15 K and then milled into particles of less than 0.1 mm for further analysis. The XRF analysis of the ZPFC presented in Figure 2. The percentage of extraction

was determined by using Equation (2):

$$\text{Extraction (\%)} = \frac{C_i - C_{aq}}{C_i} \times 100 \quad (1)$$

$$D = \frac{[C]_{org}}{[C]_{aq}} \quad (2)$$

where, C_i is the initial metal ions concentration in the aqueous phase and C_{aq} is the metal ions concentration in the aqueous phase after extraction and C_{org} is the metal ions concentration in the organic phase after extraction.

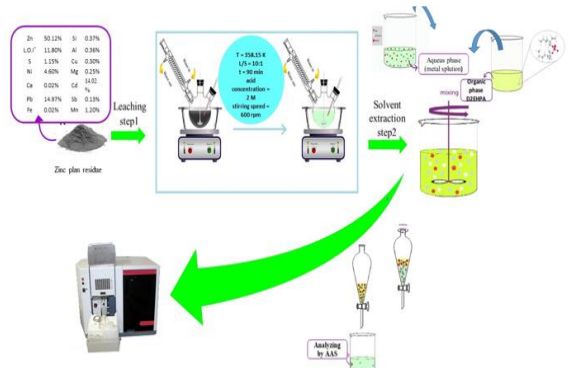


Figure 1. The schematic of the experimental process

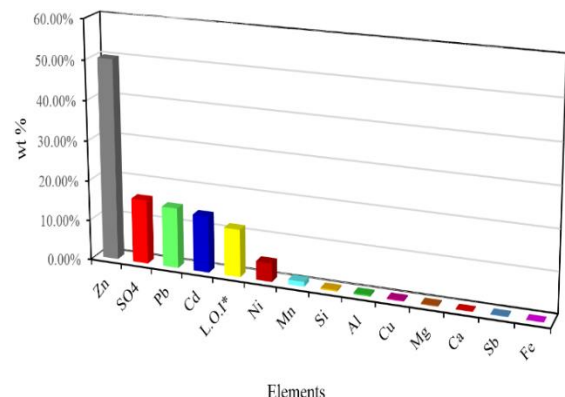


Figure 2. The chemical composition of the ZPFC using XRF analysis

*loss on ignition – the filter cake weight reduction after being ignited

3. RESULTS AND DISCUSSION

3. 1. Leaching

3. 1. 1. Result of Acid Concentration The influence of some important factors, containing temperature, operation time and acid concentration are studied on the leaching process. ZPFC is leached with nitric acid solution followed by dissolution and solvent extraction of objective ions from the leached solutions [52]. Nevertheless, hydrometallurgical behavior creates a vast acidic wastes value that if disposed in environment reasons dangerous health problems and ecological imbalance. Among a huge number of acids, HNO_3 is most accomplished leaching agent as high oxidation potential of HNO_3 and less non-soluble residue evolution. Despite high value of HNO_3 , it can be recovered again with hydrometallurgical behavior. HNO_3 can be easily recycled via external NO_x oxidation [53-56]. Generally, concentration of acid has pronounced influence on the extraction of metal and it is one of the main factors to be investigated for optimization condition for dissolution of metal ions, range of which was studied with conducting a number of experiments at various acid concentration using ZPFC. Figure 3(a) illustrates dissolution of metal ions from ZPFC by changing HNO_3 concentration in the range of 0.25-2 M, 1:10 L/S, temperature (358.15 K) and contact time (1.5 h). Ni^{2+} (100%) and Zn^{2+} (99%) ions were recovered in 2 M HNO_3 . But for 0.25 M HNO_3 the extraction of Ni^{2+} (33%) and Zn^{2+} (23%) was low. Also, Pb^{2+} ion was quite leached from the ZPFC (almost 89%).

3. 1. 2. Result of Temperature and Time Figure 3 (b-d) illustrates the influence of both time reaction and operating temperature on dissolution of metal ions with 2 M HNO_3 . As can be seen, both temperature and

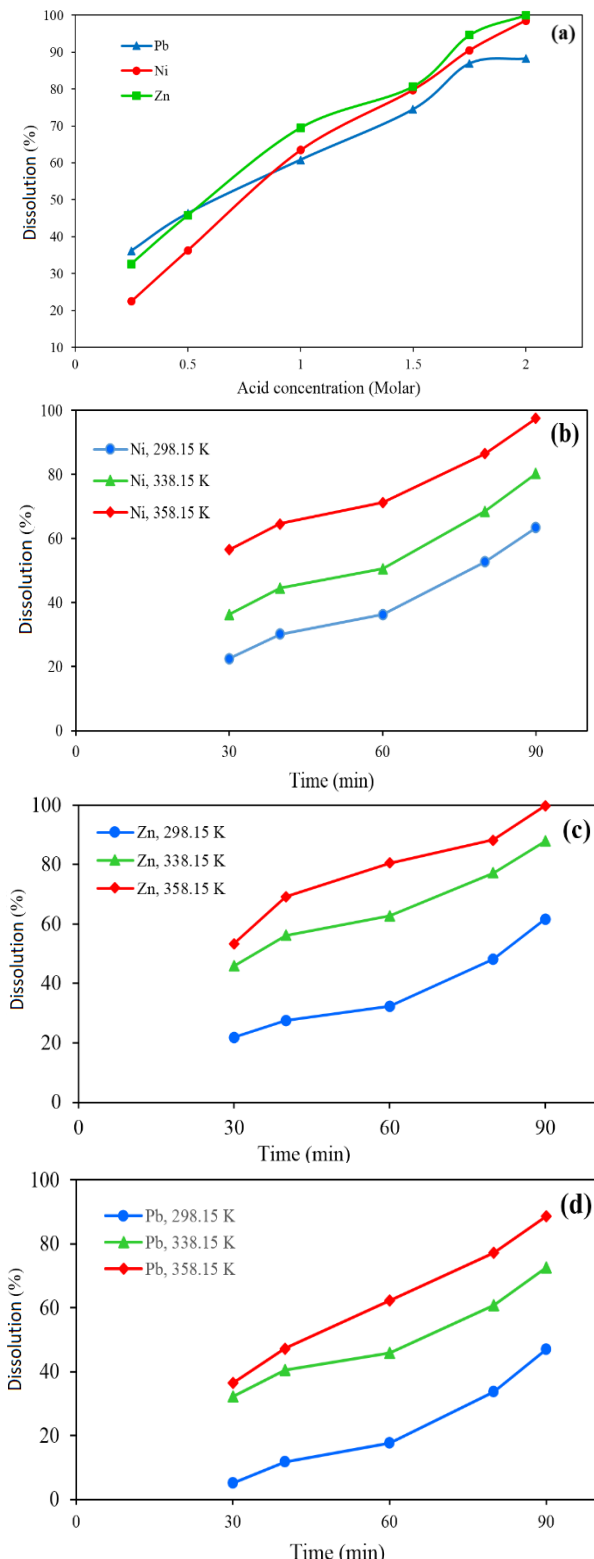


Figure 3. Factors affecting metal ions dissolution from ZPFC, S/L=1/10, (a) Influence of amount of acid on Zn^{2+} , Ni^{2+} , and Pb^{2+} dissolution at $T = 358.15\text{ K}$, and $t = 1.5\text{ h}$, Effect of temperature and time on (b) Ni^{2+} , (c) Zn^{2+} , and (d) Pb^{2+} dissolution in concentration of 2 M acid, S/L=1/10, speed of agitation: 600 rpm

reaction time had a significant influence on Zn^{2+} , Ni^{2+} , and Pb^{2+} leaching. For instance, at 298.15 K only 22.5% Ni^{2+} and 21.8% Zn^{2+} was recovered and recovery was finalized at 358.15 K.

3.2. Solvent Extraction

After investigating leaching process, the extraction of Zn^{2+} , Ni^{2+} , and Pb^{2+} were studied. All experimental tests were performed at the pH range 2-6, O/A=1/1, and $T = 298.15\text{ K}$. Referring to Figure 4(a), complete extraction of Ni^{2+} and Zn^{2+} ions, was occurred at higher value of pH. According to Equation (4) di-(2-ethylhexyl) phosphoric acid release hydrogen ion (H^+) during extraction process. Thus, increasing pH leads to increase extraction of metal from aqueous media. The extraction of Ni^{2+} and Zn^{2+} is remarkably being depending on an acidic extractant like D2EHPA and pH. There is significant difference in the treatment of each metal. The roughly a half of Zn^{2+} and almost all of Ni^{2+} ions were extracted by D2EHPA whereas Pb^{2+} remained in the aqueous solution. Furthermore, the percentage of the extraction of Pb^{2+} was 12.8 % and the pH variations had negligible effect on it.

The influence of concentration of D2EHPA on the Zn^{2+} , Ni^{2+} and Pb^{2+} extraction using 2-25 percent volume/volume of D2EHPA in kerosene at pH = 5.5, and $T = 298.15\text{ K}$ was studied. Referring to Figure 4(b), increasing D2EHPA concentration have no remarkable effect on Pb^{2+} extraction, while the extraction percentage of Zn^{2+} and Ni^{2+} had different behavior. The obtained experimental results showed rising in D2EHPA concentration leads to remarkable extraction of Ni^{2+} (95.5%) and Zn^{2+} (96.1%). Consequently, the high values of D2EHPA concentration had effective influence on Zn^{2+} and Ni^{2+} extraction.

Aghazadeh et al. [56] studied zinc extraction from synthetic sulfate solution using D2EHPA diluted with kerosene. In their study tributyl-phosphate (TBP) showed positive synergism at concentration of 5% (v/v) and negative synergism effect at concentrations of 2% and 10%. Zinc extraction efficiency increased from 90 to 98% for experiments with 5%, 15%, and 20% D2EHPA concentrations when TBP concentration was 5%. However, their study was limited to zinc extraction from synthetic sulfate solution. Aghdam et al. [57] also, studied the possibility of separation of Zn^{2+} and Cd^{2+} metal ions from chloride solutions by (D2EHPA) in kerosene as a diluent. In fact, the aqueous phase was obtained by brine leaching of zinc leaching filter cakes. They concluded D2EHPA is capable of extracting and separating zinc from cadmium in chloride solutions at pH = 3 with approximately 99% yield a negligible co-extraction of cadmium.

3.3. Thermodynamic Modeling

The γ_i in organic and aqueous phases are needed for calculation

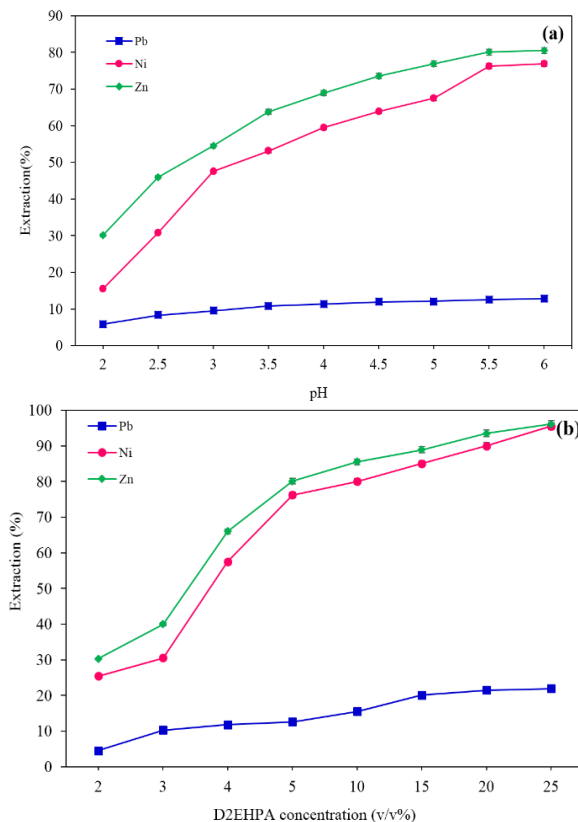


Figure 4. Factors affecting Zn^{2+} , Ni^{2+} , and Pb^{2+} extraction from ZPFC, 2 M HNO_3 solution ($[\text{Zn}^{2+}] = 49.51 \text{ g/L}$, $[\text{Ni}^{2+}] = 4.42 \text{ g/L}$ and $[\text{Pb}^{2+}] = 14.06 \text{ g/L}$), (a) Effect of pH on Zn^{2+} , Ni^{2+} , and Pb^{2+} extraction at $T = 298.15 \text{ K}$, 5 percent v/v solution of D2EHPA in kerosene, and $\text{O/A}=1/1$, (b) Effect of concentration of D2EHPA in kerosene on Zn^{2+} , Ni^{2+} , and Pb^{2+} ions extraction at $\text{pH} = 5.5$, $T = 298.15 \text{ K}$, and $\text{O/A}=1/1$

K_{ex} parameter (equilibrium constant), which can be utilized to predict the concentration equilibrium of ion in the organic phase. In this study, Electrolyte-UNIQUAC-NRF (for aqueous phase) and UNIQUAC-NRF (for organic phase) models were used for γ_i calculation. These models also were compared with NRTL and a new NRTL-based local composition model [58-66]. The more details of used models are given in Appendix A. The Genetic Algorithm (GA) was used to calculate the factors of the models and K_{ex} by a regression analysis of the extraction equilibrium data. The objective function (OF) for GA is as following (Equation (3)):

$$OF = \frac{100}{N} \left(\sum \left| \frac{[\text{Zn}]^{\text{cal.}} - [\text{Zn}]^{\text{exp.}}}{[\text{Zn}]^{\text{exp.}}} \right| + \left| \frac{[\text{Ni}]^{\text{cal.}} - [\text{Ni}]^{\text{exp.}}}{[\text{Ni}]^{\text{exp.}}} \right| \right) \quad (3)$$

The superscripts “cal.” of and “exp.” are the calculated and the experimental values, respectively and N is the number of experimental points. The thermodynamic modeling will be performed based on following algorithm:

Algorithm 1: Proposed method

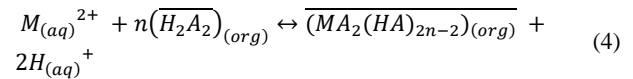
-
- 1: Input Initial concentration and experimental equilibria date for pH and $[\text{Ni}^{2+}]$ and $[\text{Zn}^{2+}]$
 - 2: Initial assumption for parameters of models and K_{ex}
 - 3: Calculate the concentration of each species $[i]'$ from the equation system at $\gamma_i = 1$
 - 4: Calculate γ_i from models using $[i]$
 - 5: Calculate the concentration of each species $[i]'$ from the equation system and return to step 4
 - 6: Calculation F parameter

$$OF = \frac{100}{Np} \sum \left(\left| \frac{[\text{Zn}] - [\text{Zn}]'}{[\text{Zn}]} \right| + \left| \frac{[\text{Ni}] - [\text{Ni}']}{{[\text{Ni}']}^2} \right| \right)$$
 - 7: If $OF > \epsilon$
 $[i] = [i]'$ and return to step 4
 If $OF < \epsilon$

$$OF = \frac{100}{Np} \left(\sum \left| \frac{[\text{Zn}]^{\text{cal.}} - [\text{Zn}]^{\text{exp.}}}{[\text{Zn}]^{\text{exp.}}} \right| + \left| \frac{[\text{Ni}]^{\text{cal.}} - [\text{Ni}]^{\text{exp.}}}{[\text{Ni}]^{\text{exp.}}} \right| \right)$$
 - 8: If $OF > \epsilon$
 Calculate the concentration of each species $[i]'$ from the equation system and return to step 3
 If $OF < \epsilon$
 Print parameters of models and K_{ex}
-

3. 3. 1. Extraction Mechanism of Ni and Zn by D2EHPA

In this study, D2EHPA was used as a solvent extraction, which extracts Zn^{2+} and Ni^{2+} ions. The divalent extraction metals such as Ni^{2+} and Zn^{2+} using di-(2-ethylhexyl) phosphoric acid is shown using the equilibrium reaction (Equation (4)):



H_2A_2 is the extractant in dimeric form and the stoichiometric coefficient of H_2A_2 displayed by n . The D2EHPA molecules is well known being generally as dimers in the non-polar organic diluents. H_2A_2 shows the dimer of di-(2-ethylhexyl) phosphoric acid and the over -bar symbol illustrates the substances in the organic phase. K_{ex} parameter of the extraction reaction of Ni^{2+} , Zn^{2+} and D2EHPA can be given as Equation (5):

$$K_{ex} = \frac{[\overline{(MA_2(HA)_{2n-2})}][H^+]^2 \overline{\gamma}_{(MA_2(HA)_{2n-2})} \gamma_{H^+}^2}{[M^{2+}] [\overline{H_2A_2}]^n \gamma_{M^{2+}} \overline{\gamma}_{(H_2A_2)}^n} \quad (5)$$

and the distribution coefficient, D , can be expressed as Equation (6):

$$D = \frac{[\overline{(MA_2(HA)_{2n-2})}]}{[M^{2+}]} \quad (6)$$

By taking the logarithm of Equation (5) and by Equation (7):

$$\log D - 2pH = n\log [\overline{(H_2A_2)}] + \log K_{ex} - \log \frac{\overline{\gamma}_{(MA_2(HA)_{2n-2})} \gamma_{H^+}^2}{\gamma_{M^{2+}} \overline{\gamma}_{(H_2A_2)}^n} \quad (7)$$

The equilibrium concentration of H_2A_2 in Equation (4) was considered by following (Equation (8)):

$$[(\overline{H_2A_2})] = [(\overline{H_2A_2})]^0 - n \overline{[(MA_2(HA)_{2n-2})]} \quad (8)$$

The plot of $\log D - pH$ vs. $\log [(\overline{H_2A_2})]$ is linear if the ideality is assumed for the system, i.e. $\gamma_i = 1$. The line slope (n) characterizes H_2A_2 stoichiometric coefficient whereas its intercept denotes K_{ex} without considering the non-ideality of the substances.

In ionic strength calculation, it is required to consider H^+ , Na^+ , NO_3^- , Zn^{2+} , and Ni^{2+} ions in the aqueous solution. According to Equation (4), the metal ions during the extraction reaction are substituted with H^+ . The organic solution contains of three components: Zn^{2+} and Ni^{2+} , free extractant dimers (H_2A_2), and kerosene as diluent. Therefore, the system contains five unknown concentrations and five equations were needed. The equations were obtained by charge and mass balances in the aqueous solution as following Equations (9-14):

$$[Kerosene] = [Kerosene]^0 \quad (9)$$

$$[(H_2A_2)] = [(H_2A_2)]^0 - n [M^{2+}] \quad (10)$$

$$[Na^+] = [M^{2+}]^0 \quad (11)$$

$$[H^+] = [H^+]^0 + [M^{2+}]^0 \quad (12)$$

$$[Ni^{2+}] = [Ni^{2+}]^0 - \overline{[Ni^{2+}]} \quad (13)$$

$$[Zn^{2+}] = [Zn^{2+}]^0 - \overline{[Zn^{2+}]} \quad (14)$$

3. 3. 2. Determination of Stoichiometric Coefficient

The obtained experimental data that are used to obtain stoichiometric coefficient are shown in Table 1. The experimental tests were performed by D2EHPA (2-25 (v/v%)), at 298.15 K, $3.8 < pH < 4.5$. In Equation (2), the slope analysis procedure is applied to calculate the organic complex of Zn^{2+} and Ni^{2+} and unknown n (stoichiometric coefficient) of D2EHPA dimer. Thus, the behavior of $\log D - pH$ vs. $\log [(\overline{H_2A_2})]$ must be plotted. Figure 5 demonstrates this behavior. Based on Figure 5, accuracy

TABLE 1. The extraction experimental data of zinc and nickel (O/A=1/1 and T = 298.15 K)

[Kerosene] (mol/L)	[H_2A_2] ⁰ (mol/L)	[Ni] ⁰ (mol/L)	[Zn] ⁰ (mol/L)	$\overline{[Ni]}$ (mol/L)	$\overline{[Zn]}$ (mol/L)	pH
4.175	0.025	0.0037	0.067	0.0002	0.0028	4.10
4.175	0.025	0.0037	0.067	0.0003	0.0028	4.15
4.067	0.050	0.0037	0.067	0.0005	0.0027	4.26
4.067	0.050	0.0037	0.067	0.0006	0.0039	4.10
4.019	0.075	0.0037	0.067	0.0007	0.0049	4.16
4.019	0.075	0.0037	0.067	0.0008	0.0073	4.20
4.067	0.050	0.0079	0.138	0.0017	0.0318	4.30
4.067	0.050	0.0079	0.138	0.0021	0.0987	4.10
4.067	0.050	0.0079	0.138	0.0018	0.1101	4.10
4.019	0.075	0.0079	0.138	0.0053	0.1269	3.99
4.019	0.075	0.0079	0.138	0.0093	0.1449	3.97
3.895	0.143	0.0079	0.138	0.0131	0.1591	4.10
3.895	0.143	0.0185	0.271	0.0154	0.1749	4.30
3.895	0.143	0.0185	0.271	0.0182	0.1914	4.32
3.690	0.287	0.0185	0.271	0.0252	0.2109	4.50
3.690	0.287	0.0185	0.271	0.0298	0.2564	4.31
3.690	0.287	0.0185	0.271	0.0356	0.3116	4.26
3.280	0.574	0.0438	0.469	0.0393	0.3378	4.18
3.280	0.574	0.0438	0.469	0.0397	0.3869	4.22
3.280	0.574	0.0438	0.469	0.0399	0.4125	4.13
3.280	0.574	0.0438	0.469	0.0432	0.4310	4.10
3.280	0.574	0.0438	0.469	0.0443	0.4364	4.11

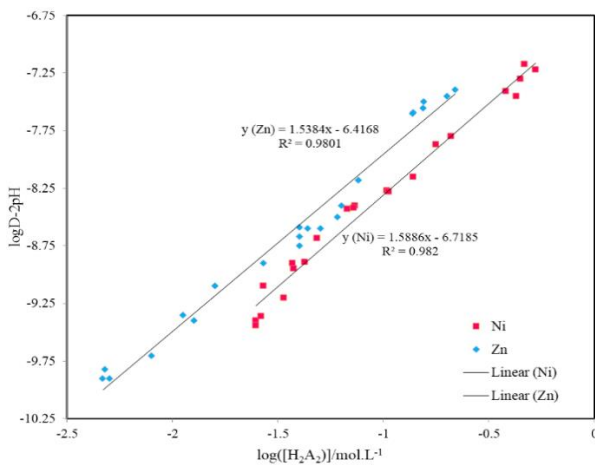
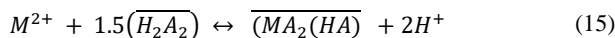


Figure 5. The $\log(D-2pH)$ behavior vs. $\log([H_2A_2J])$

of both correlations are satisfactory ($R^2 \geq 0.98$, R^2 is R-squared). According to curve fitting results, extraction reaction between D2EHPA, Zn^{2+} and Ni^{2+} dimers is as following Equation (15):



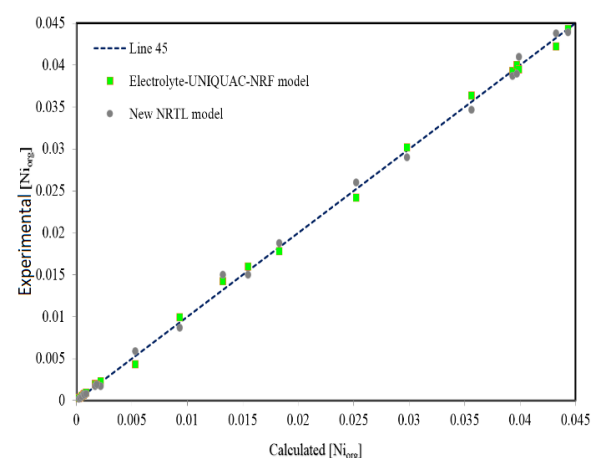
Using UNIQUAC-NRF, Electrolyte-UNIQUAC-NRF, NRTL and a new NRTL-based local composition model, the constant of Equation (15) was measured. All unknown parameters of four thermodynamic models are obtained based on experimental data. The obtained results were tabulated in Table 2. The unknown parameters were 17 and the details of them are as following: 12 unknown parameters of UNIQUAC-NRF and NRTL model and five unknown parameters of K_{ex} and Electrolyte-UNIQUAC-NRF and new NRTL-based local composition model. Furthermore, the values of q_i (surface parameter) and r_i (volume parameter), as structural parameters, of ionic and any molecular species were required in order to calculate γ_i coefficients. These coefficients are presented in literature [61].

To investigate the thermodynamic consistency of modeling of Zn^{2+} and Ni^{2+} extraction and to validate K_{ex} value and for calculation of the model factors, the obtained equilibrium concentration in the both phases were correlated with the experimental data. Consequently, the data that is given in Table 1 was classified in two parts. The first part of experimental data was related to find correctness of K_{ex} and factors of model, though the another part was compared to values predicted by these factors. Correctness of the calculations, in addition, was verified for both experimental data parts. According to Equation (4), the calculated values were achieved with adjusted correctness of K_{ex} values. γ_i were computed NRF by adjusted interaction factors and according to NRTL, new NRTL-based local composition model,

TABLE 2. The adjustable parameters based on all used models for zinc and nickel

Parameter		UNIQUAC-NRF	NRTL
I	j	α_{ij}	α_{ij}
Zn	Ni	5.64	4.90
Zn	HA	-6.43	-5.49
Zn	Kerosene	-2.02	-2.52
Ni	Zn	-4.51	-3.24
Ni	HA	6.16	5.12
Ni	Kerosene	1.15	1.58
HA	Zn	1.67	1.84
HA	Ni	-3.35	-3.56
HA	Kerosene	-0.27	-0.39
Kerosene	Zn	1.82	1.79
Kerosene	Ni	4.74	4.60
Kerosene	HA	-4.11	-4.28
		Electrolyte- UNIQUAC-NRF	New NRTL
		λ_{ij}	λ_{ij}
Zn^{2+}	NO_3^-	1.27	1.72
Ni^{2+}	NO_3^-	-4.65	-3.95
H^+	NO_3^-	-4.65	-4.28
Na^+	NO_3^-	3.10	3.67
Ion	Water	1.28	1.91

UNIQUAC-NRF and Electrolyte-UNIQUAC. Next, the values of equilibrium concentration were calculated by using the trust region dogleg iteration method. As can be shown in Figure 6, all obtained and calculated experimental data of Ni^{2+} and Zn^{2+} in the aqueous solution and organic media the at equilibrium condition.



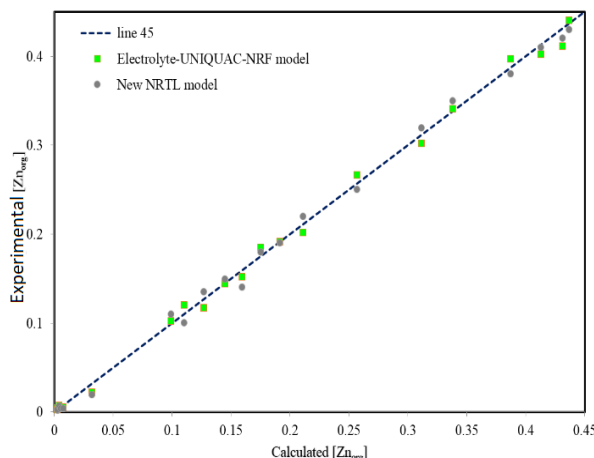


Figure 6. The Ni^{2+} and Zn^{2+} concentration in organic phase at 298.15 K: The experimental results vs. thermodynamic modeling.

4. CONCLUSIONS

This work was devoted to a comprehensive study of the extraction of Zn and Ni from zinc plant residue. The leaching behavior of metals in HNO_3 solution was investigated and the effect of some important parameter such as acid concentration, time, and temperature was studied. The result showed that increasing all these factors contributed to increase the leaching efficiency. About 100% of metal ions at the optimum extraction conditions: acid concentration of 2 M, temperature 358.15 K, S/L = 1/10, and 1.5 h was leached. The solvent extraction of Ni^{2+} , Zn^{2+} , and Pb^{2+} were examined from the leaching solution with D2EHPA. In one stage, the separation of Ni^{2+} and Zn^{2+} from Pb^{2+} was performed and about 99.8% of Ni^{2+} and Zn^{2+} were extracted (25 (v/v%) D2EHPA, pH = 5.5, (O/A) = 1/1, and T = 298.15). Afterward, using various thermodynamic models, the concentration of organic and aqueous phases was simulated. The stoichiometry of the solvent extraction reaction was investigated by the slope analysis method, subsequently it was found that 1.5 D2EHPA molecules were required for the extraction of Ni^{2+} and Zn^{2+} . Therefore, the reaction was defined as $M^{2+} + 1.5(\overline{H_2A_2}) \leftrightarrow \overline{(MA_2(HA))} + 2H^+$. Ni^{2+} and Zn^{2+} equilibrium concentrations were computed using a thermodynamic modeling. The γ_i for both organic and aqueous solutions were determined by UNIQUAC-NRF model, Electrolyte-UNIQUAC-NRF model, NRTL model and a new NRTL-based local composition model for electrolyte and non-electrolyte solution. The prediction of the equilibrium data of Ni^{2+} and Zn^{2+} by the calculated adjustable parameters demonstrated the accuracy of used thermodynamic models. As a result, Electrolyte-UNIQUAC-NRF and UNIQUAC-NRF equations in comparison the NRTL and a new local

based NRTL had more accuracy to calculate the extraction of Ni^{2+} and Zn^{2+} extraction by D2EHPA extractant from nitric solution and statistical processing of the results showed good consistency of experimental and calculated values.

5. REFERENCES

- Kashyap, V. and Taylor, P., "Extraction and recovery of zinc and indium from residue rich in zinc ferrite", *Minerals Engineering*, Vol. 176, (2022), 107364. doi: 10.1016/j.mineng.2021.107364.
- Kani, O.S.M., Azizitorghabeh, A. and Rashchi, F., "Recovery of zn (ii), mn (ii) and co (ii) from the zinc plant residue using the solvent extraction with cyanex 302 and d2ehpa/tbp: Stoichiometry and structural studies", *Minerals Engineering*, Vol. 169, (2021), 106944. doi: 10.1016/j.mineng.2021.106944.
- Li, S., Yang, J., Wang, J., Han, B., Zhang, H., Yang, S. and Chen, Y., "Efficient zinc extraction with novel phenyl phosphate ptopp in sulfuric acid system", *Journal of Cleaner Production*, Vol. 417, (2023), 138052. doi: 10.1016/j.jclepro.2023.138052.
- Asadollahzadeh, M., Shakib, B., Torab-Mostaedi, M. and Outokesh, M., "Extraction of molybdenum (vi) and vanadium (v) from nitrate solutions using coupling of acid and solvating extractants (research note)", *International Journal of Engineering, Transactions A: Basics*, Vol. 32, No. 10, (2019), 1366-1371. doi: 10.5829/IJE.2019.32.10A.05
- Zhang, K., Qiu, L., Tao, J., Zhong, X., Lin, Z., Wang, R. and Liu, Z., "Recovery of gallium from leach solutions of zinc refinery residues by stepwise solvent extraction with n235 and cyanex 272", *Hydrometallurgy*, Vol. 205, (2021), 105722. doi: 10.1016/j.hydromet.2021.105722.
- Liu, W., Li, J., Zheng, J., Song, Y., Shi, Z., Lin, Z. and Chai, L., "Different pathways for cr (iii) oxidation: Implications for cr (vi) reoccurrence in reduced chromite ore processing residue", *Environmental Science & Technology*, Vol. 54, No. 19, (2020), 11971-11979. doi: 10.1021/acs.est.0c01855
- Igosawa, T., Matsumiya, M. and Sasaki, Y., "Recovery of tungsten compounds from spent tungstophosphate catalyst using leaching, solvent extraction with phosphonium-based ionic liquids and precipitation", *Hydrometallurgy*, Vol. 208, (2022), 105803. doi: 10.1016/j.hydromet.2021.105803.
- Yuxin, Z., Ting, S., Hongyu, C., Ying, Z., Zhi, G., Suiyi, Z., Xinfeng, X., Hong, Z., Yidi, G. and Yang, H., "Stepwise recycling of fe, cu, zn and ni from real electroplating sludge via coupled acidic leaching and hydrothermal and extraction routes", *Environmental Research*, Vol. 216, (2023), 114462. doi: 10.1016/j.envres.2022.114462
- Ahmadi, A., Sheibani, S., Mokmeli, M., Khorasani, S. and Yaghoobi, N., "Factors affecting the cathode edge nodulation in copper electrorefining process", *International Journal of Engineering, Transactions C: Aspects*, Vol. 35, No. 12, (2022), 2370-2376. doi: 10.5829/IJE.2022.35.12C.13.
- Hosseinzadeh, M. and Alizadeh, M., "Improvement of the solvent extraction of rhenium from molybdenite roasting dust leaching solution using counter-current extraction by a mixer-settler extractor", *International Journal of Engineering, Transactions A: Basics*, Vol. 27, No. 4, (2014), 651-658. doi: 10.5829/idosi.ije.2014.27.04a.17.
- Mohammadzadeh, M., Bagheri, H. and Ghader, S., "Study on extraction and separation of ni and zn using [bmim][pf6] il as selective extractant from nitric acid solution obtained from zinc plant residue leaching", *Arabian Journal of Chemistry*, Vol. 13, No. 6, (2020), 5821-5831. doi: 10.1016/j.arabjc.2020.04.019.

12. Suliman, S.S., Othman, N., Noah, N.F.M. and Kahar, I.N.S., "Extraction and enrichment of zinc from chloride media using emulsion liquid membrane: Emulsion stability and demulsification via heating-ultrasonic method", *Journal of Molecular Liquids*, Vol. 374, (2023), 121261. doi: 10.1016/j.molliq.2023.121261.
13. Asadollahzadeh, M., Torkaman, R. and Torab-Mostaedi, M., "Optimization of green technique develop for europium (iii) extraction by using phosphonium ionic liquid and central composite design approach", *International Journal of Engineering, Transactions B: Applications*, Vol. 34, No. 2, (2021), 508-516. doi: 10.5829/IJE.2021.34.02B.24.
14. Santanilla, A.J.M., Aliprandini, P., Benvenuti, J., Tenorio, J.A.S. and Espinosa, D.C.R., "Structure investigation for nickel and cobalt complexes formed during solvent extraction with the extractants cyanex 272, versatic 10 and their mixtures", *Minerals Engineering*, Vol. 160, (2021), 106691. doi: 10.1016/j.mineng.2020.106691.
15. Mahmoudi, A., Shakibania, S., Rezaee, S. and Mokmeli, M., "Effect of the chloride content of seawater on the copper solvent extraction using acorga m5774 and lix 984n extractants", *Separation and Purification Technology*, Vol. 251, (2020), 117394. doi: 10.1016/j.seppur.2020.117394.
16. Barnard, K.R., Zeng, L. and Shiers, D.W., "Stoichiometry of the nickel complex formed with lix 63 hydroxyoxime under acidic chloride conditions", *Solvent Extraction and Ion Exchange*, Vol. 40, No. 5, (2022), 477-492. doi: 10.1080/07366299.2021.1992891.
17. Odegbemi, F., Idowu, G.A. and Adebayo, A.O., "Nickel recovery from spent nickel-metal hydride batteries using lix-84i-impregnated activated charcoal", *Environmental Nanotechnology, Monitoring & Management*, Vol. 15, (2021), 100452. doi: 10.1016/j.enmm.2021.100452.
18. Valeev, D., Shoppert, A., Dogadkin, D., Romashova, T., Kuz'mina, T. and Salazar-Concha, C., "Extraction of al and rare earth elements via high-pressure leaching of boehmite-kaolinite bauxite using nh4hs04 and h2so4", *Hydrometallurgy*, Vol. 215, No., (2023), 105994. doi: 10.1016/j.hydromet.2022.105994.
19. Li, C., Jia, Y., Lu, X. and Chen, H., "Transport of zn (ii) through matrix enhanced polymer inclusion membrane containing oha and d2ehpa", *Chemical Engineering Journal*, Vol. 452, (2023), 139288. doi: 10.1016/j.cej.2022.139288.
20. Hou, H., Shao, S., Ma, B., Li, X., Shi, S., Chen, Y. and Wang, C., "Sustainable process for valuable-metal recovery from circulating fluidized bed fly ash through nitric acid pressure leaching", *Journal of Cleaner Production*, Vol. 360, (2022), 132212. doi: 10.1016/j.jclepro.2022.132212.
21. Martins, J.M.A., Guimaraes, A.S., Dutra, A.J.B. and Mansur, M.B., "Hydrometallurgical separation of zinc and copper from waste brass ashes using solvent extraction with d2ehpa", *Journal of Materials Research and Technology*, Vol. 9, No. 2, (2020), 2319-2330. doi: 10.1016/j.jmrt.2019.12.063.
22. Azizi, A., Nozhati, R.A. and Sillanpää, M., "Solvent extraction of copper and zinc from sulfate leach solution derived from a porcelain stone tailings sample with chemorex cp-150 and d2ehpa", *Journal of Sustainable Metallurgy*, Vol. 6, (2020), 250-258. doi: 10.1007/s40831-020-00271-w.
23. Hosseini, T., Mostoufi, N., Daneshpayeh, M. and Rashchi, F., "Modeling and optimization of synergistic effect of cyanex 302 and d2ehpa on separation of zinc and manganese", *Hydrometallurgy*, Vol. 105, No. 3-4, (2011), 277-283. doi: 10.1016/j.hydromet.2010.10.015
24. Babakhani, A., Rashchi, F., Zakeri, A. and Vahidi, E., "Selective separation of nickel and cadmium from sulfate solutions of spent nickel-cadmium batteries using mixtures of d2ehpa and cyanex 302", *Journal of Power Sources*, Vol. 247, (2014), 127-133. doi: 10.1016/j.jpowsour.2013.08.063.
25. Innocenzi, V. and Veglio, F., "Separation of manganese, zinc and nickel from leaching solution of nickel-metal hydride spent batteries by solvent extraction", *Hydrometallurgy*, Vol. 129, (2012), 50-58. doi: 10.1016/j.hydromet.2012.08.003.
26. Bagheri, H., Karimi, N., Dan, S., Notej, B. and Ghader, S., "Ionic liquid excess molar volume prediction: A conceptual comparison", *Journal of Molecular Liquids*, Vol. 336, (2021), 116581. doi: 10.1016/j.molliq.2021.116581.
27. Bagheri, H., Hashemipour, H., Ghalandari, V. and Ghader, S., "Numerical solution of particle size distribution equation: Rapid expansion of supercritical solution (ress) process", *Particulology*, Vol. 57, (2021), 201-213. doi: 10.1016/j.partic.2020.12.011.
28. Mokhtari, A., Bagheri, H., Ghazvini, M. and Ghader, S., "New mathematical modeling of temperature-based properties of ionic liquids mixture: Comparison between semi-empirical equation and equation of state", *Chemical Engineering Research and Design*, Vol. 177, (2022), 331-353. doi: 10.1016/j.cherd.2021.10.039.
29. Maraki, M., Tagimalek, H., Azargoman, M., Khatami, H. and Mahmoodi, M., "Experimental investigation and statistical modeling of the effective parameters in charpy impact test on az31 magnesium alloy with v-shape groove using taguchi method", *International Journal of Engineering, Transactions C: ASPECTS*, Vol. 33, No. 12, (2020), 2521-2529. doi: 10.5829/IJE.2020.33.12C.13.
30. Illoeje, C.O., Jové Colón, C.F., Cresko, J. and Graziano, D.J., "Gibbs energy minimization model for solvent extraction with application to rare-earths recovery", *Environmental Science & Technology*, Vol. 53, No. 13, (2019), 7736-7745. doi: 10.1021/acs.est.9b01718
31. Razavi, S.M., Haghtalab, A. and Khanchi, A.R., "Thermodynamic modeling of the solvent extraction equilibrium for the recovery of vanadium (v) from acidic sulfate solutions using di-(2-ethylhexyl) phosphoric acid", *Fluid Phase Equilibria*, Vol. 474, (2018), 20-31. doi: 10.1016/j.fluid.2018.07.007.
32. Razavi, S.M., "A new nrtl-based local composition model for thermodynamic modeling of electrolyte solutions", *The Journal of Chemical Thermodynamics*, Vol. 161, (2021), 106534. doi: 10.1016/j.jct.2021.106534.
33. Liu, F., Ning, P.-G., Cao, H.-B. and Zhang, Y., "Measurement and modeling for vanadium extraction from the (navo3+ h2so4+ h2o) system by primary amine n1923", *The Journal of Chemical Thermodynamics*, Vol. 80, (2015), 13-21. doi: 10.1016/j.jct.2021.106534.
34. Aman-Pommier, F. and Jallut, C., "Solubility of diazepam in water+ tert-butyl alcohol solvent mixtures: Part 2. Correlation using scatchard-hildebrand and combined scatchard-hildebrand/flory-huggins excess gibbs energy models", *Fluid Phase Equilibria*, Vol. 458, (2018), 84-101. doi: 10.1016/j.jct.2021.106534.
35. Mörters, M. and Bart, H.-J., "Extraction equilibria of zinc with bis (2-ethylhexyl) phosphoric acid", *Journal of Chemical & Engineering Data*, Vol. 45, No. 1, (2000), 82-85. doi: 10.1021/je990200u.
36. Shi, D., Cui, B., Li, L., Xu, M., Zhang, Y., Peng, X., Zhang, L., Song, F. and Ji, L., "Removal of calcium and magnesium from lithium concentrated solution by solvent extraction method using d2ehpa", *Desalination*, Vol. 479, (2020), 114306. doi: 10.1016/j.desal.2019.114306.
37. Tanong, K., Tran, L.-H., Mercier, G. and Blais, J.-F., "Recovery of zn (ii), mn (ii), cd (ii) and ni (ii) from the unsorted spent batteries using solvent extraction, electrodeposition and

- precipitation methods", *Journal of Cleaner Production*, Vol. 148, (2017), 233-244. doi: 10.1016/j.jclepro.2017.01.158.
38. Babakhani, A. and Sartaj, M., "Removal of cadmium (ii) from aqueous solution using tripolyphosphate cross-linked chitosan", *Journal of Environmental Chemical Engineering*, Vol. 8, No. 4, (2020), 103842. doi: 10.1016/j.jece.2020.103842.
 39. Pitzer, K.S. and Silvester, L.F., "Thermodynamics of electrolytes. Vi. Weak electrolytes including h 3 po 4", *Journal of Solution Chemistry*, Vol. 5, (1976), 269-278. doi: 10.1016/j.jece.2020.103842.
 40. Pitzer, K.S. and Mayorga, G., "Thermodynamics of electrolytes. II. Activity and osmotic coefficients for strong electrolytes with one or both ions univalent", *The Journal of Physical Chemistry*, Vol. 77, No. 19, (1973), 2300-2308. doi: 10.1021/j100638a009.
 41. Pitzer, K.S., "Activity coefficients in electrolyte solutions, CRC press, (2018).
 42. Pitzer, K.S., "Thermodynamics of electrolytes. I. Theoretical basis and general equations", *The Journal of Physical Chemistry*, Vol. 77, No. 2, (1973), 268-277. doi: 10.1021/j100621a026.
 43. Cruz, J.L. and Renon, H., "A new thermodynamic representation of binary electrolyte solutions nonideality in the whole range of concentrations", *AICHE Journal*, Vol. 24, No. 5, (1978), 817-830. doi: 10.1002/aic.690240508.
 44. Zhao, E., Yu, M., Sauvé, R.E. and Khoshkbarchi, M.K., "Extension of the wilson model to electrolyte solutions", *Fluid Phase Equilibria*, Vol. 173, No. 2, (2000), 161-175. doi: 10.1016/S0378-3812(00)00393-9.
 45. Thomsen, K., Rasmussen, P. and Gani, R., "Correlation and prediction of thermal properties and phase behaviour for a class of aqueous electrolyte systems", *Chemical Engineering Science*, Vol. 51, No. 14, (1996), 3675-3683. doi: 10.1016/0009-2509(95)00418-1.
 46. Chen, C.C. and Evans, L.B., "A local composition model for the excess gibbs energy of aqueous electrolyte systems", *AICHE Journal*, Vol. 32, No. 3, (1986), 444-454. doi: 10.1208/s12249-019-1373-4.
 47. Haghtalab, A. and Vera, J., "A nonrandom factor model for the excess gibbs energy of electrolyte solutions", *AICHE Journal*, Vol. 34, No. 5, (1988), 803-813. doi: 10.1002/aic.690340510.
 48. Sadeghi, R., "New local composition model for electrolyte solutions", *Fluid Phase Equilibria*, Vol. 231, No. 1, (2005), 53-60. doi: 10.1016/j.molliq.2011.10.015.
 49. Chen, C.-C. and Mathias, P.M., "Applied thermodynamics for process modeling", *American Institute of Chemical Engineers. AICHE Journal*, Vol. 48, No. 2, (2002), 194. doi: 10.1002/aic.690480202.
 50. Renon, H. and Prausnitz, J.M., "Local compositions in thermodynamic excess functions for liquid mixtures", *AICHE Journal*, Vol. 14, No. 1, (1968), 135-144. doi: 10.1002/aic.690140124.
 51. Haghtalab, A. and Peyvandi, K., "Generalized electrolyte-uniquac-nrf model for calculation of solubility and vapor pressure of multicomponent electrolytes solutions", *Journal of Molecular Liquids*, Vol. 165, No., (2012), 101-112. doi: 10.1016/j.molliq.2011.10.015.
 52. Mohammadzadeh, M., Bagheri, H. and Ghader, S., "Solvent extraction of nickel and zinc from nitric acid solution using d2ehpa: Experimental and modeling", *Journal of Solution Chemistry*, Vol. 51, No. 4, (2022), 424-447. doi: 10.1007/s10953-022-01151-5.
 53. Sethurajan, M., Huguenot, D., Jain, R., Lens, P.N., Horn, H.A., Figueiredo, L.H. and van Hullebusch, E.D., "Leaching and selective zinc recovery from acidic leachates of zinc metallurgical leach residues", *Journal of Hazardous Materials*, Vol. 324, (2017), 71-82. doi: 10.1016/j.hazmat.2021.125664.
 54. Safarzadeh, M.S., Moradkhani, D., Ilkhchi, M.O. and Golshan, N.H., "Determination of the optimum conditions for the leaching of cd-ni residues from electrolytic zinc plant using statistical design of experiments", *Separation and Purification Technology*, Vol. 58, No. 3, (2008), 367-376. doi: 10.1016/j.seppur.2007.05.016.
 55. Randhawa, N.S., Gharami, K. and Kumar, M., "Leaching kinetics of spent nickel-cadmium battery in sulphuric acid", *Hydrometallurgy*, Vol. 165, (2016), 191-198. doi: 10.1016/j.hydromet.2015.09.011.
 56. Aghazadeh, S., Gharabaghi, M. and Shafaei, Z., "Thermodynamical and catalytic aspects of zinc separation from aqueous solution", *Chinese Journal of Chemical Engineering*, Vol. 26, No. 12, (2018), 2455-2460. doi: 10.1016/j.cjche.2018.07.022.
 57. Aghdam, A.A.B., Yoozbashizadeh, H. and Moghaddam, J., "Simple separation method of zn (ii) and cd (ii) from brine solution of zinc plant residue and synthetic chloride media using solvent extraction", *Chinese Journal of Chemical Engineering*, Vol. 28, No. 4, (2020), 1055-1061. doi: 10.1016/j.cjche.2019.12.003.
 58. Sheik, A., Ghosh, M., Sanjay, K., Subbaiah, T. and Mishra, B., "Dissolution kinetics of nickel from spent catalyst in nitric acid medium", *Journal of the Taiwan Institute of Chemical Engineers*, Vol. 44, No. 1, (2013), 34-39. doi: 10.1016/j.jtice.2012.08.003.
 59. Assefi, M., Maroufi, S., Mayyas, M. and Sahajwalla, V., "Recycling of ni-cd batteries by selective isolation and hydrothermal synthesis of porous nio nanocuboid", *Journal of Environmental Chemical Engineering*, Vol. 6, No. 4, (2018), 4671-4675. doi: 10.1016/j.jece.2018.07.021.
 60. Yu, S., Xing, W., Xue, F., Cheng, Y. and Li, B., "Solubility and thermodynamic properties of nimodipine in pure and binary solvents at a series of temperatures", *The Journal of Chemical Thermodynamics*, Vol. 152, (2021), 106259. doi: 10.1016/j.jct.2020.106259.
 61. Ravichandran, A., Khare, R. and Chen, C.C., "Predicting nrtl binary interaction parameters from molecular simulations", *AICHE Journal*, Vol. 64, No. 7, (2018), 2758-2769. doi: 10.1002/aic.16117.
 62. Pinto, I.S. and Soares, H.M., "Selective leaching of molybdenum from spent hydrodesulphurisation catalysts using ultrasound and microwave methods", *Hydrometallurgy*, Vol. 129, (2012), 19-25. doi: 10.1016/j.hydromet.2012.08.008.
 63. Spooren, J., Binnemans, K., Björkmalm, J., Breemersch, K., Dams, Y., Folens, K., González-Moya, M., Horckmans, L., Komnitsas, K. and Kurylak, W., "Near-zero-waste processing of low-grade, complex primary ores and secondary raw materials in europe: Technology development trends", *Resources, Conservation and Recycling*, Vol. 160, (2020), 104919. doi: 10.1016/j.resconrec.2020.104919.
 64. Haghtalab, A. and Peyvandi, K., "Electrolyte-uniquac-nrf model for the correlation of the mean activity coefficient of electrolyte solutions", *Fluid Phase Equilibria*, Vol. 281, No. 2, (2009), 163-171. doi: 10.1016/j.fluid.2009.04.013.
 65. Asamoah, R.K., Skinner, W. and Addai-Mensah, J., "Alkaline cyanide leaching of refractory gold flotation concentrates and bio-oxidised products: The effect of process variables", *Hydrometallurgy*, Vol. 179, (2018), 79-93. doi: 10.1016/j.hydromet.2018.05.010.
 66. Shen, X., Shao, H., Liu, Y. and Zhai, Y., "Extraction, phase transformation and kinetics of valuable metals from nickel-chromium mixed metal oxidized ore", *Minerals Engineering*, Vol. 161, (2021), 106737. doi: 10.1016/j.mineng.2020.106737.

6. Appendix A

6.1. UNIQUAC-NRF Model

In order to correlate the activity coefficient for aqueous nonelectrolyte systems the UNIQUAC-NRF model is investigated [32, 51]. This model consists of two terms as a combinatorial for entropic contribution, and a residual for enthalpy contribution. Therefore, the activity coefficient equations for each component in a multicomponent mixture are given as following:

$$\ln \gamma_i = \ln \gamma_i^c - \ln \gamma_i^r \quad (\text{A.1})$$

$$\ln \gamma_i^c = \ln \left(\frac{\Phi_i}{x_i} \right) + 1 - \left(\frac{\Phi_i}{x_i} \right) - \frac{z}{2} q_i \left[\ln \left(\frac{\Phi_i}{\theta_i} \right) + 1 - \left(\frac{\Phi_i}{\theta_i} \right) \right] \quad (\text{A.2})$$

$$\begin{aligned} \ln \gamma_i^r &= q_i \left[1 + \ln \Gamma_{ii} \sum_{j=1}^n (\theta_j \Gamma_{ij}) + \right. \\ &\quad \left. (1 - \theta_i) \sum_{j=1}^n \left(\theta_j \ln \frac{\Gamma_{ij} \Gamma_{ji}}{\Gamma_{ii} \Gamma_{jj}} \right) - \right. \\ &\quad \left. \frac{1}{2} \sum_{k=1}^n \sum_{l=1, k \neq i, l}^n \left(\theta_k \theta_l \ln \frac{\Gamma_{kl} \Gamma_{lk}}{\Gamma_{kk} \Gamma_{ll}} \right) \right] \end{aligned} \quad (\text{A.3})$$

where Z is the coordination number, x_i denotes mole fraction of each component. The volume fraction (ϕ_i) and area fraction (θ_i) of each species are defined as following:

$$\theta_i = \frac{x_i q_i}{\sum_j x_j q_j} \quad (\text{A.4})$$

$$\Phi_i = \frac{x_i r_i}{\sum_j x_j r_j} \quad (\text{A.5})$$

The nonrandom factor, Γ_{ij} , is defined as following:

$$\Gamma_{ij} = \frac{\tau_{ij}}{\sum_k \theta_k \tau_{kj}} \quad (\text{A.6})$$

where τ_{ij} and τ_{ji} are the interaction parameters of UNIQUAC-NRF model for i and j components that are related to the interaction energies (u_{ij}) as following:

$$\tau_{ij} = \exp \left(-\frac{(u_{ij} - u_{ji})}{RT} \right) = \exp(-\alpha_{ij}) \quad (\text{A.7})$$

$$\begin{aligned} \alpha_{ij} &= (\alpha_{ij})_0 + (\alpha_{ij})_0 \left(\frac{1}{T} - \frac{1}{298.15} \right) + \\ &\quad (\alpha_{ij})_2 \left(\frac{298.15 - T}{T} + \ln \frac{T}{298.15} \right) \end{aligned} \quad (\text{A.8})$$

where x_i is mole fraction, Z is coordination number, τ_{ij} and τ_{ji} are the interaction factors.

6.2. Electrolyte-UNIQUAC-NRF Model

The Electrolyte-UNIQUAC-NRF model is based on the local composition approach for the calculation of activity coefficients in electrolyte solutions. Here the main equations of the model were provided. This activity coefficient model consists of a long range interaction contribution represented by the Pitzer-Debye-Hückel equation, and a short range interaction contribution which itself is stated as the sum of a

combinatorial term and a residual term as following [62]:

$$\ln \gamma_i = (\ln \gamma_i^*)^{PDH} + (\ln \gamma_i^*)^c + (\ln \gamma_i^*)^r \quad (\text{A.9})$$

where star superscript stands for unsymmetrical normalization.

$$(\ln \gamma_i^*)^{PDH} = -A_\phi \left(\frac{1000}{M_S} \right)^{0.5} \left[\left(\frac{2z_e^2}{\rho} \right) \ln \left(1 + \frac{z_e^2 I_x^{0.5} - 2I_x^{1.5}}{1 + \rho I_x^{0.5}} \right) \right] \quad (\text{A.10})$$

where M_S is the molecular weight of solvent, z is the charge number of each ion, ρ is closest approach parameter, A_ϕ is the Debye-Hückel constant, and I_x stands for the ionic strength on a mole fraction basis.

$$(\ln \gamma_i^*)^c = (\ln \gamma_i^c) - (\ln \gamma_i^\infty)^c \quad (\text{A.11})$$

$$\begin{aligned} (\ln \gamma_i^c) &= \ln \left(\frac{\Phi'_i}{X_i} \right) + 1 - \left(\frac{\Phi'_i}{X_i} \right) - \\ &\quad \frac{z}{2} q_i \left[\ln \left(\frac{\Phi'_i}{\theta'_i} \right) + 1 - \left(\frac{\Phi'_i}{\theta'_i} \right) \right] \end{aligned} \quad (\text{A.12})$$

$$\begin{aligned} (\ln \gamma_i^\infty)^c &= \ln \left(\frac{r_i}{r_s} \right) - \frac{z}{2} q_i \left[\ln \left(\frac{r_i q_s}{r_s q_i} \right) - \left(\frac{r_i q_s}{r_s q_i} \right) + \right. \\ &\quad \left. 1 \right] - \left(\frac{r_i}{r_s} \right) + 1 \end{aligned} \quad (\text{A.13})$$

where Z is coordination number, and r_i and q_i denote the volume and surface parameters of ion i or solvent molecules. The effective volume and area fractions of each species are expressed as following:

$$\Phi'_i = \frac{x_i r_i}{\sum_j x_j r_j} \quad (\text{A.14})$$

$$\theta'_i = \frac{x_i q_i}{\sum_j x_j q_j} \quad (\text{A.15})$$

where X stands for the effective mole fraction that is expressed by the bulk mole fraction as $X_i = C_i x_i$, in which $C_i = z_i$ for ions and $C_i = 1$ for solvent molecules. Finally, the residual term of activity coefficient as following:

$$(\ln \gamma_i^r) = (\ln \gamma_i^r) - (\ln \gamma_i^\infty)^r \quad (\text{A.16})$$

$$\begin{aligned} \frac{1}{q_a z_a} (\ln \gamma_a)^r &= \sum_{a'} \frac{\theta'_{a'}}{z_{a'}} \left(1 - \right. \\ &\quad \left. \sum_{c'} \theta'_{c'} \ln (\tau_{c'a'}) \right) + \sum_{c'} \frac{\theta'_{c'}}{z_{c'}} \left(1 - \Gamma_{ac'} + \right. \\ &\quad \left. \ln (\tau_{ac'}) - \sum_{a'} \theta'_{a'} \ln (\tau_{c'a'}) \right) + \theta'_m \left(1 - \right. \\ &\quad \left. \Gamma_{am} + \ln (\tau_{am}) - \sum_i \theta'_i \ln (\tau_{im}) \right) - \\ &\quad \frac{1}{z_a} \left(\ln \left(\sum_{c'} \theta'_{c'} \tau_{c'a} + \theta'_m \right) - \sum_{c'} \theta'_{c'} \ln (\tau_{c'a}) \right) \end{aligned} \quad (\text{A.17})$$

$$\begin{aligned} \frac{1}{q_c z_c} (\ln \gamma_c)^r &= \sum_{c'} \frac{\theta'_{c'}}{z_{c'}} \left(1 - \right. \\ &\quad \left. \sum_{a'} \theta'_{a'} \ln (\tau_{a'c'}) \right) + \sum_{a'} \frac{\theta'_{a'}}{z_{a'}} \left(1 - \Gamma_{ca'} + \right. \\ &\quad \left. \ln (\tau_{ca'}) - \sum_{c'} \theta'_{c'} \ln (\tau_{c'a'}) \right) + \theta'_m \left(1 - \right. \\ &\quad \left. \Gamma_{cm} + \ln (\tau_{cm}) - \sum_i \theta'_i \ln (\tau_{im}) \right) - \\ &\quad \frac{1}{z_c} \left(\ln \left(\sum_{a'} \theta'_{a'} \tau_{a'c} + \theta'_m \right) - \sum_{a'} \theta'_{a'} \ln (\tau_{a'c}) \right) \end{aligned} \quad (\text{A.18})$$

$$(Ln \gamma_i^\infty)^r = q_i z_i (1 - \tau_{im} + Ln \tau_{im}) \quad (A.19)$$

where c , a , and m subscripts show the cations, anions, and solvent molecules, respectively. The ion-molecule and ion-ion interaction energy parameters are represented by τ . The interaction energy parameters of the model are written as following:

$$\tau_{am} = \tau_{am} = exp(-\lambda_{ion,m}) \quad (A.20)$$

$$\tau_{ac} = \tau_{ac} = exp(-\lambda_{c,a}) \quad (A.21)$$

$$\lambda_{ij} = (\lambda_{ij})_0 + (\lambda_{ij})_0 \left(\frac{1}{T} = \frac{1}{298.15} \right) + (\lambda_{ij})_2 \left(\frac{298.15-T}{T} + Ln \frac{T}{298.15} \right) \quad (A.22)$$

where $\lambda_{ion,m}$ and $\lambda_{c,a}$ are the adjustable parameters of the model.

6. 3. NRTL Model

The NRTL model is following [59]:

$$\frac{g^M}{RT} = \sum_{i=1}^n x_i Ln(x_i) + \frac{g^E}{RT} \quad (A.23)$$

$$\frac{g^E}{RT} = \sum_{i=1}^n x_i \frac{\sum_{i=1}^n \tau_{ji} G_{ji} x_j}{\sum_{i=1}^n G_{Ki} x_k} \quad (A.24)$$

$$G_{ij} = exp(-\alpha_{ij} \tau_{ij}) \quad (A.25)$$

$$\tau_{ij} = \frac{g_{ij}-g_{jj}}{RT} = \frac{\Delta g_{ij}}{RT} \quad (A.26)$$

Here, g_{ij} is an energy factor that illustrates the interaction of species i and j , and the factor R_{ij} , R_{ji} is correlated to the non-randomness in the mixture (R_{ij}) corresponds to complete randomness, or an ideal solution.

6. 4. New NRTL-based Local Composition Model

The new NRTL model is given as following [61]:

$$g_c = Z_c (\sum_{a'} X_{a'c} g_{a'c} + \sum_{m'} X_{m'c} g_{m'c}) \quad (A.27)$$

$$g_a = Z_a (\sum_{c'} X_{c'a} g_{c'a} + \sum_{m'} X_{m'a} g_{m'a}) \quad (A.28)$$

$$g_m = \sum_i X_{im} g_{im} \quad (A.29)$$

where the g_c (cation Gibbs energy), g_a (anion Gibbs energy) and g_m (solvent Gibbs energy) are as following [59, 61]:

$$g_c^{ref} = Z_c \left(\frac{\sum_{a'} X_{a'} g_{a'c} + \sum_{m'} X_{m'} g_{m'c}}{\sum_{a'} X_{a'} + \sum_{m'} X_{m'}} \right) \quad (A.30)$$

$$g_a^{ref} = Z_a \left(\frac{\sum_{c'} X_{c'} g_{c'a} + \sum_{m'} X_{m'} g_{m'a}}{\sum_{c'} X_{c'} + \sum_{m'} X_{m'}} \right) \quad (A.31)$$

$$g_m^{ref} = \frac{\sum_i X_{im} g_{im}}{\sum_i X_i} \quad (A.32)$$

The excess molar Gibbs energy function is obtained as following [61]:

$$\begin{aligned} \frac{(g^E)_{SR}}{RT} = & \sum_{a'} X_{a'} \left[\sum_{j \neq a} \frac{X_j}{\sum_{j \neq a} X_j} \left(\frac{\sum_{k \neq a} X_k G_{ka',ia'} \tau_{ka',ia'}}{\sum_{k \neq a} X_k G_{ka',ia'}} \right) \right] + \\ & \sum_{c'} X_{c'} \left[\sum_{i \neq c} \frac{X_i}{\sum_{i \neq c} X_j} \left(\frac{\sum_{k \neq c} X_k G_{kc',ic'} \tau_{kc',ic'}}{\sum_{k \neq c} X_k G_{kc',ic'}} \right) \right] + \\ & \sum_{m'} X_{m'} \left[\left(\frac{\sum_k X_k G_{km',m'm'} \tau_{km',m'm'}}{\sum_k X_k G_{km',m'm'}} \right) - \right. \\ & \left. \left(\sum_k X_k \tau_{km',m'm'} \right) \right] \end{aligned} \quad (A.33)$$

And activity coefficients are given as following [61]:

$$Ln\gamma_i = \frac{\partial (n_i \frac{g^E}{RT})}{\partial n_i} \quad (A.34)$$

$$Ln\gamma_i = (Ln\gamma_i^*)_{LR} + (Ln\gamma_i^*)_{SR} \quad (A.35)$$

$$(Ln\gamma_i^*)_{LR} = -A_\phi \left(\frac{1000}{M_S} \right)^{0.5} \left[\left(\frac{2z_e^2}{\rho} \right) Ln(1 + \rho I_x^{0.5}) + \frac{z_e^2 I_x^{0.5} - 2I_x^{1.5}}{1 + \rho I_x^{0.5}} \right] \quad (A.36)$$

$$(Ln\gamma_i^*)_{LR} = -A_\phi \left(\frac{1000}{M_S} \right)^{0.5} \frac{2I_x^{1.5}}{1 + \rho I_x^{0.5}} \quad (A.37)$$

$$(Ln\gamma_i^*)_{SR} = (Ln\gamma_i)_{SR} + (Ln\gamma_i^\infty)_{SR} \quad (A.38)$$

$$(Ln\gamma_i^\infty)_{SR} = Z_i (G_{im,mm} - 1) \tau_{im,mm} \quad (A.39)$$

$$\begin{aligned} \tau_{ij,kj} = & (\lambda_{ij})_0 + (\lambda_{ij})_0 \left(\frac{1}{T} = \frac{1}{298.15} \right) + \\ & (\lambda_{ij})_2 \left(\frac{298.15-T}{T} + Ln \frac{T}{298.15} \right) \end{aligned} \quad (A.40)$$

COPYRIGHTS

©2023 The author(s). This is an open access article distributed under the terms of the Creative Commons Attribution (CC BY 4.0), which permits unrestricted use, distribution, and reproduction in any medium, as long as the original authors and source are cited. No permission is required from the authors or the publishers.

**Persian Abstract****چکیده**

پسماند فیلترکیک روی حاوی فلزات ارزشمندی است که می‌توان از آنها به عنوان منبعی برای به دست آوردن این فلزات استفاده مجدد کرد. این مطالعه یک مطالعه تجربی دو مرحله‌ای استخراج روی و نیکل از فیلترکیک روی را توصیف می‌کند که شامل لیچینگ فیلترکیک روی و سپس استخراج فلزات به کمک فاز آبی از محلول لیچینگ است. برای تعیین شرایط بهینه لیچینگ، یک مطالعه جامع از بازیابی عناصر شیمیایی از فیلتر کیک مصرف شده به صورت تجربی در سطوح مختلف غلظت اسید در ماهای مختلف در حالی که غلظت عناصر شیمیایی با زمان اندازه‌گیری شد، مورد مطالعه قرار گرفت. نتایج تجربی نشان داد که ۹۹ درصد از سرب در شرایط بهینه دومولار نیتریک اسید، زمان $t=1.5\text{ h}$ ، دمای $T=358.15\text{ K}$ و $\text{S/L}=10/1$ قابل دستیابی هستند. سپس استخراج نیکل روی و سرب توسط استخراج کننده دی-(۲)-اتیل هگزیل (D2EHPA) به همراه رقیق کننده کروزن بررسی گردید. pH و غلظت استخراج کننده به عنوان متغیرهای موثر بر استخراج در نظر گرفته شدند. نتایج نشان داد افزایش pH و غلظت استخراج کننده تاثیر چشم گیری در استخراج نیکل و روی دارد و در شرایط بهینه $5.5 = \text{D2EHPA}, \text{pH} = 5.5, (\text{O/A}) = 25\text{ v/v\%}$ و $90\text{ درصد از روی و نیکل استخراج شدند}$. برای مدل‌سازی غلظت‌های تعادل در فازهای آبی و آبی و محاسبه ضرایب فعالیت، از مدل‌های ترکیب موضعی مبتنی بر NRTL-based local composition models NRTL، UNIQUAC-NRF، Electrolyte-UNIQUAC-NRF استفاده شد. پس از آن، پارامترهای تنظیم شده با موافقیت برای محاسبه ثابت تعادل پارامترهای مجھول و واکنش استخراج استفاده شد. نتایج بدست آمده از مدل‌سازی ترمودینامیکی با داده‌های تجربی مطابقت خوبی داشت.



A Multiple Kernel Learning Based Model with Clustered Features for Cancer Stage Detection using Gene Datasets

A. Mohammadjani, F. Zamani*

Department of Electrical and Computer Engineering, Nooshirvani University of Technology, Babol, Iran

PAPER INFO

ABSTRACT

Paper history:

Received 06 June 2023

Received in revised form 06 August 2023

Accepted 07 August 2023

Keywords:

Machine Learning

Multiple Kernel Learning

Bioinformatics

Cancer Stage

Dimension Reduction

The Cancer Genome Atlas(TCGA)

Genomic data is used in various fields of medicine including diagnosis, prediction, and treatment of diseases. Stage detection of cancer progression is crucial for treating patients because the mortality rate of cancer is higher when it is diagnosed in the late stages. Furthermore, the type of treatment varies depending on the cancer stage. This paper presents a Multiple Kernel Learning based algorithm to predict the stage of cancer using genomic data. Because of the high dimension of genomic data, the curse of dimensionality may degrade the stage prediction. To reduce the dimension, features are clustered first in the proposed algorithm. Then, the original data samples are clustered into smaller subsets with reduced dimensions based on the computed feature clusters. Afterward, for each subset, a kernel matrix is calculated. The kernel matrices are weighted and then combined linearly. Finally, a cancer stage prediction model is trained using the combined kernel matrix and Support Vector Machine. The proposed algorithm is compared with the baseline methods. The classification accuracy of the proposed method outperforms the other methods in 13 cancer groups of 15 from the cancer genome atlas program (TCGA) dataset.

doi: 10.5829/ije.2023.36.11b.08

1. INTRODUCTION

The increasing generation of genomic data and the need to store, retrieve, and properly analyze them led to the emergence of bioinformatics. Bioinformatics deals with mathematical and computational aspects to understand and process biological data. In other words, the aim of bioinformatics is to increase understanding of biological processes through the use of computational techniques [1].

With the significant growth of biological data generation, they play important role in analyzing and resolving problems in medicine such as cancer diagnosis and treatment [2]. Before the advent of machine learning methods, bioinformatics algorithms were written manually, which made them difficult to be used in applications such as protein structure prediction [3]. Today, machine learning tools and methods are widely used in bioinformatics applications [4].

This paper proposes a machine learning based algorithm to predict the stage of cancer using genomic data. Diagnosing the stage of cancer progression is critical because the mortality rate of cancer is high in its late stages. Furthermore, the type of treatment is different at different stages.

Different types of genomic data are available. The genomic data used in this paper is gene expression, which is commonly used in bioinformatics applications such as cancer diagnosis, treatment, survival, and stage detection.

In this paper, the problem of detecting the stage of cancer progress is considered as a classification problem. The results of machine learning algorithms such as support vector machine, Random Forest, and Multiple Kernel Learning in genomic data classification problems are satisfying. In this paper, we proposed a Feature Clustering Multiple Kernel Learning (FCMKL) algorithm to detect the cancer stage of patients.

*Corresponding Author Institutional Email: [\(F. Zamani\)](mailto:zamani@nit.ac.ir)

The dimension of gene expression data is very high, such that may influence the performance of classification algorithms due to the curse of dimensionality. Curse of dimensionality problem is addressed by dimension reduction. Principle Component Analysis is a widely used method to reduce the dimension of data.

To reduce the gene expression dimension, a novel method is employed in this paper. To this end, the features are clustered first, then data is divided into groups such that in each group, data is represented by the corresponding feature cluster. It is worth noting that the number of clusters and the number of data groups is equal. Finally, in their new representation, data are combined with a Multiple Kernel Learning classifier in order to determine the stage of cancer progression.

The key contributions of the proposed algorithm, Feature Clustering Multiple Kernel Learning (FCMKL), are as follows:

- The genomic data used for cancer stage detection, which is the main focus of this paper, is gene expression. The dimension of gene expression data is high. To avoid the curse of the dimensionality problem, the features are clustered into smaller groups. By grouping features, the classifier does not suffer from the curse of the dimensionality problem because of the reduced dimension of data. Also, this method does not change or remove features.
- For each data group, a kernel matrix is calculated. Then a weighted linear combination of kernel matrices is computed in a Multiple Kernel Learning framework which is used to detect the cancer stage of the patient.
- This paper combines clustering and classification algorithms together to predict the cancer stage of patients.

A block diagram of the proposed method is depicted in Figure 1.

This paper is organized as follows. In the second section, related works are reviewed. The third section explains the proposed algorithm in detail. In section four, the experiment results of the proposed algorithm are demonstrated and discussed. The last section concludes the paper.

2. RELATED WORKS

This section reviews some works related to machine learning based cancer diagnosis and treatment including cancer stage detection.

An integrated model based on logistic regression and support vector machine for the classification of Colorectal Cancer (CRC) into cancerous and normal samples was proposed by Zhao et al. [5].

The method proposed by Bhalla et al. [6] identifies genes to detect the progress of renal cell cancer. For this

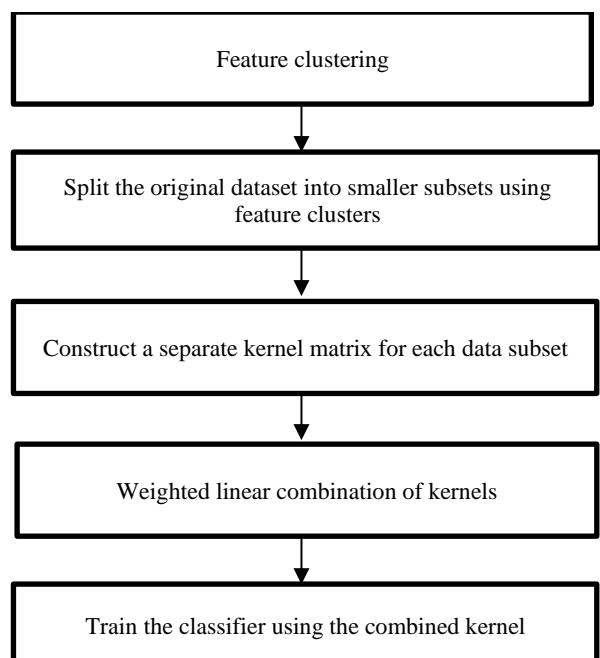


Figure 1. The block diagram of the proposed method

purpose, gene expression data from the KIRC cancer group of TCGA dataset is used. This method is based on the fact that there are only a few genes that are important to determine the stage of cancer. In this method, a threshold value is selected for each gene such that determines whether the desired sample is in an early stage or a late one according to the expression of that gene. Finally, the selected genes were fed to the support vector machine.

Huo et al. [7] used the gene expression data for tumor classification based on the sparsity characteristics of genes. To this end, related genes are selected via the sparse group lasso method. Then, tumors are classified by a support vector machine. Ranjani Rani and Ramyachitra [8] proposed a similar framework for cancer classification. They employed the Spider Monkey Optimization algorithm to select related genes.

After detecting differentially expressed genes, in the framework proposed by Xu et al. [9], a Protein Preotein Interaction (PPI) network based neighborhood scoring technique was used in combination with Support Vector Machine for colon cancer diagnosis and recurrence prediction.

Medjahed et al. [10] employed Support Vector Machine in two phases to select the best gene set of DNA microarray for cancer diagnosis task. A two-stage feature selection method based on Multiple Kernel Learning method was proposed by Du et al. [11] to predict cancer. In the first step of the proposed method, relevant features are identified by Multiple Kernel Learning. In the second step, a subset of features from the set of candidate features obtained in the first step is specified.

Data fusion based on Multiple Kernel Learning is proposed by Speicher and Pfeifer [12] to identify cancer subtypes. In order to reduce the dimension of gene data, the proposed method was combined with a graph embedding framework.

A model based on the combination of clustering and Multiple Kernel Learning framework was proposed by Speicher and Pfeifer [13] to identify cancer subtypes. In the proposed model, the features are clustered based on the combination of several kernels, then the effect of each feature cluster on a patient cluster is measured.

The proposed method by Tao et al. [14] deals with the classification of five subtypes of breast cancer based on Multiple Kernel Learning. The data used in this research are gene expression, DNA methylation, and copy number variation from the TCGA dataset. Some genes may have little or no effect on the classification of breast cancer subtypes, which should be identified. For this purpose, the p-values of genes were calculated using the Wilcoxon rank sum. The Benjamini-Hochberg false discovery rate is then determined to adjust the computed p-values. Genes with p-value less than 0.05 are selected as significant genes.

Four types of genomic data in addition to pathological images were used by Sun et al. [15] to predict the survival of breast cancer patients. In the proposed method, Multiple Kernel Learning is employed to integrate different data types.

To predict the survival of patients with squamous cell lung cancer who underwent surgery, a new method based on Multiple Kernel Learning is proposed by Zhang et al. [16]. Due to the small number of samples, to deal with the problem of the curse of dimensionality, a linear correlation algorithm is employed to select the optimal features.

Multiple Kernel Learning was used by Wilson et al. [17] to determine the best kernels calculated from two types of data, including clinical data and microRNA from the TCGA dataset. The goal is to predict whether a patient with ovarian cancer would live more than three years after diagnosis or not.

A method to determine the cancer stage using Multiple Kernel Learning was proposed by Rahimi and Gönen [18]. In this paper, instead of identifying clusters of gene expression features and computing kernel matrices, it was proposed to combine these two steps into a single model using prior knowledge about pathways and sets of genes. For this purpose, they create a separate kernel matrix for each gene set, then combine them using a Multiple Kernel Learning algorithm.

A set of pathways/genes along with gene data were used by Rahimi and Gönen [19] to detect the cancer stage. Different types of cancers with distinct biological mechanisms, have similarities. In this paper, each cancer group is considered as a specific task. A multi-task learning formula is used in which different tasks are

being trained simultaneously. In fact, the goal is to identify similarities between cancer groups (i.e., tasks) in terms of their basic mechanisms. Joint clustering is used for this purpose.

Deep learning based methods generally have very high accuracy in data classification. Zohrevand et al. [20] introduced Convolutional Neural Network, which is a powerful deep learning approach, that was employed to Finger-Knuckle-Print recognition. A Fully Convolutional Network in combination with the graph's shortest layer path has been used for fluid segmentation in retina images [21]. Also, a fully automated model was trained by Azimi et al. [22] for fluid segmentation. In this two-path method, the first and last layers of the retina are segmented in the Neutrosophic domain. Then, a Fully Convolutional Network is used for fluid segmentation. Assigning appropriate values for parameters is very important in machine learning based methods. Chegeni et al. [23] proposed a mathematical model to compute the Convolutional Neural Network model parameters automatically. Deep learning based methods suffer from high computational complexity in the training phase and a large number of parameters including weights. To address the mentioned problems a compact version of the Convolutional Neural Network which is called SqueezeNet is employed for document classification while its classification results were comparable to Convolutional Neural Network [24].

Salimy et al. [25] proposed a deep learning framework to predict the survival of colon cancer patients. This method integrates three types of genomic data including gene expression, DNA methylation, and clinical data by autoencoder. Slimene et al. [26] used microRNA for cancer classification. After converting the microRNA data into images, ResNet, which is a pretrained Deep Neural Network is employed to classify data.

3. PROPOSED FCMKL

This paper focuses on diagnosing the early and late cancer stages by using a gene expression data set. Cancer stage detection is considered as a binary classification problem. In the problems like cancer stage detection in which data samples are usually not separable, the use of the kernel function, which implicitly maps data to a high dimension space, improves the classification accuracy (Figure 2a).

The dimension of data samples in the gene expression dataset is very high, which degrades the performance of cancer stage classification due to the curse of dimensionality. To address this problem, it is necessary to reduce the data dimension (Figure 2b).

In order to reduce the data dimension, features are clustered in the first step of the proposed method. The

idea is to compute a separate kernel for each cluster of features. After reducing the feature dimension, a Multiple Kernel Learning classifier is trained to classify cancer stages by using the computed kernels (Figure 2c).

Figure 2 illustrates three different ways to compute kernel matrix for high dimension Gene Expression data. (a) In this case, a kernel function is used to compute kernel matrix simply. Since the dimension of Gene Expression Data is high, cure of dimensionality problem will reduce classification accuracy in this method. (b) To address the curse of dimensionality problem, it is recommended to reduce the dimension of data by employing dimension reduction algorithms like PCA before computing kernel. (c) Another approach to reduce the dimension of Gene Expression Data, is to cluster features. This method, which is used in this paper, does not change or remove features.

Suppose the dataset contains N data samples and the feature dimension of each data sample is d . The features are clustered into c clusters. Therefore, each cluster contains N data samples which are d/c dimensional. For each d/c -dimensional cluster, a separate $N \times N$ kernel is computed.

The ratio of the number of features to the number of samples is determinanat in the classification performance. It should be noted that for a fixed sample size, if the number of features grows, the classification error will decrease first and then will increase [27]. In the case that the features are independent, its enough that the number of features does not exceed $N-1$. As the feature correlation increases, this number decreases such that if the correlation is very high, this number decreases to \sqrt{N} which is used as the number of clusters in the proposed method [27].

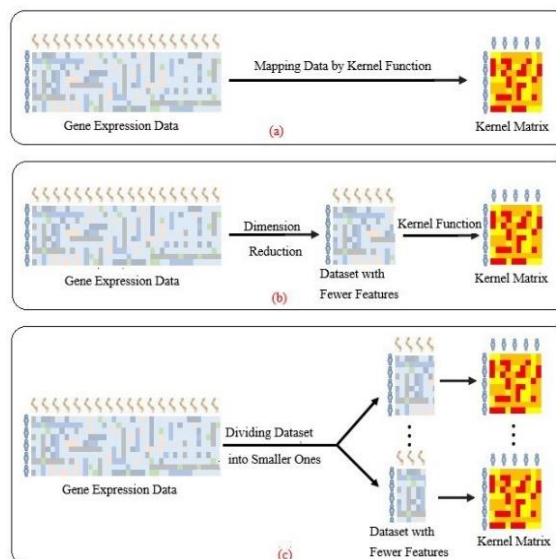


Figure 2. Kernel matrix for high dimension Gene Expression data

The architecture of FCMKL is illustrated in Figure 3. In the following sections, the training and testing phases are explained in detail.

Figure 3 illustrates the architecture of FCMKL. First, the dataset is divided into training and testing sets. In the training phase, the features of the training data are clustered. Then, a kernel matrix is computed for each *feature* cluster. A single kernel is obtained by weighted linear combination of computed kernels. Then, the kernel based Support Vector Machine is trained. In the testing phase, after calculating the kernel corresponding to the testing data based on the feature clusters detected in the training phase, the testing data are classified by the trained support vector machine.

3.1. Training Phase Following are the main steps of the FCMKL algorithm.

Step 1: Feature clustering

As described before, to address the curse of dimensionality problem in the proposed algorithm, the original data set is divided into smaller ones. To this end, the features are clustered by the k-means clustering algorithm. More precisely, the rows (samples) and columns (features) of the data set are interchanged and given as input to the kmeans algorithm. Kmeans algorithm clusters features based on samples, the output of which is feature clusters.

Step 2: Split the dataset into smaller datasets based on feature clusters

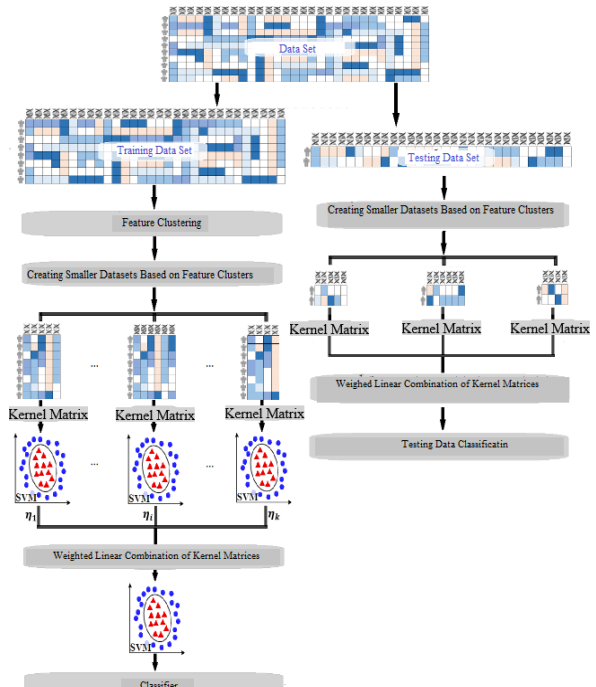


Figure 3. FCMKL architecture

By using the feature clusters obtained in the previous step, the dataset is divided into smaller subsets such that each subset uses one feature cluster. In each small subset, the rows are samples of the original dataset and the columns are the features in the corresponding cluster. In this way, there will be data subsets that have N samples with different features.

Step 3: Computing the kernel matrix for each data subset
 Each data subset is implicitly mapped to a high-dimensional feature space by using a separate kernel function. Eventually, for each data subset, an $N \times N$ kernel matrix is computed based on the corresponding kernel function.

Step 4: Kernel weighting

Before combining kernels calculated in the previous step, we should weight them. To this end, the AUC classification accuracy of each kernel based on Support Vector Machine is computed. Then, weights are assigned to the each kernel by using Equation (1).

$$\eta_i = \frac{(AUC_i)^2}{\sum_{j=1}^P (AUC_j)^2} \quad (1)$$

where η_i is the weight of the i^{th} kernel, P is the number of kernels and AUC_i is the result of predicting the cancer stage by using i^{th} kernel.

Step 5: Weighted linear combination of kernel matrices
 In this step, the kernels are linearly combined based on the weights calculated in the previous step. Then the kernel matrices are combined according to Equation (2) and a single kernel matrix is created.

$$k_s(x_i, x_j) = \sum_{l=1}^P \eta_l k_l(x_i, x_j) \quad (2)$$

where $k_l(x_i, x_j)$ is the l^{th} kernel matrix and $k_s(x_i, x_j)$ is the combined kernel matrix.

Step 6: Training kernel-based support vector machine
 Finally, by using the combined kernel matrix, a kernel based Support Vector Machine is trained.

3. 2. Testing Phase The proposed method is evaluated by measuring the testing data classification accuracy. The main steps of the testing phase are as follows:

Step 1: Split the testing dataset into smaller datasets based on feature clusters

In first step, using the feature clusters obtained in the training phase, the testing set is divided into smaller subsets.

Step 2: Constructing training-testing kernel matrices
 The kernel matrices of training-testing data are calculated in this step using training and testing subsets.

Step 3: Weighted linear combination of training-testing kernel matrices

The training-testing kernels computed in the previous step are combined using the weights calculated in the training phase by Equation (2).

Step 4: Classification of testing data using kernel-based Support Vector Machine

Finally, by using the combined training-testing kernel matrix, testing data are classified by trained Support Vector Machine.

4. EXPERIMENTAL RESULTS

In this section, some experiments have been conducted to evaluate the performance of the proposed algorithm using the TCGA dataset. Then, the proposed method is compared with some baseline methods.

4. 1. TCGA Dataset

In the experiments, several groups of cancers available in the TCGA dataset were used to detect the cancer stage. In this dataset, gene expression values of cancer patients, which includes more than 10,000 tumors, are available. In the experiments, HTSeq-FPKM records including primary tumors have been downloaded and used for each disease group.

The TCGA database includes clinical annotations for cancer patients. One of the annotated items, is the degree of cancer progression, which is a number between 1 and 4 for each patient.

Due to the fact that it is clinically significant to distinguish between early and late stages of cancer, in this paper, primary tumors annotated with stage 1 are considered as early stage and the remaining tumors annotated with stages 2, 3, and 4 are considered as late. Disease group information used in this paper is summarized in Table 1.

4. 2. Experiment Settings

For each cancer group, 80% of tumors were selected as training data and the remaining 20% as testing data. The data was divided in such a way that the proportion of positive and negative classes in the training and testing sets is almost equal.

The range of gene expression value is large. After adding a fixed value, the gene expression values have been converted to a more limited range using log 2. The training set was normalized to have zero mean and standard deviation of one, and then the testing set was as well.

The efficiency of the proposed algorithm is compared with Support Vector Machine, Random Forest, combination of PCA and Support Vector Machine, Deep Neural Network and also Multiple Kernel Learning using Hallmark gene dataset which includes 50 gene sets [18]. It was extracted from some molecular databases. Each gene set contains information about a specific biological state or a biological process. Rahimi and Gönen [19] divided the gene expression dataset into 50 smaller ones based on the features available in the Hallmark gene set.

TABLE 1. Summary of 15 cancer groups in the TCGA dataset

Cancer Group	RF	SVM	PCA+SVM	DNN	MKL[H]	FCMKL
BRCA	0.55	0.62	0.64	0.64	0.63	0.65
COAD	0.58	0.65	0.66	0.67	0.68	0.71
ESCA	0.74	0.67	0.69	0.67	0.71	0.81
HNSC	0.53	0.67	0.67	0.67	0.69	0.79
KICH	0.69	0.66	0.69	0.69	0.65	0.86
KIRC	0.76	0.75	0.75	0.78	0.75	0.77
KIRP	0.79	0.78	0.79	0.77	0.80	0.81
LIHC	0.67	0.65	0.65	0.65	0.65	0.68
LUAD	0.63	0.62	0.62	0.58	0.62	0.64
LUSC	0.63	0.62	0.62	0.64	0.62	0.65
PAAD	0.67	0.69	0.71	0.68	0.74	0.80
READ	0.64	0.55	0.61	0.53	0.63	0.72
STAD	0.71	0.72	0.70	0.67	0.69	0.76
TGCT	0.73	0.76	0.75	0.68	0.72	0.82
THCA	0.68	0.67	0.68	0.72	0.68	0.70
MEAN	0.67	0.67	0.68	0.67	0.68	0.74

To implement random forest, the randomForestSRC package was used [28]. The number of trees for this algorithm was selected from the set {500, 1000, 1500, 2000, 2500} using 4-fold cross validation.

The code shared by Ma et al. [29] was also used to implement the deep neural network.

To implement Support Vector Machine and Multiple Kernel Learning using Hallmark gene set, code shared by Rahimi and Gönen [18] was used and the MOSEK package is used to solve the quadratic optimization problems¹.

To compute kernel matrices, Gaussian kernel function was used:

$$k(x_i, x_j) = \exp\left(-\frac{(x_i - x_j)^T(x_i - x_j)}{2\sigma^2}\right) \quad (3)$$

such that σ , the kernel width parameter, was set to the average euclidean distance between all pairs of training data.

In the proposed algorithm, the regularization parameter C was set to 1. Moreover, as discussed in section 3, since genomic data have a very high correlation [18, 19], the number of clusters should be equal to the ratio of the number of features in the dataset to the square root of the number of training data samples [27]. In this way, the features are clustered in such a way that the average number of features in each feature cluster is equal to the square root of the number of training data samples as proposed by Zhang et al. [16].

To compare classification performance of the mentioned algorithms, the evaluation measurement AUC (area under the ROC curve) has been calculated.

To achieve more reliable results, all the experiments were repeated 100 times, and the average of the AUC values were reported (Table 2).

Also, the results of the experiments are illustrated and compared in Figure 4. As Figure 4 shows, the average performance of the algorithms in all datasets is better than random case (in which AUC equal to 0.5). Therefore, the gene expression dataset has significant information about the stages of cancers.

By comparing the classification accuracy of PCA+SVM algorithm with SVM, it is observed that PCA+SVM achieved better results in 8 of 15 cancer groups, while SVM was better in only two groups. The greatest performance improvement of PCA+SVM was in READ cancer group (6%), and the greatest performance reduction was in STAD cancer group (2%).

By comparing the classification accuracy of FCMKL algorithm with RF, it is observed that FCMKL achieved better results in all 15 cancer groups. Performance improvement was significantly better in all groups. For example, compared to RF, FCMKL has improved the classification performance of BRCA by 10%, HNSC by 26%, KICH by 17%, PAAD and COAD by 13%, READ by 8%, STAD by 5%, and TGCT by 9%.

By comparing the classification accuracy of FCMKL algorithm with SVM, it is observed that FCMKL has

¹ <https://www.mosek.com/>

TABLE 2. Average of AUC values of Random Forest (RF), Support Vector Machine (SVM), Multiple Kernel Learning using Hallmark dataset (MKL[H]), combination of PCA and SVM (PCA+SVM), Deep Neural Network (DNN) and proposed algorithm (FCMKL) on 15 cancer groups from the TCGA dataset

Cancer Group	Cancer Name	Early Stage	Late Stage	Total
BRCA	Adrenocortical carcinoma	202	995	1197
COAD	Colon adenocarcinoma	85	422	507
ESCA	Esophageal carcinoma	21	130	151
HNSC	Head and neck squamous carcinoma	27	450	477
KICH	Kidney chromophobe	29	60	89
KIRC	Kidney renal clear cell carcinoma	297	311	608
KIRP	Kidney renal papillary cell carcinoma	187	105	292
LIHC	Liver hepatocellular carcinoma	191	201	392
LUAD	Lung adenocarcinoma	324	261	585
LUSC	Lung squamous cell carcinoma	271	276	547
PAAD	Pancreatic adenocarcinoma	21	158	179
READ	Rectum adenocarcinoma	34	132	166
STAD	Stomach adenocarcinoma	59	324	383
TGCT	Testicular germ cell tumors	56	26	82
THCA	Thyroid carcinoma	321	245	566

obtained better results in all 15 cancer groups. Performance improvements in some groups have been remarkable. Compared to SVM, FCMKL has improved the classification performance of ESCA by 14%, HNSC by 12%, KICH by 20%, PAAD by 11%, READ by 17%, COAD and TGCT by 6%.

By comparing the classification accuracy of FCMKL algorithm with PCA+SVM, it is observed that FCMKL has obtained better results in all 15 groups. Compared to PCA+SVM, FCMKL has improved the classification performance of ESCA and HNSC by 12%, KICH by 17%, PAAD by 9%, READ by 11%, TGCT by 7%, and STAD by 6%.

By comparing the classification accuracy of FCMKL algorithm with DNN, it is observed that FCMKL has obtained better results in 13 of 15 data sets, while DNN was better in only two data sets. The greatest performance improvement of FCMKL was 19%, in READ cancer group and the greatest performance reduction was 2% in THCA cancer group.

By comparing the classification performance of FCMKL algorithm with Multiple Kernel Learning using Hallmark dataset [18], it is observed that FCMKL has obtained better results in all 15 groups. The performance

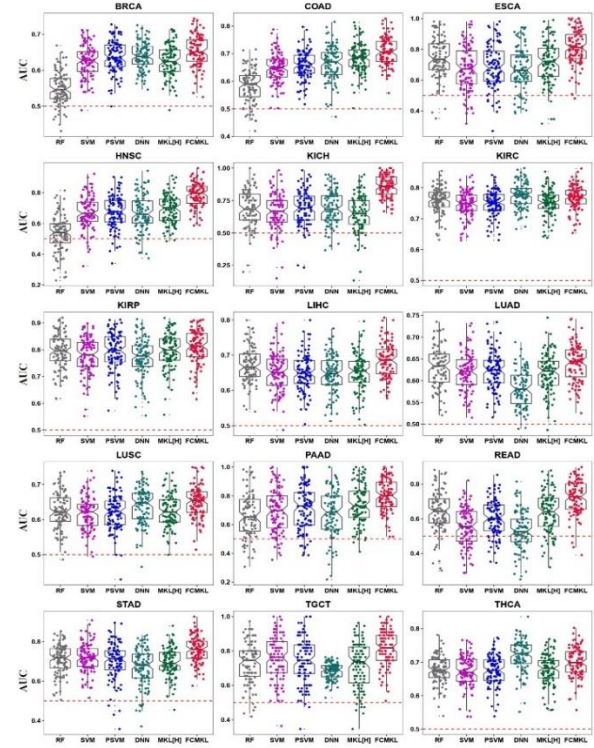


Figure 4. Performance comparison of Random Forest (RF), Support Vector Machine (SVM), Multiple Kernel Learning using Hallmark dataset (MKL[H]), combination of PCA and SVM (PCA+SVM), Deep Neural Network (DNN) and proposed algorithm (FCMKL) on 15 cancer groups from TCGA dataset. The box and dot plots compare the averages AUC values. Orange dashed lines indicate baseline performance level ($AUC = 0.5$).

improvement on some datasets has been significantly better. Compared to Rahimi and Gönen's work [18], FCMKL improved the classification performance of HNSC and ESCA by 10%, KICH by 21%, READ by 9% and STAD by 7%, TGCT by 10% and PAAD by 6%.

Table 3 shows the number of clusters computed in the FCMKL algorithm for each cancer group.

Figure 5 shows the number of cluster members in the proposed algorithm for 15 cancer groups. The dot chart and the violin chart display the range, mean and distribution of the number of cluster members. Each black dot represents a cluster. The red dot indicates the average number of cluster members for each cancer group. The largest cluster has 234 members and the smallest one has one member. Considering that the total number of features is more than 19,000, the distribution of features in the clusters seems to be appropriate.

The computed weights for each kernel in the FCMKL algorithm for 15 cancer groups are shown in Figure 6. Violin and box plots represent the range, mean, and weight distribution of kernels. Since the maximum weight assigned to the kernels is equal to 0.0026, we can

TABLE 3. The number of clusters computed in the FCMKL algorithm for each cancer group

Cancer Group	Cluster Number
THCA	921
TGCT	2393
STAD	1120
READ	1680
PAAD	1624
LUSC	937
LUAD	906
LIHC	1104
KIRP	1281
KIRC	890
KICH	2286
HNSC	1004
ESCA	1785
COAD	973
BRCA	635

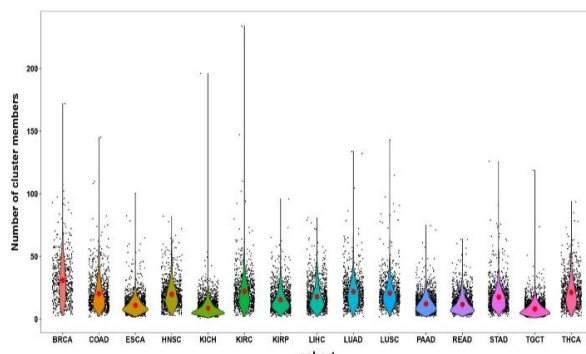


Figure 5. The number of cluster members in the FCMKL algorithm for each cancer group is shown in this figure. The black dots represent the clusters and the red dots represent the average number of cluster members in each group. The violin diagram shows the range and distribution of the clusters in terms of the number of their members

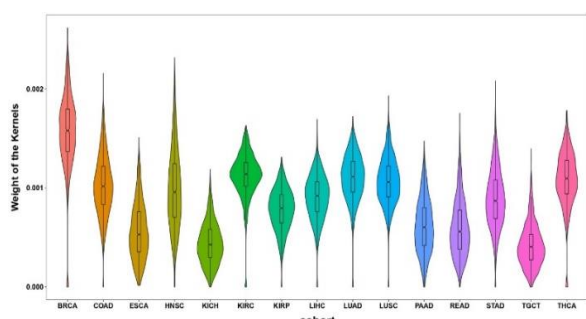


Figure 6. Computed weights for each kernel in the FCMKL algorithm for each cancer group are shown in this figure. Violin diagram and box diagram show the range, mean and weight distribution of kernels

conclude the majority of kernels are effective in classification. The maximum number of zero kernel weights in a cancer group is 20.

The proposed algorithm is implemented by R language. The experiments are conducted on a Windows 10 system, which contains a core i7 CPU with 8 cores and 16GB RAM. The training time of the proposed algorithm varies between 15 minutes to one hour and 10 minutes for different cancer groups.

5. CONCLUSION

Genomic data are useful in many medical applications including disease diagnosis, prevention and treatment. Cancer is one of the most dangerous and life-threatening diseases in the world and is considered as one of the most important causes of death. It is vital to detect the stage of cancer in a patient because if the disease is detected at an early stage, it will be curable. Also, the type of treatment is different in different stages of the disease.

In this paper, an algorithm, FCMKL, is proposed to improve cancer stage detection using feature clustering based Multiple Kernel Learning. Due to the fact that genomic data have a very high dimension, we are facing the problem of the curse of dimensionality. To address this problem, the features of the original dataset are first clustered based on samples. Then, using feature clusters, the original dataset which has a high dimension is divided into smaller datasets in terms of the number of features. For each of these smaller data sets, a kernel matrix is computed. The kernel matrices are weighted and linearly combined. Finally, using the resulting kernel matrix, the Support Vector Machine is trained to determine the cancer stage. The experiments indicate promising performance of the proposed algorithm.

Employing another clustering algorithms may result in reducing the number of clusters. By reducing the number of clusters, the computation time will decrease. Also, there are another genomic data type like microRNA and DNA methylation which we did not used in our proposed method. By using multimodal data, the classification accuracy will increase.

6. REFERENCES

1. Chicco, D., "Ten quick tips for machine learning in computational biology", *BioData Mining*, Vol. 10, No. 1, (2017), 35. doi: 10.1186/s13040-017-0155-3.
2. Yang, Y., Gao, J., Wang, J., Heffernan, R., Hanson, J., Paliwal, K. and Zhou, Y., "Sixty-five years of the long march in protein secondary structure prediction: The final stretch?", *Briefings in Bioinformatics*, Vol. 19, No. 3, (2018), 482-494. doi: 10.1093/bib/bbw129.
3. Larrañaga, P., Calvo, B., Santana, R., Bielza, C., Galdiano, J., Inza, I., Lozano, J.A., Armananzas, R., Santafé, G. and Pérez, A.,

- "Machine learning in bioinformatics", *Briefings in Bioinformatics*, Vol. 7, No. 1, (2006), 86-112. doi: 10.1093/bib/bbk007.
4. Wang, J.T., Zaki, M.J., Toivonen, H.T. and Shasha, D., Introduction to data mining in bioinformatics, in Data mining in bioinformatics. 2005, Springer.3-8.
 5. Zhao, D., Liu, H., Zheng, Y., He, Y., Lu, D. and Lyu, C., "A reliable method for colorectal cancer prediction based on feature selection and support vector machine", *Medical & Biological Engineering & Computing*, Vol. 57, (2019), 901-912. doi: 10.1007/s11517-018-1930-0.
 6. Bhalla, S., Chaudhary, K., Kumar, R., Sehgal, M., Kaur, H., Sharma, S. and Raghava, G.P., "Gene expression-based biomarkers for discriminating early and late stage of clear cell renal cancer", *Scientific Reports*, Vol. 7, No. 1, (2017), 44997. doi: 10.1038/srep44997.
 7. Huo, Y., Xin, L., Kang, C., Wang, M., Ma, Q. and Yu, B., "Sgl-svm: A novel method for tumor classification via support vector machine with sparse group lasso", *Journal of Theoretical Biology*, Vol. 486, (2020), 110098. doi: j.jtbi.2019.110098.
 8. Rani, R.R. and Ramyachitra, D., "Microarray cancer gene feature selection using spider monkey optimization algorithm and cancer classification using svm", *Procedia Computer Science*, Vol. 143, (2018), 108-116. doi: 10.1016/j.procs.2018.10.358.
 9. Xu, G., Zhang, M., Zhu, H. and Xu, J., "A 15-gene signature for prediction of colon cancer recurrence and prognosis based on svm", *Gene*, Vol. 604, (2017), 33-40. doi: 10.1016/j.gene.2016.12.016.
 10. Medjahed, S.A., Saadi, T.A., Benyettou, A. and Ouali, M., "Kernel-based learning and feature selection analysis for cancer diagnosis", *Applied Soft Computing*, Vol. 51, (2017), 39-48. doi: 10.1016/j.asoc.2016.12.010.
 11. Du, W., Cao, Z., Song, T., Li, Y. and Liang, Y., "A feature selection method based on multiple kernel learning with expression profiles of different types", *BioData mining*, Vol. 10, No. 1, (2017), 1-16. doi: 10.1186/s13040-017-0124-x.
 12. Speicher, N.K. and Pfeifer, N., "Integrating different data types by regularized unsupervised multiple kernel learning with application to cancer subtype discovery", *Bioinformatics*, Vol. 31, No. 12, (2015), i268-i275. doi: 10.1093/bioinformatics/btv244.
 13. Speicher, N.K. and Pfeifer, N., "An interpretable multiple kernel learning approach for the discovery of integrative cancer subtypes", arXiv preprint arXiv:1811.08102, (2018). doi: 10.48550/arXiv.1811.08102.
 14. Tao, M., Song, T., Du, W., Han, S., Zuo, C., Li, Y., Wang, Y. and Yang, Z., "Classifying breast cancer subtypes using multiple kernel learning based on omics data", *Genes*, Vol. 10, No. 3, (2019), 200. doi: 10.3390/genes10030200.
 15. Sun, D., Li, A., Tang, B. and Wang, M., "Integrating genomic data and pathological images to effectively predict breast cancer clinical outcome", *Computer Methods and Programs in Biomedicine*, Vol. 161, (2018), 45-53. doi: 10.1016/j.cmpb.2018.04.008.
 16. Zhang, A., Li, A., He, J. and Wang, M., "Lscdfs-mkl: A multiple kernel based method for lung squamous cell carcinomas disease-free survival prediction with pathological and genomic data", *Journal of Biomedical Informatics*, Vol. 94, (2019), 103194. doi: 10.1016/j.jbi.2019.1031.
 17. Wilson, C.M., Li, K., Yu, X., Kuan, P.-F. and Wang, X., "Multiple-kernel learning for genomic data mining and prediction", *BMC bioinformatics*, Vol. 20, (2019), 1-7. doi: 10.1186/s12859-019-2992-1.
 18. Rahimi, A. and Gönen, M., "Discriminating early-and late-stage cancers using multiple kernel learning on gene sets", *Bioinformatics*, Vol. 34, No. 13, (2018), i412-i421. doi: 10.1093/bioinformatics/bty239.
 19. Rahimi, A. and Gönen, M., "A multitask multiple kernel learning formulation for discriminating early-and late-stage cancers", *Bioinformatics*, Vol. 36, No. 12, (2020), 3766-3772. doi: 10.1093/bioinformatics/btaa168.
 20. Zohrevand, A., Imani, Z. and Ezoji, M., "Deep convolutional neural network for finger-knuckle-print recognition", *International Journal of Engineering, Transactions A:Basics*, Vol. 34, No. 7, (2021), 1684-1693. doi: 10.5829/ije.2021.34.07a.12.
 21. Azimi, B., Rashno, A. and Fadaei, S., "Fully convolutional networks for fluid segmentation in retina images", in 2020 International Conference on Machine Vision and Image Processing (MVIP), IEEE. (2020), 1-7.
 22. Azimi, B., Rashno, A. and Fadaei, S., "Two-path neutrosophic fully convolutional networks for fluid segmentation in retina images", *AUT Journal of Modeling and Simulation*, Vol. 54, No. 1, (2022), 85-104. doi: 10.22060/miscej.2022.21258.5277.
 23. Chegeni, M.K., Rashno, A. and Fadaei, S., "Convolution-layer parameters optimization in convolutional neural networks", *Knowledge-Based Systems*, Vol. 261, (2023), 110210. doi: 10.1016/j.knosys.2022.110210.
 24. Hassanpour, M. and Malek, H., "Learning document image features with squeeze-net convolutional neural network", *International Journal of Engineering, Transactions A:Basics*, Vol. 33, No. 7, (2020), 1201-1207. doi: 10.5829/ije.2020.33.07a.05.
 25. Salimy, S., Lanjanian, H., Abbasi, K., Salimi, M., Najafi, A., Tapak, L. and Masoudi-Nejad, A., "A deep learning-based framework for predicting survival-associated groups in colon cancer by integrating multi-omics and clinical data", *Helijon*, Vol. 9, No. 7, (2023). doi: 10.1016/j.helijon.2023.e17653.
 26. Slimene, I., Messaoudi, I., Oueslati, A.E. and Lachiri, Z., "Deep learning-based cancer disease classification through microRNA expression", in 2022 IEEE Information Technologies & Smart Industrial Systems (ITSIS), IEEE. (2022), 1-6.
 27. Hua, J., Xiong, Z., Lowey, J., Suh, E. and Dougherty, E.R., "Optimal number of features as a function of sample size for various classification rules", *Bioinformatics*, Vol. 21, No. 8, (2005), 1509-1515. doi: 10.1093/bioinformatics/bti171.
 28. Ishwaran, H. and Kogalur, U.B., "Fast unified random forests for survival, regression, and classification (rfsrc)", *R Package Version*, Vol. 2, No. 1, (2019).
 29. Ma, B., Meng, F., Yan, G., Yan, H., Chai, B. and Song, F., "Diagnostic classification of cancers using extreme gradient boosting algorithm and multi-omics data", *Computers in Biology and Medicine*, Vol. 121, (2020), 103761. doi: 10.1016/j.combiomed.2020.103761.

COPYRIGHTS

©2023 The author(s). This is an open access article distributed under the terms of the Creative Commons Attribution (CC BY 4.0), which permits unrestricted use, distribution, and reproduction in any medium, as long as the original authors and source are cited. No permission is required from the authors or the publishers.

**Persian Abstract****چکیده**

داده های ژنومی در زمینه های مختلف پزشکی از جمله تشخیص، پیش بینی و درمان بیماری ها استفاده می شود. تشخیص میزان پیشرفت سرطان برای درمان بیماران بسیار مهم است زیرا میزان مرگ و میر سرطان زمانی که در مراحل پایانی تشخیص داده می شود، بیشتر است. علاوه بر این، نوع درمان با توجه به میزان پیشرفت، این بیماری متفاوت است. این مقاله یک الگوریتم مبتنی بر یادگیری چند هسته‌ای برای پیش‌بینی میزان پیشرفت سرطان با استفاده از داده‌های ژنومی پیشنهاد می‌کند. به دلیل ابعاد بالای داده های ژنومی، نفرین ابعاد ممکن است دقت پیش بینی پیشرفت سرطان را کاهش دهد. برای کاهش ابعاد، در الگوریتم پیشنهادی ویژگی ها ابتدا خوشبندی می شوند. سپس، نمونه های داده اصلی به زیر مجموعه های کوچک‌تر با ابعاد کاهش یافته بر اساس خوشبندی ویژگی محاسبه شده خوشبندی می شوند. پس از آن، برای هر زیر مجموعه، یک ماتریس هسته ساخته شده به آنها وزن اختصاص داده می شود. سپس ماتریس های وزن دار به صورت خطی ترکیب می شوند. در نهایت، یک مدل پیش بینی میزان پیشرفت سرطان با استفاده از ماتریس هسته ترکیبی و ماشین بردار پشتیبان آموزش داده می شود. الگوریتم پیشنهادی با روش های پایه مقایسه شده است. دقت طبقه‌بندی روش پیشنهادی از روش های دیگر در ۱۳ گروه سرطانی از ۱۵ گروه مجموعه داده TCGA بهتر است.



An Integrated Production-distribution Problem of Perishable Items with Dynamic Pricing Consideration in a Three-echelon Supply Chain

B. Y. Yegane*

Department of Industrial Engineering, Faculty of Engineering Management, Kermanshah University of Technology, Kermanshah, Iran

PAPER INFO

ABSTRACT

Paper history:

Received 16 June 2023

Received in revised form 18 July 2023

Accepted 26 July 2023

Keywords:

Production

Distribution

Pricing

Genetic Algorithm

Perishable Goods

The importance of employing appropriate pricing strategies for perishable products within the supply chain cannot be overstated. Pricing is a cross-functional driver of each supply chain, playing an irrefutable role in the success and profitability of the supply chain alongside other factors such as inventory and production policies which has been investigated in this research. The research emphasizes the significant role of pricing in profitability, along with the interplay of production policies and inventory control, highlighting their collective influence on financial outcomes, the subject of dynamic pricing within a multi-product, multi-period problem in a three-level supply chain with perishable products has garnered relatively limited attention. The study focuses on optimizing an integrated production-distribution system with multiple producers and distribution centers serving specific customer groups. Direct shipments between production centers, distribution centers, and retailers are optimized using a vehicle routing problem approach. A mixed-integer programming model is formulated, and a genetic algorithm-based metaheuristic approach is proposed. The BARON solver was initially used to solve two simplified test problems, with results compared to a self-designed genetic algorithm implemented in C#. After confirming the efficiency and effectiveness of our genetic algorithm (GA), the investigation is further extended to encompass five distinct problems, each comprising nine sub-problems. The GA demonstrates its power and adaptability by providing high-quality solutions efficiently within a reasonable computational time.

doi: 10.5829/ije.2023.36.11b.09

1. INTRODUCTION

Effective pricing strategies play a pivotal role in the supply chain management of perishable items, including food and pharmaceuticals. Given the perishable nature of these goods, pricing decisions significantly impact various aspects of the supply chain. The right pricing approach helps optimize revenue generation while minimizing losses due to spoilage or expiration. By strategically setting prices, businesses can balance supply and demand, ensure product availability, and enhance profitability. Dynamic pricing mechanisms, tailored to factors like demand fluctuations, product freshness, market conditions, and inventory levels, enable businesses to stay competitive and maximize revenue. Moreover, pricing decisions in the supply chain of perishable items necessitate careful consideration of cost

factors, market dynamics, consumer behavior, product quality, and regulatory requirements. By implementing effective pricing strategies, businesses can mitigate risks associated with perishable items, improve waste reduction efforts, optimize inventory management, and meet consumer expectations for both quality and affordability.

The delay in product delivery to customers can lead to dissatisfaction and long-term damage to a producer's credibility, resulting in reduced supply chain competitiveness. Various factors, starting from the lowest level of the supply chain with customer needs identification, influence the rapid delivery of products. It is crucial to plan and schedule operations effectively to meet these needs. Additionally, effective inventory management plays a significant role in meeting a portion of customer demands. Moreover, an abundance of

*Corresponding Author Email: bys.yegane@gmail.com (B. Y. Yegane)

inventory intensifies supply chain reliance and heightens the vulnerability of fashion products, such as clothes, bags, and shoes, to becoming outdated. Furthermore, industries dealing with perishable items like food, drugs, or oil and gas products face the risk of inventory reduction due to product decay when increasing inventory levels. The importance of perishable items has significantly heightened in recent years, notably due to the COVID-19 pandemic, resulting in profound alterations in the supply chain policies of retail chains and restaurants [1].

Apart from having appropriate plans for efficient production of goods, adopting appropriate policies to control inventory in a way that keeps holding cost and decay rate at an acceptable level and also meets customer needs are essential. Furthermore, if there are no efficient transportation systems providing customers with products promptly then efforts and plans aimed at production and inventory control will not be effective. Thus, integration is inevitable in every supply chain for determination of production, inventory and distribution policies to achieve strategic alignment. Achieving these goals requires the utilization of appropriate and relevant technologies associated with the industry 4.0 (I4.0). I4.0 proposes an industrialization model in which humans, machines, learning algorithms, and products communicate with each other via both physical and cybernetic means [2]. The supply chain studied in this research is a forward or traditional supply chain (SC). The forward SC, also known as the traditional SC or the linear economy of take-make-waste, is a one-directional material flow beginning with raw material extraction, continuing with the process of manufacturing a product, and ending with customers disposing of the same product after use. In the opposite direction of the forward SC, products move through the reverse SC. The reverse SC includes acquisition of the used products from customers, recovering the products' residual value, and remarketing the products [3]. The forward and reverse activities of a supply chain are combined by the Closed-Loop supply chain (CLSC) network into an integrated system with the aim of improving the economic, environmental, and social criteria; In the CLSC, a manufacturer may decide to handle the return process separately [4]. For obtaining more information about the structures of traditional and closed-loop supply chains, it is advised to refer to literature [5].

Given the importance of pricing policies used as a control lever for coordination in the supply chain [6]; this study investigates a multi-product multi-period mixed-integer programming mathematical model for a three-echelon supply chain to maximize profit. In this model, product demand is dependent on price and is determined for each period. The supply chain consists of manufacturers, distribution centers, and retailers. Manufacturers have the capability to produce all products, and a distribution center may be supplied by

one or more manufacturers. Products are directly delivered from production centers to the distribution centers; while customer deliveries are managed using a vehicle routing problem. Since it is probable for customer demand for a product to exceed a vehicle's capacity, each customer may be served by multiple vehicles in this study.

The reminder of the paper is organized as follows. In section 2, the related works are reviewed in order to examine the different aspects of the research problem in terms of structure and solution methods. Then, the assumptions, notations and mathematical model are presented in section 3. Section 4 describes the framework of the genetic algorithm used to solve the problem. Computational results are provided in section 5; and finally, section 6 presents the conclusion and future research directions.

2. LITERATURE REVIEW

Modeling and solving integration problems in production, inventory, and distribution have garnered attention from researchers in recent years. This is because the integration of production and distribution not only significantly impacts the profitability of the supply chain but also enhances responsiveness to market needs. Several researchers have conducted reviews of related studies and categorized them based on different perspectives. For instance, Farahani et al. [7] have provided a comprehensive classification of integrated production-distribution models. The majority of previous studies addressing this research problem have considered the following issues:

1. Determining the quantity of regular-time and overtime production, as well as identifying the production that needs to be outsourced during each period. The inventory number of manufacturers;
2. The quantity of products delivered from manufacturer to warehouses or distribution centers;
3. The inventory of warehouses or distribution centers;
4. The quantity of backlog or lost sales on different products in each period.

Considering the complex nature of the integrated production-distribution problem and the large number of decision variables involved, researchers have often turned to heuristic or metaheuristic approaches in order to obtain efficient and effective solutions. In the following sections, we will delve into a selection of notable studies from reputable journals that have tackled this problem.

Bilgen and Günther [8], introduce a block planning approach that establishes cyclical production patterns based on setup families. The study examines two transportation modes, full truckload and less than truckload, for delivering final goods from plants to distribution centers. The proposed approach employs a

mixed-integer linear optimization model to minimize overall production and transportation costs. They utilized two distribution methods, Full Truckload (FTL) and Less than Truckload (LTL), in the distribution process and finally the results of their work were evaluated through a case study conducted in a fruit juice production factory. A mixed-integer linear model was proposed by Coccolla et al. [9] to integrate production and distribution policies into a supply chain with a number of manufacturers in multi-site network. The model addresses the problem of managing single-stage parallel-line multiproduct batch plants together with multi-echelon distribution networks transporting multiple products from factories to customers through direct shipping and/or via intermediate depots using warehousing and cross docking strategies. The supply chain of chemical materials in several European countries has been used as a case study in the article. Nasiri et al. [10] studied the integrated production-distribution problem by considering stochastic demands. They considered a three-echelon supply chain including a number of suppliers, production centers, and distribution centers. They employed a hierarchical approach to determine the production-distribution plans for a one-year time horizon. Marchetti et al. [11] investigated an integrated production-distribution problem to determine the optimal policies in a gas supply chain. The problem was regarded as a multi-period mixed-integer linear programming model to minimize production and distribution costs. Sy [12] investigated the production-distribution problem in a hybrid system in which products are transferred from top level to bottom level and vice versa to reduce the bullwhip effect in the supply chain. Devapriya et al. [13] considered perishable items to investigate the integration of production and distribution scheduling. Given different features of perishable products in previous studies, the lifetime of items was regarded as a criterion for making decisions.

Li and Wang [14] examine a centralized production/distribution system. The objective is to develop an integrated policy that mitigates the negative effects of inventory inaccuracy. Roostaie and Nakhai Kamal Abadi [15] focused on the integrated decision-making process for production, routing, and inventory in a two-echelon supply chain. They addressed the inventory routing problem, where the supplier manages inventory replenishment, delivery timing, quantity, and customer sequence and a heuristic method to overcome the complexity of the problem is considered by them. Izadi et al. [16] studied an integrated production scheduling, vehicle routing, inventory, and outsourcing problem. They developed a model using Mixed Integer Linear Programming (MILP) to minimize total costs. They combined dominance properties with a Genetic Algorithm (GA) to solve the problem. The proposed hybrid algorithm was evaluated through a computational study using randomly generated instances. Azami and

Saidi-Mehrabad [17] developed a new multi-period production-distribution planning (PDP) model for perishable products in a three-level supply chain including the factories, distribution centers, and retailers. The objective was to maximize the seller's profit while ensuring the optimality of the buyer. In this paper, factors such as price, discounts, and credit terms have been utilized to enhance competitiveness and incentivize customers. Due to the high complexity of the problem, both genetic algorithms and a hierarchical decomposition-based approach have been utilized to solve the problem. Haghshenas et al. [18] proposed a new mathematical model in a three level supply chain considering location, inventory and pricing of products. They consider a new separate and autonomous channel in this model for the sale of Reman products, with the aim of increasing the manufacturer's profitability. Their developed model has been solved in small dimensions using the LINGO software and in larger dimensions with the assistance of genetic algorithm and particle swarm optimization algorithm. Ghomi-Avili et al. [19] presents an integrated production and distribution model that combines Stackelberg competition and Make-to-Order production system, investigating the impact of discounts on chain profits. They used blockchain technology for enhancing transparency in supply chains. A modified algorithm based on smart contract prices is used to solve the model, demonstrating improved performance and increased network efficiency. Simultaneous decision-making of pricing policies and inventory control for perishable items has been examined by Edalatpour et al [20]; two interrelated price-sensitive linear demand functions to consider the possibility of shortage with both budget and warehouse capacity constraints is considered in their study; Furthermore, they incorporate an upper bound for environmental pollution and a lower bound for job opportunities as additional constraints to their proposed mathematical model.

The research literature has extensively investigated the integration of pricing policies and inventory control in various studies. However, there has been a lack of attention or omission of the pricing aspect when considering production-related decisions in conjunction with inventory control. This discrepancy arises due to the inherent differences in decision-making nature between pricing and production/inventory, resulting in increased complexity when integrating multiple decision levels. Thus, this study aims to address this gap by examining the simultaneous decision-making of pricing, production, and inventory control, along with products distribution decisions, is the novelty of this research. Considering these policies for perishable items constitutes another notable feature of this research.

The importance and contributions of this research can be summarized as follows:

- This study makes a significant contribution to the field of supply chain management by delving into the

- intricate realm of dynamic pricing strategies in a multi-level supply chain context.
- One of the main contributions of this research is the development of a novel pricing approach within a multi-product, multi-period problem, which has been relatively overlooked in the existing literature.
 - By introducing this unique pricing model, our research fills a critical research gap and presents a new perspective on dynamic pricing strategies in the context of perishable goods.
 - The findings of this study offer valuable insights into the dynamic pricing practices that can be adopted in a complex three-level supply chain, contributing to the advancement of pricing strategies in the field.
 - Moreover, this research provides practical implications for businesses operating in industries dealing with perishable products, such as food and pharmaceuticals, by offering an optimized approach to pricing decisions and inventory management.

3. MATHEMATICAL MODEL

As mentioned in the preceding section, this study focuses on a multi-period and multi-product production-distribution system with demand that is dependent on price. The assumptions and notations are explained as follows:

- All of the parameters in the problem are deterministic and pre-determined.
- The production-distribution problem is investigated in a multi-period multi-product mode with price-dependent demands to maximize profit in a three-echelon supply chain including several manufacturers, distribution centers and retailers.
- Demand of Each retailer (customer) in each period is represented by $demand_{j_w} = a_{tip{j_w}} - b_{tip{j_w}} p_{tp}$, where p_{tp} indicates the price of product p in the period t .
- The products are perishable and they are instantaneously deteriorated in a constant rate α .
- Each manufacturer has a number of production lines and each of them is able to produce all the products.
- The goods are shipped directly from the manufacturer to the distribution centers.
- The production capacity of each manufacturer is definite and deterministic.
- Each customer is only supplied by one distribution center.
- Each distribution center has a number of heterogeneous fleet of vehicles which are different in transportation cost and capacity.
- The goods are shipped from the distribution centers to the customers based on vehicle routing problem.
- Split delivery of products is permitted.
- Backlog is not permitted.

3. 1. Problem Formulation

In this section, we first provide the notations and definitions used in the current formulation, followed by the introduction of the mathematical formulation.

Sets and indices

t	Index that represents time periods $t \in \{1, 2, \dots, T\}$
i	Index that represents manufacturers $i \in \{1, 2, \dots, I\}$
w	Index that represents warehouses $w \in \{1, 2, \dots, W\}$
j_w	Index that represents Set of customers of warehouse w ; $j_w \in \{1, 2, \dots, J_w\}$
N_w	Total number of customers of warehouse w
p	Index that represents products $p \in \{1, 2, \dots, P\}$
l	Index that represents production lines for each manufacturer $l \in \{1, 2, \dots, L\}$
v_i	Index that represents Sets vehicles of manufacturer i ; $v_i \in \{1, 2, \dots, V_i\}$
vw_w	Index that represents vehicles of warehouse w ; $vw_w \in \{1, 2, \dots, VW_w\}$

Parameters

F	Fixed cost of production
$a_{tip{j_w}}$	Intercept value of demand function of customer j_w in period t
$b_{tip{j_w}}$	Slope of the demand function of customer j_w in period t
$c_{v,i}$	Unit transportation cost of vehicle v of manufacturer i
H_{1i}	Unit holding cost of products at manufacturer i
$cap_{max}^{l,p,i}$	Maximum production capacity of line l at manufacturer i for product p
$setup_{p,p'}$	Sequence dependent setup time between product p and p'
$Sc_{p,p'}$	Sequence dependent setup cost between product p and p'
$proc_{p,l,i}$	Processing time of product p in line l of manufacturer i
$PC_{p,l,i}$	Unit cost of product p in line l of manufacturer i
λ_p	Unit volume of product p
w_p	Unit weight of product p
vol_{v_i}	Volume Capacity of vehicle v of manufacturer i
wei_{v_i}	Weight capacity of vehicle v of manufacturer i
Inv_{min}	Minimum inventory level for manufacturer and warehouses
$cv_{(vw_w)}$	Unit transportation cost of vehicle vw of warehouse w
H_{2w}	Unit holding cost of products at warehouse w
vol_{vw}	Volume Capacity of vehicle vw of warehouse w

wei_{vw}	Weight capacity of vehicle vw of warehouse w
c_{perish}	Perishable unit cost
α	Deterioration rate

Decision Variables

p_{tp}	Price of product p at period t
$pr_{t,p,l,i}$	Amount of product p which assigned to line l of manufacturer i at period t
$Inv_{t,p,i}$	Inventory level of product p at manufacturer i at time t
$Iw_{t,p,w}$	Inventory level of product p at warehouse w at time t
$z_{t(vw_w)m,n}$	Binary variable denoting that if vehicle vw of warehouse w exactly visit node m after node n
$q_{vw_w,m,t}$	Total number of visiting nodes m by vehicle vw of warehouse w at time t
$x_{t,p,w,l,i}$	Binary variable denoting that product p produced by line l for warehouse w at time t
$y_{p,p',l,i}$	Binary variable denoting that product p is processed before p' in line l of manufacturer i
$seq_{p,p',l,i}$	Variable determining that product p is processed right before p' in line l of manufacturer i
$VU_{t,p,v_i,i,w}$	Amount of product p shipped from manufacturer i to warehouse w at time t by vehicle v_i
VL_{t,j_w,p,vw_w}	Amount of product p shipped from warehouse w to customer j_w at time t by vehicle vw_w

The mathematical model of the integrated production-distribution problem is presented as follows:

$$\begin{aligned}
 & \text{Min } \sum_{t,i,j_w} (a_{tipj_w} p_{tip} - b_{tipj_w} p_{tip}^2) - [F + \\
 & \sum_{t,p,p',l,i} pr_{t,p,l,i} \cdot PC_{p,l,i} + \\
 & \sum_{t,p,p',l,i} seq_{t,p,p',l,i} \cdot Sc_{p,p'} \\
 & + \sum_{v_i,w} c_{v_i} \cdot d_{iw} \cdot zz_{tv_i iw} + \sum_{t,p,i} H_{1i} \cdot Inv_{t,p,i} \\
 & \sum_{t,p,w} H_{2w} \cdot Iw_{t,p,w} \\
 & + \sum_{t,w,j_w} (vw_w)_m \cdot d_{wj_w} \cdot cv_{(vw_w)} \cdot z_{t(vw_w)m,n} + \\
 & \sum_{t,w,p,(vw)_j_w} \pi_{t,p,(vw)_j_w} \cdot B_{t,p,vw_w,j_w} + \\
 & + \sum_{t,p} c_{perish} \cdot \alpha \cdot (Inv_{t,p,i} + Iw_{t,p,w}) \\
 & \text{s.t.}
 \end{aligned} \tag{1}$$

$$\sum_{l,i} x_{t,p,w,l,i} = 1 \quad \forall t, p, w \tag{2}$$

$$\sum_{l,i} pr_{t,p,l,i} \leq cap_{max}^{l,p} \cdot x_{t,p,w,l,i} \quad \forall t, p, w \tag{3}$$

$$\begin{aligned}
 & start_{t,p,l,i} \geq finish_{t,p,l,i} + \\
 & setup_{p,p'} \cdot seq_{t,p,p',l,i} - M \cdot (1 - \\
 & y_{p,p',l,i}) \quad \forall t, p, p', l, i
 \end{aligned} \tag{4}$$

$$finish_{t,p,l,i} \geq start_{t,p,l,i} + pr_{t,p,l,i} \cdot proc_{p,l,i} \quad \forall t, p, p', l, i \tag{5}$$

$$y_{t,p,p',l,i} + y_{t,p',p,l,i} \geq x_{t,p,w,l,i} + x_{t,p',w,l,i} - 1 \quad \forall t, p, p', l, i, w \tag{6}$$

$$y_{t,p,p',l,i} \leq x_{t,p,w,l,i} \quad \forall t, p, p', l, i, w \tag{7}$$

$$y_{t,p',p,l,i} \leq x_{t,p',w,l,i} \quad \forall t, p, p', l, i, w \tag{8}$$

$$\begin{aligned}
 pos_{t,p,p',l,i} = & \sum_{(p,p') \neq p''} (y_{t,p,p'',l,i} - y_{t,p,p',l,i}) + \\
 & M \cdot (1 - y_{t,p,p',l,i}) \quad \forall t, p, p', p'', l, i
 \end{aligned} \tag{9}$$

$$pos_{t,p,p',l,i} + seq_{t,p,p',l,i} \geq 1 \quad \forall t, p, p', l, i \tag{10}$$

$$\sum_{t,w} zz_{tv_i iw} \leq 1 \quad \forall i, v_i \tag{11}$$

$$\sum_p \lambda_p VU_{t,p,v_i,i,w} \leq zz_{tv_i iw} \cdot vol_{v_i} \quad \forall t, v_i, i \tag{12}$$

$$\sum_p w_p VU_{t,p,v_i,i,w} \leq zz_{tv_i iw} \cdot wei_{v_i} \quad \forall t, v_i, i \tag{13}$$

$$\sum_p \lambda_p VU_{t,p,v_i,i,w} \leq vol_{v_i} \quad \forall t, v_i, i \tag{14}$$

$$\sum_p w_p VU_{t,p,v_i,i,w} \leq wei_{v_i} \quad \forall t, v_i, i \tag{15}$$

$$\begin{aligned}
 Inv_{t,p,i} = & Inv_{t-1,p,i} (1 - \alpha) + \sum_l pr_{t,p,l,i} - \\
 & \sum_{v_i,w} zz_{tv_i iw} \cdot VU_{t,p,v_i,i,w} \quad \forall t, p, i
 \end{aligned} \tag{16}$$

$$Inv_{t,p,i} \geq Inv_{min} \quad \forall t, p, i \tag{17}$$

$$Iw_{t,p,w} \geq Iw_{min} \tag{18}$$

$$\begin{aligned}
 Iw_{t,p,w} = & Iw_{t-1,p,w} (1 - \alpha) + \sum_{v_i,i} VU_{t,p,v_i,i,w} - \\
 & \sum_{vw_w,j_w} VL_{t,j_w,p,vw_w} \quad \forall t, p, w
 \end{aligned} \tag{19}$$

$$\sum_{v_i,i} VU_{t,p,v_i,i,w} \geq \sum_{vw_w,j_w} VL_{t,j_w,p,vw_w} \quad \forall t, p, w \tag{20}$$

$$\sum_{vw_w} z_{t(vw_w)m,n} \geq 1 \quad \forall t, w, m, n \tag{21}$$

$$\sum_m z_{t(vw_w)m,n} = \sum_n z_{t(vw_w)n,m} \quad \forall t, w \tag{22}$$

$$\begin{aligned}
 \sum_{vw_w} VL_{t,j_w,p,vw_w} \cdot z_{t(vw_w)m,n} = & a_{tipj_w} - \\
 & b_{tipj_w} p_{tp} \quad \forall t, w, p, j_w
 \end{aligned} \tag{24}$$

$$\sum_{p,j_w} \lambda_p VL_{t,j_w,p,vw_w} \leq vol_{vw_w} \quad \forall t, w \tag{25}$$

$$\sum_{p,j_w} w_p VL_{t,j_w,p,vw_w} \leq wei_{vw_w} \quad \forall t, w \tag{26}$$

$$\begin{aligned}
 x_{t,p,w,l,i} \in \{0,1\}; & y_{p,p',l,i} \in \{0,1\}; seq_{p,p',l,i} \in \\
 & \{0,1\};
 \end{aligned} \tag{27-37}$$

$$\begin{aligned}
 z_{t(vw_w)m,n} \in \{0,1\} \\
 BC_{t,j_w} \in \{0,1\}; & p_{tp} \geq 0; pr_{t,p,l,i} \geq 0; Inv_{t,p,i} \geq \\
 & 0; Iw_{t,p,w} \geq 0;
 \end{aligned} \tag{27-37}$$

$$VU_{t,p,v_i,i,w} \geq 0; VL_{t,j_w,p,vw_w} \geq 0$$

Equation (1) represents the maximization of the manufacturer's net profit, calculated as the total revenue

minus the sum of the total cost. Equation (2) states that a warehouse-related product known as a product order, can only be allocated to one production line in each period. Constraint (3) ensures that the amount of production on a production line within a production center does not exceed its capacity. Constraints (4) and (5) determine the start and finish times of different production batches. The production sequence of two batches is determined by Constraints (6-10). For each period, each vehicle is assigned to transport goods from one production center to one warehouse; These constraints are expressed in Equations (11) to (13). Constraints (14) and (15) impose limitations on the total products shipped from each manufacturer to each warehouse, ensuring that they do not exceed the maximum weight and volume capacity of the vehicles. Equations (16-19) specify the inventory levels of different products in the manufacturing warehouses and distribution centers. In equation (16), the term $Iw_{t-1,p,w}(1 - \alpha)$ shows that the items which are non-deteriorated will be received from previous period. The quantity of products received from each warehouse should be greater than or equal to that of products sent by the warehouse which is ensured by Constraint (20). Equation (21) states the condition under which each customer can be visited by the vehicles more than once. Consecutive movements of vehicles are stated by Constraint (22); this means that every vehicle should exit a node after entering it. Equation (23) is a subtour elimination constraint. Equation (24) guarantees that total number of delivered products to each customer should be equal to its demand. Constraints (25) and (26) are similar to Constraints (14) and (15) but they relate to distribution centers. The domains of the decision variables are set by Constraints (27) to (37).

4. PROPOSED GENETIC ALGORITHM

Evolutionary algorithms (EAs) depict the simulation of nature process to invent the metaheuristic algorithm [21]. Genetic algorithm is one of the most effective search methods which have been successfully applied to many combinatorial optimization problems in which the regeneration process of living beings is simulated for solving complicated problems in different areas of science and engineering. It is a type of evolutionary algorithm that utilizes biological processes like inheritance, biology mutation, and Darwin's selection principles to find the optimal solution [21]. GAs are the special type of EAs and include so many methods in this classification. Chromosomes are the structure of cells in animals, plants and humans. In GA, we define an array of variables which is called chromosome. Chromosomes are altered by two operators: mutation and crossover; The types of two mentioned operators are addressed by several recent studies [22]. The framework proposed in this research for implementation of the genetic algorithm

will be described in the following subsection. Each step of implementing the algorithm will be outlined below:

1. Generating the initial population randomly;
2. Calculating the fitness functions of the chromosomes;
3. Selecting parents for creation of the next generation;
4. Applying the crossover and mutation operators;
5. Updating the population;
6. Iterating Steps 2-6 until the termination condition is met (determining the number of iterations);

4. 1. Representation

The solution vector representation in every EA should be as compact as possible but should contain enough information to represent any solution of the problem. The way of representing solutions significantly affect the choice of searching operators. Accordingly, efficient representation of the solutions helps to use well-known operators in the literature that their high performance has been proved [23]. In this paper, a hybrid chromosome representation is utilized to represent the chromosomes in each generation. Considering that each customer's demand in each period is price-dependent, initially the price of each product in each period is generated randomly in range $[p_{tp}^U, p_{tp}^L]$ where p_{tp}^U and p_{tp}^L are the upper and lower bound for the price of product p in period t and it will be determined as follows. As mentioned in previous section, demand of each customer is price-dependent and considered as:

$demand_{j_w} = a_{tipj_w} - b_{tipj_w}p_{tp}$ which is simply a linear function. We assume that the price of a product is the same for all customers but may change during different periods. The primary condition to determine the acceptable range of the price for each product will be determined by solving the following inequality:

$$a_{tipj_w} - b_{tipj_w}p_{tp} \geq d_{tipj_w}^{min} \quad (38)$$

Consequently, for each customer we have:

$$p_{tp} \leq \frac{a_{tipj_w} - d_{tipj_w}^{min}}{b_{tipj_w}} \quad \forall w, j \quad (39)$$

Thus, considering above results will determine the upper bound for price of each product in each period as follows:

$$p_{tp}^U = \text{Min}\{p_{tp}\} = \text{Min}_{w,j} \left\{ \frac{a_{tipj_w} - d_{tipj_w}^{min}}{b_{tipj_w}} \right\} \quad (40)$$

Now, suppose that maximum demand of each customer is represented by $d_{tipj_w}^{max}$; therefore, we have:

$$a_{tipj_w} - b_{tipj_w}p_{tp} \leq d_{tipj_w}^{max} \quad (41)$$

And thus:

$$p_{tp} \geq \frac{a_{tipj_w} - d_{tipj_w}^{max}}{b_{tipj_w}} \quad \forall w, j \quad (42)$$

Based on the aforementioned results, the lower bound for the price of each product in each period can be determined as follows:

$$p_{tp}^L = \text{Max}\{p_{tp}\} = \text{Max}_{w,j} \left\{ \frac{a_{tipj_w} - d_{tipj_w}^{max}}{b_{tipj_w}} \right\} \quad (43)$$

Now, we can present the proposed chromosome structure of the problem. In this study, to describe a solution to the problem, a mixed representation is utilized in which each chromosome includes four sections.

For example, assume that the production-distribution problem is to be designed for the bi-product mode with four time periods. Figure 1(a) indicates the first section of the hybrid chromosome structure namely pricing sub-chromosome.

The demand of each customer for each product is determined based on the specified price structure. For example, the demand for the first product from all customers is set at a price of 35 in the first period, while for the second product it is set at a price of 28 in the second period. This process is repeated for each period and customer, ensuring that the demand is aligned with the corresponding price. Each customer's demand for each product in each period will be determined by having the price specification. Therefore, it is necessary to specify the number of products shipped to each customer by each vehicle. Furthermore, visiting different customers should be arranged for every vehicle. Assume that there are two warehouses, the first one with five customers and the second one with three customers. It means that there are 8 customers among which customers 6-8 represent those of the second warehouse and if there are more customers then they will be numbered in the same way. In each period, one vehicle is selected randomly for each warehouse. Then, the order of customers' visits is randomly generated (it should be noted that each vehicle starts at and ends in a warehouse; however, it is not represented in the chromosome structure). Figure 1(b) shows the order of visits of the different customers in four time periods.

Now, the selected vehicle can ship all the customer demand. After each gene is filled, a part of the weight and size capacity of the vehicle is occupied which should be considered when the next genes are in action. If the weight or volume capacity of the vehicle is reached, any remaining customers will be assigned to another vehicle (the order of remaining customers can be considered in the same way as the order of vehicles, or a new order can be established). Figure 1(c) shows the quantity of products shipments to customers in each period. For example, 45, 20, and 30 units of the first, second, and third product respectively are sent to customer 2 in the first period.

Based on the quantity of goods transported by the vehicles from each warehouse to the customers, and taking into account the minimum inventory requirements for each product, the total demand for each product is calculated. Now, the production of these products needs to be scheduled in the production lines of the manufacturer. For example, let's consider two production centers, each equipped with two production lines, where each line has a maximum production capacity. Figure 1(d) shows the structure used to determine the production

order of a product in the production centers. The first number indicates the product, the second represents the warehouse, the third refers to the production line, and the fourth indicates the manufacturer.

Now, a population of chromosomes is generated according to the described structure and based on the size of the population.

4. 2. Determining the Fitness Function

The fitness function of each chromosome is calculated once the initial population is generated. In this study, only feasible chromosomes are generated, and therefore the objective function is used directly as the fitness function.

4. 3. Selection

The process of parent selection is carried out to generate a new generation within the current population. The genetic operators (crossover and mutation) are then applied to produce the new generation; Since the population size is fixed, a certain number of chromosomes are removed from the current population based on the fitness function. Although there are various methods available for selection of parents from the population to produce the generation, some methods may decrease the likelihood of producing high-quality offspring from parents with unfavorable fitness values by favoring the best fitness functions and selecting the best parents. Among different selection methods, the roulette wheel technique is a method in which each chromosome has the chance of being selected. Therefore, the roulette wheel method was used according to the rules described below:

$$1. \quad F'(ch) = F_{max} - F(ch)$$

		Pricing sub-chromosome						
a	35	24	28	31				
	26.4	28	30	18				
Vehicle Routing Sub-chromosome								
b	2	4	1	3	5			
	1	3	2	4	5			
	4	2	5	1	3			
	3	4	5	2	1			
Sub-chromosome of distribution quantity of products for customers								
c	45- 20- 30 15	30- 20- 20 20	50- 45- 20 20	15- 25- 30- 25	60- 30- 20 30	25- 40- 18 25	30- 20- 40 30	30- 25-15
	25- 20- 30 20	10- 40- 25 25	30- 35- 45- 30	20- 25- 25- 25	25- 25- 15 25	30- 20- 15 30	40- 25- 30- 40	15- 20-40
	35- 28- 50 48	25- 22- 50 45	35- 20- 50 45	20- 30- 30 30	15- 10- 45 30	25- 30- 45 40	22- 38- 40 30	24- 10-5
	15- 25- 20 35	20- 15- 35 24	30- 42- 42 16	18- 32- 32 45	30- 19- 25 45	18- 25- 20 20	35- 30- 22 22	24- 10-5
Assignment of demand of warehouses to production lines of manufacturer								
d	2211	3221	2121	3122	1111	1211		

Figure 1. An example of chromosome encoding

2. $RW(ch) = \frac{\sum_{i=1}^{i=ch} F(i)}{\sum_{j=1}^{pop_size} F(j)}$
3. Generate a random number between 0 and 1;
4. If $RW(ch - 1) < rand \leq RW(ch)$ and $RW(0) = 0$ then select chromosome ch

4.4. Crossover

Crossover operator is used to diversify the search process. In this study, the crossover operator will be applied to two selected chromosomes from the population. The process will be described in the following section.

- I. Generate a random number R_1 between 0 and 1, if $R_1 \leq \eta$ go to step II and go to step III otherwise;
- II. Apply crossover operator to vehicle routing sub-chromosome;
- III. Apply crossover operator to production sub-chromosome;

η is the probability that shows whether the crossover operator should be applied to vehicle routing sub-chromosome or production sub-chromosome.

An example of crossover operator is as follows. In each period, a number of genes are randomly selected from the first parent and transferred to the first offspring. Then, the genes of the second parent are compared with the genes transferred to the first child from left to right, and are transferred to the first empty gene in the case of absence. In the first period of the first offspring, for instance, the second parent is considered after genes 4-1-3 of the first parent are transferred. The value of the first gene is 3 which belongs to the first child and accordingly skipped to the next gene. The value of the second gene is 2 which is put into the first empty gene because 2 is not involved with the first child. The next value is 5 which is put into the next empty gene that will be in the first child and finally, 4 is inserted. The procedure is repeated for the second period. The genes selected from the first parent are shown in yellow which are seen in the same order and color in the first child. The same procedure is repeated with regard to the second child; however, the genes are selected from the second parent. Figure 2 shows the proposed crossover operator for vehicle routing sub-chromosome. The crossover operator can be utilized to allocate lots to the production lines. In this case, for the first offspring, certain genes are randomly selected from the first parent and transferred to the first offspring. Then, the genes of the second parent are compared with the genes transferred to the first child, and any remaining empty genes are filled with the corresponding genes from the second parent. This crossover process follows the same principles as the crossover operator used in previous sub-chromosomes. This process is shown in Figure 3.

For the second child, a number of genes are selected from the second parent. It should be noted that only the first two numbers, representing the product and warehouse, are considered in comparison with the genes of a parent with the filled genes of each offspring.

3.5. Mutation

After the crossover operator, the mutation operator is applied to explore portions of the solution space that may not be accessible through the crossover operation alone. Typically, the mutation operator is applied to individual chromosomes. In this study, the mutation operator is defined as follows:

- I. Generate a random number R_2 between 0 and 1, if $R_1 \leq \lambda$ go to step II and go to step III otherwise;
- II. Apply mutation operator to vehicle routing sub-chromosome;
- III. Apply mutation operator to production sub-chromosome;

λ is the probability that shows whether the mutation operator should be applied to vehicle routing sub-chromosome or production sub-chromosome.

Two genes are selected in each period which are then replaced with each other. Figure 4 shows the mutation operator used for the current study.

4. COMPUTATIONAL RESULTS

In this section, computational results of the proposed genetic algorithm are presented. The generation of instances is described in section 5.1 while the parameters of proposed genetic algorithm are presented in section 5.2; This section is dedicated to discussing the numerical results.

Due to the high complexity of the research problem and the difficulty in obtaining optimal solutions, even in small-sized problems is difficult therefore 2 simple test problems, each of them consists of 9 sub-problems, are first solved by BARON solver of GAMS software. The results are then compared with those obtained from the GA, which has been implemented in C#. After confirming the efficiency of the designed genetic

	2	4	1	3	5	8	6	7
First parent	1	3	2	4	5	6	7	8
	4	2	5	1	3	6	7	8
	3	4	5	2	1	7	6	8
Second parent	3	2	5	1	4	7	6	8
	5	1	2	3	4	6	7	8
	1	2	3	4	5	8	6	7
	2	3	1	5	4	8	6	7
First offspring	2	4	1	3	5	8	6	7
	1	3	5	2	4	6	7	8
	2	4	5	1	3	6	7	8
	3	1	5	2	4	6	7	8

Figure 2. An example of crossover operator for Vehicle Routing Sub-chromosome

2211	3221	2121	3122	1111	1211
1121	2112	2222	3211	1221	3112
1121	3221	2121	3122	2222	1221

Figure 3. Crossover operator for two warehouses and three products

algorithm, five problems, each with nine sub-problems, are solved using the genetic algorithm.

5.2. Generation of Instances Problem instances have been generated and divided into two groups: test and main problems where there are 9 instances in each group as shown in Table 1.

The values of the parameters are shown in Table 2. Given the fact that the parameters of metaheuristic algorithms have great impact on the convergence and good performance of the algorithm, therefore a variety of combination of parameter values have been tested in order to set the GA parameters. Experimental results have shown that the following values can obtain satisfactory results and therefore are used for all examples: population size=100, crossover probability=0.8, $\eta = 0.7$, mutation Probability=0.3, $\lambda = 0.45$ and Maximum number of iterations=1500.

5.2. Results In this section, numerical results on the performance of the proposed genetic algorithm are presented. All of the sample problems were coded in GAMS24.7.4 and C# executed on a computer operating system with a Core i5 processor and 8 GB of RAM. The genetic algorithm was executed 10 times on each sample problem; Numerical reports were generated for the average, best, and worst solutions obtained, along with the standard deviation of the objective function across the

parent	2	4	1	3	5	8	6	7
	1	3	2	4	5	6	7	8
	4	2	5	1	3	6	7	8
	3	4	5	2	1	7	6	8
offspring	2	5	1	3	4	6	8	7
	3	1	2	4	5	7	6	8
	3	2	5	1	4	6	8	7
	2	4	5	3	1	8	6	7

Figure 4. Mutation operator

TABLE 1. Problem instances

	A	B	C	D	E	F	G		H
							1	2	
Test problems	1	1	1	5	3	3	2	4	2
	2	1	2	5	3	3	2	4	2
	1	2	2	4	3	3	2	4	2
Main problems	2	2	3	6	5	4	2	4	2
	3	2	4	8	7	5	2	4	2
	4	2	5	15	10	6	2	4	2
	5	2	6	20	10	7	2	4	2
									4

A: Problem No. B: No. of manufacturer; C: No. of Distribution Centers; D: No. of customers of each DCs; E: No. of Vehicles of manufacturer; F: No. of Vehicles of each DC; G: No. of Products; H: Time periods;
1: Min and 2: Max

TABLE 2. The values of parameters

Parameter	Value	Parameter	Value
a_{tipjw}	$U[50,100]$	b_{tipjw}	$U[1,1.5]$
$F, c_{v,i}, c_{v(vw_w)}$			
$\pi_{t,p,(vw_w),j_w}$	1	α, β	0.1
c_{perish}			
$cap_{max}^{l,p,i}$	$3.5N \sum_{t,i,j_w} (a_{tipjw} \cdot b_{tipjw} p_{tip})$	$setup_{p,p'}$	$U[0.1,0.5]$
$Sc_{p,p'}$	$U[0.1,0.5]$	$proc_{p,l,i}$	0.1
$PC_{p,l,i}$	$U[4,6]$	λ_p	$U[0.1,1]$
w_p	$U[2,5]$	vol_{v_i}	$U[300,400]$
wei_{v_i}	$U[1000,1500]$	Inv_{min}	$U[20,30]$

10 runs and the obtained results were reported in the table of results. Tables 3-5 show the computational results of solving different sample problems. According to Tables 3-5, it is obvious that the proposed genetic algorithm is efficient as the average gap between the solutions provided by the genetic algorithm and the optimal ones is 1.6% for the first test problem and 3.3% for the second test problem which demonstrates that the solutions to the medium and large sample problems can be trusted. Comparison of the performance of the genetic algorithm with the optimal solution of the problem for two cases, as shown in Figures 5 and 6, respectively. Table 6 shows the computational results for Main problems which have been solved by genetic algorithm.

Considering the importance of the price parameter and its significant impact on management policies, Table 5 reports the obtained price values solely for the first test problem at different periods. As observed, the obtained prices have very minor differences compared to the values reported by the BARON algorithm, indicating the effectiveness of the proposed algorithm in solving the problems.

The outcomes achieved by applying the Genetic Algorithm to two experimental problems validate the robustness of the algorithm's evolutionary framework. Thus, we can exclusively employ the proposed Genetic Algorithm to solve the primary problems and confidently utilize the obtained solutions. Table 6 provides the solution outcomes for 5 main problems, each comprising 9 subproblems, encompassing the objective function values and the corresponding solution times.

The development of the multi-objective formulation and the utilization of hybrid multi-objective evolutionary algorithms (HMOEAs), the incorporation of novel approaches in genetic algorithms or using state-of-the-art algorithms such as NGO or SEO algorithms and integration of deep learning and machine learning techniques for future research are suggested as highly intriguing topics[24-29].

TABLE 3. Objective function of first test problem and CPU time

Prob. No.	Constraints	Variables	Objective function	Genetic algorithm					Standard Deviation
				Time (s)	(Best)	(Average)	(Worst)	Time (s)	
1	409	353	51689.41	205.2	52018.21	52083.73	52102.72	1.86	36.20
2	613	525	83032.27	398.12	85921.287	86482.19	87157.62	2.1	505.45
3	817	697	111817.65	221.5	113501.67	113968.02	114727.21	2.43	505.06
4	555	459	80258.12	119.1	81981.34	82476.98	83022.54	2.99	425.23
5	832	679	146867.34	276.4	148156.18	149002.42	150202.77	4.76	839.67
6	1109	899	167429.57	548.23	169218.561	169460.33	169813.49	11.21	244.29
7	757	585	115712.27	432.8	118721.16	119276.44	120019.27	4.01	531.79
8	1135	861	172046.19	542.1	174281.786	174822.36	175113.52	6.89	344.60
9	1513	1137	264293.38	845.8	266716.187	267392.01	268347.31	26.91	669.15

TABLE 4. Objective function of second test problem and CPU time

Prob. No.	Constraints	Variables	Objective function	Genetic algorithm					Standard Deviation
				Time (s)	(Best)	(Average)	(Worst)	Time (s)	
1	601	417	88382.16	867.2	89219.432	89967.296	91056.06	11.3	781.23
2	901	621	115371.07	971.3	117376.19	118257.86	119714.26	21.7	943.35
3	1201	825	166815.34	826.1	171572.189	171874.34	172113.60	38.87	248.02
4	817	529	114107.56	1421.3	118671.102	119965.32	121258.74	49.16	1081.12
5	1225	784	173317.86	602.1	182098.17	182098.17	182625.82	80.9	253.24
6	1633	1039	230168.25	1034.4	236715.74	236715.74	239101.23	121.54	1113.21
7	1113	661	166749.43	897.3	172786.17	172786.17	173429.94	76.91	321.78
8	1669	975	205753.12	926.12	208761.65	208761.65	212495.47	110.17	1746.17
9	2225	1289	325720.388	5892.1	351023.512	351023.512	355372.72	132.78	2081.62

TABLE 5. Obtained price for sub-problems of the first sample problem

Problem No.	Time Period	Product 1		Product 2		Product 3		Product 4	
		BARON	GA	BARON	GA	BARON	GA	BARON	GA
1	1	64	63.03	77	76.82				
	2	61	62.17	61	59.43				
2	1	80	80.24	78	79.32				
	2	84	83.96	72	71.43				
3	3	63	63	72	72.23				
	1	76	75.42	69	69.94				
4	2	64	64.7	70	69.63				
	3	61	60.67	61	62.01				
4	4	62	61.9	61	61				
	1	66	65	61	61.1	63	61.76		
	2	64	64.85	97	97.67	67	67.39		

	1	84	84.06	79	78.3	79	78.12	
5	2	66	67.57	73	73.16	70	69.12	
	3	66	67.9	64	63.9	64	64.16	
	1	65	64.38	64	62.89	65	65.19	
6	2	67	67.11	70	71.01	63	63.12	
	3	61	59.81	65	64.38	66	66.15	
	4	60	59.19	56	55.61	56	55.81	
7	1	55	54.1	61	60.14	55	54.9	56
	2	66	66.09	67	67.09	66	67.01	66
	1	68	67.21	69	69.18	67	68.19	67
8	2	59	58.32	60	60.21	59	58.41	59
	3	64	63.01	62	61.67	62	61.78	62
	1	98	99.78	90	92	82	83	81
9	2	79	81	66	66.12	74	74.3	73
	3	64	63.9	85	85.62	85	86.01	85
	4	68	68.14	70	70.15	70	70.91	70

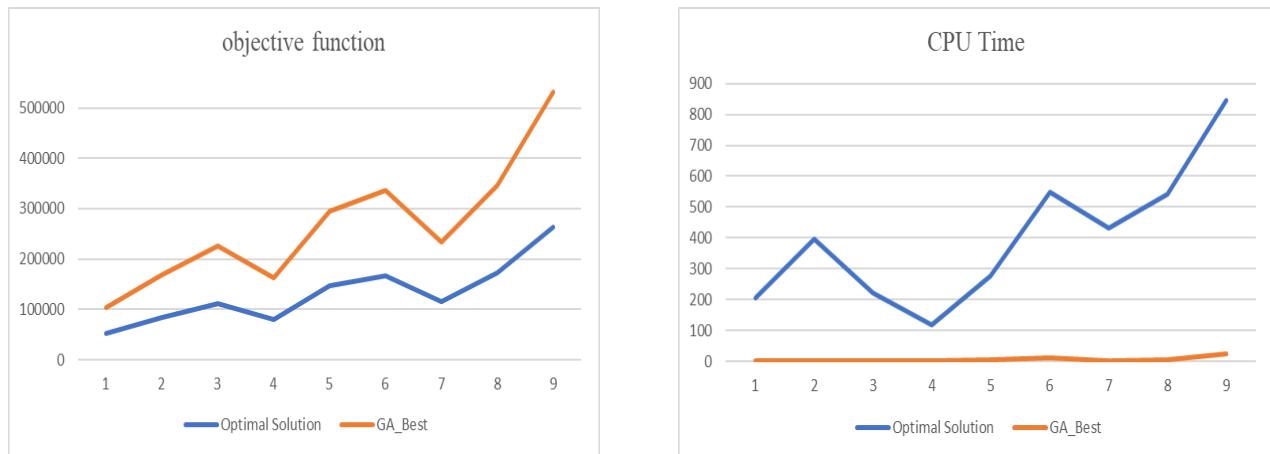


Figure 5. Optimal solution VS best reported value by the genetic algorithm for the first test problems

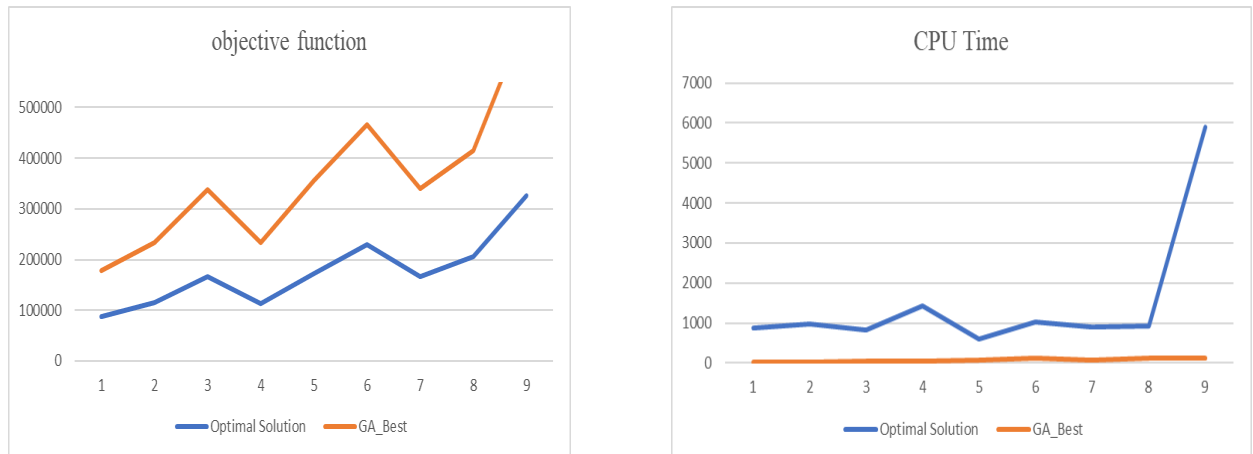


Figure 6. Optimal solution VS best reported value by the genetic algorithm for the second test problems

TABLE 6. Objective function of main problems with CPU time

Sub-problem	1-1	1-2	1-3	1-4	1-5	1-6	1-7	1-8	1-9
Obj. Fun.	97326.172	136098.016	194738.648	122254.19	188097.143	217943.92	177218.176	220715.81	257876.12
Time (s)	15.2	22.1	24.7	36.5	42.7	78.9	72.2	93.6	105.4
Sub-problem	2-1	2-2	2-3	2-4	2-5	2-6	2-7	2-8	2-9
Obj. Fun.	632.118745	308.140392	619.200593	678.131056	191267.7	63.232645	190678.732	228765.32	156.265328
Time (s)	6.17	2.23	56.39	5.52	3.84	3.126	4.86	7.117	1.138
Sub-problem	3-1	3-2	3-3	3-4	3-5	3-6	3-7	3-8	3-9
Obj. Fun.	316.142089	217.175456	18.237651	278.162345	76.209867	26.269017	86.193796	278.254871	112.304768
Time (s)	2.23	9.28	4.46	3.61	3.89	2.134	7.96	22.126	3.148
Sub-problem	4-1	4-2	4-3	4-4	4-5	4-6	4-7	4-8	4-9
Obj. Fun.	027.194219	706.227691	064.271237	786.222612	723.285675	717.316234	2.269432	367.300492	212.364765
Time (s)	1.28	6.34	32.52	9.83	4.102	45.156	32.116	4.138	2.167
Sub-problem	5-1	5-2	5-3	5-4	5-5	5-6	5-7	5-8	5-9
Obj. Fun.	067.238543	167.291324	634.338178	154.28821	475.323423	098.37232	965.319869	991.363567	675.410025
Time (s)	3.41	8.58	3.72	6.116	2.141	9.175	2.132	3.163	8.193

6. CONCLUSION, FINDINGS, LIMITATION AND FUTURE DIRECTIONS

This paper investigates an integrated multi-product and multi-period production-distribution system involving multiple manufacturers, distribution centers, and customers. The system considers split delivery and focuses on delivering perishable goods without allowing shortages. Since limited research has focused on pricing in production-distribution systems, this study proposes a mathematical formulation to maximize profit by incorporating dynamic pricing policies, which serves as a significant contribution of the study. Due to the high complexity of the developed mathematical model, a genetic algorithm is employed as an appropriate tool for solving the problem instances. Additionally, a set of test problems is initially solved to achieve optimality, and the efficiency of the proposed genetic algorithm is evaluated by comparing its results with the optimal solutions. Considering the effective performance of the genetic algorithm on the test problems, the main problems are also solved using the genetic algorithm, resulting in near-optimal or optimal solutions. Advanced optimization algorithms have proven their effectiveness in multiple domains, including online learning, scheduling, multi-objective optimization, transportation, medicine, and

data classification. Their success in these areas demonstrates their potential for various decision-making problems, extending beyond the specific focus of this study. These algorithms offer valuable tools for decision-making across different contexts and present opportunities for enhancing problem-solving capabilities.

In the following, the most significant findings of the research and the limitations associated with conducting this study will be described.

In this research, all the parameters of the problem have been assumed to be deterministic, while in the case of parameters such as demand, it is not easy to assume certainty, as we always expect fluctuations in product demand. On the other hand, the price of a product is influenced by numerous factors, many of which have not been considered in this study. All of these factors are simply disregarded to prevent increasing the complexity of the mathematical model.

The solution of an integrated model that addresses production planning and scheduling, inventory control, routing and distribution, and ultimately pricing of products over multiple periods is the most significant finding of the research. Future researchers can propose better and stronger approaches to solving the problem and dealing with its inherent complexities by taking a

closer look at this issue. Another limitation inherent in this study is the failure to empirically implement the findings derived from the mathematical model within a practical context; It is imperative that future research endeavors involve the application of the developed model to a real-world problem, thereby facilitating a comprehensive analysis of the results.

The research contributes to the advancement of vehicle scheduling in warehouses and cross-docking operations. In addition, it would be interesting to consider reverse logistics in the mathematical model. Given that the genetic algorithm was only used for the problems, appropriate approaches to determine upper and lower bounds to control and navigate the genetic algorithm may improve the solutions. Considering the complexity of the problem examined in this research, it appears that employing simulation approaches as an attractive method can be highly effective in achieving high-quality solutions. Furthermore, it presents an intriguing research area for the further development of recent studies.

7. REFERENCES

1. Moosavi, J., Fathollahi-Fard, A.M. and Dulebenets, M.A., "Supply chain disruption during the covid-19 pandemic: Recognizing potential disruption management strategies", *International Journal of Disaster Risk Reduction*, Vol. 75, (2022), 102983. <https://doi.org/10.1016/j.ijdrr.2022.102983>
2. Simonetto, M., Sgarbossa, F., Battini, D. and Govindan, K., "Closed loop supply chains 4.0: From risks to benefits through advanced technologies. A literature review and research agenda", *International Journal of Production Economics*, (2022), 108582. <https://doi.org/10.1016/j.ijpe.2022.108582>
3. Berlin, D., Feldmann, A. and Nuur, C., "The relatedness of open- and closed-loop supply chains in the context of the circular economy; framing a continuum", *Cleaner Logistics and Supply Chain*, Vol. 4, (2022), 100048. <https://doi.org/10.1016/j.clscn.2022.100048>
4. Asghari, M., Afshari, H., Mirzapour Al-e-hashem, S.M.J., Fathollahi-Fard, A.M. and Dulebenets, M.A., "Pricing and advertising decisions in a direct-sales closed-loop supply chain", *Computers & Industrial Engineering*, Vol. 171, (2022), 108439. <https://doi.org/10.1016/j.cie.2022.108439>. <https://www.sciencedirect.com/science/article/pii/S0360835222004740>
5. Fathollahi-Fard, A., Dulebenets, M., Hajiaghaei-Keshteli, M., Tavakkoli-Moghaddam, R., Safaeian, M. and Mirzahosseiniyan, H., "Two hybrid meta-heuristic algorithms for a dual-channel closed-loop supply chain network design problem in the tire industry under uncertainty", *Advanced Engineering Informatics*, Vol. 50, (2021), 101418. doi: 10.1016/j.aei.2021.101418.
6. Chopra, S. and Meindl, P., "Supply chain management: Strategy, planning, and operation, Pearson, (2016).
7. Farahani, R.Z., Rezapour, S., Drezner, T. and Fallah, S., "Competitive supply chain network design: An overview of classifications, models, solution techniques and applications", *Omega*, Vol. 45, (2014), 92-118. <https://doi.org/10.1016/j.omega.2013.08.006>
8. Bilgen, B. and Günther, H.O., "Integrated production and distribution planning in the fast moving consumer goods industry: A block planning application", *OR Spectrum*, Vol. 32, No. 4, (2010), 927-955. doi: 10.1007/s00291-009-0177-4.
9. Coccolla, M.E., Zamarripa, M., Méndez, C.A. and Espuña, A., "Toward integrated production and distribution management in multi-echelon supply chains", *Computers & Chemical Engineering*, Vol. 57, (2013), 78-94. <https://doi.org/10.1016/j.compchemeng.2013.01.004>.
10. Nasiri, G.R., Zolfaghari, R. and Davoudpour, H., "An integrated supply chain production-distribution planning with stochastic demands", *Computers & Industrial Engineering*, Vol. 77, (2014), 35-45. doi: <https://doi.org/10.1016/j.cie.2014.08.005>.
11. Marchetti, P.A., Gupta, V., Grossmann, I.E., Cook, L., Valton, P.-M., Singh, T., Li, T. and André, J., "Simultaneous production and distribution of industrial gas supply-chains", *Computers & Chemical Engineering*, Vol. 69, (2014), 39-58. <https://doi.org/10.1016/j.compchemeng.2014.06.010>.
12. Sy, C., "A policy development model for reducing bullwhips in hybrid production-distribution systems", *International Journal of Production Economics*, Vol. 190, (2017), 67-79. <https://doi.org/10.1016/j.ijpe.2016.09.005>
13. Devapriya, P., Ferrell, W. and Geismar, N., "Integrated production and distribution scheduling with a perishable product", *European Journal of Operational Research*, Vol. 259, No. 3, (2017), 906-916. <https://doi.org/10.1016/j.ejor.2016.09.019>
14. Li, M. and Wang, Z., "An integrated robust replenishment/production/distribution policy under inventory inaccuracy", *International Journal of Production Research*, Vol. 56, No. 12, (2018), 4115-4131. doi: 10.1080/00207543.2018.1444808.
15. Roostaei, A. and Nakhai Kamal Abadi, I., "Considering production planning in the multi-period inventory routing problem with transshipment between retailers", *International Journal of Engineering, Transaction C: Aspects*, Vol. 31, No. 9, (2018), 1568-1574. https://www.ije.ir/article_73294_56d823c2a4725045279477cd326ca693.pdf
16. Izadi, L., Ahmadizar, F. and Arkat, J., "A hybrid genetic algorithm for integrated production and distribution scheduling problem with outsourcing allowed", *International Journal of Engineering, Transaction B: Applications*, Vol. 33, No. 11, (2020), 2285-2298. doi: 10.5829/ije.2020.33.11b.19.
17. Aazami, A. and Saidi-Mehrabad, M., "A production and distribution planning of perishable products with a fixed lifetime under vertical competition in the seller-buyer systems: A real-world application", *Journal of Manufacturing Systems*, Vol. 58, (2021), 223-247. <https://doi.org/10.1016/j.jmsy.2020.12.001>
18. Haghshenas, P., Sahraeian, R. and Golmohammadi, A.M., "A state-of-the-art model of location, inventory, and pricing problem in the closed-loop supply chain network", *International Journal of Engineering, Transaction B: Applications*, Vol. 35, No. 8, (2022), 1558-1570. doi: 10.5829/ije.2022.35.08B.12.
19. Ghomi-Avili, M., Akhavan Niaki, S.T. and Tavakkoli-Moghaddam, R., "A joint pricing and sustainable closed-loop supply chain network design problem using blockchain technology", *Journal of Industrial and Systems Engineering*, Vol. 14, No. 4, (2023), 121-137.
20. Edalatpour, M.A., Mirzapour Al-e-Hashem, S.M.J. and Fathollahi-Fard, A.M., "Combination of pricing and inventory policies for deteriorating products with sustainability considerations", *Environment, Development and Sustainability*, (2023). doi: 10.1007/s10668-023-02988-6.
21. Hashemi, Z. and Tari, F.G., "A prufer-based genetic algorithm for allocation of the vehicles in a discounted transportation cost system", *International Journal of Systems Science: Operations & Logistics*, Vol. 5, No. 1, (2018), 1-15. doi: 10.1080/23302674.2016.1226980.

22. Abdi, A., Abdi, A., Fathollahi-Fard, A.M. and Hajiaghaei-Keshteli, M., "A set of calibrated metaheuristics to address a closed-loop supply chain network design problem under uncertainty", *International journal of systems science: Operations & logistics*, Vol. 8, No. 1, (2021), 23-40. doi: 10.1080/23302674.2019.1610197.
23. Karimi-Mamaghan, M., Mohammadi, M., Pirayesh, A., Karimi-Mamaghan, A.M. and Irani, H., "Hub-and-spoke network design under congestion: A learning based metaheuristic", *Transportation Research Part E: Logistics and Transportation Review*, Vol. 142, (2020), 102069. https://doi.org/10.1016/j.tre.2020.102069
24. Müller-Zhang, Z., Kuhn, T. and Antonino, P.O., "Towards live decision-making for service-based production: Integrated process planning and scheduling with digital twins and deep-q-learning", *Computers in Industry*, Vol. 149, (2023), 103933. doi: https://doi.org/10.1016/j.compind.2023.103933
25. Gholizadeh, H., Fazlollahtabar, H., Fathollahi-Fard, A.M. and Dulebenets, M.A., "Preventive maintenance for the flexible flowshop scheduling under uncertainty: A waste-to-energy system", *Environmental Science and Pollution Research*, (2021). doi: 10.1007/s11356-021-16234-x.
26. Zhao, H. and Zhang, C., "An online-learning-based evolutionary many-objective algorithm", *Information Sciences*, Vol. 509, No., (2020), 1-21. https://doi.org/10.1016/j.ins.2019.08.069
27. Dulebenets, M.A., "An adaptive island evolutionary algorithm for the berth scheduling problem", *Memetic Computing*, Vol. 12, No. 1, (2020), 51-72. doi: 10.1007/s12293-019-00292-3.
28. Tian, G., Zhang, X., Fathollahi-Fard, A.M., Jiang, Z., Zhang, C., Yuan, G. and Pham, D.T., "Hybrid evolutionary algorithm for stochastic multiobjective disassembly line balancing problem in remanufacturing", *Environmental Science and Pollution Research*, (2023). doi: 10.1007/s11356-023-27081-3.
29. Zhang, X., Zhou, H., Fu, C., Mi, M., Zhan, C., Pham, D.T. and Fathollahi-Fard, A.M., "Application and planning of an energy-oriented stochastic disassembly line balancing problem", *Environmental Science and Pollution Research*, (2023). doi: 10.1007/s11356-023-27288-4.

COPYRIGHTS

©2023 The author(s). This is an open access article distributed under the terms of the Creative Commons Attribution (CC BY 4.0), which permits unrestricted use, distribution, and reproduction in any medium, as long as the original authors and source are cited. No permission is required from the authors or the publishers.



Persian Abstract

چکیده

اهمیت استفاده از استراتژی‌های قیمت‌گذاری مناسب برای محصولات فاسدشدنی در زنجیره تأمین بیانگر نیاز اساسی است. قیمت‌گذاری به عنوان یک رانده عملکردی مشترک در هر زنجیره تأمین نقشی قاطع در موفقیت و سودآوری زنجیره تأمین را در کنار عوامل دیگری نظر سیاست‌های موجودی و تولید ایفا می‌کند که در این پژوهش مورد بررسی قرار گرفته‌اند. این پژوهش بر تأکید بر نقش مهم قیمت‌گذاری در سودآوری، همراه با تداخل سیاست‌های تولید و کنترل موجودی، و تأثیر مشترک آنها بر نتایج مالی تمرکز دارد. موضوع قیمت‌گذاری پویا در یک مسئله چندمحصوله و چنددوره‌ای در یک زنجیره تأمین سه سطحی با محصولات فاسدشدنی تاکنون به طور محدود مورد توجه قرار گرفته است. این مطالعه به بررسی قیمت‌گذاری پویا در یک زنجیره تأمین سه‌سطحی با محصولات فاسدپذیر با تأکید بر نقش مهم قیمت در سودآوری می‌پردازد. سیستم یکپارچه تولید-توزیع مورد مطالعه شامل تولیدکنندگان و مرکز توزیع متعدد است و هر یک از آن‌ها به یک گروه خاص از مشتریان خدمات ارائه می‌دهد. ارسال محصولات بین مرکز توزیع و مرکز توزیع بصورت مستقیم و همچنین بین مرکز توزیع و خردفروشان براساس مسئله مسیریابی وسیله تقلیلی است. به منظور بیشینه‌سازی تابع هدف، یک مدل برنامه‌ریزی عدد صحیح مختلط توسعه یافته و روشی الگوریتم ژنتیک برای دستیابی به جواب‌های با کیفیت ارائه شده است. به دلیل پیچیدگی بالای مسئله تحقیق (حتی در ابعاد کوچک) حل بهینه مساله به سادگی امکان‌پذیر نیست، به همین دلیل در ابتدا 2 دسته مسائل آزمایشی ساده که هر کدام شامل نه زیرمسئله هستند، توسط حل کننده GAMS نرم‌افزار BARON حل می‌شوند و نتایج حاصل با نتایج الگوریتم ژنتیک که با زبان سی‌شارپ پیاده‌سازی شده است، مقایسه می‌شوند. پس از تأیید کارآیی الگوریتم ژنتیک طراحی شده، پنج مسئله اصلی با نه زیرمسئله برای هر کدام، توسط الگوریتم ژنتیک حل شده‌اند.



A Hybrid Approach to Detect Researchers' Communities Based on Deep Learning and Game Theory

A. Torkaman^a, K. Badie^b, A. Salajegheh^{*a}, M. H. Bokaei^c, S. F. Fatemi Ardestani^d

^a Department of Computer, South Tehran Branch, Islamic Azad University, Tehran, Iran

^b E-Services and E-Content Research Group, IT Research Faculty, ICT Research Institute, Tehran, Iran

^c Department of Information Technology, ICT Research Institute, Tehran, Iran

^d Sharif University of Technology, Tehran, Iran

PAPER INFO

Paper history:

Received 18 June 2023

Received in revised form 24 July 2023

Accepted 25 July 2023

Keywords:

Complex Networks

Community Detection

Deep Learning

Cooperative Game

Non-Cooperative Game

ABSTRACT

Today, with the proliferation of complex networks and their large amounts of data, researchers have great concerns about the accurate community detection methods. The difficulty in analyzing these networks stems from their enormous size and the complex relationships among the members of the networks. It is difficult to analyze the deep relationships and mechanisms by just looking at the whole. Traditional methods have some problems and limitations when analyzing these networks such as feature extraction, high reliance on the initial phase settings, computational complexity, neglect of network relationships and content. From the perspective of relationships and interactions between individuals, the environment of complex networks can be compared to a game in which nodes acting as players or agents may join or leave a community based on similar structural or semantic characteristics. Consequently, there is a strong tendency to use cooperative and non-cooperative games to detect communities. Moreover, the amalgamation of deep learning techniques and game theory has recently been proven to be highly effective in extracting communities. Deep learning techniques have demonstrated enhanced capability in feature engineering and automate the process. In this study, the authors make effort to detect rational and accurate communities based on structural and content features with the help of traditional approaches, deep learning, as well as cooperative and non-cooperative games. The efficiency of this study is demonstrated by experimental findings on real datasets, and confirming that it is able enough to identify those communities that are more meaningful.

doi: 10.5829/ije.2023.36.11b.10

1. INTRODUCTION

One of the most crucial research area of study in complex networks is community detection. This has motivated many researchers over the years to find node groups based on modular patterns .

The ability to detect communities gives us further intuition into how groups function and how they form. Nodes within a community share similar characteristics and interests with one another and are more closely connected than other nodes within the network.

Various studies have provided different perspectives on communities extraction, such as partitioning approaches, hierarchical methods, edge removal

methods, as well as factorization-based and modularity-based approaches [1-3]. However, these scenarios may work well in some situations, as the issue of detecting community is inherently challenging and involves multiple factors, it is better to look at this issue from a different aspect.

In citation networks, communities are formed solely based on individuals self-interest. It is only in the interest of individuals to decide on their membership [4]. In one hand, we can conceive about a cooperative environment in which individuals connect with each other, form communities, and seek to promote the utility of the group, so there is also a kind of coordination between them.

*Corresponding Author Email: a_salajegheh@azad.ac.ir
(A. Salajegheh)

On the other hand, we can also imagine a competitive environment where agents compete to join or leave their communities and increase their profits.

Arguably, understanding these relationships requires rationality. By applying the theoretical economic principles of game theory, makes it easy to analyze these relationships.

In order to produce logical and ideal answers in challenging circumstances, game theory is a highly helpful mathematical instrument for analyzing strategic conditions and modelling the competition and collaboration between decision-makers [5]. Game theory is generally divided into cooperative and non-cooperative types. Games in which emphasize member cooperation is referred to cooperative game [6], in which each player attempts to increase the utility of the coalition [7]. In contrast, in non-cooperative games, players ignore the gains of the group and focus on increasing their individual utility.

Therefore, we address the idea of using cooperative and non-cooperative games to obtain more satisfying and trustworthy communities.

Recently, deep learning techniques along with game theory have proven to be extremely useful in extracting communities. Deep learning can provide features that are more informative and open up new perspectives in solving the community detection problems in large-scale networks.

In this respect, we utilized three well-known deep learning algorithms to obtain instructive characteristics. First, we learnt the embedding vectors from the network structure through the DeepWalk method [8]. Then, to extract the content features, we used LSTM [9] and Doc2vec [10] algorithms. After preparing the features, to identify the primary clusters, we applied a popular partitioning technique such as K-means to divide the network and provide the initial clusters. This helps reduce computational complexity. Rather than trying to initiate clustering through an agglomerative hierarchical approach.

Then, to stabilize the initial clusters and decrease them, we utilized the advantages of cooperative games. Meanwhile, we need to make sure that the nodes are properly assigned to the communities. So, we considered the privileges of non-cooperative games (Figure 1).

As the cooperative game is applied based on k-means clustering results instead of singleton clustering, the complexity is reduced. Additionally, since the non-cooperative game applied on the stabilized clusters extracted by cooperative game, so nodes as selfish players can only be compared with the significant and important nodes who have a high degree in their communities. As a result, there are fewer comparisons conducted as well as fewer nodes planning to leave their community due to improving their utilities.

Totally, the suggested method is more efficient and the computing cost noticeably reduced.

The main contributions of this paper are as follows.

- In this research, we used three well-known deep learning algorithms to obtain instructive features. Both structural and content features have been extracted through deep learning to help identify more meaningful communities. The proposed model can deal with long-term dependencies and solve the vanishing gradient problem.
- In order to reduce the computational complexity, rather than trying to initiate clustering by using an agglomerative hierarchical approach, we used a traditional clustering method, k-means, to divide the network and provide the initial clusters.
- Use of traditional clustering methods such as K-means does not guarantee the clusters obtained and may generate more clusters than the actual ones, so by using cooperative game theory we can reduced and stabilized the extracted communities.
- In some cases, there may be a limited number of nodes belonging to different communities, or there may be single nodes that do not belong to a proper community. In such cases, we utilized the benefits of non-cooperative game which helps rationally

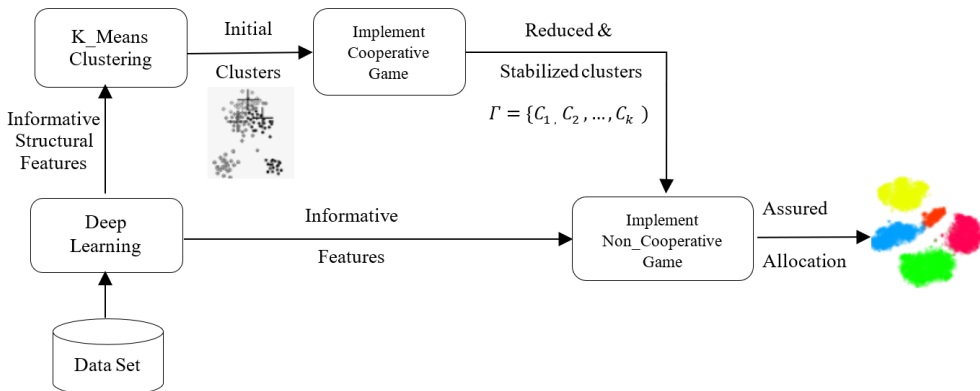


Figure 1. The proposed framework

allocate these nodes to well-established communities.

- Individual nodes which have no connections with the rest of the network can also be assigned to communities according to their content.

The following sections of this essay are structured as follows: Section 2 reviews the literature on several approaches to the challenge of community detection. In section 3, the suggested model is mentioned. Section 4 discusses the analysis of the experimental findings, and section 5 presents concluding remarks and further research.

2. RELATED WORK

A community consists of multiple components that are in close proximity to each other only within their respective groups, in contrast to the rest of the network. Individuals that reside in the same community share similar characteristics, such as interests, social links, locations, occupations, etc. [11, 12].

The nodes belonging to the same community typically have similar responsibilities and/or functions [13].

Community detection is one of the most exciting research areas, which has caught the interest of numerous researchers in a variety of fields of study, including biology, statistics, and computer science [14]. Community detection is typically an NP-complete issue [13, 14].

Several studies published in the literature attempt to extract high-quality communities. Some of them used the graph partitioning techniques such as K-means to detect communities [15-19].

However, these methods have significant drawbacks like weak cluster descriptors and high sensitivity to initialization. Hierarchical clustering based on agglomerative or divisive methods is another aspect widely used in literatures [20-23]. Some researchers focused on improving quality metrics such as modularity for obtaining a high-quality community structure [24].

In recent years, methods based on network representations by using deep learning have become popular for community detection. Some of them respected the structure perspective [8, 25-27]. Salehi and Pouyan [11] proposed a model for detecting communities within social networks based on deep learning. In this method, a nonlinear embedding of the original graph is fed to stacked auto-encoders to train. Then a clustering algorithm is employed to extract communities. However, These methods work well, but they only consider the structural information and ignore node content information.

Other methods, incorporate the node content information into network representation [28-30].

These approaches work logically. However, it is beneficial to use methods that are based on both structural and content information to detect communities.

Over the past two decades, various studies have proposed game-theoretic approaches to identify communities.

In fact, community detection can be likened to a game in which each node makes rational decisions about which community to join in order to maximize its score. Additionally, community members try to increase the utility of group.

Many researches addressed the challenge of community detection by using the non-cooperative game, while others use cooperative one. In line with the cooperative game, McSweeney et al. [31] treated each node as a player in a hedonic game, which aims to create an stable community structure.

The Shapley value was recommended by Zhou et al. [32] to identify communities within a specific social network. They also suggested a coalitional game for detecting communities based on the node structure in 2015.

Each node was envisioned by Hajibagheri et al. [33] as a logical being attempting to maximize the Shapley value. Avrachenkov and his colleagues [34] suggested two cooperative game theory methods based on hedonic and Myerson value games for detecting communities. Both methods extract communities with varying resolutions.

Nodes were taken into account by Zhou et al. [35] as players attempted to increase the utility of their coalitions by taking part in a cooperative games. In this study, an edge weight computation was proposed to determine the Shapley value for coalitions and nodes.

According to Chen et al. [36], on the non-cooperative side, agent's utility is computed as a gain and loss function based on modularity and community membership, respectively. Therefore, the game's local equilibrium reveals community organization at the end. Furthermore, Narayananam and Narahari [37] believed that the utility of each vertex is a linear function, imagining each node as an agent wanting to join a community. In this study, community stability is ensured via Nash stability.

A methodology based on the iterative game have been considered by Alvari et al. [38] for detecting communities in complex networks. They considered nodes as logical players who enter the game to increase their utility.

A weighted potential game was developed by Havvaei and Deo [39] to demonstrate community structure. When a community reaches the Nash equilibrium point, it stabilizes. Co-game is a game-theoretical method for identifying communities in real-world networks, as described by Zhao et al. [40]. This technique combines individual games and

equilibrium to create finer-grained partitions in the detection process.

A game-theoretical algorithm for detecting communities in online complex networks was developed by Vincenzo et al. [41]. They modeled the process of community formation as a game, in which each node as a player aiming to maximize its goals. They used a game theory approach to simulate how communities form. Each node is regarded as a player trying to maximize its utility.

SIMGT [42] is a useful method for identifying communities, which assumes nodes as self-interested players participating in a non-cooperative game. To update players identities, they used a stochastic gradient ascent.

Zhou et al. [43] proposed a novel method for detecting communities based on both cooperative and non-cooperative games. This method imagined nodes as players in coalitional form games who want to increase the utility of the group, meanwhile playing non-cooperative games to increase their own utility.

Similar to the hierarchical agglomerative method, this approach considers a cooperative game in the initial phase, where nodes or agents are clustered as singletons, and coalitions with the highest utility value are combined into larger coalitions until high-quality coalitions are attained. This method, like other agglomeration approaches typically has considerable computational cost for large data sets. Therefore, it is recommended to integrate the first phase with other clustering techniques.

In this regard, Torkaman et al. [44] proposed a Four-Stage Algorithm (FSA), which find the important central nodes, propagate labels, and identify initial communities to solve this problem. However, this method focuses only on structural information and omits content information.

Therefore, in this study, we proposed a new community detection model based on both structural and content features, using a traditional clustering method to reduce the initial computational cost, and integrate cooperative and non-cooperative games to provide reliable and stable communities.

3. PROPOSED METHOD

3.1. Preliminary A citation network is a type of complex network that may include various papers, books, linked by co-citation relationships. A key issue in network analysis is how to represent these networks. Assume a network $G=(V,E,D)$ and a set of vertices $V=\{v_1, v_2, v_3, \dots, v_n\}$, n is the number of vertices. $E = \{e_{ij}\}_{i,j=1}^n$ the set of edges, and the edge among v_i and v_j is encoded as e_{ij} . D is the set of textual data which relates to each node of v_i .

The goal of the network-embedding problem is to develop the mapping function: $f: V \rightarrow \mathbb{R}^d$ which maps

each node into a low-dimensional space and extracts the network's structural and content characteristics. Nodes in this representation space that have similar structure or content are located close to one another.

3.1.1. Community Detection

Community detection is an operation to detect M communities; $C = \{C_1, C_2, \dots, C_M\}$, so $M \ll N$ and $\cup_{m=1}^M C_m = V$. if $C_i \neq C_j$ for any subset of V , then nodes can only join one community and are referred to as non-overlapping communities. If it can join more than one community, it entitled as overlapping communities [45].

3.1.2. Game Theory Background

Game theory is a mathematical tool that focuses on decision-making problems between two or more entities engaged in strategic scenarios where one player's decisions affect the other players' payoffs [46].

The interaction between vertices in a complex network may be compared to a game in which a node acts like a player and seeks to join or leave the community depending on its utility in a target community.

Let u_i be the utility of vertex $i \in V$. For every C_i , $u_i(C_i)$ is the utility function of i by existing in a community C_i . Every vertex seeks to become a member of a community and increase its own utility. It should be emphasized any node's utility is depends on the community to which is it belongs.

3.2. Our Proposed Model

This study utilizes deep learning approaches and game theory to find established and accurate communities, as previously described.

Figure 1 shows our suggested framework. First, according to our previous work [44], we extract informative features by using three popular deep learning approaches.

The architecture of the proposed representation is shown in Figure 2. It projects each node into a low dimensional region to capture the network's structural and content properties [44].

As shown in Figure 2, we learn embedding vectors from network structure by DeepWalk [8] method, to provide deep structural features to the K-means clustering algorithm. Then, to extract the content features, we used the concatenated vectors of both Long Short-Term Memory (LSTM) [9] and Doc2vec [10] algorithms, to enhance each other to extract the context sequence from the paper's titles or abstracts more accurately. Therefore, in this paper, we applied the same loss function used by Torkaman et al. [44] to extract the structural and content properties of the nodes:

$$\mathcal{L} = \mathcal{L}_{Doc2Vec} + \mathcal{L}_{LSTM} + \mathcal{L}_{Deepwalk} \quad (1)$$

Afterward, in order to partition the network and find initial communities, we applied a common partitioning

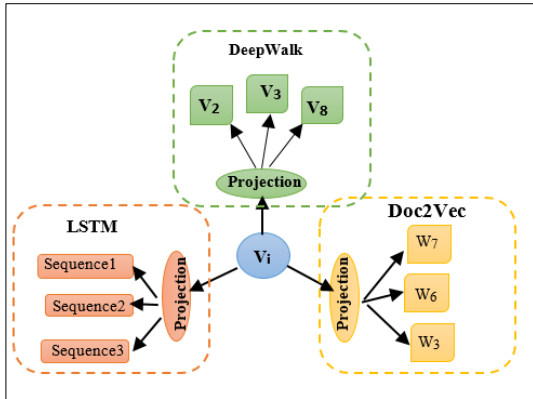


Figure 2. Architecture of our network representation

technique such as the k-means algorithm [47]. This helps reduce computational complexity rather than trying to initiate clustering by using an agglomerative hierarchical approach.

The elbow approach is used to find the optimum value of K [48], which is one of the most popular methods for choosing the ideal value of K.

Therefore, the initial clusters $B = \{B_1, B_2, \dots, B_k\}$, or coalition structure is prepared. In many instances, the number of initially extracted communities is numerous or located far from the actual desired communities that they become unsustainable. Thus, we used the advantages of cooperative (coalitional form) and non-cooperative games to decrease the number of these communities, make them similar to the actual ones and precisely map nodes to communities.

Implementing Cooperative Game: Nodes in a citation network are assumed to act as rational agents striving to form communities (coalitions) and increase the utility of groups. Fewer nodes communities are merged with bigger ones until the merge operation no longer improves the utility of the merged coalitions. In this case, neither coalition intends to cooperate with the other because the game has reached equilibrium. The game starts with an initial cluster from the K-Means algorithm.

Given B_i is a coalition of $G = \langle V, E \rangle$, which is achieved by k-means method.

Definition 1: The utility function of coalition, $u(B_i)$ of B , is based on the function was described in our previous work [43]:

$|E|$ is the total number of edges in G , $e(B_i)$ is the number of edges connecting vertices within B_i , and $D(B_i)$ is the sum of the degree of the vertices in B_i . In fact, $u(B_i)$ comes from Newman's modularity metric Q [49].

In general, if $\Delta u(B_i, B_{ij}) > 0$ and $\Delta u(B_j, B_{ij}) > 0$ then two coalitions are merged [43]. Communities that recently joined are added to a new list $\Gamma = \{C_1, C_2, \dots, C_n\}$.

The final extracted coalitions are stable if there are no coalition intends to participate in merge operation to

increase its utility. That is, if $u(B_i) > u(B_i + B_j) \forall B_j \neq B_i$, B_i does not want to join B_j and it favors to remain within the past situation. In this way, an equilibrium state of the coalition is achieved.

Implementing Non-Cooperative Games: After reaching a set of stable communities, non-cooperative games are played. Single nodes with connections that might not satisfy with their utilities may not be in their correct coalition.

Each node in this game is viewed as a selfish agent who seeks to join or leave a community from Γ depending on its utility measure. It would leave its existing alliance and join a new one, if joining a coalition would increase its utility.

Since nodes in a citation network have structure and content information, the utility function should be the combination of them, especially in the case of single nodes, which can only be determined based on their content similarity.

Definition 2: The utility function of an individual (node): Let $v \in V$, $C_i \in \Gamma$, the utility function is as follows:

$$u_v(C_i) = \alpha W + \beta \frac{e(v, C_i)}{d(v)} \quad (3)$$

$e(v, C_i)$; the number of edges among v and coalition C_i . $d(v)$ is the degree of v and W is the informative feature vector. α, β are binary value $\alpha = 0$, which means the network only consist of structural value. $\beta = 0$ means v is a singleton node and just the similarity determines the closeness between node v and C_i . $u_v(C_i)$ measures the similarity between v and the targeted community C_i . The greater value of $u_v(C_i)$, indicates more similarity between v and C_i .

Definition 3: (Join & Leave): node v join the community C_i :

$$C_i \leftarrow C_i + \{v\}$$

If $v \notin C_i$ and $u_v(C_i)$ is the maximum value that v can achieve through joining communities.

Node v leave its community C_n and join community C_i :

$$C_n \leftarrow C_n - \{v\}$$

if $v \in C_n$ and $u_v(C_n) < u_v(C_i)$.

Finally, when agents have no incentive to leave their own community and join others, a kind of equilibrium has prevailed and communities have reached a stable state.

Cooperative and non-cooperative algorithms described in Algorithms 1 and 2.

$$u(B_i) = \sum_{B_i \in B} \left(\frac{e(B_i)}{|E|} - \left(\frac{D(B_i)}{2|E|} \right)^2 \right) \quad (2)$$

Algorithm 1 Cooperative Game

1: Input: the initial coalitions achieved by k-means algorithm

$$B = \{B_1, B_2, \dots, B_k\}$$

2: Output: Community reduction and stabilization $\Gamma = \{C_1, C_2, \dots, C_n\}$

```

3:  $\Gamma = \emptyset$ 
4: for all  $(B_i, B_j \in B \text{ and } B_j \neq B_i)$  do
5:   if  $\Delta u(B_{ij}) > \Delta u(B_j) \& \Delta u(B_j) > 0$  then
6:      $\Gamma = \{B_{ij}\} - \{B_i\} - \{B_j\}$ 
7:   else
8:     return  $\Gamma$ 
9:   end if
10: end for
(Continue until no coalition is willing to join the other in order to
enhance its utility)

```

As already mentioned, the initial set of communities (B) is provided by the K-means algorithm. Then, the game initials are between these communities. Given B_i, B_j two communities in B , If the union of these two communities (B_{ij}) has more benefits than either community alone, a join operation takes place and B_{ij} is added to the new list Γ . The algorithm may terminate when no coalition intends to use the join mechanism and improve its utility.

Algorithm 2 non-Cooperative game

```

1: Input: the cooperative game's reduced and stabilized communities
 $\Gamma = \{C_1, C_2, \dots, C_n\}$ 
2: Output: Node allocation assurance and ultimate stable community
structure  $C = \{C_1, C_2, \dots, C_n\}$ 
3:  $\delta = \emptyset$ 
4: for all  $(v \in C_i)$  do
5:    $\delta = C - C_i$ 
6:   for all  $(C_j \in \delta)$  do
7:     if  $(\Delta u_v(C_j)) > (\Delta u_v(C_i))$ 
8:        $C_j = C_j + \{v\}$ 
9:        $C_i = C_i - \{v\}$ 
10:    end if
11:   return  $C_i, C_j$ 
12: end for
(Continue until nodes are not eager to leave their current communities
and join new ones.)

```

All nodes are initially placed in their own community provided by Algorithm 1. Each vertex assesses other communities and determines how useful it is to join them. If the value exceeds the utility, it quits its current coalition and joins the new one. The algorithm will stop when the agents chooses to remain in their current situation rather than join other communities to increase their utility values.

4. EXPERIMENTS

In this section, extensive experiments are conducted to validate the effectiveness of our proposed method. two widely used real-world datasets and six state-of-the-art baselines are adopted for the experiment.

4. 1. Datasets

We use actual networks to demonstrate the potential and efficiency of the suggested approach, and observe the experimental results. In this regard, we run the proposed approach on two real citation networks (DBLP [50], Citeseer [51]).

Dblp: Dblp is a well-known citation network containing bibliography data in computer science. In total, it includes 60,744 papers and 52,890 edges and four research areas consist of data mining, database, the artificial intelligent, and computer vision.

Citeseer [51]: This data set is a citation network of computer science publications. It contains 3312 publications and 4,732 edges, each of the papers is labeled as one of six categories, artificial intelligence, agents, database, human-computer interaction, information retrieval, and machine learning.

4. 2. Baseline Learning Algorithms

For a comprehensive evaluation, we compare our proposed algorithm with a number of methods from different categories.

K-means [47]: A popular classical shallow partitioning algorithm for clustering, alternately updates the location of the cluster center and the distance of the sample from the cluster center.

Spectral [52]: A classical shallow clustering method based on graph theory, using the node adjacency matrix as the similarity matrix.

Louvain [53]: The Louvain Method is a widely used greedy algorithm for community detection by network modularity maximization.

ARGAE [54]: The Adversarial Regularized Graph Autoencoder (ARGAE) method is a graph clustering method, where a discriminator is utilized to ensure the deep representation calculated by encoder matching a prior distribution.

DAEGC [55]: deep attentional embedded graph clustering (DAEGC), is a graph clustering method utilizing a self-optimizing module to learn a clustering-oriented deep representation.

MGCCN [56]: Multilayer Graph Contrastive Clustering Network (MGCCN), a generic and effective autoencoder framework for multilayer graph clustering.

4. 3. Analysis of Experimental Results

We calculated the accuracy(ACC) [57], the Normalized mutual information (NMI) [32], the purity measure [13] and between the extracted community structures, taking into account the ground truth of the datasets as an evaluation metric.

We evaluate the effectiveness of the suggested algorithm based on the above metrics, Table 1 and Figure 3 show the accuracy, purity and NMI values of only k-means after applying the cooperative game and eventually running the non-cooperative game.

All the algorithms were run in Python on a desktop PC with an Intel Core i7 CPU (3.4 GHz) and 8 GB RAM.

According to the results (Table 1), after executing the cooperative game with k-means results, ACC, NMI and purity scores improved due to the cluster merging process and a stable point was reached. K-means method does not work well in this situation due to its restrictions such as weak cluster descriptors and its high degree of sensitivity to initial parameters such as determination of the K values.

As is shown in Figure 3, promising results were obtained by running the non-cooperative game on the results of the cooperative strategy.

This is because each node tries to join a community or leave the current community based on its semantic and

structural features. In particular, individual nodes that are not connected to a community can easily increase their utility by joining a community based on semantic features. This situation is obvious because the dblp dataset contains a significant amount of single nodes. Once the equilibrium point is reached, all nodes and communities are in stable state.

For a comprehensive evaluation, we compared our proposed model with different methods in different categories.

As shown in Table 2 and Figure 4, it can be observed that our proposed method achieves competitive performance compared with all the baseline methods according to two clustering metrics, which demonstrates

TABLE 1. Accuracy (ACC), Normalized mutual information (NMI) and Purity evaluation metrics after running each method on the Dblp, Citeseer dataset with ground truth

Metric	Purity		NMI		ACC	
	Datasets		Citeseer	Dblp	Citeseer	Dblp
Methods	Citeseer	Dblp	Citeseer	Dblp	Citeseer	Dblp
K_Means	0.618	0.735	0.312	0.431	0.544	0.604
Cooperative Game	0.678	0.739	0.345	0.433	0.612	0.709
Non-Cooperative Game	0.853	0.886	0.597	0.762	0.788	0.907

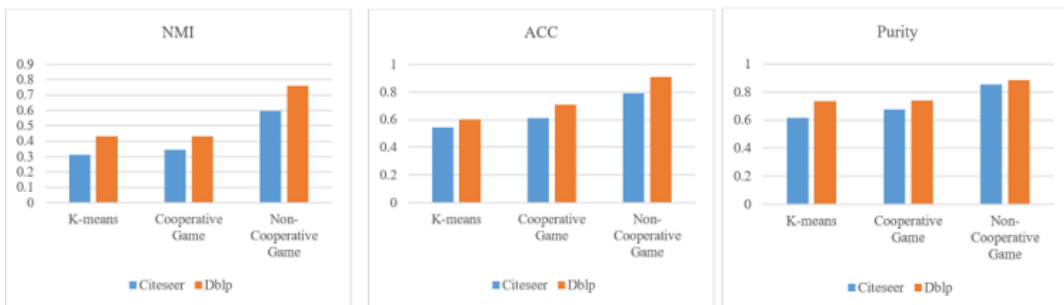


Figure 3. Accuracy (ACC), Normalized mutual information (NMI) and Purity evaluation metrics after running each method on the dblp dataset with ground truth

TABLE 2. Clustering results on Citeseer and Dblp datasets

Metric Methods	NMI		ACC	
	Datasets			
	Citeseer	Dblp	Citeseer	Dblp
K-means	0.312	0.431	0.544	0.604
Spectral	0.056	0.223	0.239	0.402
Louvain	0.409	0.504	0.437	0.513
ARGAE	0.350	0.495	0.573	0.605
DAEGC	0.397	0.561	0.672	0.869
MGCCN	0.455	0.615	0.715	0.830
Ours	0.512	0.762	0.788	0.907

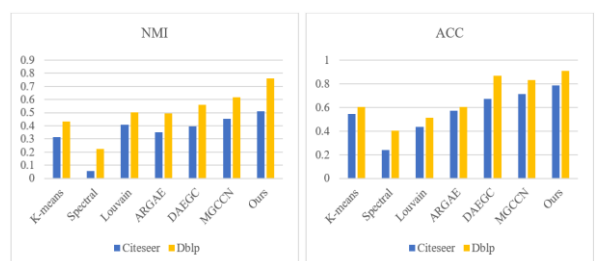


Figure 4. ACC and NMI comparison results on different datasets and methods

the effectiveness of our method. Specifically, we can make the following interesting observations:

- The proposed method and other Graph Convolutional Network (GCN) based methods (DAEGC, MGCCN) show superiority over K-Means, Louvain and Spectral methods, which demonstrates that methods based on both structural and information characteristics, performs better than only using one of them.
- According to the results, our proposed algorithm outperformed other methods in Dbip and Citeseer. In fact, this algorithm yielded higher values of accuracy and NMI than the other existing methods. This is due to utilizing the combination of deep learning and game theory to find established and accurate communities.
- Our method yields a relative increase in NMI values of 35.03% for ARGAE and 26.3% for DAEGC for the Dbip dataset, and the increase is even greater for the Citeseer dataset. These GCN-based approaches use adjacency matrices to represent topological features, but have limitations on large datasets.
- MGCCN is a close competitor to our method, but as we can see, our method has better performance. MGCCN is a generic framework which designed for multi-view graph clustering. MGCCN employs a self-supervised component that iteratively updates the node embedding and clustering, so, there is no guarantee that samples will be assigned to the correct clusters. Therefore, in some cases, “highly confident” nodes are used that act as a soft label to supervise the clustering process. While our method uses both cooperative and non-cooperative methods to solve this problem, and the resulting clusters are reliable and stable.

4.4. Parameter Sensitivity We have used the same parameter settings that are reported by Torkaman et al. [44] for deep learning part. We set window size $b=8$, The embedding size is set to $k = 300$ (100 for each proposed deep learning methods), the learning rate= 0.001 and Adam [58] as the optimizer.

Game theory has been used as a tool to achieve more reliable and stable communities. The game parameters are generic and we do not interfere in its settings.

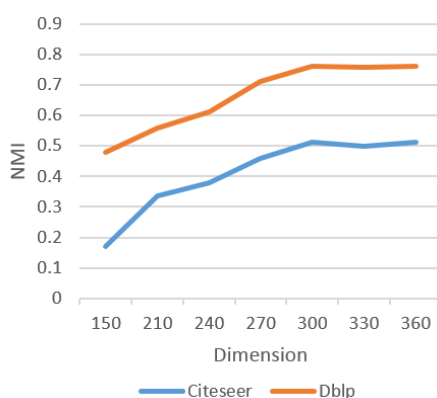


Figure 5. The effect of embedding size on the NMI result

One of the important parameters in the proposed model is the embedding size. the proper size for this vector is 100 for each structural and content vectors. If the size of the vector exceeds this value, the efficiency of the proposed algorithm does not change significantly, only the dimensionality of the problem increases (Figure 5).

4.5. Network Visualization Finally, we leverage 2D t-SNE projection [59, 60] to visualize the results of the community detection method applied to the dblp dataset.

As shown in Figure 6(a), in the visualization of K_Means, the clusters are not so clear. In Figure 6(b), the cooperative game method outperforms K_Means, but for some classes do not have a clear resolution. In Figure 6(c), after using the non-cooperative approach, the clusters become clearer and almost have a meaningful layout for each community.

5. CONCLUDING REMARKS

In this paper, we proposed a robust and efficient community detection approach that integrates both the topological and content information for community detection. To find the initial clusters, we first used a traditional clustering technique, K-means. Then, to decrease the obtained clusters and fix them, we used a cooperative game, and finally play a non-cooperative game on each node to guarantee a fair and rational allocation of nodes to the established communities.

Experimental findings support the effectiveness of our method, showing how cooperative and non-cooperative game techniques complement each other to identify safer and more stable communities, thereby improving K-means results.

The proposed algorithm shows high performance on medium-sized datasets. However, there are limitations for very large networks with many extracted communities, it takes time to identify the right communities.

Future work may use a different splitting method to split the network and provide initial communities instead of using K-means.

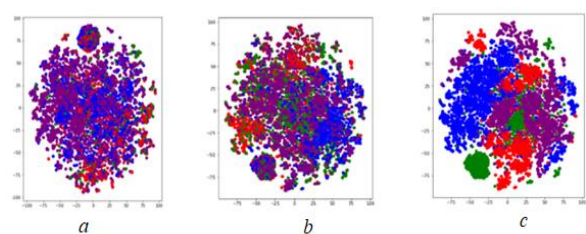


Figure 6. Visualization on the dblp dataset. Colors demonstrate the ground-truth communities

Additionally, various deep learning techniques can be used to extract more advantageous features. The utility functions of the game components, are supposed to be replaced by the other deep learning methods. Finally, this framework can be extended not only to weighted networks, but also to overlapping networks with semantic content.

6. REFERENCES

1. Fortunato, S., "Community detection in graphs", *Physics Reports*, Vol. 486, No. 3-5, (2010), 75-174. <https://doi.org/10.1016/j.physrep.2009.11.002>
2. Coscia, M., Giannotti, F. and Pedreschi, D., "A classification for community discovery methods in complex networks", *Statistical Analysis and Data Mining: The ASA Data Science Journal*, Vol. 4, No. 5, (2011), 512-546. <https://doi.org/10.1002/sam.10133>
3. Krishna Prasad, M. and Rao Chintalapudi, S., "Mining overlapping communities in real-world networks based on extended modularity gain", *International Journal of Engineering, Transactions A: Basics*, Vol. 30, No. 4, (2017), 486-492. doi: 10.5829/idosi.ije.2017.30.04a.05.
4. Jonnalagadda, A. and Kuppusamy, L., "A survey on game theoretic models for community detection in social networks", *Social Network Analysis and Mining*, Vol. 6, (2016), 1-24. doi: 10.1007/s13278-016-0386-1.
5. Nash, J., "Non-cooperative games. The annals of mathematics, second series, volume 54, issue 2", (1951).
6. Zlotkin, G. and Rosenschein, J.S., "Coalition, cryptography, and stability: Mechanisms for coalition formation in task oriented domains", Alfred P. Sloan School of Management, Massachusetts Institute of Technology, (1994).
7. Fadaei, M., Tavakkoli-Moghaddam, R., Taleizadeh, A. and Mohammaditabar, D., "Cooperative benefit and cost games under fairness concerns", *International Journal of Engineering, Transactions B: Applications*, Vol. 31, No. 8, (2018), 1250-1257. doi: 10.5829/ije.2018.31.08b.09.
8. Perozzi, B., Al-Rfou, R. and Skiena, S., "Deepwalk: Online learning of social representations", in Proceedings of the 20th ACM SIGKDD international conference on Knowledge discovery and data mining, (2014), 701-710.
9. Taheri, A., Gimpel, K. and Berger-Wolf, T., "Sequence-to-sequence modeling for graph representation learning", *Applied Network Science*, Vol. 4, (2019), 1-26. <https://doi.org/10.1007/s41109-019-0174-8>
10. Mikolov, T., Sutskever, I., Chen, K., Corrado, G.S. and Dean, J., "Distributed representations of words and phrases and their compositionality", *Advances in Neural Information Processing Systems*, Vol. 26, No., (2013). doi: 10.48550/arXiv.1310.4546.
11. Salehi, S. and Pouyan, A., "Detecting overlapping communities in social networks using deep learning", *International Journal of Engineering, Transactions C: Aspects*, Vol. 33, No. 3, (2020), 366-376. doi: 10.5829/ije.2020.33.03c.01.
12. Indrawan, G., Setiawan, H. and Gunadi, A., "Multi-class svm classification comparison for health service satisfaction survey data in bahasa", *HighTech and Innovation Journal*, Vol. 3, No. 4, (2022), 425-442. doi: 10.28991/HIJ-2022-03-04-05.
13. Chakraborty, T., Dalmia, A., Mukherjee, A. and Ganguly, N., "Metrics for community analysis: A survey", *ACM Computing Surveys (CSUR)*, Vol. 50, No. 4, (2017), 1-37. doi: 10.1145/3091106.
14. Cavallari, S., Zheng, V.W., Cai, H., Chang, K.C.-C. and Cambria, E., "Learning community embedding with community detection and node embedding on graphs", in Proceedings of the 2017 ACM on Conference on Information and Knowledge Management, (2017), 377-386.
15. Van Laarhoven, T. and Marchiori, E., "Local network community detection with continuous optimization of conductance and weighted kernel k-means", *The Journal of Machine Learning Research*, Vol. 17, No. 1, (2016), 5148-5175.
16. Liu, J., "Comparative analysis for k-means algorithms in network community detection", in Advances in Computation and Intelligence: 5th International Symposium, ISICA 2010, Wuhan, China, October 22-24, 2010. Proceedings 5, Springer, (2010), 158-169.
17. Ferreira, L.N., Pinto, A. and Zhao, L., "Qk-means: A clustering technique based on community detection and k-means for deployment of cluster head nodes", in The 2012 International Joint Conference on Neural Networks (IJCNN), IEEE, (2012), 1-7.
18. Niu, Y., Kong, D., Liu, L., Wen, R. and Xiao, J., "Overlapping community detection with adaptive density peaks clustering and iterative partition strategy", *Expert Systems with Applications*, Vol. 213, (2023), 119213. <https://doi.org/10.1016/j.eswa.2022.119213>
19. Wu, Y., Fu, Y., Xu, J., Yin, H., Zhou, Q. and Liu, D., "Heterogeneous question answering community detection based on graph neural network", *Information Sciences*, Vol. 621, (2023), 652-671. <https://doi.org/10.1016/j.ins.2022.10.126>
20. Chen, J., Li, Y., Yang, X., Zhao, S. and Zhang, Y., "Vghc: A variable granularity hierarchical clustering for community detection", *Granular Computing*, Vol. 6, (2021), 37-46. <https://doi.org/10.1007/s41066-019-00195-1>
21. Yin, C., Zhu, S., Chen, H., Zhang, B. and David, B., "A method for community detection of complex networks based on hierarchical clustering", *International Journal of Distributed Sensor Networks*, Vol. 11, No. 6, (2015), 849140. <https://doi.org/10.1155/2015/849140>
22. Zhou, L., Lü, K., Yang, P., Wang, L. and Kong, B., "An approach for overlapping and hierarchical community detection in social networks based on coalition formation game theory", *Expert Systems with Applications*, Vol. 42, No. 24, (2015), 9634-9646. <https://doi.org/10.1016/j.eswa.2015.07.023>
23. Li, C., Bai, J., Wenjun, Z. and Xihao, Y., "Community detection using hierarchical clustering based on edge-weighted similarity in cloud environment", *Information Processing & Management*, Vol. 56, No. 1, (2019), 91-109. <https://doi.org/10.1016/j.ipm.2018.10.004>
24. Newman, M.E., "Modularity and community structure in networks", *Proceedings of the National Academy of Sciences*, Vol. 103, No. 23, (2006), 8577-8582. <https://doi.org/10.1073/pnas.0601602103>
25. Grover, A. and Leskovec, J., "Node2vec: Scalable feature learning for networks", in Proceedings of the 22nd ACM SIGKDD international conference on Knowledge discovery and data mining, (2016), 855-864.
26. Wang, D., Cui, P. and Zhu, W., "Structural deep network embedding", in Proceedings of the 22nd ACM SIGKDD international conference on Knowledge discovery and data mining, (2016), 1225-1234.
27. Tang, J., Qu, M., Wang, M., Zhang, M., Yan, J. and Mei, Q., "Line: Large-scale information network embedding", in Proceedings of the 24th international conference on world wide web, (2015), 1067-1077.
28. Yang, C., Liu, Z., Zhao, D., Sun, M. and Chang, E.Y., "Network representation learning with rich text information", in IJCAI. Vol. 2015, (2015), 2111-2117.

29. Pan, S., Wu, J., Zhu, X., Zhang, C. and Wang, Y., "Tri-party deep network representation", *Network*, Vol. 11, No. 9, (2016), 12.
30. Chang, J. and Blei, D., "Relational topic models for document networks", in Artificial intelligence and statistics, PMLR. (2009), 81-88.
31. McSweeney, P.J., Mehrotra, K. and Oh, J.C., "A game theoretic framework for community detection", in 2012 IEEE/ACM International Conference on Advances in Social Networks Analysis and Mining, IEEE. (2012), 227-234.
32. Zhou, L., Lü, K., Cheng, C. and Chen, H., "A game theory based approach for community detection in social networks", in Big Data: 29th British National Conference on Databases, BNCOD 2013, Oxford, UK, July 8-10, 2013. Proceedings 29, Springer. (2013), 268-281.
33. Hajibagheri, A., Alvari, H., Hamzeh, A. and Hashemi, S., "Social networks community detection using the shapley value", in The 16th CSI International Symposium on Artificial Intelligence and Signal Processing (AISP 2012), IEEE. (2012), 222-227.
34. Avrachenkov, K.E., Kondratev, A.Y., Mazalov, V.V. and Rubanov, D.G., "Network partitioning algorithms as cooperative games", *Computational Social Networks*, Vol. 5, No. 1, (2018), 1-28. doi: 10.1186/s40649-018-0059-5.
35. Zhou, X., Cheng, S. and Liu, Y., "A cooperative game theory-based algorithm for overlapping community detection", *IEEE Access*, Vol. 8, (2020), 68417-68425. doi: 10.1109/ACCESS.2020.2985397.
36. Chen, W., Liu, Z., Sun, X. and Wang, Y., "A game-theoretic framework to identify overlapping communities in social networks", *Data Mining and Knowledge Discovery*, Vol. 21, (2010), 224-240. https://doi.org/10.1007/s10618-010-0186-6
37. Narayanan, R. and Narahari, Y., "A game theory inspired, decentralized, local information based algorithm for community detection in social graphs", in Proceedings of the 21st International Conference on Pattern Recognition (ICPR2012), IEEE. (2012), 1072-1075.
38. Alvari, H., Hashemi, S. and Hamzeh, A., "Detecting overlapping communities in social networks by game theory and structural equivalence concept", in Artificial Intelligence and Computational Intelligence: Third International Conference, AICI 2011, Taiyuan, China, September 24-25, 2011, Proceedings, Part II 3, Springer. (2011), 620-630.
39. Havvaei, E. and Deo, N., "A game-theoretic approach for detection of overlapping communities in dynamic complex networks", *International Journal of Computational Methods*, Vol. 1, (2016), 313-324. https://doi.org/10.48550/arXiv.1603.00509
40. Zhao, X., Wu, Y., Yan, C. and Huang, Y., "An algorithm based on game theory for detecting overlapping communities in social networks", in 2016 International Conference on Advanced Cloud and Big Data (CBD), IEEE. (2016), 150-157.
41. Moscato, V., Picariello, A. and Sperli, G., "Community detection based on game theory", *Engineering Applications of Artificial Intelligence*, Vol. 85, (2019), 773-782. https://doi.org/10.1016/j.engappai.2019.08.003
42. Wang, Y., Bu, Z., Yang, H., Li, H.-J. and Cao, J., "An effective and scalable overlapping community detection approach: Integrating social identity model and game theory", *Applied Mathematics and Computation*, Vol. 390, (2021), 125601. https://doi.org/10.1016/j.amc.2020.125601
43. Zhou, L., Yang, P., Lü, K., Wang, L. and Chen, H., "A fast approach for detecting overlapping communities in social networks based on game theory", in Data Science: 30th British International Conference on Databases, BICOD 2015, Edinburgh, UK, July 6-8, 2015, Proceedings 30, Springer. (2015), 62-73.
44. Torkaman, A., Badie, K., Salajegheh, A., Bokaei, M.H. and Ardestani, S.F.F., "A four-stage algorithm for community detection based on label propagation and game theory in social networks", *AI*, Vol. 4, No. 1, (2023), 255-269. https://doi.org/10.3390/ai4010011
45. Torkaman, A., Badie, K., Salajegheh, A., Bokaei, M.H. and Fatemi, S.F., "A hybrid deep network representation model for detecting researchers' communities", *Journal of AI and Data Mining*, Vol. 10, No. 2, (2022), 233-243. https://doi.org/10.22044/jadm.2022.11243.2277
46. Myerson, R., "Game theory: Analysis of conflict harvard univ", *Press, Cambridge*, Vol. 3, (1991). https://doi.org/10.2307/j.ctvjsf522
47. MacQueen, J., "Some methods for classification and analysis of multivariate observations", in Proceedings of the fifth Berkeley symposium on mathematical statistics and probability, Oakland, CA, USA. Vol. 1, (1967), 281-297.
48. Bholowalia, P. and Kumar, A., "Ebk-means: A clustering technique based on elbow method and k-means in wsn", *International Journal of Computer Applications*, Vol. 105, No. 9, (2014). doi: 10.5120/18405-9674.
49. Newman, M.E. and Girvan, M., Mixing patterns and community structure in networks, in Statistical mechanics of complex networks. 2003, Springer.66-87.
50. Lusseau, D., "The emergent properties of a dolphin social network", *Proceedings of the Royal Society of London. Series B: Biological Sciences*, Vol. 270, No. suppl_2, (2003), S186-S188. doi: 10.1098/rspb.2003.0057.
51. Giles, C.L., Bollacker, K.D. and Lawrence, S., "Citeseer: An automatic citation indexing system", in Proceedings of the third ACM conference on Digital libraries. (1998), 89-98.
52. Ng, A., Jordan, M. and Weiss, Y., "On spectral clustering: Analysis and an algorithm", *Advances in Neural Information Processing Systems*, Vol. 14, (2001).
53. Blondel, V.D., Guillaume, J.-L., Lambiotte, R. and Lefebvre, E., "Fast unfolding of communities in large networks", *Journal of Statistical Mechanics: Theory and Experiment*, Vol. 2008, No. 10, (2008), P10008. doi: 10.1088/1742-5468/2008/10/P10008.
54. Pan, S., Hu, R., Long, G., Jiang, J., Yao, L. and Zhang, C., "Adversarially regularized graph autoencoder for graph embedding", arXiv preprint arXiv:1802.04407, (2018). https://doi.org/10.48550/arXiv.1802.04407
55. Wang, C., Pan, S., Hu, R., Long, G., Jiang, J. and Zhang, C., "Attributed graph clustering: A deep attentional embedding approach", arXiv preprint arXiv:1906.06532, (2019). https://doi.org/10.48550/arXiv.1802.04407
56. Liu, L., Kang, Z., Ruan, J. and He, X., "Multilayer graph contrastive clustering network", *Information Sciences*, Vol. 613, (2022), 256-267. https://doi.org/10.1016/j.ins.2022.09.042
57. Qin, M., Jin, D., He, D., Gabrys, B. and Musial, K., "Adaptive community detection incorporating topology and content in social networks", in Proceedings of the 2017 IEEE/ACM International Conference on Advances in Social Networks Analysis and Mining 2017. (2017), 675-682.
58. Kingma, D.P. and Ba, J., "Adam: A method for stochastic optimization", arXiv preprint arXiv:1412.6980, (2014). dhttps://doi.org/10.48550/arXiv.1412.6980
59. Yang, H., Kong, Q. and Mao, W., "A deep latent space model for graph representation learning", arXiv preprint arXiv:2106.11721, (2021). https://doi.org/10.48550/arXiv.2106.11721
60. Tatarkanov, A., Alexandrov, I., Muranov, A. and Lampezhov, A., "Development of a technique for the spectral description of curves of complex shape for problems of object classification", *Emerging Science Journal*, Vol. 6, No. 6, (2022), 1455-1475. doi: 10.28991/ESJ-2022-06-06-015.

COPYRIGHTS

©2023 The author(s). This is an open access article distributed under the terms of the Creative Commons Attribution (CC BY 4.0), which permits unrestricted use, distribution, and reproduction in any medium, as long as the original authors and source are cited. No permission is required from the authors or the publishers.

**Persian Abstract**

چکیده

امروزه با گسترش شبکه‌های پیچیده و حجم بالای داده‌های آن‌ها، یافتن روش‌های آشکارسازی دقیق همپویه‌ها (جوامع) در این نوع شبکه‌ها از اهمیت بالایی برخوردار است. دشواری تجزیه و تحلیل این شبکه‌ها از حجم بالا و روابط پیچیده بین اعضای شبکه ناشی می‌شود. تحلیل روابط و سازوکار عمیق بین اعضاء، تنها با در نظر گرفتن کلیت آن، دشوار است. روش‌های سنتی، برای تحلیل این شبکه‌ها مشکلات و محدودیت‌هایی نظیر استخراج ویژگی، وابستگی زیاد به تنظیمات اولیه، پیچیدگی محاسباتی بالا و نادیده گرفتن روابط و محتویات شبکه دارند. از نظر روابط و تعاملات بین افراد، محیط شبکه‌های پیچیده را می‌توان به بازی‌ای تشبیه کرد که در آن گره‌ها، به عنوان بازیکن یا عامل، تلاش می‌کنند تا بر اساس ویژگی‌های ساختاری یا معنایی مشابه به یک همپویه بپیوندند یا از آن خارج شوند. در نتیجه، می‌توان برای آشکارسازی همپویه‌ها از بازی‌های همکاری و غیر-همکاری بهره ببریم. اخیراً ادغام تکنیک‌های یادگیری ژرف و نظریه بازی‌ها جهت استخراج همپویه‌ها بسیار مؤثر بوده است. تکنیک‌های یادگیری ژرف قابلیت‌های پیشرفت‌تری را در مهندسی ویژگی‌ها نشان داده‌اند و این فرآیند را خودکار نموده است. بنابرایان، در این پژوهش، نویسنده‌گان تلاش می‌کنند تا با کمک رویکردهای سنتی، یادگیری ژرف و همچنین بازی‌های همکاری و غیر-همکاری، همپویه‌های منطقی و دقیقی را بر اساس ویژگی‌های ساختاری و محتوایی آشکارسازی کنند. کارایی این مطالعه با یافته‌های تجربی بر روی مجموعه داده‌های واقعی نشان داده شده است و تأیید می‌کند که روش پیشنهادی، به قدر کافی قادر به آشکارسازی همپویه‌هایی است که معنی دارترند.



Evaluating Traffic Performance on Basra City Urban Roads Network

Z. Nassrullah*

Department of Civil Engineering, Collage of Engineering, University of Basrah, Iraq

PAPER INFO

Paper history:

Received 19 June 2023

Received in revised form 27 July 2023

Accepted 28 July 2023

Keywords:

Traffic Congestion

Traffic Flow

Average Speed

Average Travel Time

Delay

ABSTRACT

The continuous growth of the economy and population around the world has led to an increase in transportation demand. Consequently, the number of vehicles keeps increasing to satisfy the continued demand for transportation. Traffic congestion and delay, as a result, is becoming the norm in many big cities. The first step to alleviate the traffic congestion and delay is to gain a better understanding of the traffic operations at the city's road network. This study tries to investigate and report about the traffic operations at urban roadways in Basra City, Southern of Iraq. With the focus of studying some of the main traffic parameters such as traffic flow, speed, travel time and delay at some selected sites with interrupted traffic flow within Basra City. Field traffic data from 30 roadways sites has been collected by using two techniques, camcorders and floating car technique. Data analysis showed that most of the selected sites are running under their capacity with an average speed close to the posted speed limit. However, the analysis of data also showed that for the majority of times on these selected sites long travel time and traffic delays were experienced, with an average delay of around 3.0 minutes for each 1.0 km road length. This could be attributed to deficiencies in the operation of traffic signals at intersections, presence of illegal on-street curb parking (with double parking sometimes) and the absence of traffic enforcement controls (with associated penalties).

doi: 10.5829/ije.2023.36.11b.11

1. INTRODUCTION

With the rapid growth and development of the economy and population, transportation demand for both passenger and freight is also increasing. According to SLOCAT the global gross domestic product (GDP) grew by 27% between 2010 and 2019 whereas the global population increased 12% and the urban population grew by nearly 20% between 2010 and 2020. The continuous growing of populations and a denser concentration of people in urban areas around the world has led to increase the transportation demand which affects traffic flow conditions negatively in urban roads [1-3]. In addition, Lukina et al. [4] reported that the city center could create up to 40% of job opportunities which increases the transportation demand for accessing work and other attraction points in the city center. Consequently, the number of vehicles is increasing. The number of private sector vehicles in Iraq has increased nearly fivefolds

between 2010 and 2020. The number of vehicles for private sector only in Iraq has reached 7 million vehicles by the end of 2020 and continued increasingly. However, the corresponding road capacity has not been significantly improved. Lengths of paved highways grew only by 7% between 2015 and 2020 [6]. This situation may have exacerbated the situation with serious traffic congestion in some locations leading to higher delays and higher rate of traffic accidents. In 2020, the number of fatalities involving traffic accidents was 2016 accidents whereas the non-fatal traffic accidents were 6170 accidents. Traffic congestion and unsafe driving behavior are the main motivations of the higher rate of traffic accidents [5-7]. Even though, a comprehensive solution of the traffic issues in Basra City's urban roads might not be achieved. European Conference of Ministers of Transport [8] stated that "*dynamic, affordable, livable and attractive urban regions will never be free of congestion*". However, a good understanding of traffic

*Corresponding Author Email: zaid.abbas@uobasrah.edu.iq
(Z. Nassrullah)

operations at Basra urban roads might help to alleviate traffic congestion and delay and to enhance safety. The present study tries to investigate and report about the traffic operations at urban roadways in Basra City, Southern of Iraq (in Basra Governorate). To inform Basra City's traffic engineers, urban planners, and policymakers about the existing traffic issues.

2. LITRETURE REVIEW

Several previous studies have been found in the literature that deal with traffic performance of roads in urban areas. Liao et al. [9] stated that traffic congestion is commonly occurred in urban areas, especially during peak hours. They reported that analysis and estimation of traffic flow in urban areas is required to understand the causes of traffic congestion. Zang et al. [10] reported that for alleviating traffic congestion, scientific and quantitative evaluation of the traffic congestion should be carried out. Alkaissi and Hussain [11] estimated traffic volumes, vehicle compositions and travel time for some selected interrupted streets in Baghdad City to understand the causes of traffic congestion. Falih [12] studied the causes and remedies of traffic congestion in Samawa city. He reported that the illegal parking of vehicles, lack of vehicles parking, physical constraints of some roads and mismanagements of roads intersections are main reasons for traffic congestion. AlGhanim et al. [13] studied the traffic performance for some selected streets in Al-Najaf City. The researchers estimated traffic volume, travel time, average travel speeds and level of service (LOS). Abbas et al. [14] studied the negative impact of freight transportation on Hilla City roads. The researchers proposed adding new roads to enhance the road network in the city. Hafram et al. [15] evaluating the traffic performance by using simulation model. The researchers used traffic volume, speed, road geometry and roadside parking as input data for modeling process. Yigitcanlar et al. [16] suggested adopting intelligent transport systems (such as traffic control applications and big data analytics) and smart mobility services to optimize traffic conditions. Reddy and Srivastava [17] reported that traffic operations are considered as one of the important factors for dealing with and managing traffic congestion in urban areas. Alkaissi [18] reported that travel time and delay can be considered as one of the important factors that can be used in evaluating traffic performance in an urban road network. Ahmed et al. [19] reported that estimating travel time and average speed are very important to enhance the efficiency and safety of roads. Garber and Hoel [20] reported that the travel time and delay data can be used to identify the traffic problem locations. Skovajsa et al. [21] stated that traffic delay is one of the principal factors that can be used to evaluate the quality of traffic management. Noor et al. [22] studied

the traffic congestion in urban areas by measuring traffic volume and speed. Abed et al. [23] studied the effects of traffic operations (such as traffic volume, traffic speed and traffic composition) and characteristics of roads geometry on noise pollution. It can be concluded from the abovementioned studies that the most important factors of traffic operations that affect traffic performance are traffic flow, average speed, average travel time and delay which will be taken into consideration into the present study.

Rashid [24] studied the causes of traffic congestion in Basra. He found that the growing population and number of vehicles in Basra are the most significant factors for the traffic congestion. He reported that the number of vehicles in Basra has increased by threefolds for the period from 2004 to 2009. Rashid [24] studied the impacts of traffic accidents on the city of Basra. He reported that traffic accidents in Basra have resulted in 19 fatalities for every 100 injuries. However, traffic operations have not been taken into consideration in both studies, by Rashid [24].

Although many previous researchers studied the traffic performance in urban areas, very limited studies have been found in the literature for Basra city. Therefore, this study will try to furnish investigations about traffic operations at urban roadways in Basra City. With the focus of studying traffic flow, average speed, average travel time and delay (as suggested by previous studies) at some selected interrupted traffic flow roadways in Basra City.

3. DATA COLLECTION

One of the challenges in this study was selecting the sites in the crowded urban center of Basra City to collect field traffic data. However, most of the main roads in Basra City center have been selected. The field traffic data have been collected from 30 roadway sites by using two techniques, these are camcorders and floating car technique, as will be discussed in the following sections.

The approach of this study involves understanding traffic flow conditions by measuring traffic operations (such as flow, speed, travel time and delay as described in the previous studies). Figure 1 shows the research flowchart.

3. 1. Data Collected by Camcorders Field traffic data has been collected by using camcorders from 22 sites dual carriageways roads with 4, 3 and 2 lanes in each direction. The collected data by camcorders were then used to compute traffic flow and average speed.

3. 1. 1. Four Lanes Dual Carriageway Roads Six sites' roadways (with 4-lane) have been selected. The four lanes dual carriageway roads is characterized by

traffic travelling in opposite directions separated by a central median with four lanes in each direction and different posted speed limits for each lane. The posted speed limit for the four lanes dual carriageway roads in Basra City is 40 km/h for lane 1 (inside lane), 40 km/h for lane 2, 60 km/h for lane 3 and 80 km/h for lane 4 (offside lane). Figure 2 shows lanes notations used in this study. These sites have been surveyed during 2021 and 2022. Table 1 summarizes the details of the selected sites, whereas Figure 3 shows locations of these sites.

3. 1. 2. Three Lanes Dual Carriageway Roads

Eight sites' roadways (with 3-lane) have been selected. The selected sites for the three lanes dual carriageway roads is also characterized by traffic travelling in opposite directions separated by a central median with three lanes in each direction. The posted speed limit is 40 km/h for all lanes in each direction. These sites have been surveyed during 2021 and 2022. Table 2 summarizes the details of the selected sites, whereas Figure 4 shows the locations of these sites.

3. 1. 3. Two Lanes Dual Carriageway Roads

Eight sites' roadways (with 2-lane) have been selected and surveyed as summarized in Table 3 and the location map

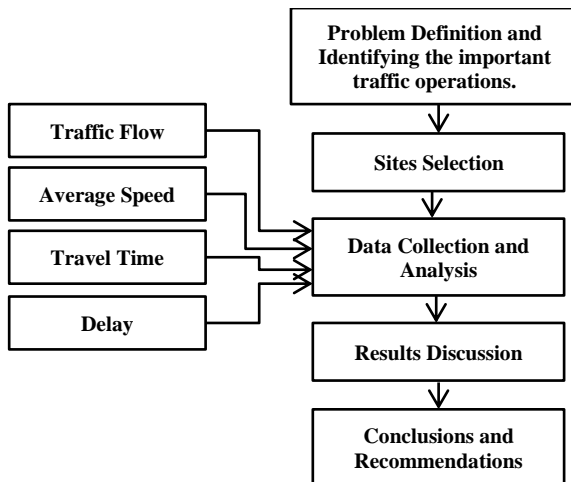


Figure 1. Illustration of research flowchart

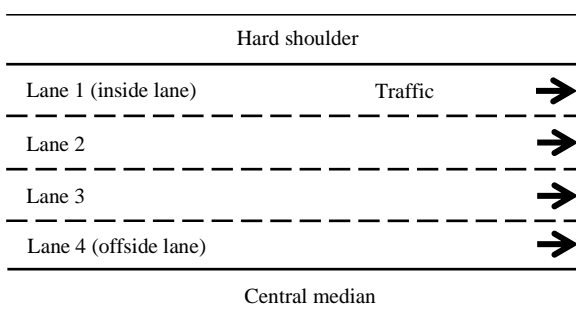


Figure 2. Illustration of four lanes dual carriageway roads

TABLE 1. Sites' location and details for selected 4-lane roads

Site No.	Site location	Traffic direction	Date	Time and duration
1	Lebanon Street	Eastbound	Tuesday 30/11/2021	10:00-13:00 3 hours
2	Lebanon Street	Westbound	Tuesday 30/11/2021	10:00-13:00 3 hours
3	Azzubair street	Eastbound	Wednesday 12/01/2022	07:40-10:40 3 hours
4	Azzubair street	Westbound	Wednesday 12/01/2022	07:40-10:40 3 hours
5	Baghdad street	Northbound	Sunday 21/11/2021	07:40-10:10 2.5 hours
6	Baghdad street	Southbound	Sunday 21/11/2021	07:40-10:10 2.5 hours



Figure 3. Sites' locations map (camcorders, 4 Lanes roads)
(Source of map: Google Maps, 2023)

TABLE 2. Sites' location and details for selected 3-lane roads

Site No.	Site's location	Traffic direction	Date	Time and duration
7	Al-Basra street	Eastbound	Sunday 28/11/2021	07:00-10:00 3 hours
8	Al-Basra street	Westbound	Sunday 28/11/2021	07:00-10:00 3 hours
9	AlJomhoria street	Eastbound	Sunday 09/01/2022	08:00-11:00 3 hours
10	AlJomhoria street	Westbound	Sunday 09/01/2022	08:00-11:00 3 hours
11	Ashar Street	Eastbound	Sunday 16/01/2022	08:00-11:00 3 hours
12	Ashar Street	Westbound	Sunday 16/01/2022	08:00-11:00 3 hours
13	Trade Street	Eastbound	Wednesday 05/01/2022	11:05-14:05 3 hours
14	Trade Street	Westbound	Wednesday 05/01/2022	11:05-14:05 3 hours

shown in Figure 5. Likewise, the traffic is travelling in opposite directions separated by a central median with two lanes in each direction. The posted speed limit is 40 km/h for all lanes.



Figure 4. Sites' locations map (camcorders, 3 Lanes streets)

TABLE 3. Sites' location and details for selected 2-lane roads

Site No.	Site location	Traffic direction	Date	Time and duration
15	Dinar Street	Northbound	Wednesday 12/01/2022	11:00-13:30 2.5 hours
16	Dinar Street	Southbound	Wednesday 12/01/2022	11:00-13:30 2.5 hours
17	14 July Street	Eastbound	Tuesday 09/11/2021	07:00-10:00 3 hours
18	14 July Street	Westbound	Tuesday 09/11/2021	07:00-10:00 3 hours
19	Al-Saadi Street	Northbound	Sunday 02/01/2022	11:30-14:30 3 hours
20	Al-Saadi Street	Southbound	Sunday 02/01/2022	11:30-14:30 3 hours
21	Al-Jaza'ar Street	Northbound	Sunday 23/01/2022	11:00-14:00 3 hours
22	Al-Jaza'ar Street	Southbound	Sunday 23/01/2022	11:00-14:00 3 hours

TABLE 4. Sites' locations and details for the data collected by floating car technique

Site No.	Site location	Traffic direction	Date and Time	Street length covered (m)
23		Northbound	Sunday 15/05/2022	4200
24	Baghdad Street	Southbound	07:30-09:20	4200
25		Eastbound	Monday 14/03/2022	2200
26	Al-Basra Street	Westbound	07:30-09:00	2200
27		Eastbound	Thursday 19/05/2022	1800
28	14 July Street	Westbound	19:00-21:32	1800
29		Northbound	Wednesday 02/03/2022	2300
30	Dinar Street	Southbound	07:30-09:20	2300



Figure 6. Sites' locations map (floating car technique)



Figure 5. Sites locations map (camcorders, 2 Lanes streets)

3. 2. Data Collected by Floating Car Technique
Field traffic data have been collected by using floating car technique from 8 sites dual carriageways roads with 4, 3 and 2 lanes in each direction. The collected data by floating car technique were then used to compute average travel time and delay. Likewise, these 8 roadways sites have been surveyed during 2021 and 2022. Table 4 summarizes the details of the selected sites, whereas Figure 6 shows locations of these sites.

4. DATA ANALYSIS

4. 1. Traffic Flow Field data from 22 sites with 4 lanes, 3 lanes and 2 lanes dual carriageways roads have been collected and analyzed to calculate the traffic flow parameter. The traffic flow data has been measured manually by displaying the video recording on the screen of a computer and drawing a thin line across the computer screen by using a marker pen to help in counting the vehicles. The collected flow data were then grouped into five-minute intervals and converted to hourly flows for each five-minute interval, as recommended by many previous researchers such as [25]. Figures 7, 8 and 9 show traffic flow for 4 lanes dual carriageways sites, 3 lanes dual carriageways sites and 2 lanes dual carriageways sites, respectively.

It can be seen from Figure 7 that the traffic flow conditions for Lebanon Street (Site no. 1 and Site no. 2) can be considered as a moderate traffic flow conditions and it is ranging from around 2000 to 3000 pcu/h. The data taken from Sites no. 1 and 2 was collected at off peak hours from 10:00 am to 13:00 pm. Where, the traffic flow

conditions for Azzubair Street (Site no. 3 and Site no. 4) and Baghdad Street (Site no. 5 and Site no. 6) can be considered as a heavy traffic flow conditions and it is ranging from around 4000 to 6000 pcu/h. The data for both sites was collected at peak hours, as mentioned in Table 1. Also, It is worth mentioning here that the heavy vehicles percentages for Site no. 1 are 5% and 4% for Site no. 2, 5% for Site no. 3, 8% for Site no. 4, and 16% for both Sites no. 5 and 6.

Figure 8 showed that the traffic flow conditions for all the observed sites range from 1000 to 3000 pcu/h. Also, it can be seen from Figure 8 – A that there are some fluctuations in flow rates for Site no. 7 and it reached zero at 08:35 am. This could be attributed to the influence of the nearby intersection. The heavy vehicles percentages for all observed 3-lanes dual carriageways streets is around 5%.

Figure 9 shows that the traffic flow conditions for all the observed two lanes dual carriageways roads is

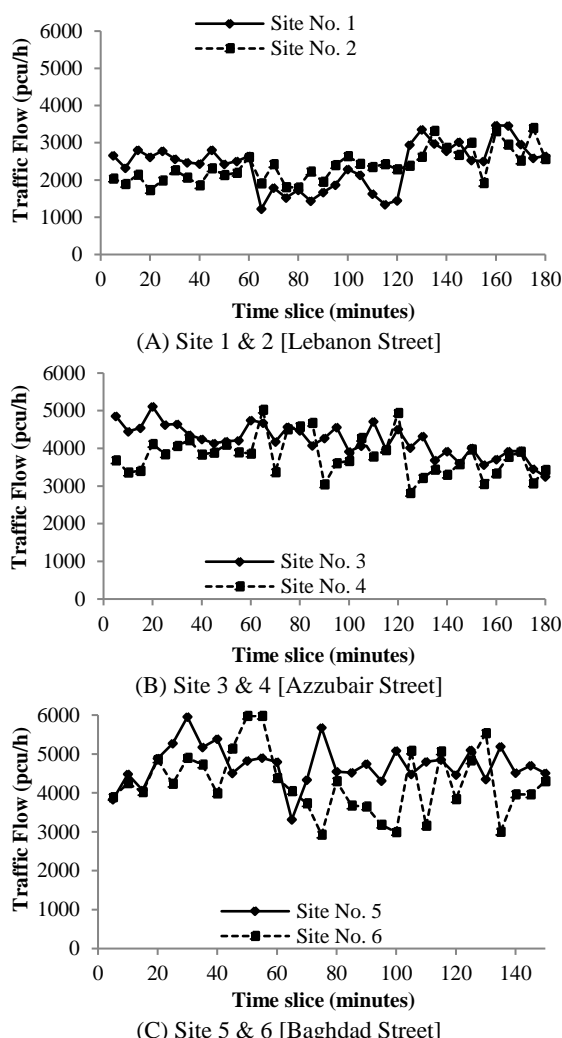


Figure 7. Traffic flow for 4-lanes streets (A) Lebanon, (B) Azzubair and (C) Baghdad Street

ranging from 1000 to 2000 pcu/h and can be considered. Likewise, the heavy vehicles percentages for all observed two lanes dual carriageways streets is around 5%.

In general, it can be concluded from Figures 7, 8 and 9 that the traffic flow conditions for sites with 4 lanes can be considered as heavy traffic flow conditions. Where, for sites with 3 lanes and 2 lanes the traffic flow conditions can be considered as moderate traffic.

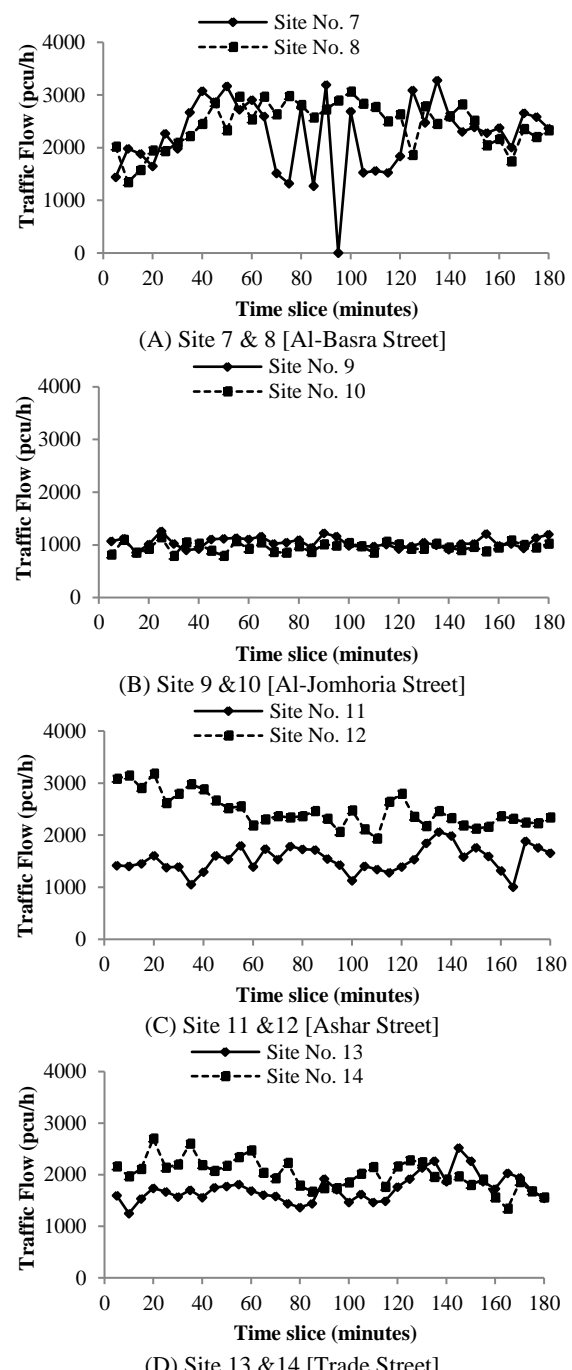


Figure 8. Traffic flow for 3-lanes streets (A) Al-Basra, (B) Al-Jomhoria, (C) Ashar and (D) Trade Street

4.2. Average Speed Field data from 22 sites with 4 lanes, 3 lanes and 2 lanes dual carriageways roads have been collected and analyzed to calculate the average speed. The average speed data has been measured manually by displaying the video recording on the screen of a computer and sketching two reference lines on the computer screen to cover a specified distance. A stopwatch was used to measure the required time for a vehicle to cross this distance. Simple calculations of distance over the measured time have been used to convert the readings into speeds. Figures 10, 11 and 12 show average speed for 4 lanes dual carriageways sites, 3 lanes dual carriageways sites and 2 lanes dual carriageways sites, respectively.

It can be seen from Figure 10 that the average speed for Site no. 1 and Site no. 2 (Lebanon Street) is ranging from around 30 km/h to 70 km/h. It should be noted that the posted speed limit for both sites is 40 km/h. The average speed for Azzubair Street (Site no. 3 and Site no. 4) is ranging from 60 km/h to 80 km/h, whereas the average speed for Baghdad Street (Site no. 5 and Site no. 6) is ranging from 50 km/h to 100 km/h. The posted speed limit for both Azzubair street and Baghdad Street is variable speed limits based on the lane's location (as mentioned in section 3.1) with a maximum value of 80 km/h for off-side lane.

Figure 11 shows that the average speed for Site no. 7 and Site no. 8 (Al-Basra Street) is ranging from 20 km/h to 50 km/h with a value of 0.0 km/h at 08:35 am (i.e., stationary traffic), as shown in Figure 10– A and discussed in section 4.1. For Sites no. 9 and 10 (Al-Jomhoria Street) and Site no. 11 and 12 (Ashar Street), the average speed is ranging from around 30 km/h to 60 km/h. Where, the average speed for Trade Street (Sites no. 13 and 14) is ranging 20 km/h to 40 km/h. It is worth mentioning here that the posted speed limit for all the observed 3 lanes dual carriageways streets is 40 km/h. The lower value of observed average speed (i.e., 20 km/h), especially for Al-Basra Street and Trade Street, could be attributed to the higher number of vehicles that were parking illegally on curb with double parking sometimes on both streets.

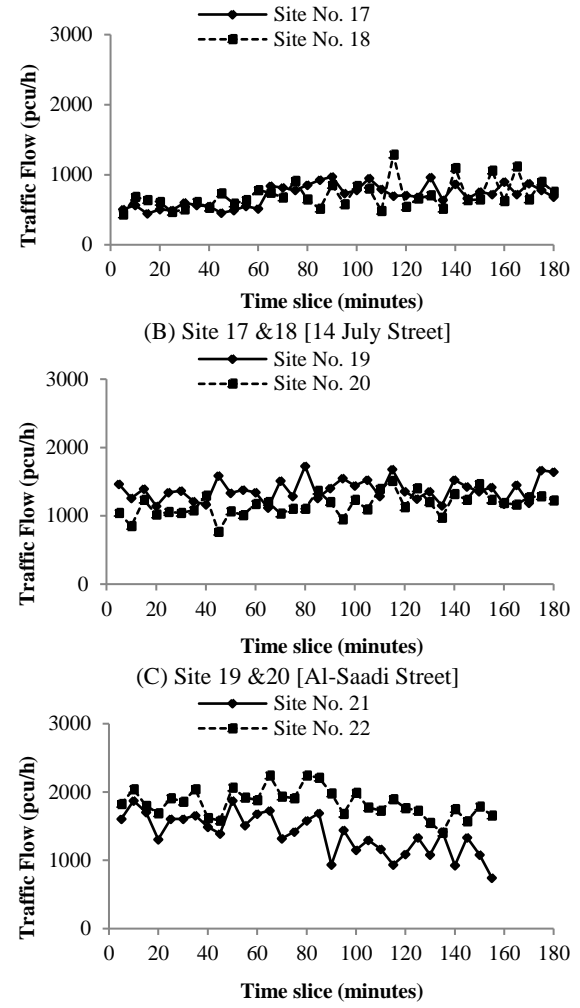
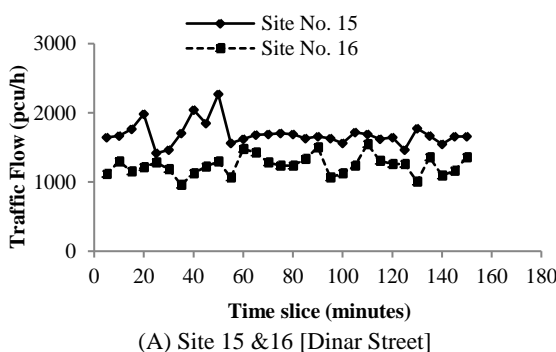
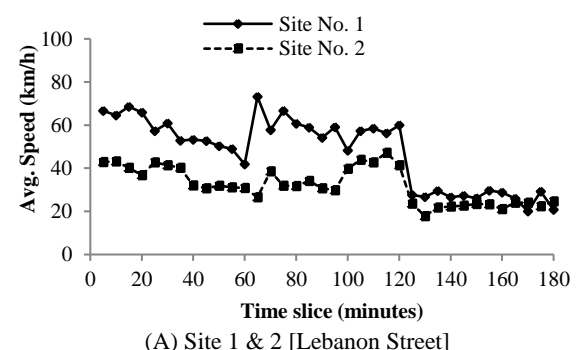


Figure 9. Traffic flow for 2-lanes streets (A) Dinar, (B) 14 July, (C) Al-Saadi and (D) Al-Jaza'ar Street

Figure 12 shows that the average speed for Sites no. 15 and 16 (Dinar Street) and Sites no. 17 and 18 (14 July Street) ranges from around 25 km/h to 40 km/h. For Al-Saadi Street (i.e., Sites no. 19 and 20) the average speed is ranging from around 40 km/h to 60 km/h. Where, the average speed for Al-Jaza'ar Street (i.e., Sites no. 21 and



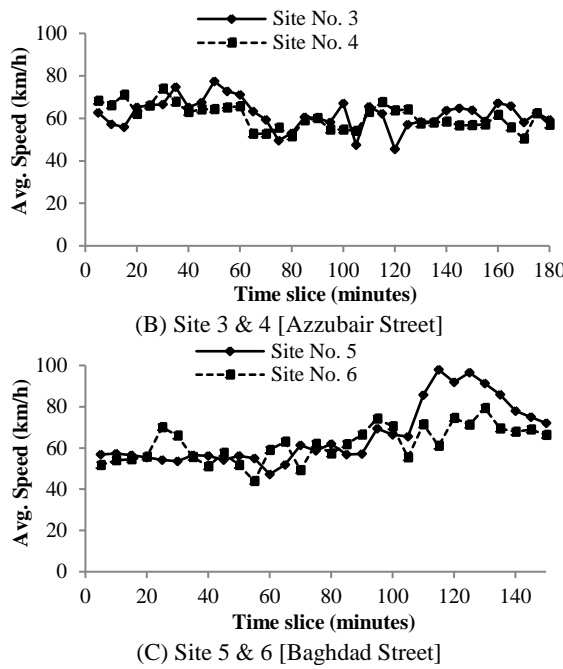


Figure 10. Average speed for 4-lanes streets (A) Lebanon, (B) Azzubair and (C) Baghdad Street

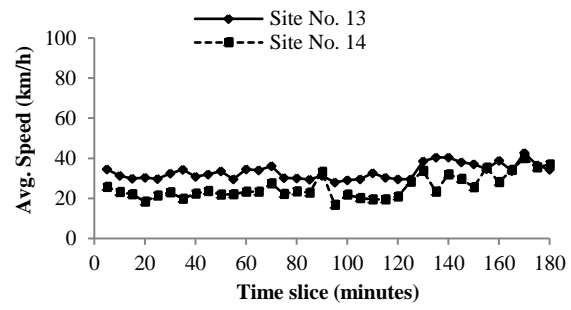
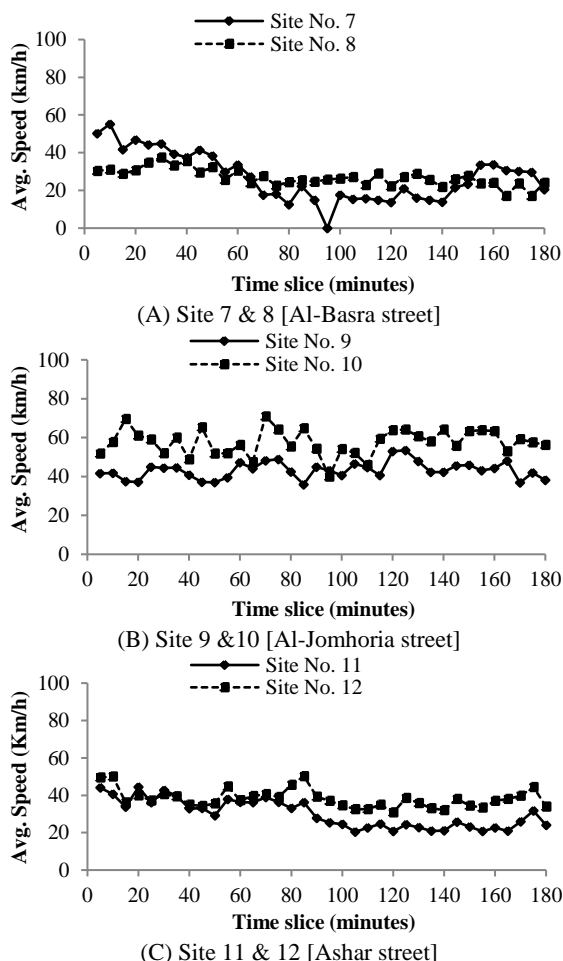
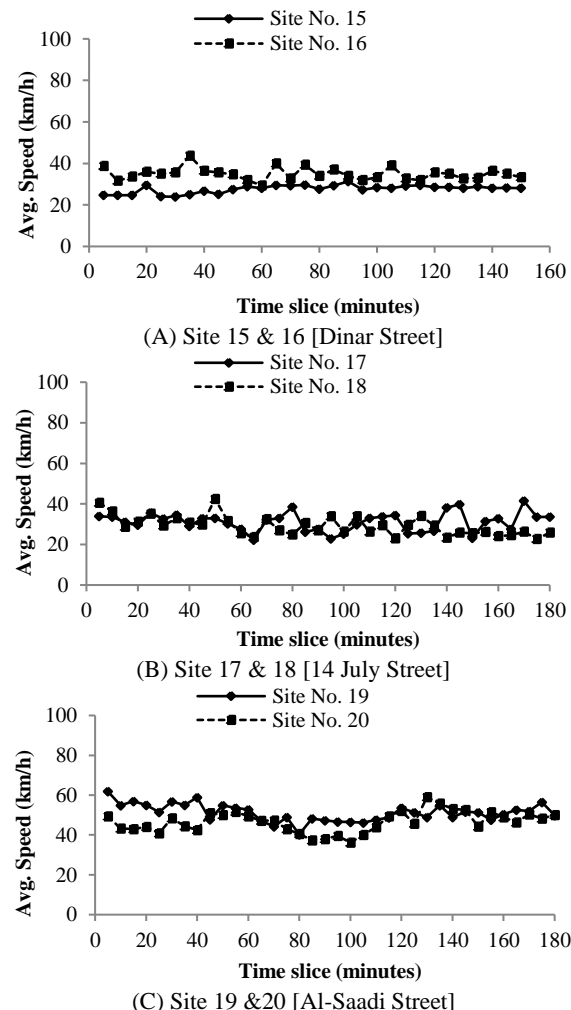
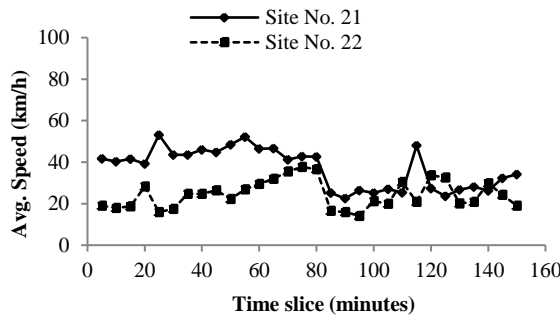


Figure 11. Average speed for 3-lanes streets (A) Al-Basra, (B) Al-Jomhoria, (C) Ashar and (D) Trade Street

22) ranges from around 15 km/h to 50 km/h. Likewise, the posted speed limit for all the observed 2 lanes dual carriageways streets is 40 km/h. Similarly, the lower value of observed average speed (i.e., 15 km/h), especially for Al-Jaza'ar Street, could be due to the higher number of vehicles that were parking unofficially on the street.





(D) Site 21 & 22[Al-Jaza'ar Street]

Figure 12. Average speed for 2-lanes streets (A) Dinar, (B) 14 July, (C) Al-Saadi and (D) Al-Jaza'ar Street

4. 3. Average Travel Time and Delay As mentioned in section 2.2, the floating car technique was used to compute the average travel time. Six runs for each site have been conducted to compute the travel time as recommended by the Highway Capacity Manual (HCM, 2010) [26]. The required travel time to traverse the selected site is recorded and this is repeated for six runs. Then, the recorded travel times are averaged. Table 5 summarizes the average travel time and delay for the selected 8 sites.

It can be seen from Table 5 that the busiest street is the “14 July Street” with around 10 minutes of delay for only 1.8 km length covered of the street. This could be attributed to the nearby intersections which have improperly designed traffic signals. Iftikhar et al. [27] reported that the weak traffic signals timing is one of the factors that leads to traffic congestion and delay. The other reason of the delay is because of the highly number of motorists that were observed illegally parked on curb and some of them were even observed doing double parking on curb on a street with 2 lanes. This is because the 14 July street is a commercial street which contains many commercial facilities and restaurants located on both sides of the street. Also, due to the absence of traffic

enforcement and associated penalties. It is worth mentioning here that the field data was collected on the evening peak hours started from 7:00 pm, as shown in Table 4. However, these two reasons are not restricted for only this street, but it can be found almost for all the streets in Basra City.

As discussed in sections 4.1, 4.2, and 4.3, all the collected data (i.e., traffic flow, average speed, travel time and delay) were measured manually, which may be affected by human errors. Therefore, an attempt was carried out to check the accuracy of the measurements. This has been done by requesting two well-trained observers to extract the traffic data from same sample separately then compare their results, a sample of 15 minutes from each video recording was chosen. The comparison of the results showed a very close fit between the two observers.

5. RESULTS DISCUSSION

The results of data analysis show that the traffic flow rates for all observed roads are running under moderate traffic flow conditions. Except, the traffic flow conditions for Baghdad and Azzubair streets (both are 4 lanes streets) which are ranging from moderate to heavy flow rates. The results of average speed data showed that on average most of the motorists are driving at speeds close to the posted speed limit. However, the average travel time and delay data showed that all observed sites experienced longer travel time and delays. This is in good agreement with the study by Noor et al. [22]. The study's results showed that the surveyed roads experienced traffic congestion although they were running with traffic flow under their designed capacity. The causes of the traffic congestion are fragile public transportation and pedestrians' behavior, illegal road occupancy by roadside vendors and weak law enforcement [22]. Also, Noor et al. [22] reported that these causes could lead to decrease the road efficiency by 32 to 82% in different areas.

Field observations showed that a high number of the motorists in Basra City are illegally parking on streets and sometimes they are even doing double parking on curb. This needs further investigations, since the on streets parking has a significant impact on reducing road capacity [28]. Yousif and Purnawan [29] reported that on busy roads inappropriate parking can lead to severe delays. In addition to the absence of traffic enforcement and associated penalties.

Other field observations showed that all at-grade intersections in Basra City are operated by a traffic police officer due to the deficiency of the traffic signals. This has led to the cycle length of intersection to be extended highly and sometimes it reaches 10 – 15 minutes, which makes travel time and delay longer. Also, this needs further investigation and documentation.

TABLE 5. Average travel time and delay for the selected sites

Site No.	Site location	Traffic direction	Average Travel Time (minutes)	Delay (minutes)
23	Baghdad Street	Northbound	8.2	4.0
24	Baghdad Street	Southbound	10.1	5.9
25	Al-Basra Street	Eastbound	7.7	4.4
26	Al-Basra Street	Westbound	7.5	4.2
27	14 July Street	Eastbound	12.8	10.1
28	14 July Street	Westbound	12.5	9.8
29	Dinar Street	Northbound	7.8	4.3
30	Dinar Street	Southbound	10.6	7.1

Also, it is worth mentioning here that all observed streets have good pavement surfaces, however, 65% of the observed streets have no road markings.

6. CONCLUSIONS

The aim of this study is to investigate and report on the traffic operations on some selected urban roads in Basra City. This paper tries to help inform traffic engineers and urban planners who are working with the local authorities in Basra City to put the required plans to mitigate the existing traffic congestion and delays in the city urban roads. Bear in mind that roads are the main and viable mode of commuting in urban areas for Iraqis. The results showed that, although, most of the observed sites were running under their capacity flow with driving speeds close to the posted speed limit. However, all the observed sites experienced longer travel time and delays. This could be attributed (1) high number of the motorists are doing illegal parking on streets with doing double parking on curb sometimes, (2) absence of traffic enforcement and associated penalties, (3) the deficiency of the traffic signals at the intersections, and (4) the physical constraints of some 2 lanes streets. In addition to the very weak public transportation services in Basra City. To overcome the longer travel time and delay; the traffic signals at all Basra City intersections should be properly designed and activated, providing adequate parking lots, activating traffic enforcement and associated penalties, in addition to enhance public transportation services. Further investigation on the impacts of physical parameters of roads on traffic operations is required.

7. REFERENCES

- Humphrey, M., Dona, S., Singh, A. and Swe, T.T., "A comparison of traffic performance in highly congested urban areas", *International Journal of Traffic and Transportation Engineering*, Vol. 5, No. 3, (2016), 47-63. doi: 10.5923/j.ijtte.20160503.01.
- Mohammadi, M., Dideban, A. and Moshiri, B., "A novel approach to modular control of highway and arterial networks using petri nets modeling", *International Journal of Engineering, Transactions B: Applications*, Vol. 36, No. 8, (2023), 1578-1588. doi: 10.5829/ije.2023.36.08b.17.
- Abdulrazzaq, L.R., Abdulkareem, M.N., Yazid, M.R.M., Borhan, M.N. and Mahdi, M.S., "Traffic congestion: Shift from private car to public transportation", *Civil Engineering Journal*, Vol. 6, No. 8, (2020), 1547-1554. doi: 10.28991/cej-2020-03091566.
- Lukina, A.V., Sidorchuk, R.R., Mkhitaryan, S.V., Stukalova, A.A. and Skorobogatkh, I.I., "Study of perceived accessibility in daily travel within the metropolis", *Emerging Science Journal*, Vol. 5, No. 6, (2021), 868-883. doi: 10.28991/esj-2021-01316.
- Sumi, L. and Ranga, V., "Intelligent traffic management system for prioritizing emergency vehicles in a smart city", *International Journal of Engineering, Transactions B: Applications*, Vol. 31, No. 2, (2018), 278-283. doi: 10.5829/ije.2018.31.02b.11.
- Damodariya, S.M. and Patel, C.R., "Identification of factors causing risky driving behavior on high-speed multi-lane highways in india through principal component analysis", *International Journal of Engineering, Transactions B: Applications*, Vol. 35, No. 11, (2022), 2130-2138. doi: 10.5829/ije.2022.35.11b.08.
- Retallack, A.E. and Ostendorf, B., "Current understanding of the effects of congestion on traffic accidents", *International Journal of Environmental Research and Public Health*, Vol. 16, No. 18, (2019), 3400. doi: 10.3390/ijerph16183400.
- Congestion, M.U.T., "Managing urban traffic congestion". ISBN 978-92-821-0128-5, OECD Publishing, France, 2007.
- Liao, Z., Huang, H., Zhao, Y., Liu, Y. and Zhang, G., "Analysis and forecast of traffic flow between urban functional areas based on ride-hailing trajectories", *ISPRS International Journal of Geo-Information*, Vol. 12, No. 4, (2023), 144. https://doi.org/10.3390/ijgi12040144
- Zang, J., Jiao, P., Liu, S., Zhang, X., Song, G. and Yu, L., "Identifying traffic congestion patterns of urban road network based on traffic performance index", *Sustainability*, Vol. 15, No. 2, (2023), 948. https://doi.org/10.3390/su15020948
- Alkaissi, Z.A. and Hussain, R.Y., "Estimation of traffic volumes distribution of urban streets in baghdad city", *Journal of The Planner & Development*, Vol. 26, No. 2, (2021).
- Falih, Y.A.H., "Traffic congestion in the central business district of samawah; causes and remedies", *Basic Education College Magazine For Educational and Humanities Sciences*, Vol. 12, No. 49, (2020).
- Al Ghanim, A.M., Asad, F.H. and Al-Jameel, H.A., "Traffic performance evaluation for selected streets within the southern part of al-najaf city network", in Journal of Physics: Conference Series, IOP Publishing. Vol. 1973, (2021), 012226.
- Abbas, H.A., Obaid, H.A. and Alwash, A.A.A., "Enhanced road network to reduce the effect of (external-external) freight trips on traffic flow", *Civil Engineering Journal*, Vol. 8, No. 11, (2022), 2573-2584. doi: 10.28991/CEJ-2022-08-11-015.
- Hafram, S.M., Valery, S. and Hasim, A.H., "Calibrating and validation microscopic traffic simulation models vissim for enhanced highway capacity planning", *International Journal of Engineering, Transactions B: Applications*, No. Articles in Press, (2023). doi: 10.5829/ije.2023.36.08b.11.
- Yigitcanlar, T., Li, R.Y.M., Inkmen, T. and Paz, A., "Public perceptions on application areas and adoption challenges of ai in urban services", *Emerging Sciences Journal*, Vol. 6, No. 6, (2022), 1199-1236. doi: 10.28991/ESJ-2022-06-06-01.
- Reddy, K.J.M. and Srivastava, P., "Traffic operations and capacity analysis in india", in IOP Conference Series: Materials Science and Engineering, IOP Publishing. Vol. 925, (2020), 012029.
- Al-Kaissi, Z.A., "Travel time prediction models and reliability indices for palestine urban road in baghdad city", *Al-Khwarizmi Engineering Journal*, Vol. 13, No. 3, (2017), 120-130. https://doi.org/10.22153/kej.2017.01.007
- Ahmed, R.M., Alkaissi, Z.A. and Hussain, R.Y., "Travel time analysis of selected urban streets in baghdad city", *Journal of Engineering and Sustainable Development (JEASD)*, Vol. 25, No. Special Issue 2021, (2021). https://doi.org/10.31272/jeasd.conf.2.3.15
- Garber, N.J. and Hoel, L.A., "Traffic and highway engineering", Cengage Learning, (2019).
- Skovajsa, J., Přibyl, O., Přibyl, P., Ščerba, M. and Janota, A., "Evaluation of a mobile highway management system at roadwork zones", *International Journal of Engineering*,

- Transactions B: Applications**, Vol. 35, No. 5, (2022), 900-907.
doi: 10.5829/ije.2022.35.05b.06.
22. Noor, M.A., Ashrafi, S., Fattah, M.A., Morshed, S.R. and Rahman, S., "Assessment of traffic congestion scenario at the cbd areas in a developing city: In the context of khulna city, bangladesh", **Transportation Research Interdisciplinary Perspectives**, Vol. 11, No., (2021), 100435. <https://doi.org/10.1016/j.trip.2021.100435>
 23. Abed, A., Albayati, A. and Wang, Y., "Effect of vehicular stream characteristics on traffic noise", **Civil Engineering Journal**, Vol. 8, No. 12, (2022). doi: 10.28991/CEJ-2022-08-12-016.
 24. Qasim Rashid, W., "An economic study of the problem of traffic congestion in the city of basra", **Basra Studies Journal**, Vol. 13, No. 1994, (2012), 268-297.
 25. Nassrullah, Z. and AbdulJaleel, L., "Traffic operations at the approaches to the highway checkpoint sites", in **Journal of Physics: Conference Series**, IOP Publishing. Vol. 1973, (2021), 012228.
 26. Manual, H.C., "Washington, dc: Transportation research board, 2010", **Google Scholar**, (2010).
 27. Iftikhar, A., Khan, Z.H., Gulliver, T.A., Khattak, K.S., Khan, M.A., Ali, M. and Minallahe, N., "Macroscopic traffic flow characterization at bottlenecks", **Civil Engineering Journal**, Vol. 6, No. 7, (2020), 1227-1242. doi: 10.28991/cej-2020-03091543.
 28. Caroles, L., Adisasmitta, S.A. and Pamungkas, P.B., "Concept of an intelligent parking system; efforts to resolve traffic conflicts regulations", **Civil Engineering Journal**, Vol. 9, (2023), 65-74. doi: 10.28991/CEJ-SP2023-09-05.
 29. Yousif, S., "A study into on-street parking: Effects on traffic congestion", **Traffic Engineering and Control**, Vol. 40, (1999), 424-427.

COPYRIGHTS

©2023 The author(s). This is an open access article distributed under the terms of the Creative Commons Attribution (CC BY 4.0), which permits unrestricted use, distribution, and reproduction in any medium, as long as the original authors and source are cited. No permission is required from the authors or the publishers.



Persian Abstract

چکیده

رشد مداوم اقتصاد و جمعیت در سراسر جهان منجر به افزایش تقاضای حمل و نقل شده است. در نتیجه، تعداد وسایل نقلیه برای اراضی تقاضای مداوم برای حمل و نقل درک بهتر از عمليات ترافیکی در شبکه راه های شهر است. اولین گام برای کاهش ازدحام و تاخیر ترافیک، دستیابی به بر مطالعه برخی از پارامترهای اصلی ترافیک مانند جریان ترافیک، سرعت، زمان سفر و تأخیر در برخی از سایت های منتخب با جریان ترافیک قطع شده در شهر بصره. داده های ترافیکی میدانی از 30 سایت جاده با استفاده از دو تکنیک دوربین فیلمبرداری و تکنیک ماشین شناور جمع آوری شده است. تجزیه و تحلیل داده ها نشان داد که اکثر سایت های منتخب تحت ظرفیت خود با سرعت متوسط نزدیک به حد مجاز اعلام شده در حال اجرا هستند. با این حال، تجزیه و تحلیل داده ها همچنین نشان داد که در اکثر موقع در این مکان های انتخابی، زمان سفر طولانی و تاخیر های ترافیکی با میانگین تاخیر حدود 3 دقیقه برای هر 1.0 کیلومتر طول جاده تجربه شده است. این را می توان به نقص در عملکرد عالم راهنمایی و رانندگی در تقاطع ها، وجود پارکینگ غیرقانونی در حاشیه خیابان (با پارکینگ دوبل) و عدم وجود کنترل های اجرایی ترافیک (با مجازات های مرتبه) نسبت داد.



Exploring Factors Influencing Cryptocurrency Adoption: A Comprehensive Modeling Based on Fuzzy Cognitive Maps Approach

S. Mohammadi*, M. Yadegari

Department of Information Technology, Faculty of Industrial Engineering, K. N. Toosi University of Technology, Tehran, Iran

PAPER INFO

Paper history:

Received 09 July 2023

Received in revised form 04 August 2023

Accepted 13 August 2023

Keywords:

Cryptocurrency

Cryptocurrency Adoption

Technology Adoption Model

Technology Acceptance Model

Fuzzy Cognitive Map

ABSTRACT

Cryptocurrencies, with their decentralized nature, are gaining rapid international adoption as a means of payment or a valuable digital asset, independent of the economic policies of governments and without the need for a supervisory institutions such as banks. However, limited research has been conducted on the adoption of cryptocurrencies, most of which employ a general technology acceptance/ adoption model with a positivist approach. The main problem with previous studies is that they have been limited to the structure of general adoption models and only examined a few constructs due to the increasing complexity of the model. On the other hand, due to cryptocurrencies' unique nature and rapid developments, it is necessary to create new comprehensive models that include different dimensions. This paper aims to identify influential factors in the adoption of cryptocurrency technology, understand their interrelationships, and ultimately develop a comprehensive model. With a constructivist approach, this study uses the most important research of the past decade in the field of cryptocurrency adoption and creates a cognitive model of their constructs through a systematic approach. The focal point of our approach is constructivism, accompanied by considering the impact of constructs on each other using fuzzy cognitive maps, which has not been previously done in cryptocurrency adoption. The results of the proposed model indicate that perceived usefulness, attitude, financial value, and perceived ease of use are the most significant constructs that influence the creation of positive intention toward the use and adoption of cryptocurrencies.

doi: 10.5829/ije.2023.36.11b.12

1. INTRODUCTION

According to many researchers, blockchain technology and cryptocurrencies are radical or disruptive innovations in the sense that they have the potential to destroy previous technologies and replace them [1-3]. Although some consider them complementary to existing technologies, not as a replacement for them [4]. In any case, due to the increasing trend of using cryptocurrencies worldwide and their acceptance by some countries, it seems that cryptocurrencies' popularity is increasing, and this technology is very close to achieving widespread adoption [5]. However, prohibitions in certain countries and inadequate regulation can temporarily hinder their acceptance in some regions of the world. Nevertheless, with the

cryptocurrency market exceeding one trillion dollars in value, it demonstrates global interest in this technology and its potential for investment and income generation in the future. Although research on the reasons for their popularity and understanding the reasons for user adoption can significantly impact the future of this technology [2], limited studies have been conducted in this area [6]. Therefore, the need for qualitative and conceptual research for technologies at the beginning of adoption is essential [4], and it even seems that this is a higher priority for cryptocurrency technology compared to other emerging technologies. Understanding the reasons for the adoption of cryptocurrencies can be highly valuable for policymakers, legislators, and many governmental and private organizations due to creating a proper understanding of citizens' behavior and even

*Corresponding Author Email: mohammadi@kntu.ac.ir
(S. Mohammadi)

predicting their future acceptance. Properly understanding this phenomenon can pave the way for adopting correct cryptocurrency strategies and policies [7, 8].

The speed of cryptocurrency adoption in recent years has increased, and in the same way, the factors influencing their adoption have also increased; Therefore, understanding and modeling the effective constructs in cryptocurrency adoption has become more complex in this new space. This research aims to extract these constructs based on the most important studies of cryptocurrency adoption to identify the most important adoption factors through cognitive modeling. It is worth mentioning that most of the research conducted on the acceptance/ adoption of cryptocurrencies has adopted a positivist approach, where the authors conducted surveys to collect data from respondents and then analyzed them to prove their hypothesis. However, with a constructivist approach, this research independently examined and analyzed existing studies and their frameworks, independent of acceptance/adoption model structures and personal opinions. The approach in this stage is construct-oriented rather than model-centric, as all the constructs of the models and technology acceptance/adoption theories in the literature on cryptocurrencies were encoded and transformed into a fuzzy cognitive model.

The rest of this paper is organized as follows: In the second section (literature review), relevant research has been reviewed and analyzed, and a categorization of studies in this field has been presented. In the third section (explanation of the gap and the proposed method), the deficiencies of existing research have been explained, and the reasons for the need for the proposed method have been outlined. The fourth section (fuzzy cognitive map) provides a brief overview of the history and functioning of fuzzy cognitive mapping. Then in the fifth section (methodology), the research steps are described. The sixth section (model design) explains the proposed method and the model construction process from the influential adoption factors. The seventh section (model implementation) explains the model's implementation method and extracting the most important constructs. Finally, in the eighth section (discussion and interpretation of results), the most important constructs of the model's output will be described and interpreted.

2. LITERATURE REVIEW

Blockchain technology has gained fame primarily due to cryptocurrencies [9]; also, our focus in this study is only

on the adoption of cryptocurrencies and does not include other applications of blockchain technology. In general, academic research in the field of cryptocurrencies can be divided into four categories: technical, economic, regulatory, and social sciences, with the social sciences category having the least amount of research devoted to it [10, 11] and the technical category is the most popular research area in the field of cryptocurrencies [12]. Most research in cryptocurrencies considers Bitcoin as the representative of this technology and has focused its research on it. This point is also true in the acceptance/adoption field, where the adoption of Bitcoin is considered the adoption of all cryptocurrencies. Research conducted on the adoption of cryptocurrency technology can be categorized into five groups, as presented in Table 1. Qualitative research studies have not been included in future reviews due to their lack of relevance to this article.

Most research on the adoption of cryptocurrency technology has used a general technology adoption/acceptance model (Category 1). However, it appears that well-known models such as "Technology Acceptance Model (TAM)", models adapted from TAM (TAM2, TAM3), or "Unified Theory of Acceptance And Use Of Technology" (UTAUT) may not be sufficiently

TABLE 1. Classification of cryptocurrency technology adoption studies

Category	Description	Sample
1. Use a basic model	Studies that have used the structure of the models or general theories of acceptance/ adoption.	[4] - TBP ¹
2. Combination of basic models	Studies that combined the constructs of two or more acceptance/ adoption models or theories.	[13] - UTAUT 2 and DOI ²
3. Combination of basic models and external constructs	Studies that used one or more basic models but developed them with new constructs according to cryptocurrency technology.	[14] - Adding "security" and "awareness" constructs to UTAUT
4. Other systematic methods	Studies that used systematic methods with a constructivist approach to modeling the acceptance/ adoption of cryptocurrencies. In some cases, the structure of these researches originates from basic models.	[15] - Neural network, PLS-SEM ³ and TAM
5. Purely qualitative	Studies that did not use acceptance/ adoption models and were often based on open or semi-structured interviews.	[16]

¹ Theory of Planned Behavior

² Diffusion of Innovation Theory

³ Partial Least Squares Structural Equation Modeling

qualified to study emerging technologies [17]. This can be exacerbated for emerging technologies such as cryptocurrencies due to the unique nature of the adoption process compared to other technologies [18, 19]. For example, the complexity of this technology can significantly affect the design of hypotheses regarding usage intention and actual usage [20]. In other words, many theories and models have been criticized for their poor fit with innovation and the absence of some of their specific features [2]. To the extent that some researchers believed that a particular model does not apply to a wide range of technologies, which is a fundamental and limiting factor for researchers who only use a specific model for studying the adoption of technology [3].

Furthermore, many researchers have concluded that combining multiple theories (Category 2) creates more research power to investigate the adoption of innovation and a better understanding of that innovation [3, 21-24]. However, merely combining models and theories with past structures sometimes lacks the necessary innovation to provide new insights [25]. Adding new constructs to previous models (Category 3) is another way to overcome previous models' complexity and lack of comprehensiveness in accepting/adopting cryptocurrencies. However, this can also carry the risk of bias.

3. EXPLANATION OF THE GAP AND THE PROPOSED METHOD

Limiting oneself to the structure of technology acceptance/adoption models will result in the loss of information. Given that understanding all the main reasons for technology adoption is often complicated [25]. Generally, acceptance/adoption model structures are usually limited and focus on the most critical factors. On the other hand, considering more constructs due to the structure of acceptance/adoption models causes the model to become more complex [26]. In fact, researchers are reluctant to increase the minimum constructs in the base model. Some researchers have even removed some constructs from the base models to reduce complexity. For instance, Sun et al. [27] eliminated the moderating constructs from the UTAUT model [28] to cope with complexity. However, acceptance/ adoption modeling requires considering various constructs related to individual characteristics [25] and technology characteristics [23]. From a structural point of view, there are criticisms of models and theories of technology adoption in cryptocurrencies. For example, none of the studies on cryptocurrency adoption consider the internal causal relationships between different adoption constructs and the measurement of the influence or impact of constructs on each other. Additionally, the uncertainty of relationships has been overlooked, while

the need for a map of causal relationships and dependencies between constructs in adoption models has been considered necessary [26] as uncertainty-based techniques are essential for understanding emerging technologies [29, 30].

Also, a technology adoption model should simultaneously consider both human and technological variables and characteristics that may affect the use of technology. On the other hand, the constructs of existing technology adoption models rarely focus on a specific technology's features [25]. This is more important for cryptocurrencies, which have unique features compared to other technologies [18, 19, 31], and the structure of the designed model should be able to consider different dimensions as well. Besides that, the characteristics of cryptocurrency technology adoption are large-scale and highly complex [32]. Therefore, the proposed method to overcome the mentioned shortcomings is to innovatively use a fuzzy cognitive map (FCM) based on the structure of cryptocurrency research. FCM can describe different dimensions of adoption by showing causal relationships and the influence of constructs on each other. Also, considering that the current research area is in the category of social science research, the determination of adoption structures is generally done qualitatively, and modeling these structures, even with mathematical relationships, is complicated. When mathematical models cannot be used due to the system's complexity, cognitive maps by modeling this complex system are considered a very suitable tool to show a qualitative perspective [33].

4. FUZZY COGNITIVE MAP (FCM)

The fuzzy cognitive map was first introduced in 1986 by Kosko based on Lotfizadeh's fuzzy logic and Axelrod's cognitive models. FCMs evolved from cognitive maps developed by social scientists to record and analyze the cognitions of decision-makers and experts. A cognitive map is a mental model that shows the causal knowledge of experts and is obtained experimentally through social learning [34, 35]. Fuzzy cognitive maps are one of the most widely used graphic models for modeling dynamic systems and seek to model the system as it is understood [36].

In the fuzzy cognitive mapping method, a system is shown and modeled with several nodes and directional lines. Nodes represent the system's states, characteristics, inputs, outputs, and effective parameters. In the basic structure of FCM, each node has a number in the range [0 1]. Each edge between nodes indicates the influence of one node on another node. The weight of each edge means the degree of connection between nodes. In the structure of fuzzy cognitive maps, the weight of each is a number between [-1 1], where the weight of 1 indicates a

complete direct connection and the weight of -1 indicates a full reverse connection. The numbers between these two numbers show the relative degree of relationship [36]. A simple example of FCM is shown in Figure 1.

5. METHODOLOGY

This article's method is adapted from the process introduced by Jetter and Kok [37]. Based on this process, a standard and general methodology for modeling fuzzy cognitive maps is presented in 6 steps.

We need a set of basic information to create a fuzzy cognitive map. In general, the following methods can be used to create a cognitive map [36-38]:

- (1) Experts: The relationships between nodes are determined based on experts' opinions, and their views can also be used to determine the nodes themselves.
- (2) Extracting nodes and relationships from previous research
- (3) Existence of previous FCMs and their consolidation with new rules
- (4) Network training: In this method, there is no need for an expert or a commenter to determine the influence of one node on another node, and relationships are extracted by network training.

We will use a combination of the first three methods to consider each of the past studies as an expert, and based on the results of that research, we will consider each of the factors affecting adoption as a node of the fuzzy cognitive map. Then, based on the structure of each study, we will draw causal relationships to reach an FCM of each study (first and second methods). Then we will combine each of the obtained mappings considering a specific weight (third method).

Extracting the important points of the text and adapting them to some of the desired functions is always one of the crucial concerns [39]. Since the previous studies are considered experts, we will use the method developed by Alizadeh and Jetter [40] to extract nodes and relationships from secondary data. In fact, in phases 4 and 5 of Figure 2, the following steps will be followed:

- Drawing raw FCM from the results of each research
- Consolidating identical concepts

- Adopting consistent terms for similar concepts
- Determining details for concepts and sub-concepts
- Identification and managing island FCMs

6. MODEL DESIGN

According to section 5, to create a comprehensive cryptocurrency adoption model, it is necessary to get help from past researchers as experts to form each FCM. For this purpose, the most important studies in the field of cryptocurrency adoption were carefully examined in two phases, and their structures and relationships were extracted.

In the first phase, a structural approach developed by Webster and Watson [41] was used to find related works in four general steps. Keywords such as acceptance, adoption, attitude to use, and cryptocurrency were used in Google Scholar and Scopus databases to find studies (step 1). After reviewing valid studies (step 2); Fast scanning of full text (step 3); and preliminary analysis (step 4), 30 studies were selected for more detailed review, which is shown in Table 2.

In the second phase, the "citation average per year" index based on the Google Scholar database was used to identify the most important studies. This index shows its relative importance by adjusting the publication time of the research [42, 43]. Using this index is to ensure the benefit of valid experts. Because as past research in different fields has shown, experts play a very important role in developing new models and should be carefully selected [44, 45].

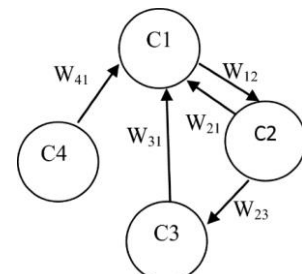


Figure 1. A simple example of a fuzzy cognitive map

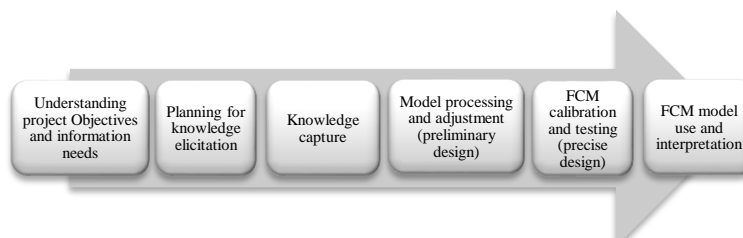


Figure 2. Standard steps of modeling with fuzzy cognitive mapping derived from [37]

Table 2 shows potential experts in order of importance (based on citation average per year). Should note that the data of each study has been examined in a country/region. Therefore, if a study conducted in a

country is considered as one of the experts of the final model, related studies in that country will not be included at a lower rank in the proposed model to ensure an appropriate distribution of input data.

TABLE 2. Researches in the field of cryptocurrency adoption (as FCM experts)

Rank	Authors	Citation average per year	Total cites	Theory/Model/Method used	Country/Region	Sample size	Included in the proposed model?
1	Arias-Olive et al. [46]	45.5	182	UTAUT, PLS- SEM	Spain	402	Yes
2	Abbasi et al. [47]	37.5	75	UTAUT2, PLS-SEM, ANN ¹	Malaysia	314	Yes
3	Shahzad et al. [2]	33.8	169	TAM	China	376	Yes
4	Folkinshteyn and Lennon [4]	32.29	226	TAM	USA	-	Yes
5	Mazambani and Mutambara [48]	31.6	95	TPB	South Africa	269	Yes
6	Sas and Kheyrodin [16]	25.33	152	-	England	20	No/ Purely qualitative and small sample size
7	Sohaib et al. [15]	23.25	93	TAM, PLS-SEM, ANN	Australia	140	Yes
8	Miraz et al. [49]	21	21	UTAUT 2	Malaysia	263	No/ Existence of Malaysia
9	Bhimani et al. [50]	21	21	Correlation and regression analysis	137 Countries	-	No/ Review national development issues
10	Alharbi and Sohaib [51]	20	40	PLS-SEM, ANN	Australia	160	No/ Existence of Australia
11	Yeong, et al. [24]	18	18	UTAUT2, PLS-SEM	Malaysia	176	No/ Existence of Malaysia
12	Jonker [32]	17.25	69	Binomial probit	Netherlands	768	No/ Review at the retailer level
13	Schaupp and Festa [52]	16.8	84	TPB	USA	117	No/ Existence of USA
14	Chen et al. [53]	15	15	PLS-SEM	Malaysia	295	No/ Existence of Malaysia
15	Walton and Johnston [54]	14	70	TAM, TPB	South Africa	237	No/ Existence of South Africa
16	Schaupp et al. [55]	11	11	TPB	USA	492	No/ Existence of USA
17	Jalan et al. [8]	10	10	GLM on WVS ² wave 7	48 Countries	70867	No/ Results based on tweets and Google trends
18	Alaklabi and kang [56]	9.5	19	TRA ³	Saudi Arabia	368	Yes
19	Lee et al. [57]	9	36	UTAUT	USA	127	No/ Existence of USA
20	Gunawan and Novendra [58]	8.33	50	UTAUT	Indonesia	49	Yes
21	Mahomed Nadim [20]	6.17	37	UTAUT 2	South Africa	300	No/ Existence of South Africa

¹ Artificial Neural Network

² Generalized Linear Models Analysis in the World Values Survey

³ Theory of Reasoned Action

22	Esmailzadeh et al. [59]	4.75	19	UTAUT	USA	165	Existence of USA
23	Nseke [13]	4.4	22	UTAUT 2 DOI	African Countries	-	No/ Disconfirmation of hypotheses
24	Kumpajaya and Dhewanto [60]	4	32	TAM DOI	Indonesia	108	No/ Existence of Indonesia
25	Silinskyte [18]	3.78	34	UTAUT	-	111	Yes
26	García-Monleón et al. [6]	2	2	UTAUT PLS-SEM	-	175	Yes
27	Bommer et al. [31]	2	2	Meta-analysis	-	42	No/ Meta-analysis
28	Andraschko and Britzelmaier [61]	2	6	TAM2	Germany	31	No/ Organizational level
29	Liew et al. [62]	1	1	Questionnaire	27 Countries	42223	No/ Purely qualitative
30	Wesley [3]	0.8	4	DOI	USA	20	No/ Existence of USA

According to Table 2, 10 studies were selected as experts, and we will create an FCM from each of them. The raw FCMs formed from each study will be based on the results of the confirmed hypotheses of that study and do not include all the mentioned constructs. Also, if the weight of the relations was clear in the research, the same weight is used as the FCM edge weight; otherwise, the weight of all edges will be the same and equal to the fixed value of 0.5.

6. 1. FCM Creation from Each of the Selected Studies

Based on UTAUT, Arias-Olive et al. [46] propose six hypotheses for the constructs affecting the adoption of cryptocurrencies, and three hypotheses are rejected after analyzing the model. The confirmed constructs are shown in Table 3.

Due to failing to confirm all hypotheses, the Social Influence, Perceived Risk, and Financial Literacy constructs were not used in the final FCM construction shown in Figure 3. In this study, the final node is the intention to use cryptocurrencies.

The above method can be applied to other selected studies similarly. The constructs and FCM adapted from Abbasi et al. [47] study are as follows (Table 4 and Figure 4).

The constructs and FCM adapted from Shahzad et al. [2] study are as follows (Table 5 and Figure 5):

TABLE 3. Effective adoption constructs derived from [46]

Symbol	Node	Output edge weight
A1	Intention to use	-
C1-1	Performance expectancy	0.68
C1-2	Effort expectancy	0.05
C1-3	Facilitating conditions	0.15

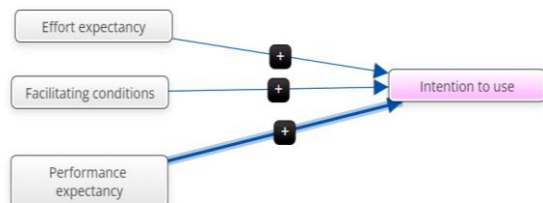


Figure 3. Raw FCM designed from [46]

TABLE 4. Effective adoption constructs derived from [47]

Symbol	Node	Output edge weight
A2	intention to adopt	-
C2-1	Performance expectancy	0.09 to A2-1; 0.21 to C2-5
C2-2	Effort expectancy	A2-1 to 0.17 ; 0.24 to C2-1
C2-3	Trust	0.3
C2-4	Hedonic Motivation	0.26 to C2-5; 0.42 to C2-1
C2-5	Price Value	0.15
C2-6	Personal Innovativeness	0.23

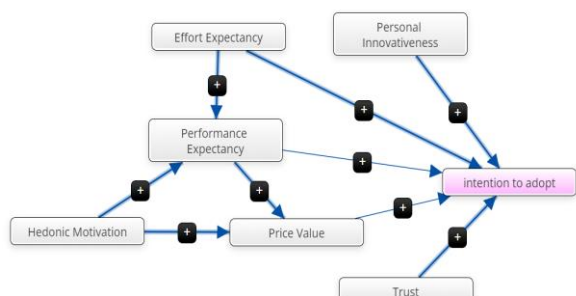
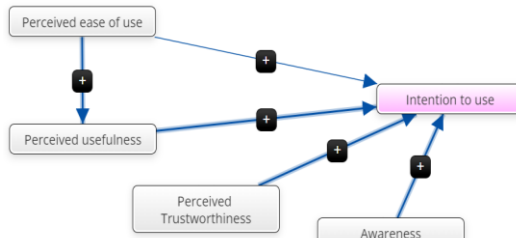


Figure 4. Raw FCM designed from [47]

TABLE 5. Effective adoption constructs derived from [2]

Symbol	Node	Output edge weight
A3	Intention to use	-
C3-1	Perceived ease of use	0.125 to A3; 0.353 to C3-2
C3-2	Perceived usefulness	0.236
C3-3	Perceived Trustworthiness	0.33
C3-4	Awareness	0.229

**Figure 5.** Raw FCM designed from [2]

The constructs and FCM adapted from Folkinshteyn and Lennon [4] study are as follows (Table 6 and Figure 6):

The constructs and FCM adapted from Mazambani and Mutambara [48] study are as follows (Table 7 and Figure 7):

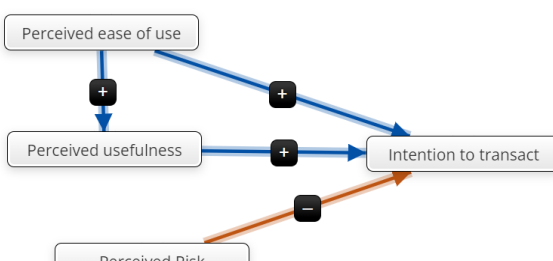
The constructs and FCM adapted from Sohaib et al. [15] study are as follows (Table 8 and Figure 8):

The constructs and FCM adapted from Alaklabi and Kang [56] study are as follows (Table 9 and Figure 9):

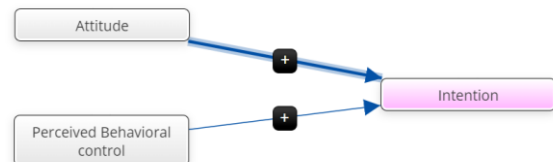
The constructs and FCM adapted from Gunawan and Novendra [58] study are as follows (Table 10 and Figure 10):

TABLE 6. Effective adoption constructs derived from [4]

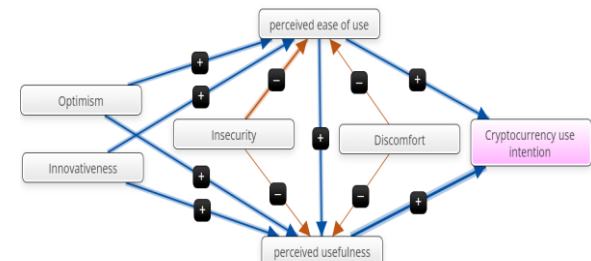
Symbol	Node	Output edge weight
A4	Intention to transact	-
C4-1	Perceived ease of use	0.5 to A4; 0.5 to C4-2
C4-2	Perceived usefulness	0.5
C4-3	Perceived Risk	-0.5

**Figure 6.** Raw FCM designed from [4]**TABLE 1.** Effective adoption constructs derived from [48]

Symbol	Node	Output edge weight
A5	Intention	-
C5-1	Attitude	0.74
C5-2	Perceived Behavioural control	

**Figure 7.** Raw FCM designed from [48]**TABLE 2.** Effective adoption constructs derived from [15]

Symbol	Node	Output edge weight
A6	Cryptocurrency use intention	-
C6-1	perceived ease of use	0.486 to A6, 0.321 to C6-2
C6-2	perceived usefulness	0.514
C6-3	Discomfort	-0.08 to C6-2; -0.1 to C6-1
C6-4	Insecurity	-0.16 to C6-2; -0.21 to C6-1
C6-5	Optimism	0.242 to C6-2; 0.4 to C6-1
C6-6	Innovativeness	0.191 to C6-2; 0.285 to C6-1

**Figure 8.** Raw FCM designed from [15]**TABLE 9.** Effective adoption constructs derived from [56]

Symbol	Node	Output edge weight
A7	Intention to adopt cryptocurrency	-
C7-1	Attitude	0.5
C7-2	Subjective norm	0.5
C7-3	Security Risk (Perceived Risk)	-0.5
C7-4	perceived usefulness	0.5 to A7 and C7-1
C7-5	Perceived Enjoyment	0.5 to A7 and C7-1

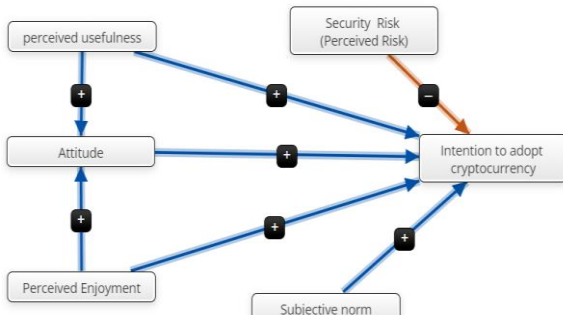


Figure 9. Raw FCM designed from [56]

TABLE 10. Effective adoption constructs derived from [58]

Symbol	Node	Output edge weight
A8-1	use behavior	-
A8-2	behavioral intention	0.5
C8-1	Performance expectancy	0.5
C8-2	Social influence	0.5
C8-3	Facilitating condition	0.5

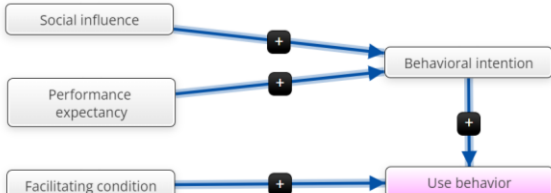


Figure 10. Raw FCM designed from [58]

The constructs and FCM adapted from Silinskyte [18] study are as follows (Table 11 and Figure 11):

The constructs and FCM adapted from García-Monleón et al. [6] study are as follows (Table 12 and Figure 12):

6. 2. Unification of Similar Concepts and Integration of FCMs

In the previous stages, the cognitive network structure of each research was

TABLE 3. Effective adoption constructs derived from [18]

Symbol	Node	Output edge weight
A9-1	Use Behavior	
A9-2	Behavioural intentions	0.487
C9-1	Effort expectancy	0.473
C9-2	Facilitating conditions	0.448
C9-3	Performance expectancy	0.707

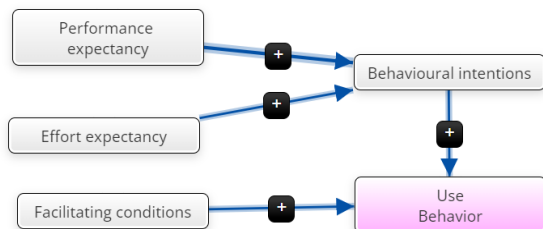


Figure 11. Raw FCM designed from [18]

TABLE 12. Effective adoption constructs derived from [6]

Symbol	Node	Output edge weight
A10-1	Intention to use cryptocurrency	-
C10-1	Emotional perceived value	0.533
C10-2	Financial perceived value	0.545
C10-3	knowledge path	0.677
C10-4	Hedonic motivation	0.027
C10-5	Social influence	0.004
C10-6	Trust	0.243
C10-7	Effort expectancy	0.093
C10-8	Performance expectancy	0.26
C10-9	Facilitating conditions	0.149
C10-10	Environmental sustainability	0.238
C10-11	Social sustainability	0.169

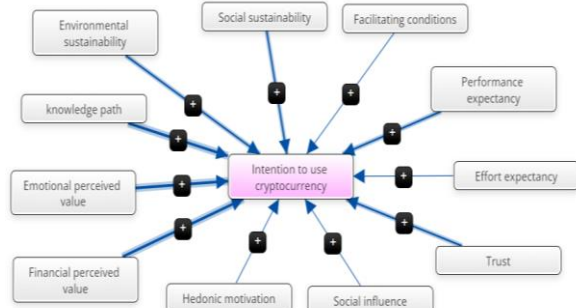


Figure 12. Raw FCM designed from [6]

prepared; now, all constructs in similar concepts used in the above FCMs should be unified and coded. Table 13 shows the final constructs for creating a comprehensive FCM.

In Table 13, some constructs (second column) have been integrated into one code (first column) based on Yadegari et al. [43]. For example, Effort expectancy and Perceived ease of use have the same concept and are mapped to the PEU code, or perceived usefulness is similar to performance expectancy [63] and receives the same code (PU).

TABLE 4. Coding model concepts

Final code	Symbol	Node	References
ITU (Intention to use)	A1	Intention to use	[2, 6, 46]
	A3		
	A9-1		
	A2	Intention to adopt	[47, 56]
	A7		
	A4	Intention to transact	[4]
	A5	Intention	[48]
	A6	Cryptocurrency use intention	[15]
	A8-2		
	A10-2	Behavioral intention	[18, 58]
USE	A8-1		
	A10-1	Use behavior	[18, 58]
(PU) Performance usefulness	C1-1		
	C2-1		
	C8-1	Performance expectancy	[6, 18, 46, 47, 58]
	C9-8		
	C10-3		
	C3-2		
	C4-2	Perceived usefulness	[2, 4, 15, 56]
	C6-2		
	C7-4		
	C1-2		
PEU (Perceived ease of use)	C2-2		
	C9-7	Effort expectancy	[6, 18, 46, 47, 58]
	C10-1		
	C3-1		
FC (Facilitating conditions)	C4-1	Perceived ease of use	[2, 4, 15]
	C6-1		
	C1-3		
	C8-3	Facilitating conditions	[6, 18, 46, 58]
PT (Perceived Trust)	C9-9		
	C10-2		
	C2-3	Trust	[6, 47]
HM (Hedonic Motivation)	C9-6		
	C3-3	Perceived trustworthiness	[2]
	C2-4		
FV (Financial value)	C9-4	Hedonic motivation	[6, 47]
	C7-5	Perceived enjoyment	[56]
INV (Innovativeness)	C2-5	Price value	[47]
	C9-2	Financial perceived value	[6]
AW (Awareness)	C6-6	Innovativeness	[15]
	C2-6	Personal innovativeness	[47]
PR (Perceived Risk)	C3-4	Awareness	[2]
	C9-3	Knowledge path	[6]
	C4-3	Perceived risk	[4]
	C7-3	Security risk (perceived risk)	[56]

	C6-4	Insecurity	[15]
AT (Attitude)	C5-1 C7-1	Attitude	[48, 56]
PBC	C5-2	Perceived behavioural Control	[48]
DC	C6-3	Discomfort	[15]
OP	C6-5	Optimism	[15]
SN	C7-2	Subjective norm	[56]
SI	C8-2 C9-5	Social influence	[6, 58]
EPV	C9-1	Emotional perceived value	[6]
ES	C9-10	Environmental sustainability	[6]
SS	C9-11	Social sustainability	[6]

One of the great features of fuzzy cognitive maps is the possibility of combining several maps; in such a way that the nodes are added to each other, and a weighted average is taken from the common edges. Figure 14 shows the graphical representation of the aggregated fuzzy cognitive map. This figure shows the causal relationship of all the constructs mentioned in the first column of Table 13 based on the structure of the previous models.

7. MODEL IMPLEMENTATION

In fuzzy cognitive maps, an initial value should be considered for each node. In this research, this value is assumed to be 0 for all nodes so that the conditions of all

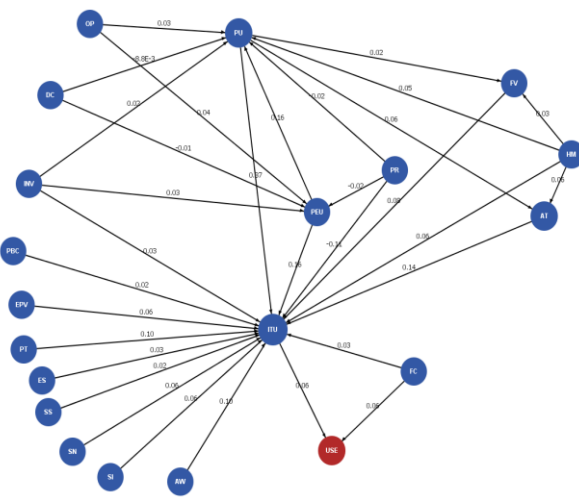


Figure 14. Aggregated fuzzy cognitive map

nodes are the same for the final selection. In each iteration, the effect value of the nodes on each other is added to or subtracted from this initial value. It can be said that choosing any initial value does not affect the final result as long as it is the same for all nodes.

Equation (1) to calculate the value of each node recursively. According to this Equation, the value of a node is the sum of the effects of all nodes that influence it, as well as the node's previous value [36].

$$A_i^t = f \left(\sum_{j=1}^n A_j^{t-1} W_{ji} + A_i^{t-1} \right) \quad (1)$$

t = iteration

A_i^t = the value of concept i in the t^{th} iteration

W_{ji} = the impact value of concept i on concept j

To ensure that the values of concepts remain within the range of [0 1], a compression function f is employed, which is typically represented by Equation (2). This equation is commonly referred to as a logistic compression function.

$$f(X) = \frac{1}{1+e^{-\lambda x}} \quad (2)$$

In Equation (2), λ determines the slope of the logistic function, and it must be a number greater than zero, which is considered 1 in this research. Also, e is the number of Neper (=2.71).

To calculate the final value of each node, the iteration is done until either the node's value reaches a stable state or its value changes in a finite state cycle. A stable state means that the values of all concepts have reached the final stable values without changing in future iterations. Only in this case can the model outputs be interpreted and used for decision-making [59, 64].

As it is clear in Figure 15, in the first iteration, the value of all the nodes goes from 0 to 0.5. After the first iteration, according to the strength of each edge, the nodes affect each other, and finally, after seven repetitions, the value of all nodes will be stable without

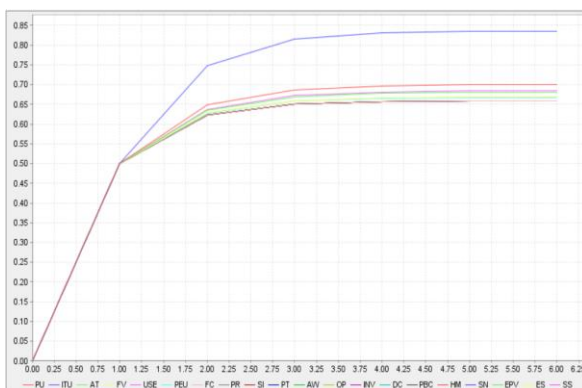


Figure 15. Stability of the cryptocurrency adoption constructs in the proposed model

change. Table 14 shows the final value of the most important constructs. In this table, a higher value means a greater impact on the adoption of cryptocurrencies.

8. DISCUSSION AND INTERPRETATION OF RESULTS

As many studies have pointed out, the intention to use cryptocurrencies (ITU) is the main factor in cryptocurrency adoption. In fact, the stage before adoption and then using cryptocurrencies is the intention of the user to this technology, which is positive means adoption, and being negative means not adopting it. Although we must distinguish between acceptance, adoption, and use ("technology acceptance can be considered to precede technology adoption, and these two precede technology use" [43, 65]). What is clear is that any constructs that significantly affect this factor will ultimately directly influence the adoption of cryptocurrencies. According to the results of the proposed model, perceived usefulness (PU), attitude (AT), financial value (PV), and perceived ease of use (PEU) of this technology are the most important factors that positively influence the adoption of cryptocurrencies.

Perceived usefulness refers to the degree to which a person believes using cryptocurrency can improve their performance [66]. If a person evaluates that a cryptocurrency helps him/her to do his work and is useful, the probability of using it increases. Presenting real applications and successful examples where cryptocurrencies have been used can be one of the ways to familiarize a person with the applicability of this technology and lead to the intention of using it. Due to the high importance of this construct, paying attention to the current and future needs of users and expressing the benefits of a specific cryptocurrency that can cover that need more efficiently than before can lead to the user's intention to use it.

Another factor affecting the adoption of cryptocurrencies is attitude, which means A person's feeling of the positive or negative effect of a certain behavior [67]. In other words, attitude refers to how a

TABLE 5. The final value of the most important constructs

Code	Node	Final value
ITU	Intention to use	0.8359
PU	Perceived usefulness	0.7001
AT	Attitude	0.6801
FV	Financial value	0.669
PEU	Perceived ease of use	0.6668
Other	-	Less than 0.659

person feels and believes about technology, including its advantages and disadvantages, its actual value, and how it relates to his/her environment. Perceived usefulness directly makes a person's attitude towards use positive. Therefore, clearly stating the benefits of this technology and how to deal with the risks can significantly improve a person's attitude toward cryptocurrencies.

The financial value that the user perceives from cryptocurrencies is another important factor that leads to user adoption. Historical data also shows that whenever the financial value of cryptocurrencies has increased, the number of users of this technology has also grown significantly; As the predictions show, the value of cryptocurrencies will grow significantly due to the decentralized future of financial systems, which will lead to greater adoption in the future.

Also, perceived ease of use is the degree to which a person can effortlessly use cryptocurrencies [66]. Considering the existence of this construct in the selected factors, it seems that the complexity of using cryptocurrency technology for end users is still high, and it can hurt the users' attitude. Therefore, cryptocurrency service providers should focus on simplifying the user interface, training users, and adapting the processes as much as possible to the systems that the user used before.

9. CONCLUSION

Cryptocurrency adoption models can provide comprehensive insight to policymakers, legislators, and organizations interested in cryptocurrency. Legislators and policymakers can use the adoption model to create regulations that support cryptocurrency adoption factors while reducing cryptocurrency risks. Organizations interested in cryptocurrency can also use adoption models to inform product designs, promotions, and services. Organizations can increase their chances of success in the cryptocurrency market by aligning their strategies with the affecting adoption factors.

For the first time, this research has developed a comprehensive modeling of the factors influencing the adoption of cryptocurrencies using the fuzzy cognitive mapping approach based on the results of credible research in this field. This approach considered each selected study on the acceptance/ adoption of cryptocurrencies as an expert and used the research outputs as input for the model to take advantage of global data prevalence systematically to create a comprehensive model. This method enabled the integration of all the previous models into one scalable fuzzy cognitive map. The results of the final FCM indicate the most important constructs and their greater effect on the final node.

The findings of the presented model show that the perceived usefulness, attitude, financial value, and Perceived ease of use of cryptocurrency technology are

the most important factors that cause a positive attitude toward adopting this technology. Considering the conditions of each society, finding tools and methods that can satisfy these factors can significantly impact the adoption of cryptocurrencies on a large scale.

This study was also faced with some limitations and challenges, the most important of which was the dependence on past studies and the selection of the most important ones. The constructs of the past models form the initial structure of the fuzzy cognitive map, and if they are not carefully selected, they may affect the final results. In this study, we used one selected study from each country. Using more studies with different selection criteria can produce different results than this research. Another limitation was due to the nature of fuzzy cognitive maps. In some technology acceptance models, moderator variables such as age and gender are used. Since these moderator variables affect the relationship between two constructs, they cannot be directly modeled on the fuzzy cognitive map and were not considered in this model.

For future studies, it is suggested to define a criterion to define the importance of fuzzy cognitive maps adapted from each study so that when combining the maps, studies with higher importance have a greater contribution to the final results. For example, this criterion can be adapted from conventional criteria for evaluating and measuring the credibility of articles and then normalizing it for use in FCM. Also, converting the moderator variables into intermediate nodes in FCM and considering their impact on the constructs of adopting cryptocurrencies can result in a more accurate model and is of interest to researchers. Finally, collecting all the studies related to digital currencies in a country and modeling them comprehensively in the manner described in this study can provide an applicable model specific to that country.

10. REFERENCES

1. Joseph M. Woodside, Fred K. Augustine Jr, and Will Giberson, "Blockchain Technology Adoption Status and Strategies", *Journal of International Technology and Information Management*, Vol. 26, No. 2, (2017), 65-93, doi: 10.58729/1941-6679.1300.
2. Shahzad, F., Xiu, G., Wang, J., and Shahbaz, M., "An empirical investigation on the adoption of cryptocurrencies among the people of mainland China", *Technology in Society*, Vol. 55, (2018), 33-40, doi: 10.1016/j.techsoc.2018.05.006.
3. Wesley, M., "An investigation into the diffusion of the cryptocurrency innovation", Jyväskylä University. Master Thesis, (2018).
4. Folkinshteyn, D. and Lennon, M., "Braving Bitcoin: A technology acceptance model (TAM) analysis", *Journal of Information Technology Case and Application Research*, Vol. 18, No. 4, (2016), 220-249, doi: 10.1080/15228053.2016.1275242.

5. Derbentsev, V., Babenko, V., Khrustalev, K., Obruch, H., and Khrustalova, S., "Comparative Performance of Machine Learning Ensemble Algorithms for Forecasting Cryptocurrency Prices", *International Journal of Engineering, Transactions A: Basics*, Vol. 34, No. 1, (2021), 140-148, doi: 10.5829/ije.2021.34.01a.16.
6. García-Monleón, F., Erdmann, A., and Arilla, R., "A value-based approach to the adoption of cryptocurrencies", *Journal of Innovation & Knowledge*, Vol. 8, No. 2, (2023), 100342, doi: 10.1016/j.jik.2023.100342.
7. Tauda, G. A., Omara, A., and Arnone, G., "Cryptocurrency: Highlighting the Approach, Regulations, and Protection in Indonesia and European Union", *BESTUUR*, Vol. 11, (2023), 1-25, doi: 10.20961/bestuur.v11i1.67125.
8. Jalan, A., Matkovskyy, R., Urquhart, A., and Yarovaya, L., "The role of interpersonal trust in cryptocurrency adoption", *Journal of International Financial Markets, Institutions and Money*, Vol. 83, (2023), p. 101715, doi: 10.1016/j.intfin.2022.101715.
9. Moosavi, J., Naeni, L. M., Fathollahi-Fard, A. M., and Fiore, U., "Blockchain in supply chain management: a review, bibliometric, and network analysis", *Environmental Science and Pollution Research*, (2021), 1-15, doi: 10.1007/s11356-021-13094-3.
10. Baur, A. W., Bühler, J., Bick, M., and Bonorden, C. S., "Cryptocurrencies as a Disruption? Empirical Findings on User Adoption and Future Potential of Bitcoin and Co", in *14th Conference on e-Business, e-Services and e-Society (I3E)*, (2015), 63-80.
11. Holub, M. and Johnson, J., "Bitcoin research across disciplines", *The Information Society*, Vol. 34, No. 2, (2018), 114-126, doi: 10.1080/01972243.2017.1414094.
12. Alzahrani, S. and Daim, T. U., "Technology Adoption: Case of Cryptocurrency", in *Recent Developments in Individual and Organizational Adoption of ICTs*, O. Yildiz, Ed., (2020), 96-119.
13. Nseke, P., "How Crypto-Currency Can Decrypt the Global Digital Divide: Bitcoins a Means for African Emergence", *International Journal of Innovation and Economic Development*, Vol. 3, No. 6, (2018), 61-70, doi: 10.18775/ijied.1849-7551-7020.2015.36.2005.
14. Alomari, A. S. A. and Abdullah, N. L., "Factors influencing the behavioral intention to use Cryptocurrency among Saudi Arabian public university students: Moderating role of financial literacy", *Cogent Business & Management*, Vol. 10, No. 1, (2023), doi: 10.1080/23311975.2023.2178092.
15. Sohaib, O., Hussain, W., Asif, M., Ahmad, M., and Mazzara, M., "A PLS-SEM Neural Network Approach for Understanding Cryptocurrency Adoption", *IEEE Access*, Vol. 8, (2019), 13138-13150, doi: 10.1109/ACCESS.2019.2960083.
16. Sas, C. and Khairuddin, I. E., "Design for Trust", Proceedings of the 2017 CHI Conference on Human Factors in Computing Systems, New York, NY, USA, (2017).
17. Lai, P. C., "The literature review of technology adoption models and theories for the novelty technology", *Journal of Information Systems and Technology Management*, Vol. 14, No. 1, (2017), 21-38, doi: 10.4301/s1807-17752017000100002.
18. Silinskyte, J., "Understanding Bitcoin adoption: Unified Theory of Acceptance and Use of Technology (UTAUT) application", Leiden University. Master thesis, (2014).
19. Catalini, C. and Tucker, C., "When early adopters don't adopt", *Science*, Vol. 357, No. 6347, (2017), 135-136, doi: 10.1126/science.aal4476.
20. Mahomed Nadim, "Understanding consumer adoption of cryptocurrencies", Gordon Institute of Business Science, University of. Master thesis, (2017).
21. Tiago Oliveira and Maria Fraga Martins, "Literature Review of Information Technology Adoption Models at Firm Level", *Electronic Journal of Information Systems Evaluation*, Vol. 14, No. 1, (2011), 110-121.
22. Lee, Y.-H., Hsieh, Y.-C., and Hsu, C.-N., "Adding innovation diffusion theory to the technology acceptance model: Supporting employees' intentions to use e-learning systems", *Journal of Educational Technology Society*, Vol. 14, No. 4, (2011), 124-137.
23. Al-Amri, R., Zakaria, N. H., Habbal, A., and Hassan, S., "Cryptocurrency adoption: current stage, opportunities, and open challenges", *International Journal of Advanced Computer Research*, Vol. 9, No. 44, (2019), 293-307, doi: 10.19101/ijacr.pid43.
24. Yeong, Y.-C., Kalid, K. S., Savita, K. S., Ahmad, M. N., and Zaffar, M., "Sustainable cryptocurrency adoption assessment among IT enthusiasts and cryptocurrency social communities", *Sustainable Energy Technologies and Assessments*, Vol. 52, Part A, (2022), 102085, doi: 10.1016/j.seta.2022.102085.
25. Shaw, H., Ellis, D. A., and Ziegler, F. V., "The Technology Integration Model (TIM). Predicting the continued use of technology", *Computers in Human Behavior*, Vol. 83, (2018), 204-214, doi: 10.1016/j.chb.2018.02.001.
26. Rahimi, N., Jetter, A. J., Weber, C. M., and Wild, K., "Soft Data Analytics with Fuzzy Cognitive Maps: Modeling Health Technology Adoption by Elderly Women", in *Advanced Data Analytics in Health*: Springer, Cham, (2018), 59-74.
27. Sun, Y., Bhattacharjee, A., and Ma, Q., "Extending technology usage to work settings: The role of perceived work compatibility in ERP implementation", *Information & Management*, Vol. 46, No. 6, (2009), 351-356, doi: 10.1016/j.im.2009.06.003.
28. Venkatesh, V., Thong, J. Y., and Xu, X., *Unified Theory of Acceptance and Use of Technology: A Synthesis and the Road Ahead*, (2016).
29. Kazemifard, N., Bashir, L., and Rahmani, D., "A Novel Hybrid Model for Technology Strategy Formulating in High-tech Industries under Uncertainty: A Case Study", *International Journal of Engineering, Transactions C: Aspects*, Vol. 36, No. 6, (2023), 1166-1178, doi: 10.5829/ije.2023.36.06c.15.
30. Moosavi, J., Fathollahi-Fard, A. M., and Dulebenets, M. A., "Supply chain disruption during the COVID-19 pandemic: Recognizing potential disruption management strategies", *International Journal of Disaster Risk Reduction*, Vol. 75, (2022), p. 102983, doi: 10.1016/j.ijdrr.2022.102983.
31. Bommer, W. H., Milevoj, E., and Rana, S., "The intention to use cryptocurrency: A meta-analysis of what we know", *Emerging Markets Review*, Vol. 55, (2023), 100962, doi: 10.1016/j.ememar.2022.100962.
32. Jonker, N., "What drives the adoption of crypto-payments by online retailers?", *Electronic Commerce Research and Applications*, Vol. 35, (2019), 100848, doi: 10.1016/j.elerap.2019.100848.
33. Aguilar, J., "Multilayer Cognitive Maps in the Resolution of Problems using the FCM Designer Tool", *Applied Artificial Intelligence*, Vol. 30, No. 7, (2016), 720-743, doi: 10.1080/08839514.2016.1214422.
34. Özesmi, U. and Özesmi, S. L., "Ecological models based on people's knowledge: a multi-step fuzzy cognitive mapping approach", *Ecological Modelling*, Vol. 176, 1-2, (2004), 43-64, doi: 10.1016/j.ecolmodel.2003.10.027.
35. Kosko, B., "Fuzzy cognitive maps", *International Journal of Man-Machine Studies*, Vol. 24, No. 1, (1986), 65-75, doi: 10.1016/S0020-7373(86)80040-2.
36. Glykas, M., Fuzzy cognitive maps: Advances in theory, methodologies, tools and applications: Springer Science & Business Media., (2010). <https://link.springer.com/content/pdf/10.1007/978-3-642-03220-2.pdf>
37. Jetter, A. J. and Kok, K., "Fuzzy Cognitive Maps for futures studies—A methodological assessment of concepts and methods", *Futures*, Vol. 61, (2014), 45-57, doi: 10.1016/j.futures.2014.05.002.

38. Sánchez, H., Aguilar, J., Terán, O., and Gutiérrez de Mesa, J., "Modeling the process of shaping the public opinion through Multilevel Fuzzy Cognitive Maps", *Applied Soft Computing*, Vol. 85, (2019), 105756, doi: 10.1016/j.asoc.2019.105756.
39. Tayefeh Mahmoudi, M. and Badie, K., "A Fuzzy Fusion Framework for Generating Purpose-oriented Texts", *International Journal of Engineering, Transactions A: Basics*, Vol. 36, No. 7, (2023), 1219-1229, doi: 10.5829/ije.2023.36.07a.03.
40. Alizadeh, Y. and Jetter, A., "Content Analysis Using Fuzzy Cognitive Map (FCM): A Guide to Capturing Causal Relationships from Secondary Sources of Data", 2017 Portland International Conference on Management of Engineering and Technology (PICMET), (2017).
41. Webster, J., & Watson, R. T., "Analyzing the past to prepare for the future: Writing a literature review", *MIS Quarterly*, Vol. 26, No. 2, (2002), xiii-xxiii.
42. Sousa, A., Calçada, E., Rodrigues, P., and Pinto Borges, A., "Cryptocurrency adoption: a systematic literature review and bibliometric analysis", *EuroMed Journal of Business*, Vol. 17, No. 3, (2022), 374-390, doi: 10.1108/EMJB-01-2022-0003.
43. Yadegari, M., Mohammadi, S., and Masoumi, A. H., "Technology adoption: an analysis of the major models and theories", *Technology Analysis & Strategic Management*, (2022), 1-15, doi: 10.1080/09537325.2022.2071255.
44. Fallahpour, A., Wong, K. Y., Rajoo, S., Fathollahi-Fard, A. M., Antucheviciene, J., and Nayeri, S., "An integrated approach for a sustainable supplier selection based on Industry 4.0 concept", *Environmental Science and Pollution Research*, (2021), 1-19, doi: 10.1007/s11356-021-17445-y.
45. Ghadami, N., Gheibi, M., Kian, Z., Faramarz, M. G., Naghedi, R., Eftekhari, M., Fathollahi-Fard, A. M., Dulebenets, M. A., and Tian, G., "Implementation of solar energy in smart cities using an integration of artificial neural network, photovoltaic system and classical Delphi methods", *Sustainable Cities and Society*, Vol. 74, (2021), doi: 10.1016/j.scs.2021.103149.
46. Arias-Oliva, M., Pelegrín-Borondo, J., and Matías-Clavero, G., "Variables Influencing Cryptocurrency Use: A Technology Acceptance Model in Spain", *Frontiers in psychology*, Vol. 10, (2019), doi: 10.3389/fpsyg.2019.00475.
47. Abbasi, G. A., Tiew, L. Y., Tang, J., Goh, Y.-N., and Thurasamy, R., "The adoption of cryptocurrency as a disruptive force: Deep learning-based dual stage structural equation modelling and artificial neural network analysis", *PLoS ONE*, Vol. 16, No. 3, (2021), e0247582, doi: 10.1371/journal.pone.0247582.
48. Mazambani, L. and Mutambara, E., "Predicting FinTech innovation adoption in South Africa: the case of cryptocurrency", *African Journal of Economic and Management Studies*, Vol. 11, No. 1, (2020), 30-50, doi: 10.1108/AJEMS-04-2019-0152.
49. Miraz, M. H., Hasan, M. T., Rekabder, M. S., and Akhter, R., "Trust-transaction-transparency-volatility-facilitating-condition-performance-expectancy-towards-cryptocurrency-adoption-through-intention-to-use", *Journal of Management Information and Decision Sciences*, Vol. 25, S5, (2021), 1-20.
50. Bhimani, A., Hausken, K., and Arif, S., "Do national development factors affect cryptocurrency adoption?", *Technological Forecasting and Social Change*, Vol. 181, (2022), 121739, doi: 10.1016/j.techfore.2022.121739.
51. Alharbi, A. and Sohaib, O., "Technology Readiness and Cryptocurrency Adoption: PLS-SEM and Deep Learning Neural Network Analysis", *IEEE Access*, Vol. 9, (2021), 21388-21394, doi: 10.1109/access.2021.3055785.
52. Schaupp, L. C. and Festa, M., "Cryptocurrency adoption and the road to regulation", Proceedings of the 19th Annual International Conference on Digital Government Research: Governance in the Data Age, New York, NY, USA, (2018).
53. Chen, X., Miraz, M. H., Gazi, M. A. I., Rahaman, M. A., Habib, M. M., and Hossain, A. I., "Factors affecting cryptocurrency adoption in digital business transactions: The mediating role of customer satisfaction", *Technology in Society*, Vol. 70, (2022), p. 102059, doi: 10.1016/j.techsoc.2022.102059.
54. J Walton, A. and A. Johnston, K., "Exploring Perceptions of Bitcoin Adoption: The South African Virtual Community Perspective", *Interdisciplinary Journal of Information, Knowledge, and Management*, Vol. 13, (2018), 165-182, doi: 10.28945/4080.
55. Schaupp, L. C., Festa, M., Knotts, K. G., and Vitullo, E. A., "Regulation as a pathway to individual adoption of cryptocurrency", *Digital Policy, Regulation and Governance*, Vol. 24, No. 2, (2022), 199-219, doi: 10.1108/DPRG-08-2021-0101.
56. Alaklabi, S. and Kang, K., "Perceptions towards Cryptocurrency Adoption: A case of Saudi Arabian Citizens", *Journal of Electronic Banking Systems*, (2021), 1-17, doi: 10.5171/2021.110411.
57. Lee, C. C., Kriscenski, J. C., and Lim, H. S., "An Empirical Study of Behavioral Intention to Use Blockchain Technology", *Journal of International Business Disciplines*, Vol. 14, No. 1, (2019).
58. Gunawan, G. and Novendra, R., "2017-gunavan: An Analysis of Bitcoin Acceptance in Indonesia", *Computer, Mathematics and Engineering Applications*, Vol. 8, No. 4, (2017), 241-247.
59. Esmaeilzadeh, P. and Subramanian, H., "Individuals' cryptocurrency adoption: A proposed moderated-mediation model", Twenty-fifth Americas Conference on Information Systems, (2019).
60. Kumpajaya, A. and Dhewanto, W., "The acceptance of Bitcoin in Indonesia: extending TAM with IDT", *Journal of Business and Management*, Vol. 4, No. 1, (2015), 28-38.
61. Andraschko, L. and Britzelmaier, B., "Adaptation of cryptocurrencies in listed companies: empirical findings of a CFO survey in the German capital market", *International Journal of Big Data Management*, Vol. 1, No. 1, (2020), 26-49.
62. Liew, E. J. Y., Peh, W. L., and Leong, Z. K., *Perceived Trust and Confidence for Cryptocurrency Adoption: What Lies Ahead?*: IGI Global, (2022).
63. Safaie, N., Hamidi, H., and Vali, M., "A Framework for Analysis of Predictors of Mobile-marketing Use by Expanding Unified Theory of Acceptance and Use of Technology and Artificial Neural Networks", *International Journal of Engineering, Transactions B: Applications*, Vol. 36, No. 5, (2023), 1012-1022, doi: 10.5829/ije.2023.36.05b.17.
64. Motlagh, O., Tang, S. H., Jafar, F. A., and Khaksar, W., "FCM Relationship Modeling for Engineering Systems", in *Fuzzy Cognitive Maps for Applied Sciences and Engineering*: Springer, Berlin, Heidelberg, (2014), 49-64.
65. Liu, L., Cruz, A. M., and Rincon, A. M. R., "Technology Acceptance, Adoption, and Usability: Arriving at Consistent Terminologies and Measurement Approaches", in *Rehabilitation science in practice series, Everyday technologies in healthcare*, C. M. Hayre, D. J. Müller, and M. J. Scherer, Eds., 1st ed., Boca Raton: CRC Press, (2019), 319-338.
66. Venkatesh, V. and Bala, H., "Technology Acceptance Model 3 and a Research Agenda on Interventions", *Decision Sciences*, Vol. 39, No. 2, (2008), 273-315, doi: 10.1111/j.1540-5915.2008.00192.x.
67. Bahrami, L., Safaie, N., and Hamidi, H., "Effect of motivation, opportunity and ability on human resources information security management considering the roles of Attitudinal, behavioral and organizational factors", *International Journal of Engineering, Transactions C: Aspects*, Vol. 34, No. 12, (2021), 2624-2635, doi: 10.5829/ije.2021.34.12c.07.

COPYRIGHTS

©2023 The author(s). This is an open access article distributed under the terms of the Creative Commons Attribution (CC BY 4.0), which permits unrestricted use, distribution, and reproduction in any medium, as long as the original authors and source are cited. No permission is required from the authors or the publishers.

**Persian Abstract**

چکیده

رمزارزها با ماهیت غیرمت مرکز خود، مستقل از سیاست های اقتصادی دولت ها و بدون نیاز به نهادهای نظارتی مانند بانک ها، به سرعت به عنوان وسیله ای پرداخت یا دارایی دیجیتال ارزشمند، در حال پذیرش بین المللی هستند. با این حال، تحقیقات محدودی در مورد پذیرش رمزارزها انجام شده است، که اکثر آنها از یک مدل پذیرش فناوری عمومی با رویکرد اثبات گرایانه استفاده می کنند. مشکل اصلی مطالعات قبلی این است که آنها به ساختار مدل های فناوری محدود شده اند و تنها چند سازه محدود را به دلیل افزایش پیچیدگی مدل، بررسی می کنند. از سوی دیگر، با توجه به ماهیت منحصر به فرد و پیشرفت های سریع رمزارزها، ایجاد مدل های جامع جدید که ابعاد مختلف را در بر می گیرد، ضروری به نظر می رسد. هدف این مقاله شناسایی عوامل تأثیرگذار در پذیرش فناوری رمزارزها، درک روابط متقابل آنها و در نهایت توسعه یک مدل جامع است. این پژوهش با رویکرد سازه انگاری، از مهم ترین تحقیقات دهه گذشته در زمینه پذیرش رمزارزها استفاده کرده و با رویکردی نظام ممند، مدلی شناختی از سازه های آنها ایجاد می کند. نقطه کانونی رویکرد ما ساخت گرایی، همراه با در نظر گرفتن تأثیر سازه ها بر یکدیگر با استفاده از نقشه های شناختی فازی، که قبلاً در پذیرش ارزهای دیجیتال انجام نشده است می باشد. نتایج مدل پیشنهادی نشان می دهد که سودمندی درک شده، نگرش، ارزش مالی و سهولت استفاده درک شده مهم ترین سازه هایی هستند که بر ایجاد قصد مثبت نسبت به استفاده و پذیرش ارزهای دیجیتال تأثیر می گذارند.



Numerical Study and Comparison of Two-dimensional Ferrofluid Flow in Semi-porous Channel under Magnetic Field

P. Jalili^a, M. D. Afifi^b, B. Jalili^{*a}, A. M. Mirzaei^b, D. D. Ganji^b

^aDepartment of Mechanical Engineering, North Tehran Branch, Islamic Azad University, Tehran, Iran

^bDepartment of Mechanical Engineering, Babol Noshirvani University of Technology, Babol, Iran

PAPER INFO

Paper history:

Received 22 July 2023

Received in revised form 14 August 2023

Accepted 15 August 2023

Keywords:

Ferrofluid

Magnetic Field

Akbari-Ganji Method

Finite Element Method

Semi-porous Channel

ABSTRACT

In this article, the equations governing the constant ferromagnetic current are investigated. The Lorentz force restrains this ferrofluid flow in a semi-porous valve. Analyses were performed on three sub-particle fluids: kerosene and blood, water and magnetite. Modeling in the Cartesian coordinate system using the relevant equations was investigated. A slight thinning should be considered in the lower part of this channel. This research has used two Akbari-Ganji methods (AGM) and finite element method (FEM) to solve the equations. Nonlinear differential equations are solved using the above two methods. In the finite element model, the effect of changing the Hartmann number and the Reynolds number on the flow velocity and the derivatives of the velocity and shear stress of the fluid were investigated. As the Hartmann number increases, the velocity decreases in both directions. The Reynolds number changes in different slip parameters, which shows the opposite behavior for the two directions. Also, the insignificant effect of volume fraction of nanoparticles on velocity and its derivatives and shear stress was investigated. The results of solving the equations with the above two methods were compared with HAM. The results obtained using AGM and FEM and their comparison with previous researches have led to complete agreement, which shows the efficiency of the techniques used in this research.

doi: 10.5829/ije.2023.36.11b.13

NOMENCLATURE

L_x	characteristic length [m]
u, v	dimensionless velocity components
x, y	dimensionless variables
U, V	dimensionless velocity
u^*, v^*	velocity vector components in x^* and y^* directions, respectively [ms^{-1}]
x^*, y^*	spatial coordinates [m]
h	channel's width [m]
u_0	x velocity of plate [ms^{-1}]
l	slip length [m]
B	constant magnetic field [$\text{m}^{-1} \text{A}$]
Re	Reynolds number
Ha	Hartmann number [= $Bh\sqrt{\sigma/\mu_f}$]
q	transpiration velocity

P dimensionless pressure [= hq/v_f]

p^* hydrostatic pressure [$\text{kgm}^{-1} \text{s}^{-2}$]

Greek Symbols

β	slip parameter [= l/h]
ν	kinematic viscosity [$\text{m}^2 \text{s}^{-1}$]
ρ	density [kgm^{-3}]
σ	electrical conductivity [s m^{-1}]
ε	the ratio of h and L_x
ϕ	nanoparticle volume fraction
μ	dynamic viscosity [$\text{kgm}^{-1} \text{s}^{-1}$]

Subscripts

s	nano-solid particles
f	base fluid
nf	nanofluid

1. INTRODUCTION

Recently, the wide and abundant use of non-Newtonian fluids in industry and engineering sciences has caused

them to pay special attention to these materials. The characteristic and importance of this type of fluid can be seen in polymer compounds and edible substances. Ferrofluid is one of the non-Newtonian fluids that has

*Corresponding Author Email: b.jalili@iau-mb.ac.ir (B. Jalili)

recently been investigated by scientists. The physical structure of this fluid is very complex and no model can fully show all its features. For these reasons, investigation and analysis of the behavior of ferrofluid is very important.

Abbas et al. [1] investigated second-order fluid in the presence of a chemical reaction in a semi-porous channel. In this research, homotopy method was used to approximate analytical solution of the differential equations. Abdel Rahim and Rahman [2] analyzed heat transfer and fluid mass transfer in a magnetic field, which was assumed to be slow flow under electric conduction. Abbas and Hasnain [3], Abbas et al. [4, 5] have conducted studies on a two-phase fluid flow in an entirely porous medium. In this research, magnetite (Fe_3O_4) fluid was selected, and the sliding flow of nanomaterials in an inclined channel with thermal radiation was investigated and analyzed.

For the investigation of fluid properties, it can be mentioned that the fluid in the semi-porous channel is chemically conductive, and the mass transfer of the fluid is second-order with chemical reaction, Abbas et al. [6] investigated Maxwell fluid flow with radiation in an axisymmetric semi-porous channel. The natural convection micropolar fluid flow problem developed by Ashmawy [7]. According to that study, it was observed that the enhancement of the micropolar parameter includes the decrease or an increase in the fluid velocity. There are various medical mechanisms, such as blood circulation in the veins, the presence of oxygen generators in the blood, blood dialysis in the artificial kidney, and various types of engineering activities such as filter design; all of these mechanisms, despite the presence of a fluid flow in a channel semi-porous flows, it can be analyzed and investigated. Ayaz [8] used it for nonlinear ordinary differential equations. Also, in electrical engineering, new problems are presented, which are linear and nonlinear. It should also be noted that solving the governing equations of medical flow using DTM was investigated by Bég et al. [9]. One of the most effective analyses of fluid flow inside the channel is presented by Berman [10]. This article gives equations governing the smooth flow of a rectangular channel with semi-porous walls.

To fully describe a fluid flow in Manal with porous walls, solving the Navier-Stokes equations in two-dimensional laminar flow was necessary. This work was done by Brinkman [11], which is clearly shown the dependence of pressure and velocity components on fluid properties and channel dimensions. Due to the development and evolution of components, researchers are trying to create a variety of advanced fluids. These types of fluids should be closer to the real state in terms of heat exchange. For this purpose, they focused their studies on nanofluids because nanofluids release nano-sized particles. Chen and Ho [12] extended DTM to solve

partial differential equations. Therefore, using these materials in liquids can achieve lower thermal conductivity. Choi and Eastman [13], Choi et al. [14] proposed the first idea for these advanced fluids and discussed the extraordinary physical and chemical properties of these fluids that ferrofluids are also considered part of these fluids.

Ghasemian et al. [15] investigated forced displacement heat transfer on magnetite and numerically compared them with the presence of fluid under constant and alternating fields. Analysis of the flow of two fluids with the same density and varying viscosity in a horizontal channel and an unsteady state was recorded by Ghosh et al. [16]. According to this study, when the viscous fluid is near the channel, it is unstable for many parameters. Koriko et al. [17] conducted studies on the importance of partial slip and buoyancy on the boundary flow of a nanofluid, where the viscosity was considered to be zero. The equations governing nanoparticles were solved using the classic Runge-Kutta method; they found that it can be concluded that the maximum flow velocity occurs in larger values of partial slip and buoyancy parameters. We need analytical approximations often broken nonlinearly to solve nonlinear problems. Liao [18] mentioned the homotopy method in his book and solved difficult nonlinear problems with the help of this method. Mousavi et al. [19] investigated the hydrodynamic behavior of ferrofluid with 3D simulation in a wave channel and used the mathematical model with matching magnetohydrodynamics and ferrohydrodynamics to formulate the problem. Also, this research investigated the efficacy of changes in the Nusselt number and the amount of magnetic gradient. The use of semi-numerical techniques such as the homotopy analysis method (HAM) and differential transform method (DTM) has been presented by Parsa et al. [20]. They solved the governing equations of fluid flow in a semi-porous channel and investigated the effect of some parameters, such as Reynolds and Hartmann numbers in the heat transfer rate.

With the help of this method in an analytical function and using unknown and known boundary conditions, the derivative of n can be calculated at a known point. Rashidi et al. [21, 22] by using the differential transform method (DTM), were able to provide a solution for studying a non-Newtonian fluid flow inside a channel with semi-porous boundaries. This research was done using the parametric perturbation method. Salehpour and Ashjaee [23] investigated on the ferrofluid flow in a miniature channel under alternating and constant fields in a two-dimensional space. They found that the constant magnetic field enhancement heat transfer and the heat transfer rate decreases with increasing Reynolds number. They also calculated the optimal frequency for maximum heat transfer at high Reynolds numbers. In addition to that, Sanyal and Sanyal [24] studied on the two-

dimensional steady flow in an inclined rectangular channel with the presence of a magnetic field. From the outcomes of this research, we can refer to the graphical comparison of velocity, temperature, and magnetic field numerically. Also, the fluid flow has been investigated as a two-dimensional steady Maxwell flow in a symmetric semi-porous channel with a heat transfer rate. By using DTM and a semi-numerical solution with Taylor series expansion, Zhou [25] has formulated such existing problems.

The composition of ferrofluid includes substances such as Ferrum (Fe_3O_4) and suspension liquid of nanoparticles in several domains. Due to surface tension between solid particles and traditional fluid, a coating such as surfactants can be used to reduce it. If there is a magnetic field next to these particles, their behavior differs from ordinary metals. Also, these particles become magnetized inside the magnetic field. The location of the fluid under the magnetic force can be affected. Insomuch, the response of the ferrofluid to the external magnetic field is evident. One of the characteristics of sub-fluids is that they have very small particles. This makes them maintain their position and not settle down despite the magnetic force for a long time. In fact, papers and researches on ferrofluid flow in non-repetitive geometries are very limited.

Abbas et al. [26] developed a steady ferrofluid flow study in a semi-porous channel. In this research, fluids such as water, kerosene, blood, and magnetite are subjected to the Lorentz force in a semi-porous channel. The solution methods in this paper are the homotopy analysis method (HAM), differential transformation method (DTM), and Runge-Kutta method. The efficacy of Hartmann and Reynolds number changes on the flow velocity is shown and analyzed. Jalili et al. [27] investigated ferrofluid microstructure and inertial characteristics using homotopy and Akbari-Ganji methods. Also, the efficacy of related parameters on flow performance, temperature, and velocity has been analyzed. It should be noted that the fluid velocity in the vicinity of the sheet and at a distance from the sheet has been compared. In a study with a semi-analytical solution method on the Lorentz force and the efficacy of viscosity on nanofluid, the viscosity is variable, and the temperature parameter changes in a linear function. The semi-analytical AGM is used in this paper presented by Jalili et al. [28]. Changes in fluid velocity have been investigated by changing parameters such as Prantel, Hartmann, and Nusselt numbers. In another study conducted by Jalili et al. [29], the performance of magnetohydrodynamic heat transfer in a porous circular chamber was analyzed using Darcy's law. Also, by using the eddy current function formula and solving it numerically, a good comparison has been made with FEM. This material is placed in a magnetic field under a horizontal magnetic force, and its behavior has been

investigated with changes in the volume fraction of nanoparticles, inclination angle, Lorentz, and buoyancy forces. The use of three methods of comparing them to investigate the characteristics of a ferrofluid on a shrinking plate was demonstrated in a research conducted by Jalili et al. [30], which are AGM, FEM, and HPM. The base fluid in it is water and Fe_3O_4 . According to this paper, it can be seen that the boundary and magnetic parameters have the same efficacy on the fluid velocity. This is not the case for the micro-rotation parameter.

Recent studies have investigated the nanofluid flow between two parallel plates under magnetic and electric fields in a rotating system. According to the research conducted by Jalili et al. [31], the velocity profile and micro-rotation velocity increased with the magnetic and rotation parameters also increased. Also, the efficacy of changes in Reynolds, Prantel, and Schmidt numbers, thermophoretic parameters, and Brownian motion have been analyzed.

Jalili et al. [32] conducted a study on a two-dimensional viscous fluid located between two porous spaces in a calm and incompressible manner. Based on this research, the equations between two discs have been solved using the Akbari-Ganji and finite element methods. With the help of the findings, the velocity, pressure, and temperature parameters have been analyzed. Also, sliding in the boundaries and changing the Reynolds number causes changes in the fluid velocity, which are obvious.

In the article presented by Jalili et al. [33], all heat transfer processes in non-Newtonian fluid flow have been investigated. AGM and FEM methods have been used to solve this fluid flow's governing equations, showing complete agreement. Several values for Hartmann number and electromagnetic force affect the velocity profiles. Also, an extensive analytical research has been done in this field [34-36].

As a result, the general approach of this article and research is to provide numerical and semi-numerical solutions for ferrofluid flow in a semi-porous channel under a magnetic field with two basic fluids such as water and kerosene. Finally, the fluid velocity is obtained in its final form by solving the relevant equations with three homotopy methods: the Akbari-Ganji and finite element methods. Also, comparing these three different techniques and the efficacy of fixed parameters on fluid velocity are analyzed.

The use of other numerical and experimental solution methods such as Euler, Taylor, and RK-4 methods can also be used to solve the governing equations of fluid flow. The very good agreement of the obtained results from the used methods is one of the advantages of adopting this approach in this article. The error caused by the mentioned methods is very small and negligible and finally it is acceptable.

A comprehensive literature above motivated us to investigate and analyze a ferrofluid flow in a transverse magnetic field (see Figure 1). In the continuation of this research, the effect of changes in Reynolds and Hartmann numbers, velocity slip parameter and volume fraction of nanoparticles is shown using the finite element method. The results help the readers to have a better understanding of the effect of the above parameters on the velocity profile, velocity derivatives and ferrofluid shear stress in two directions. The comparison of the values obtained from the present research with other researches is presented in order to show the validity of the proposed solution methods.

2. FORMULATION OF PROBLEM AND BASIC EQUATION

According to Figure 1, two infinitely rigid parallel plates located at a distance h from each other, where the desired fluid enters this range (see Figure 1). The slip condition is applied on the plate of length L_x along the x^* -axis at $y^* = 0$. The rate of transpiration in an infinite porous plate is equal to q . The physical properties of the flow are two-dimensional, steady, and slow flow.

Water and kerosene-carrying magnetite Fe_3O_4 are two fluids considered nanoparticles in this research. Applying a magnetic field with intensity B is assumed in the desired channel. The magnetic field is transverse to the fluid flow. The effects of the induced magnetic field are not taken into account. Considering the above assumptions, the equations governing the flow are as follows [19, 20].

$$\frac{\partial u^*}{\partial x} + \frac{\partial v^*}{\partial y} = 0 \quad (1)$$

$$u^* \frac{\partial u^*}{\partial x} + v^* \frac{\partial u^*}{\partial y} = -\frac{1}{\rho_{nf}} \frac{\partial p^*}{\partial x} + \frac{\mu_{nf}}{\rho_{nf}} \left(\frac{\partial^2 u^*}{\partial x^*} + \frac{\partial^2 u^*}{\partial y^*} \right) - \frac{u^* \sigma B^2}{\rho_{nf}} \quad (2)$$

$$u^* \frac{\partial v^*}{\partial x} + v^* \frac{\partial v^*}{\partial y} = -\frac{1}{\rho_{nf}} \frac{\partial p^*}{\partial y} + \frac{\mu_{nf}}{\rho_{nf}} \left(\frac{\partial^2 v^*}{\partial x^*} + \frac{\partial^2 v^*}{\partial y^*} \right) \quad (3)$$

Also, the effective dynamic viscosity is calculated as follows [11]:

$$\mu_{nf} = \frac{\mu_f}{(1-\phi)^{2.5}}$$

The nanoparticle volume fraction is represented by the symbol ϕ (<0.05 for most practical cases). The shape of the particles can be considered spherical or non-

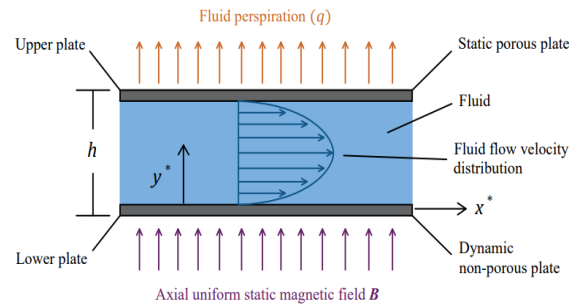


Figure 1. An overview of the physics of the problem

spherical. It should be noted that the effective density has been analysed by Mousavi et al. [19].

The physical properties of magnetic nanoparticles and the base fluid are shown in Table 1 [17-19].

$$\rho_{nf} = \rho_f (1-\phi) + \rho_s$$

In specific situations, the boundary conditions (BCs) are as follows:

$$y^* = 0 : u^* = u_0 + \frac{\partial u}{\partial y}, v^* = 0, y^* = h : u^* = 0, v^* = -q, \quad (4)$$

Scientists and researchers are trying to investigate the conditions of the sliding velocity of Navier in the walls and their use. Some articles and research that have used these boundary conditions as well [1, 3, 7, 16, 24].

Using the following equation, the average velocity $U(y)$ is calculated)

$$Uh = \int_0^h u^* dy^* = L_x q \quad (5)$$

With the help of the following non-dimensional variables, solutions to the problem can be found.

$$x = \frac{x^*}{L_x}, y = \frac{y^*}{h}, u = \frac{u^*}{U}, v = \frac{v^*}{q}, P_y = \frac{p^*}{\rho q} \quad (6)$$

By substituting the above variables in Equations (1), (3), and (6) is obtained

$$\frac{\partial u}{\partial x} + \frac{\partial v}{\partial y} = 0 \quad (7)$$

$$u \frac{\partial u}{\partial x} + v \frac{\partial u}{\partial y} = -\epsilon^2 \frac{\partial P_y}{\partial x} - u \frac{Ha^2}{Re((1-\phi+\phi(\frac{\rho_s}{\rho_f})))} \frac{\partial \rho_f}{\rho_f} + \frac{1}{Re} \left(\frac{1}{(1-\phi)^{2.5}(1-\phi+\phi(\frac{\rho_s}{\rho_f}))} \right) \epsilon^2 \left(\frac{\partial^2 u}{\partial x^2} + \frac{\partial^2 u}{\partial y^2} \right) \quad (8)$$

$$u \frac{\partial v}{\partial x} + v \frac{\partial v}{\partial y} = -\frac{\partial P_y}{\partial y} + \frac{1}{Re} \left(\frac{1}{(1-\phi)^{2.5}(1-\phi+\phi(\frac{\rho_s}{\rho_f}))} \right) (\epsilon^2 \frac{\partial^2 v}{\partial x^2} + \frac{\partial^2 v}{\partial y^2}) \quad (9)$$

TABLE 1. Physical properties of magnetic nanoparticles

Physical property	Water	Kerosene	Blood	Fe ₃ O ₄
Density(ρ)	997	783	1050	5180
Viscosity(μ)	0.001003	0.00164	0.003-0.004	-

Hartmann and Reynolds numbers in Equations (8) and (9) are equal to:

$$Ha = Bh \sqrt{\frac{\sigma}{\mu_f}} \quad Re = \frac{hq}{v_f}$$

The term ϵ , is very tiny because it is the ratio of h and L_x . To remove ϵ from Equations (8) and (9), Berman [10] similarity transformations are used

$$u = u^* U^{-1} = x \frac{dV}{dx} + u^* U(y), v = -V(y). \quad (10)$$

According to the above relationships, it can be seen that in Equation (9), the quantity $\partial P_y / \partial y$ is independent of the x variable. According to Equation (8), it can be said that $\partial^2 P_y / \partial x^2$ is not a function of the longitudinal variable x . If the asterisks are ignored for ease of work, the following relationships will appear after changing the variables

$$\begin{aligned} V^{'''} + VV''' - \frac{1}{Re} \left(\frac{1}{(1-\phi)^{2.5} (1-\phi+\phi(\frac{\rho_s}{\rho_f}))} \right) V''' \\ + \frac{Ha^2}{Re(1-\phi+\phi(\frac{\rho_s}{\rho_f}))} V' = \epsilon \frac{\partial^2 P_y}{\partial x^2} = \epsilon \frac{1}{x} \frac{\partial P_y}{\partial x}. \end{aligned} \quad (11)$$

$$\begin{cases} u(x) = u_0, u'(x) = u_1, \dots, u^{(m-1)}(x) = u_{m-1} & \text{at } x = 0 \\ u(x) = u_{L_0}, u'(x) = u_{L_1}, \dots, u^{(m-1)}(x) = u_{L_{m-1}} & \text{at } x = L \end{cases}$$

In Equation (17), a series of order n is assumed according to the boundary conditions at $x = L$, where the coefficients are considered constant. This series is written as the answer to the first differential equation as follows:

$$u(x) = \sum_{i=0}^n a_i x^i = a_0 + a_1 x^1 + a_2 x^2 + \dots + a_n x^n \quad (18)$$

In order to enhance the accuracy in solving Equation (16), it is necessary to enhance the series expressions in Equation (18). Due to the order of the above series being n , there are $(n+1)$ unknown coefficients, which we usually need $(n+1)$ equations to solve. In Equation

$$\begin{cases} u(L) = a_0 + a_1 L + a_2 L^2 + \dots + a_n L^n = u_{L_0} \\ u'(L) = a_1 + 2a_2 L + 2a_3 L^2 + \dots + n a_n L^{n-1} = u_{L_1} \\ u''(L) = 2a_2 + 6a_3 L + 12a_4 L^2 + \dots + n(n-1)a_n L^{n-2} = u_{L_{m-1}} \\ \vdots \quad \vdots \quad \vdots \quad \vdots \quad \vdots \quad \vdots \end{cases}$$

$$UV''' - VU''' = \frac{1}{Re} \left(\frac{1}{(1-\phi+\phi(\frac{\rho_s}{\rho_f}))} \right) \left(\frac{U''}{(1-\phi)^{2.5}} - Ha^2 U \right). \quad (12)$$

If Equation 11 is calculated in terms of variable y , it will be as follows:

$$\begin{aligned} V''' &= (1-\phi)^{2.5} Ha^2 V'' \\ &+ Re(1-\phi+\phi(\frac{\rho_s}{\rho_f})) (V''' - VV'''). \end{aligned} \quad (13)$$

The boundary conditions governing the equations are written as follows:

$$V(0) = 0, V'(0) = \beta V''(0), U(0) = 1 + \beta U'(0). \quad (14)$$

$$V(1) = 1, V'(1) = 0, U(1) = 0. \quad (15)$$

where $\beta = l/h$.

3. THE GENERALITIES OF AKBARI GANJI'S METHOD (AGM)

Considering the boundary conditions, the differential equations are as follows:

$$p_k: f(u, u', u'', \dots, u^{(m)}) = 0; u = u(x) \quad (16)$$

The p function in a nonlinear differential equation is assumed as a function of u . Also, the u parameter is considered a function of x and its derivatives. In this way, the boundary conditions of the equations are established as follows:

$$(17)$$

(17), boundary conditions are applied for the $(n+1)$ equation.

3. 1. Apply BCs with AGM

Boundary conditions are used to solve Equation (18) as follows

When $x = 0$:

$$\begin{cases} u(0) = a_0 = u_0 \\ u'(0) = a_1 = u_1 \\ u''(0) = a_2 = u_2 \\ \vdots \quad \vdots \quad \vdots \end{cases} \quad (19)$$

and when $x = L$:

$$(20)$$

After inserting Equation (20) into Equation (16) and applying boundary conditions in differential Equation (16), it is obtained based on the following technique:

$$\begin{aligned} p_0: f(u(0), u'(0), u''(0), \dots, u^{(m)}(0)) \\ p_1: f(u(L), u'(L), u''(L), \dots, u^{(m)}(L)) \end{aligned} \quad (21)$$

According to the selection of n ($n < m$) terms from Equation (18), to create a set of equations consisting of $(n+1)$ equations and $(n+1)$ unknowns, there will be additional unknowns. Therefore, to solve this problem, due to these additional unknowns in the mentioned equations, m times should be derived from Equation (23), and then the BCs should be applied to them. The solution process in Flowchart 1 has been fully investigated.

$$\begin{aligned} p'_k: f(u', u'', u''', \dots, u^{(m+1)}) \\ p''_k: f(u'', u''', u^{(IV)}, \dots, u^{(m+2)}) \\ \vdots \quad \vdots \quad \vdots \quad \vdots \quad \vdots \quad \vdots \end{aligned} \quad (22)$$

In Equation (22), the boundary conditions are applied to the derivatives of the differential equation p_k .

$$p'_k: \left\{ \begin{array}{l} f(u'(0), u''(0), u'''(0), \dots, u^{(m+1)}(0)) \\ f(u'(L), u''(L), u'''(L), \dots, u^{(m+1)}(L)) \end{array} \right. \quad (23)$$

$$p''_k: \left\{ \begin{array}{l} f(u''(0), u'''(0), u^{(IV)}(0), \dots, u^{(m+2)}(0)) \\ f(u''(L), u'''(L), u^{(IV)}(L), \dots, u^{(m+2)}(L)) \end{array} \right. \quad (24)$$

$(n+1)$ equation is obtained from Equations (19) to (24), so $(n+1)$ unknown coefficient in Equation (18),

including a_0, a_1, \dots, a_n will be calculated. Solving the nonlinear differential Equation (16) is done by calculating the coefficients of Equation (18).

3.2. Solving Equations Governing Fluid Flow with AGM

In this method, using appropriate functions, polynomial series with constant coefficients can be considered:

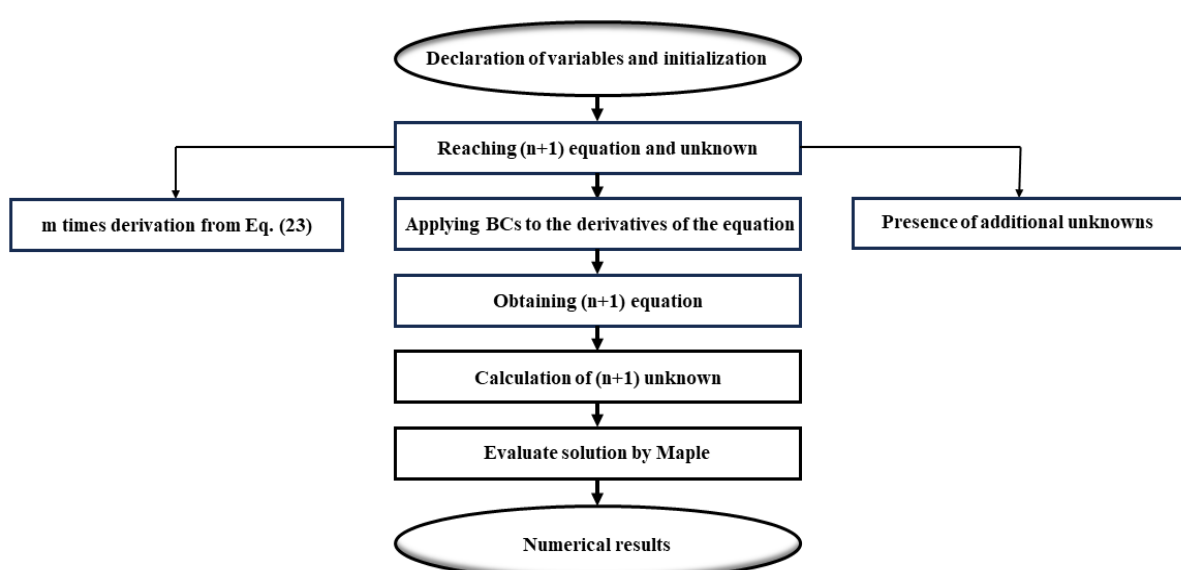
$$\begin{aligned} U = \sum_{i=0}^5 a_i x^i \\ U = x^5 a_5 + x^4 a_4 + x^3 a_3 + x^2 a_2 + x a_1 + a_0 \end{aligned} \quad (25)$$

$$\begin{aligned} V = \sum_{i=0}^5 b_i x^i \\ V = x^5 b_5 + x^4 b_4 + x^3 b_3 + x^2 b_2 + x b_1 + b_0 \end{aligned} \quad (26)$$

Equations (12) and (13) are written as follows:

$$\begin{aligned} U * \text{diff}(V, x) - V * \text{diff}(U, x) = \\ \frac{1}{\text{Re}} \left(\frac{1}{(1-\phi+\phi(\frac{\rho_s}{\rho_f}))} \right) \left(\frac{\text{diff}(U, x, x)}{(1-\phi)^{2.5}} - H a^2 * U \right) \\ \text{diff}(V, x, x, x, x) = (1-\phi)^{2.5} (H a^2 * \text{diff}(V, x, x)) \\ + \text{Re}((1-\phi+\phi(\frac{\rho_s}{\rho_f}))) (\text{diff}(V, x) \\ * \text{diff}(V, x, x) - V * \text{diff}(V, x, x))). \end{aligned}$$

The use of BCs in Equations (14) and (15) is as follows:



Flowchart 1. Showing the process of solving equations with AGM

$$V(0) = 0 \rightarrow b_0 = 0 \quad (27)$$

$$V'(0) = \beta * V''(0) \rightarrow b_1 = 0.4b_2 \quad (28)$$

$$U(0) = 1 + \beta * U'(0) \rightarrow a_0 = 1 + 0.2a_1 \quad (29)$$

$$V(1) = 1 \rightarrow b_5 + b_4 + b_3 + b_2 + b_1 + b_0 = 1 \quad (30)$$

$$V'(1) = 0 \rightarrow 5b_5 + 4b_4 + 3b_3 + 2b_2 + b_1 = 0 \quad (31)$$

$$U(1) = 0 \rightarrow a_5 + a_4 + a_3 + a_2 + a_1 + a_0 = 0 \quad (32)$$

According to the considered series in Equations (25) and (26), there are 12 unknown coefficients. Therefore, 12 equations are needed. Six equations are obtained by applying boundary conditions, and six more equations are added as follows:

$$\begin{aligned} S7 &= F(0) \rightarrow S7 = a_0b_1 - a_1b_0 \\ &= 1.895700084a_2 - 0.8558895353a_0 \end{aligned} \quad (33)$$

$$\begin{aligned} S8 &= F'(0) \rightarrow S8 = 2a_0b_2 - 2a_2b_0 \\ &= 5.687100252a_3 - 0.8558895353a_1 \end{aligned} \quad (34)$$

$$\begin{aligned} S9 &= F''(0) \rightarrow S9 = 6a_0b_3 + 2a_1b_2 - 2a_2b_1 - 6a_3b_0 \\ &= 22.74840102a_4 - 1.711779071a_2 \end{aligned} \quad (35)$$

$$\begin{aligned} S10 &= F'''(0) \rightarrow S10 = 24a_0b_4 + 12a_1b_3 - 12a_2b_2 - 24a_3b_1 \\ &= 113.7420050a_5 - 5.135337212a_3 \end{aligned} \quad (36)$$

$$\begin{aligned} S11 &= G(0) \rightarrow S11 = 24b_4 \\ &= 1.805959798b_2 + 2.110038414b_1b_2 - 6.330115242b_0b_3 \end{aligned} \quad (37)$$

$$\begin{aligned} S12 &= G'(0) \rightarrow S12 = 120b_5 \\ &= 5041787939b_3 + 4.220076828b_2^2 - 25.32046097b_0b_1 \end{aligned} \quad (38)$$

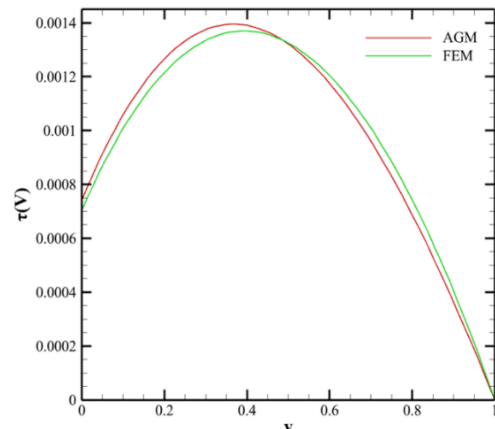
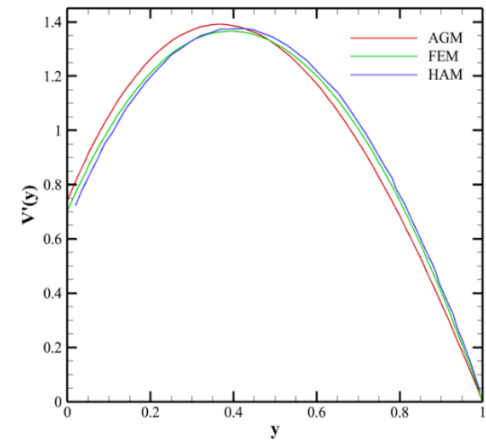
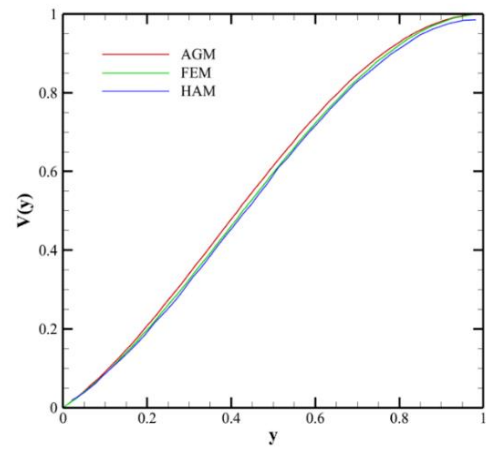
Finally, the values of V and U are equal to:

$$\begin{aligned} V &= 0.03526533002x^5 + 0.2595824095x^4 \\ &- 1.884935683x^3 + 1.850062816x^2 + 0.7400251266x \\ U &= 0.2981496437x^5 - 0.5758048195x^4 + 0.2737060224x^3 \\ &+ 0.6157135630x^2 - 1.343137008x + 0.7313725984 \end{aligned}$$

4. RESULTS AND DISCUSSION

Equations (12) and (13) were solved with AGM and FEM to obtain velocity fields $V(y)$, $V'(y)$, $U(y)$, $U'(y)$, τ_V and τ_U according to Equations (14) and (15). Drawing and displaying graphs $V(y)$, $V'(y)$, $U(y)$, $U'(y)$, τ_V and τ_U and the efficacy of changes in relevant parameters have

been done in them. Figure 2 shows $V(y)$, $V'(y)$, $U(y)$, $U'(y)$, τ_V and τ_U profiles. Also, the comparison of three solution methods AGM, FEM, and HAM has been done when $Re = Ha = 1.0$, $\beta = 0.2$ and $\phi = 0.04$. By comparing the figures, it can be concluded that the outcome obtained from all methods are very close to each other. This result proves and confirms the validity of the methods.



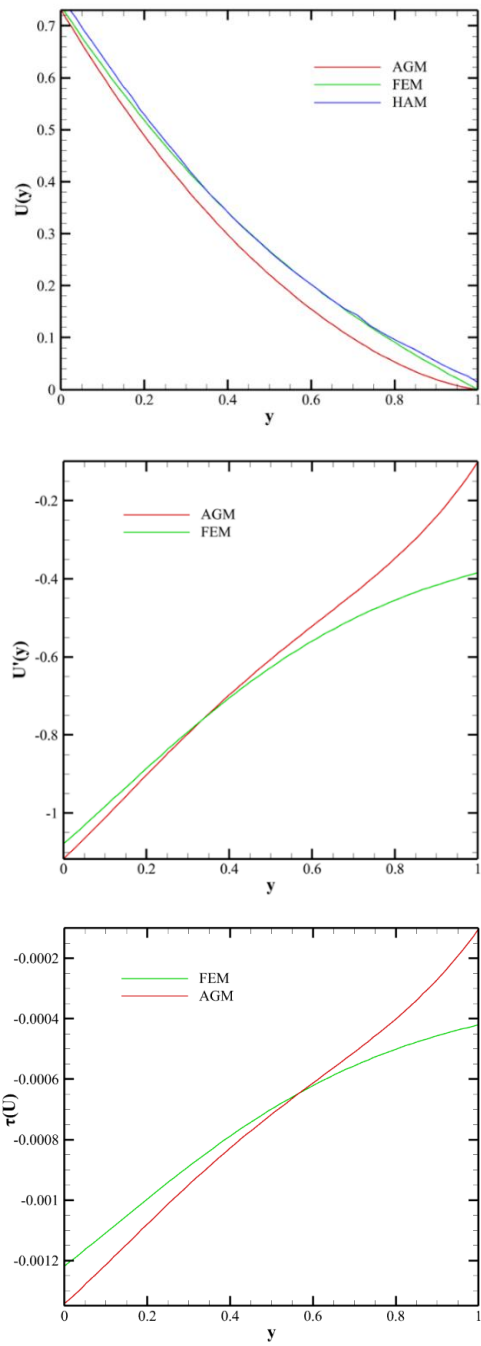
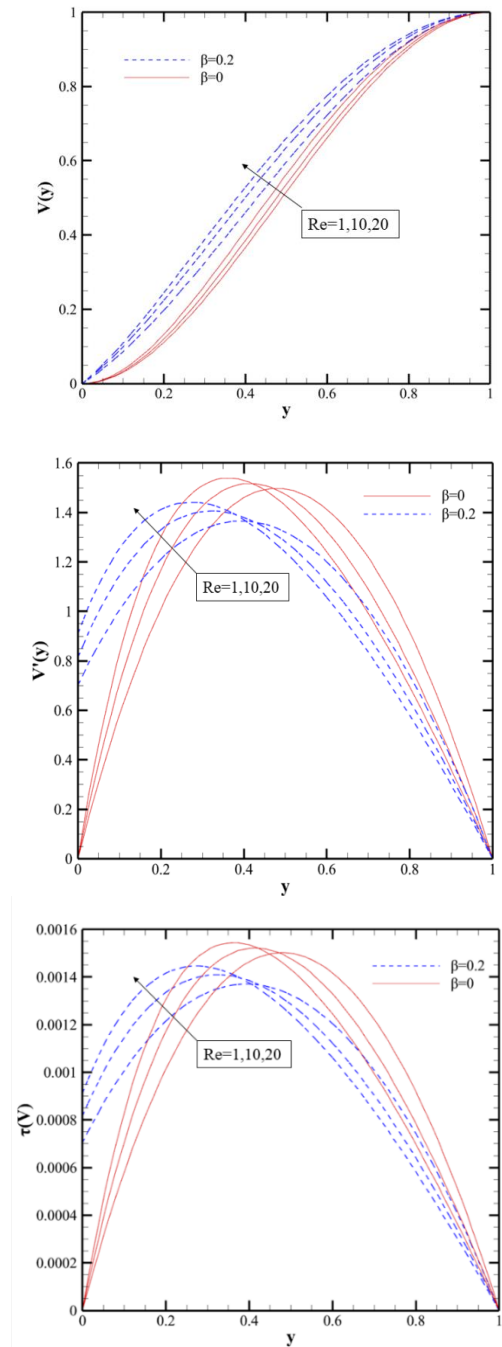


Figure 2. Comparison of the conclusion obtained for $V(y)$, $V'(y)$, $U(y)$, $U'(y)$, τ_V and τ_U with three methods of AGM, FEM, HAM, and comparison of $U'(y)$, τ_V and τ_U with two methods of AGM and FEM where $Re = Ha = 1.0$, $\phi = 0.04$, $\beta = 0.2$

Changes in $V(y)$, $V'(y)$, $U(y)$, $U'(y)$, τ_V and τ_U for fixed values of $\phi = 0.04$ and $Ha = 1.0$ and several values of Re with two boundary conditions of slip and no-slip are shown in Figure 3. With the enhancement of Reynolds number, the flux of the side body on the upper

plane increases and the fluid flow approaches the upper plane as an outcome. Decreasing the velocity in the x -direction $U(y)$ and increasing the velocity in the y -direction $V(y)$ is the outcome of the previous movement. By increasing the Reynolds number from 1 to 20, the velocity enhancement in the y -direction and the velocity decrease in the x -direction are tangible. Also, according to Figure 3, it can be seen that with the enhancement of the Reynolds number, $V'(y)$ also increases. But when approaching the top page ($y = 0.45$), it shows a reverse



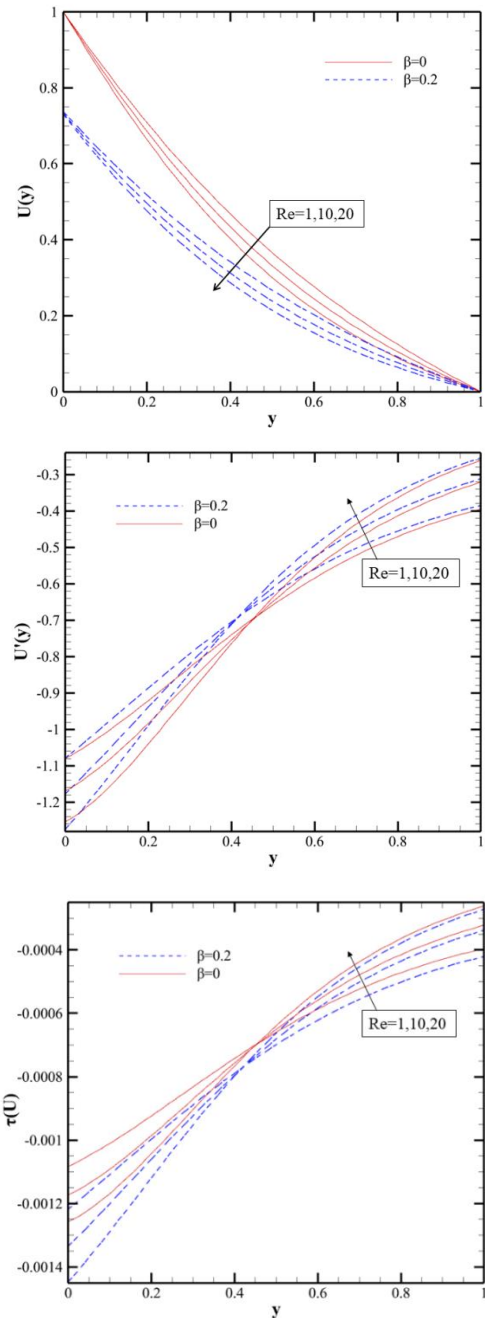


Figure 3. Comparison of diagrams obtained for $V(y)$, $V'(y)$, $U(y)$, $U'(y)$, τ_V and τ_U with FEM for several values of β and Re when $\phi = 0.04$, $Ha = 0.0$

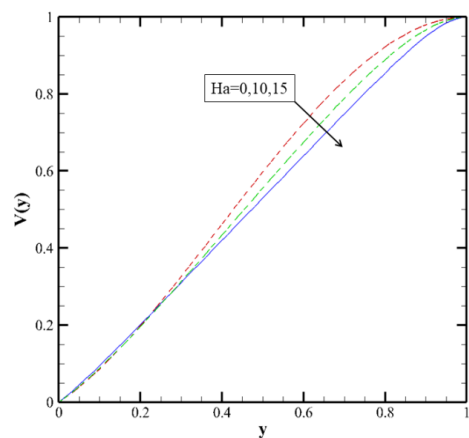
behavior. But $U'(y)$ shows the opposite behavior. That is, in the range of $0 \leq y \leq 0.45$, with an increase in Reynolds number, $U'(y)$ decreases, and then it takes an increasing trend in $0.45 \leq y \leq 1$. Based on this, it can be concluded that the values of τ_U and τ_V also behave similar to the derivatives of velocity, because the constant coefficient (μ) is multiplied in the derivatives and shear stresses appear. According to Figure 3, it can

be seen that there is no difference in the efficacy of Reynolds number changes in the boundary conditions of sliding and non-slipping.

According to Figure 4, the distribution of fluid flow velocity decreases with the enhancement of the Hartmann number. This decrease is much higher in $U(y)$. The Lorentz force enters in the x -direction because the magnetic field is placed in the y -direction. Thus, the magnetohydrodynamic force generated in $V(y)$ and $V'(y)$ can be ignored, although it plays a significant role in $U(y)$ and $U'(y)$. With an increase in Hartmann's number in the range of $0 \leq y \leq 0.6$, a decrease in $V'(y)$ can be seen, and in $0.6 \leq y \leq 1$, the value of $V'(y)$ increases. This behavior is also shown in shear stress (τ_V). The algebraic value of $U'(y)$ in the range of $0 \leq y \leq 0.4$ increases with an increase in Hartmann's number, but its value is negative. In the range of $0.4 \leq y \leq 1$, its behavior is reversed and the same process is repeated for τ_U in a smaller order.

The efficacy of ϕ sub-particle volume fraction and β slip on fluid flow velocity distribution $V(y)$ and $U(y)$ Likewise Re and ϕ are shown in Figure 5. Also, in the vicinity of the upper and lower plates, for boundary conditions with slip and no-slip, the opposite behavior can be observed for $V'(y)$ and $U'(y)$. If the volume fraction of nanoparticles (ϕ) increases, $V(y)$ decreases and $U(y)$ increases. This behavior is similar for both velocity profiles with an increase in slip parameter (β). As the value of ϕ increases, in the range of $0 \leq y \leq 0.5$, the value of $V'(y)$ and the algebraic value of $U'(y)$ decrease, and then at $0.5 \leq y \leq 1$, the algebraic value of $U'(y)$ and $V'(y)$ increases. A similar behavior is also shown for shear stresses (τ_V and τ_U) in two directions.

Figures 6 and 7 show the effect of changes in Reynolds and Hartmann numbers and the volume fraction parameter of nanoparticles. As can be seen, with an increase in Reynolds number, $V(y)$ increases, but if the Hartmann number or volume fraction of nanoparticles increases, $V(y)$ decreases.



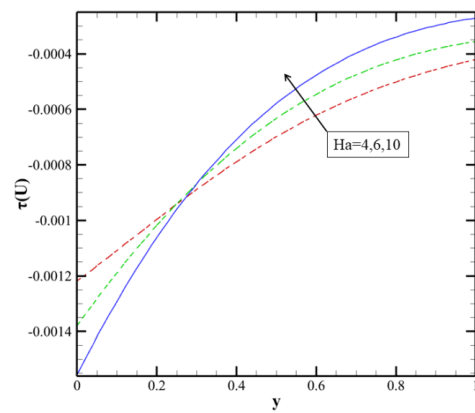
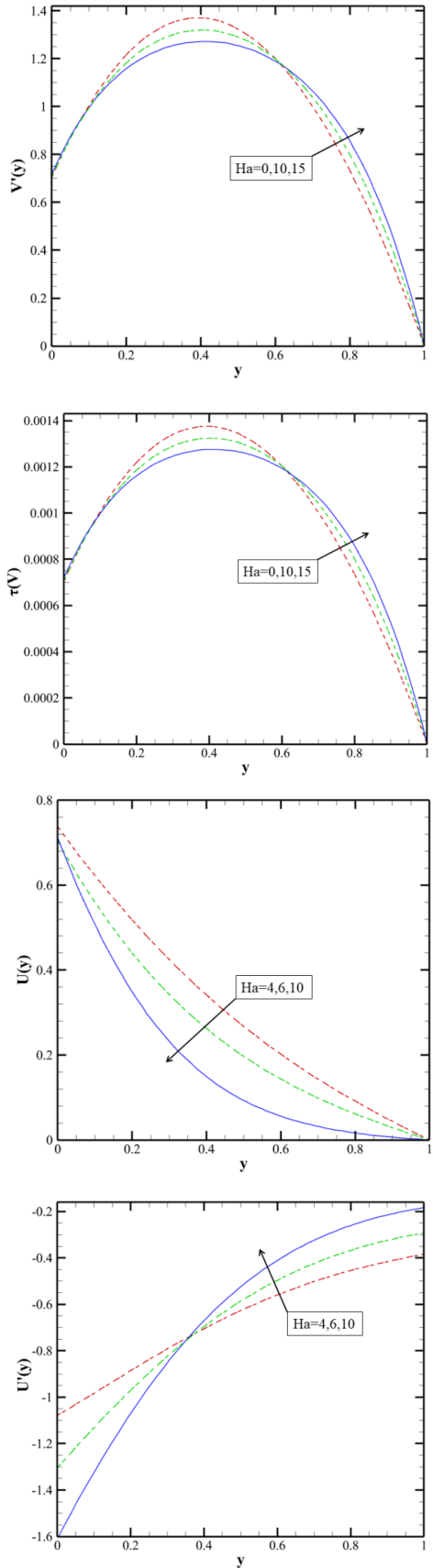
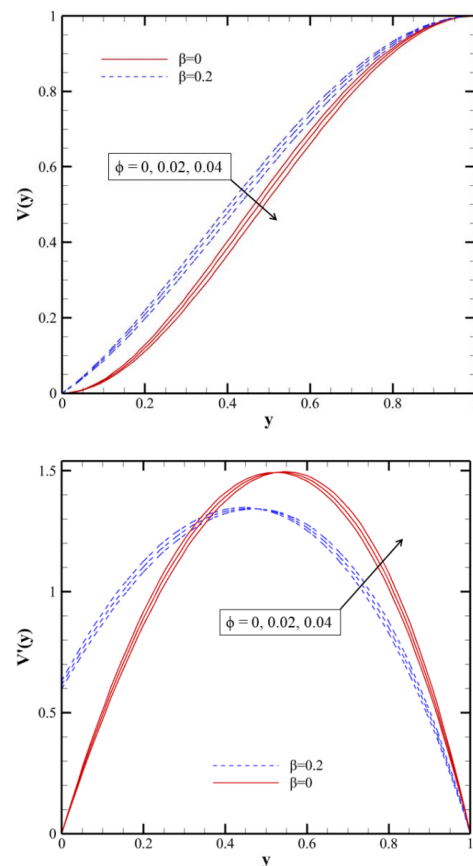


Figure 4. Comparison of $V(y)$, $V'(y)$, $U(y)$, $U'(y)$, τ_V and τ_U diagrams using FEM with several values for Ha when $Re = 1.0$, $\beta = 0.2$, $\phi = 0.04$

Based on Figures 8 and 9, it can be concluded that $U(y)$ decreases with an increase in Hartman and Reynolds numbers. But if the volume fraction of nanoparticles is increased, $U(y)$ increases.

Convergence for several values of $V(y)$, $U(y)$, τ_V and τ_U in terms of y is listed in Table 2 to 5. In Tables 2 and 3, the results obtained for the values of water velocity



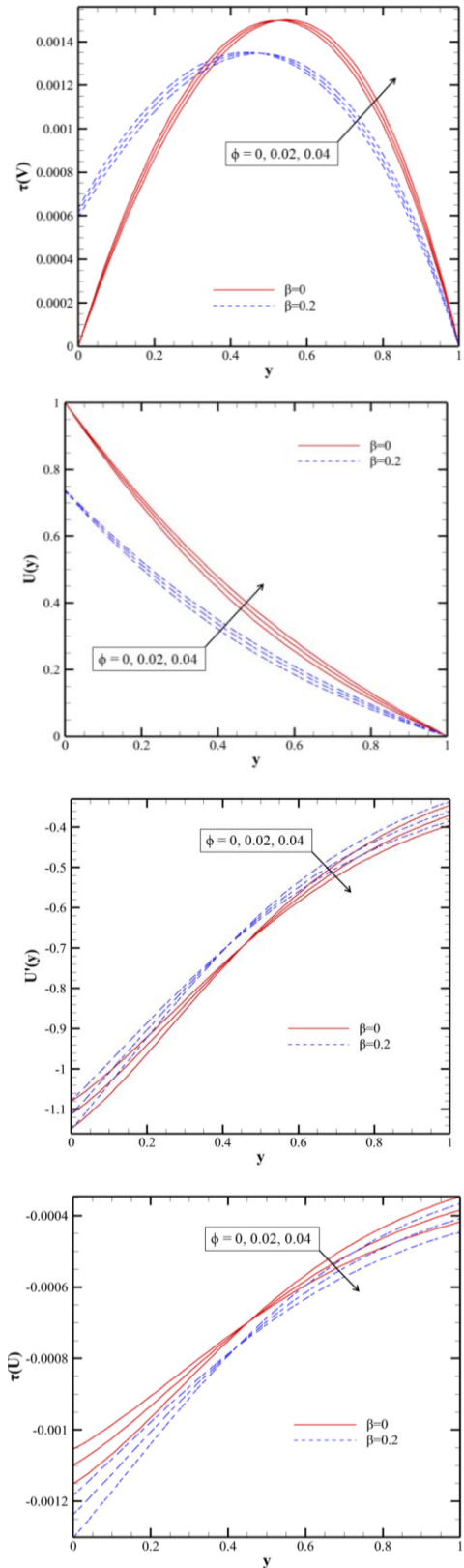


Figure 5. Comparison of $V(y)$, $V'(y)$, $U(y)$, $U'(y)$, τ_V and τ_U diagrams with FEM for several values of ϕ and β when $Re = Ha = 1.0$

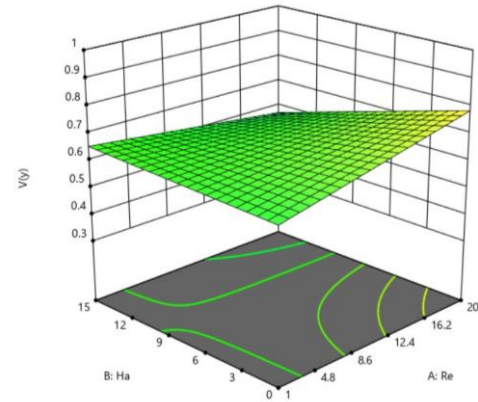


Figure 6. Efficacy of changes in Reynolds number and Hartmann number on constant Phi number equal to 0.02

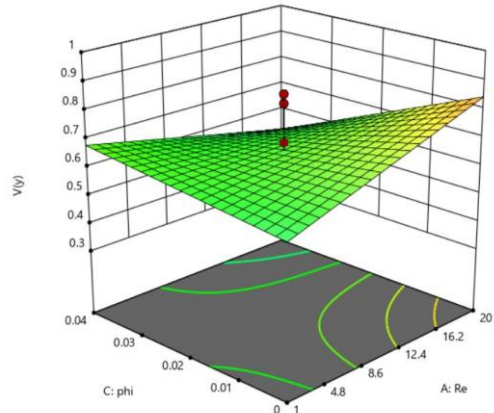


Figure 7. The efficacy of changes in Reynolds number and Phi number on the constant Hartmann number equal to 7.5

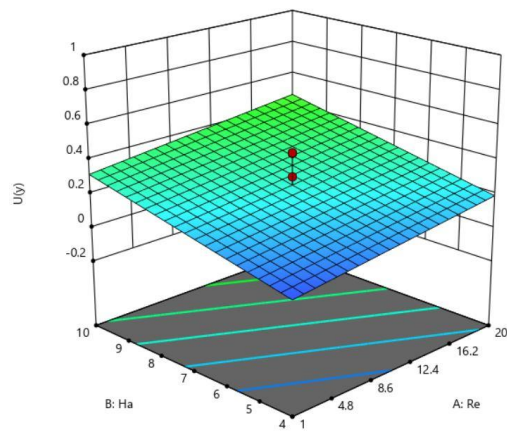


Figure 8. The efficacy of changes in Reynolds number and Hartmann number on constant Phi number is equal to 0.02

in two directions in the current research with the two methods of AGM and FEM and the values obtained with

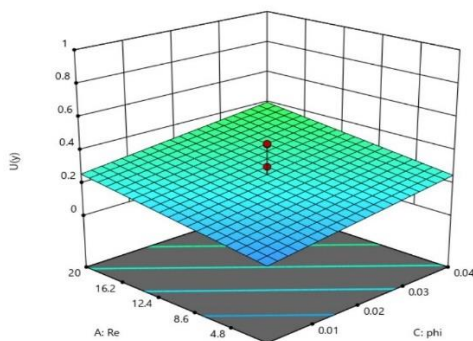


Figure 9. The efficacy of changes in Reynolds number and Phi number on Hartmann's constant number equal to 7

the three methods of HAM, DTM and Numerical are presented. The comparison of the present results and their correspondence with the results of other researches [26] shows the efficiency of the methods used in this article. In addition, in Tables 4 and 5, the values obtained from the current research with two AGM and FEM methods are given.

The changes related to the three parameters of Re , Ha and ϕ in a 3D space in the form of optimization are given in Figures 6 and 7 for $V(y)$.

The changes related to the three parameters of Re , Ha and ϕ in a 3D space in the form of optimization are given in Figures 8 and 9 for $U(y)$.

TABLE 2. The analogy of the obtained outcome for the velocity of $V(y)$ when $\phi = 0.04$, $Re = 1.0$, $Ha = 1.5$, $\beta = 0.3$ for the Water base.

y	AGM	FEM	HAM [26]	DTM [26]	Numerical solution [26]
0	0.000000	0.000000	0.000000	0.000000	0.000000
0.1	0.098899	0.097758	0.097758	0.097758	0.097758
0.2	0.220465	0.215312	0.215311	0.215312	0.215311
0.3	0.365673	0.344513	0.344742	0.344742	0.344742
0.4	0.498575	0.479145	0.478699	0.478699	0.478699
0.5	0.644486	0.610354	0.610245	0.610246	0.610245
0.6	0.754926	0.732942	0.732703	0.732703	0.732703
0.7	0.851991	0.839491	0.839514	0.839515	0.839514
0.8	0.932754	0.924120	0.924121	0.924122	0.924121
0.9	0.981562	0.979879	0.979879	0.979880	0.979879
1	1.000000	1.000000	1.000000	1.000000	1.000000

TABLE 3. The analogy of the obtained outcome for the velocity of $U(y)$ when $\phi = 0.04$, $Re = 1.0$, $Ha = 1.5$, $\beta = 0.3$ for the Water base.

y	AGM	FEM	HAM [26]	DTM [26]	Numerical solution [26]
0	0.619974	0.602783	0.620077	0.620077	0.620077
0.1	0.486728	0.498574	0.502367	0.502367	0.502367
0.2	0.379256	0.399492	0.401721	0.401721	0.401721
0.3	0.272567	0.315897	0.316599	0.316599	0.316599
0.4	0.182456	0.245170	0.245171	0.245171	0.245171
0.5	0.137496	0.185479	0.185479	0.185479	0.185479
0.6	0.102891	0.135577	0.135577	0.135577	0.135577
0.7	0.075286	0.093610	0.093624	0.093624	0.093624
0.8	0.045872	0.057189	0.057961	0.057961	0.057961
0.9	0.022378	0.026981	0.027150	0.027150	0.027150
1	0.000000	0.000000	0.000000	0.000000	0.000000

TABLE 4. The analogy of the obtained outcome for τ_V when $\phi = 0.04, Re = 1.0, Ha = 1.5, \beta = 0.3$ for the Water base

y	AGM	FEM
0	0.000749	0.000711
0.1	0.001080	0.001033
0.2	0.001279	0.001219
0.3	0.001374	0.001334
0.4	0.001390	0.001365
0.5	0.001320	0.001321
0.6	0.001160	0.001201
0.7	0.000943	0.000994
0.8	0.000704	0.000711
0.9	0.000385	0.000434
1	0.000000	0.000000

TABLE 5. The analogy of the obtained outcome for τ_U when $\phi = 0.04, Re = 1.0, Ha = 1.5, \beta = 0.3$ for the Water base

y	AGM	FEM
0	-0.001400	-0.001255
0.1	-0.001247	-0.001120
0.2	-0.001110	-0.001001
0.3	-0.000971	-0.000889
0.4	-0.000844	-0.000780
0.5	-0.000712	-0.000660
0.6	-0.000575	-0.000571
0.7	-0.000446	-0.000502
0.8	-0.000316	-0.000444
0.9	-0.000179	-0.000390
1	0.000000	-0.000349

5. CONCLUSION

One of the most important goals of this research was to investigate and analyze two-dimensional fluid flow in relation to sliding efficiency on a nanofluid with a porous wall. The equations governing the flow were solved with the mentioned simplifications and two methods. Among the achievements of this article, the following factors can be mentioned:

- The area of convergence in $V''(0)$ is larger than that of $U'(0)$.
- The difference in AGM, FEM, and HAM outcomes is negligible, and all three methods are acceptable.
- As the Reynolds number enhancement, the velocity of the $V(y)$ fluid increases. This is while it reduces with the enhancement of Hartmann's number.

- As the Hartmann and Reynolds numbers increase, $U(y)$ decreases.
- As the nanoparticle volume fraction parameter increases, $U(y)$ increases and $V(y)$ decreases.
- If there are changes for Hartmann, Reynolds numbers and volume fraction of nanoparticles, the opposite behavior is reported for the derivatives of velocity and shear stress in the range of $0 \leq y \leq 1$.

6. REFERENCES

1. Abbas, Z., Ahmad, B. and Ali, S., "Chemically reactive hydromagnetic flow of a second-grade fluid in a semi-porous channel", *Journal of Applied Mechanics and Technical Physics*, Vol. 56, (2015), 878-888. <https://doi.org/10.1134/S0021894415050156>
2. Abdel-Rahim, Y.M. and Rahman, M.M., "Laminar semi-porous channel electrically conducting flow under magnetic field, International Conference on Heat Transfer, Fluid Mechanics and Thermodynamics. (2014).
3. Abbas, Z. and Hasnain, J., "Two-phase magnetoconvection flow of magnetite (Fe_3O_4) nanoparticles in a horizontal composite porous annulus", *Results in Physics*, Vol. 7, (2017), 574-580. <https://doi.org/10.1016/j.rinp.2016.12.022>
4. Abbas, Z., Hasnain, J. and Sajid, M., "Mhd two-phase fluid flow and heat transfer with partial slip in an inclined channel", *Thermal Science*, Vol. 20, No. 5, (2016), 1435-1446. <https://doi.org/10.2298/TSCI130327049A>
5. Abbas, Z., Rahim, T. and Hasnain, J., "Slip flow of magnetite-water nanomaterial in an inclined channel with thermal radiation", *International Journal of Mechanical Sciences*, Vol. 122, (2017), 288-296. <https://doi.org/10.1016/j.ijmecsci.2017.01.040>
6. Abbas, Z., Naveed, M., Naeem, M. and Zia, Q., "Analytical investigation of a maxwell fluid flow with radiation in an axisymmetric semi-porous channel by parameterized perturbation method", *Journal of the Brazilian Society of Mechanical Sciences and Engineering*, Vol. 40, (2018), 1-8. <https://doi.org/10.1007/s40430-018-0985-z>
7. Ashmawy, E., "Fully developed natural convective micropolar fluid flow in a vertical channel with slip", *Journal of the Egyptian Mathematical Society*, Vol. 23, No. 3, (2015), 563-567. <https://doi.org/10.1016/j.joems.2014.06.019>
8. Ayaz, F., "Solutions of the system of differential equations by differential transform method", *Applied Mathematics and Computation*, Vol. 147, No. 2, (2004), 547-567. <https://doi.org/10.1016/j.amc.2004.06.019>
9. Bég, T., Rashidi, M., Bég, O.A. and Rahimzadeh, N., "Differential transform semi-numerical analysis of biofluid-particle suspension flow and heat transfer in non-darcian porous media", *Computer Methods in Biomechanics and Biomedical Engineering*, Vol. 16, No. 8, (2013), 896-907. doi: 10.1080/10255842.2011.643470.
10. Berman, A.S., "Laminar flow in channels with porous walls", *Journal of Applied Physics*, Vol. 24, No. 9, (1953), 1232-1235. <https://doi.org/10.1063/1.1721476>
11. Brinkman, H.C., "The viscosity of concentrated suspensions and solutions", *The Journal of Chemical Physics*, Vol. 20, No. 4, (1952), 571-571. <https://doi.org/10.1063/1.1700493>
12. Chen, C.O.K. and Ho, S.H., "Solving partial differential equations by two-dimensional differential transform method", *Applied Mathematics and Computation*, Vol. 106, No. 2-3, (1999), 171-179. [https://doi.org/10.1016/S0096-3003\(98\)10115-7](https://doi.org/10.1016/S0096-3003(98)10115-7)

13. Choi, S.U. and Eastman, J.A., *Enhancing thermal conductivity of fluids with nanoparticles*. 1995, Argonne National Lab.(ANL), Argonne, IL (United States).
14. Choi, S., Zhang, Z.G., Yu, W., Lockwood, F. and Grulke, E., "Anomalous thermal conductivity enhancement in nanotube suspensions", *Applied Physics Letters*, Vol. 79, No. 14, (2001), 2252-2254. <https://doi.org/10.1063/1.1408272>
15. Ghasemian, M., Ashrafi, Z.N., Goharkhah, M. and Ashjaee, M., "Heat transfer characteristics of fe₃o₄ ferrofluid flowing in a mini channel under constant and alternating magnetic fields", *Journal of Magnetism and Magnetic Materials*, Vol. 381, No., (2015), 158-167. <https://doi.org/10.1016/j.jmmm.2014.12.078>
16. Ghosh, S., Usha, R. and Sahu, K.C., "Absolute and convective instabilities in double-diffusive two-fluid flow in a slippery channel", *Chemical Engineering Science*, Vol. 134, No., (2015), 1-11. <https://doi.org/10.1016/j.ces.2015.04.049>
17. Koriko, O.K., Animasaun, I., Mahanthesh, B., Saleem, S., Sarojamma, G. and Sivaraj, R., "Heat transfer in the flow of blood-gold carreau nanofluid induced by partial slip and buoyancy", *Heat Transfer—Asian Research*, Vol. 47, No. 6, (2018), 806-823. <https://doi.org/10.1002/htj.21342>
18. Liao, S., "Beyond perturbation: Introduction to the homotopy analysis method", CRC press, (2003).
19. Mousavi, S.M., Biglarian, M., Darzi, A.A.R., Farhadi, M., Afrouzi, H.H. and Toghraie, D., "Heat transfer enhancement of ferrofluid flow within a wavy channel by applying a non-uniform magnetic field", *Journal of Thermal Analysis and Calorimetry*, Vol. 139, (2020), 3331-3343. <https://doi.org/10.1007/s10973-019-08650-6>
20. Parsa, A.B., Rashidi, M.M., Bég, O.A. and Sadri, S., "Semi-computational simulation of magneto-hemodynamic flow in a semi-porous channel using optimal homotopy and differential transform methods", *Computers in Biology and Medicine*, Vol. 43, No. 9, (2013), 1142-1153. <https://doi.org/10.1016/j.combiomed.2013.05.019>
21. Rashidi, M., Keimanesh, M., Bég, O.A. and Hung, T., "Magneto hydrodynamic biorheological transport phenomena in a porous medium: A simulation of magnetic blood flow control and filtration", *International Journal for Numerical Methods in Biomedical Engineering*, Vol. 27, No. 6, (2011), 805-821. <https://doi.org/10.1002/cnm.1420>
22. Rashidi, M., Pour, S.M. and Laraqi, N., "A semi-analytical solution of micro polar flow in a porous channel with mass injection by using differential transform method", *Nonlinear Analysis: Modelling and Control*, Vol. 15, No. 3, (2010), 341-350. <https://doi.org/10.15388/NA.15.3.14329>
23. Salehpour, A. and Ashjaee, M., "Effect of different frequency functions on ferrofluid fhd flow", *Journal of Magnetism and Magnetic Materials*, Vol. 480, (2019), 112-131. <https://doi.org/10.1016/j.jmmm.2019.02.045>
24. Sanyal, D. and Sanyal, M., "Hydromagnetic slip flow with heat transfer in an inclined channel", *Czechoslovak Journal of Physics B*, Vol. 39, No. 5, (1989), 529-536. <https://doi.org/10.1007/BF01597717>
25. Zhou, J., *Differential transformation and its applications for electrical circuits*. 1986, Huazhong University Press, Wuhan, China.
26. Abbas, Z., Hasnain, J., Aly, S. and Sheikh, M., "Comparative analysis for partial slip flow of ferrofluid fe₃o₄ nanoparticles in a semi-porous channel", *Journal of King Saud University-Science*, Vol. 32, No. 5, (2020), 2646-2655. <https://doi.org/10.1016/j.jksus.2020.05.007>
27. Jalili, B., Sadighi, S., Jalili, P. and Ganji, D.D., "Characteristics of ferrofluid flow over a stretching sheet with suction and injection", *Case Studies in Thermal Engineering*, Vol. 14, (2019), 100470. <https://doi.org/10.1016/j.csite.2019.100470>
28. Jalili, B., Ganji, A.D., Jalili, P., Nourazar, S.S. and Ganji, D., "Thermal analysis of williamson fluid flow with lorentz force on the stretching plate", *Case Studies in Thermal Engineering*, Vol. 39, (2022), 102374. <https://doi.org/10.1016/j.csite.2022.102374>
29. Jalili, B., Sadighi, S., Jalili, P. and Ganji, D.D., "Numerical analysis of mhd nanofluid flow and heat transfer in a circular porous medium containing a cassini oval under the influence of the lorentz and buoyancy forces", *Heat Transfer*, Vol. 51, No. 7, (2022), 6122-6138. <https://doi.org/10.1002/htj.22582>
30. Jalili, B., Jalili, P., Sadighi, S. and Ganji, D.D., "Effect of magnetic and boundary parameters on flow characteristics analysis of micropolar ferrofluid through the shrinking sheet with effective thermal conductivity", *Chinese Journal of Physics*, Vol. 71, (2021), 136-150. <https://doi.org/10.1016/j.cjph.2020.02.034>
31. Jalili, P., Narimisa, H., Jalili, B., Shateri, A. and Ganji, D., "A novel analytical approach to micro-polar nanofluid thermal analysis in the presence of thermophoresis, brownian motion and hall currents", *Soft Computing*, Vol. 27, No. 2, (2023), 677-689. <https://doi.org/10.1007/s00500-022-07643-2>
32. Jalili, B., Roshani, H., Jalili, P., Jalili, M., Pasha, P. and Ganji, D.D., "The magnetohydrodynamic flow of viscous fluid and heat transfer examination between permeable disks by agm and fem", *Case Studies in Thermal Engineering*, Vol. 45, (2023), 102961. <https://doi.org/10.1016/j.csite.2023.102961>
33. Jalili, P., Sharif Mousavi, S., Jalili, B., Pasha, P. and Ganji, D.D., "Thermal evaluation of mhd jeffrey fluid flow in the presence of a heat source and chemical reaction", *International Journal of Modern Physics B*, (2023), 2450113. <https://doi.org/10.1142/S0217979224501133>
34. Nagiredla, S., Joladarashi, S. and Kumar, H., "Rheological properties of the in-house prepared magneto-rheological fluid in the pre-yield region", *International Journal of Engineering, Transactions B: Applications*, Vol. 35, No. 11, (2022), 2238-2246. doi: 10.5829/IJE.2022.35.11B.19.
35. Pasha, P., Nabi, H., Peiravi, M., Pourfallah, M. and Domiri Ganji, D., "The application of analytical methods in the investigation effects of magnetic parameter and brownian motion on the fluid flow between two equal plates", *International Journal of Engineering, Transactions A: Basics*, Vol. 34, No. 10, (2021), 2341-2350. doi: 10.5829/IJE.2021.34.10A.15.
36. Tajik Jamal-Abad, M., "Analytical investigation of forced convection in thermally developed region of a channel partially filled with an asymmetric porous material-lme model", *International Journal of Engineering, Transactions A: Basics*, Vol. 29, No. 7, (2016), 975-984.

COPYRIGHTS

©2023 The author(s). This is an open access article distributed under the terms of the Creative Commons Attribution (CC BY 4.0), which permits unrestricted use, distribution, and reproduction in any medium, as long as the original authors and source are cited. No permission is required from the authors or the publishers.

**Persian Abstract****چکیده**

در این مقاله، معادلات حاکم بر جریان فرومغناطیسی ثابت بررسی شده است. نیروی لورنتس، این جریان فرومغناطیسی را در یک دریچه نیمه متخلخل مهار می کند. آنالیزها بر روی سه سیال زیر ذرماهی انجام شد: نفت سفید و خون، آب و مگنتیت. مدلسازی در میهم مختصات دکارتی با استفاده از معادلات مربوطه بررسی شده است. در قسمت پایینی این کاتال باشد کمی نازک شدن در نظر گرفته شود. در این تحقیق از دو روش اکبری-گنجی و روش اجزاء محدود برای حل معادلات استفاده شده است. معادلات دیفرانسیل غیرخطی با استفاده از دو روش فوق حل می شوند. در مدل اجزاء محدود، اثر تغییر عدد هارتمن و عدد رینولدز بر سرعت جریان و مشتقات سرعت و تنش برشی سیال بررسی شده است. با افزایش عدد هارتمن، سرعت در هر دو جهت کاهش می یابد. عدد رینولدز در پارامترهای لغزش مختلف تغییر می کند که رفتار مخالف را برای دو جهت نشان می دهد. همچنین اثر ناچیز کسر حجمی نانوذرات بر سرعت و مشتقات آن و تنش برشی بررسی شده است. نتایج حل معادلات با دو روش فوق با روش هموتوپی مقایسه شده است. نتایج به دست آمده با استفاده از روش اکبری-گنجی و روش اجزاء محدود و مقایسه آنها با تحقیقات قبلی منجر به مطابقت کامل شده است که نشان دهنده کارایی تکنیک های مورد استفاده در این تحقیق است.



Deep Multi-task Convolutional Neural Networks for Efficient Classification of Face Attributes

M. Rohani, H. Farsi*, S. Mohamadzadeh

Department of Electrical and Computer Engineering, University of Birjand, Birjand, Iran

PAPER INFO

A B S T R A C T

Paper history:

Received 23 July 2023

Received in revised form 01 August 2023

Accepted 06 August 2023

Keywords:

Age Detection

Convolutional Neural Networks

Gender Classification

Multi-task Learning

Smile Detection

Facial feature recognition is an important subject in computer vision with numerous applications. The human face plays a significant role in social interaction and personology. Valuable information such as identity, age, gender, and emotions can be revealed via facial features. The purpose of this paper is to present a technique for detecting age, smile, and gender from facial images. A multi-task deep learning (MT-DL) framework was proposed that can simultaneously estimate three important features of the human face with remarkable accuracy. Additionally, the proposed approach aims to reduce the number of trainable network parameters while leveraging the combination of features from different layers to increase the overall accuracy. The conducted tests demonstrate that the proposed method outperforms recent advanced techniques in all three accuracy criteria. Moreover, it was demonstrated that multi-task learning (MTL) is capable of improving the accuracy by 1.55% in the smile task, 2.04% in the gender task, and 3.52% in the age task even with less available data, by utilizing tasks with more available data. Furthermore, the trainable parameters of the network in the MTL mode for estimating three tasks simultaneously increase only by about 40% compared to the single-task mode. The proposed method was evaluated on the IMDB-WIKI and GENKI-4K datasets and produced comparable accuracy to the state-of-the-art methods in terms of smile, age detection, and gender classification.

doi: 10.5829/ije.2023.36.11b.14

NOMENCLATURE

M	Total number of training sample	L_t	Cross-Entropy
N_t	Number of classes associated with each task	λ	Weight decay
C_i^t	Class score vector for the i th sample in the t th task	W	Output weights
S_i^t	Label corresponding to the i th sample in the t th task	μ_t	Significance factor in each loss function
X_i^t	One-hot Encoding of the i th sample	L_r	Learning rate
\hat{X}_i^t	Probability distribution in the t th task over the i th sample	$Decay_step$	Steps the learning rate
β_i^t	The kind of sample	β_i^t	The kind of sample

1. INTRODUCTION

Deep learning (DL), a branch of artificial intelligence (AI), has made significant advancements in computer vision. Many AI developments and products have lifted living standards, increased productivity, and conserved social and human resources. In many instances, artificial intelligence has surpassed human skills. The study of human emotions and behavior; however, greatly benefited from the active research into automatic face detection [1, 2]. Hence, the present research addresses

facial feature recognition, such as smile, emotion, and gender detection. Subsequently, each of these features is expressed as a task associated with the human face. In each task, facial images are used as inputs. In the smile task, the presence or absence of a smile is detected on each facial image. Then, the ages of the persons in the images are classified into six age groups. Finally, each person's gender is revealed. These tasks are typically investigated as separate problems, which makes model training challenging, especially when there is a lack of adequate training data. On the other hand, the

*Corresponding Author Email: hfarsi@birjand.ac.ir (H. Farsi)

information related to different facial analysis tasks frequently includes joint facial traits. Therefore, simultaneous learning from several facial datasets improves the detection accuracy of each task. The paper outlines the methodology for facial image analysis, which involves preprocessing images from different datasets using a convolutional neural network (CNN) to extract faces. A deep convolutional neural network (D-CNN) is then trained using a combination of common features for smile detection, age detection, and gender classification. To achieve this, the tasks are divided into three branches with their own loss functions, and a final loss function is defined by combining these. The approach allows each task to receive images from its corresponding dataset and share the features for training with other tasks. The second section of the paper offers a concise overview of CNNs and their application to the gender, smile, and age tasks. The section concludes with an examination of multi-task learning (MTL) methods. In section 3, a novel multi-task deep learning (MT-DL) framework is introduced, which enables the simultaneous estimation of three significant facial features with remarkable precision. A key aspect of the proposed approach is its focus on minimizing the number of trainable network parameters by proposing a new CNN, while effectively harnessing feature combinations from various layers to improve overall accuracy. Through comprehensive tests and evaluations, the proposed method consistently outperforms recent advanced techniques across all three accuracy criteria, underscoring its superiority and effectiveness in facial feature recognition tasks.

2. LITERATURE REVIEW

This section provides a comprehensive examination of the existing research on deep neural networks applied to smile detection, age detection, gender classification, and multi-task learning in the context of facial feature recognition. This section explores the methodologies, techniques, and approaches employed in previous studies, focusing on their utilization of deep neural networks for these specific tasks. Through critical analysis of the accomplishments, limitations, and advancements in these areas, this literature review establishes the foundation for the proposed method, highlighting the gaps that this present study aims to address and emphasizing the significance of the proposed approach in advancing the field of facial analysis.

2. 1. Deep Neural Networks Over the past ten years, there has been significant research in the field of computer vision, with a focus on deep learning techniques, which has led to the development of numerous methods. D-CNNs are common in the area of

DL, such that they constitute a major DL method. In these networks, a large number of layers in these networks are trained with a powerful approach. This technique is extremely effective and is also frequently utilized in a variety of computer vision applications [3, 4]. The major CNN was AlexNet, introduced by Krizhevsk [5] fourteen years after LeNet in 2017. The network can be categorized as a shallow network as it has a total of eight layers, including three fully connected layers and five convolutional layers [5]. Subsequently, deeper neural networks were introduced. Recently, Google presented a network called Inception, which was based on deepening convolutional networks [6]. The VGG-16 network was introduced by Simonyan and Zisserman [7]. This network is highly popular due to its simple structure. Later, Microsoft presented a network named Residual Network, abbreviated as ResNet. In addition to the convolutional network, this network incorporates connections between layers to directly transfer inputs from one layer to the next, as well as errors during backpropagation, allowing for a faster and deeper training process without the need for intermediate layers [8]. After the introduction of deeper and more accurate networks, those such as ResNext and WideResNet were proposed. ResNext was a multi-branch version of ResNet, presented in 2017 by Xie et al. [9]. The aim of this network was to improve efficiency by increasing the network's width. In order to increase network width and decrease network depth, this network tried to improve efficiency by adding more filters. The performance of the presented neural networks was demonstrated in ImageNet, one of the most well-known computer vision competitions.

2. 2. Smile Detection

Recent studies have concentrated on using neural networks to detect smiles in images. In research by Sang et al. [10], a network similar to the VGG network, named BK-Net, was designed. This is highly capable of smile detection. In 2018, Cui et al. [11] presented the extreme learning machine (ELM) with the aim of feature dimensionality reduction and focusing on the regions surrounding the mouth. Subsequently, in 2019, Vo et al. [12] extracted features from facial images using a CNN and carried out smile detection via an extreme gradient boosting (XGB) classifier. In the same year, Nguyen [13] employed the YOLO network for smile detection. In 2020, Wu et al. [14] proposed a method for fast smile detection in a working environment based on Multilayer Perceptron (MLP) network. Additionally, they used two different databases for training the network instead of one. In 2021, Hassen et al. [15] proposed a method based on MLP neural network and Cascade Classifier. The accuracy of these methods is challenged in low-light conditions and when the facial image is angled or distorted. In another study in 2022, Hassen et al. [16] used an ensemble classification

approach and multiple classifiers to detect smiles. This method also has a high speed, but its accuracy decreases when dealing with low-resolution images [16]. In the same year in 2022, Liu et al. [17] utilized the MobileNetV2 network for smile detection.

2.3. Age Detection Recent years have witnessed the widespread use of CNNs for age detection [18]. To this end, they designed a network inspired by the VGG-16 architecture and implemented this model using the ResNet network [19]. In 2018, Rothe et al. [20] proposed a method for age estimation based on the ResNet. They then estimated the age of individuals using a unique network. They employed the Adience dataset to evaluate their methods. In 2019, Zhang et al. [21] combined the ResNet and LSTM networks into AL-ResNet networks in order to extract age-sensitive local regions. To accomplish this, they used a ResNet model that was pre-trained on the ImageNet dataset as a base model, and then identified age intervals using age-related datasets. Cao et al. [22] estimated age using two neural networks. First, they extracted features using a simple neural network, and then they estimated age using the Rank Consistent Ordinal Regression Network (RCORN) network. In another study, Xia et al. [23] extracted features using a neural network through multi-stage learning and estimated the age of individuals from facial images using a Feedforward Neural Network.

2.4. Gender Classification In recent years, the use of CNNs for age detection has considerably increased. Zhang et al. [24] utilized both ResNet and LSTM networks to extract age-related features from facial images, which were then combined to estimate gender. In 2018, Amit Dhomne et al. [25] proposed a gender detection approach based on the VGG network, which achieved acceptable accuracy. In a recent study, Nga et al. [26] employed the ImageNet network to detect gender and utilized a combination of features from multiple layers for improved performance. They believed that using pre-trained weights in the ImageNet network would improve their results. In 2022, Bekhet et al. [27] estimated individuals' gender using a proposed convolutional neural network with selfie images. However, a limitation of this approach is the low diversity of images in the dataset.

2.4. Multi-Task Learning MTL refers to multiple classifications with different objectives in different classes. In MTL, multiple tasks are simultaneously trained using CNNs. This type of learning exploits the similarities and differences between various tasks [28, 29]. In 2017, Ranjan et al. [30] presented an AlexNet-based MTL model named Hyper Face with face detection, landmark localization, facial gesture estimation, and gender estimation capabilities. These

four tasks were trained simultaneously on a dataset named ALFW, and the network output was used to predict each of the tasks. In another study in multi task learning, Ran et al. [31] used multi-task learning to estimate human pose and shape and remove occlusions. In 2021, Savchenko [32] proposed a multi-task learning approach for facial expression and attribute recognition. The aim of the proposed method in this paper was to detect facial features and components. In 2022, Yu et al. [33] introduced a multi-task learning based approach for facial parameter detection. They used attention modules to focus on each part of the image in their method. The use of these modules improved the accuracy of detecting each parameter [33].

3. MATERIAL AND METHODS

The proposed framework utilizes multi-task learning to simultaneously learn and solve multiple tasks. Moreover, D-CNNs were simultaneously used for all the tasks and named the “shared convolutional neural network” (S-CNN). To this end, several independent datasets were used to train the network after being combined. The advantage of using several datasets along with the S-CNN is learning shared features from several datasets in different tasks. In addition, shared learning allows tasks with fewer data to use tasks with more data. Moreover, it seems that using features learned in shared learning leads to better results compared to the single-task mode. In the next step, the network was divided into three separate branches. Each of these branches was assigned to one task and sought to learn the features related to that task. In the end, an appropriate loss function was defined for each task. Figure 1 displays the combination of the datasets.

3.1. Implementation of Method with MTL The proposed framework has been presented and modified based on the BKNet network. In this method, the CNN was constructed by removing the last three fully connected layers of the BKNet and concatenating the output of the first layer with the last layer before the fully connected layers. Table 1 shows the BKNet architecture. In order to use the facial images from the datasets, one first needs to crop the face images from the original images. A multi-task convolutional neural network (MTCNN) was used for this purpose [34]. The comprehensive preprocessing begins by reading the images from a designated folder and utilizing MTCNN to identify the positions of faces within the images. Subsequently, a series of preprocessing steps, including face cropping, grayscale conversion, and resizing the images to a fixed dimension of 48x48 pixels. Furthermore, the quality and diversity of the dataset can be enhanced by incorporating additional preprocessing

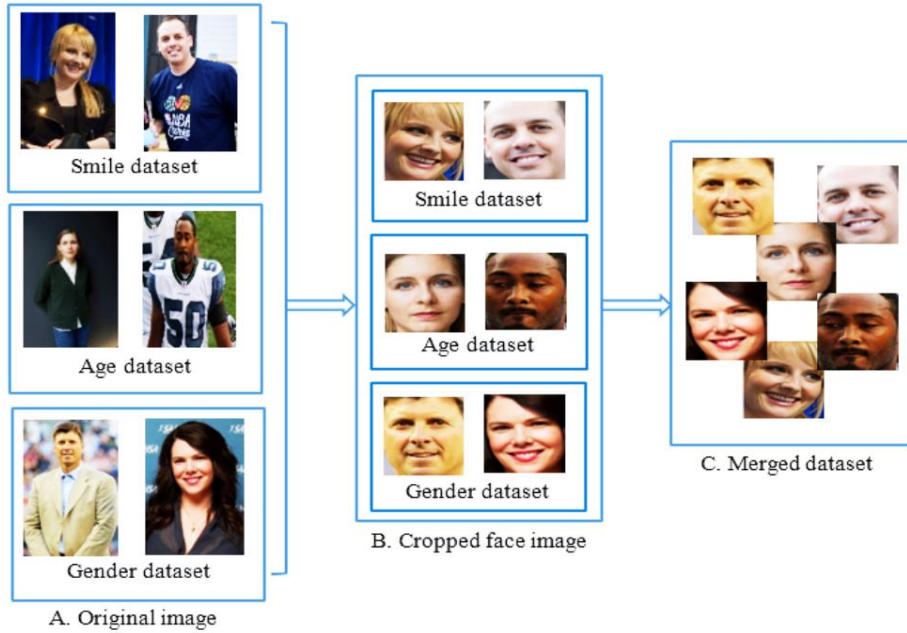


Figure 1. Dataset combination: original images (A); cropped facial images (B); and dataset combination (C)

TABLE 1. Architecture of the BKNet CNN [10]

Input image

Convolutional layer 64 filters 3×3 , stride 1 and ReLU
Convolutional layer 64 filters 3×3 , stride 1 and ReLU
Max pooling layer with a 2×2 filter and stride of 2
Convolutional layer 128 filters 3×3 , stride 1 and ReLU
Convolutional layer 128 filters 3×3 , stride 1 and ReLU
Convolutional layer 128 filters 3×3 , stride 1 and ReLU
Max pooling layer with a 2×2 filter and stride of 2
Convolutional layer 256 filters 3×3 , stride 1 and ReLU
Convolutional layer 256 filters 3×3 , stride 1 and ReLU
Max pooling layer with a 2×2 filter and stride of 2
Convolutional layer 512 filters 3×3 , stride 1 and ReLU
Convolutional layer 512 filters 3×3 , stride 1 and ReLU
Max pooling layer with a 2×2 filter and stride of 2

3.2. Shared Convolutional Neural Network Four convolution blocks were used in this section. At first, the CNN was comprised of three blocks, each consisting of two convolutional layers with 32, 64, and 128 neurons, respectively, all with a 3×3 filter and a stride equal to 1. Each block had a max pooling layer with a 2×2 filter and stride equal 2. The fourth and final block had convolutional layers with 256 neurons and a 3×3 filter, stride equal 1, and the same max pooling layer. Also, the first block's output and the last block's output were concatenated. This allows the features of the first layer, which focuses on the overall facial features, to combine with those of the last layer, which focuses on the details,



Figure 2. An example of a facial picture cropped by the MTCNN: original images (first row); face location (second row); and cropped images corresponding to the first row obtained from the WIKI dataset (third row)

techniques such as normalization and data augmentation. The inclusion of normalization ensures that the intensity values of the grayscale images are within a specific range, facilitating optimal model training. Figure 2 shows an illustration of a face image that the MTCNN has been cropped. Furthermore, the augmentation method was employed to increase the number of training data. This method reduces overfitting and improves learning. The augmentation was carried out using the Random Crop, Random Flip, and Random Rotate techniques.

to produce better results. Figure 3 presents the proposed method's block diagram.

3. 3. Separated Convolutional Neural Network

To facilitate smile detection, age detection, and gender detection, the network was divided into three sections following the S-CNN. The split CNN learns the characteristics of each task in the associated branch, whereas S-CNN learns the shared features of the three tasks from various datasets. Each individual layer consists of three fully connected layers, with the final layer containing N neurons. N is the number of classes for each task and the first two layers each containing 256 neurons. For smile detection, age detection, and gender detection, respectively, these parameters are equivalent to 2, 7, and 2. An activation function for the ReLU and a batch normalization function come after the first two fully connected layers. To prevent overfitting, the three fully connected layers utilized dropout. The first layer's output, which contains features that are closely related to the original images and have a significant impact on the output tasks, including the eyes, nose, and mouth, was concatenated with the last layer before the network was divided into three parts.

3. 4. Loss Functions

An effective CNN was presented in the proposed method for training from several datasets. In this section, all the data from different datasets were combined to form a larger shared training dataset. Each training datum may correspond to one or more tasks. Accordingly, the following points must be taken into account. M represents the total number of training samples collected from two datasets. N_t

represents the number of classes associated with each task. C_i^t is the class score vector for the i th sample in the t th task. S_i^t is the true label corresponding to the i th sample in the t th task. X_i^t is the one-hot Encoding of the i th sample's true class label in the t th task ($X_i^t(S_i^t) = 1$). \hat{X}_i^t is the probability distribution in the t th task over the i th sample. $\beta_i^t \in (0,1)$ indicates the kind of sample. ($\beta_i^t = 1$ if the i th sample matches the t th task; $\beta_i^t = 0$ otherwise) L_t represents the loss function that is specific to each task. L_t is named the Cross-Entropy, and according to Equation (1), the L_t corresponding to the t th task is defined.

$$L_t = -\frac{1}{M} \sum_i^M (\beta_i^t \sum_j^{N_t} X_i^t(j) \log (\hat{X}_i^t(j))) \quad (1)$$

In this equation, $\beta_i^t \in (0,1)$ states whether the label j is true for the i th sample or not. The value $\hat{X}_i^t(j)$ within the range of (0,1) represents the estimated probability of the j th label being true for the i th sample. To compute the overall loss function for the network, the weights generated by the loss functions of each task are added together. To mitigate overfitting in the network, the L2 regularization term is incorporated into the total loss function. The total loss function is expressed by Equation (2). In the equation, λ represents the weight decay, which is a hyperparameter that controls the strength of the L2 regularization term, and W refers to the output weights. Moreover, the t th task's significance factor in each loss function is denoted by the μ_t .

$$L_{total} = \sum_i^T (\sum_j^{N_t} \mu_t L_t + \lambda \|W\|^2) \quad (2)$$

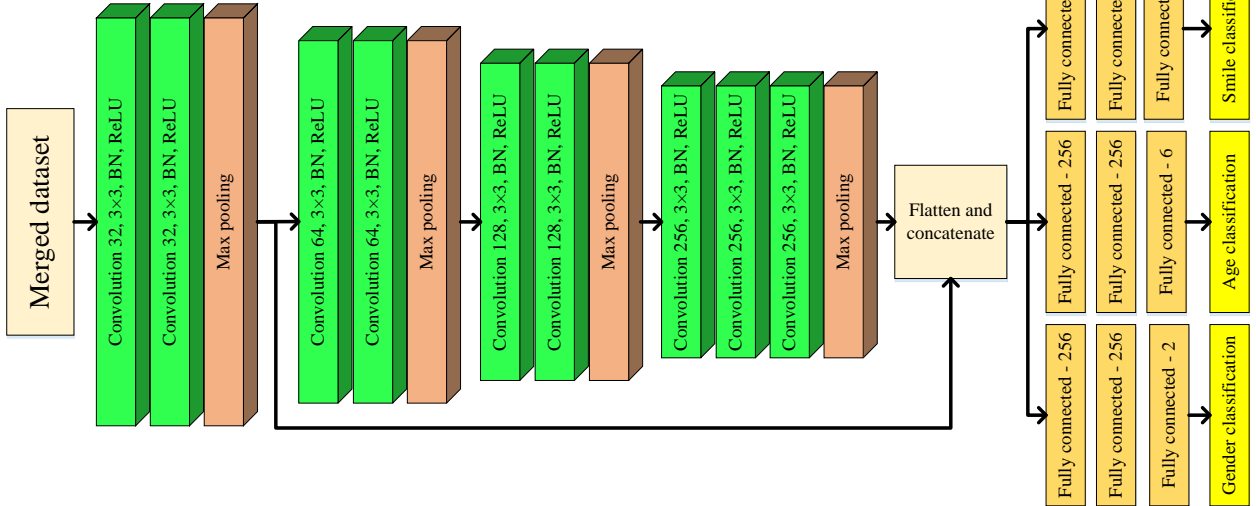


Figure 3. Block diagram of the proposed method

4. RESULTS AND DISCUSSION

4.1. Dataset The GENKI-4K dataset is a widely used dataset for smile detection. It was published by the MPLab GENKI Database. This dataset consists of 4000 labeled images of the human face taken from individuals of various ages and races. 1838 of these images have the label "non-smiling," and 2162 have the label "smiling". This dataset was procured from the Internet, and the backgrounds of the images are different, which makes smile detection more challenging. In other words, unlike datasets that have identical backgrounds, this dataset was constructed from actual images. Another challenge involved in this dataset is that the smile is unclear in some of the images. Some previous studies have eliminated these images from the training and testing processes. These images may cause errors in the training process, complicate the network evaluation, and significantly reduce the overall accuracy. Despite this, all images in the GENKI-4K dataset were utilized for training and testing the proposed method. Figure 4 showcases some samples of images from the GENKI-4K dataset [33].

Also, the proposed method was trained and evaluated using the IMDB-WIKI dataset [34]. This dataset was introduced in 2016 to compensate for the shortage of images in related datasets. This dataset contains images of famous actors prepared from the IMDB website. In addition, it contains images from persons on Wikipedia. This dataset includes the date of birth, name, and gender of every person. Moreover, there are several images of each person in this dataset. In total, there are 460723 images of 20284 persons from IMDB and 62328 images of the same persons from Wikipedia, making up a total of 523051 images. Furthermore, there are six age classes (0-15, 16-25, 26-35, 36-45, 46-60, and 60-100 years) in this dataset. Also, the genders are labeled either male or female. Figure 5 presents samples of images from the IMDB-WIKI dataset.

4.2. Evaluation Criteria The accuracy evaluation criterion measures the accuracy of the smile, gender, and age tasks. This criterion is calculated as the number of correct predictions to the total number of ground-truth labels. It assesses the proportion of face images correctly classified as smiling or not, the accurate age range, and correct gender identification. It is determined by Equation (3) [20, 35].

$$\text{Accuracy} = \frac{\text{Number of accurate prediction}}{\text{Total number of prediction}} \quad (3)$$

4.3. Simulation Details The study utilized the GENKI-4K dataset to detect smiles and the IMDB-WIKI dataset for gender and age detection. Initially, the two datasets were merged to create a larger dataset, and 3000

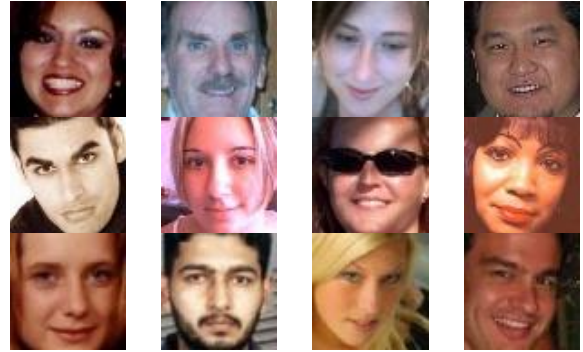


Figure 4. Samples of the GENKI-4K dataset's images [33]

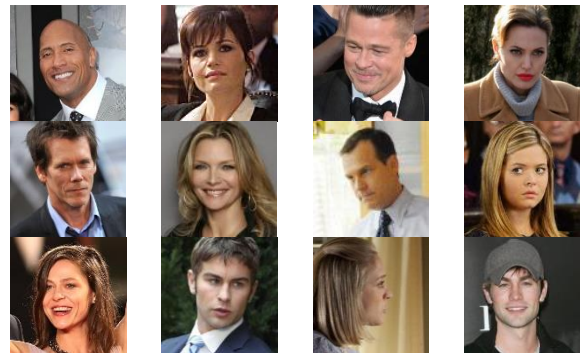


Figure 5. Samples of the images in the IMDB-WIKI dataset [34]

samples from the GENKI-4K dataset were selected for training, while 1000 samples were reserved for testing purposes. Moreover, 20000 samples were utilized for testing and 150000 samples for training using the IMDB-WIKI dataset. The label corresponding to each task was assigned to every sample from each dataset. The vector composed of these labels is designated as β_i^t . Moreover, the batch size was considered to be 128. Additionally, all initial weights were taken into account using a Gaussian distribution with a variance of 0.01 and zero mean. It was assumed that L2 weight decay would be $\lambda=0.01$. Furthermore, the importance factors of all tasks were assumed to be $\mu_t = \mu_1 = \mu_2 = \mu_3 = 1$. The dropout rate was considered to be 0.5 for all the fully connected layers. An exponential function was used to reduce the learning rate. This rate is calculated in the p^{th} step of Equation (4).

$$L_r = \text{Initial } L_r \times \text{Decay_rate}^{\text{Step}/\text{Decay_step}} \quad (4)$$

In this equation, L_r denotes the learning rate at the p^{th} step. Moreover, Decay_step is the step in which the learning rate declines, and $\text{Initial } L_r$ is the initial learning rate. In the conducted experiments, $\text{Initial } L_r = 0.01$, $\text{Decay}_step = 2000$, and $\text{Decay}_rate = 0.8$. Also, the proposed model was executed for over 500 epochs.

Figure 6 shows the accuracy and loss function graphs for the three tasks for 100 epochs. In this paper, three groups of experiments were performed. The first network training method was single-task training. In this method, the network output was considered only for one task and was trained using the corresponding dataset.

4. 4. Results The evaluation of the network is presented in Table 2 under Config A (Single BK-Net). The second method, designated Config B, involves MTL without combining the features of the first and last convolutional layers (MTL-BK-Net). The third case, Config C, corresponds to the method proposed (MTL-MBK-Net) in Figure 3. The proposed method was initially trained on the two datasets. The results of the proposed method are compared to those of the state-of-the-art methods in Table 2. The proposed method MTL-MBKNet (Config C) achieved a smile detection accuracy of 96.63% on the IMDB-WIKI dataset according to the Table 2, which is superior to previous methods.

In addition, an accuracy of 95.08% was achieved in the single-task mode for the smile task, indicating that the smile task uses the other tasks to improve the results. In the gender task, the proposed method attained an accuracy of 93.20%, which outperformed the other methods. The RoR-34 method came in second place with an accuracy of 92.24%. Additionally, the proposed method achieved a gender detection accuracy of 91.16% in the single-task mode. This difference in accuracy

between the multi-task and single-task modes shows that the gender task has used the other tasks during training. In the age detection task, MTL-MBK-Net (Config C) produced the best accuracy at 68.92%, followed by AL-ResNet-34 with an accuracy of 67.83%. MTL performed better than single-task learning also in this task. MTL-MBK-Net (Config B) exhibited better results than Single BK-Net (Config A) in all the tasks. The proposed method suffered some errors during the evaluation in some tasks. These errors are present in smile, gender, and age detection. Figure 7 depicts the errors in the smile, gender, and age detection tasks. Specifically, the first, second, and third rows of the Figure represent the errors in smile, gender, and age detection, respectively. In smile detection, these errors can be attributed to the facial form and the presence or absence of the teeth during smiling or a special form of the smile in some persons. In gender detection, the errors may be due to the makeup used by some persons and their genetics. A major challenge in age detection is the makeup used by women, which modifies the lip, eye, and skin features.

The results of comparing the three proposed models based on the number of parameters of execution time and Fps are presented in Table 3. Single BK-Net (Config A) results in the lowest number of parameters, with only 2418146, and the fastest execution time of 6.23 seconds. It also has a relatively high processing speed of 20.54 Fps. MTL-BK-Net (Config B) provides 3731946 processing speed of 13.30 Fps. Finally, MTL-MBK-Net

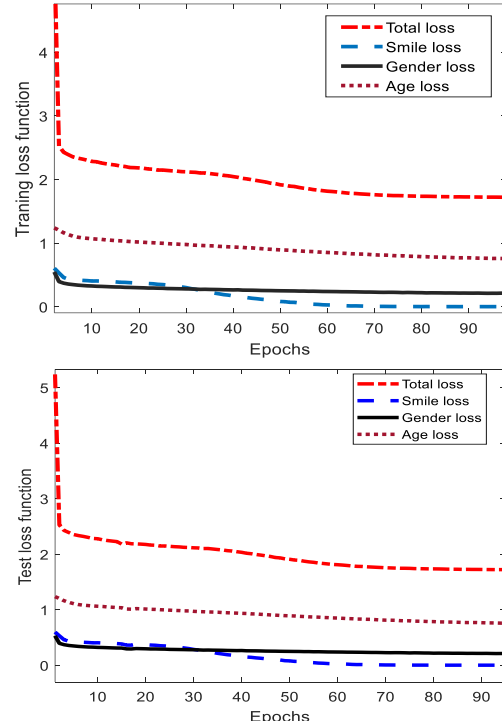
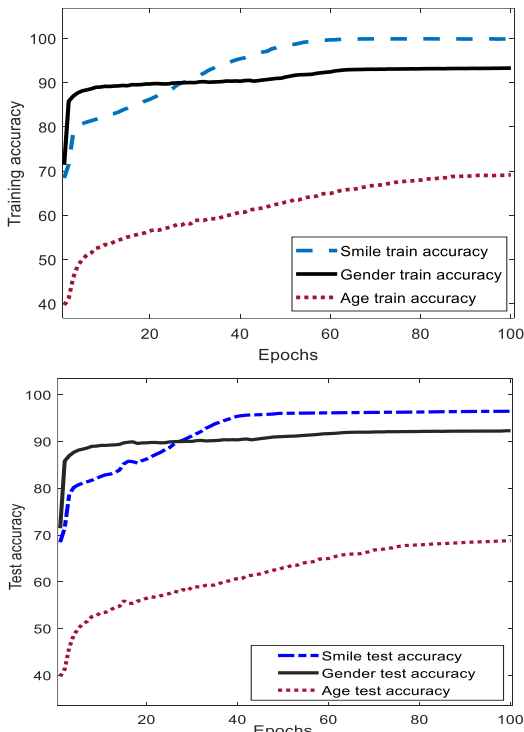
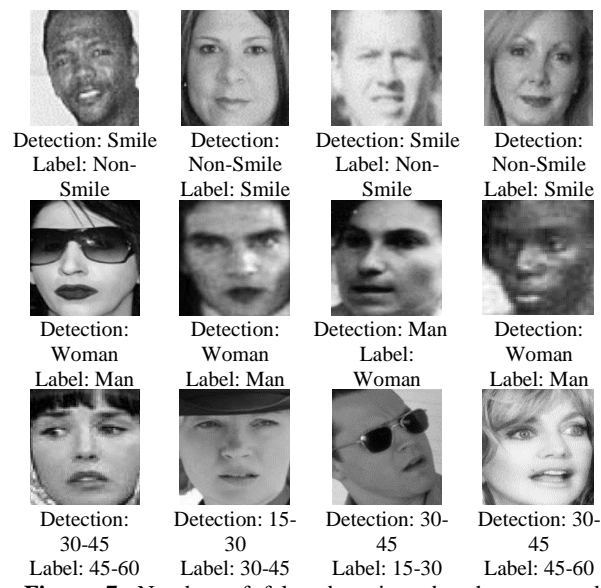


Figure 6. A view of the accuracy and loss functions for the three tasks during training and testing

TABLE 2. Numerical results of the proposed method and other state-of-the art methods

Task	Methods	Accuracy (%)
Smile accuracy comparison results	PDV-ELM [11]	93.42
	HF-SD [12]	93.60
	YOLO [13]	93.17
	MNV2 [17]	94.37
	Single BKNet (Config A)	95.08
	MTL-BKNet (Config B)	<u>95.60</u>
Gender accuracy comparison results	MTL-MBKNet (Config C)	96.63
	RoR-34 [24]	<u>92.24</u>
	TL-VGG19 [26]	91.09
	TL-DenseNet-169 [26]	70.48
	GSI-CNN [27]	89.00
	Single BKNet (Config A)	91.16
Age accuracy comparison results	MTL-BKNet (Config B)	91.28
	MTL-MBKNet (Config C)	93.20
	ResNet-34 [24]	64.63
	RoR-34 [24]	65.74
	AL-ResNet-34 [21]	67.83
	DEX-w [20]	64.00
Age accuracy comparison results	Single BKNet (Config A)	65.40
	MTL-BKNet (Config B)	<u>67.81</u>
	MTL-MBKNet (Config C)	68.92

**Figure 7.** Number of false detections by the proposed method**TABLE 3.** Proposed models parameters and execution time comparison

Methods	Parameters	Execution time (s)	Fps
Single BK-Net (Config A)	2418146	6.23	20.54
MTL-BK-Net (Config B)	3731946	9.62	13.30
MTL-MBK-Net (Config C)	3953130	10.19	12.56

(Config C), has 3953130 parameters and takes 10.19 seconds to execute with a processing speed of 12.56 Fps. In order to evaluate three tasks, three single-task networks must be parallelized with each other. In this case, the parameters of the network are tripled and it has more parameters compared to the multi-task state. However, using multi-task learning causes that the parameter ratio of the network decreases and the computational burden reduces as well. Furthermore, according to Table 3, with the training of three single-task networks, the execution time of the network also increases compared to the multi-task state.

5. CONCLUSION

The present paper proposed a DL framework using MTL on facial images. In the proposed method, a D-CNN was shared to extract features related to smiling, gender, and age group from facial images from the well-known GENKI-4K and IMD-WIKI datasets. This improved the accuracy of smile detection, which had fewer available data than the other tasks. In addition, the proposed separated network was used along with a combination of layers to detect smile, age, and gender. In comparison to current methodologies used in both the multi-task mode and the single-task mode, the proposed framework achieved good results. In future studies, potential applications and challenges of the proposed architecture, including its scalability and robustness under different conditions and environments, will be investigated. Additionally, the use of more challenging datasets and auxiliary losses to improve the training procedure and increase the accuracy of neural networks in various tasks will be explored. Furthermore, the potential of the proposed framework for real-time face recognition in practical applications such as security, healthcare, and entertainment will be examined.

6. REFERENCES

- Shahbakhsh, M.B. and Hassanpour, H., "Empowering face recognition methods using a gan-based single image super-resolution network", *International Journal of Engineering*,

- Transactions A: Basics**, Vol. 35, No. 10, (2022), 1858-1866. doi: 10.5829/ije.2022.35.10a.05.
2. Firouzian, I., Firouzian, N., Hashemi, S. and Kozegar, E., "Pain facial expression recognition from video sequences using spatio-temporal local binary patterns and tracking fiducial points", **International Journal of Engineering, Transactions B: Applications**, Vol. 33, No. 5, (2020), 1038-1047. doi: 10.5829/ije.2020.33.05b.38.
 3. Charoqdouz, E. and Hassanpour, H., "Feature extraction from several angular faces using a deep learning based fusion technique for face recognition", **International Journal of Engineering, Transactions B: Applications**, Vol. 36, No. 8, (2023), 1548-1555. doi: 10.5829/ije.2023.36.08b.14.
 4. Thepade, S., Dindorkar, M., Chaudhari, P. and Bang, S., "Enhanced face presentation attack prevention employing feature fusion of pre-trained deep convolutional neural network model and thepade's sorted block truncation coding", **International Journal of Engineering, Transactions A: Basics**, Vol. 36, No. 4, (2023), 807-816. doi: 10.5829/ije.2023.36.04a.17.
 5. Krizhevsky, A., Sutskever, I. and Hinton, G.E., "Imagenet classification with deep convolutional neural networks", **Advances in Neural Information Processing Systems**, Vol. 25, (2012). doi: 10.1145/3065386.
 6. Szegedy, C., Liu, W., Jia, Y., Sermanet, P., Reed, S., Anguelov, D., Erhan, D., Vanhoucke, V. and Rabinovich, A., "Going deeper with convolutions", in Proceedings of the IEEE conference on computer vision and pattern recognition. (2015), 1-9.
 7. Simonyan, K. and Zisserman, A., "Very deep convolutional networks for large-scale image recognition", **arXiv preprint arXiv:1409.1556**, (2014). doi: 10.48550/arXiv.1409.1556.
 8. He, K., Zhang, X., Ren, S. and Sun, J., "Deep residual learning for image recognition", in Proceedings of the IEEE conference on computer vision and pattern recognition. (2016), 770-778.
 9. Xie, S., Girshick, R., Dollár, P., Tu, Z. and He, K., "Aggregated residual transformations for deep neural networks", in Proceedings of the IEEE conference on computer vision and pattern recognition. (2017), 1492-1500.
 10. Sang, D.V., "Facial smile detection using convolutional neural networks", in 2017 9th International Conference on Knowledge and Systems Engineering (KSE), IEEE. (2017), 136-141.
 11. Cui, D., Huang, G.-B. and Liu, T., "Elm based smile detection using distance vector", **Pattern Recognition**, Vol. 79, (2018), 356-369. doi: 10.1016/j.patcog.2018.02.019.
 12. Vo, T., Nguyen, T. and Le, C., "A hybrid framework for smile detection in class imbalance scenarios", **Neural Computing and Applications**, Vol. 31, No. 12, (2019), 8583-8592. doi: 10.1007/s00521-019-04089-w.
 13. Nguyen, C.C., Tran, G.S., Nghiêm, T.P., Burie, J.-C. and Luong, C.M., "Real-time smile detection using deep learning", **Journal of Computer Science and Cybernetics**, Vol. 35, No. 2, (2019), 135-145. doi: 10.15625/1813-9663/35/2/13315.
 14. Wu, H., Liu, Y., Liu, Y. and Liu, S., "Fast facial smile detection using convolutional neural network in an intelligent working environment", **Infrared Physics & Technology**, Vol. 104, (2020), 103061. doi: 10.1016/j.infrared.2019.103061.
 15. Hassen, O.A., Abu, N.A., Abidin, Z.Z. and Darwish, S.M., "A new descriptor for smile classification based on cascade classifier in unconstrained scenarios", **Symmetry**, Vol. 13, (2021), 805-816. doi: 10.3390/sym13050805.
 16. Hassen, O.A., Abu, N.A., Abidin, Z.Z. and Darwish, S.M., "Realistic smile expression recognition approach using ensemble classifier with enhanced bagging", **Computers, Materials & Continua**, Vol. 70, No. 2, (2022). doi: 10.32604/cmec.2022.019125.
 17. Liu, Y., Liu, Z., Zhao, Y. and Xu, J., "A robust approach for smile recognition via deep convolutional neural networks", in 2022 7th International Conference on Image, Vision and Computing (ICIVC), IEEE. (2022), 60-64.
 18. Mavaddati, S., "Voice-based age and gender recognition using training generative sparse model", **International Journal of Engineering, Transactions C: Aspects**, Vol. 31, No. 9, (2018), 1529-1535. doi: 10.5829/ije.2018.31.09c.08.
 19. Zhang, K., Sun, M., Han, T.X., Yuan, X., Guo, L. and Liu, T., "Residual networks of residual networks: Multilevel residual networks", **IEEE Transactions on Circuits and Systems for Video Technology**, Vol. 28, No. 6, (2017), 1303-1314. doi: 10.1109/TCSVT.2017.2654543.
 20. Rothe, R., Timofte, R. and Van Gool, L., "Deep expectation of real and apparent age from a single image without facial landmarks", **International Journal of Computer Vision**, Vol. 126, No. 2-4, (2018), 144-157. doi: 10.1007/s11263-016-0940-3.
 21. Zhang, K., Liu, N., Yuan, X., Guo, X., Gao, C., Zhao, Z. and Ma, Z., "Fine-grained age estimation in the wild with attention lstm networks", **IEEE Transactions on Circuits and Systems for Video Technology**, Vol. 30, No. 9, (2019), 3140-3152. doi: 10.1109/TCSVT.2019.2936410.
 22. Cao, W., Mirjalili, V. and Raschka, S., "Rank consistent ordinal regression for neural networks with application to age estimation", **Pattern Recognition Letters**, Vol. 140, (2020), 325-331. doi: 10.1016/j.patrec.2020.11.008.
 23. Xia, M., Zhang, X., Weng, L. and Xu, Y., "Multi-stage feature constraints learning for age estimation", **IEEE Transactions on Information Forensics and Security**, Vol. 15, (2020), 2417-2428. doi: 10.1109/TIFS.2020.2969552.
 24. Zhang, K., Gao, C., Guo, L., Sun, M., Yuan, X., Han, T.X., Zhao, Z. and Li, B., "Age group and gender estimation in the wild with deep ror architecture", **IEEE Access**, Vol. 5, (2017), 22492-22503. doi: 10.1109/ACCESS.2017.2761849.
 25. Dhomne, A., Kumar, R. and Bhan, V., "Gender recognition through face using deep learning", **Procedia computer science**, Vol. 132, (2018), 2-10. doi: 10.1016/j.procs.2018.05.053.
 26. Nga, C.H., Nguyen, K.-T., Tran, N.C. and Wang, J.-C., "Transfer learning for gender and age prediction", in 2020 IEEE International Conference on Consumer Electronics-Taiwan (ICCE-Taiwan), IEEE. (2020), 1-2.
 27. Bekhet, S., Alghamdi, A.M. and Taj-Eddin, I., "Gender recognition from unconstrained selfie images: A convolutional neural network approach", **International Journal of Electrical & Computer Engineering**, Vol. 12, No. 2, (2022), 2066-2078. doi: 10.11591/ijece.v12i2.pp2066-2078.
 28. Thung, K.-H. and Wee, C.-Y., "A brief review on multi-task learning", **Multimedia Tools and Applications**, Vol. 77, (2018), 29705-29725. doi: 10.1007/s11042-018-6463-x.
 29. Zhang, Y. and Yang, Q., "A survey on multi-task learning", **IEEE Transactions on Knowledge and Data Engineering**, Vol. 34, No. 12, (2021), 5586-5609. doi: 10.1109/TKDE.2021.3070203.
 30. Ranjan, R., Patel, V.M. and Chellappa, R., "Hyperface: A deep multi-task learning framework for face detection, landmark localization, pose estimation, and gender recognition", **IEEE Transactions on Pattern Analysis and Machine Intelligence**, Vol. 41, No. 1, (2017), 121-135. doi: 10.1109/TPAMI.2017.2781233.
 31. Ran, H., Ning, X., Li, W., Hao, M. and Tiwari, P., "3d human pose and shape estimation via de-occlusion multi-task learning", **Neurocomputing**, (2023), 126284. doi: 10.1016/j.neucom.2023.126284.
 32. Savchenko, A.V., "Facial expression and attributes recognition based on multi-task learning of lightweight neural networks", in

- 2021 IEEE 19th International Symposium on Intelligent Systems and Informatics (SISY), IEEE. (2021), 119-124.
33. Yu, W. and Xu, H., "Co-attentive multi-task convolutional neural network for facial expression recognition", *Pattern Recognition*, Vol. 123, (2022), 108401. doi: 10.1016/j.patcog.2021.108401.
34. Wu, C. and Zhang, Y., "Mtcnn and facenet based access control system for face detection and recognition", *Automatic Control and Computer Sciences*, Vol. 55, (2021), 102-112. doi: 10.3103/S0146411621010090.
35. Agbo-Ajala, O. and Viriri, S., "Deeply learned classifiers for age and gender predictions of unfiltered faces", *The Scientific World Journal*, Vol. 2020, (2020). doi: 10.1155/2020/1289408.

COPYRIGHTS

©2023 The author(s). This is an open access article distributed under the terms of the Creative Commons Attribution (CC BY 4.0), which permits unrestricted use, distribution, and reproduction in any medium, as long as the original authors and source are cited. No permission is required from the authors or the publishers.



Persian Abstract

چکیده

تشخیص ویژگی‌های انسان از روی چهره یکی از موضوعات مهم و دارای کاربردهای مختلف در حوزه بینایی کامپیوتر است. چهره انسان ویژگی‌های مهمی را در تعاملات اجتماعی و شخصیت شناسی افراد دارد. اطلاعات بر جسته‌ای مانند هویت فرد، سن، جنسیت و احساسات را می‌توان با استفاده از چهره افراد تشخیص داد. در همین راستا در این مقاله روشی به منظور تشخیص سن، لیختن و جنسیت از روی تصویر چهره معرفی شده است. چهارچوب یادگیری عمیق چند وظیفه‌ای پیشنهاد شده است که می‌تواند به طور مشترک سه ویژگی مهم از چهره انسان را با دقت قابل توجهی تخمین بزند. آزمایش‌های انجام شده نشانگر این است که روش پیشنهادی نسبت به روش‌های پیشرفتی اخیر در هر سه وظیفه در معیارهای رایج به دقت برتری دست یافته است. همچنین نشان داده شده است که یادگیری چند وظیفه‌ای قادر است با استفاده از داده‌های کمتر در یکی از ویژگی‌ها از سایر ویژگی‌های دارای داده‌های بیشتر بهره بگیرد تا دقت تشخیص را در آن ویژگی بالا ببرد. به منظور ارزیابی روش پیشنهادی از دو پایگاه داده IMDB-WIKI و GENKI-4K استفاده گردیده است.



A Numerical Study to Investigate Shear Behavior of High-strength Concrete Beams Externally Retrofitted with Carbon Fiber Reinforced Polymer Sheets

A. M. Jabbar^{*a}, D. H. Mohammed^b, Q. A. Hasan^b

^a Civil Engineering Department, College of Engineering, Wasit University, Iraq

^b Civil Engineering Department, University of Technology, Baghdad, Iraq

PAPER INFO

Paper history:

Received 27 July 2017

Received in revised form 03 August 2023

Accepted 06 August 2023

ABSTRACT

This paper aims to numerically investigate the structural behavior of reinforced high-strength concrete (HSC) beams retrofitted by Carbon Fiber Reinforced Polymer (CFRP) sheets after cracking. Six pre-cracked HSC beams retrofitted with CFRP sheets having identical reinforcement are numerically tested by four-point loading until failure using Abaqus software, besides two others without CFRP as control beams. CFRP sheets are attached on three beam sides in the shear span after cracking under 60 % of loading. Two shear span distances, two inclinations of CFRP sheets, and the number of sheets are adopted as parameters to compare with the experimental results obtained previously. Test results are matched with the practical findings to calibrate the Abaqus parameters. The results show that retrofitting the cracked beam by CFRP raised its tolerance to the applied load by a range of (13-36) % depending on the shear span to depth ratio and the arrangement of CFRP sheets. When the beam tends to fail in shear, the effect of CFRP is more pronounced than when it tends to fracture in flexure. The inclined sheets are more effective than the vertical ones. Furthermore, two additional parameters are regarded to clarify their effects on the behavior of retrofitted beams: sheet width and concrete compressive strength. Altering the CFRP width does not affect the tolerance, whereas increasing concrete compressive strength raises the beam loading.

doi: 10.5829/ije.2023.36.11b.15

1. INTRODUCTION

Several causes contribute to the necessity of retrofitting the existing facilities, such as strength loss due to corrosion, erosion, or deterioration caused by nature effects. Changing the use, expanding the facility, and upgrading the structure to resist higher loads also require correcting design or construction weaknesses [1, 2]. Retrofitting of facilities is a common practice; therefore, retrofitting approaches have been offered and evolved over years of practical and experimental work. The finding of the method used to retrofit a structural component relies on financial regard and the practicality of the assumed approach. However, choosing an inappropriate retrofitting manner can worsen the structure's function or even lastly causes failure [3].

Modern installations, like buildings, towers, and bridges, may deteriorate for different reasons. These installations are pricey to rebuild, and the construction time may cause trouble for many users. Therefore, it is significant to maintain enduring structures with long lifetimes and low maintenance costs. The most common manner for enhancing lifetime and durability is upgrading [4]. Establishments can be boosted to meet the changing demands or restored to an initial implementation status. The implementation status indicates load-carrying capacity, durability, operation, and aesthetic impression [5]. Retrofitting is usually complicated way because the structural components are already established. Therefore, it is not easy to reach the areas that require retrofitting [6]. Conventional approaches, including shotcrete, steel overlays, and post-

*Corresponding Author Email: [\(A. M. Jabbar\)](mailto:adilmahdi@uowasit.edu.iq)

tensioned cables, usually need broad space [7, 8]. Consequently, materials having higher strength and better application procedures than conventional ones should be most suitable for retrofitting and of high benefits in practice [9].

Recently, the most appropriate material used to retrofit and strengthen installations is Fiber Reinforced Polymer Composite (FRP) [10]. That material is a desirable rehabilitation substance due to its characteristics, like high strength-to-weight ratio and noncorrosive features that permit enhancing installation life [11]. Carbon FRP (CFRP) is a good strengthening fabric due to its distinguished tensile strength and stiffness compared to other composite substances [12, 13]. Externally bonded CFRP can use to repair and strengthen damaged structural elements. In such structures, the complete strengthening work takes a little while, which is faster than an alternative of replacing the beams with new ones [14]. The polymer matrix is applied to tie the fibers together, transfer the forces among the fibers and protect them from external effects. The shear strength erected between the fibers depends on the tie-matrix properties [4, 11, 15]. Therefore, it is significant that the matrix must have the ability to maintain higher strains than the fibers. If not, there will be cracks in the matrix before the fibers fail, and the fibers will be unprotected [14, 16].

This paper describes the potential and weakness of adding composite materials to retrofit cracked concrete beams. The prime aims are to investigate the impact of using CFRP sheets to rehabilitate cracked high-strength concrete beams on its shear behavior. The parameters include shear span-to-depth ratio (a/d), CFRP sheet number, and orientation.

2. EXPERIMENTAL DATA FOR SIMULATION OF RETROFITTED BEAMS

Practically performed RC beams were chosen to capture the required data to simulate the retrofitted beams for comparative study. Eight simple supported beams cast with high-strength concrete were performed by Al-Saeedi [17]. The beams were tested under a four-point load. All beams have an equal cross-section of (150x220) mm and a length of 1500 mm. The beams are designed according to ACI-318-19 [18] to avoid flexural failure using a 3-rebar of 20 mm diameter at the bottom and a 3-rebar of 12 mm diameter at the top so that shear is controlled, as shown in Figure 1. A concrete cover of 20 mm is applied for all sides of the beam cross-section. The tests were performed after curing in water for 28 days according to ASTM C31/C31 M-19 [19]. Three parameters were adopted in the experimental work. These are the shear span to depth ratio (a/d), CFRP sheet angle, and the number of CFRP sheets.

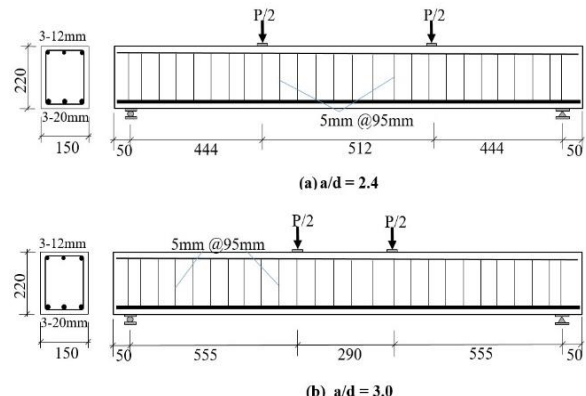


Figure 1. Details of beams' dimensions and reinforcement

The beams were categorized into two groups according to the a/d ratio. The first group had $a/d = 2.4$ while the second had a/d of 3.0. Each group consisted of four beams, the first beam (BA) without CFRP sheets is cast as a control beam, and the second (BRA1) had two CFRP sheets as a U-Shape on the beam sides and bottom at the mid-distance between the support and the nearby loading point with 90° configurations. A third beam (BRA2) had two CFRP sheets as U-Shape at the same place as the beam (BRA1) but with a 45° configuration. The fourth one (BRA3) had three CFRP sheets as U-Shape on the beam sides at the mid-distance between the support and the loading point with 45° configurations. The CFRP sheets had a 40 mm width and 0.131 mm thickness. Each group was represented with an a/d ratio [17]. Figure 2 illustrates the configuration of CFRP sheets on the beams.

2. 1. Materials and Mix Proportions Ordinary Portland cement (ASTM type I), natural fine aggregate with a 2.61 specific gravity, and natural crushed gravel with a maximum size of 10 mm and specific gravity of 2.58 were used for the mix. Silica fume of 91 % silicon dioxide with a surface area of 20000 m^2/kg is added as a cementitious material. Glenium 54, as a high-range water reducer (HRWR), is used as a percentage of cement weight to modify the workability of the mixture at a slump of 100 mm. The w/c ratio is constant at 0.28 [17]. Mix proportions and mechanical properties of concrete are listed in Table 1.

SikaWarp-300 C/60 woven carbon fiber fabric for concrete strengthening is used for retrofitting the beams experimentally. The CFRP does not exhibit plastic behavior before rupture, where the tensile stress-strain relationship is linear until failure. Therefore, CFRP failure is sudden and catastrophic. The tensile strength of carbon fiber is 3900 MPa, the elastic modulus is 230 GPa, and the elongation percentage at rupture is 1.5 %. Sikadur-330 epoxy glue is used as a bonding material for CFRP sheets. It has 30 MPa tensile strength and 4500

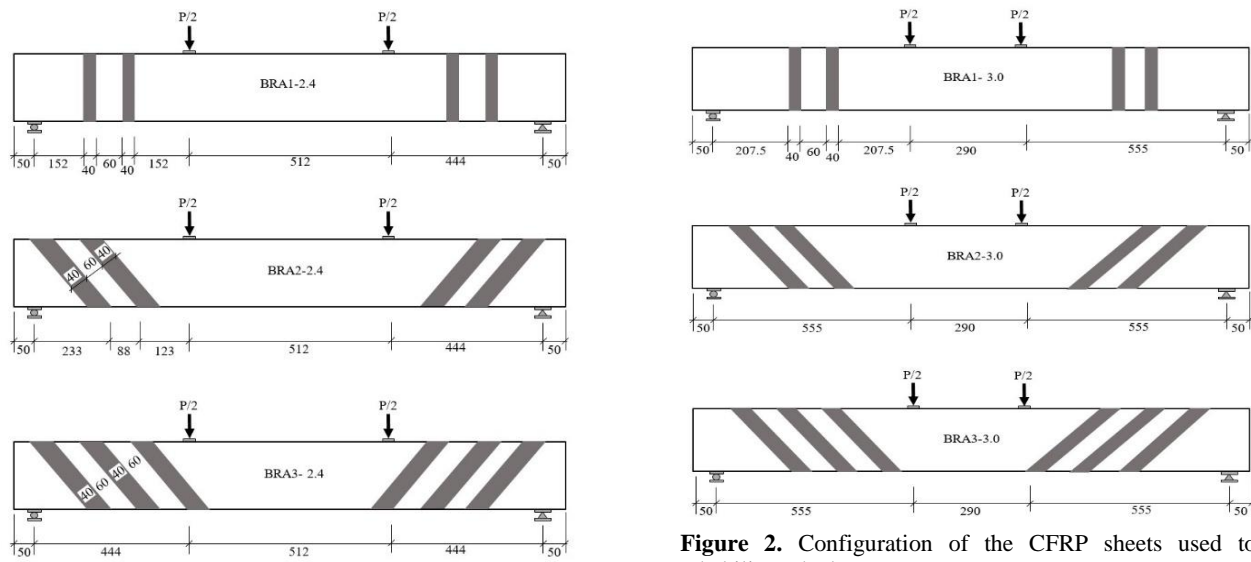


Figure 2. Configuration of the CFRP sheets used to rehabilitate the beams

TABLE 1. Mix proportioning and concrete strength

Mix Proportion						
Material	Cement (kg/m^3)	Silica fume (kg/m^3)	Sand (kg/m^3)	Crushed gravel (kg/m^3)	w/cm	HRWR (% of cement)
Quantity	450	50	750	1000	0.28	2.8
Concrete Mechanical Properties						
f'_c 7-day		f'_c 28-day		$f_{spt.}$, MPa	E_c , MPa	
65		72.5		6.0	41770	

MPa elastic modulus in tension. Three rebar diameters are used for reinforcing the beams, as shown in Figure 1. Table 2 lists the mechanical properties of steel rebars.

All beams were tested before retrofitting under four-point loading in the first test stage without any strengthening or retrofitting with CFRP to reach the specified damage. The beams arrived at the degree of the damaged ratio at 60% of the ultimate load of the control beam. Then, the beams were retrofitted using CFRP sheets [17].

3. EXPERIMENTAL RESULTS

Concrete cylinders of (150 x 300) mm were cast from the same concrete batch used for casting the beams as control

specimens and tested at the same age as the beam test. Three cylinders were cast with each beam and the average value was considered. The average compressive strength was 72.5 MPa and the splitting tensile strength was 6.0 MPa, as illustrated in Table 1.

At initial loading, all beams elastically behaved up to about 20 % of ultimate load when first cracking appeared with proportional deflection. The first crack occurred in the tension zone at the lower portion between loading points. Then, flexural cracks vertically propagated to a short distance due to increasing tensile stresses. However, the elastic behavior continued, even after the initiation of flexural cracks, up to a load of approximately 40% of the ultimate loading. The stresses resulting from the imposed load on the beam were transmitted initially to the tensile region. When the steel rebars contributed to bearing stresses, they were redistributed to the shear zone. Shear cracks propagated diagonally between supports and the adjacent loading point. The first diagonal crack was observed at the loading level (40-52) % of the ultimate load, as shown in Figure 3. Upon increasing the loading, shear cracks expanded and extended down towards the support and up to the point load.

TABLE 2. Mechanical properties of steel rebars

Nominal rebar diameter, mm	Yield stress, MPa	Tensile strength, MPa	Elongation
20	450	667	0.00229
12	520	611	0.00263
5	480	590	0.00243

All beams were preloaded to 60 % of the ultimate load, except the control one, in which the loading continued to fail. The others were rehabilitated using the CFRP sheets. The test results are listed in Table 3.

4. NUMERICAL ANALYSIS OF THE BEAMS

Despite the symmetry, the beams are simulated with their entire dimensions. Abaqus CAE is used for the Finite Element Analysis (FEA) of beams. The analysis was performed in two static general steps by displacement control method.

4. 1. Numerical Simulation of Beams The beam components simulated in Abaqus consist of concrete, steel rebars, CFRP sheets, and steel plates for supporting and loading the beam. The concrete beam and steel plates are discretized into C3D8R as homogenous solid elements. C3D8R is a 3-dimensional continuum element that has 8 nodes as a brick element where each node has 3 degrees of freedom in the three directions with reduced

integration upon iteration process to calculate the stiffness matrix for each load increment [20, 21].

The rebars are discretized by the T3D2 truss element that has 2 nodes with 3 degrees of freedom per node. The CFRP sheets are discretized as a composite layup shell of the S4R element, which is a 4-node doubly curved thin shell with reduced integration [22].

The steel plates are considered rigid bodies to transfer the loading to the beam without distortion. The steel rebars are assigned as embedded regions inside the host region of the concrete beam. The CFRP sheets are constrained as a tie between two surfaces, the master surface is the concrete beam, and the slave one is the sheet [22-24]. The interaction between steel plates and the concrete beam is a surface-to-surface contact type with two properties; tangential behavior with a friction coefficient of 0.45 and normal behavior of hard contact with no penetration between the adjacent surfaces. The boundary conditions are created at the initial step. The lower supporting plate is designated as fixed boundary conditions, which are assumed for the supporting plates by preventing the translations and rotations in all directions.

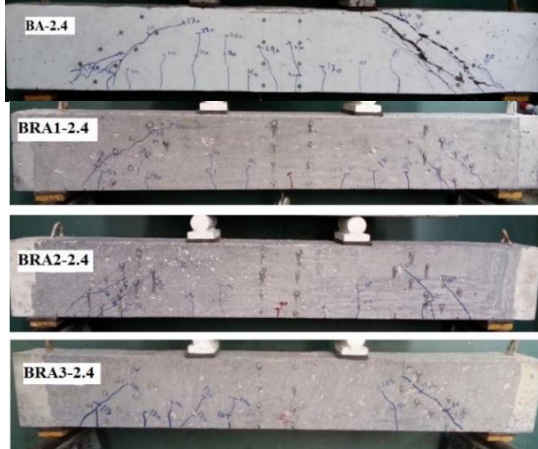


Figure 3. Cracking of the experimental beams at the first stage of loading before retrofitting [17]

TABLE 3. Test results of the beams [17]

Beam ID	CFRP sheet	a/d	Cracking State		Peak State		Failure Mode
			Pcr	Acr	Pu	Au	
BA-2.4	--	2.4	55	0.92	260	13.35	Diagonal shear
BRA1-2.4	2 at 90	2.4	53	0.71	310	14.25	Diagonal shear and debonding CFRP
BRA2-2.4	2 at 45	2.4	50	0.75	335	13.05	Debonding CFRP sheets
BRA3-2.4	3 at 45	2.4	58	0.63	375	13.58	Compression failure + debonding CFRP
BB-3.0	--	3.0	38	0.90	225	12.15	Diagonal shear
BRB1-3.0	2 at 90	3.0	42	0.85	260	12.53	Diagonal shear and debonding CFRP
BRB2-3.0	2 at 45	3.0	47	0.94	275	12.90	Debonding CFRP sheets
BRB3-3.0	3 at 45	3.0	48	0.95	317	13.20	Compression failure + debonding CFRP

A download vertical displacement is applied on upper steel plates to simulate the loading in a displacement control method in two loading steps. The first loading was up to 60 % of the ultimate load of the control beam. The other loading step was to complete the loading on the beam. All beam components are seeded into 20 mm mesh size, as shown in Figure 4.

4. 2. Concrete, Steel Rebar, and CFRP Sheet

Modelling

Modelling The compressive strength used to simulate the concrete in the beam is 72.5 MPa, and the cracking stress is assumed to be 40 % of compressive strength as the experimentally obtained value. Therefore, the concrete is numerically simulated by two behaviors as is required in Abaqus; linear behavior by the elastic modulus and Poisson's ratio. The plastic behavior is described in two stages; strain hardening to the concrete strength and strain softening after peak strength. The Concrete Damage Plasticity (CDP) model is adopted to define the plastic behavior of concrete after cracking [25, 26]. The compressive stress-strain relationship of the concrete is formulated using Hognestad equation as described in Equation (1) below, which awards a reasonable approach to the experimental results;

$$\sigma_c = 2f'_c \left[\frac{\varepsilon_c}{\varepsilon_{co}} - \left(\frac{\varepsilon_c}{\varepsilon_{co}} \right)^2 \right] \quad (1)$$

where: σ_c is the concrete compressive stress at the

corresponding strain (ε_c) in MPa, ε_c is the concrete strain at compression, and ε_{co} is the strain at compressive strength. The modulus of elasticity and inelastic strain are formulated using Euro code2-2004 [27] approach as illustrated in the following equations:

$$E_c = 3320\sqrt{f'_c} + 6900 \quad (2)$$

$$\varepsilon_{pl.} = \varepsilon_c - \frac{\sigma_c}{E_c} \quad (3)$$

E_c is the elastic modulus of concrete in MPa. ε_{pl} is the plastic strain. The damage parameter (dc) in compression is defined as follows;

$$d_c = 1 - \frac{\sigma_c}{f'_c} \quad (4)$$

The five parameters required to define the failure surface of the elements, including eccentricity, biaxial to uniaxial stress, and the shape of failure, were set as default values regarded in Abaqus. However, the dilation angle and viscosity were calibrated to obtain the maximum loading of the beams recorded in the experimental works, as illustrated in Table 4 [28]. These five parameters present concrete cracking in Abaqus. The rebar stress-strain relationship was represented by elastic-perfect plastic behavior. Table 4 illustrates the mechanical properties and parameters of concrete and steel rebars used to simulate the beams in Abaqus [29].

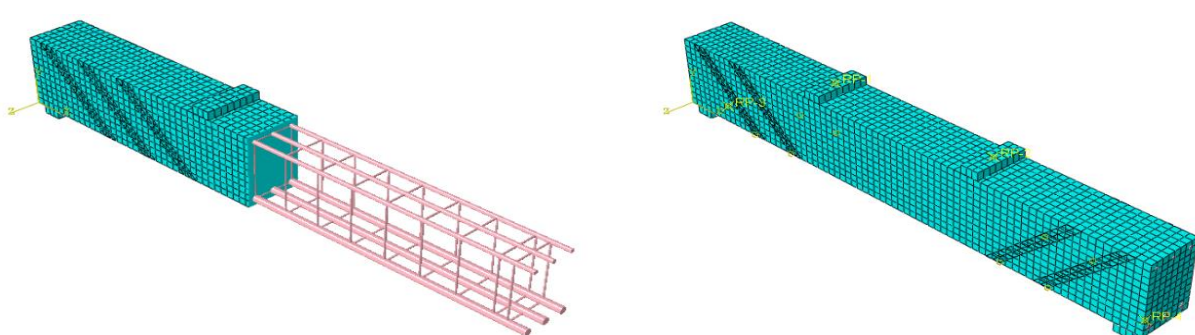


Figure 4. Simulation of concrete beams via Abaqus software

TABLE 4. The properties of materials used to simulate the retrofitted beams

Material	Properties				
concrete	Elastic modulus, Ec		35168.78 MPa		Poisson ratio
	Compressive strength		72.5 MPa		Tensile strength
	Dilation angle, ψ	Eccentricity, ϵ	biaxial to uniaxial stress ratio, fbo/fco	Shape Parameter, K	viscosity parameter, μ
	45	0.1	1.16	0.677	0.02
Steel rebars	Diameter = 20 mm			Diameter = 12 mm	
	Es	Yield stress	Poisson's ratio	Es	Yield stress
	200 GPa	450 MPa	0.3	200 GPa	520 MPa
				0.3	200 GPa
				480 MPa	0.3

The CFRP sheets are simulated in elastic and plastic status. Lamina type is used for elastic behavior, and Hashin Damage is used for plastic behavior to define the damage features of fiber-reinforced composites [30]. The calibrated data depends on the experimental values provided by the manufacturer. The mechanical properties of the CFRP sheets are listed in Table 5.

Where E1 and E2 are the elastic modulus in the x and y-directions, μ_{12} is the Poisson's ratio in the xy-plane, G12, G13, and G23 are the shear modulus in xy, xz, and yz-directions [25, 31].

4.3. FEA Results of the Beams The analysis results of all beams are illustrated in Table 6. The cracking load was approximately equal for all beams in each group. At a/d of 2.4, the cracking load was about 58 kN, while at a/d of 3.0, it was about 45 kN. At the cracking state, the experimental results recorded a lower load than the finite element results by a range of (85-99) % for a/d = 2.4. For a/d = 3.0, the variation between experimental and FE loads ranges between (85-106) %, as shown in Table 6.

These variations may be due to several reasons, such as the micro-cracks normally occurring in concrete due to shrinkage, handling the beams for testing, and environmental effects. However, concrete simulation in FE does not contain such micro cracks. Other reasons relate to the materials' definition in the Abaqus, which depends on the stress-strain relationship at the cracking state.

At the ultimate state and for a/d = 2.4, the variation in load occurred due to the impact of CFRP sheets and their orientations. The increment in ultimate load was 17 %, 23 %, and 36 % upon using 2 CFRP sheets at 90, 2 CFRP sheets at 45, and 3 CFRP sheets at 45, respectively, over the control beam maximum load. For a/d = 3.0, the increment in the ultimate load was 13 %, 19 %, and 35 % upon using 2 sheets of CFRP at 90, 2 CFRP sheets at 45, and 3 CFRP sheets at 45, respectively, over the control beam maximum load, as illustrated in Figure 5. Based on the findings of this study, it appears that utilizing 3-CFRP sheets in rehabilitation efforts yields the highest increase in loading capacity. This information could be valuable

TABLE 5. Mechanical properties of the CFRP sheets used in Abaqus

	E1, MPa	E2, MPa	μ_{12}	G12, MPa	G13, MPa	G23, MPa
Elastic	131900	9510	0.326	5270	7030	3390
Type				Hashin Damage		
Long. tensile strength	Long. compressive strength	Transverse tensile strength	Transverse compressive strength	Long. shear strength	Transverse shear strength	
1328 MPa	1064 MPa	70.9 MPa	221 MPa	71.2 MPa	94.5 MPa	
Plastic	Damage Evolution		Type	Energy	Softening	Linear
	Longitudinal tensile fracture energy	Longitudinal compressive fracture energy		Transverse tensile fracture energy	Transverse compressive fracture energy	
	0.33 mJ/mm ²	0.33 mJ/mm ²		2.00 mJ/mm ²	2.00 mJ/mm ²	

TABLE 6. Results of FEA for the beams

Beam ID	CFRP sheet	a/d	Cracking State						Peak State					
			Exp.		FEA		Per (Exp/FEA)	Δc_r (Exp/FEA)	Exp.		FEA		Pu (Exp/FEA)	Δu (Exp/FEA)
			Per, kN	Δc_r , mm	Pcr, kN	Δc_r , mm			Pu, kN	Δu , mm	Pu, kN	Δu , mm		
BA-2.4	-	2.4	55	0.92	57.7	0.74	0.95	1.24	260	13.35	272.8	13.25	0.95	1.01
BRA1-2.4	2 at 90	2.4	53	0.71	58.4	0.74	0.91	0.96	310	14.25	319.6	15.78	0.97	0.90
BRA2-2.4	2 at 45	2.4	50	0.75	58.5	0.74	0.85	1.01	335	13.05	334.9	16.41	1.00	0.80
BRA3-2.4	3 at 45	2.4	58	0.63	58.8	0.74	0.99	0.85	375	13.58	370.7	17.81	1.01	0.76
BB-3.0	-	3.0	38	0.90	44.8	0.66	0.85	1.36	225	12.15	223.4	11.54	1.01	1.05
BRB1-3.0	2 at 90	3.0	42	0.85	44.9	0.66	0.94	1.29	260	12.53	252.1	14.01	1.03	0.89
BRB2-3.0	2 at 45	3.0	47	0.94	44.9	0.67	1.05	1.40	275	12.90	265.8	14.82	1.03	0.87
BRB3-3.0	3 at 45	3.0	48	0.95	45.2	0.66	1.06	1.44	317	13.20	301.1	18.23	1.05	0.72

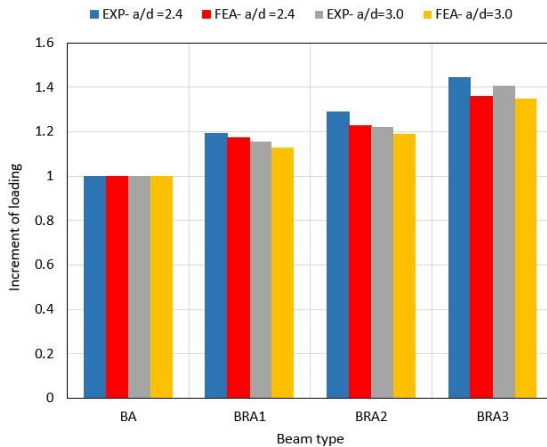


Figure 5. Increment in loading due to adding CFRP sheets

for those looking to improve the strength and durability of structures or materials. For $a/d = 2.4$, the beam tends to fail in shear. Therefore, the action of CFRP sheets in enhancing the shear capacity of the beam was more pronounced than that of $a/d = 3.0$. When the stresses are redistributed to the shear span on both sides of the beam, and this case occurs faster when a/d is 2.4, the effect of the CFRP sheets appears more clearly in enhancing the shear resistance. In the case of a/d is 3.0, the stresses transmitted to the shear span are less. That means the stress redistribution is between the tension area below the mid-span of the beam and the shear span. Then the effect of CFRP sheets is less because they resist the shear and do not resist the tensile due to their absence in the tension zone. Therefore, the beam tends to fail in flexure in the case of a/d is 3.0.

Generally, the use of inclined CFRP sheets is more effective than perpendicular ones in terms of loading and specifically for shear in beams. That could be interrupted as the CFRP sheets are perpendicular to the path of the inclined cracks of shear, which hinder the progression of cracks.

4. 4. Beams' Deflection Results The cracking deflection of FEA was equal for all beams in the case of $a/d=2.4$ and 3.0, as shown in Table 6. On the other hand, the ratio of experiment to FEA deflection at the cracking state ranges between (0.84-1.24) for $a/d = 2.4$, while for $a/d = 3.0$, the experimental cracking deflection was higher than the FE one. That may be due to the constraint provided by FE simulation.

At the ultimate state, the ratio between the experimental to FEA deflection ranges between (0.81-1.05). Generally, the increment in deflection recorded in the case of $a/d=3.0$ is higher than that of $a/d = 2.4$. The action of CFRP sheets on deflection occurred after the cracking state. For $a/d=2.4$, the three inclined CFRP sheets increased deflection by 27 % over that of the

control beam, while for $a/d = 3.0$, the three inclined CFRP sheets raised the deflection by 41 %. The increment in deflection upon using 2/90 and 2/ 45 CFRP sheets was 19% and 24% at $a/d = 2.0$, and 21%, 28%, at $a/d = 3.0$, as shown in Figure 6.

The increment in deflection for $a/d=3.0$ is more than that for $a/d=2.4$. That is because the beam with $a/d = 3.0$ tends to fail in flexural, while the one with $a/d = 2.4$ tends to fail on shear. The distribution of stresses in the first case is partially focused on a flexural zone, while the stresses are redistributed to the shear span in the second case.

Figures 7 and 8 show the load-deflection relationship of the beams. The behavior of beams was similar in both groups up to about 100 kN load, which is greater than the cracking load of 58 kN for $a/d=2.4$ and 45 kN for $a/d = 3.0$. This behavior is consistent with what was recorded in the experimental behavior of the beams. Then the behavior altered according to the number and configuration of CFRP sheets. Since all rehabilitated beams were manufactured with the same concrete and

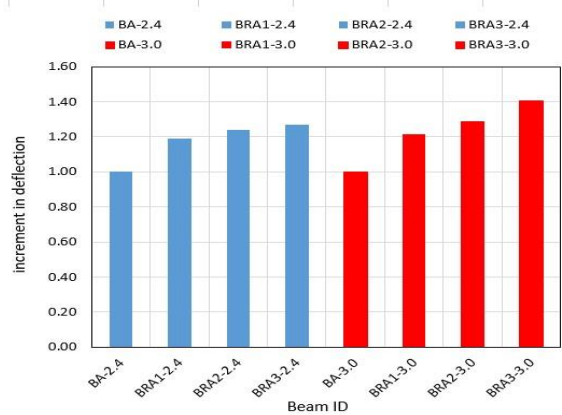


Figure 6. The percentage of deflection variation for all beams

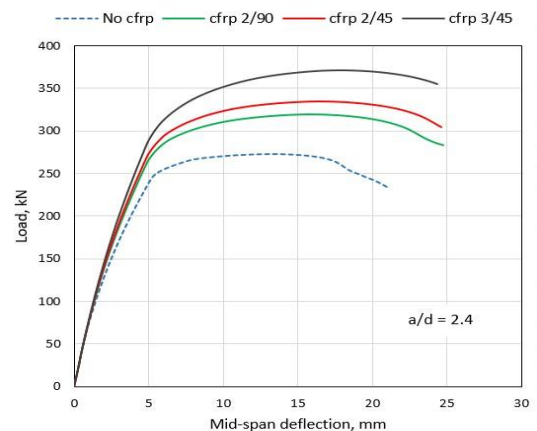


Figure 7. Load-deflection of beams with $a/d=2.4$

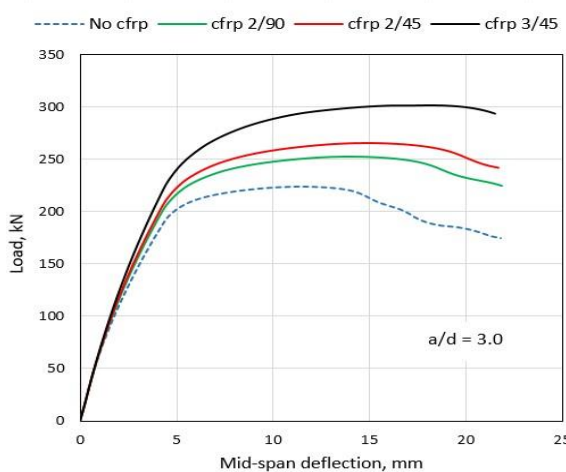


Figure 8. Load-deflection of beams with $a/d = 3.0$

similar reinforcement, the variation in the behavior and ultimate loads depends on the CFRP sheets.

On the other hand, all beams did not exhibit high ductility after peak load. That could be because the behavior of CFRP is linear to failure.

4.5. Impact of a/d Ratio on Beam Behavior When a/d decreases, the tolerance of the beam to the applied loads improves. The load capacity of the control beam increases by 22 % upon reducing a/d from 3.0 to 2.4. In the case of retrofitted beams by CFRP, the beam tolerance increases by (23-27) % at $a/d = 2.4$. This behavior is because the beam bears more shear loads, and the presence of CFRP helps it increases endurance.

4.6. Steel Rebar Stresses In all beams with $a/d = 2.4$ and 3.0, the longitudinal rebars in the tension and compression zone have yielded at the peak load, as illustrated in Figure 9. That means the beam failed due to the yielding of the tensile rebars before the fracturing of concrete in compression zone because the CFRP sheets enhanced the shear resistance of the beam and that increases the stress in the flexural region.

On the other hand, the vertical stirrups do not yield along the shear spans between the supports and adjacent loading points. However, in beams with 2 CFRP at 45, 2 CFRP at 90, and 3 CFRP at 45 with $a/d = 3.0$, the mid-span stirrup yield at the upper portion near the compression zone. That is due to the fracturing of the concrete at the compression region after reaching the ultimate concrete strain, as shown in Figure 10.

4.7. Crack Pattern For all beams that were retrofitted by CFRP sheets with $a/d = 2.4$ and 3.0, the failure was due to diagonal shear cracking and debonding the CFRP sheets except for the one with 3 CFRP sheets at 45 and $a/d = 3.0$, where they failed due to concrete

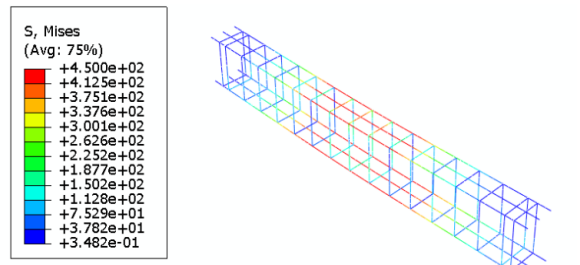


Figure 9. Stress distribution in steel rebars at the ultimate load

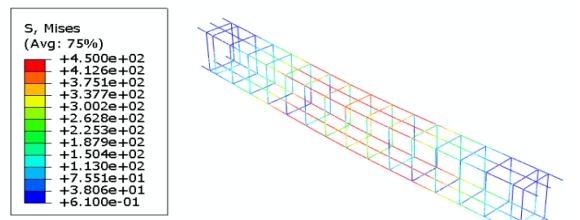


Figure 10. Yielding of the middle stirrup in beams BRA1-3.0, BRA2-3.0, and BRA3-3.0

compression fracture, as shown in Figure 11. That indicates that the number of inclined CFRP affects changing the behavior of the beam and its failure pattern. That behavior is consistent with experimental failures as mentioned in Table 3.

Generally, the CFRP sheets attached to the shear spans of the beam enhance the beam load capacity in shear and may alter the failure from diagonal shear to concrete compression fracture. Figure 11 illustrates the cracking pattern that occurs in the analyzed beams compared to the experimental cracking of the counterpart beams, in which the agreement of the type of failure is observed in the experimental beams and the ones simulated by Abaqus.

5. PARAMETRIC STUDY

5.1. Effect of Variation of CFRP Sheet Width The first parameter considered was changing the CFRP sheet width. Two additional widths were examined to show their effect on beam behavior. The width changed to 80 mm and 120 mm, and they were placed in the same positions on the sides and bottom of the beam as in the case of 40 mm wide CFRP. However, changing the CFRP width did not affect the beam maximum loading and the corresponding deflection, as shown in Figure 12.

5.2. Effect of Altering Concrete Compressive Strength Undoubtedly, changing the concrete strength affects the beam behavior; but how is the effect in the case of retrofitted beams?

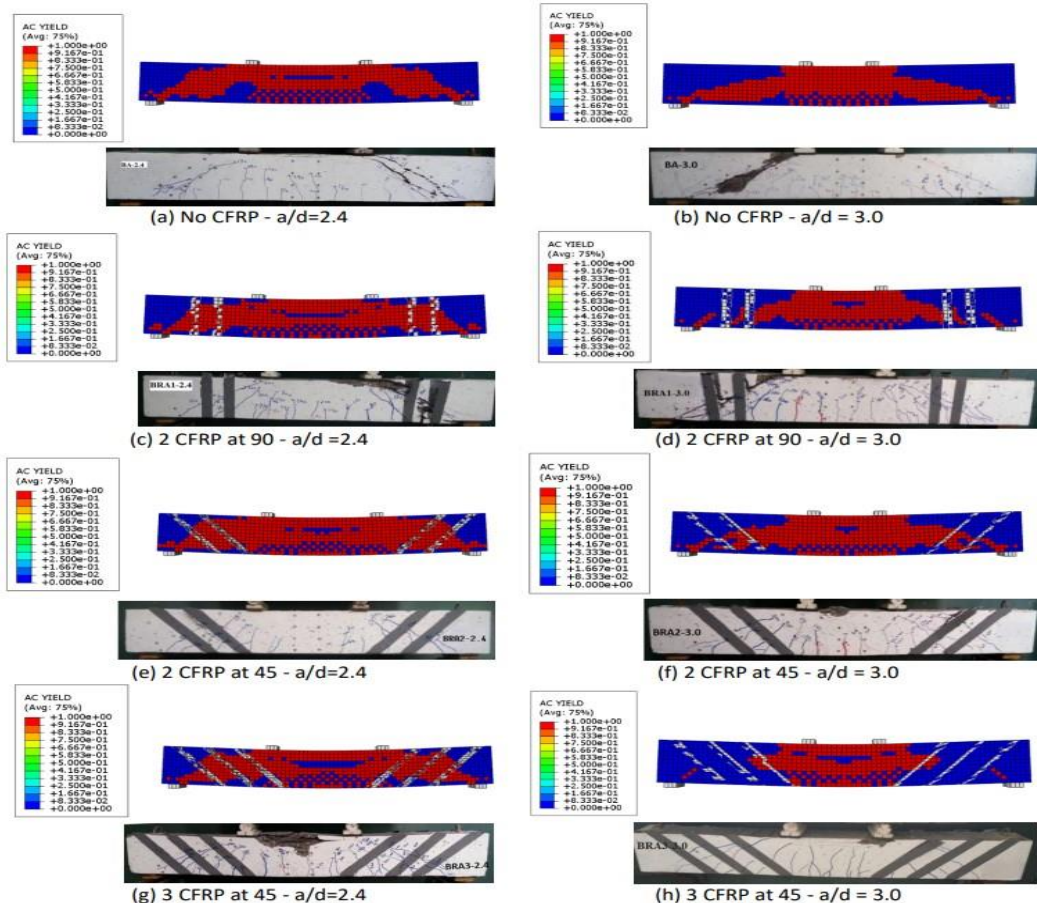


Figure 11. A cracking pattern of the beams in experiments and in FEA

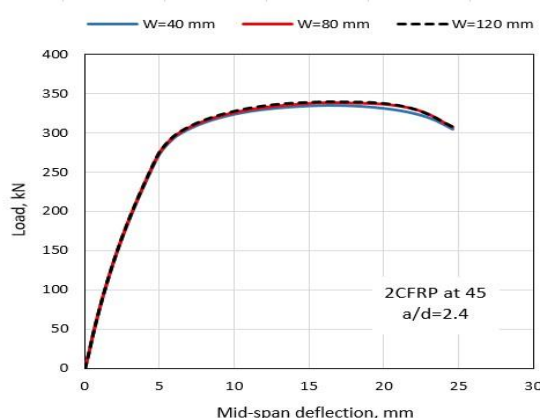


Figure 12. Load-deflection relationship in case of changing CFRP width

Therefore, the second parameter adopted is changing concrete compressive strength. Three compressive strengths are examined, and the results are shown in Table 7.

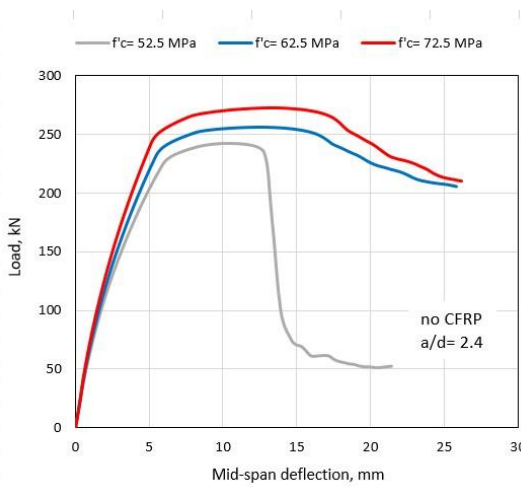
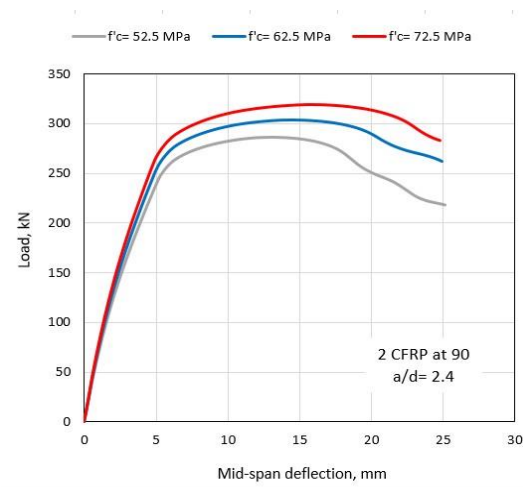
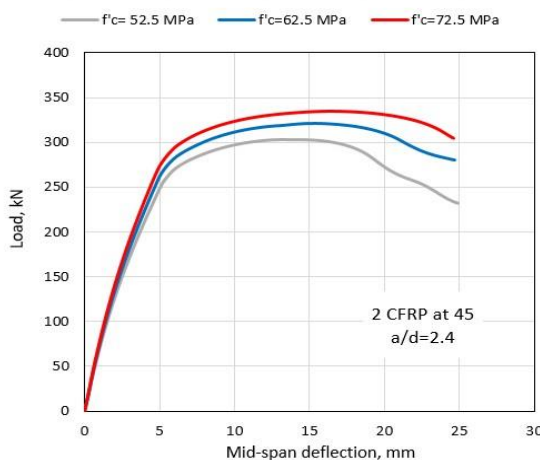
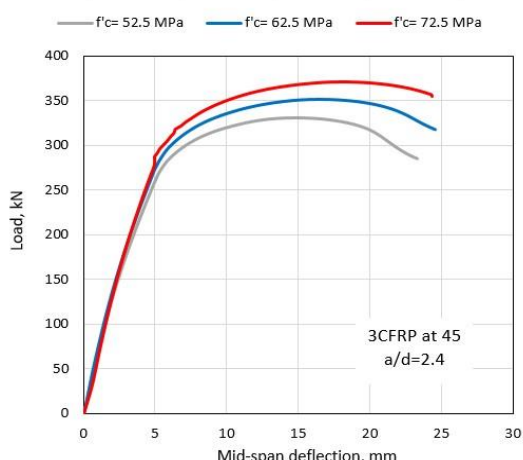
Upon decreasing concrete compressive strength, the maximum loading that withstands by the beam decreases. The deflection also decreases with decreasing compressive strength. Reducing the concrete compressive strength by 10 MPa and 20 MPa from 72.5 MPa decreases the beam loading tolerance by about (4-6) % and (10-12) % at both cracking and ultimate states, respectively. However, the failure pattern does not change.

The effect of compressive strength and the accompanying change in the tensile strength is on resisting the stresses transmitted through the beam section along its length and reaching the maximum stress the beam can bear. Therefore, lowering the compressive strength causes a lowering of the maximum stress that the beam can withstand.

Figures 13-16 show the load-deflection relationships for the control and rehabilitated beams with CFRP sheets at a/d of 2.4 and 3.0. Adding CFRP sheets to retrofit the beams can slightly enhance the ductility of the beams, but to a specific limit due to the linear behavior of CFRP until failure.

TABLE 7. Effect of variation of concrete compressive strength on retrofitted beams

Beam ID	f'c = 52.5 MPa			f'c = 62.5 MPa			f'c = 72.5 MPa					
	Pcr, kN	Δcr, mm	Pu, kN	Δu, mm	Pcr, kN	Δcr, mm	Pu, kN	Δu, mm	Pcr, kN	Δcr, mm	Pu, kN	Δu, mm
BA-2.4	50.9	0.74	242.3	10.30	55.4	0.74	256.5	12.65	57.7	0.74	272.8	13.25
BRA1-2.4	52.5	0.74	286.7	13.10	55.6	0.74	303.5	14.48	58.4	0.74	319.6	15.78
BRA2-2.4	52.8	0.74	302.6	13.24	55.8	0.74	321.8	15.27	58.5	0.74	334.9	16.41
BRA3-2.4	53.1	0.74	330.6	14.86	56.1	0.74	351.5	16.45	58.8	0.74	370.7	17.81

**Figure 13.** Load-deflection relationship of beams without CFRP**Figure 14.** Load-deflection relationship of beams with vertical CFRP**Figure 15.** Load-deflection relationship of beams with two inclined CFRP at 45°**Figure 16.** Load-deflection relationship of beams with three inclined CFRP at 45°

6. CONCLUSIONS

This paper introduces a numerical investigation of using CFRP sheets to retrofit high-strength concrete beams after exposure to preload of 60 % of the ultimate resisting load. Three configurations of CFRP sheets and two a/d ratios are adopted to show their effects on the beam

behavior. The FE results were compared and matched with the results of a previously implemented work. Two further parameters are tested. These are the CFRP sheet's width and concrete compressive strength. The following conclusions can reach:

Using CFRP sheets to retrofit cracked beams raises the ultimate load that the beam can bear. The increment

in peak load depends on the number and configuration of the attached CFRP sheets. Upon using 2 vertical sheets, 2-inclined at 45, and 3- inclined at 45 sheets, they can raise the ultimate load by (13-17) %, (19-23) %, and (35-36) %, respectively, for a/d of 2.4 and 3.0.

For a/d of 2.4, the impact of CFRP on shear resistance is more pronounced than for a/d of 3.0. When a/d increases, the loading capacity of the beam decreases by a range od (18-23) %. Also, the inclined sheets are more effective than the perpendicular ones.

The deflection corresponding to maximum loading increases according to CFRP sheets numbers and orientation. The increment ranges between (16-25) % for a/d of 2.4 and between (18-37) % for a/d of 3.0.

The failure of retrofitted beams was due to the yielding of longitudinal rebars, while the shear rebars did not yield.

Altering CFRP sheet width did not affect the beam tolerance for the applied load. However, increasing concrete compressive strength increases the beam tolerance for loading. Increasing the compressive strength by 10 MPa and 20 MPa raises beam capacity for loading by (4-6) % and (10-12) % at cracking and ultimate states, respectively.

7. REFERENCES

1. Gemert, D., "Design applications and durability of plate bonding technique", in Proceedings of the International Conference on Concrete Repair, Rehabilitation and Protection, Scotland. London: Chapman & Hall. (1996), 559-569.
2. Abbas, S., Ali, I. and Abdulridha, A., "Behavior and strength of steel fiber reinforced self-compacting concrete columns wrapped by carbon fiber reinforced polymers strips", *International Journal of Engineering, Transactions B: Applications*, Vol. 34, No. 2, (2021), 382-392. doi: 10.5829/IJE.2021.34.02B.10.
3. Täljsten, B., "Strengthening of existing concrete structures by epoxy bonded steel plates of steel or fibre reinforced plastics", in International Conference Radical Concrete Technology: 24/06/1996-28/06/1996, Taylor and Francis Group. (1996), 623-632.
4. Faez, A., Sayari, A. and Manei, S., "Retrofitting of rc beams using reinforced self-compacting concrete jackets containing aluminum oxide nanoparticles", *International Journal of Engineering, Transactions B: Applications*, Vol. 34, No. 5, (2021), 1195-1212. doi: 10.5829/ije.2021.34.05b.13.
5. Osman, B.H., Wu, E., Ji, B. and Abdulhameed, S.S., "Repair of pre-cracked reinforced concrete (RC) beams with openings strengthened using frp sheets under sustained load", *International Journal of Concrete Structures and Materials*, Vol. 11, (2017), 171-183. doi: 10.1007/s40069-016-0182-3.
6. Rahimi, S.B., Jalali, A., Mirhoseini, S.M. and Zeighami, E., "Experimental comparison of different types of frp wrapping in repairing of rc deep beams with circular openings", *International Journal of Engineering, Transactions B: Applications*, Vol. 34, No. 8, (2021), 1961-1973. doi: 10.5829/ije.2021.34.08b.17.
7. Miller, M. and Frye, M., "Scc proves successful in repair and strengthening projects", *Concrete Construction Website*, (2009).
8. Daniel, I.M., Ishai, O., Daniel, I.M. and Daniel, I., "Engineering mechanics of composite materials, Oxford university press New York, Vol. 1994, (2006).
9. Soudki, K. and Alkhrdaji, T., "Guide for the design and construction of externally bonded frp systems for strengthening concrete structures (aci 440.2 r-02)", in Structures Congress 2005: Metropolis and Beyond. (2005), 1-8.
10. Haj Seiyed Taghia, S.A., Darvishvand, H.R. and Pourhasan, M., "An economic approach to the confinement of different concrete classes with carbon and glass fibers reinforced polymers", *International Journal of Engineering, Transactions A: Basics*, Vol. 36, No. 4, (2023), 776-787. doi: 10.5829/ije.2023.36.04a.14.
11. Osman, B.H., Wu, E., Ji, B. and S Abdelgader, A.M., "A state of the art review on reinforced concrete beams with openings retrofitted with frp", *International Journal of Advanced Structural Engineering*, Vol. 8, (2016), 253-267. doi: 10.1007/s40091-016-0128-7.
12. Ali, A., Abdalla, J., Hawileh, R. and Galal, K., "Cfrp mechanical anchorage for externally strengthened rc beams under flexure", *Physics Procedia*, Vol. 55, (2014), 10-16. doi: 10.1016/j.phpro.2014.07.002.
13. Hafiz, T., "Life prediction of carbon fiber reinforced polymers using time temperature shift factor", *International Journal of Engineering, Transactions A: Basics*, Vol. 33, No. 7, (2020), 1340-1346. doi: 10.5829/ije.2020.33.07a.21.
14. Mhanna, H.H., Hawileh, R.A. and Abdalla, J.A., "Shear strengthening of reinforced concrete beams using cfrp wraps", *Procedia Structural Integrity*, Vol. 17, (2019), 214-221. doi: 10.1016/j.prostr.2019.08.029.
15. Mohsenzadeh, S., Maleki, A. and Lotfollahi-Yaghin, M., "Strengthening of rc beams using scc jacket consisting of glass fiber and fiber-silica fume composite gel", *International Journal of Engineering, Transactions B: Applications*, Vol. 34, No. 8, (2021), 1923-1939. doi: 10.5829/ije.2021.34.08b.14.
16. Kaw, A.K., "Mechanics of composite materials, CRC press, (2005).
17. AlSaeedi, A., "Shear retrofitting of reinforced high strength concrete beams using cfrp", MSc Thesis, Civil Engineering Department, University of Technology, Iraq: 172, (2017),
18. Committee, A., "Building code requirements for structural concrete (aci 318-08) and commentary, American Concrete Institute. (2008).
19. Standard, A., C31/c31m, 2010, "standard practice for making and curing concrete test specimens in the field," astm international, west conshohocken, pa, 2010, doi: 10.1520/c0031_c0031m.
20. Pawar, A.J., Patel, M. and Suryawanshi, S., "Finite element modelling of laboratory tests on reinforced concrete beams containing recycled aggregate concrete", *International Journal of Engineering, Transactions B: Applications*, Vol. 36, No. 5, (2023), 991-999. doi: 10.5829/ije.2023.36.05b.15.
21. Inc, A., "Abaqus version 6.10-1 analysis user's manual", *Dassault Systèmes Simulia Corp*, Vol. 3, (2017), 1-10. doi.
22. Abulqasim, S.A., Noori, A.Q.N. and Çelik, T., "Numerical investigation on flexural behavior of rc beams with large web opening externally strengthened with cfrp laminates under cyclic load: Three-point bending test", (2022). doi: 10.5937/jaes0-32985.
23. Paul, S.K. and Sahu, P., "Finite element analysis of retrofitting of rc beam with cfrp using abaqus", *International Research Journal of Engineering and Technology (IRJET)*, Vol. 7, No., (2020), 1268-1273.
24. Aljazaeri, Z. and Al-Jaberi, Z., "Numerical study on flexural behavior of concrete beams strengthened with fiber reinforced cementitious matrix considering different concrete compressive strength and steel reinforcement ratio", *International Journal of Engineering*, Vol. 34, No. 4, (2021), 793-802. doi: 10.5829/ije.2021.34.04a.05.
25. Zhang, D., Wang, Q. and Dong, J., "Simulation study on cfrp strengthened reinforced concrete beam under four-point

- bending", *Computers and Concrete*, Vol. 17, No. 3, (2016), 407-421. doi: 10.12989/cac.2016.17.3.407.

26. Ibrahim, S.K. and Rad, M.M., "Numerical plastic analysis of non-prismatic reinforced concrete beams strengthened by carbon fiber reinforced polymers", in Proceedings of the 13th fib International PhD Symposium in Civil Engineering, Marne-la-Vallée, Paris, France. (2020), 26-28.

27. Beckett, D. and Alexandrou, A., "Introduction to eurocode 2: Design of concrete structures (including seismic actions)", New York, (1997).

28. Mahdi, A.M., "Impact of failure-surface parameters of concrete damage plasticity model on the behavior of reinforced ultra-high performance concrete beams", *Periodica Polytechnica Civil Engineering*, Vol. 67, No. 2, (2023), 495-504. doi: 10.3311/PPci.21345.

29. Jabbar, A.M., Danha, L.S. and Hasan, Q.A., "Numerical simulation of ultra-high-performance concrete's compressive and tensile behaviour in beams", *Journal of Applied Engineering Science*, Vol. 21, No. 2, (2023), 532-546. doi: 10.5937/jaes0-40769.

30. Systèmes, D., "Getting started with abaqus: Interactive edition 6.12", *Getting Started with Abaqus: Interactive Edition*, Vol., (2012), 4.50-54.54. http://www.maths.cam.ac.uk/computing/software/abaqus_docs/docs/v6.12/pdf_books/GET_STARTED.pdf

31. Kumar, N.M., Sameer, S. and Divya, K., "Numerical simulations of composite materials", in IOP Conference Series: Earth and Environmental Science, IOP Publishing. Vol. 982, (2022), 012019.

COPYRIGHTS

©2023 The author(s). This is an open access article distributed under the terms of the Creative Commons Attribution (CC BY 4.0), which permits unrestricted use, distribution, and reproduction in any medium, as long as the original authors and source are cited. No permission is required from the authors or the publishers.



Persian Abstract

چکیدہ

هدف این مقاله بررسی عده‌ی رفتار ساختاری تیرهای بتن با مقاومت بالا (HSC) مقاوم سازی شده توسط ورق‌های پلیمر تقویت شده با فیبر کربن (CFRP) پس از ترک خوردنگی است. شش تیر HSC پیش‌ترک شده مجهز به ورق‌های CFRP که دارای تقویت‌کننده‌های یکسان هستند، به علاوه دو تیر دیگر بدون CFRP به عنوان تیرهای کنترل، به صورت عده‌ی با پارگذاری چهار نقطعه‌ای ترازمان شکست با استفاده از نرم افزار Abaqus آزمایش می‌شوند. ورق‌های CFRP در سه طرف تیر در دهانه برشی پس از ترک در زیر ۶۰ درصد بارگذاری متصل می‌شوند. دو فاصله دهانه برشی، دو شبیب صفحات CFRP و تعداد ورق‌ها به عنوان پارامترهایی برای مقایسه با نتایج تحریکی به دست آمده قابلی اتخاذ می‌شوند. نتایج آزمایش با یافته‌های عملی برای کالیبره کردن پارامترهای Abaqus مطابقت دارد. نتایج نشان می‌دهد که مقاوم سازی تیر ترک خورده توسط CFRP تحمل آن را در برابر با اعمال شده با دامنه (۳۶-۱۳) درصد بسته به نسبت دهانه برشی به عمق و آرایش ورق‌های CFRP افزایش می‌دهد. هنگامی که تیر در برش تمایل به شکست دارد، اثر CFRP نسبت به زمانی که تمایل به شکستگی در خمش دارد، بارزتر است. ورق‌های شبیدار نسبت به ورق‌های عمودی موثرتر هستند. علاوه بر این، دو پارامتر اضافی برای روشن شدن اثرات آنها بر رفتار تیرهای مقاوم سازی شده در نظر گرفته شده است: عرض ورق و مقاومت فشاری بتن. تغییر عرض CFRP بر تحمل تاثیر نمی‌گذارد، در حالی که افزایش مقاومت فشاری بتن با پارگذاری تیر را افزایش می‌دهد.



Novel Scheme for Data Hiding in Binary Images using Cover Pattern Histogram

G. Chhajed^a, B. Garg^b

^aDepartment of Computer Engineering, BV(DU)COE, Pune, VPKBIET, Baramati, Pune, Maharashtra, India

^bDepartment of Computer Engineering, BV(DU)COE, Pune, Maharashtra, India

PAPER INFO

Paper history:

Received 13 April 2023

Received in revised form 22 July 2023

Accepted 23 July 2023

Keywords:

Decision Tree

Information Hiding

Encryption

Watermarking

Steganography

Histogram

Pattern Series

A B S T R A C T

In today's digital age, security and safe communication are necessities. Applications frequently transport large amounts of private data as binary images. This research proposes a unique scheme that uses a cover pattern histogram-based decision tree for information concealment and extraction from binary images. This research aims to provide a data-hiding approach with a large capacity for data concealment, possible minor distortion, security, and difficulty discovering hidden data. This method uses high-frequency 3X3 pixel block patterns to obscure data. The two series of pattern's are identified based on sorted block pattern frequency. To construct a decision tree for embedding, these series patterns, key bits, and information bits work together as parameters. Information is encrypted using a secret key to ensure message security before being hidden. A decision tree decides the block suitability and bit embedding with or without flipping at the sender side. A histogram of 3X3 pixel block patterns gets generated for the received image containing concealed data, and two series are recognized similarly to the embedding procedure at the receiver side. A decision tree assesses whether an image block carries an information bit and decides whether the bit is "0" or "1". This decision tree extracts hidden data bits by analyzing series patterns and key bits. The secret key decodes retrieved concealed bits and reveal the original data. According to research, 50-80 % of hidden bits are transmitted without flipping the pixels, automatically reducing visual distortion. This scheme performs better than comparable methods and is applicable in steganography and watermarking.

doi: 10.5829/ije.2023.36.11b.16

1. INTRODUCTION

Digital media has become a daily need due to its widespread. Images, movies, and audio are examples of digital media used for various applications. Transaction receipts, medical imaging, and scanned document images are typically binary. Significant concerns exist regarding the security and confidentiality of these images as data carriers. Cryptography is a mechanism that serves this purpose. The disadvantage of cryptography is that it is easily noticeable that some critical information exists in the carrier medium. Steganography and watermarking, which hide the existence of the information, are preferred solutions to this restriction. A combination of encryption and information hiding [1], i.e., steganography or watermarking, can improve further information security. Information hiding in the binary medium is complex due to using only two colors for painting binary images. For

researchers in this discipline, maintaining visual quality with high-capacity embedding is a significant difficulty. Numerous data hiding techniques are developed to conceal data in black and white images. The techniques used edge pixels [2], boundaries [3], blocks [1-8], transformation functions [9], and run lengths [10] to locate the suitable pixels for hiding data. The steganalysis techniques confirm using the same to locate whether we can hide data at a particular location [11]. We can evaluate the performance of the data hiding technique using the peak signal-to-noise ratio (PSNR), Mean square error (MSE), and distortion matrix. We can also evaluate the data-hiding techniques with other parameters like hiding capacity and security [10]. In the current work, the hiding capacity is directly proportional to visual distortion. So there is scope to identify a better solution. Compared to the currently existing methods, using a decision tree for choosing data-hiding locations is not

*Corresponding Author Email: gjchhajed@gmail.com (G. Chhajed)

recommended. So this research proposed a scheme to determine whether to embed information bits in patterns or to bypass them using a decision tree. We have used the decision trees to retrieve exactly hidden information bits. We encrypted the message before hiding the information to increase the security of confidential data. The paper is organized as: section 1 introduces the proposed work, section 2 addresses related work; section 3 examines the details of the proposed scheme; section 4 discusses the details of block processing and decision tree; section 5 discusses performance analysis; and section 6 conclusion.

2. RELATED WORK

Grayscale and color images are among the main focus of information concealment efforts. There is ample scope to define new methods and design new techniques for grey and color media, as 256 shades for grey and 256 shares for each RGB color are available to maintain visual artifacts. However, binary medium faces a significant challenge due to its limited number of shades. Maintaining high information hiding capacity and less distortion is crucial for binary images. In studied literature, many techniques generally use pixels at edges, image boundaries, image blocks, and transformation functions to hide information in binary images. The extended boundary pairs with 5 pixels, and the center foreground pixel is added or deleted for information hiding [3]. The trading between a modified bit of the host image is applied, and the adjacent bit to the former's new value provides an invisible hiding effect [1]. To check the feasibility of watermark embedding in the discrete cosine transform (DCT) domain is used [5]. The image blocks are examined for smoothness and connection with neighboring pixels to select them for data hiding [6]. A blind data-hiding method preserves the connectivity of pixels in a local neighborhood [7]. A two-layer scheme proposed to authenticate and identify tempering locations [8]. A morphological transform domain is used for location identification for embedding watermarks for authentication purposes [12]. By creating an RL pair, a run-length (RL) histogram is used to improve reversible data concealing [10]. A spatial domain steganographic scheme considering HVS and statistics was proposed [13]. For precise authentication and the verification of modification, a fragile embedding developed [14]. A hybrid authentication scheme utilizes many good DCPLs for embedding and extraction [15]. An arbitrary additive distortion function is proposed, performing near the theoretical bound [2]. A framework is proposed for designing distortion functions [16]. A secret position matrix increases the hiding capacity, which minimizes distortion based on combination theory [17]. Confidential information is secured using a binary weight matrix and keys [11]. Pixels are manipulated in a certain

way to hide a message to minimize distortion to achieve higher security without compromising visual artifacts [18]. A high-capacity scheme with a distortion function to check distortion uses pixels cluster and boundary connectivity to evaluate the flipping distortion [19]. The text data hiding in text documents discussed [20]. In contrast to state-of-the-art techniques, coding tables based on HVS were used to hide information in blocks of binary images [21]. Data identifying the best changeable pixel to hide data using the cover image's edge. Pixels are changed by changing the distance matrix dynamically and computing its changeable score by weighting mechanism [22]. The RDH schemes are applied for authentication and proving ownership of images captured by robots [23]. For binary images, a block classification identifies the complex sections to insert secret data [24]. Hamming codes-based data hiding scheme is proposed, which claims to flip a small number of pixels. An algorithm suggests the flipping of selected particular pixel to minimize visual distortion [25]. An RDH approach decides flipping pattern pairs with opposite center pixels (PPOCPs) in binary image [26]. Shared pixel prediction and halving compression propose a new reversible data hiding scheme in an encrypted binary image [27]. A 3x3 image block used to hide and extract groups of four bits of data using a decision tree technique [28, 29]. A diagonal partition patterns analysis of a 3X3 image block to hide data [30, 31]. Petri net modeling, which offers security and regulates user access to massive data databases to analyze the privacy issue [32].

As per the literature survey analysis, there is always a scope to identify a new approach to hide data in images, creating difficulty for steganalysis. For this, there is a requirement to design a technique that provides a new way for searching locations in the image to hide data so that confidential data will be unnoticeable. The design should also satisfy the characteristics such as imperceptibility, security to data, high data hiding capacity, and minimum visual distortion caused due to data hiding. The best way to make this possible is to utilize existing image patterns to their maximum for hiding data and increase the difficulty level of locating, extracting, and understanding the hidden data.

3. PROPOSED SYSTEM

In the proposed work, a novel approach is identified where frequently occurring block patterns in the image are used to hide data bits. The frequently occurring blocks supports the increased data hiding capacity.

The frequently occurring blocks supports the increased data hiding capacity. The novelty of the proposed method is that it uses a decision tree to decide whether the image block is suitable to carry information bits and whether the bits transmitted to be '0' or '1'. The utilization of decision tree also secures the hidden data as

the key bit pattern is used in making decision. Next, the encryption prior to hiding also secures the from detectability. This method has two phases: building a decision tree and applying it for embedding and extraction. The decision tree constructed using block patterns found in cover images. After creating and sorting the histogram of the pattern's occurrences in the input image, two pattern series, S1, and S2, are identified, thoroughly detailed in section four. The steps for creating and using a decision tree are about similar for the sender and receiver.

Let I represent the image of size $m \times n$, and B represent the image pixel block of size 3×3

$$I = \{B_{00}, B_{01}, \dots, B_{ij}\} \text{ where } i=1 \text{ to } m/3 \text{ and } j=1 \text{ to } n/3$$

Each B_{ij} is represented by 9 bits as it corresponds to a image pixel block of size 3×3

$$B = \{b_0, \dots, b_8\}$$

Let H represent the sorted histogram of distinct block patterns B of the image I in descending order excluding the uniform block patterns, i.e., whole black or white.

$$H = \{h_1, h_2, \dots, h_n\} \text{ where } n \text{ is number of distinct } B \text{ pattern}$$

Let $S1$ represent the set of sorted odd-numbered frequency block patterns in H

$$S1 = \{B(h_1), B(h_3), B(h_5) \dots\}$$

Let $S2$ represent the set of sorted even-numbered frequency block patterns of H

$$S2 = \{B(h_2), B(h_4), B(h_6) \dots\}$$

Let F_S1 represent the set of frequency block patterns with the flipped bit for blocks of series represented by $S1$

$$F_S1 = \{B'(h_1), B'(h_3), B'(h_5) \dots\}$$

Let F_S2 represent the set of frequency block patterns with the flipped bit for blocks of series represented by $S2$

$$F_S2 = \{B'(h_2), B'(h_4), B'(h_6) \dots\}$$

Let B' represents the block after flipping the one bit in it where b' represents the flipped bit in B which results to B'

If flipping the first bit does not result in uniform pattern, then B' represented as

$$B' = \{b'_0, \dots, b'_8\}$$

Else if flipping first bit results in uniform pattern, then B' represented as

$$B' = \{b_0, b'_1, \dots, b_8\}$$

Figure 1 shows the process for building a decision tree. After creating a decision tree for a given input image, it is used to conceal information inside that image.

Figure 2 depicts the suggested workflow at the sender side. The input image divided into blocks of size 3×3 pixels. Then, block by block, the image scanned from left to right. As it scans, a 3×3 block gets represented as a 9-bit pattern. An image-based decision tree receives this block pattern at its root node as input. On the basis of a shared secret key and encrypted data bit, a decision tree provides the decision. The decision tree decides whether or not to embed information bits in the current pattern, along with whether or not the flipping of pixels is required to embed data bits. The hidden data is first encrypted with the help of a shared secret key between the sender and the receiver to increase security.

At the receiver side, the work flow shown in Figure 3. The first thing done to partition the obtained image into 3×3 block segments. The subsequent steps involve processing the block pattern histogram and identifying the series. The image is then scanned left to right, block by block, and each block examined using a decision tree to determine whether it contains concealed data and, if so, whether it is a "0" or "1". The sender-side flow explanation and the flow described here are about

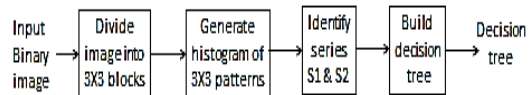


Figure 1. Decision tree building process

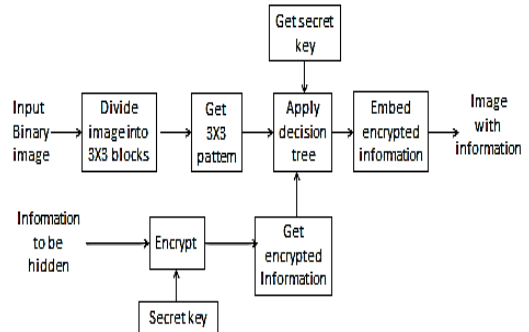


Figure 2. The process on the sender side

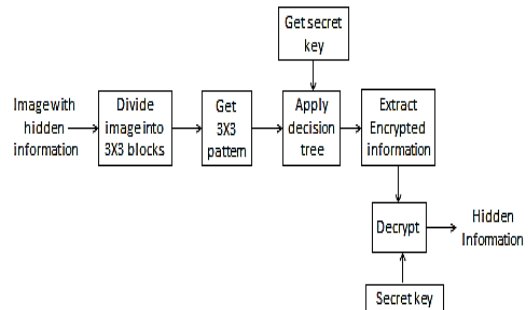
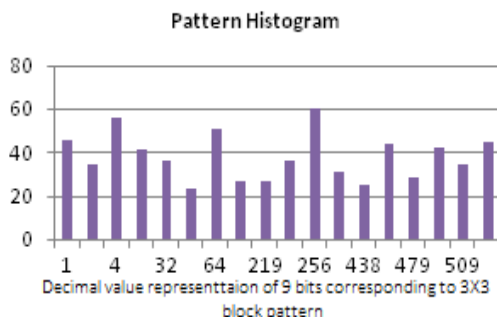


Figure 3. The process on the receiver side

TABLE 1. Sorted patterns as per their decimal values

Sr. no	Decimal value	Pattern	Pattern Frequency
1	0	000000000	748
2	1	000000001	46
3	2	000000010	34
4	4	000000100	56
5	8	000001000	41
6	32	000100000	36
7	48	000110000	23
8	64	001000000	51
9	128	010000000	27
10	219	011011011	27
11	255	011111111	36
12	256	100000000	60
13	383	101111111	31
14	438	110110110	25
15	447	110111111	44
16	479	111011111	28
17	507	111111011	42
18	509	111111101	34
19	510	111111110	45
20	511	111111111	924

**Figure 4.** Histogram of top 20 patterns

similar. The decision tree only considers the current block pattern and the shared secret key bit when determining if the current block pattern includes information and which information bits, '0', or '1', are embedded. Since the extracted data is encrypted, next, it is decrypted by a shared key. This information is the original hidden information sent by the sender.

4. BLOCK PROCESSING AND DECISION TREE

4. 1. Block Processing Technique The image is divided into 3X3 pixel blocks, and these blocks are processed to hide information. The following steps make up the block processing method.

Algorithm : Block Processing

1. Get input image
2. Divide into 3x3 blocks and consider it as 9 bits pattern
3. Generate a histogram of distinct patterns
4. Sort the patterns in descending order according to the frequency of patterns in the image.
5. Ignore the uniform patterns if they are in frequent top patterns
6. Get corresponding patterns to the above-arranged patterns after flipping one pixel. Call it a Flipped pattern.
7. Sum the frequency of sorted and corresponding flipped pattern
8. Again arrange the patterns according to the sorted sum of frequencies in descending order.
9. Select a suitable number of top patterns for embedding.

The patterns with all 9 bits 0's or 1's corresponding to a 3X3 block, i.e., all 9 pixels are black or white pixel, are called uniform pattern. The images generally have more frequency of uniform blocks patterns. However, they are not considered for data hiding because the change in a single pixel is easily noticeable in a block. The top 20 frequently occurring patterns for the test image baboon of size 200 X 200 are listed in descending order. The uniform patterns are at the top, which means they are the frequently occurring patterns in the image. The top 20 most frequent 3X3 block patterns are shown in Table 1, arranged according to their corresponding decimal values in ascending order and is depicted graphically in Figure 4.

4. 2. Series Identification

The following steps explain the steps of series identification.

The outcome of applying the steps mentioned is provided in Table 2, which also includes the top 20 frequently occurring patterns with their frequency as well

Algorithm : Series Identification

1. Get the top frequency patterns
2. Get the patterns after flipping one pixel of above-top frequency patterns called flipped patterns.
3. Get the frequency of flipped patterns.
4. Sum up the frequencies of patterns in step1 and step 3
5. Arrange the patterns in descending order of sum
6. Create two series called S1 and S2
7. S1 has patterns at odd places in ordered patterns
8. S2 has patterns at even places in ordered patterns
9. Create two more series, flipped S1 and flipped S2.
10. Flipped S1 has flipped patterns corresponding to patterns in S1
11. Flipped S2 has flipped patterns corresponding to patterns in S2

as corresponding patterns with their initial bit flipped, i.e. changing '1' to '0' and '0' to '1'. Although uniform patterns inverted pattern's have high frequencies, they also get ignored for conveying data bits, similar to how uniform patterns are. As opposed to typical pattern's where the first bit is flipped, in such case, the second bit flipped. Pattern "10000000" has the highest frequency, as indicated in Table 2, but it is actually the inverted version of pattern "00000000". The inverted pattern "10000000" is likewise not used since uniform patterns discarded. So for this case , the second bit is flipped as "11000000". The number of information bits to be hidden dictates how many top-frequency pattern selections should be made in a series. This decision impacts the hiding capacity. The capacity to hide data would increase when more number of top-frequency patterns in a series were taken into consideration.

For the experiment, the top eight frequencies considered discarding uniform patterns. Tables 3 and 4 display the pattern analysis on the transmitter and receiver side respectively. It is observed that the sum of

frequencies shown in the sum column is equal. The correct encrypted message can be decoded by adding the frequencies of the pattern and the reversed pattern at the receiver side , which is believed to be used at the sender side.

4. 3. Building Decision Tree The key component of this technique is the building of a decision tree. Two decision trees are constructed, one of which is, for embedding and the other for extraction.The sender-side decision tree uses the series pattern at the first level, a key bit at the second level, and a message bit at the third level. The tree finally decides whether the bit is to be embedded in the current testing block and as well with or without flipping.

4. 3. 1. Building Decision Tree At Sender Side

The decision tree at sender side is built using following steps described using the decision table in Table 5 and the decision tree in Figure 5.

TABLE 2. Patterns in series S1 and S2

Pattern	Pattern Frequency	Flipped Pattern	Flipped Pattern Frequency	Sum	Series
100000000	60	110000000	17	77	s1
001000000	51	101000000	14	65	s2
000000100	56	100000100	6	62	s1
000100000	36	100100000	21	57	s2
000000001	46	100000001	10	56	s1
011111111	36	001111111	11	47	s2
111111110	45	011111110	2	47	s1
111111101	34	011111101	11	45	s2
110111111	44	010111111	0	44	s1
010000000	27	110000000	17	44	s2
111111011	42	011111011	0	42	s1
101111111	31	001111111	11	42	s2
111011111	28	011011111	14	42	s1
011011011	27	111011011	15	42	s2
000001000	41	100001000	0	41	s1
000000010	34	100000010	6	40	s2
110110110	25	010110110	1	26	s1
000110000	23	100110000	3	26	s2

Algorithm : Building Decision Tree At Sender Side

1. Consider a 9-bit pattern at the root.
2. Patterns are categorized into Uniform patterns, S1, S2,flipped S1 , flipped S2 and other patterns at next level
3. Shared key bits are considered at the next level with values 0 and 1.

4. Information bits are considered at the next lower level and have two values, 0 and 1
5. The next decision level is whether to embed without flipping or after flipping.
6. The decision is at the leaf level, which signifies whether to discard the pattern for embedding or embed bit 0 or embed bit 1
7. The decision is based on a combination of the type of pattern, key bit, and Information bit.

4. 3. 2. Building Decision Tree At Receiver Side

The receiver-side decision tree uses a series pattern at the first level and the secret key bit at the second level. This tree determines whether the current block has a hidden

bit and, if so, whether it is a '0' or a '1'. The steps for building a receiver-side decision tree are explained below. The decision tree in Figure 6 and decision Table 6 are used to describe these steps.

TABLE 3. Selected series for embedding

Pattern	Pattern Frequency	Flipped Pattern	Flipped Pattern Frequency	Sum	Series
100000000	60	110000000	17	77	s1
001000000	51	101000000	14	65	s2
000000100	56	100000100	6	62	s1
000000001	46	100000001	10	56	s2
110111111	44	010111111	9	53	s1
000001000	41	100001000	7	48	s2
111111011	42	011111011	5	47	s1
111111110	45	011111110	2	47	s2

TABLE 4. Series for extraction based on sample Table 3

Pattern	Pattern Frequency	Flipped Pattern	Flipped Pattern Frequency	Sum	Series
100000000	52	110000000	25	77	s1
001000000	49	101000000	16	65	s2
000000100	47	100000100	15	62	s1
000000001	43	100000001	13	56	s2
110111111	44	010111111	9	53	s1
000001000	41	100001000	7	48	s2
111111011	42	011111011	5	47	s1
111111110	45	011111110	2	47	s2

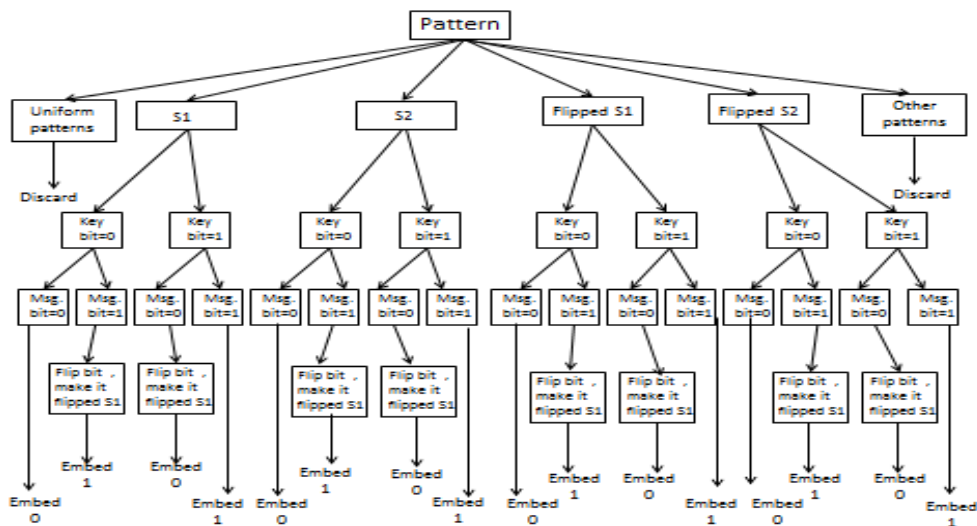


Figure 5. Decision tree for embedding at sender side

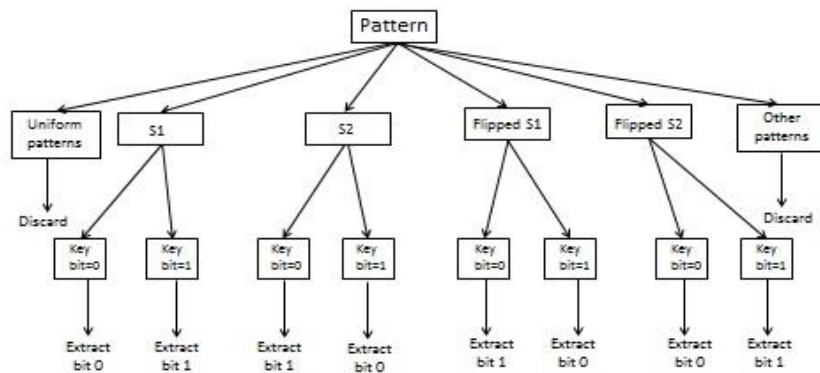


Figure 6. Decision tree for extraction at receiver side

TABLE 5. Decision table for embedding

Series	Key bit	Encrypted information bit	Decision (Embedding of encrypted information bit)
S1	1	1	Embed without flipping
S1	0	0	Embed without flipping
S1	0	1	Flip bit in S1 and make it Flipped S1
S1	1	0	Flip bit in S1 and make it Flipped S1
S2	0	1	Embed without flipping
S2	1	0	Embed without flipping
S2	0	0	Flip bit in S2 and make it Flipped S2
S2	1	1	Flip bit in S2 and make it Flipped S2
Flipped S1	1	0	Embed without flipping
Flipped S1	0	1	Embed without flipping
Flipped S1	0	0	Flip bit in S1 and make it Flipped S1
Flipped S1	1	1	Flip bit in S1 and make it Flipped S1
Flipped S2	0	0	Embed without flipping
Flipped S2	1	1	Embed without flipping
Flipped S2	0	1	Flip bit in S2 and make it Flipped S2
Flipped S2	1	0	Flip bit in S2 and make it Flipped S2

Algorithm : Building Decision Tree At Receiver Side

1. The pattern is at the root.
2. Patterns are categorized into Uniform patterns, S1, S2, flipped S1, flipped S2, and other patterns
3. The shared key is at the next level and has two values, 0 and 1, as it is in binary bits.
4. The decision is at the leaf level, which signifies whether to skip the pattern for the extraction or extract information bit 0 or 1
5. The decision is based on a combination of the type of pattern and key bit.

Algorithm : Embedding Using Decision Tree

1. Scan the image block by block of size 3 X 3 pixels
2. Get the block pattern of size 9 bits
3. Check the category of pattern from the decision tree
4. Get the Key bit
5. Move to the branch with the combination of pattern category and key bit
6. Get the encrypted Information bit
7. Move to the branch with the combination of pattern category, key bit, and information bit
8. Get the decision if reaching to reach a leaf node or perform the action of flipping bit, making flipped pattern, and then get the decision reaching to a leaf node.

4.4. Embedding Using Decision Tree

Following are the steps for embedding in the binary image using a decision tree:

Figure 7 pictorially represents the embedding of encrypted information 11010111. The sequence of

patterns belonging to series is shown cells , and the key is 11011000 in Figure 7(a). The square inside the cell represents flipping the pattern to hide data bit and making it flipped pattern is shown in Figure 7(b). In this example, S2 and S1 are converted to flipped S2 and flipped S1, respectively.

4.5. Extraction Using Decision Tree

Following are the steps for extracting information using decision tree

Algorithm : Extraction Using Decision Tree

1. Scan the image block by block of size 3 x 3
2. Get the pattern of the block of size 9 bits
3. Check the category of pattern from the decision tree
4. Get the Key bit
5. Move to the branch with the combination of pattern category and key bit
6. Get the decision reaching to leaf node whether to discard or extract 0/1 bit

Figure 8 pictorially represents the extraction of encrypted information. The sequence of patterns in cells and the key is 11011000, is shown in Figure 8 square

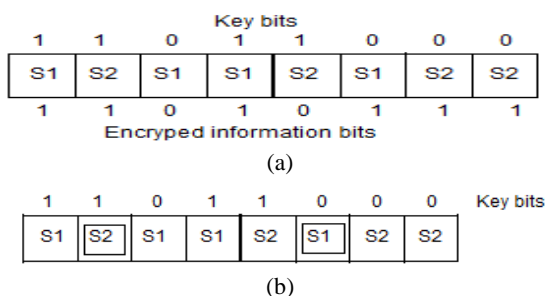


Figure 7. Embedding example (a) before embedding (b) after embedding

TABLE 6. Decision table for extraction

Series	Key bit	Decision (Extraction of encrypted information bit)
S1	1	Extract 1
S1	0	Extract 0
Flipped S1	1	Extract 0
Flipped S1	0	Extract 1
S2	0	Extract 1
S2	1	Extract 0
Flipped S2	0	Extract 0
Flipped S2	1	Extract 1

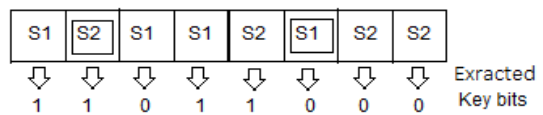


Figure 8. Extraction example

inside the cell represents flipped patterns. Applying decision tree the bit sequence 11010111 will be extracted.

5. PERFORMANCE ANALYSIS

For an experimentation, a set of 1431 binary images used. Various sizes and the variety of messages and the key combinations used to test the system. The sample set of images with the message "success" with the key "abcabca" in binary form is embedded in different images of different sizes. The sample images with some standard images are presented below with a total of 64 encrypted bits embedded in them where the first 8 bits are encrypted message length and later 56 bits represent an encrypted message. Figure 9 represents images before hiding the data. Figure 10 shows images after embedding 64-bit encrypted data using 2 patterns and 4 patterns in each series respectively. Figure 11 represents the eye part of the baboon image in original and zoomed size before and after embedding data.

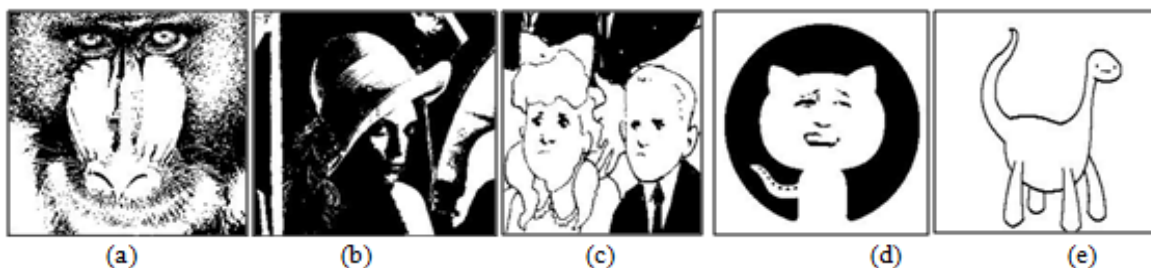


Figure 9. Original images before information hiding

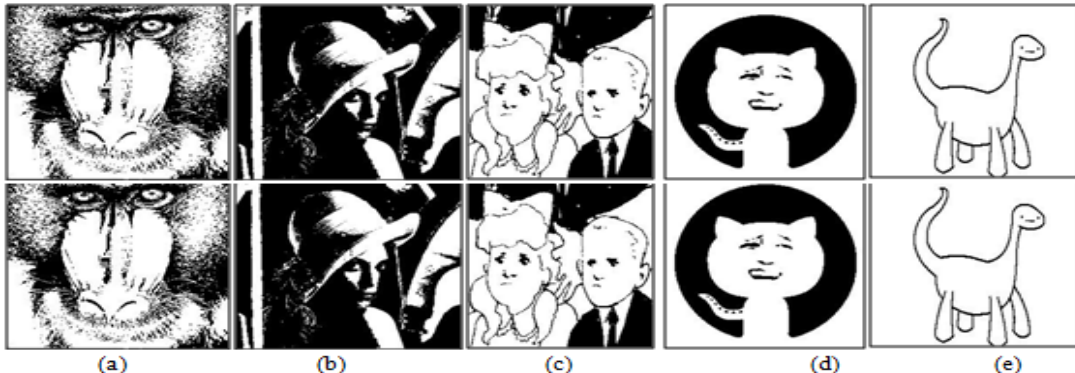


Figure 10. Images after hiding 64-bit data with series S1 and S2 having 2(top) and 4(bottom) patterns respectively a)Baboon b) Lena c) Cartoon1 d) Cat e) Dinosaur f) Hero



Figure 11. Eye part of baboon image using 4 patterns in series (a) before hiding data (b) zoomed part before hiding (c) after hiding data (d) zoomed part after hiding data

With the experimentation, it is noticed that the visual differences between the original cover images and the cover images with the hidden data are hardly detected with the naked eye. The Mean Square Error (MSE) and Peak Signal to Noise Ratio (PSNR) are two common quality measurements to measure the difference between the cover image and the image with hidden data.

As shown in Tables 7, 8 and Figure 12, this technique performs well. For the above cases, the number of pixels flipped for series considering two patterns and four patterns are analyzed. As per observations, 50-80 % of total number of bits to be hidden is possible without changing the pixel colour. The performance of this technique is dependent on the arrangement of pixels in the cover image and key bits. If more patterns are considered in series, then there will be availability of more patterns for embedding, and distortion will reduce.

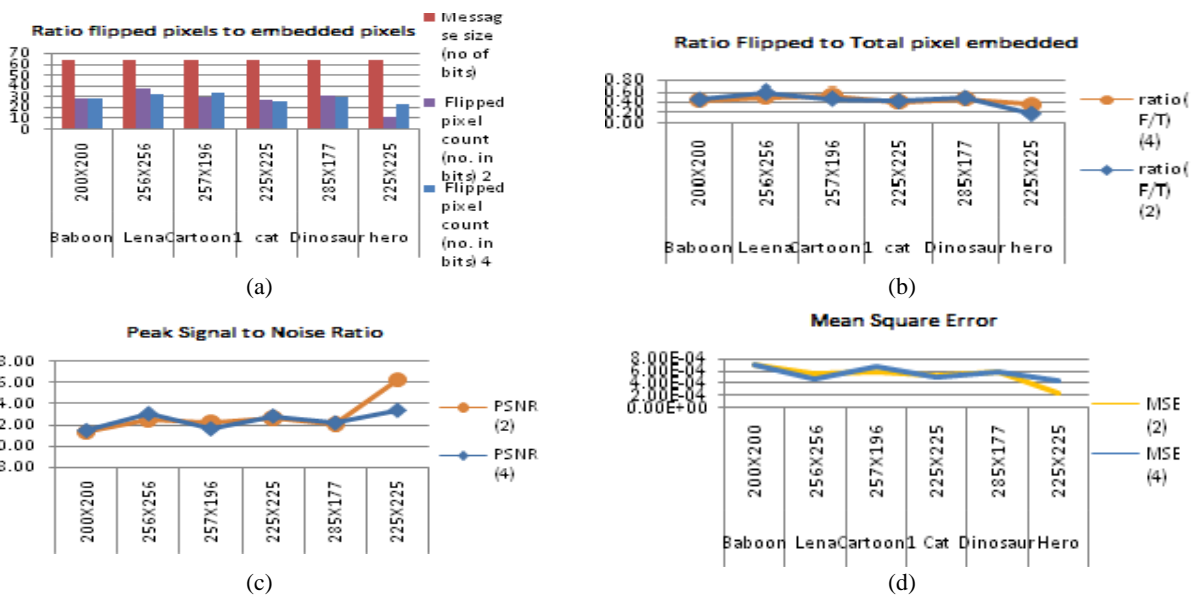
This method is compared with the method discussed in [6], where a lookup table of flip-score for 69 patterns is presented. The flip scores of the pattern decide whether the block is embeddable or not. The flip-scores greater than or equal to 0.125 were selected from literature [6] for data hiding from the range of calculated scores 0, 0.01, 0.125, 0.25, 0.375, 0.625 considering all 512 patterns for 3X3 block. Similarly, patterns were considered for hiding data in [31]. The other schemes based on special pixel selection [13] and edge based grid pattern [32] are also compared, and it is identified that this method performs better, providing more data hiding capacity. Table 9 and Figure 13 shows the comparative analysis, where our method using 2 and 4 patterns in series S1 and S2 is compared with other methods using block based technique, edge grid based and special selection of pixel based on texture of the image. The data hiding capacity

TABLE 7. MSE and PSNR for series having 2 and 4 patterns for Figures 9 and 10

Image	Image size	Flipped pixel count (no. in bits) 2 patterns in each series	Flipped pixel count (no. in bits) 4 patterns in each series	MSE (2) in 10^{-4}	PSNR (2)	MSE (4) in 10^{-4}	PSNR (4)
Baboon	200X200	29	28	7.25	31.40	7.00	31.55
Lena	256X256	37	32	5.65	32.48	4.88	33.11
Cartoon1	257X196	30	34	5.96	32.25	6.75	31.71
Cat	225X225	27	26	5.33	32.73	5.14	32.89
Dinosaur	285X177	31	30	6.15	32.11	5.95	32.26
Hero	225X225	12	23	2.37	36.25	4.54	33.43

TABLE 8. The ratio of flipped pixel to message length for Figures 9 and 10

Image	Image size	Image DPI	Msg. size (no of bits)	Flipped pixel count (no. in bits) 2 patterns in each series	Flipped pixel count (no. in bits) 4 patterns in each series	Ratio (F/T) (2)	Ratio (F/T) (4)
Baboon	200X200	96	64	29	28	0.45	0.44
Lena	256X256	96	64	37	32	0.58	0.50
Cartoon1	257X196	96	64	30	34	0.47	0.53
Cat	225X225	96	64	27	26	0.42	0.41
Dinosaur	285X177	96	64	31	30	0.48	0.47
Hero	225X225	96	64	12	23	0.19	0.36

**Figure 12.** Performance analysis plots with 2 and 4 patterns in series S1 & S2 respectively (a) Message size Vs. flipped pixels (b) ratio of flipped pixels to no. of bits in message (c) MSE (d) PSNR**TABLE 9.** Comparative Analysis

Method	Image	Image size	Flipped pixel count	Ratio (F/T)	MSE in 10^{-4}	PSNR
(patterns 2) Ours			29	0.45	7.25	31.40
(patterns 4) Ours			28	0.44	7.00	31.55
[4]			34	0.53	8.50	30.71
[9]	Baboon	200X200	33	0.52	8.25	30.84
[31]			31	0.48	7.75	31.11
[32]			35	0.55	8.75	30.58
(patterns 2) Ours			37	0.58	5.65	32.48
(patterns 4) Ours			32	0.50	4.88	33.11
[4]			37	0.58	5.65	32.48
[9]	Lena	256X256	27	0.42	4.12	33.85
[31]			30	0.47	4.58	33.39
[32]			31	0.48	4.73	33.25
(patterns 2) Ours			30	0.47	5.96	32.25
(patterns 4) Ours			34	0.53	6.75	31.71

[4]			31	0.48	6.15	32.11
[9]	Cartoon1	257X196	33	0.52	6.55	31.84
[31]			30	0.47	5.96	32.25
[32]			37	0.58	7.35	31.34
(patterns 2) Ours			27	0.42	5.33	32.73
(patterns 4) Ours			26	0.41	5.14	32.89
[4]			33	0.52	6.52	31.86
[9]	Cat	225X225	31	0.48	6.12	32.13
[31]			30	0.47	5.93	32.27
[32]			34	0.53	6.72	31.73

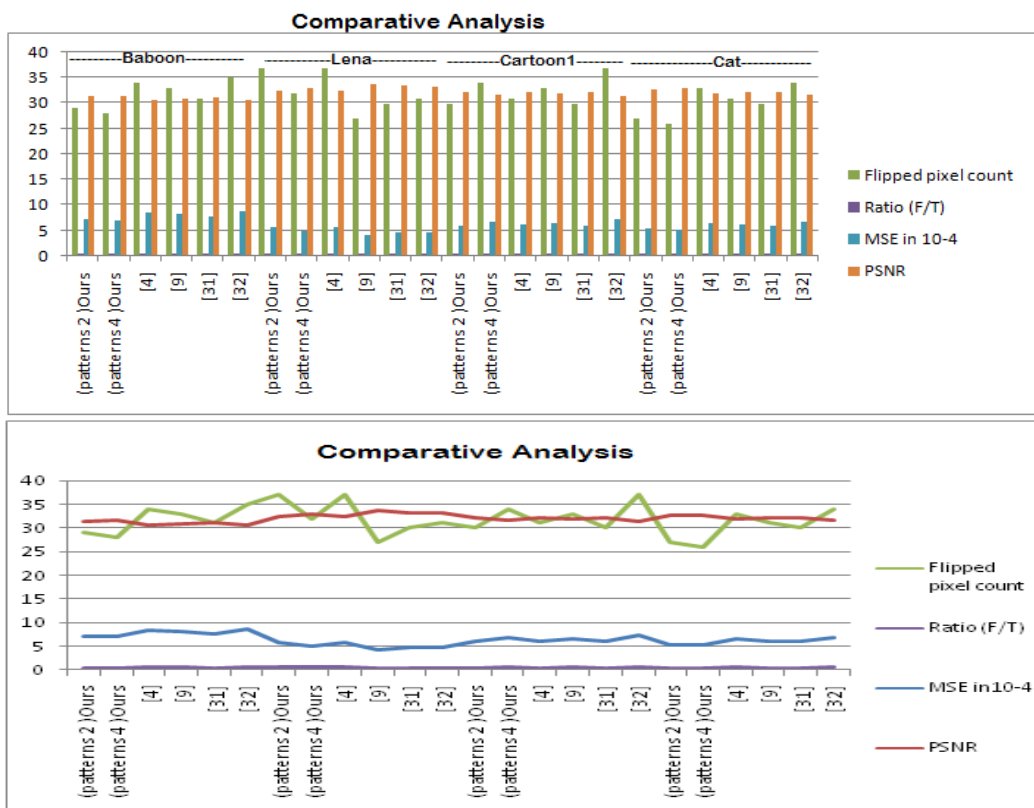


Figure 13. Comparative analysis plots with 2 and 4 patterns in series S1 & S2 respectively (a) Message size Vs. flipped pixels (b) ratio of flipped pixels to no. of bits in message (c) MSE (d) PSNR

varies depending on patterns frequency, arrangement of patterns considered in series S1 and S2. The distortion caused due to flipping pixels for data hiding depends on the sequence of series pattern occurrence in the image, secret key bit, and encrypted information bit. More the match, the less the distortion. So this technique performs well for providing good data hiding capacity for images providing more number of non-uniform blocks. For the test images, the flipped pixel count is 20-50 % of the number of bits to be hidden; hence visual distortion is also comparable to other techniques.

6. CONCLUSION

In this paper, a novel information-hiding method in the binary image is proposed. The decision tree is used to decide whether the pattern is suitable for information hiding or not, as well as which bit, 0 or 1, to be embedded. The decision tree uses three parameters for making any decision. First, it requires the series of 3X3 block patterns represented in 9 bits of the input image, the second information bit to be embedded, and third, the secret key bit. Once the decision tree is built for the input image at

the sender side, it can be applied for any information to be hidden. To enhance the security of information, it is encrypted before embedding. This method utilizes cover image patterns as much as possible and hence minimizes visual distortion. A similar decision tree is built and applied at the receiver side, which requires two parameters, the series of 3X3 block patterns represented in 9 bits of an input image with hidden information, i.e., watermarked or stego image, and the secret key bit. Decryption is applied to extract information to get the original information. This method is applicable in applications that use a binary medium for secret communication in sensitive domains like military, defense, and medical imaging. In experiments, two and four patterns are considered in series. The results show that 50-80% of pixels are utilized in their original form to hide sample data and images. From this observation, it's concluded that 50-80% of data bits are hidden without flipping pixels, which means distortion is less. It is also concluded that the need to flip pixels to hide the data bit depends on the pattern of the input image as frequencies of the 9-bit pattern are based on image 3X3 pixel block pattern occurrences second, the secret key bit sequence, and information bit sequences. Best the match less will be distortion. The hiding capacity depends on a number of patterns considered in series and their occurrences. This will prove to be an efficient information-hiding method for binary images in which the original image is not required for extracting information. Next, it will not be possible to identify the block that is carrying which bit without knowing the secret key. Next, the encryption applied to hidden data further enhances the security of hidden information. In future perspective, this method is applicable for Steganography and watermarking applications. To further reduce the distortion factor of the proposed work, pixel to be flipped for data hiding can be selected by checking the surrounding pixels in a block. If this is incorporated, than accordingly, the receiver side will also need to identify the strategy to locate the block carrying the data bit.

7. REFERENCES

1. Tseng, Y.-C. and Pan, H.-K., "Data hiding in 2-color images", *IEEE Transactions on Computers*, Vol. 51, No. 7, (2002), 873-880. doi: 10.1109/TC.2002.1017706.
2. Filler, T., Judas, J. and Fridrich, J., "Minimizing additive distortion in steganography using syndrome-trellis codes", *IEEE Transactions on Information Forensics and Security*, Vol. 6, No. 3, (2011), 920-935. doi: 10.1109/TIFS.2011.2134094.
3. Mei, Q.G., Wong, E.K. and Memon, N.D., "Data hiding in binary text documents", in Security and watermarking of multimedia contents III, SPIE. Vol. 4314, (2001), 369-375.
4. Chhajed, G.J., Inamdar, V. and Attar, V., "Steganography in black and white picture images", in 2008 Congress on Image and Signal Processing, IEEE. Vol. 2, (2008), 141-144.
5. Deshmukh, K.V. and Chhajed, G.J., "A steganographic method for data hiding in binary image using edge based grids", *International Journal of Computer Applications in Technology*, Vol. 5, No. 4, (2014), 1369-1374.
6. Lu, H., Shi, X., Shi, Y.Q., Kot, A.C. and Chen, L., "Watermark embedding in dc components of dct for binary images", in 2002 IEEE Workshop on Multimedia Signal Processing., IEEE. (2002), 300-303.
7. Wu, M. and Liu, B., "Data hiding in binary image for authentication and annotation", *IEEE Transactions on Multimedia*, Vol. 6, No. 4, (2004), 528-538. doi: 10.1109/TMM.2004.830814.
8. Yang, H. and Kot, A.C., "Pattern-based data hiding for binary image authentication by connectivity-preserving", *IEEE Transactions on Multimedia*, Vol. 9, No. 3, (2007), 475-486. doi: 10.1109/TMM.2006.887990.
9. Yang, H., Kot, A.C. and Rahardja, S., "Orthogonal data embedding for binary images in morphological transform domain-a high-capacity approach", *IEEE Transactions on Multimedia*, Vol. 10, No. 3, (2008), 339-351. doi: 10.1109/TMM.2008.917404.
10. Tseng, Y.-C., Chen, Y.-Y. and Pan, H.-K., "A secure data hiding scheme for binary images", *IEEE Transactions on Communications*, Vol. 50, No. 8, (2002), 1227-1231. doi: 10.1109/ICWAPR.2007.4420668.
11. Yang, H. and Kot, A.C., "Binary image authentication with tampering localization by embedding cryptographic signature and block identifier", *IEEE Signal Processing Letters*, Vol. 13, No. 12, (2006), 741-744. doi: 10.1109/LSP.2006.879829.
12. Xuan, G., Shi, Y.Q., Chai, P., Tong, X., Teng, J. and Li, J., "Reversible binary image data hiding by run-length histogram modification", in 2008 19th International Conference on Pattern Recognition, IEEE. (2008), 1-4.
13. Feng, B., Lu, W. and Sun, W., "Secure binary image steganography based on minimizing the distortion on the texture", *IEEE Transactions on Information Forensics and Security*, Vol. 10, No. 2, (2014), 243-255. doi: 10.1109/TIFS.2014.2368364.
14. Cao, H. and Kot, A.C., "On establishing edge adaptive grid for bilevel image data hiding", *IEEE Transactions on Information Forensics and Security*, Vol. 8, No. 9, (2013), 1508-1518. doi: 10.1109/TIFS.2013.2274041.
15. Guo, M. and Zhang, H., "High capacity data hiding for binary image authentication", in 2010 20th International Conference on Pattern Recognition, IEEE. (2010), 1441-1444.
16. Pevný, T., Filler, T. and Bas, P., "Using high-dimensional image models to perform highly undetectable steganography", in Information Hiding: 12th International Conference, IH 2010, Calgary, AB, Canada, June 28-30, 2010, Revised Selected Papers 12, Springer. (2010), 161-177.
17. Wu, N.-I. and Hwang, M.-S., "Development of a data hiding scheme based on combination theory for lowering the visual noise in binary images", *Displays*, Vol. 49, (2017), 116-123. doi: <https://doi.org/10.1016/j.displa.2017.07.009>
18. Mol, M.H. and Reji, P., "A secure binary data hiding and comparison technique", *International Journal of Scientific Engineering and Research*, Vol. 7, No. 7, (2016), 810.
19. Feng, B., Lu, W. and Sun, W., "High capacity data hiding scheme for binary images based on minimizing flipping distortion", in Digital-Forensics and Watermarking: 12th International Workshop, IWDW 2013, Auckland, New Zealand, October 1-4, 2013. Revised Selected Papers 12, Springer. (2014), 514-528.
20. Bhattacharyya, D., Haveliya, A. and Kim, T.-h., "Secure data hiding in binary text document for authentication", *Applied Mathematics*, Vol. 8, No. 1L, (2014), 371-378. doi: 10.12785/amis/081L47.
21. Ding, W. and Wang, Y., "Data hiding in binary image with high payload", *Arabian Journal for Science and Engineering*, Vol.

- 43, No., (2018), 7737-7745. doi. <https://doi.org/10.1007/s13369-018-3130-5>
22. Liu, T.-H. and Chang, L.-W., "An adaptive data hiding technique for binary images", in Proceedings of the 17th International Conference on Pattern Recognition, 2004. ICPR 2004., IEEE. Vol. 4, (2004), 831-833.
23. Manikandan, V. and Masilamani, V., "Reversible data hiding scheme during encryption using machine learning", *Procedia Computer Science*, Vol. 133, (2018), 348-356. doi. <https://doi.org/10.1016/j.procs.2018.07.043>
24. Nguyen, T.-S., Chang, C.-C. and Hsueh, H.-S., "High capacity data hiding for binary image based on block classification", *Multimedia Tools and Applications*, Vol. 75, (2016), 8513-8526. doi. <https://doi.org/10.1007/s11042-015-2768-1>
25. Lee, Y., Kim, H. and Park, Y., "A new data hiding scheme for binary image authentication with small image distortion", *Information Sciences*, Vol. 179, No. 22, (2009), 3866-3884. doi. <https://doi.org/10.1016/j.ins.2009.07.014>
26. Yin, X., Lu, W., Zhang, J., Chen, J. and Liu, W., "Reversible data hiding in binary images by flipping pattern pair with opposite center pixel", *Journal of Visual Communication and Image Representation*, Vol. 70, (2020), 102816. doi. <https://doi.org/10.1016/j.jvcir.2020.102816>
27. Li, F., Zhang, L. and Wei, W., "Reversible data hiding in encrypted binary image with shared pixel prediction and halving compression", *EURASIP Journal on Image and Video Processing*, Vol. 2020, (2020), 1-21. doi. <https://doi.org/10.1186/s13640-020-00522-6>
28. Chhajed, G.J. and Garg, B.R., Applying decision tree for hiding data in binary images for secure and secret information flow, in Cybersecurity measures for e-government frameworks. 2022, IGI Global.175-186.
29. Chhajed, G. and Garg, B., "Data hiding in binary images for secret and secure communication using decision tree", in 4th EAI International Conference on Big Data Innovation for Sustainable Cognitive Computing: BDCC 2021, Springer. (2022), 69-84.
30. Chhajed, G. and Garg, B., "Information security by hiding data in binary images based on block-diagonal partition pattern", in 2022 IEEE International Conference on Blockchain and Distributed Systems Security (ICBDS), IEEE. (2022), 1-6.
31. J Chhajed, G. and Garg, B.R., "Hiding data in binary images using block-diagonal partition pattern", *International Journal of Computing and Digital Systems*, (2023). doi. <http://dx.doi.org/10.12785/ijcds/130176>
32. Asadi Saeed Abad, F. and Hamidi, H., "An architecture for security and protection of big data", *International Journal of Engineering, Transactions A: Basics*, Vol. 30, No. 10, (2017), 1479-1486.

COPYRIGHTS

©2023 The author(s). This is an open access article distributed under the terms of the Creative Commons Attribution (CC BY 4.0), which permits unrestricted use, distribution, and reproduction in any medium, as long as the original authors and source are cited. No permission is required from the authors or the publishers.



Persian Abstract

چکیده

در عصر دیجیتال امروز، امنیت و ارتباطات ایمن از ضروریات است. برنامه ها اغلب مقادیر زیادی از داده های خصوصی را به عنوان تصاویر باینری منتقل می کنند. این تحقیق یک طرح منحصر به فرد را پیشنهاد می کند که از درخت تصمیم گیری مبتنی بر هیستوگرام الگوی پوشش برای پنهان کردن اطلاعات و استخراج از تصاویر باینری استفاده می کند. هدف این تحقیق ارائه یک رویکرد پنهان کردن داده با ظرفیت بزرگ برای پنهان کردن داده ها، اعوجاج جزئی احتمالی، امنیت و مشکل در کشف داده های پنهان است. این روش از الگوهای بلوك پیکسلی 3×3 با فرکанс بالا برای مبهم کردن داده ها استفاده می کند. دو سری از الگوها بر اساس فرکانس الگوی بلوك مرتب شده شناسایی می شوند. برای ساختن یک درخت تصمیم برای جاسازی، این الگوهای سری، بیت های کلیدی و بیت های اطلاعاتی با هم به عنوان پارامتر کار می کنند. اطلاعات با استفاده از یک کلید مخفی برای اطمینان از امنیت پیام قبل از پنهان شدن داده های پنهان تولید می شوند. درخت تصمیم مناسب بودن بلوك و تعییه بیت را با یابدون چرخش در سمت فرستنده تعیین می کند. یک هیستوگرام از الگوهای بلوك پیکسل X33 برای تصویر دریافتی حاوی تولید می شود و دو سری مشابه با روش جاسازی در سمت گیرنده شناسایی می شوند. درخت تصمیم ارزیابی می کند که آیا یک بلوك تصویر حاوی بیت اطلاعات است و تصمیم می گیرد که آیا بیت "0" یا "1" باشد. این درخت تصمیم، بیت های داده پنهان را با تجزیه و تحلیل الگوهای سری و بیت های کلید استخراج می کند. کلید مخفی بیت های پنهان بازیابی شده را رمزگشایی می کند و داده های اصلی را آشکار می کند. بر اساس تحقیقات، 50 تا 80 درصد از بیت های پنهان بدون برگرداندن پیکسل ها منتقل می شوند و به طور خودکار اعوجاج بصری را کاهش می دهند. این طرح نسبت به روش های مشابه بهتر عمل می کند و در استگانوگرافی و واترمارکینگ قابل استفاده است.

AIMS AND SCOPE

The objective of the International Journal of Engineering is to provide a forum for communication of information among the world's scientific and technological community and Iranian scientists and engineers. This journal intends to be of interest and utility to researchers and practitioners in the academic, industrial and governmental sectors. All original research contributions of significant value focused on basics, applications and aspects areas of engineering discipline are welcome.

This journal is published in three quarterly transactions: Transactions A (Basics) deal with the engineering fundamentals, Transactions B (Applications) are concerned with the application of the engineering knowledge in the daily life of the human being and Transactions C (Aspects) - starting from January 2012 - emphasize on the main engineering aspects whose elaboration can yield knowledge and expertise that can equally serve all branches of engineering discipline.

This journal will publish authoritative papers on theoretical and experimental researches and advanced applications embodying the results of extensive field, plant, laboratory or theoretical investigation or new interpretations of existing problems. It may also feature - when appropriate - research notes, technical notes, state-of-the-art survey type papers, short communications, letters to the editor, meeting schedules and conference announcements. The language of publication is English. Each paper should contain an abstract both in English and in Persian. However, for the authors who are not familiar with Persian, the publisher will prepare the latter. The abstracts should not exceed 250 words.

All manuscripts will be peer-reviewed by qualified reviewers. The material should be presented clearly and concisely:

- *Full papers* must be based on completed original works of significant novelty. The papers are not strictly limited in length. However, lengthy contributions may be delayed due to limited space. It is advised to keep papers limited to 7500 words.
- *Research notes* are considered as short items that include theoretical or experimental results of immediate current interest.
- *Technical notes* are also considered as short items of enough technical acceptability with more rapid publication appeal. The length of a research or technical note is recommended not to exceed 2500 words or 4 journal pages (including figures and tables).

Review papers are only considered from highly qualified well-known authors generally assigned by the editorial board or editor in chief. Short communications and letters to the editor should contain a text of about 1000 words and whatever figures and tables that may be required to support the text. They include discussion of full papers and short items and should contribute to the original article by providing confirmation or additional interpretation. Discussion of papers will be referred to author(s) for reply and will concurrently be published with reply of author(s).

INSTRUCTIONS FOR AUTHORS

Submission of a manuscript represents that it has neither been published nor submitted for publication elsewhere and is result of research carried out by author(s). Presentation in a conference and appearance in a symposium proceeding is not considered prior publication.

Authors are required to include a list describing all the symbols and abbreviations in the paper. Use of the international system of measurement units is mandatory.

- On-line submission of manuscripts results in faster publication process and is recommended. Instructions are given in the IJE web sites: www.ije.ir-www.ijeir.info
- Hardcopy submissions must include MS Word and jpg files.
- Manuscripts should be typewritten on one side of A4 paper, double-spaced, with adequate margins.
- References should be numbered in brackets and appear in sequence through the text. List of references should be given at the end of the paper.
- Figure captions are to be indicated under the illustrations. They should sufficiently explain the figures.
- Illustrations should appear in their appropriate places in the text.
- Tables and diagrams should be submitted in a form suitable for reproduction.
- Photographs should be of high quality saved as jpg files.
- Tables, Illustrations, Figures and Diagrams will be normally printed in single column width (8cm). Exceptionally large ones may be printed across two columns (17cm).

PAGE CHARGES AND REPRINTS

The papers are strictly limited in length, maximum 8 journal pages (including figures and tables). For the additional to 8 journal pages, there will be page charges. It is advised to keep papers limited to 3500 words.

Page Charges for Papers More Than 8 Pages (Including Abstract)

For International Author ***	\$55 / per page
For Local Author	100,000 Toman / per page

AUTHOR CHECKLIST

- Author(s), bio-data including affiliation(s) and mail and e-mail addresses).
- Manuscript including abstracts, key words, illustrations, tables, figures with figure captions and list of references.
- MS Word files of the paper.



Scopus®

